

Ahmed F. Zobaa

Shady H. E. Abdel Aleem *Editors*

Modernization of Electric Power Systems

Energy Efficiency and Power Quality

 Springer

Modernization of Electric Power Systems

Ahmed F. Zobaa • Shady H. E. Abdel Aleem
Editors


Modernization of Electric Power Systems

Energy Efficiency and Power Quality

 Springer

Editors

Ahmed F. Zobaa 
Electrical and Power Engineering
Brunel University, Uxbridge
Uxbridge, UK

Shady H. E. Abdel Aleem 
Electrical Engineering and Electronics
Valley Higher Institute of Engineering and
Technology
Qalubia, Egypt

ISBN 978-3-031-18995-1 ISBN 978-3-031-18996-8 (eBook)
<https://doi.org/10.1007/978-3-031-18996-8>

© The Editor(s) (if applicable) and The Author(s), under exclusive license to Springer Nature Switzerland AG 2023

This work is subject to copyright. All rights are solely and exclusively licensed by the Publisher, whether the whole or part of the material is concerned, specifically the rights of translation, reprinting, reuse of illustrations, recitation, broadcasting, reproduction on microfilms or in any other physical way, and transmission or information storage and retrieval, electronic adaptation, computer software, or by similar or dissimilar methodology now known or hereafter developed.

The use of general descriptive names, registered names, trademarks, service marks, etc. in this publication does not imply, even in the absence of a specific statement, that such names are exempt from the relevant protective laws and regulations and therefore free for general use.

The publisher, the authors, and the editors are safe to assume that the advice and information in this book are believed to be true and accurate at the date of publication. Neither the publisher nor the authors or the editors give a warranty, expressed or implied, with respect to the material contained herein or for any errors or omissions that may have been made. The publisher remains neutral with regard to jurisdictional claims in published maps and institutional affiliations.

This Springer imprint is published by the registered company Springer Nature Switzerland AG
The registered company address is: Gewerbestrasse 11, 6330 Cham, Switzerland

Contents

Modeling Combined Shunt/Series FACTS in Power Flow Solutions: A Comprehensive Review	1
Mohamed Ebeed, Salah Kamel, Francisco Jurado, Shady H. E. Abdel Aleem, and Ahmed F. Zobaa	
Comparison of Different Configurations of Saturated Core Fault Current Limiters in a Power Grid by Numerical Method: A Review	49
Aydin Zaboli	
Optimized Settings of Over Current Relays in Electric Power Systems ...	79
Abdelmonem Draz, Mahmoud Elkholy, and Attia El-Fergany	
Optimal Allocation of Active and Reactive Power Compensators and Voltage Regulators in Modern Distribution Systems	99
Heba M. Elaraby, Ahmed M. Ibrahim, Muhyaddin Rawa, Essam El-Din Abou El-Zahab, and Shady H. E. Abdel Aleem	
Analysis of Impacts of Multiple Renewable Energy Sources and D-STATCOM Devices on Distribution Networks	141
R. Satish, K. Vaisakh, and Almoataz Y. Abdelaziz	
A Convex Formulation for Hosting Capacity Analysis in Power Distribution Networks	161
Alejandro Garcés and José Maria Yusta	
Power Quality in Modern Power Systems: A Case Study in Bosnia and Herzegovina	181
Mia Lešić Aganović, Tatijana Konjić, Miloš Milovanović, Martin Čalasan, Ahmed I. Omar, and Shady H. E. Abdel Aleem	

Optimal Coordination of Distributed Generation Units and Shunt Capacitors in Egyptian Distribution System Using Sine-Cosine Optimization Algorithm	205
Moustafa M. Ahmed, Muhyaddin Rawa, Ahmed M. Ibrahim, Hala M. Abdel Mageed, and Shady H. E. Abdel Aleem	
Power Quality Enhancement of Balanced/Unbalanced Distribution Systems Using Metaheuristic Optimizations	235
Ahmad Eid	
Knowledge Discovery in Database Process Used to Analyze Voltage THD of a Computer Factory	269
Edson Farias de Oliveira, Ítalo Rodrigo Soares Silva, Ricardo Silva Parente, Paulo Oliveira Siqueira Junior, Manoel Henrique Reis Nascimento, Jandecy Cabral Leite, and David Barbosa de Alencar	
Optimization of Economic and Environmental Dispatch Using Bio-inspired Computer Metaheuristics	305
Manoel Henrique Reis Nascimento, Jandecy Cabral Leite, Alexandra Amaro de Lima, Edson Farias de Oliveira, Ítalo Rodrigo Soares da Silva, Ricardo Silva Parente, Jorge Laureano Moya Rodríguez, and Paulo Oliveira Siqueira Junior	
A Stochastic Multi-period Transmission Expansion Planning Using Whale Optimization Algorithm	377
Mohamed M. Refaat, Muhyaddin Rawa, Yousry Atia, Ziad M. Ali, Shady H. E. Abdel Aleem, and Mahmoud M. Sayed	
Energy Storage Devices	407
Samuel Raafat Fahim and Hany M. Hasanien	
Stochastic Approach for Economic-Technical-Environmental Operation of Microgrids with Battery Storage Considering Parameters Uncertainty	443
Mostafa H. Mostafa, Muhyaddin Rawa, Ahmed I. Omar, Shady H. E. Abdel Aleem, Almoataz Y. Abdelaziz, Ziad M. Ali, and Ahmed F. Zobaa	
A Resilient Hybrid Renewable Energy System for DC Microgrid with Inclusion of the Energy Storage	463
Siddharth Joshi, Praghness Bhatt, Bhinal Mehta, and Amit Sant	
High Impedance Fault Detection and Classification Based on Pattern Recognition	487
Zahra Moravej and Mehrdad Ghahremani	
Designing of Efficient Lighting System for Smart Homes	513
Suprava Chakraborty and Abhishek Nemani	

Reliability Analysis of a Group of Internal Combustion Engines (ICM) in Thermoelectric Power Plants Using Optimization Methods for Artificial Neural Networks (ANN) 525
Ítalo Rodrigo Soares Silva, Ricardo Silva Parente,
Paulo Oliveira Siqueira Junior, Manoel Henrique Reis Nascimento,
Milton Fonseca Júnior, Jandecy Cabral Leite,
and David Barbosa de Alencar

Index 557

Modeling Combined Shunt/Series FACTS in Power Flow Solutions: A Comprehensive Review



Mohamed Ebeed, Salah Kamel, Francisco Jurado,
Shady H. E. Abdel Aleem , and Ahmed F. Zobaa 

1 Introduction

Flexible Alternating Current Transmission System (FACTS) are power electronic-based controllers that can regulate electrical systems' power flow [1–5]. FACTS plays a vital role in electrical systems where several benefits can be captured by integration of FACTS devices, which can be summarized as follows:

- Enhance the system loadability and the power transfer capability
- Reduce the generation cost
- Alleviate the thermal loading of the congested transmission lines and limit the overloads
- Provide the controllability of systems parameters such as the power flow, the line impedance, the magnitudes, and phase angles of voltages of certain buses

M. Ebeed (✉)

Electrical Engineering Department, Faculty of Engineering, Sohag University, Sohag, Egypt
e-mail: mebeed@eng.sohag.edu.eg

S. Kamel

Electrical Engineering Department, Faculty of Engineering, Aswan University, Aswan, Egypt
e-mail: skamel@aswu.edu.eg

F. Jurado

Department of Electrical Engineering, University of Jaen, Linares, Spain
e-mail: fjurado@ujaen.es

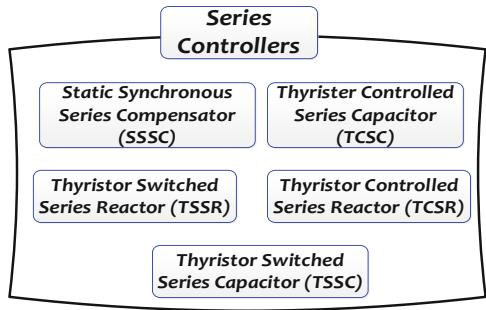
S. H. E. Abdel Aleem

Electrical Engineering and Electronics Department, Valley High Institute of Engineering and Technology, Science Valley Academy, Qalyubia, Egypt
e-mail: engyshady@ieee.org

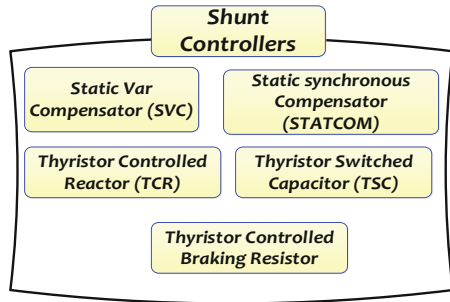
A. F. Zobaa

Electrical and Power Engineering, Brunel University, Uxbridge, Uxbridge, UK
e-mail: azobaa@ieee.org

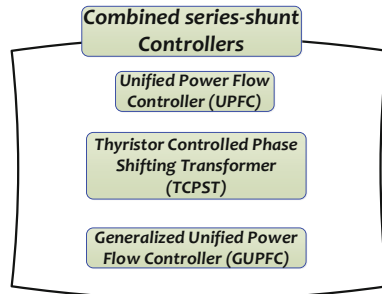
Fig. 1 Types of FACTS controllers based on their connection. (a) Series controller, (b) shunt controller, (c) combined series-shunt controller, and (d) combined series-series controller



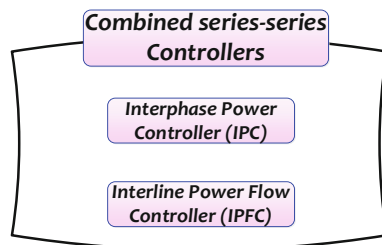
(a)



(b)



(c)



(d)

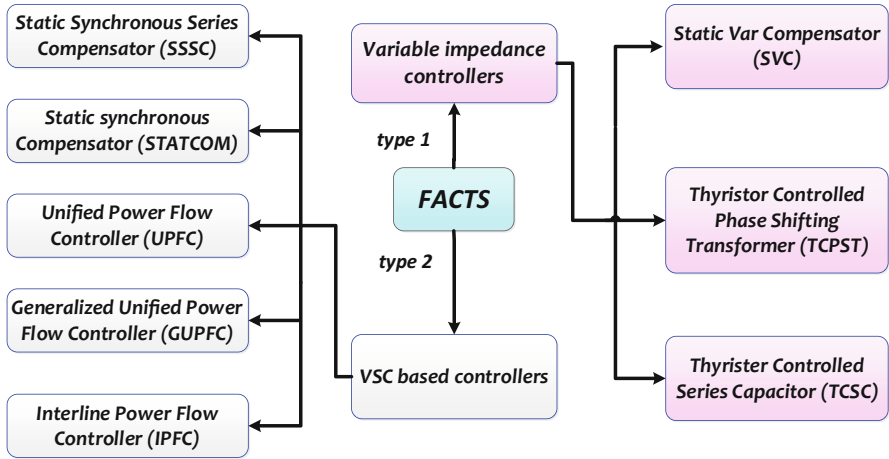


Fig. 2 Types of FACTS controllers based on the power electronic devices

- Reduce the system active and reactive power loss
- Improve the power factor
- Mitigate the harmonics
- Enhance the system security
- Limit the faults currents
- Damp the oscillations
- Enhance the transient and dynamic stability

With the continued progress of the power electronics manufacturing technologies, several types of FACTS devices are produced. Figure 1 shows types of FACTS devices based on their connection, while Fig. 2 shows classifications of FACTS based on power electronic devices.

Modeling FACTS devices is an important issue to assess and evaluate the impact of the inclusion of the FACTS devices on modern power systems. It should point out here that the capital costs of these devices are very high. Thus, it is crucial to investigate the influence of the inclusion of FACTS devices before installing them in the system.

Modeling of the FACTS devices into power flow solution methods (Gauss-Seidel method, Newton-Raphson (NR) method, the decoupled Method) needs several modifications which can be summarized as follows:

- Changes in the original admittance matrix to incorporate the impedances of the FACTS devices
- Auxiliary reference buses to the original networks are added, representing the FACTS devices’ terminals
- Modifications of the Jacobian matrix, the correction matrix, and the power mismatch matrix to consider parameters of the FACTS devices as control variables

Table 1 Types of buses in load flow solution

Classification	Known	Unknown
Load bus (PQ)	P, Q	V, δ
Voltage-controlled bus (PV)	P, V	Q, δ
Slack bus (swing bus)	V, δ	P, Q

This chapter presents a survey about modeling the common FACTS devices in power flow solutions and the advantages and disadvantages in each way.

2 Power Flow Solutions

The power flow analysis is essential for planning, controlling, and operating the electric power systems and planning for future expansion. Power system analysis includes several technical activities in transmission planning, such as power flow, optimal power flow, voltage stability, contingency analysis, transient stability, and others.

The power flow problem solution was studied earlier by Ward and Hale method in 1956. The primary goal of the power flow solution is to determine the bus voltages and line power flows in an extensive electrical grid for known loads and generation schedules – the nonlinear relationship between the system voltages, currents, consumed powers, and the generated powers. Hence, the power flow problem is solved by iterative methods. The most common methods that have been implemented in the system analysis are the Gauss-Seidel method, Newton-Raphson method and decoupled method.

2.1 Power Flow Methods

The main work of the power flow solution is to provide accurate information on the steady-state operating characteristics of the electric system under particular load demands. Generally, in an electric network, the four quantities include the voltage magnitude $|V|$, phase angle δ , real power P , and reactive power Q are associated with each bus. The buses in the load flow problem are classified as: (1) Slack bus, (2) Load buses, and (3) Voltage-controlled buses. Each bus has known and unknown quantities, illustrated in Table 1.

The relationship between the injected current at bus i voltage and current is defined as follows:

$$I_i = V_i \sum_{j=0}^n y_{ij} - \sum_{j=1}^n y_{ij} V_j \quad j \neq i \quad (1)$$

The active and reactive powers are represented as follows:

$$P_i + jQ_i = VI_i^* \quad (2)$$

By substituting of I_i form (1) in (2).

$$\frac{P_i - jQ_i}{V_i^*} = V_i \sum_{j=0}^n y_{ij} - \sum_{j=1}^n y_{ij} V_j \quad j \neq i \quad (3)$$

where, y_{ij} is the actual impedance between buses i and j . From expanding Eq. (3), the active and reactive powers flow can be defined as:

$$P_{i,\text{calc}} = V_i \sum_{j=1}^{\text{NB}} V_j (G_{ij} \cos \delta_{ij} + B_{ij} \sin \delta_{ij}) \quad (4)$$

$$Q_{i,\text{calc}} = V_i \sum_{j=1}^{\text{NB}} V_j (G_{ij} \sin \delta_{ij} - B_{ij} \cos \delta_{ij}) \quad (5)$$

$P_{i,\text{calc}}$ and $Q_{i,\text{calc}}$ denote the calculated net active and reactive powers injected of bus i . G_{ij} and B_{ij} are the conductance and susceptance between bus i and bus j , respectively.

The scheduled active and reactive powers at bus i are set as follows:

$$P_{i,\text{sch}} = P_{g,i} - P_{d,i} \quad (6)$$

$$Q_{i,\text{sch}} = Q_{g,i} - Q_{d,i} \quad (7)$$

where, $P_{g,i}$ and $Q_{g,i}$ denote the generated active and reactive powers of bus i , respectively. $P_{d,i}$ and $Q_{d,i}$ denote the active and reactive load demands of bus i . The mismatched of active and reactive powers of bus i are given as:

$$\Delta P_i = P_{i,\text{sch}} - P_{i,\text{calc}} \quad (8)$$

$$\Delta Q_i = Q_{i,\text{sch}} - Q_{i,\text{calc}} \quad (9)$$

(a) Gauss-Seidel Power Flow Solution Method

This method is one of the common methods implemented to solve the power flow solution problem. Gauss-Seidel is an iterative method where the voltages are updated in the iterative process, according to (3), as follows:

$$V_i^{(m+1)} = \left[\frac{\frac{P_{i,\text{sch}} - jQ_{i,\text{sch}}}{V_i^{*(m)}} + \sum_{j=1}^n y_{ij} V_j^{(m)}}{\sum_{j=0}^n y_{ij}} \right] \quad (10)$$

Hence, Eq. (10) can be represented in terms of the admittance matrix Y_{bus} as:

$$V_i^{(m+1)} = \left[\frac{\frac{P_{i,\text{sch}} - jQ_{i,\text{sch}}}{V_i^{*(m)}} - \sum_{j \neq i}^n Y_{ij} V_j^{(m)}}{Y_{ii}} \right] \quad (11)$$

where m is the iteration number. $Y_{ij} = -y_{ij}$ and $Y_{ii} = \sum_{j=0}^n y_{ij}$. The solution procedures of the Gauss-Seidel method are summarized as given below:

1. Read the system data, including the bus, line, and tolerance values (typical tolerance is 0.00001 p.u).
2. Form the admittance matrix.
3. Initialize the voltages as:
 - For PQ buses, $V = 1 \angle 0$.
 - For PV buses (including the swing bus), $V = V_{\text{sp}} \angle 0$.
4. Update the initialize voltage according to (11). The voltage angle is only updated for PV buses, while the voltage magnitude is set constant at the specified value.
5. According to (8) and (9), check the mismatch between active and reactive power. Suppose the maximum value of power mismatch is more than the selected tolerance value, repeat steps (4) and (5). Otherwise, stopover the iterative process and find the final solution.

– *Merits of Gauss-Seidel Method*

- Simplicity in the application.
- It needs less computer memory.
- It needs less commotional time per iteration.

– *Demerits of Gauss-Seidel Method*

- It is applied for small-scale systems.
- It has a slow convergence rate.

It should be highlighted that the Gauss-Seidel method is applied for small-scale systems.

(b) **Newton Raphson (NR) Power Flow Solution Method**

Newton Raphson solution is the commonly applied method, especially in large-scale systems. The Newton Raphson method is applied to solve the Taylor series's nonlinear equations. Thus, linearize Eqs. (4) and (5) by Newton Raphson method, the following equation can be returned:

$$\begin{bmatrix} \Delta P \\ \Delta Q \end{bmatrix} = \begin{bmatrix} J_{P\delta} & J_{PV} \\ J_{Q\delta} & J_{QV} \end{bmatrix} \begin{bmatrix} \Delta \delta \\ \Delta V/V \end{bmatrix} \quad (12)$$

where, $J_{P\delta}$, J_{PV} , J_{QV} , $J_{Q\delta}$ are elements of an $N \times N$ matrix of partial derivatives, known as the Jacobian matrix. These elements can be originated as follows:

$$(J_{P\delta})_{ij} = \frac{\partial P_i}{\partial \delta_j} \quad (13)$$

$$(J_{PV})_{ij} = \frac{\partial P_i}{\partial V_j} V_j \quad (14)$$

$$(J_{Q\delta})_{ij} = \frac{\partial Q_i}{\partial \delta_j} \quad (15)$$

$$(J_{QV})_{ij} = \frac{\partial Q_i}{\partial V_j} V_j \quad (16)$$

If $i \neq j$, the members in the Jacobian matrix are given as follows:

$$(J_{P\delta})_{ij} = -V_i V_j (G_{ij} \sin \delta_{ij} - B_{ij} \cos \delta_{ij}) \quad (17)$$

$$(J_{PV})_{ij} = -V_i V_j (G_{ij} \cos \delta_{ij} - B_{ij} \sin \delta_{ij}) \quad (18)$$

$$(J_{Q\delta})_{ij} = V_i V_j (G_{ij} \cos \delta_{ij} - B_{ij} \sin \delta_{ij}) \quad (19)$$

$$(J_{QV})_{ij} = -V_i V_j (G_{ij} \sin \delta_{ij} - B_{ij} \cos \delta_{ij}) \quad (20)$$

If $i = j$, the members in the Jacobian matrix are given as follows:

$$(J_{P\delta})_{ii} = -Q_i - B_{ii} |V_i|^2 \quad (21)$$

$$(J_{PV})_{ii} = P_i + G_{ii} |V_i|^2 \quad (22)$$

$$(J_{Q\delta})_{ii} = P_i - G_{ii} |V_i|^2 \quad (23)$$

$$(J_{QV})_{ii} = Q_i - B_{ii} |V_i|^2 \quad (24)$$

After initializing the values of V and δ , the Jacobian matrix is constructed from (12), the values of $\Delta\delta$ and ΔV are determined, and then V and δ are updated. The solution procedures of Newton Raphson are summarized as follows:

1. Read the system data, including the bus, line, and tolerance values (typical tolerance is 0.00001 p.u).
2. Form the admittance matrix.
3. Initialize the voltages as:
 - For PQ buses, $V = 1 \angle 0$.
 - For PV buses (including the swing bus), $V = V_{sp} \angle 0$.
4. Construct Jacobian matrix elements according to (13) and (24).
5. Find the values of $\Delta\delta$ and ΔV by solving Eq. (12).
6. Update the voltages as follows:

$$(V)^{m+1} = (V)^m + \Delta V \quad (25)$$

$$(\delta)^{m+1} = (\delta)^m + \Delta\delta \quad (26)$$

The voltage angle is only updated for PV buses, while the voltage magnitude is set constant at the specified value.

7. According to (8) and (9), check the mismatch between active and reactive power. Suppose the maximum value of power mismatch is more than the selected tolerance value; repeat steps (4) and (6). Otherwise, halt the iterative process and get the final solution.

– *Merits of Newton Raphson Method*

- More robust and it is suitable for large scale systems.
- It converges rapidly where it needs about 3–5 iterations.
- It needs low commotional time.

– *Demerits of Newton Raphson Method*

- It needs large computer memory.
- It has more calculations, whereas the Jacobian matrix is calculated per iteration.
- Its programming code is complicated.

(c) Decoupled Power Flow Solution Method

The decoupled method is driven from the NR method, which is considered an approximate version of the NR method by modifying the Jacobian matrix. It should be pointed out that the change of real power flow is primarily affected with voltage phase angle (δ) while the reactive power flow is unchanged with $|V|$. Thus $(J_{PV})_{ij}$ equals to zero. Likewise, the change of reactive power flow is primarily affected by voltage magnitude ($|V|$) while the reactive power flow is unchanged with δ . Thus $(J_{Q\delta})_{ij}$ equals to zero. Hence, Eq. (12) reveals to:

$$\begin{bmatrix} \Delta P \\ \Delta Q \end{bmatrix} = \begin{bmatrix} J_{P\delta} & 0 \\ 0 & J_{QV} \end{bmatrix} \begin{bmatrix} \Delta\delta \\ \Delta V/V \end{bmatrix} \quad (27)$$

hence,

$$\Delta P = (J_{P\delta}) \Delta\delta \quad (28)$$

$$\Delta Q = (J_{QV}) \Delta V/V \quad (29)$$

Several considerations related to transmission system can be taken into consideration as follows:

- The voltage phase angles between buses are small. Thus,

$$\cos(\delta_i - \delta_j) \approx 1, \quad \sin(\delta_i - \delta_j) \approx \delta_i - \delta_j \quad (30)$$

- The X/R value is high in transmission system, thereby

$$G_{ij} \sin \delta_{ij} \ll B_{ij} \cos \delta_{ij} \quad (31)$$

- The reactive power injected into bus i is less than the reactive power flow if all the lines are connected. Thus,

$$Q_i \ll |V_i| B_{ij} \quad (32)$$

$$(J_{P\delta})_{ij} = \frac{\partial P_i}{\partial \delta_j} = \frac{\partial Q_i}{\partial V_j} V_j = -V_i V_j B_{ij} \quad (33)$$

$$(J_{P\delta})_{ii} = \frac{\partial P_i}{\partial \delta_i} = \frac{\partial Q_i}{\partial V_i} V_i = -V_i^2 B_{ii} \quad (34)$$

The decoupled method is much faster than the NR method. Also, storage requirements are more diminutive.

3 Modeling Methods of the FACTS Devices

3.1 Modeling of the Variable Impedance-Based FACTS

3.1.1 Static VAR Compensator (SVC)

The Static VAR Compensator (SVC) is a shunt-connected FACTS device that absorbs or generates reactive power. SVC consists of a set of capacitors parallel with Thyristor Controlled Reactor (TCR), as shown in Fig. 3. Thus, SVC can be considered a controllable shunt reactance that can control the reactive compensation and the voltage magnitude of the connected bus [6, 7]. The equivalent circuit of the SVC is shown in Fig. 4, where the SVC is represented as a variable reactance for shunt compensation, and the injected reactive power can be calculated as a function of equivalent susceptance (B_{SVC}) follows:

$$I = jBV_k \quad (35)$$

Reactive power drawn by SVC that is the same as injected power to bus k is written as follows:

Fig. 3 Schematic diagram of SVC

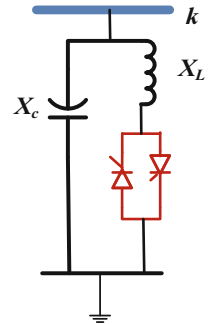
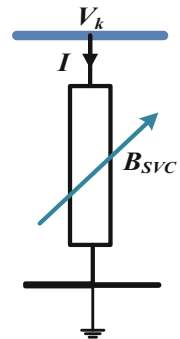


Fig. 4 Variable shunt susceptance



$$Q_k = -V_k^2 B \quad (36)$$

The equivalent susceptance can be calculated as a function of the firing angle (α) as follows:

$$B_{eq} = -\frac{X_L - \frac{X_C}{\pi} (2(\pi - \alpha) + \sin(2\alpha))}{X_C \dot{X}_L} \quad (37)$$

where $X_L = \omega L$, and $X_C = 1/\omega C$.

(a) Total Susceptance Model

In this model, the susceptance of the SVC is taken as a state variable in NR power flow as follows:

$$\begin{bmatrix} \Delta P_k \\ \Delta Q_k \end{bmatrix}^t = \begin{bmatrix} 0 & 0 \\ 0 & Q_k \end{bmatrix}^t \begin{bmatrix} \Delta \theta_k \\ \Delta B_{SVC}/B_{SVC} \end{bmatrix} \quad (38)$$

Thus, the value of B_{SVC} will be updated with the iterative process as follows:

$$B_{SVC}^{t+1} = B_{SVC}^t + \left(\frac{\Delta B_{SVC}}{B_{SVC}} \right)^t B_{SVC}^t \quad (39)$$

If the specified voltage is satisfied by variation of the B_{SVC} .

(b) The Firing Angle Model

In this model $B = B_{SVC}$ and the SVC is represented as depicted in Fig. 4. The Firing angle in this model is considered as a state variable which can be calculated as follows:

$$\begin{bmatrix} \Delta \beta_k \\ \Delta Q_k \end{bmatrix}^i = \begin{bmatrix} 0 & 0 \\ 0 & \frac{\partial Q_k}{\partial \alpha} \end{bmatrix}^i \begin{bmatrix} \Delta \theta_k \\ \alpha \end{bmatrix}^i \quad (40)$$

Where:

$$\frac{\partial Q_k}{\partial \alpha} = \frac{2V_k^2}{X_L} (\cos(2\alpha) - 1) \quad (41)$$

Thus, the value of α will be updated with the iterative process as follows:

$$\alpha^{i+1} = \alpha^i + \Delta \alpha^i \quad (42)$$

The equivalent susceptance will be calculated as follows:

$$B_{eq} = -\frac{X_L - \frac{X_C}{\pi} (2(\pi - \alpha) + \sin(2\alpha))}{X_C \dot{X}_L} \quad (43)$$

3.1.2 Thyristor Controlled Series Capacitors (TCSC)

The TCSC comprises a Thyristor Controlled Reactor (TCR) parallel with a fixed capacitor to provide the series compensation, as shown in Fig. 5 [8, 9]. The TCSC can rapidly change the impedance of the TL, and it can control the active power flow in TL. Figure 6 shows the equivalent circuit of the TCSC. The power flow equations between bus m and n can be described as follows:

$$P_{mn} = V_m^2 G_{mn} - V_m V_n G_{mn} \cos(\delta_m - \delta_n) - V_m V_n B_{mn} \sin(\delta_m - \delta_n) \quad (44)$$

$$Q_{mn} = -V_m^2 B_{mn} - V_m V_n G_{mn} \sin(\delta_m - \delta_n) + V_m V_n B_{mn} \cos(\delta_m - \delta_n) \quad (45)$$

$$P_{nm} = V_n^2 G_{mn} - V_m V_n G_{mn} \cos(\delta_m - \delta_n) + V_m V_n B_{mn} \sin(\delta_m - \delta_n) \quad (46)$$

$$Q_{nm} = -V_n^2 B_{mn} + V_m V_n G_{mn} \sin(\delta_m - \delta_n) + V_m V_n B_{mn} \cos(\delta_m - \delta_n) \quad (47)$$

Where:

Fig. 5 Configuration of the TCSC

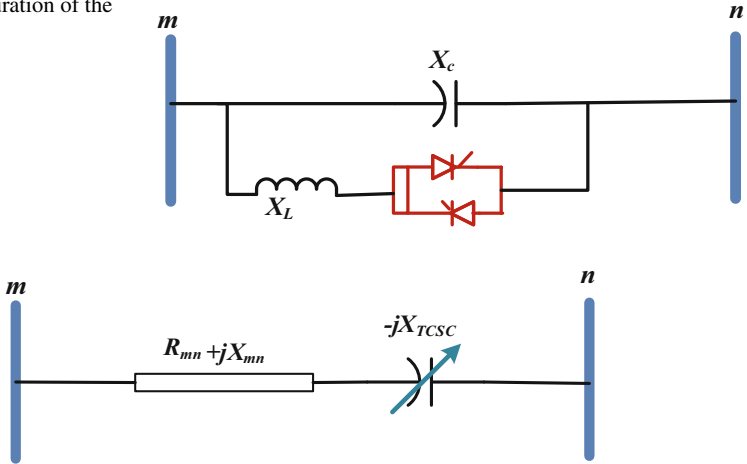
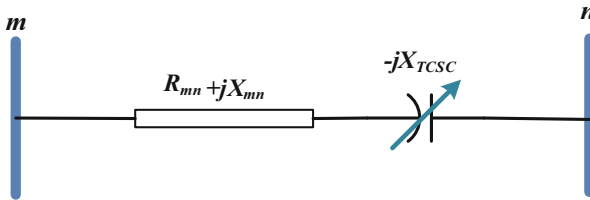


Fig. 6 Model of the TCSC



$$G_{mn} = \frac{R_{mn}}{R_{mn}^2 + (X_{mn} - X_c)^2} \quad (48)$$

$$B_{mn} = -\frac{X_{mn} - X_c}{R_{mn}^2 + (X_{mn} - X_c)^2} \quad (49)$$

The reactance of the TCSC is variable with changing the firing angle of the thyristors, as follows:

$$X_{\text{TCSC}}(\gamma) = \frac{X_c X_L(\gamma)}{X_L(\gamma) - X_c} \quad (50)$$

The equivalent reactance (X_{eq}) of the transmission line with incorporating TCSC can be expressed as follows:

$$X_{\text{eq}} = X_{mn} - X_{\text{TCSC}} = (1 - \tau) X_{mn} \quad (51)$$

Where:

$$\tau = \frac{X_{\text{TCSC}}}{X_{mn}} \quad (52)$$

(a) The Conventional Ybus Matrix Model

For modeling the TCSC, the Y_{bus} matrix will be modified to consider the reactance of TCSC in the line between buses m and n [10] as follows:

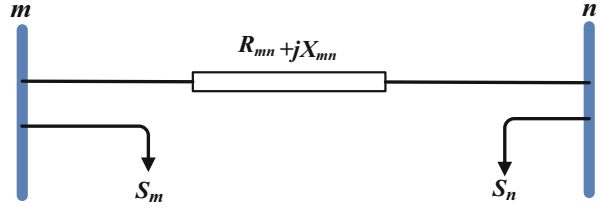
$$Y_{\text{bus}}^{\text{TCSC}} = Y_{\text{bus}} + \begin{bmatrix} 0 & 0 & 0 & \dots & 0 & 0 \\ 0 & \Delta y_{mn} & 0 & \dots & -\Delta y_{mn} & 0 \\ 0 & 0 & 0 & \dots & 0 & 0 \\ \dots & \dots & \dots & \dots & \dots & 0 \\ 0 & -\Delta y_{mn} & 0 & \dots & \Delta y_{mn} & 0 \\ 0 & 0 & 0 & \dots & 0 & 0 \end{bmatrix} \quad (53)$$

(b) TCSC-Firing Angle Model

The authors in [11–14] presented an efficient firing angle model. In this model, the firing angle is considered a state variable. The equivalent reactance of the TCSC as a function of the firing angle can be expressed as follows:

$$X_{\text{tssc}} = \frac{X_c \left[\pi (k^2 - 1)^2 - k^2 (k^2 - 1) (2\beta + \sin 2\beta) + 4k^2 \cos^2 \beta (k \tan k\beta - \tan \beta) \right]}{\pi (k^2 - 1)^2} \quad (54)$$

Fig. 7 The power injection model of TCSC



where $k = \sqrt{\frac{X_c}{X_L}}$, $\beta = \pi - \alpha$. The NR equation for the firing angle model of TCSC can be expressed as follows:

$$n \begin{bmatrix} \frac{\partial P_m}{\partial V_m} & \frac{\partial P_m}{\partial \theta_m} & \frac{\partial P_m}{\partial V_n} & \frac{\partial P_m}{\partial \theta_n} & \frac{\partial P_m}{\partial \alpha} \\ \frac{\partial Q_m}{\partial V_m} & \frac{\partial Q_m}{\partial \theta_m} & \frac{\partial Q_m}{\partial V_n} & \frac{\partial Q_m}{\partial \theta_n} & \frac{\partial P_n}{\partial \alpha} \\ \frac{\partial P_n}{\partial V_m} & \frac{\partial P_m}{\partial \theta_m} & \frac{\partial P_m}{\partial V_m} & \frac{\partial P_n}{\partial \theta_n} & \frac{\partial P_n}{\partial \alpha} \\ \frac{\partial Q_b}{\partial V_a} & \frac{\partial P_b}{\partial \theta_a} & \frac{\partial Q_n}{\partial V_n} & \frac{\partial Q_n}{\partial \theta_n} & \frac{\partial Q_n}{\partial \alpha} \\ \frac{\partial P_{mn}}{\partial V_n} & \frac{\partial P_{mn}}{\partial \theta_m} & \frac{\partial P_{mn}}{\partial V_n} & \frac{\partial P_{mn}}{\partial \theta_n} & \frac{\partial P_{mn}}{\partial \alpha} \end{bmatrix} \begin{bmatrix} \Delta V_m \\ \Delta \theta_m \\ \Delta V_n \\ \Delta \theta_n \\ \Delta \alpha \end{bmatrix} = \begin{bmatrix} \Delta P_m \\ \Delta Q_m \\ \Delta P_n \\ \Delta Q_n \\ \Delta P_{mn} \end{bmatrix} \quad (55)$$

It should be pointed out that the firing angle can be changed within the range $[90^\circ-180^\circ]$.

(c) The Power Injection Model

The power injection modeling of the TCSC is similar to the power injection models of FACTS devices. In this model, the TCSC is represented by injected loads at the terminal of the TL at buses m and n , as depicted in Fig. 7. The injected power can be calculated in the following manner [15, 16]:

$$P_m = V_m^2 \Delta G_{mn} - V_m V_n [\Delta G_{mn} \cos \delta_{mn} + \Delta B_{mn} \sin \delta_{mn}] \quad (56)$$

$$P_n = V_n^2 \Delta G_{mn} - V_m V_n [\Delta G_{mn} \cos \delta_{mn} - \Delta B_{mn} \sin \delta_{mn}] \quad (57)$$

$$Q_m = -V_m^2 \Delta B_{mn} - V_m V_n [\Delta G_{mn} \sin \delta_{mn} - \Delta B_{mn} \cos \delta_{mn}] \quad (58)$$

$$Q_n = -V_n^2 \Delta B_{mn} + V_m V_n [\Delta G_{mn} \sin \delta_{mn} + \Delta B_{mn} \cos \delta_{mn}] \quad (59)$$

where $\Delta G_{mn} = \frac{X_c R_{mn} (X_c - 2X_{mn})}{(R_{mn}^2 + X_{mn}^2)(R_{mn}^2 + (X_{mn} - X_c)^2)}$ and $\Delta B_{mn} = \frac{-X_c (R_{mn}^2 - X_{mn}^2 + X_c X_{mn})}{(R_{mn}^2 + X_{mn}^2)(R_{mn}^2 + (X_{mn} - X_c)^2)}$

3.1.3 Thyristor Controlled Phase Shifting Transformer (TCPST)

TCPST is a phase-shifting transformer adjusted by thyristor switches to provide a rapidly variable phase angle. TCPST is an efficient controller that consists of two transformers, one of them connected in series with TL, and the other transformer is connected in parallel with the system, as depicted in Fig. 8. TCPST can provide a fast phase angle control of the voltage across the device to regulate regional power flow [17–19]. Figure 9 shows the equivalent circuit of the TCPST. Injected loads can represent the TCPST at the sending and the receiving bus, as shown in Fig. 10. The injected loads and the power flow can be calculated as follows:

The power flow equation of the TCPST can be described as follows:

$$P_{mn} = \frac{V_m^2 g_{mn}}{\cos^2 \phi} - \frac{V_m V_n}{\cos \phi} [g_{mn} \cos (\delta_m - \delta_n + \phi) + b_{mn} \sin (\delta_m - \delta_n + \phi)] \tag{60}$$

$$Q_{mn} = -\frac{V_m^2 b_{mn}}{\cos^2 \phi} - \frac{V_m V_n}{\cos \phi} [g_{mn} \sin (\delta_m - \delta_n + \phi) - b_{mn} \cos (\delta_m - \delta_n + \phi)] \tag{61}$$

$$P_{nm} = V_n^2 g_{mn} - \frac{V_m V_n}{\cos \phi} [g_{mn} \cos (\delta_m - \delta_n + \phi) - b_{mn} \sin (\delta_m - \delta_n + \phi)] \tag{62}$$

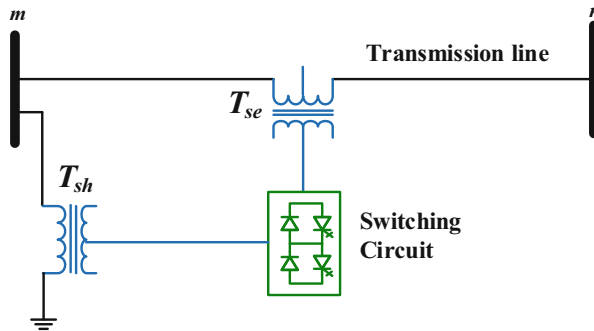


Fig. 8 Configuration of the PST

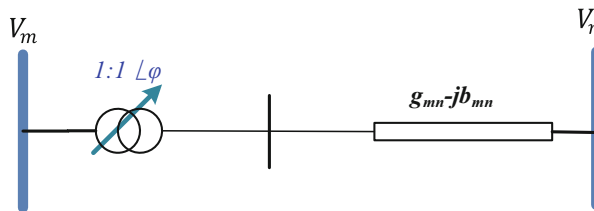


Fig. 9 The equivalent circuit diagram for TCPST

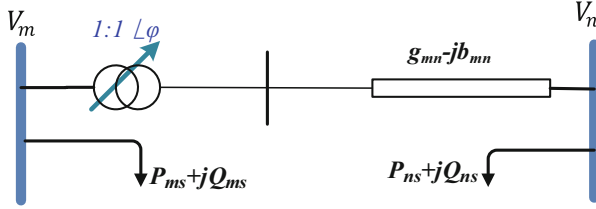


Fig. 10 Model of TCSPT

$$Q_{nm} = -V_n^2 b_{mn} + \frac{V_m V_n}{\cos \phi} [g_{mn} \sin(\delta_m - \delta_n + \phi) + b_{mn} \cos(\delta_m - \delta_n + \phi)] \quad (63)$$

The injected real and reactive power of TCPS at bus m and bus n are given as follows:

$$P_{ms} = \& - g_{mn} V_m^2 \tan^2 \phi - V_m V_n \tan \phi [g_{mn} \sin(\delta_m - \delta_n) - b_{mn} \cos(\delta_m - \delta_n)] \quad (64)$$

$$Q_{ms} = \& b_{mn} V_m^2 \tan^2 \phi + V_m V_n \tan \phi [g_{mn} \cos(\delta_m - \delta_n) + b_{mn} \sin(\delta_m - \delta_n)] \quad (65)$$

$$P_{ns} = \& - V_m V_n \tan \phi [g_{mn} \sin(\delta_m - \delta_n) + b_{mn} \cos(\delta_m - \delta_n)] \quad (66)$$

$$Q_{ns} = \& - V_m V_n \tan \phi [g_{mn} \cos(\delta_m - \delta_n) - b_{mn} \sin(\delta_m - \delta_n)] \quad (67)$$

3.2 Modeling of the VSC-based FACTS

3.2.1 Modeling of the UPFC

The UPFC is an efficient combined series-shunt FACTS device used to control the voltage magnitude of a sending bus, and the active and the reactive powers flow through the transmission line. The UPFC comprises two converters (VSC1 – VSC2) connected via a common DC link, as depicted in Fig. 11. VSC1 connects in shunt at the sending bus, while VSC2 is connected in series between the sending and the receiving bus. VSC1 and VSC2 connect to the system using two coupling transformers (Z_{se} , Z_{sh}) [1, 20].

The primary function of the shunt converter (VSC1) is to control the voltage magnitude of the sending bus by absorbing or injecting reactive power with the AC

Fig. 11 Schematic diagram of UPFC

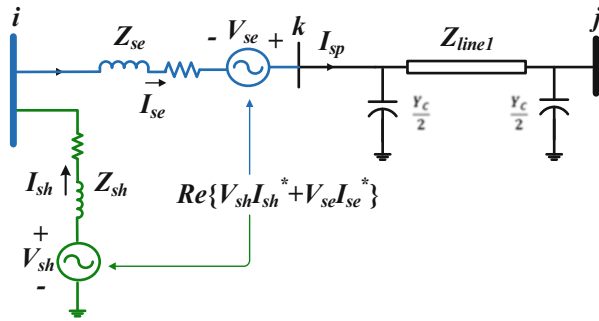
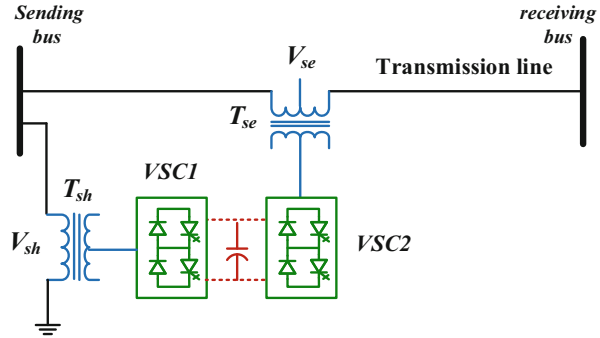


Fig. 12 The VS representation of the UPFC

system. In addition, it provides the required active power to the series converter, absorbed from the AC system. Thus, the net exchanged power in the OUPFC equals zero in case of neglecting the power losses in the converters.

The Voltage Source (VS) representation of the UPFC is depicted in Fig. 12. In Fig. 12, the UPFC is represented by two voltage sources (V_{se} , V_{sh}) which have been combined with two impedances (Z_{se} , Z_{sh}). Thus, four state variables are related to the representation of the UPFC into the power flow solution, including V_{sh} , V_{se} , θ_{sh} and θ_{se} . This requires the modification in the Jacobian, the power mismatch, and the correction matrices.

Modeling the UPFC into power flow is not an easy task. Thus, several efforts have been presented for modeling the UPFC as follows.

(a) The Comprehensive Model

This model has emerged from the voltage source representation of the UPFC (Fig. 12). In this model, the UPFC is included in the Jacobian matrix, and the linearized power equations of the UPFC are combined with the system linearized power Eq. (21). Thus, the modification in the Jacobian matrix is mandatory in this model, which can be depicted as follows:

$$\begin{bmatrix} \Delta P_i \\ \Delta P_j \\ \Delta Q_i \\ \Delta Q_j \\ \Delta P_{ij} \\ \Delta Q_{ij} \\ \Delta P_{ex} \end{bmatrix} = \begin{bmatrix} \frac{\partial P_i}{\partial \theta_i} & \frac{\partial P_i}{\partial \theta_j} & \frac{\partial P_i}{\partial V_{iR}} V_{sh} & \frac{\partial P_i}{\partial V_j} V_j & \frac{\partial P_i}{\partial \theta_{se}} & \frac{\partial P_i}{\partial V_{se}} V_{se} & \frac{\partial P_i}{\partial \delta_{vR}} \\ \frac{\partial P_j}{\partial \theta_i} & \frac{\partial P_j}{\partial \theta_j} & 0 & \frac{\partial P_j}{\partial V_j} V_j & \frac{\partial P_m}{\partial \theta_{se}} & \frac{\partial P_j}{\partial V_{se}} V_{se} & 0 \\ \frac{\partial Q_i}{\partial \theta_i} & \frac{\partial Q_i}{\partial \theta_j} & \frac{\partial Q_i}{\partial V_{iR}} V_{sh} & \frac{\partial Q_i}{\partial V_j} V_j & \frac{\partial Q_i}{\partial \theta_{se}} & \frac{\partial Q_i}{\partial V_{se}} V_{se} & \frac{\partial Q_i}{\partial \theta_{sh}} \\ \frac{\partial Q_j}{\partial \theta_i} & \frac{\partial Q_j}{\partial \theta_j} & 0 & \frac{\partial Q_j}{\partial V_j} V_j & \frac{\partial Q_j}{\partial \theta_{se}} & \frac{\partial Q_j}{\partial V_{se}} V_{se} & 0 \\ \frac{\partial P_{ji}}{\partial \theta_i} & \frac{\partial P_{ji}}{\partial \theta_j} & 0 & \frac{\partial P_{ji}}{\partial V_j} V_j & \frac{\partial P_{ji}}{\partial \theta_{se}} & \frac{\partial P_{ji}}{\partial V_{se}} V_{se} & 0 \\ \frac{\partial Q_{ji}}{\partial \theta_i} & \frac{\partial Q_{ji}}{\partial \theta_j} & 0 & \frac{\partial Q_{ji}}{\partial V_j} V_j & \frac{\partial Q_{ji}}{\partial \theta_{se}} & \frac{\partial Q_{ji}}{\partial V_{se}} V_{se} & 0 \\ \frac{\partial P_{ex}}{\partial \theta_i} & \frac{\partial P_{ex}}{\partial \theta_j} & \frac{\partial P_{ex}}{\partial V_{sh}} V_{sh} & \frac{\partial P_{ex}}{\partial V_j} V_j & \frac{\partial P_{ex}}{\partial \theta_{se}} & \frac{\partial P_{ex}}{\partial V_{se}} V_{se} & \frac{\partial P_{ex}}{\partial \theta_{sh}} \end{bmatrix} \begin{bmatrix} \Delta \theta_i \\ \Delta \theta_j \\ \frac{\Delta V_{sh}}{V_{sh}} \\ \frac{\Delta V_j}{V_j} \\ \Delta \theta_{se} \\ \frac{\Delta V_{se}}{V_{se}} \\ \Delta \theta_{sh} \end{bmatrix} \quad (68)$$

The model has a good convergence characteristic and in the UPFC can control the voltage magnitude and the power flow concurrently and individually. The significant shortage in this model is that the Jacobian matrix will be adjusted more to incorporate more UPFCs due to including their parameters in it.

(b) The Power Injection Model

In this model, the UPFC is represented by injected active and reactive loads at the terminals of this device, as depicted in Fig. 13 [22]. These loads are calculated as a function of the UPFC's terminal voltage and impedance. The admittance matrix is modified by adding the reactance of the UPFC (X_{se}). In this model, the value of the X_{se} is calculated as $rV_i < \beta$ where $0 < r < r_{max}$ and $0 < \beta < 360^\circ$. r and β refers to the control parameters that have been adjusted by the UPFC. The injected powers and their derivative have been added into the Jacobian matrix. The following equations describe the injected powers:

$$\begin{aligned} \bar{S}_j &= \bar{V}_j [-jb_{sr} \bar{V}_i e^{j\gamma}]^* \\ &= b_{sr} V_i V_j \sin(\theta_{ij} + \beta) + jb_{sr} V_i V_j \cos(\theta_{ij} + \beta) \end{aligned} \quad (69)$$

$$\begin{aligned} S_i &= \bar{V}_i [jb_{sr} \bar{V}_i e^{j\gamma}]^* \\ &= -b_{sr} V_i^2 \sin \gamma - jb_{sr} V_i^2 \cos \beta \end{aligned} \quad (70)$$

(c) The Matrix Partitioning Model

The matrix partitioning model simplifies the UPFC into Newton Raphson load flow [23]. This model depends upon on splitting the Jacobian matrix into the original matrix (J) and sub-matrices (J' , J'' and J''') related to UPFC as follows:

$$\begin{bmatrix} \boxed{J} & \boxed{J'} \\ \boxed{J''} & \boxed{J'''} \end{bmatrix} \begin{bmatrix} \boxed{X} \\ \boxed{X'} \end{bmatrix} = \begin{bmatrix} \boxed{B} \\ \boxed{B'} \end{bmatrix} \quad (71)$$

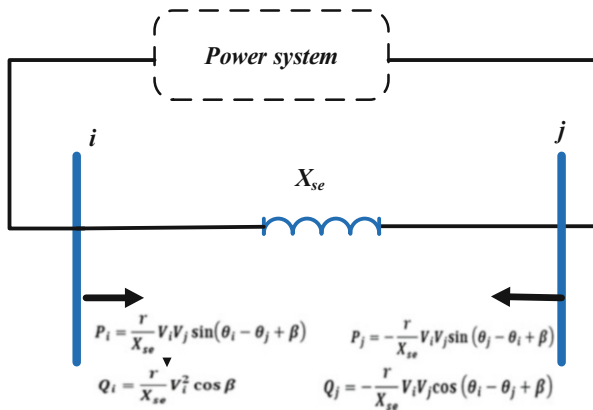


Fig. 13 Power injection model of the UPFC

The following equations describe each part in Eq. (70):

$$[B'] = [\Delta P_{ij} \Delta Q_{ij} \Delta P_{ex}]^T \quad (72)$$

$$[X'] = \left[\Delta \theta_{se} \quad \frac{\Delta V_{se}}{V_{se}} \quad \Delta \theta_{sh} \right]^T \quad (73)$$

$$[J''] = \begin{bmatrix} \frac{\partial \Delta P_{ij}}{\partial \theta_k} & \frac{\partial \Delta P_{ij}}{\partial \theta_j} & 0 & V_j \frac{\partial \Delta P_{ij}}{\partial V_j} \\ \frac{\partial \Delta Q_{ij}}{\partial \theta_i} & \frac{\partial \Delta Q_{ij}}{\partial \theta_j} & 0 & V_j \frac{\partial \Delta Q_{ij}}{\partial V_j} \\ \frac{\partial \Delta P_{ex}}{\partial \theta_i} & \frac{\partial \Delta P_{ex}}{\partial \theta_j} & V_{sh} \frac{\partial \Delta P_{ex}}{\partial V_{sh}} & V_j \frac{\partial \Delta P_{ex}}{\partial V_j} \end{bmatrix} \quad (74)$$

$$[J'] = \begin{bmatrix} \frac{\partial \Delta P_i}{\partial \theta_{se}} & V_{se} \frac{\partial \Delta P_i}{\partial V_{se}} & \frac{\partial \Delta P_i}{\partial \theta_{sh}} \\ \frac{\partial \Delta P_j}{\partial \theta_{se}} & V_{se} \frac{\partial \Delta P_j}{\partial V_{se}} & 0 \\ \frac{\partial \Delta Q_i}{\partial \theta_{se}} & V_{se} \frac{\partial \Delta Q_i}{\partial V_{sh}} & \frac{\partial \Delta Q_i}{\partial \theta_{sh}} \\ \frac{\partial \Delta Q_j}{\partial \theta_{se}} & V_{se} \frac{\partial \Delta Q_j}{\partial V_{se}} & 0 \end{bmatrix} \quad (75)$$

$$[J'''] = \begin{bmatrix} \frac{\partial \Delta P_{se}}{\partial \theta_{se}} & V_{se} \frac{\partial \Delta P_{se}}{\partial V_{se}} & 0 \\ \frac{\partial \Delta Q_{ij}}{\partial \theta_{se}} & V_{se} \frac{\partial \Delta Q_{ij}}{\partial V_{se}} & 0 \\ \frac{\partial \Delta P_{ex}}{\partial \theta_{se}} & V_{se} \frac{\partial \Delta P_{ex}}{\partial V_{se}} & V_{sh} \frac{\partial \Delta P_{sh}}{\partial V_{sh}} \end{bmatrix} \quad (76)$$

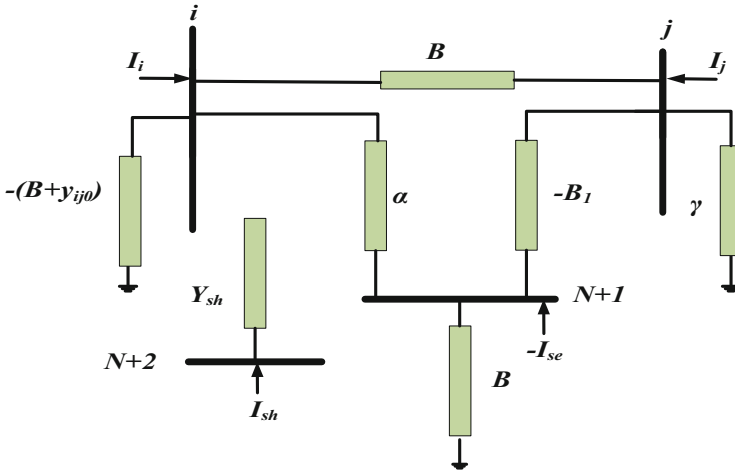


Fig. 14 Power indirect model of the UPFC

(d) The Indirect Model

The indirect model is proposed to diminish the complexities of incorporating the UPFC into the power flow solution [24]. This model represents the UPFC by an augmented circuit, as shown in Fig. 14. In this model, two fictitious buses, $N + 1$ and $N + 2$, are added to the system. The values in Fig. 14 are given as follows:

$$\alpha = \frac{Y_{se} (Y_0 + Y_{ij})}{Y_0 + Y_{ij} + Y_{se}} \quad (77)$$

$$B = \frac{Y_{ij} Y_{se}}{Y_0 + Y_{ij} + Y_{se}} \quad (78)$$

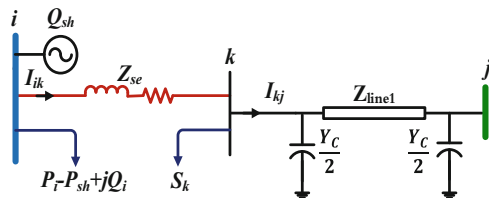
$$I_{N+1} = -I_{se} = \sum_{k=1}^{N+2} Y_{(N+1),k} V_k \quad (79)$$

$$I_{N+2} = -I_{sh} = \sum_{k=1}^{N+2} Y_{(N+2),k} V_k \quad (80)$$

(e) The Simplified Model

This model is based on representing the UPFC by injected loads which have been updating with the iterative process of the power flow as a function of the specified active and reactive powers flow in the TL, and the sending bus is converted to a PV-

Fig. 15 The simple model of the UPFC



bus as shown in Fig. 15 [25, 26]. This model is obtained from the current injection model of the series converter converted to two shunt current sources. Then, they have been converted to two injected loads at bus i and the bus the auxiliary bus k as follows:

$$S_i = V_i (I_{inj})^* \quad (81)$$

$$S_k = -V_k (I_{inj})^* \quad (82)$$

where I_{inj} denotes the injected current by the current source. The sending bus is represented as a generation bus that injects a shunt reactive power to control voltage magnitude, which can be calculated using the balanced reactive powers at bus i as follows:

$$Q_{sh} = \sum_{i=1}^n V_i V_k (G_{ik} \sin \delta_{ik} - B_{ik} \cos \delta_{ik}) + Q_i^{load} + Q_i \quad (83)$$

where, G and B represent real and imaginary components of line admittance. Q_i and Q_i^{load} are imaginary part of the S_i and reactive load at bus i . The active shunt power at bus i (P_{sh}) represents the injected power by the series converter which the shunt converter has delivered. The merit of this model is that the modification in the Jacobian matrix is avoided, and the specified voltage, active and reactive powers are predefined values. The disadvantage of this model is that the convergence of the power flow is very sensitive to the initial values of the injected loads.

(f) The Decoupled Model

Nabavi-Niaki and Iravani present the decoupled model of the UPFC [27]. This model is based on separating the sending and the receiving buses of the UPFC, and the sending bus is represented as PV while the receiving bus is illustrated by the PQ bus, as depicted in Fig. 16. The voltage magnitude of the sending bus and the injected load at the receiving buses are specified or predefined values in this model. Then, after the load flow, the UPFC's parameters can be assigned. The advantages of this model are simple to be applied, and the modification of the Jacobian matrix is avoided. In contrast, the shortcomings in this model include that the parameters of the UPFC are determined after the power flow solution, and the control in the voltage magnitude and the power flow is concurrent, not individually.

Fig. 16 The decoupled model of the UPFC

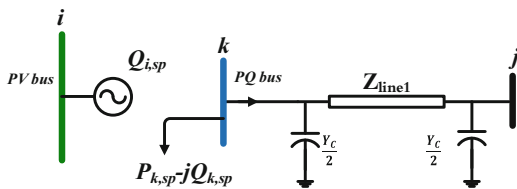
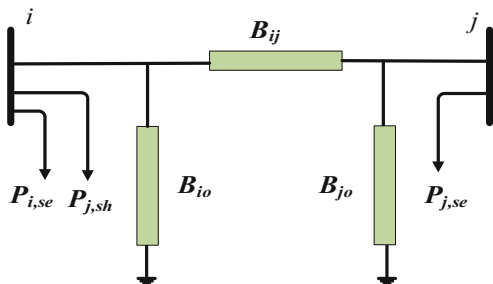


Fig. 17 The Π injection model of the UPFC



(g) The Π Injection Model

In this model, it is considered that there are no losses in the UPFC, and the resistance of the transmission line is neglected. This model is based on modeling the UPFC by a Π circuit with injected loads at the terminals of the UPFC, as shown in Fig. 17 [28, 29]. Π circuit includes the reactances of the UPFC, the transmission line reactance, and the transmission line's charging susceptance. The coefficients in Fig. 17 can be depicted as follows:

$$B_{ij} = \frac{X_c}{(X_\ell X_c + X_{se} X_c - X_{se} X_\ell)} \quad (84)$$

$$B_{io} = \frac{-1}{X_{sh}} + \frac{X_\ell}{(X_\ell X_c + X_{se} X_c - X_{se} X_\ell)} \quad (85)$$

$$B_{jo} = \frac{1}{X_c} + \frac{X_{se}}{(X_\ell X_c + X_{se} X_c - X_{se} X_\ell)} \quad (86)$$

$$P_{i,se} = V_i V_{se} \frac{(1 - y_0 X_L)}{(X_{se} - y_0 X_{se} X_L + X_L)} \sin(\theta_i - \theta_{se}) \quad (87)$$

$$P_{j,se} = \frac{-V_j V_{se}}{(X_{se} - y_0 X_{se} X_L + X_L)} \sin(\theta_j - \theta_{se}) \quad (88)$$

$$P_{j,sh} = \frac{V_n V_{sh}}{X_{sh}} \sin(\theta_n - \theta_{sh}) \quad (89)$$

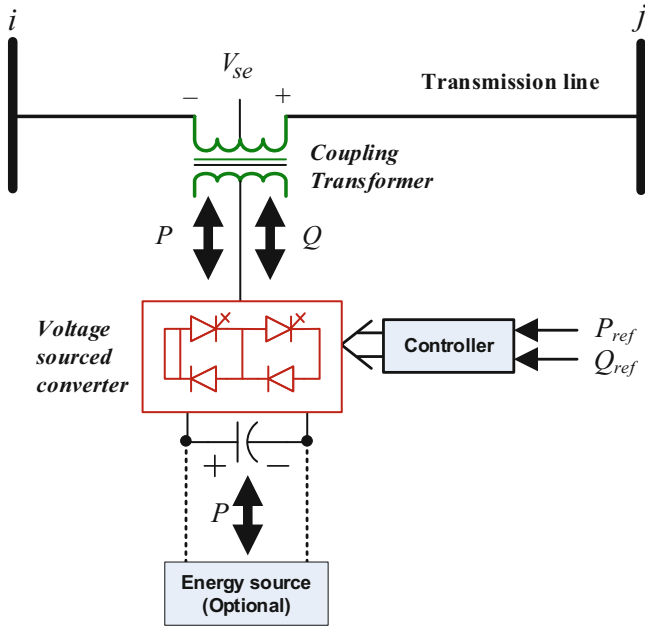


Fig. 18 Static Synchronous Series Compensator (SSSC)

In this model, the state variables of the UPFC are adjusted simultaneously with state variables of the system. The shunt susceptance of the transmission line and reactance of the coupling transformers of the UPFC are considered in this model. In addition to that, the block-diagonal of the Jacobian matrix is kept unchanged.

3.2.2 Modeling of SSSC

The SSSC is a VSC-based controller connected in series with the TL to control the TL’s active and reactive power flow. SSSC consists of a voltage source converter combined with DC linked to the bus, and it is connected to the system by a coupling transformer, as depicted in Fig. 18. SSSC injects a controllable AC voltage in series to the TL to control the active and the reactive power flow. The voltage source representation of the SSSC is shown in Fig. 19, where an AC voltage source represents the SSSC (V_{se}) connected in series with its impedance (Z_{se}). Several efforts have been presented for modeling the SSSC in power flow solution, which can be explained as follows:

The following equations describe the powers flow in the SSSC:

$$\begin{aligned}
 P_{ij} = & V_i^2 g_{ii} - V_i V_j (g_{ij} \cos(\theta_i - \theta_j) + b_{ij} \sin(\theta_i - \theta_j)) \\
 & - V_i V_{se} (g_{ij} \cos(\theta_i - \theta_{se}) + b_{ij} \sin(\theta_i - \theta_{se}))
 \end{aligned}
 \tag{90}$$

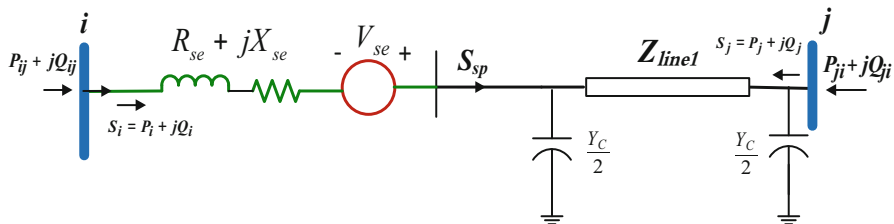


Fig. 19 Voltage sources representation of SSSC controller

$$Q_{ij} = -V_i^2 b_{ii} - V_i V_j (g_{ij} \sin(\theta_i - \theta_j) - b_{ij} \cos(\theta_i - \theta_j)) - V_i V_{se} (g_{ij} \sin(\theta_i - \theta_{se}) - b_{ij} \cos(\theta_i - \theta_{se})) \quad (91)$$

$$P_{ji} = V_j^2 g_{jj} - V_i V_j (g_{ij} \cos(\theta_j - \theta_i) + b_{ij} \sin(\theta_j - \theta_i)) + V_j V_{se} (g_{ij} \cos(\theta_j - \theta_{se}) + b_{ij} \sin(\theta_j - \theta_{se})) \quad (92)$$

$$Q_{ji} = -V_j^2 b_{jj} - V_i V_j (g_{ij} \sin(\theta_j - \theta_i) - b_{ij} \cos(\theta_j - \theta_i)) + V_j V_{se} (g_{ij} \sin(\theta_j - \theta_{se}) - b_{ij} \cos(\theta_j - \theta_{se})) \quad (93)$$

$$\text{Re}(V_{se} I_{ji}^*) = -V_i V_{se} (g_{ij} \cos(\theta_i - \theta_{se}) - b_{ij} \sin(\theta_i - \theta_{se})) + V_j V_{se} (g_{ij} \cos(\theta_j - \theta_{se}) - b_{ij} \sin(\theta_j - \theta_{se})) \quad (94)$$

where $g_{ij} + jb_{ij} = 1/Z_{se}$, $g_{ii} = g_{ij}$, $b_{ii} = b_{ij}$, $g_{jj} = g_{ij}$, $b_{jj} = b_{ij}$

(a) Multi Control Function Model

Multi control function model is based on a power injection representation [30]. The proposed model is presented in four control modes to control (1) the active power, (2) the reactive power, (3) the voltage of a particular bus, and (4) the reactance of the TL. The Jacobian matrix will be modified as follows:

$$\begin{bmatrix} \frac{\partial F}{\partial \theta_{se}} & \frac{\partial F}{\partial V_{se}} & \vdots & \frac{\partial F}{\partial \theta_i} & \frac{\partial F}{\partial V_i} & \frac{\partial F}{\partial \theta_j} & \frac{\partial F}{\partial V_j} \\ \frac{\partial PE}{\partial \theta_{se}} & \frac{\partial PE}{\partial V_{se}} & \vdots & \frac{\partial PE}{\partial \theta_i} & \frac{\partial PE}{\partial V_i} & \frac{\partial PE}{\partial \theta_j} & \frac{\partial PE}{\partial V_j} \\ \dots & \dots & \dots & \dots & \dots & \dots & \dots \\ \frac{\partial P_i}{\partial \theta_{se}} & \frac{\partial P_i}{\partial V_{se}} & \vdots & \frac{\partial P_i}{\partial \theta_i} & \frac{\partial P_i}{\partial V_i} & \frac{\partial P_i}{\partial \theta_j} & \frac{\partial P_i}{\partial V_j} \\ \frac{\partial Q_i}{\partial \theta_{se}} & \frac{\partial Q_i}{\partial V_{se}} & \vdots & \frac{\partial Q_i}{\partial \theta_i} & \frac{\partial Q_i}{\partial V_i} & \frac{\partial Q_i}{\partial \theta_j} & \frac{\partial Q_i}{\partial V_j} \\ \frac{\partial P_j}{\partial \theta_{se}} & \frac{\partial P_j}{\partial V_{se}} & \vdots & \frac{\partial P_j}{\partial \theta_i} & \frac{\partial P_j}{\partial V_i} & \frac{\partial P_j}{\partial \theta_j} & \frac{\partial P_j}{\partial V_j} \\ \frac{\partial Q_j}{\partial \theta_{se}} & \frac{\partial Q_j}{\partial V_{se}} & \vdots & \frac{\partial Q_j}{\partial \theta_i} & \frac{\partial Q_j}{\partial V_i} & \frac{\partial Q_j}{\partial \theta_j} & \frac{\partial Q_j}{\partial V_j} \end{bmatrix} \begin{bmatrix} \Delta \theta_{se} \\ \Delta V_{se} \\ \dots \\ \Delta \theta_i \\ \Delta V_i \\ \Delta \theta_j \\ \Delta V_j \end{bmatrix} = \begin{bmatrix} \frac{\partial Q}{\partial \theta} \\ -PE \\ \dots \\ -\Delta P_i \\ -\Delta Q_i \\ -\Delta P_j \\ -\Delta Q_j \end{bmatrix} \quad (95)$$

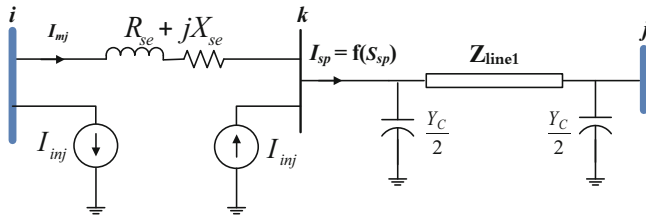


Fig. 20 The shunt injected currents representation of the SSSC

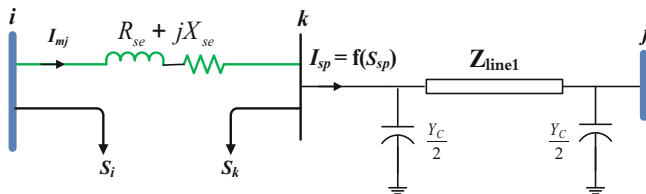


Fig. 21 The simple model of SSSC

(b) **The Simplified Model**

The simplified model in the NR power flow and the fast decouple are presented in [31] and [32]. In this model, the parameters of the SSSC are represented by the injecting loads at its terminals. This model is based on converting the voltage source (V_{se}) to current source (I_{inj}) which is calculated as a function of specified power flow in TL. Then, the current source is represented as two current sources, as shown in Fig. 20. The two current sources are converted into two injected loads, as shown in Fig. 21. Initially, the voltage source is converted to the current source as follows:

$$I_{inj} = \frac{V_{se}}{Z_{se}} \tag{96}$$

By application Kirchhoff’s Current Law at bus j in Fig. 20, the injected current is given as follows:

$$I_{inj} = I_{sp} - I_{ik} = \left(\frac{S_{sp}}{V_j} \right)^* - \left(\frac{V_i - V_k}{Z_{se}} \right) \tag{97}$$

where, $S_{sp} = P_{sp} + jQ_{sp}$ and $I_{se} = I_{sp}$. The shunt currents are converted to the complex loads using the following equations:

$$S_i = V_i (I_{inj})^* \tag{98}$$

$$S_k = -V_k (I_{inj})^* \quad (99)$$

The value of V_{se} SSSC can be calculated easily using (95).

$$V_{se} = I_{inj} \times Z_{se} \quad (100)$$

The advantages of this model are that the modification in the Jacobian matrix has been avoided, the control in active and reactive powers can be achieved separately or simultaneously in different control modes, and the constraints violations can be easily handled.

(c) The Current-Based Model

The current-based model is based on using the real component ($\text{Re}[I_{se}]$) and the imaginary component ($\text{Im}[I_{se}]$) of the SSSC's current instead of the injected voltage [33]. The active and reactive powers in the SSSC's terminal are equal to the product of I_{se} and throughout the terminal voltages (V_S , V_R). The current of the SSSC (I_{se}) can be split into real and imaginary parts $\text{Re}[I_{se}]$ and $\text{Im}[I_{se}]$, respectively. Figure 22 shows the current based model. The following equations describe the power flow due to incorporation of the SSSC:

$$S_{ST} = P_{ST} + jQ_{ST} = V_S(-I_{se})^* \quad (101)$$

$$S_{ST} = V_S (\cos(\delta_S) + j \sin(\delta_S)) (-(\text{Re}[I_{se}] - j \text{Im}[I_{se}])) \quad (102)$$

$$P_{ST} = \text{Re}[V_S(-I_{se})^*] = -V_S (\text{Re}[I_{se}] \cos(\delta_S) + \text{Im}[I_{se}] \sin(\delta_S)) \quad (103)$$

$$Q_{ST} = \text{Im}[V_S(-I_{se})^*] = -V_S (\text{Re}[I_{se}] \sin(\delta_S) - \text{Im}[I_{se}] \cos(\delta_S)) \quad (104)$$

$$S_{RT} = P_{RT} + jQ_{RT} = V_R(-I_{se})^* \quad (105)$$

$$S_{RT} = V_R (\cos(\delta_R) + j \sin(\delta_R)) \times (-(\text{Re}[I_{se}] - j \text{Im}[I_{se}])) \quad (106)$$

$$P_{RT} = \text{Re}[V_R I_{se}^*] = V_R (\text{Re}[I_{se}] \cos(\delta_R) + \text{Im}[I_{se}] \sin(\delta_R)) \quad (107)$$

$$Q_{RT} = \text{Im}[V_R I_{se}^*] = V_R (\text{Re}[I_{se}] \sin(\delta_R) - \text{Im}[I_{se}] \cos(\delta_R)) \quad (108)$$

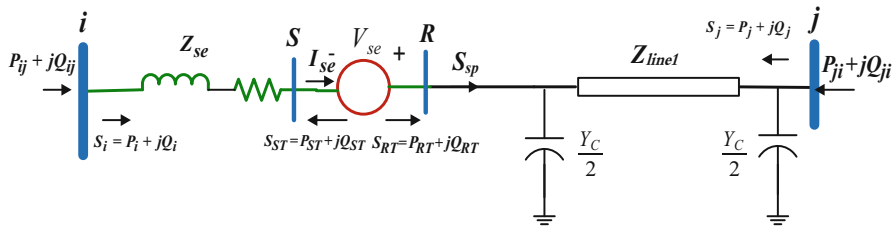


Fig. 22 The current-based model

The system equations at the sending and receiving bus of SSSC terminals that have been listed into NR power flow are listed as follows:

$$P_i = V_i^2 G_T - V_i V_S (G_{se} \cos(\delta_i - \delta_S) + B_{se} \sin(\delta_i - \delta_S)) \quad (109)$$

$$Q_i = -V_i^2 B_T - V_i V_S (G_{se} \sin(\delta_i - \delta_S) - B_{se} \cos(\delta_i - \delta_S)) \quad (110)$$

$$P_S = V_S^2 G_{se} - V_S V_j (G_{se} \cos(\delta_S - \delta_j) + B_{se} \sin(\delta_S - \delta_j)) - P_{ST} \quad (111)$$

$$Q_S = -V_S^2 B_{se} - V_S V_j (G_{se} \sin(\delta_S - \delta_j) - B_{se} \cos(\delta_S - \delta_D)) - Q_j \quad (112)$$

$$P_R = V_R^2 \left(\frac{G_L + G_C}{2} \right) - V_R V_j (G_L \cos(\delta_R - \delta_L) + B_V \sin(\delta_R - \delta_L)) - P_{RT} \quad (113)$$

$$Q_R = -V_R^2 \left(\frac{B_L + B_C}{2} \right) - V_R V_j (G_L \sin(\delta_R - \delta_L) - B_L \cos(\delta_L - \delta_R)) - Q_{RT} \quad (114)$$

$$P_j = V_j^2 \left(\frac{G_L + G_C}{2} \right) - V_j V_R (G_L \cos(\delta_L - \delta_R) + B_L \sin(\delta_L - \delta_R)) \quad (115)$$

$$Q_j = -V_j^2 \left(\frac{B_L + B_C}{2} \right) - V_j V_R (G_L \sin(\delta_L - \delta_R) - B_L \cos(\delta_L - \delta_R)) \quad (116)$$

where, G_L and B_L are the conductance and substance of the transmission line. The control variables in this model include the active power and reactive power, the injected voltage, and the reactance of the SSSC. The modification in the Jacobian matrix is required in this model. However, the merit of this model is that it has a fast convergence characteristic compared with the power injection model.

(d) The Developed Power Injection Model

In this model, the linearized power flow equations are combined with the system equations corresponding to the rest of the network. The power equations of the SSSC in this model or the injected powers by SSSC are captured from the voltage source representation of the SSSC in Fig. as follows:

$$S_i = P_i + jQ_i = V_i(I_{se})^* = V_i \left(Y''_{ii} V_i + Y''_{ij} V_j + Y'_i V_s \right)^* \quad (117)$$

$$S_j = P_j + jQ_j = V_j(I_{se})^* = V_j \left(Y''_{ji} V_i + Y''_{jj} V_j + Y'_j V_s \right)^* \quad (118)$$

$$P_i = G''_{ii} V_i^2 + \left(G''_{ij} \cos \delta_{ij} + B''_{ij} \sin \delta_{ij} \right) V_i V_j + \left(G'_{ii} \cos \delta_{is} + B'_{ii} \sin \delta_{is} \right) V_i V_s \quad (119)$$

$$Q_i = -B''_{ii} V_i^2 + \left(G''_{ij} \sin \delta_{ij} - B''_{ij} \cos \delta_{ij} \right) V_i V_j + \left(G'_{ii} \sin \delta_{is} - B'_{ii} \cos \delta_{is} \right) V_i V_s \quad (120)$$

$$P_j = G''_{jj} V_j^2 + \left(G''_{ji} \cos \delta_{ji} + B''_{ji} \sin \delta_{ji} \right) V_i V_j + \left(G'_{ji} \cos \delta_{js} + B'_{ji} \sin \delta_{js} \right) V_j V_s \quad (121)$$

$$Q_j = -B''_{jj} V_j^2 + \left(G''_{ji} \sin \delta_{ji} - B''_{ji} \cos \delta_{ji} \right) V_i V_j + \left(G'_{ji} \sin \delta_{js} - B'_{ji} \cos \delta_{js} \right) V_j V_s \quad (122)$$

where;

$$Y''_{ii} = G''_{ii} + jB''_{ii} = -\frac{Y_{ii}^2 Z_{se}}{1 + Y_{ii} Z_{se}} \quad (123)$$

$$Y''_{jj} = G''_{jj} + jB''_{jj} = -\frac{Y_{ij} Y_{ji} Z_{se}}{1 + Y_{ii} Z_{se}} \quad (124)$$

$$Y''_{ij} = Y''_{ji} = G''_{ij} + jB''_{ij} = -\frac{Y_{ij} Y_{ij} Z_{se}}{1 + Y_{ii} Z_{se}} \quad (125)$$

The original admittance and the Jacobian matrix are not modified; only a new Jacobian matrix was added for representing the SSSC in NR power flow. In addition to that, the model is presented with six control modes.

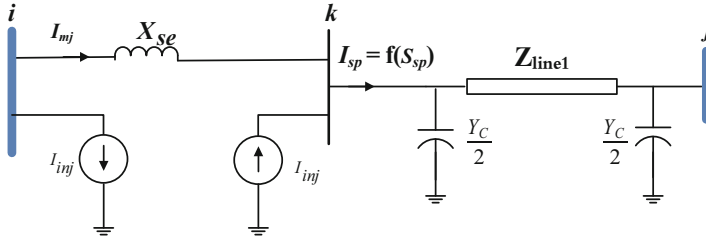


Fig. 23 The implicit model of the SSSC

(e) The Implicit Model

This model relies on representing the SSSC by injection currents at its terminal, as shown in Fig. 23 [34]. This model is established for the Newton–Raphson current injection load flow method (NR-CIM). The injected current is calculated as a function of the specified values.

$$I_{inj} = I_{sp} - I_{ik} = \left(\frac{S_{sp}}{V_j} \right)^* - \left(\frac{V_i - V_k}{Z_{se}} \right) \quad (126)$$

To model the SSSC into the NR-CIM, the injected current is split into real and imaginary parts as follows:

$$I_{inj}^{Re} = \frac{(P_{kj}^{sp} V_k^{Re} + Q_{kj} V_k^{Im})}{V_k^2} - \frac{(V_i^{Im} - V_k^{Im})}{X_s} \quad (127)$$

$$I_{inj}^{Im} = \frac{(P_{kj}^{sp} V_k^{Im} - Q_{kj} V_k^{Re})}{V_k^2} + \frac{(V_i^{Re} - V_k^{Re})}{X_s} \quad (128)$$

Where

$$I_f^{Re} = \text{Re}(I_f^{sp}) - \left(\frac{P_f^{sp} V_f^{Re} + Q_f^{sp} V_f^{Im}}{(V_f^{Re})^2 + (V_f^{Im})^2} \right) + \sum_{i=1}^n (G_{fi} V_i^{Re} - B_{fi} V_i^{Im}) \quad (129)$$

$$I_f^{Im} = \text{Im}(I_f^{sp}) - \left(\frac{P_f^{sp} V_f^{Im} - Q_f^{sp} V_f^{Re}}{(V_f^{Re})^2 + (V_f^{Im})^2} \right) + \sum_{i=1}^n (G_{fi} V_i^{Im} - B_{fi} V_i^{Re}) \quad (130)$$

$$B_{kk}^* = B_{kk} - \left(\frac{Q_k^{sp} ((V_k^{Re})^2 - (V_k^{Im})^2) - 2P_k^{sp} V_k^{Re} V_k^{Im}}{V_k^4} \right) \quad (131)$$

$$B_{kk}^{**} = -B_{kk} - \left(\frac{Q_k^{\text{sp}} \left((V_k^{\text{Re}})^2 - (V_k^{\text{Im}})^2 \right) - 2P_k^{\text{sp}} V_k^{\text{Re}} V_k^{\text{Im}}}{V_k^4} \right) \quad (132)$$

$$G_{kk}^* = G_{kk} - \left(\frac{P_k^{\text{sp}} \left((V_k^{\text{Re}})^2 - (V_k^{\text{Im}})^2 \right) + 2V_k^{\text{Re}} V_k^{\text{Im}} Q_k^{\text{sp}}}{V_k^4} \right) \quad (133)$$

$$G_{kk}^{**} = G_{kk} + \left(\frac{P_k^{\text{sp}} \left((V_k^{\text{Re}})^2 - (V_k^{\text{Im}})^2 \right) + 2V_k^{\text{Re}} V_k^{\text{Im}} Q_k^{\text{sp}}}{V_k^4} \right) \quad (134)$$

In this model, the modification in the NR-CIM is avoided, and the control in active and reactive power can be achieved through simulations or concurrently.

3.2.3 Modeling of STATCOM

STATCOM is a VSC-based controller connected in shunt to a specific bus. The STATCOM consists of an inverter and a DC capacitor connected to the system by a coupling transformer, as depicted in Fig. 24. The equivalent circuit of the STATCOM is shown in Fig. 25, which consists of a voltage source with its impedance connected to the shunt with the system. The STATCOM regulates the bus's voltage magnitude, which is connected to it by injecting reactive powers to this bus. The control in the injected reactive power can be accomplished by controlling the injected AC voltage to the system (V_{sh}). If $V_{\text{sh}} = V_m$, the STATCOM will not inject reactive power to bus m . If $V_{\text{sh}} > V_m$, the STATCOM will inject reactive power to bus m , and it works as a capacitor. If $V_{\text{sh}} < V_m$, the STATCOM will absorb reactive power from bus m , and it works as an inductor. The power flow according to the equivalent circuit can be specified as follows:

$$P_{\text{sh}} = V_i^2 g_{\text{sh}} - V_i V_{\text{sh}} (g_{\text{sh}} \cos(\theta_i - \theta_{\text{sh}}) + b_{\text{sh}} \sin(\theta_i - \theta_{\text{sh}})) \quad (135)$$

$$Q_{\text{sh}} = -V_i^2 b_{\text{sh}} - V_i V_{\text{sh}} (g_{\text{sh}} \sin(\theta_i - \theta_{\text{sh}}) - b_{\text{sh}} \cos(\theta_i - \theta_{\text{sh}})) \quad (136)$$

where $g_{\text{sh}} + jb_{\text{sh}} = 1/Z_{\text{sh}}$. V_{sh} can be calculated as follows:

$$V_{\text{sh}} = V_i + Z_{\text{sh}} \left(\frac{P_{\text{sh}} + jQ_{\text{sh}}}{V_i} \right)^* \quad (137)$$

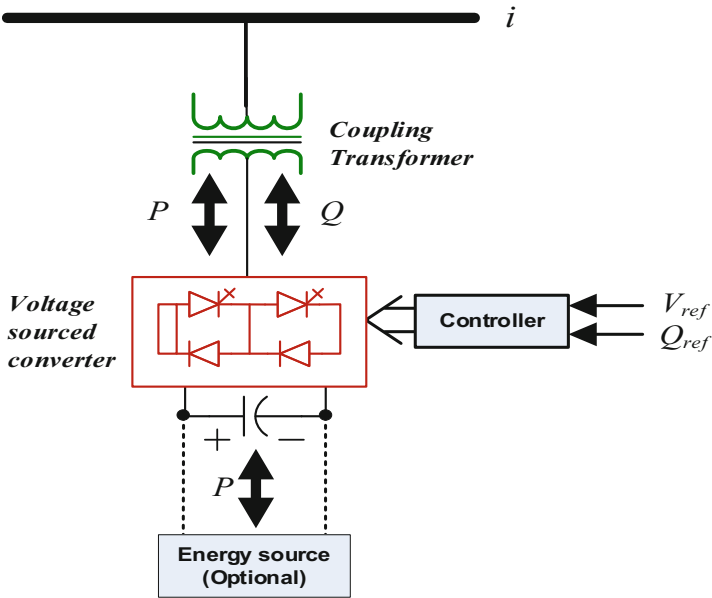
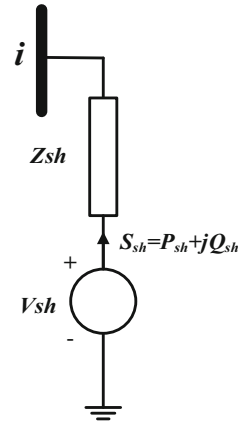


Fig. 24 Schematic diagram of STATCOM

Fig. 25 Equivalent circuit of STATCOM



The exchanged active power between the AC system and DC link is zero, which can be formulated as follows:

$$PE = \text{Re} (V_{sh} V_{sh}^*) = 0 \tag{138}$$

It should be pointed out here that STATACOM has several advantages over the SVC: (1) shows high and faster response, (2) needs less space, (3) can be combined with several energy storage systems such as the battery, SMES (superconducting

magnetic energy storage), and fuel cell. The STATACOM has healthy performance at low voltage conditions. Several efforts have been presented for modeling the STATCOM, which can be depicted as follows:

(a) **Multi-Control Functional Model**

The multi-control mode is presented in [35]. In this model, the STATACOM can control nine parameters as follows:

– *Mode 1*

In this mode, the STATACOM can control the voltage magnitude of the bus which has been connected to it as:

$$V_i - V_i^{\text{Spec}} = 0 \quad (139)$$

– *Mode 2*

In this mode, the STATACOM can control the injected reactive power as follows:

$$Q_{\text{sh}} - Q_{\text{sh}}^{\text{Spec}} = 0 \quad (140)$$

– *Mode 3*

In this mode, the STATACOM can control the equivalent impedance or the reactance, which can be calculated as a function of the V_{sh} as:

$$X_{\text{shunt}} = \text{Im} \left(\frac{V_{\text{sh}}}{I_{\text{sh}}} \right) = \text{Im} \left(\frac{V_{\text{sh}}}{(V_i - V_{\text{sh}}) / Z_{\text{sh}}} \right) \quad (141)$$

– *Mode 4*

In this mode, the STATACOM can control the magnitude of the current I_{sh} , in capacitive compensation function as follows:

$$I_{\text{sh}}^{\text{Spec}} \angle (\theta_{\text{sh}} + 90^\circ) = \frac{V_i - V_{\text{sh}}}{Z_{\text{sh}}} \quad (142)$$

$$\text{Re} \left(I_{\text{gh}}^{\text{Spec}} \angle (\theta_{\text{sh}} + 90^\circ) \right) = \text{Re} \left(\frac{V_i - V_{\text{sh}}}{Z_{\text{sh}}} \right) \text{ or} \quad (143)$$

$$\text{Im} \left(I_{\text{gh}}^{\text{Spec}} \angle (\theta_{\text{sh}} + 90^\circ) \right) = \text{Im} \left(\frac{V_i - V_{\text{sh}}}{Z_{\text{sh}}} \right)$$

– *Mode 5*

In this mode, the STATACOM can control the magnitude of the current I_{sh} in inductive compensation function as follows:

$$\text{Re} \left(I_{\text{sh}}^{\text{Spec}} \angle (\theta_{\text{sh}} - 90^\circ) \right) = \text{Re} \left(\frac{V_i - V_{\text{sh}}}{Z_{\text{gh}}} \right) \text{ or} \quad (144)$$

$$\text{Im} \left(I_{\text{sh}}^{\text{Spec}} \angle (\theta_{\text{sh}} - 90^\circ) \right) = \text{Im} \left(\frac{V_i - V_{\text{sh}}}{Z_{\text{sh}}} \right)$$

– *Mode 6*

In this mode, the STATACOM can control injected voltage magnitude V_{sh} as follows:

$$V_{sh} - V_{sh}^{Spec} = 0 \quad (145)$$

– *Mode 7*

In this mode, the STATACOM can control the voltage magnitude of a remote bus j as follows:

$$V_j - V_j^{Spec} = 0 \quad (146)$$

– *Mode 8*

In this mode, the STATACOM can control reactive power flow in TL as follows:

$$Q_{jk} - Q_{jk}^{Spec} = 0 \quad (147)$$

– *Mode 9*

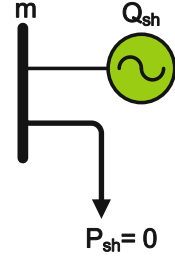
In this mode, the STATACOM can control apparent power flow in TL as follows:

$$S_{jk} - S_{jk}^{Spec} = 0 \quad (148)$$

It should be highlighted here that V_{sh} and θ_{sh} are control variables the control. The following equations express the implementation of the proposed model into the mode in NR power flow:

$$\begin{bmatrix} \frac{\partial PE}{\partial \theta_i} & \frac{\partial PE}{\partial V_{sh}} & \frac{\partial PE}{\partial \theta_i} & \frac{\partial PE}{\partial V_i} & 0 & 0 & 0 & 0 \\ \frac{\partial F}{\partial \theta_{sh}} & \frac{\partial F}{\partial V_{sh}} & \frac{\partial F}{\partial \theta_i} & \frac{\partial F}{\partial V_i} & \frac{\partial F}{\partial \theta_j} & \frac{\partial F}{\partial V_j} & \frac{\partial F}{\partial \theta_k} & \frac{\partial F}{\partial V_k} \\ \frac{\partial P_i}{\partial \theta_{sh}} & \frac{\partial P_i}{\partial V_{sh}} & \frac{\partial P_i}{\partial \theta_i} & \frac{\partial P_i}{\partial V_i} & \frac{\partial P_i}{\partial \theta_j} & \frac{\partial P_i}{\partial V_j} & \frac{\partial P_i}{\partial \theta_k} & \frac{\partial P_i}{\partial V_k} \\ \frac{\partial Q_i}{\partial \theta_{sh}} & \frac{\partial Q_i}{\partial V_{sh}} & \frac{\partial Q_i}{\partial \theta_i} & \frac{\partial Q_i}{\partial V_i} & \frac{\partial Q_i}{\partial \theta_j} & \frac{\partial Q_i}{\partial V_j} & \frac{\partial Q_i}{\partial \theta_k} & \frac{\partial Q_i}{\partial V_k} \\ 0 & 0 & \frac{\partial P_j}{\partial \theta_i} & \frac{\partial P_j}{\partial V_i} & \frac{\partial P_j}{\partial \theta_j} & \frac{\partial P_j}{\partial V_j} & \frac{\partial P_j}{\partial \theta_k} & \frac{\partial P_j}{\partial V_k} \\ 0 & 0 & \frac{\partial Q_j}{\partial \theta_i} & \frac{\partial Q_j}{\partial V_i} & \frac{\partial Q_j}{\partial \theta_j} & \frac{\partial Q_j}{\partial V_j} & \frac{\partial Q_j}{\partial \theta_k} & \frac{\partial Q_j}{\partial V_k} \\ 0 & 0 & \frac{\partial P_k}{\partial \theta_i} & \frac{\partial P_k}{\partial V_i} & \frac{\partial P_k}{\partial \theta_j} & \frac{\partial P_k}{\partial V_j} & \frac{\partial P_k}{\partial \theta_k} & \frac{\partial P_k}{\partial V_k} \\ 0 & 0 & \frac{\partial Q_k}{\partial \theta_i} & \frac{\partial Q_k}{\partial V_i} & \frac{\partial Q_k}{\partial \theta_j} & \frac{\partial Q_k}{\partial V_j} & \frac{\partial Q_k}{\partial \theta_k} & \frac{\partial Q_k}{\partial V_k} \end{bmatrix} \begin{bmatrix} \Delta \theta_{sh} \\ \Delta V_{sh} \\ \Delta \theta_i \\ \Delta V_i \\ \Delta \theta_j \\ \Delta V_j \\ \Delta \theta_k \\ \Delta V_k \end{bmatrix} = \begin{bmatrix} -PE \\ -\Delta F \\ -\Delta P_i \\ -\Delta Q_i \\ -\Delta P_j \\ -\Delta Q_j \\ -\Delta P_k \\ -\Delta Q_k \end{bmatrix} \quad (149)$$

In this model, the modification into the Jacobian is required to include the parameters of the STATACOM. However, the advantages of this model are that nine

Fig. 26 Simplified model

parameters can be controlled separately, and the operating constraints are considered in this model.

(b) Simplified Model

In this model, the STATCOM is represented as a synchronous condenser with ($P = 0$) and the bus i is converted to a PV bus as shown in Fig. 26 [36, 37]. The reactive output power can be calculated from the balanced reactive power at this bus as follows:

$$Q_{sh} = \sum_{i=1}^n V_i V_n (G_{in} \sin \delta_{in} - B_{in} \cos \delta_{in}) + Q_i^{\text{load}} \quad (150)$$

where, Q_i^{load} denotes the reactive load at bus i .

3.2.4 Modeling of IPFC

The IPFC is a developed FACTS device consisting of two or more converters connected in series with the TLs to control the power flow in multiple TLs. Figure 27 shows a simple construction of the IPFC. One of these converters is connected in series to the TL named the master converter, while the other converter, called the slave converter, is connected in series to another TL and combined through a common DC link [38, 39]. The IPFC can control three parameters: the active and reactive power flow in the master TL and the active or reactive power flow in the slave transmission line.

The voltage source representation of the IPFC is shown in Fig. 28 [39]. From Fig. 28, the power equations at the sending and receiving end buses can be listed as follows:

The power flow equations of the IPFC can be found in Fig. 28:

$$P_{in} = V_i^2 g_{in} - V_i V_n (g_{in} \cos \theta_{in} + b_{in} \sin \theta_{in}) - V_i V_{se_{in}} (g_{in} \cos (\theta_i - \theta_{se_{in}}) + b_{in} \sin (\theta_i - \theta_{se_{in}})) \quad (151)$$

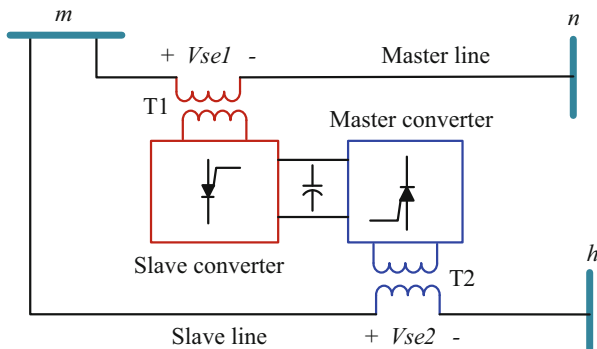


Fig. 27 IPFC schematic diagram

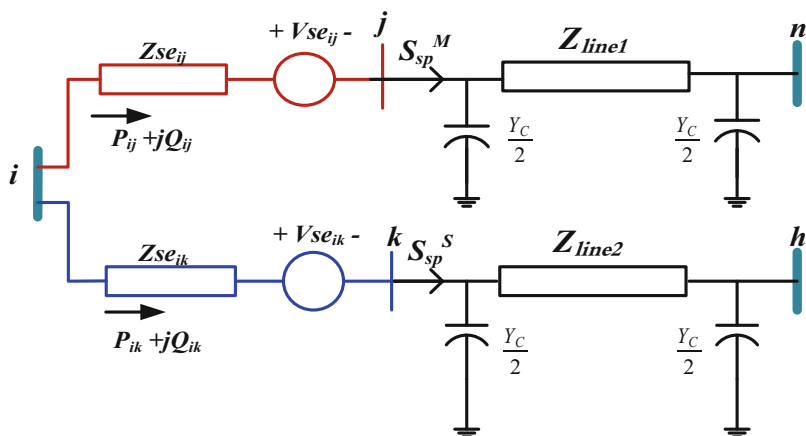


Fig. 28 Voltage sources representation of IPFC controller

$$\begin{aligned}
 P_{ni} = & V_n^2 g_{in} - V_i V_n (g_{in} \cos(\theta_n - \theta_i) + b_{in} \sin(\theta_n - \theta_i)) \\
 & + V_n V_{se_{in}} (g_{in} \cos(\theta_n - \theta_{se_{in}}) + b_{in} \sin(\theta_n - \theta_{se_{in}}))
 \end{aligned} \quad (152)$$

$$\begin{aligned}
 Q_{ni} = & -V_n^2 b_{nn} - V_i V_n (g_{in} \sin(\theta_n - \theta_i) - b_{in} \cos(\theta_n - \theta_i)) \\
 & + V_n V_{se_{in}} (g_{in} \sin(\theta_n - \theta_{se_{in}}) - b_{in} \cos(\theta_n - \theta_{se_{in}}))
 \end{aligned} \quad (153)$$

$$\begin{aligned}
 Q_{in} = & -V_i^2 b_{in} - V_i V_n (g_{in} \sin \theta_{in} - b_{in} \cos \theta_{in}) \\
 & - V_i V_{se_{in}} (g_{in} \sin(\theta_i - \theta_{in e_{in}}) - b_{in} \cos(\theta_i - \theta_{se_{in}}))
 \end{aligned} \quad (154)$$

where, $g_{in} = \text{Re}(1/Z_{se_{in}})$, $b_{in} = \text{Im}(1/Z_{se_{in}})$, P_{in} , $Q_{in}(n = j, k)$

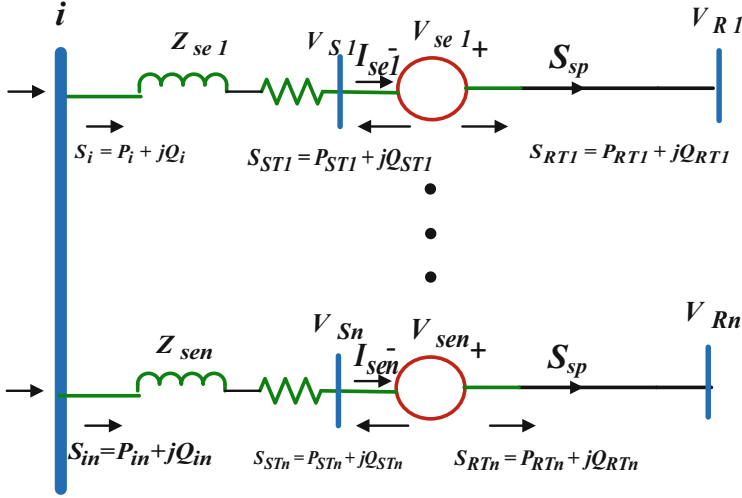


Fig. 29 The current-based model of the IPFC

(a) The Current-Based Model

The current-based model of the IPFC is similar to the current-based model of the SSSC [40]. Figure 29 shows the current-based model of the IPFC. The current-based model is based on using the real component ($\text{Re}[I_{sen}]$) and the imaginary component ($\text{Im}[I_{sen}]$) of the IPFC current multiplied by the terminal voltage according to the following equations:

$$S_{STn} = P_{STn} + jQ_{STn} = V_{Sn}(-I_{sen})^* \quad (155)$$

$$S_{STn} = V_{Sn} (\cos(\delta_{Sn}) + j \sin(\delta_{Sn})) (-(\text{Re}[I_{sen}] - j \text{Im}[I_{sen}]))) \quad (156)$$

$$P_{STn} = \text{Re}[V_{Sn}(-I_{sen})^*] = -V_S (\text{Re}[I_{sen}] \cos(\delta_{Sn}) + \text{Im}[I_{sen}] \sin(\delta_{Sn})) \quad (157)$$

$$Q_{STn} = \text{Im}[V_{Sn}(-I_{sen})^*] = -V_S (\text{Re}[I_{sen}] \sin(\delta_{Sn}) - \text{Im}[I_{sen}] \cos(\delta_{Sn})) \quad (158)$$

$$S_{RTn} = P_{RTn} + jQ_{RTn} = V_{Rn}(-I_{sen})^* \quad (159)$$

$$S_{RTn} = V_{Rn} (\cos(\delta_{Rn}) + j \sin(\delta_{Rn})) \times (-(\text{Re}[I_{sen}] - j \text{Im}[I_{sen}]))) \quad (160)$$

$$P_{RT} = \text{Re} [V_S I_-^*] = V_R (\text{Re} [I_{\text{sen}}] \cos (\delta_{Rn}) + \text{Im} [I_{\text{sen}}] \sin (\delta_{Rn})) \quad (161)$$

$$Q_{RT} = \text{Im} [V_S I_-^*] = V_R (\text{Re} [I_{\text{sen}}] \sin (\delta_{Rn}) - \text{Im} [I_{\text{sen}}] \cos (\delta_{Rn})) \quad (162)$$

The NR power flow will be modified as follows:

$$\begin{bmatrix} [A] & [B] \\ [C] & [D] \end{bmatrix} \cdot \begin{bmatrix} \Delta \delta \\ \Delta V \\ \Delta \text{Re} \begin{bmatrix} I \\ I_{\text{Se}1} \end{bmatrix} \\ \Delta \text{Im} [I_{\text{Se}1}] \\ \vdots \\ \Delta \text{Re} [I_{\text{Sen}}] \\ \Delta \text{Im} [I_{\text{Sen}}] \end{bmatrix} = \begin{bmatrix} \Delta P \\ \Delta Q \\ \Delta \text{REF}_1 \\ \vdots \\ \Delta \text{REF}_{2n-1} \\ \Delta P_0 \end{bmatrix} \quad (163)$$

$$[A] = \begin{bmatrix} \frac{\partial P}{\partial \delta} & \frac{\partial P}{\partial V} \\ \frac{\partial Q}{\partial \delta} & \frac{\partial Q}{\partial V} \end{bmatrix} \quad (164)$$

$$[B] = \begin{bmatrix} \frac{\partial P}{\partial \text{Re}[I_{S1}]} \cdots \frac{\partial P}{\partial \text{Re}[I_{Sn}]} \\ \frac{\partial Q}{\partial \text{Re}[I_{S1}]} \cdots \frac{\partial Q}{\partial \text{Im}[I_{Sn}]} \end{bmatrix} \quad (165)$$

$$[C] = \begin{bmatrix} \frac{\partial \text{REF}_1}{\partial \delta} & \frac{\partial \text{REF}_1}{\partial V} \\ \vdots & \vdots \\ \frac{\partial \text{REF}_{2n-1}}{\partial \delta} & \frac{\partial \text{REF}_{2n-1}}{\partial V} \\ \frac{\partial P_0}{\partial \delta} & \frac{\partial P_0}{\partial V} \end{bmatrix} \quad (166)$$

$$[D] = \begin{bmatrix} \frac{\partial \text{REF}_1}{\partial \text{Re}[I_{\text{Se}1}]} & \frac{\partial \text{REF}_1}{\partial \text{Im}[I_{\text{Se}1}]} & \cdots & \frac{\partial \text{REF}_1}{\partial \text{Re}[I_{\text{Sen}}]} & \frac{\partial \text{REF}_1}{\partial \text{Im}[I_{\text{Sen}}]} \\ \vdots & \vdots & \vdots & \vdots & \vdots \\ \frac{\partial \text{REF}_{2n-1}}{\partial \text{Re}[I_{\text{Se}1}]} & \frac{\partial \text{REF}_{2n-1}}{\partial \text{Im}[I_{\text{Se}1}]} & \cdots & \frac{\partial \text{REF}_{2n-1}}{\partial \text{Re}[I_{\text{Sen}}]} & \frac{\partial \text{REF}_{2n-1}}{\partial \text{Im}[I_{\text{Sen}}]} \\ \frac{\partial P_0}{\partial \text{Re}[I_{\text{Se}1}]} & \frac{\partial P_0}{\partial \text{Im}[I_{\text{Se}1}]} & \cdots & \frac{\partial P_0}{\partial \text{Re}[I_{\text{Sen}}]} & \frac{\partial P_0}{\partial \text{Im}[I_{\text{Sen}}]} \end{bmatrix} \quad (167)$$

REF is a reference quantity that represents the free parameters for each branch, which can be defined as follows:

- The real power flow in the k th IPFC branch

$$\text{REF}_i = P_{in} = V_i^2 \cdot G_{Sk} - V_i \cdot V_{Sk} \cdot (G_{Sk} \cdot \cos(\delta_i - \delta_{Sk}) + B_{Sk} \cdot \sin(\delta_i - \delta_{Sk})) \quad (168)$$

- The reactive power flow in the k th IPFC branch

$$\text{REF}_i = Q_{in} = -V_i^2 \cdot B_{Sk} - V_i \cdot V_{Sk} \cdot (G_{Sk} \cdot \sin(\delta_i - \delta_{Sk}) - B_{Sk} \cdot \cos(\delta_i - \delta_{Sk})) \quad (169)$$

- The injected voltage in the k th IPFC branch

$$\text{REF}_i = V_{sen} = \sqrt{V_{Sk}^2 + V_{Rk}^2 - 2 \cdot V_{Sk} \cdot V_{Rk} \cdot \cos(\delta_{Sk} - \delta_{Rk})} \quad (170)$$

- The line current magnitude in the k th IPFC

$$\text{REF}_i = I_{Sk} = \sqrt{\text{Re}[I_{Sk}]^2 + \text{Im}[I_{Sk}]^2} \quad (171)$$

- In this model, the parameters that can be controlled include the active power, the reactive power, the injected voltage magnitude, and the voltage bus voltage. The model has good convergence characteristics.

(b) The Developed IPFC Model

In this model, the IPFC is represented by injected loads at its terminals. These are calculated as a function of the specified power flow in the TLs. The model is conceptualized from the current source representations where the voltages are converted to current sources. Then the current sources are converted to injected loads as depicted in Fig. 30 according to the following equations:

$$S_j = -V_j (I_{M,\text{inj}})^* \quad (172)$$

$$S_k = -V_k (I_{S,\text{inj}})^* \quad (173)$$

$$S_m = V_m (I_m)^* \quad (174)$$

Where;

$$I_{M,\text{inj}} = I_{sp}^M - I_{mj} = \left(\frac{S_{sp}^M}{V_j} \right)^* - \left(\frac{V_m - V_j}{Z_{se1}} \right) \quad (175)$$

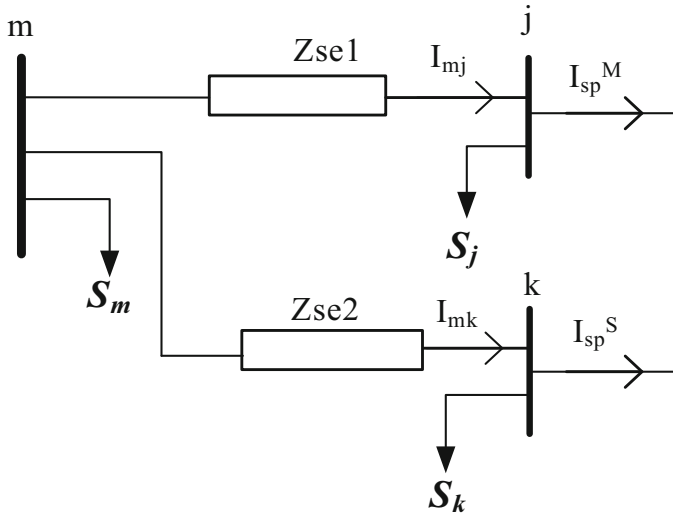


Fig. 30 Developed IPFC model based on injected fictitious loads

$$I_{S,\text{inj}} = I_{\text{sp}}^S - I_{mk} = \left(\frac{S_{\text{sp}}^S}{V_k} \right)^* - \left(\frac{V_m - V_k}{Z_{\text{se2}}} \right) \quad (176)$$

where V_j , V_k and V_m are the voltages at buses j , k and m . S_{sp}^M and S_{sp}^S are the specified apparent power flow in the master and the slave TLs. The injected voltages are calculated as follows:

$$V_{\text{se1}} = I_{M,\text{inj}} Z_{\text{se1}} \quad (177)$$

$$V_{\text{se2}} = I_{S,\text{inj}} Z_{\text{se2}} \quad (178)$$

The net exchanged active powers in the DC link of the converters, which can be described as follows:

$$\sum P_{\text{ex}} = P_{\text{ex1}} + P_{\text{ex2}} = 0 \quad (179)$$

Where

$$P_{\text{ex1}} = \text{Re} (V_{\text{se1}} (I_{\text{se1}})^*) \quad (180)$$

$$P_{\text{ex2}} = \text{Re} (V_{\text{se2}} (I_{\text{se2}})^*) \quad (181)$$

where P_{ex1} is the exchanged power between the DG link and master TL while P_{ex2} is the exchanged power between the DG link and slave TL. The main advantage of this model is that the modification in the Jacobian matrix is avoided where the parameters of the IPFC (V_{se1} , V_{se2}) are exchanged by the injected loads (S_j , S_k , S_m). The disadvantage of this model is that the required iterations for termination of the power flow are sensitive to the initial values of injected loads.

(h) The Power Injection Π Model

In this model, the IPFC is represented as a Π circuit with injected active and reactive loads at the terminals of the IPFC [41]. The series impedances of the converter are taken into consideration along with the line charging susceptance. Figure 31 shows the power injection Π Model. The advantage of this model is that the admittance matrix and the Jacobian matrix are not modified.

The following equations describe the injected powers at the terminals of the IPFC:

$$P_{s_n} = \text{Re} \{ V_{s_n} (W_{ss_n} V_{se_n})^* \} = \frac{\left(1 - \frac{B_{ln}}{2} X_{ln}\right)}{H} V_{s_n} V_{se_n} \sin(\theta_{s_n} - \theta_{se_n}) \quad (182)$$

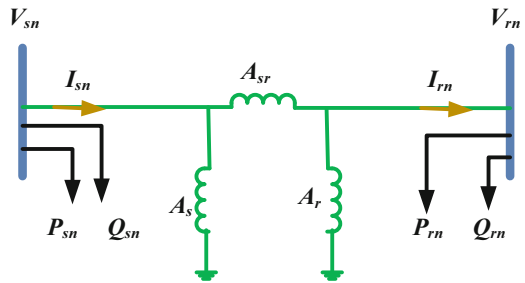
$$Q_{s_n} = \text{Im} \{ V_{s_n} (W_{ss_n} V_{se_n})^* \} = \frac{-\left(1 - \frac{B_{ln}}{2} X_{ln}\right)}{H} V_{s_n} V_{se_n} \cos(\theta_{s_n} - \theta_{se_n}) \quad (183)$$

$$P_{r_n}^{sc} = \text{Re} \{ V_{r_n} (W_{rs_n} V_{se_n})^* \} = \frac{-V_{r_n} V_{se_n}}{H} \sin(\theta_{r_n} - \theta_{se_n}) \quad (184)$$

$$Q_{r_n}^{sc} = \text{Im} \{ V_{r_n} (W_{rs_n} V_{se_n})^* \} = \frac{V_{r_n} V_{se_n}}{H} \cos(\theta_{r_n} - \theta_{se_n}) \quad (185)$$

where $H = X_{se_n} \left(1 - (B_{ln}/2) X_{ln}\right) + X_{ln}$.

Fig. 31 The power injection Π Model



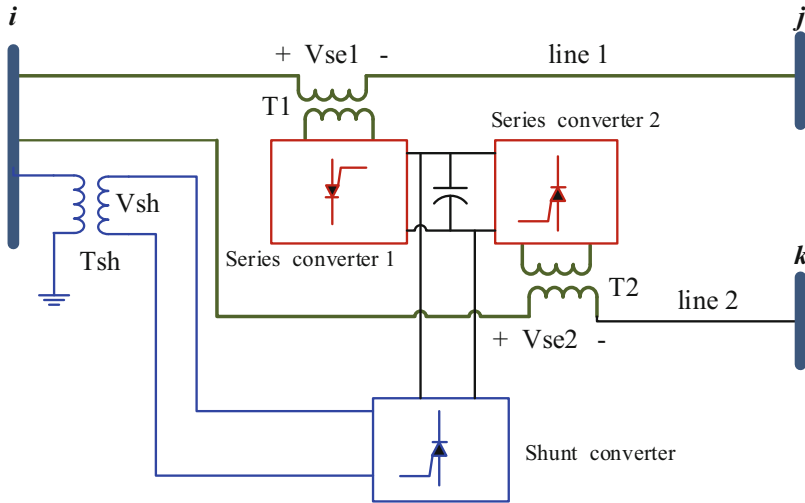


Fig. 32 Schematic diagram of GUPFC controller

3.2.5 Modeling of GUPFC

The GUPFC is a developed VSC-based controller that can control the power flow in multiple transmission lines and the voltage magnitude of common buses [39, 42, 43]. The GUPFC is comprised of three or more converters. Two or more converters connect in series with transmission lines, and another converter is connected in shunt with a common bus and connected with the series converter via a common DC link, as shown in Fig. 32. As depicted in Fig. 32, the first converter is connected in series with the first transmission line between buses m and n by the coupling transformer T1, while the second converter is connected in the second transmission line between buses m and h by the coupling transformer T2. The shunt converter is connected to the system through the shunt coupling transformer Tsh. The series converters can control the power flow in the transmission line by injecting controllable AC voltage in series to the transmission lines. The primary function of the shunt converter is injecting a reactive power to control the voltage magnitude and provide the required active power to the series converters.

(a) Voltage Source-Based Model

This model is driven from the voltage source representation of the GUPFC that has been depicted in Fig. 33 [39]. From Fig. 33, the power equations at the sending and receiving end buses can be listed as follows:

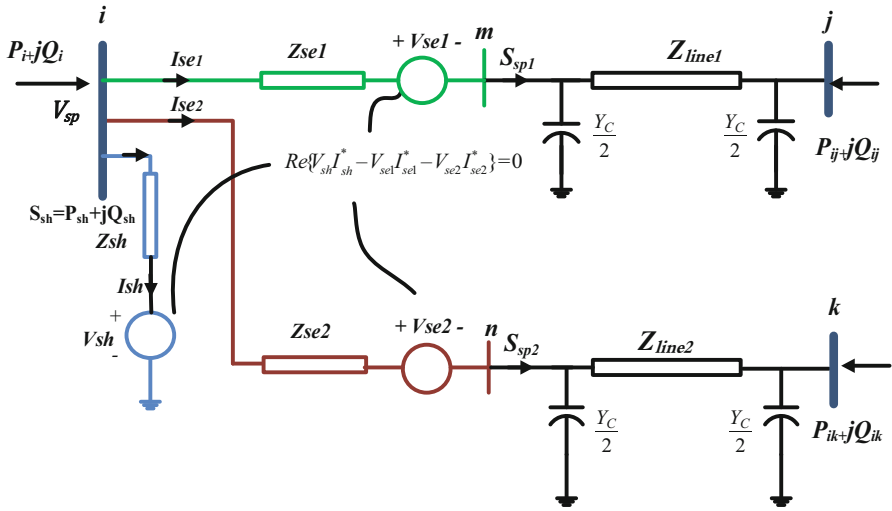


Fig. 33 Voltage sources-based representation of the GUPFC

$$\begin{aligned}
 P_i &= V_i^2 g_{ii} - V_i V_i h_i (g_{sh_i} \cos(\theta_i - \theta_{sh_i}) + b_{sh_i} \sin(\theta_i - \theta_{sh_i})) \\
 &\quad - \sum_n V_i V_n (g_{in} \cos(\theta_i - \theta_n) + b_{in} \sin(\theta_i - \theta_n)) \\
 &\quad - \sum_n V_i V_{se_{in}} (g_{in} \cos(\theta_i - \theta_{se_{in}}) + b_{in} \sin(\theta_i - \theta_{se_{in}}))
 \end{aligned} \tag{186}$$

$$\begin{aligned}
 Q_i &= -V_i^2 b_{ii} - V_i V_i h_i (g_{sh_i} \sin(\theta_i - \theta_{sh_i}) - b_{sh_i} \cos(\theta_i - \theta_{sh_i})) \\
 &\quad - \sum_n V_i V_n (g_{in} \sin(\theta_i - \theta_n) - b_{in} \cos(\theta_i - \theta_n)) \\
 &\quad - \sum_n V_i V_{in} (g_{in} \sin(\theta_i - \theta_{se_{in}}) - b_{in} \cos(\theta_i - \theta_{se_{in}}))
 \end{aligned} \tag{187}$$

$$P_{sh_i} = V_i^2 g_{sh_i} - V_i V_{sh_i} (g_{sh_i} \cos(\theta_i - \theta_{sh_i}) + b_{sh_i} \sin(\theta_i - \theta_{sh_i})) \tag{188}$$

$$Q_{sh_i} = -V_i^2 b_{sh_i} - V_i V_{sh_i} (g_{sh_i} \sin(\theta_i - \theta_{sh_i}) - b_{sh_i} \cos(\theta_i - \theta_{sh_i})) \tag{189}$$

The exchanged active power between the converter via the common DC link of the GUPFC should be as follows:

$$P_{ex1} = \text{Re}(V_{se1}(I_{se1})^*) \tag{190}$$

$$P_{ex2} = \text{Re}(V_{se2}(I_{se2})^*) \tag{191}$$

$$P_{sh} = P_{ex3} = -P_{ex1} - P_{ex2} - P_{dc} = \text{Re}(V_{se2}(I_{se2})^*) \tag{192}$$

As mentioned before, the GUPFC can control three specified values described as follows:

$$P_{ni} - P_{ni}^{\text{Spec}} = 0 \quad (193)$$

$$Q_{ni} - Q_{ni}^{\text{Spec}} = 0 \quad (194)$$

$$V_i - V_i^{\text{Spec}} = 0 \quad (195)$$

$$\begin{bmatrix} \frac{\partial P_{ji}}{\partial \theta_{seij}} & \frac{\partial P_{ji}}{\partial V_{ij}} & 0 & 0 & \frac{\partial P_{ji}}{\partial \theta_i} & \frac{\partial P_{ji}}{\partial \theta_j} & \frac{\partial P_{ji}}{\partial V_j} & 0 & 0 \\ \frac{\partial Q_{ji}}{\partial \theta_{seij}} & \frac{\partial Q_{ji}}{\partial V_{ij}} & 0 & 0 & \frac{\partial Q_{ji}}{\partial \theta_i} & 0 & \frac{\partial Q_{ji}}{\partial \theta_j} & \frac{\partial Q_{ji}}{\partial V_j} & 0 & 0 \\ 0 & 0 & \frac{\partial P_{ki}}{\partial \theta_{seik}} & \frac{\partial P_{ki}}{\partial V_{ik}} & \frac{\partial P_{ki}}{\partial \theta_i} & 0 & 0 & \frac{\partial P_{ki}}{\partial \theta_j} & \frac{\partial P_{ki}}{\partial V_j} \\ 0 & \frac{\partial Q_{ki}}{\partial \theta_{keik}} & \frac{\partial Q_{ki}}{\partial V_{ik}} & 0 & \frac{\partial Q_{ki}}{\partial \theta_i} & 0 & 0 & 0 & \frac{\partial Q_{ki}}{\partial \theta_k} & \frac{\partial Q_{ki}}{\partial V_k} \\ \frac{\partial PE}{\partial V_{ij}} & \frac{\partial PE}{\partial \theta_{seik}} & \frac{\partial PE}{\partial V_{ik}} & \frac{\partial PE}{\partial \theta_{shi}} & \frac{\partial PE}{\partial \theta_i} & \frac{\partial PE}{\partial V_{shi}} & \frac{\partial PE}{\partial \theta_j} & \frac{\partial PE}{\partial V_j} & \frac{\partial PE}{\partial \theta_k} & \frac{\partial PE}{\partial V_k} \\ \frac{\partial P_i}{\partial V_{ij}} & \frac{\partial P_i}{\partial \theta_{seik}} & \frac{\partial P_i}{\partial V_{ik}} & \frac{\partial P_i}{\partial \theta_{shi}} & \frac{\partial P_i}{\partial \theta_i} & \frac{\partial P_i}{\partial V_{shi}} & \frac{\partial P_i}{\partial \theta_j} & \frac{\partial P_i}{\partial V_j} & \frac{\partial P_i}{\partial \theta_k} & \frac{\partial P_i}{\partial V_k} \\ \frac{\partial Q_i}{\partial V_{ij}} & \frac{\partial Q_i}{\partial \theta_{seik}} & \frac{\partial Q_i}{\partial V_{ik}} & \frac{\partial Q_i}{\partial \theta_{shi}} & \frac{\partial Q_i}{\partial \theta_i} & \frac{\partial Q_i}{\partial V_{shi}} & \frac{\partial Q_i}{\partial \theta_j} & \frac{\partial Q_i}{\partial V_j} & \frac{\partial Q_i}{\partial \theta_k} & \frac{\partial Q_i}{\partial V_k} \\ \frac{\partial P_j}{\partial V_i} & 0 & 0 & \frac{\partial P_j}{\partial \theta_i} & 0 & \frac{\partial P_j}{\partial \theta_j} & \frac{\partial P_j}{\partial V_i} & 0 & 0 \\ \frac{\partial P_j}{\partial \theta_{seij}} & \frac{\partial P_j}{\partial V_{ij}} & 0 & 0 & \frac{\partial P_j}{\partial \theta} & \frac{\partial P_j}{\partial \theta_j} & \frac{\partial P_j}{\partial V_j} & \frac{\partial P_j}{\partial V_j} & 0 & 0 \\ \frac{\partial Q_j}{\partial \theta_{seij}} & \frac{\partial Q_j}{\partial V_{ij}} & 0 & 0 & \frac{\partial Q_j}{\partial \theta_i} & 0 & \frac{\partial Q_j}{\partial \theta_j} & \frac{\partial Q_j}{\partial V_j} & 0 & 0 \\ 0 & 0 & \frac{\partial P_k}{\partial \theta_{keik}} & \frac{\partial P_k}{\partial V_{ik}} & \frac{\partial P_k}{\partial \theta_i} & 0 & 0 & \frac{\partial P_k}{\partial \theta_k} & \frac{\partial P_k}{\partial V_k} \\ 0 & 0 & \frac{\partial Q_k}{\partial \theta_{seik}} & \frac{\partial Q_k}{\partial V_{ik}} & \frac{\partial Q_k}{\partial \theta_i} & 0 & 0 & \frac{\partial Q_k}{\partial \theta_k} & \frac{\partial Q_k}{\partial V_k} \end{bmatrix}$$

$$\times \begin{bmatrix} \Delta \theta_{seij} \\ \Delta V_{seij} \\ \Delta \theta_{seik} \\ \Delta V_{seik} \\ \Delta \theta_{shi} \\ \Delta \theta_i \\ \Delta V_{hi} \\ \Delta \theta_j \\ \Delta V_j \\ \Delta \theta_k \\ \Delta v_k \end{bmatrix} = \begin{bmatrix} P_{ji}^{\text{Spec}} - P_{ji} \\ Q_{ji}^{\text{Spec}} - Q_{ji} \\ P_{ki}^{\text{Spec}} - P_{ki} \\ Q_{ki}^{\text{Spec}} - Q_{ki} \\ -PE \\ \Delta P_i \\ \Delta Q_i \\ \Delta P_j \\ \Delta Q_j \\ \Delta P_k \\ \Delta Q_k \end{bmatrix} \quad (196)$$

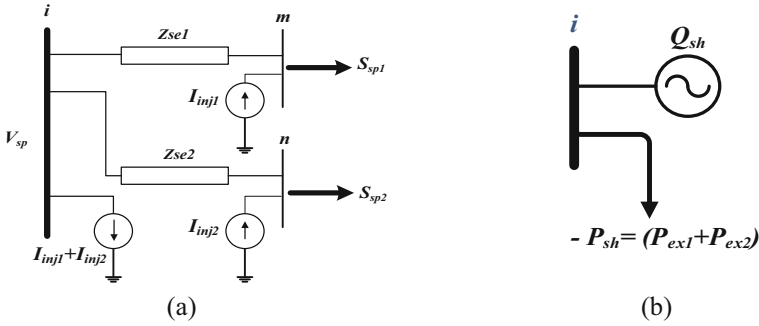


Fig. 34 The developed modeling of (a) the series converter representation and (b) the shunt converter representation

From the above clarification, the modification of the Jacobian matrix is required. The merit of this model is that the voltage magnitude and the power flow through TLs can be controlled separately or simultaneously. The operating constraints of GUPFC have been enforced in this model.

(b) The Developed Model

The developed model is based on power injection representation [44], where injected loads exchange the parameters of the GUPFC at the terminals of these devices. This representation of the series converters of the GUPFC is conceptualized from the current injection model where the V_{se1} and V_{se2} are converted to shunt current sources, calculated as a function of the specified current flow in TLs, as shown in Fig. 34a. Then these currents are converted to the injected load, whereas the shunt converter is represented as a synchronous condenser with ($P = 0$) similar to the simplified model of the STATCOM, and the common bus is converted to a PV to control the voltage magnitude of this bus. As shown in Fig. 34b. The developed model can be obtained by combining the series and the shunt converters, as shown in Fig. 34. The following equations describe the developed model:

$$S_m = -V_m (I_{inj1})^* \quad (197)$$

$$S_n = -V_n (I_{inj2})^* \quad (198)$$

$$S_i = V_i (I_i)^* \quad (199)$$

The merits of the developed model include avoiding the modifications of the Jacobian matrix, controlling the power flow in TLs, and the voltage magnitude

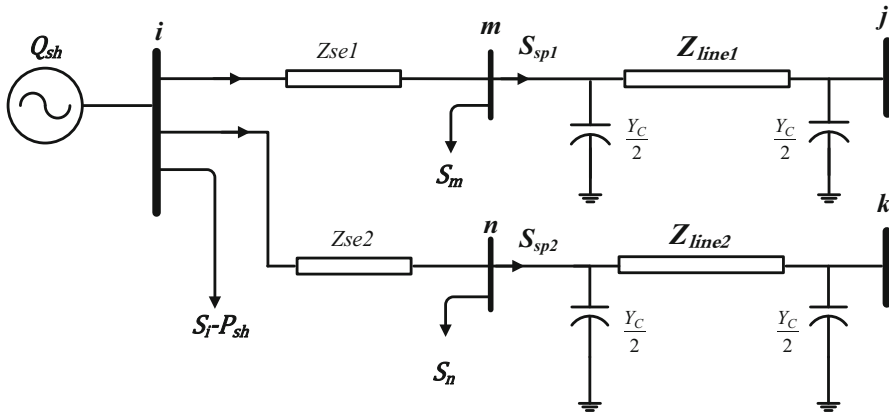


Fig. 35 The developed model of GUPFC

can be carried out simultaneously or separately. In addition to that, the operating constraints have been considered in this model (Fig. 35).

4 Summary

This chapter presented methods of modeling the FACTS devices into power flow solutions. Several models for variable impedance and VSC based type FACTS devices have been introduced, including their concepts, advantages, and shortcomings. In addition to that, the required modifications in power flow solutions. From the literature survey, it is clear that modeling the VSC-based FACTS devices is more difficult due to including the parameters of FACTS in the Jacobian matrix as state variables. For future work, combinations between these methods can be investigated to reduce the complications of modeling these controllers with fast convergence characteristics with application developed strategies for efficiently handling the FACTS controllers’ operating constraints.

References

1. Zhang X-P, Rehtanz C, Pal B (2012) Flexible AC transmission systems: modelling and control. Springer Science & Business Media
2. Hingorani NG, Gyugyi L (2000) Understanding FACTS: concepts and technology of flexible AC transmission systems. Wiley-IEEE Press
3. Acha E, Fuerte-Esquivel CR, Ambriz-Perez H, Angeles-Camacho C (2004) FACTS: modelling and simulation in power networks. Wiley
4. Song Y-H, Johns A (1999) Flexible ac transmission systems (FACTS) (no. 30). IET

5. Sood VK (2006) HVDC and FACTS controllers: applications of static converters in power systems. Springer Science & Business Media
6. Taylor CW, Scott G, Hammad A (1994) Static var compensator models for power flow and dynamic performance simulation. *IEEE Trans Power Syst* 9(1)
7. Acha E, Agelidis V, Anaya-Lara O, Miller TJE (2002) Power electronic control in electrical systems. Newnes
8. Kathal P, Bhandakkar A (2013) Power flow control in power system using FACT device thyristor controlled series capacitor (TCSC): a review. *Int J Innov Res Dev* 2(4):127–145
9. Mathur RM, Varma RK (2002) Thyristor-based FACTS controllers for electrical transmission systems. Wiley
10. Raj S, Bhattacharyya B (2018) Optimal placement of TCSC and SVC for reactive power planning using Whale optimisation algorithm. *Swarm Evol Comput* 40:131–143
11. Ambriz-Perez H, Acha E, Fuente-Esquivel CR (2006) TCSC-firing angle model for optimal power flow solutions using Newton's method. *Int J Electr Power Energy Syst* 28(2):77–85
12. Sreejith S, Simon SP, Selvan M (2010) Power flow analysis incorporating firing angle model based TCSC. In: 2010 5th International Conference on Industrial and Information Systems. IEEE, pp 496–501
13. Sekhar AH, Devi AL (2016) Voltage profile improvement and power system losses reduction with multi TCSC placement in transmission system by using firing angle control model with heuristic algorithms. In: 2016 International Conference on Signal Processing, Communication, Power and Embedded System (SCOPEs). IEEE, pp 295–301
14. Yadav P, Tiwari V, Bhowmick S (2021) A novel firing angle-based power-flow model of TCSC. In: Recent advances in power systems. Springer, pp 109–115
15. Acharya N, Mithulananthan N (2007) Locating series FACTS devices for congestion management in deregulated electricity markets. *Electr Power Syst Res* 77(3–4):352–360
16. Besharat H, Taher SA (2008) Congestion management by determining optimal location of TCSC in deregulated power systems. *Int J Electr Power Energy Syst* 30(10):563–568
17. Liu J, Hao X, Wang X, Chen Y, Fang W, Niu S (2018) Application of thyristor controlled phase shifting transformer excitation impedance switching control to suppress short-circuit fault current level. *J Mod Power Syst Clean Energy* 6(4):821–832
18. Lyman W (1930) Controlling power flow with phase shifting equipment. *Trans Am Inst Electr Eng* 49(3):825–829
19. Iravani M, Dandeno PL, Nguyen K, Zhu D, Maratukulam D (1994) Applications of static phase shifters in power systems. *IEEE Trans Power Deliv* 9(3):1600–1608
20. Padiyar K (2007) FACTS controllers in power transmission and distribution. New Age International
21. Fuente-Esquivel C, Acha E, Ambriz-Perez H (2000) A comprehensive Newton-Raphson UPFC model for the quadratic power flow solution of practical power networks. *IEEE Trans Power Syst* 15(1):102–109
22. Noroozian M, Angquist L, Ghandhari M, Andersson G (1997) Use of UPFC for optimal power flow control. *IEEE Trans Power Deliv* 12(4):1629–1634
23. Nor KM, Mokhlis H, Gani TA (2004) Reusability techniques in load-flow analysis computer program. *IEEE Trans Power Syst* 19(4):1754–1762
24. Bhowmick S, Das B, Kumar N (2008) An indirect UPFC model to enhance reusability of Newton power-flow codes. *IEEE Trans Power Deliv* 23(4):2079–2088
25. Haque M, Yam C (2003) A simple method of solving the controlled load flow problem of a power system in the presence of UPFC. *Electr Power Syst Res* 65(1):55–62
26. Ebeed M, Kamel S, Yu J, Jurado F (2019) Development of UPFC operating constraints enforcement approach for power flow control. *IET Gener Transm Distrib* 13(20):4579–4591
27. Nabavi-Niaki A, Iravani MR (1996) Steady-state and dynamic models of unified power flow controller (UPFC) for power system studies. *IEEE Trans Power Syst* 11(4):1937–1943
28. Alomoush MI (2002) Exact pi-model of UPFC-inserted transmission lines in power flow studies. *IEEE Power Eng Rev* 22(12):54–56

29. Alomoush MI (2003) Derivation of UPFC DC load flow model with examples of its use in restructured power systems. *IEEE Trans Power Syst* 18(3):1173–1180
30. Zhang X-P (2003) Advanced modeling of the multicontrol functional static synchronous series compensator (SSSC) in Newton power flow. *IEEE Trans Power Syst* 18(4):1410–1416
31. Ebeed M, Kamel S, Jurado F (2017) Constraints violation handling of SSSC with multi-control modes in Newton–Raphson load flow algorithm. *IEEJ Trans Electr Electron Eng* 12(6):861–866
32. Kamel S, Jurado F (2014) Fast decoupled load flow analysis with SSSC power injection model. *IEEJ Trans Electr Electron Eng* 9(4):370–374
33. Vinkovic A, Mihalic R (2008) A current-based model of the static synchronous series compensator (SSSC) for Newton–Raphson power flow. *Electr Power Syst Res* 78(10):1806–1813
34. Kamel S, Jurado F, Chen Z (2015) Power flow control for transmission networks with implicit modeling of static synchronous series compensator. *Int J Electr Power Energy Syst* 64:911–920
35. Zhang X-P, Handschin E, Yao M (2004) Multi-control functional static synchronous compensator (STATCOM) in power system steady-state operations. *Electr Power Syst Res* 72(3):269–278
36. Youssef H, Kamel S, Ebeed M (2018) Optimal power flow considering loading margin stability using lightning attachment optimisation technique. In: 2018 Twentieth International Middle East Power Systems Conference (MEPCON). IEEE, pp 1053–1058
37. Kamel S, Jurado F, Vera D (2014) A simple implementation of power mismatch STATCOM model into current injection Newton–Raphson power-flow method. *Electr Eng* 96(2):135–144
38. Gyugyi L, Sen KK, Schauder CD (1999) The interline power flow controller concept: a new approach to power flow management in transmission systems. *IEEE Trans Power Deliv* 14(3):1115–1123
39. Zhang X-P (2003) Modelling of the interline power flow controller and the generalised unified power flow controller in Newton power flow. *IEE Proc Gener Transm Distrib* 150(3):268–274
40. Vinkovic A, Mihalic R (2009) A current-based model of an IPFC for Newton–Raphson power flow. *Electr Power Syst Res* 79(8):1247–1254
41. Zhang Y, Chen C (2006) A novel power injection model of IPFC for power flow analysis inclusive of practical constraints. *IEEE Trans Power Syst* 21(4):1550–1556
42. Valle D, Araujo P (2015) The influence of GUPFC FACTS device on small signal stability of the electrical power systems. *Int J Electr Power Energy Syst* 65:299–306
43. Fardanesh B, Shperling B, Uzunovic E, Zelingher S (2000) Multi-converter FACTS devices: the generalised unified power flow controller (GUPFC). In: 2000 power engineering society summer meeting (Cat. No. 00CH37134), vol 2. IEEE, pp 1020–1025
44. Ebeed M, Kamel S, Jurado F (2017) Constraints violation handling of GUPFC in Newton–Raphson power flow. *Electr Power Compon Syst* 45(9):925–936

Comparison of Different Configurations of Saturated Core Fault Current Limiters in a Power Grid by Numerical Method: A Review



Aydin Zaboli

1 Introduction

Increase in fault currents in power grids is due to the ongoing expansion in energy generation and demand, as well as the trend to parallelize the network sections. As a result, there is a global effort underway to find solutions to the fault current problem in order to prevent having to replace existing circuit breakers or to postpone their replacements [1–10]. Using various types of fault current limiters (FCLs) could be an option. This device essentially makes a series connection to the power grid with a variable impedance. The impedance is low when it performs at its best situation. When a fault arises, however, the impedance of the system increases dramatically, preventing amplitude currents from flowing to greater levels. The failures in the converters and rotor circuit can cause hazardous conditions in the FCLs. Hence, they can be employed to maintain the connectivity of generators to the grid as long as possible. Short circuit current is limited by such circuits, but the generator is not disconnected from the grid [11–13]. Despite being advantageous to utilities, these new methods have created a significant problem in terms of short-circuits. Symmetrical or asymmetrical short circuits are unavoidable in power networks and result in large magnitude short circuit currents, particularly in high voltage power networks. These currents have negative thermal and mechanical consequences [14]. Different types of these devices can be classified by their functionalities, materials, structures, expenditures, and other characteristics. They may be classified into two general groups based on their most significant functional characteristics [15–18]: (1) Limiters that have a built-in reaction to a fault. (2) Limiters with a delayed

A. Zaboli (✉)

Department of Electrical Engineering, Amirkabir University of Technology, Tehran, Iran
e-mail: a.zaboli@aut.ac.ir

error response. SCFCLs offer numerous benefits over other types, however, they necessitate a significant quantity of magnetic substances, resulting in a high upfront cost and a considerable scale. These FCLs can be as non-superconducting and superconducting models, and our attention is on non-superconducting FCLs in this chapter. Superconducting FCLs have at least a superconductor tape or coil in their configurations, which can be effective in the fault current limitation, however, there are some problems in using these types of limiters. Some issues are such as cooling system volume and superconductor costs that make barriers for researchers and engineers to provide a suitable design of power grid including the superconducting FCLs [2, 19–22]. Nowadays these FCLs are constructed in small scales in laboratories and tested in some small sections of power grids [20]. There are different types of FCLs including saturated core FCL, inductive FCL, magnetic FCL, and open core FCL, that every configuration has special structure and material, but the same functionality.

The saturated core FCL is made up of three parts including, copper dc and ac coils and an iron core, each of which has its own structure. The power supply is linked in series to the ac coils, while the dc coils are connected to a separate direct current source. This type of limiters, on the other hand, confront problems such as increasing the needed magnetic material, which may be partially addressed by introducing novel structures and arrangements. To address the issues of big volume and high cost, many structures are offered during recent years [13, 15, 23–25]. By introducing an air gap into the core, the volume of the magnetic substance may be decreased. This approach is applicable to nonlinear inductors in general. The air gap is not just a component of an alternating current circuit, but it is also a component of a direct current magnetic circuit. In this situation, core saturation is difficult, and the FCL's usual impedance is decreased. As a result, designs with three legs are possible, and the arrangement of ac and dc windings may be modified such which there is no dc flux passing through the middle leg of the core. Consequently, an air gap in the intermediate branch may be generated without raising the dc excitation to saturate the core. This air gap also guarantees that the core size is reduced for the same voltage level. The configuration of the ac and dc windings allows one of the two outer legs to go out of saturation during each half cycle of the fault, limiting the fault current. The weight of the FCL may be decreased by utilizing the proper construction when compared to induction type designs, which depends on how the ac and dc coils are positioned and put on distinct legs. The ratio of the defective phase voltage to the overall fault current determines the effective fault impedance [26–28].

2 Literature Review

There are many FCL configurations tested or implemented all over the world to relieve the risks of these hazardous currents in a power grid. These can help the power system to be safe, reliable, and stable [14]. Ruiz et al. [19] have investigated

the Resistive-type Superconducting FCLs in terms of their working principles, numerical modeling, and superconducting materials with experimental concepts. Tan et al. presented a resistive SFCL with different current flowing time by an YBCO tape as a superconductor material [20]. Assessment of thermoelectric model of RSFCL by root mean squared method is conducted by Branco et al. in [29]. Related to inductive SFCL, Yamaguchi et al. presented a transformer type SFCL that analyze the relation between the current limiting characteristics and transformer ratings in [30]. Recently, a transformer-type SFCL with an external circuit has been developed that may minimize the fault current utilizing twice quench operations. The impact of current limitation on the winding path of two isolated windings has been addressed in [31]. A comprehensive review of Flux-locked type FCLs (FLSFCLs) was recently published in [32], which included a detailed assessment of research conductions and applications of FLSFCLs in power grids. A FLSFCL was used to enrich the quality of power indexes in a distribution system [33]. A voltage-sourced inverter has been used to incorporate the planned FLSFCL. The coordination of overcurrent relays with FLSFCL is discussed in [34]. In [3], the impacts of these windings on FLSFCL's performance in an iron closed-core were investigated. Tripathi et al. [35] has conducted a configuration with two ac winding and a dc winding SCFCL for improving a doubly fed induction generator (DFIG) system.

3 Principles of Fault Current Limiting

During recent years, FCLs are widely studied by researchers in terms of different configurations with materials, performance type, arrangements, and so on. Two fault current limiting bases are as follows: Adding a resistive impedance and reactive impedance (an inductor or a combination of an inductor and a capacitor) [14].

A sample transmission line with the FCL is represented, in which this device is in series with other power grid components. FCLs normally limit fault currents to a desire level, and they are dependent on the system requirements as well. That means they do not act during normal conditions of a power grid operation. Also, they do not apply any changes, damage, or restrictions to the system, so they could be safe and reliable.

Equation (1) may describe the fault current in the system, such as the single-phase fault to ground (see Fig. 1) in which $i_{\text{fault}}(t)$ represents the fault current, $U_L(t)$, the line voltage, L the phase angle of the transmission line impedance, Z_L the impedance of transmission line, $I_{L,tf}$ the value of a current of transmission line at the start time during a fault condition, t_f the start time of a fault, and τ the line time constant [17]:

$$i_{\text{fault}}(t) = \frac{U_L \sin(\omega t - \varphi_L)}{|Z_L|} + \left(I_{L,tf} - \frac{U_L \sin(\omega t - \varphi_L)}{|Z_L|} \right) e^{-\frac{t-t_f}{\tau}} \quad (1)$$

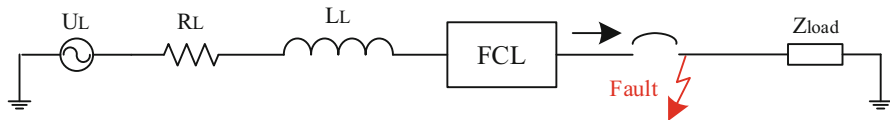


Fig. 1 Sample power system circuit

When a resistive or inductive types of FCLs are utilized, the difference in system's fault performance is in the time constant value of the system, resulting in a difference in the value of the fault current's dc portion. The transmission line time constant of a fault is less than the inductive FCL for the same FCL impedance when a resistive FCL is employed, as demonstrated by Eqs. (2) and (3) which L_L is line leakage inductance, R_L , line leakage resistance, and R_{FCL} and L_{FCL} are resistive and inductive impedances, correspondingly.

$$\tau_{RFCL} = \frac{L_L}{R_L + R_{FCL}} \quad (2)$$

$$\tau_{XFCL} = \frac{L_L + L_{FCL}}{R_L} \quad (3)$$

As a result, given the same FCL impedance, the initial fault current peak for a resistive limiting impedance is less than the inductive impedance. Another distinction is that the resistive FCL dissipates energy during the fault, whereas the inductive FCL accumulates energy in the magnetic field during the failures and restores it to the system at the end of each cycle. Hence, inductive FCLs do not result in power loss for the system if normal system operation is resumed without interruption of current flow (regardless of inductor's resistance). When the transmission line is terminated, the energy accumulated in the previous cycle is merely the power loss in the circuit breaker [20, 36].

To limit the fault current, inductive FCL can employ both an inductor and a capacitor simultaneously. The FCL can be substituted by a parallel inductor and capacitor, in this case, to arrange to conduct the network frequency to a resonance state. The C_{FCL} capacitor is connected in series via a transmission line, and its quantity is adjusted to compensate the leakage inductance of the transmission line. When a fault occurs in a power grid, the L_{FCL} inductance is connected to a capacitor in parallel, and the resonant impedance of the parallel LC circuit restricts the fault current as follows:

$$Z_{res, FCL} = j \frac{\omega L_{FCL}}{1 - \omega^2 L_{FCL} C_{FCL}} \quad (4)$$

This section briefly discussed the limitations of fault currents. Then, a comprehensive comparison will be given to assess the different configurations by numerical method in the next sections.

4 Basis of SCFCLs

The nonlinear inductor impedance is determined by the average longitude of the flux direction, l_{mean} , the cross-sectional area of the core, A_{core} , winding's turn number, N_{ind} , and the core's relative permeability, μ_r (Fig. 2). By conducting the core to a saturation mode, the inductance is smaller when the hysteresis curve's operational point is outside of the saturation zone (Fig. 3) [37].

The estimated inductances for saturated and unsaturated situations are given in the following equations:

$$L_x = \mu_0 \mu_r \frac{N_{ind}^2 A_{core}}{l_{mean}} \tag{5}$$

$$L_y = \mu_0 \mu_{r,sat} \frac{N_{ind}^2 A_{core}}{l_{mean}} \tag{6}$$

Fig. 2 Nonlinear inductor

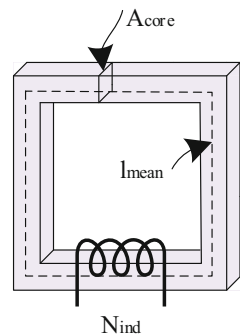


Fig. 3 Nonlinear B-H (hysteresis) curve in an iron core

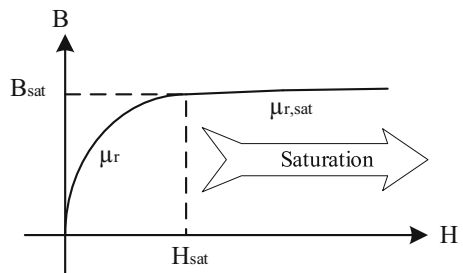
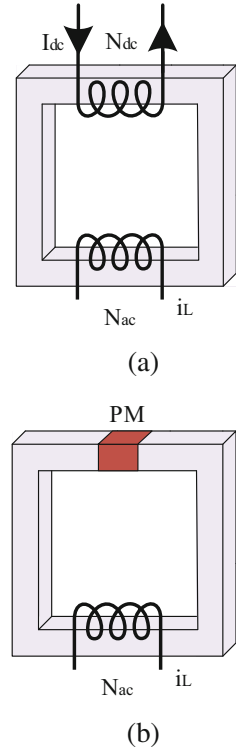


Fig. 4 Saturation methods of FCL core: (a) by direct current (b) by PM

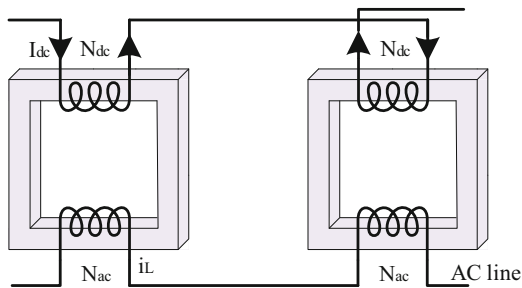


Where L_x and L_y are the FCL impedances during the fault and normal conditions, and μ_0 and $\mu_{r,sat}$ are the air permeability and relative permeability coefficients of the core at a saturation condition, respectively. The core must be saturated under normal system conditions, but not oversaturated, while the core should be de-saturated under fault situations. An additional dc current-carrying coil provided by an auxiliary source or a permanent magnet (PM) can be used to saturate the core, as illustrated in Fig. 4.

A dc coil, a copper ac coil, and an iron core make up generally the saturated core fault current limiters, the arrangement of which changes depending on the different constructions and used materials. The ac coils are linked to a power system in series, and the resulting magnetic field is directed in opposite directions. The dc coils are connected to a separate direct current source, as demonstrated in Fig. 5.

The SCFCL works in its usual non-limiting state under normal power system circumstances, which is also the mode of operation for most of the time and has no impacts on a power grid. The rated current will flow between the ac windings, and the huge current in the dc winding will make the bias of the large dc magnetic field within a core in this case. During each ac cycle, deep saturation and low magnetic permeability are maintained in iron cores. The SCFCL reactance is low and has slight impact on the rest of the power system because of the inductance relation with the permeability [2, 26, 38, 39].

Fig. 5 Schematic of main components of SCFCLs



A substantial fault current flows between the ac windings when short circuits occur, and the limiter enters its own current limiting mode. The dc current is instantly shut off for active-type SCFCLs, and regardless of the short circuit fault, the same dc bias is created for inactive-type SCFCLs. The iron cores in both types will not always be at deep saturation for a long period due to the high fault currents. The permeability rises by several thousand while the cores operate in the linear area of the hysteresis characteristic; therefore, the average limiter reactance enhances. The limiter can restrict the fault current due to reactance [21, 40]. Soft iron has nonlinear magnetic characteristics, which are dictated by the hysteresis characteristic of material, and is used to represent in this case. Figure 6 illustrates some advantages of employing this type of limiters.

The cores of limiters are adequately saturated to the point that typical current flux changes cannot restore them to the linear area depicted in Fig. 7. The operating point of B-H graph is desaturated in the case of a fault occurrence, increasing the limiter impedance. The safe margin width indicated in the figure determines the fault flow level at which the FCL commences to restrict. The width of this portion may be ignored due to the small fault current peak, and the FCL can serve on spot.

The relationship between dc current, I_{dc} , line current, I_L , and the magnetic field in the core (H) can be written as follows. To calculate the safe zone width, H_s , Eq. (7) must be rewritten as (8) [27]:

$$N_{dc}I_{dc} - N_{ac}I_{L,max} > H_{sat}l_{mean} \quad (7)$$

$$N_{dc}I_{dc} - N_{ac}I_{L,max} = (H_{sat} + H_s)l_{mean} \quad (8)$$

After the fault has been cleared, the core comes back to saturated mode. Therefore, when the amount of transmission current decreases, the ac winding's impedance decreases with no latency. As a result, the inductive FCL can limit a countless number of frequent faults.

Because of the inductive essence of the fault current limiter's impedance, there have been no energy losses throughout the restriction, but there is a loss owing to the resistance of a winding. When compared with the transmission line's nominal

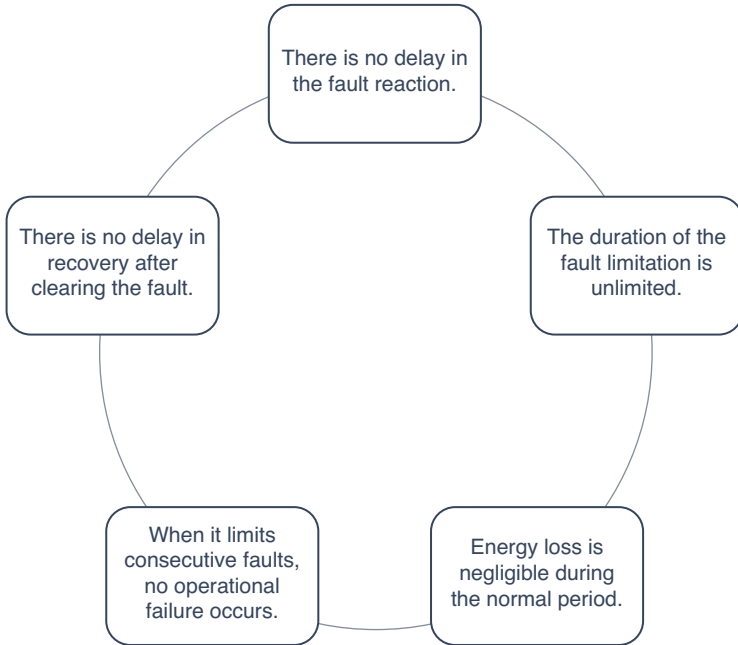
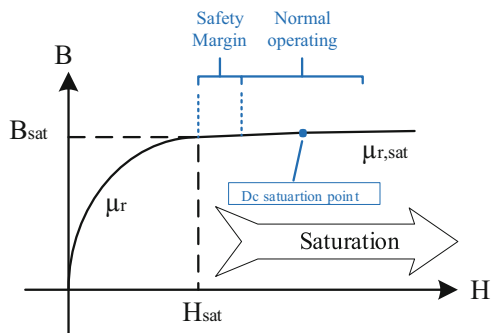


Fig. 6 SCFCL characteristics

Fig. 7 FCL performance during normal regime – flux changes



power, the dissipative power is rather low. Unlike resistive fault current limiters, the limiting operation period is not constrained by an acceptable quantity of thermal transfer at the impedance. Because inductive limiters cannot operate as a breaker, the fault current must be eliminated by other protection apparatus, like circuit breakers. However, they have not been industrialized because of the issues in design processes [41] including: (1) The scale and cost of the materials are both significant; (2) Inductive overvoltage passing through the dc current source during fault operation.

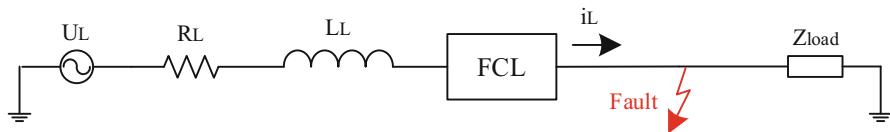


Fig. 8 Power system equivalent circuit with single phase to ground fault

Table 1 Equivalent circuit parameters

Parameter	Description
Power supply (U_L) (rms)	$10\sqrt{2}$ kV
R_L	0.1095Ω
L_L	5.63419×10^{-4} H
Z_{load}	8.79Ω

5 Circuit Diagram of a Simple Power System

Test circumstances of FCLs and their impacts on current limiting and other network parameters are in the form of a simplified power network test circuit with resistance, inductor, power supply, and load resistance, which act in fault and normal operations utilizing the various architectures of SCFCLs. The sample circuit system associated with their values is illustrated in Fig. 8 and Table 1. It is our purpose to test the different type of saturated core FCLs on the sample network by providing a model by finite element method simulated by COMSOL Multiphysics software in a computer system with Intel core i7, 6500 U, 64-bit, and 12 GB RAM and providing a comparison between them in terms of appropriate parameters. Various arrangements of these FCLs are given in the next section.

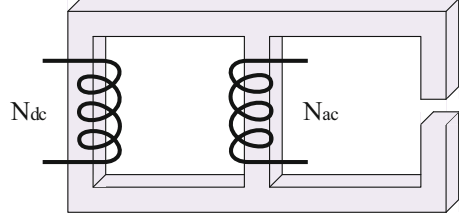
6 Different Configurations of SCFCLs

We propose some SCFCL configurations, such as 100% magnetic separation, partial magnetic separation, short-circuit dc winding, and so on. The performance of these FCLs is tested on the sample power system, and comparisons are provided.

6.1 SCFCL with 100% Magnetic Separation

Because of resistive essence of an ac winding in SCFCLs, there will be a voltage drop, which is a coefficient of voltage during normal operation (up to 2%). However, phase voltage of $U_L(t)$, is applied to the ac winding while a fault occurs. An overvoltage ($U_{FCL,dc}(t)$) is produced by a dc source as a result of windings' coupling

Fig. 9 SCFCL configuration with 100% magnetic separation of dc and ac circuit



in a transformer in which the number of turns in the ac and dc windings are N_{ac} and N_{dc} , correspondingly [12, 16].

$$U_{FCL,dc}(t) = \frac{N_{dc}}{N_{ac}} U_L(t) \quad (9)$$

The induced overvoltage problem can be solved by magnetic separation of ac and dc windings. Figure 9 depicts this arrangement in this case.

In this situation, the dc flux only crosses over the core's left and center legs and reaches the saturation mode. A leg with a significant reluctance possessing an air gap deflects the passing flux away from the path as shown in Eq. (10):

$$\left. \begin{aligned} \mathfrak{R}_m &= \frac{l_{mm}}{\mu_0 \mu_r A_{cm}} \\ \mathfrak{R}_{rr} &= \frac{l_{mr} + \mu_r l_g}{\mu_0 \mu_r A_{cr}} \end{aligned} \right\} \Rightarrow \boxed{\mathfrak{R}_m \ll \mathfrak{R}_{rr}} \quad \text{that} \quad \left\{ \begin{aligned} \mathfrak{R}_m &\text{ is middle leg reluctance} \\ \mathfrak{R}_{rr} &\text{ is right leg reluctance} \\ l_{mm} &\text{ is average length of middle leg} \\ l_{mr} &\text{ is average length of right leg} \\ l_g &\text{ is air gap length} \\ A_{cm} &\text{ is cross-section of middle leg} \\ A_{cr} &\text{ is cross-section of right leg} \end{aligned} \right. \quad (10)$$

During the fault condition, the ac flux merely flows through the center and right legs, which is induced by fault currents. The reluctance of left side is much higher than right one (with air gap) owing to a saturation state [27]:

$$\left. \begin{aligned} \mathfrak{R}_{lf} &= \frac{l_{mf}}{\mu_0 \mu_r A_{cl}} \\ \mathfrak{R}_{rr} &= \frac{l_{mr} + \mu_r l_g}{\mu_0 \mu_r A_{cr}} \end{aligned} \right\} \Rightarrow \boxed{\mathfrak{R}_{lf} \gg \mathfrak{R}_{rr}} \quad \text{that} \quad \left\{ \begin{aligned} \mathfrak{R}_{lf} &\text{ is left leg reluctance} \\ l_{mf} &\text{ is average length of left leg} \\ A_{cl} &\text{ is cross-section of left leg} \end{aligned} \right. \quad (11)$$

The dc winding does not sense any flux change in this situation since it is not aware of the ac flux. As a result, no induced overvoltage occurs. Figure 10 depicts the flow distribution, with two cores utilized for each phase.

Fig. 10 Flux distribution in SCFCL with 100% magnetic separation

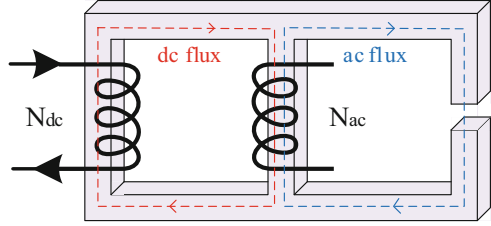
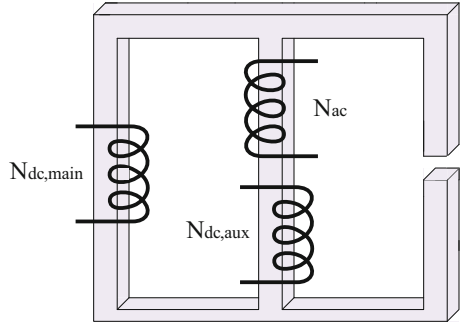


Fig. 11 SCFCL with partial magnetic separation



This configuration, however, has a design flaw. During normal operation, the ac winding has a very high impedance. Non-deep saturation of the mid-leg results in high impedance. Because the dc winding is on the opposite leg of the core, it can only saturate the same leg.

6.2 SCFCL with Partial Magnetic Separation

The saturated core FCL with 100% magnetic separation has a limiting difficulty in that a coil placed in the opposite leg of the core cannot be thoroughly saturated, as detailed in the preceding section. The ac leg falls out of saturation even with a regular current, increasing the FCL impedance during normal operation. The core size needs to be large enough to get a desire value for an impedance of the FCL in the normal state which can be inferred [1].

An improved design of a SCFCL with partial magnetic separation is illustrated in Fig. 11. There is an ac leg with an appended dc auxiliary coil to conduct it to a stronger saturated mode. The effect of the auxiliary dc coil is depicted in Fig. 12. This auxiliary coil propels the working point outside the knee area, allowing it to saturate deeper. SCFCL parameters are presented in Table 2.

Equation (12) illustrates a relationship between $N_{ac, aux}$ and N_{ac} as follows:

$$N_{dc,aux} I_{dc} = N_{ac} I_L \quad \text{that} \quad I_{dc} = \text{dc current}, \quad I_L = \text{Line current} \quad (12)$$

Fig. 12 Deep saturated mode of an AC leg provided by a dc auxiliary coil

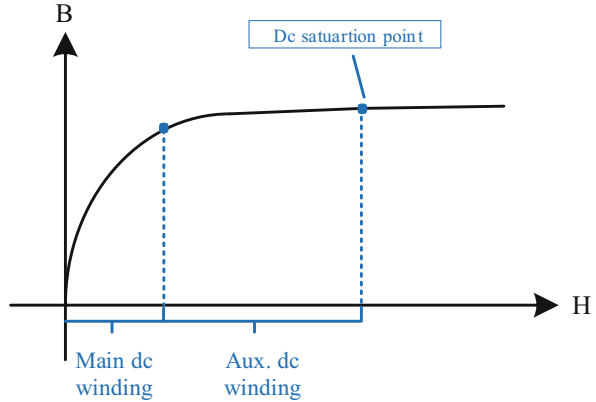


Table 2 SCFCL parameters

Parameter	Description	Value	
		100% magnetic separation	Partial magnetic separation
N_{ac}	No. of turns in ac winding	60	60
N_{dc}	No. of turns in dc winding	500	500
I_{dc}	dc current	450	450
l_{gap}	Air gap length	0.3	0.3
$N_{dc,aux}$	No. of turns in auxiliary winding	–	76

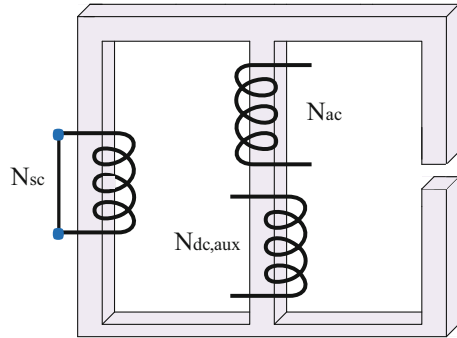
The design parameters are analogous to the previous mode for this case, and the auxiliary winding has 76 turns, which is obtained using Eq. (12). The FCL also comes with the same specifications as the auxiliary dc coil, except that the main dc coil is short-circuited.

6.3 SCFCL with DC Coil Through Short-Circuited Terminals

Even though the primary dc coil has more turns than the auxiliary one, the primary coil's share of ac leg saturation is less than that of the auxiliary dc coil illustrated in Fig. 13. To raise the dc reluctance and control the ac flux via the air gap, more turns of the dc primary coil are indispensable. Otherwise, the induced voltage at the dc source will rise due to the spreading of ac flux via the dc leg. [8, 41].

If the primary winding is cut off from the rest of the circuit, the limiter functionality will not change, as shown in the figure below. The ac current flowing via the dc leg causes a current in the coil with short-circuited terminals, which drives the ac flux. The dc leg is not fully saturated in this scenario. A supplementary coil

Fig. 13 SCFCL with DC
Coil through short-circuited
terminals



navigates it to the knee area. However, the FCL impedance does not increase when everything is running smoothly because it is where the ac flux flows.

The level of flux variation in the dc side determines the induction current in the short-circuit coil, which is oppositely proportional to N_{dc} . The quantity of induction current increases as a reduction of the coil's turn numbers. Considering that, the entire amount of material could be substantially reduced in this circumstance. The overall amount of FCL coil material is lowered by substituting the primary dc coil with a short-circuit one by partial magnetic separation [26].

7 Simulation Results for Configurations with One AC Winding

In this section, we evaluate the simulation results of these models, which we define the models as Fig. 14 and the components of this type of limiter as Fig. 15.

Also, the geometrical dimensions of the design are demonstrated in Fig. 16.

Using the sample power system for assessing the FCL performance in the circuit in fault conditions, the current curves passing through the system and the flux density and field strength curves can be obtained, as well as the distribution of flux density or field strength in different situations. A transient analysis was performed for the configurations over time, and its performance in the presence of fault is compared and assessed. Even though the limiter exists in a power system during normal situation, it should not have impacts on the circuit. Therefore, the current passing through the grid without the presence of FCL and with the presence of FCL under normal operating conditions of the system is compared, which is shown in Fig. 17. Red line demonstrated the electric current without FCL with amplitude of 1000 A. Other models illustrate some changes in current specifically at the outset of time. It originates from copper structure of FCL and is due to winding positions that reduce the amplitude of current at the models.

In models A, B, and C, the limiter is in the electric circuit. Moreover, a maximum current passing through the system is about 1000 A, which the amount of current is

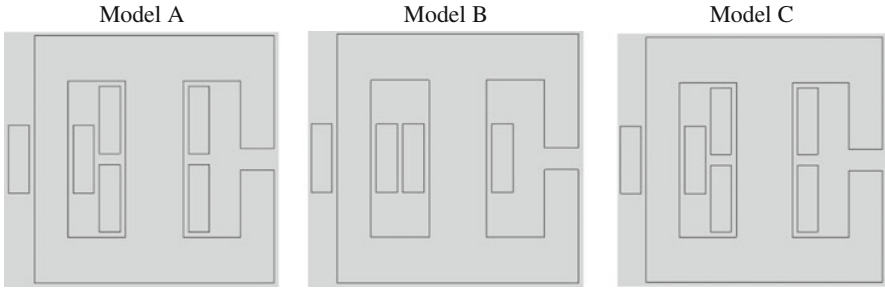


Fig. 14 SCFCL structures including partial magnetic separation (Model A), 100% magnetic separation (Model B) and a dc coil with short-circuited terminals (Model C)

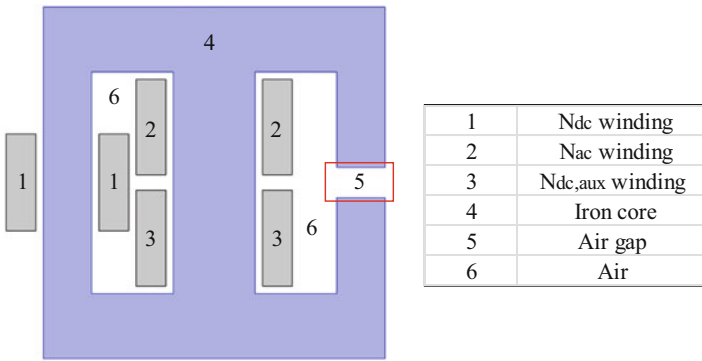


Fig. 15 SCFCL components

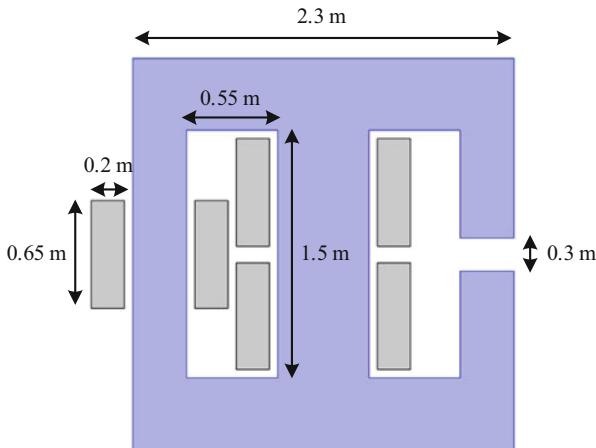


Fig. 16 Configuration dimensions

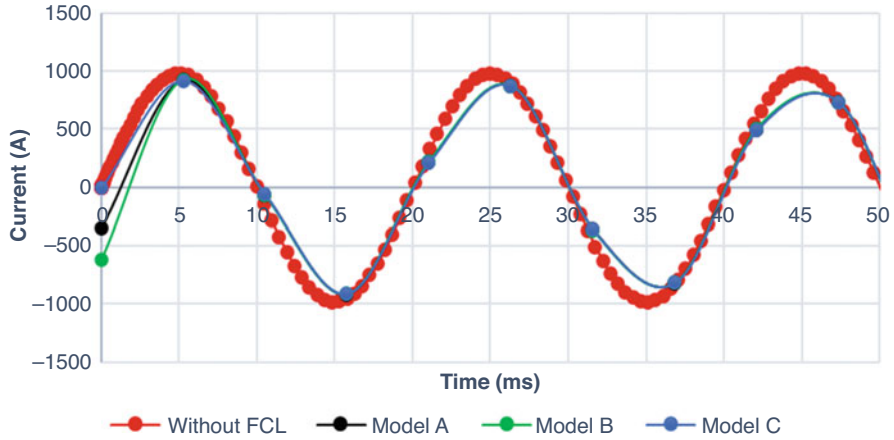


Fig. 17 Current passing through the system in normal operating conditions

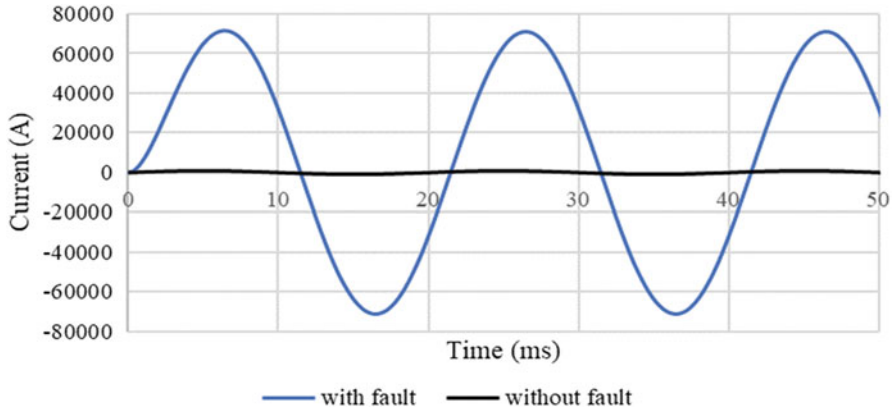


Fig. 18 Current passing through the system in normal and fault operation without SCFCL

slightly reduced because of a slight voltage drop in the presence of the FCL (due to a series connection to the circuit). Also, the general diagram of the current without the presence of FCL under normal and fault operating conditions is illustrated in Fig. 18, where the fault was initially entered into the system and the analysis was performed on the circuit for 50 ms. As can be observed, the fault impact on the electric current is highly significant.

Also, as mentioned, only the dc leg goes to deep saturation in model B, and to further saturate the ac leg, a dc auxiliary winding is added to it; a flux density diagram is shown in Fig. 19. As it can be seen, the flux density in Model A (partial mode) is slightly better saturated due to the auxiliary winding. Also, in the Model C, the dc leg is not deeply saturated and is conducted by an auxiliary winding to the knee area, which has low values of flux density, as depicted in Fig. 19.

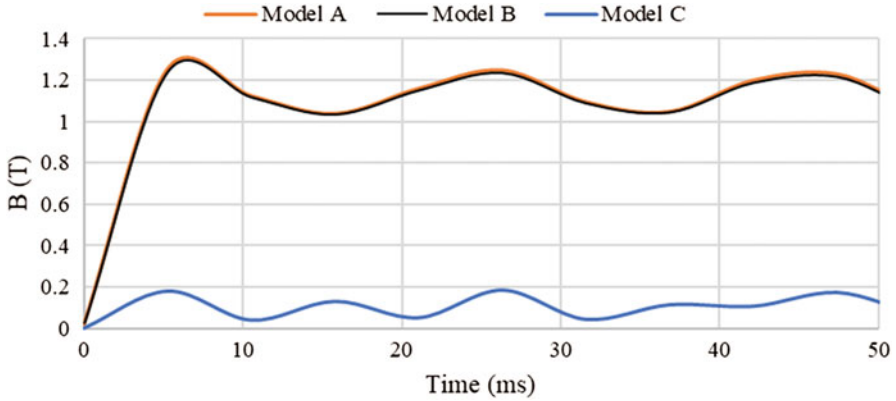


Fig. 19 Magnetic flux density changes versus time for different models

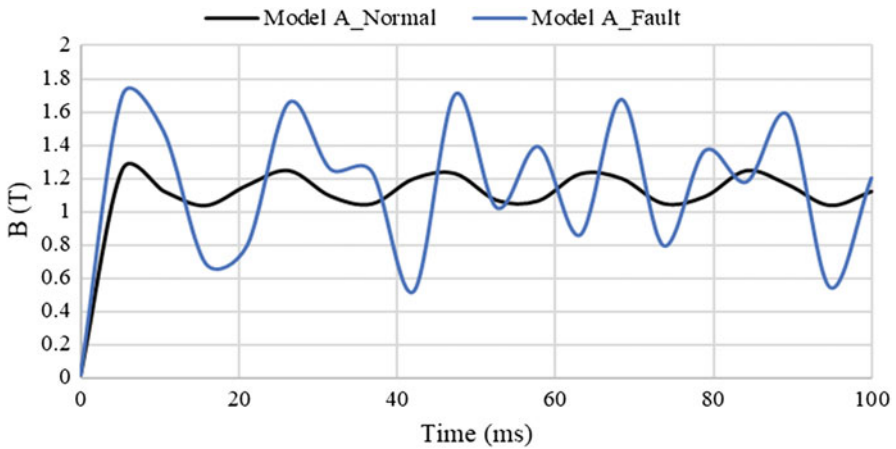


Fig. 20 Magnetic flux density passing through the core for both conditions in model A

Now, if we evaluate the flux density for the Model A in normal and fault conditions, it can be perceived that the flux density is generally higher in the faulty mode. Thus, the fault causes more saturation of the core and a larger impedance. The flux density is shown in Fig. 20 that represents this type of SCFCL is effective in density reduction and the maximum amount of B reaches almost 1.3 T.

Figure 21 depicts the magnetic field strength of the iron core for Model A as well, which is relatively higher in the fault state.

For a general comparison of flux density in the models presented above, their diagrams in normal operation and fault modes are represented in Fig. 22. The lowest flux density value is related to dc short-circuited winding mode in normal operation, which is in saturation mode. Most of the mode is related to the partial model in the fault mode, which possesses deeper saturation. Significant difference in normal and

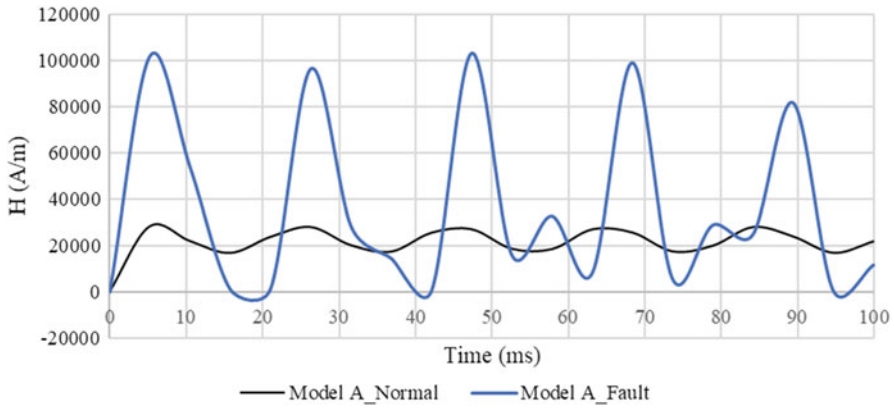


Fig. 21 Magnetic field strength passing through the iron core for model A in normal and fault modes

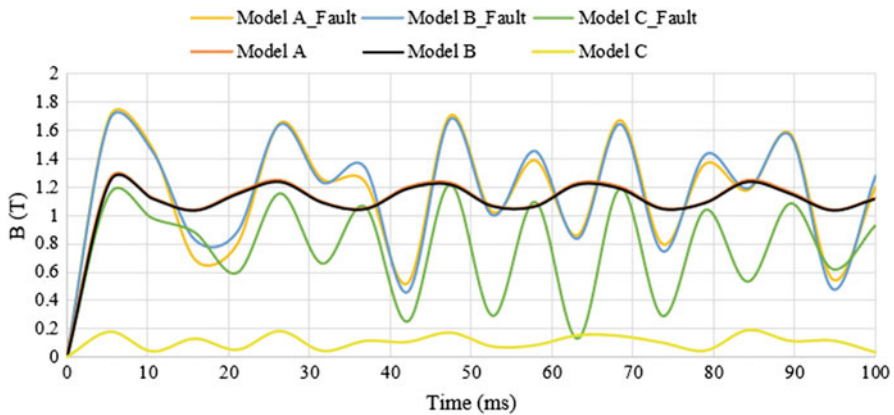


Fig. 22 Comparison of flux density in normal and fault operations

fault modes for Model C is due to the presence of short-circuited dc winding, so the impact of this type of SCFCL is very advantageous. Other structures have smaller decline in flux density than Model C.

The amount of current flow in this model in fault mode has also been investigated in the presence of SCFCL. In this case, we have:

$$B = \mu H \xrightarrow{\text{if}} B \uparrow \Rightarrow H \uparrow, \quad H = \frac{NI}{l} \xrightarrow{\text{depend on } N} NI \text{ (variable)}$$

which can be analyzed using the flux density diagram (Fig. 23).

For example, a fault has been occurred on 23 ms, and the FCL performance for Model A has been investigated, as shown in Fig. 24. As can be inferred, there is no

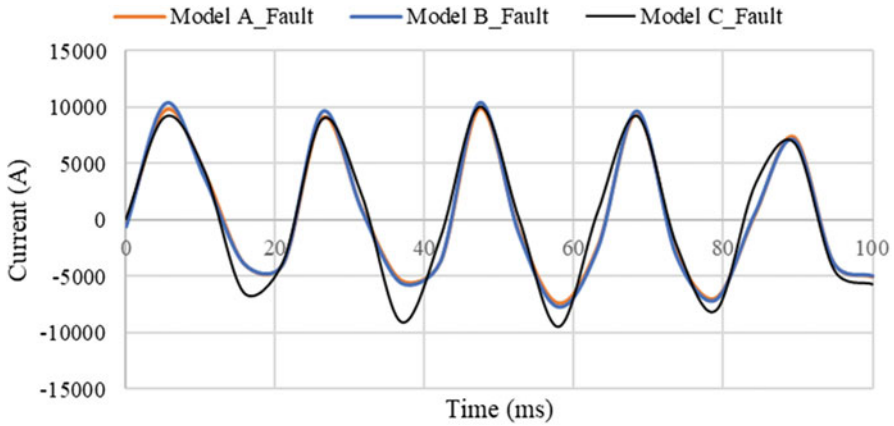


Fig. 23 Current passing through the system during a fault condition with SCFCL

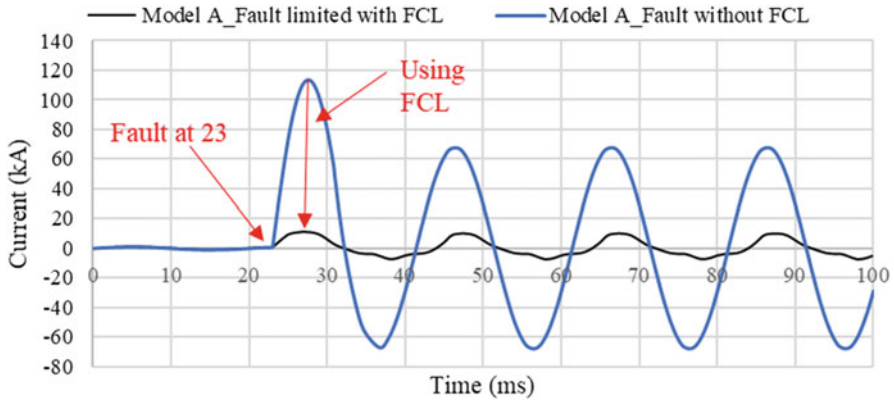


Fig. 24 Current passing through the system by applying a fault in 23 ms

fault until 23 ms and the FCL is in the circuit, so it should not normally have much of an effect on the circuit, which makes sense. After starting the fault in the first peak, the current was almost 116 kA, then the peak of fault current was reduced, which the FCL has amplified properly (we applied this type of fault on 23 ms in this section because the calculation volume is very high and time consuming and for analysis and comparison, so a fault has been applied in this moment).

We now examine the flux density distribution at different points in these three models and make a comparison between them. First, we show how the flux density changes in Model A, which is in the form of Figs. 25 and 26 (for an air gap length of 0.3 m). In Fig. 25, there is a flux density reduction in middle leg that increases near the fault point. After a fault occurrence, there is a huge drop of flux density, that density's concentration is on the top of middle leg at 5 ms. Then, the flux density distributes to other legs after 5 ms that the middle leg experiences the highest flux density. Afterwards, the high-density area transfers to the right leg.

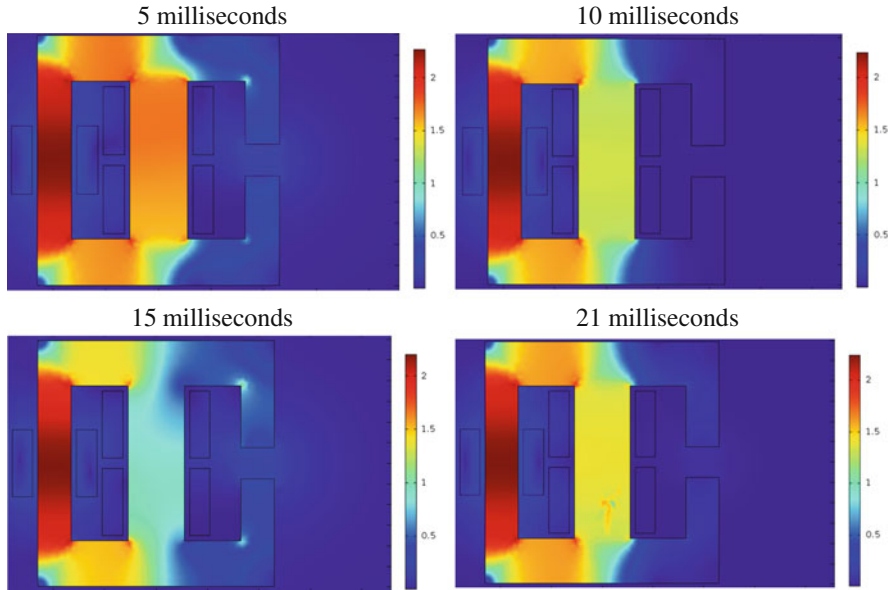


Fig. 25 Flux density illustration during normal mode for Model A

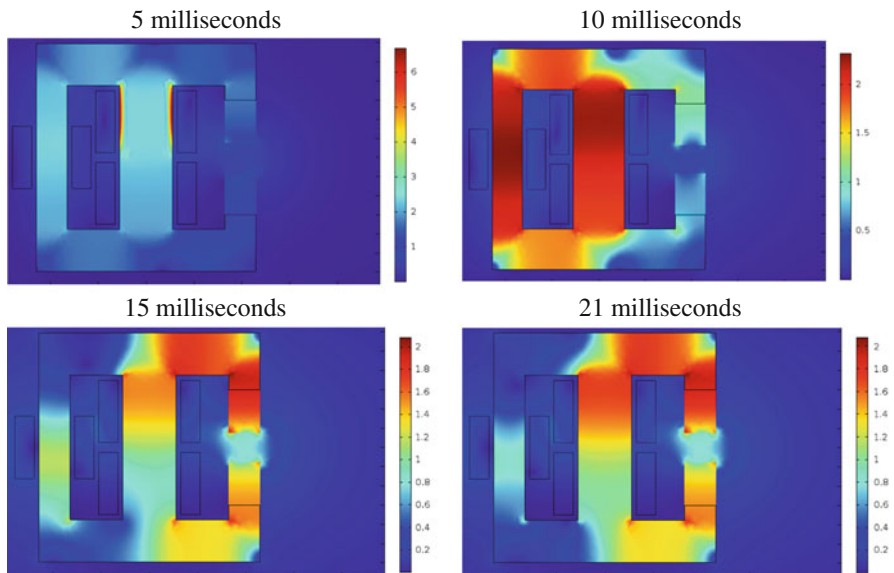


Fig. 26 Flux density distribution for Model A during fault mode

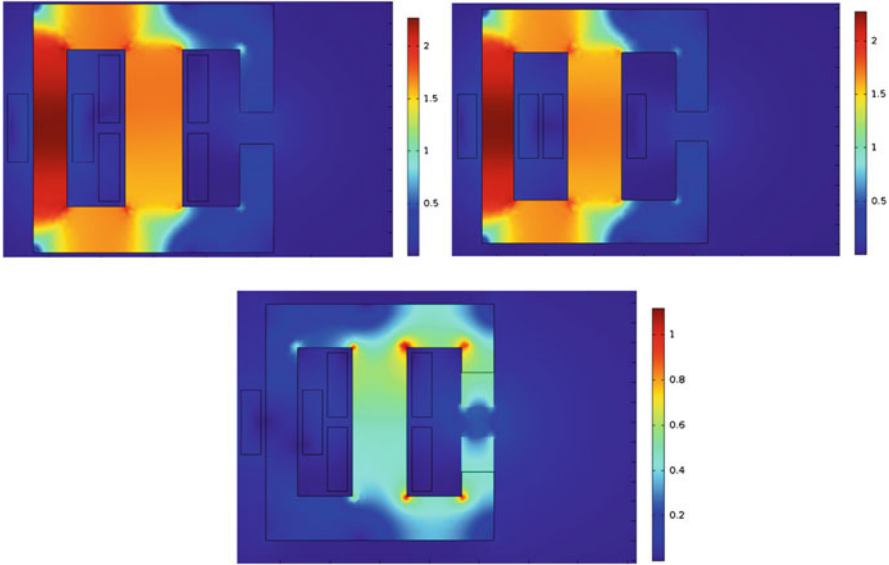


Fig. 27 Comparison of flux density distribution at 5 milliseconds

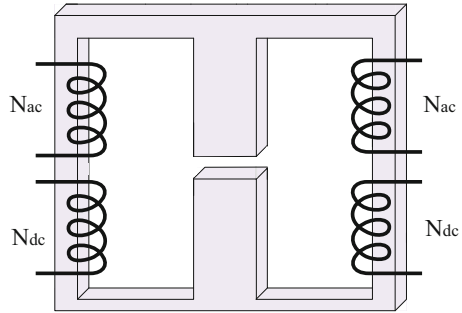
It is evident that the flux density gradually decreases in the central leg and goes out of saturation until it rises again in about 21 ms, but it has never entered deep saturation in this case. Now, the flux density is very high in some positions, due to the fault originating the passage of current through the ac windings. The middle leg is deeply saturated, which is done using the dc auxiliary winding in 10 ms. Flux density is gradually directed from the middle leg to the leg at an air gap, creating little saturation in those areas. Also, the flux density distribution is given for these three models as an example in 5 ms that the diagram has already been given (Fig. 27).

8 Inductive SCFCL

The configuration of a single phase inductive SCFCL is shown in Fig. 28. In this structure, they alternate from one half-cycle to the other half-cycle because the two legs have an ac winding separately, and the leg with the air gap directs the ac flux produced in this leg. Therefore, there are three magnetic legs in this architecture, each with dc and ac coils. The ac coils are placed to the transmission line in series, whilst the dc coils are connected to the direct current source in series [27, 28, 42].

The dc windings are connected in such a way that the dc flux receives a rotational current. As a result, the outside legs of the core are saturated, but the dc flux does not

Fig. 28 Single phase inductive SCFCL



pass through the central leg. So, the dc saturation level does not rely on the length of the air gap (l_{gap}), so we have [24]:

$$\begin{aligned}
 B_{mid} &= 0 \\
 B_o &= \mu_{r,sat} \frac{N_{dc} I_{dc}}{l_{mean,outer}} + (B_{sat} - \mu_{sat} H_{sat})
 \end{aligned}
 \tag{13}$$

Where B_o and B_{mid} and are the dc flux densities in the outer and central legs, correspondingly, and $l_{mean,outer}$ is the average lengths of the outer leg and H_{sat} is the saturation values of the magnetic field. The central leg makes a parallel route for the ac flux, allowing the air gap to be merely in the ac magnetic circuit. After the fault commences, the left and right legs of the core alternate from saturation mode. The connection of the ac windings is during a half cycle, the ac and dc fluxes are in the same direction but are in the opposite directions in another outer leg. Since the reluctance of the right leg is quite high, the ac flux of the left leg blocks its pathway via the center part due to saturation. An inductance of SCFCL can be expressed during normal and fault conditions as Eqs. (14) and (15) [22, 25, 36, 37, 43]:

$$L_{FCL,sat} = \mu_0 \frac{N_{ac}^2 A_{core,outer}}{l_{mean,outer} + l_{gap}} = \mu_0 \frac{N_{ac}^2 A_{core,outer}}{\left(\frac{l_{mean,outer}}{l_{gap}} + 1\right) l_{gap}}
 \tag{14}$$

$$L_{FCL,lin} = \mu_0 \frac{N_{ac}^2 2A_{core,outer}}{l_{gap}} = f(2A_{core,outer})
 \tag{15}$$

Where $L_{FCL,sat}$ is FCL inductance in saturation mode, $A_{core, outer}$ cross-sectional area of the outer leg, and $L_{FCL,lin}$ is FCL inductance out of saturated mode (in fault mode).

9 SCFCL with DC Single-Core Short-Circuited Windings

SCFCL with dc short-circuited windings uses two cores in each phase. The two cores can be combined to further reduce the magnetic materials, which is illustrated in Fig. 29. As can be observed, because the dc leg’s main purpose was to make a low-reluctance path for the dc flux, it was eliminated. In this setup, an extra ac leg takes over the dc leg’s role. The ac flux is directed from each ac winding to the air gap legs using short-circuited windings [18, 25, 43, 44].

In this section, we evaluate the simulation results of models D and E, which we define as the models in Fig. 30. The current passing through the system in the presence of FCL in normal operating conditions has been investigated in this case. Figure 31 shows that these two models have larger impedances than models A, B, and C in the normal operating mode, which is not desirable, and their current has reached up to 400 A or more even in the first peak, although the rated current of the system has a peak of 1000 A. Model D is more desirable than model E in this state (because model E has a larger number of windings and therefore it has more resistance and impedance in a normal operation). There is a drop at the outset of electric current of Model D because of air gap presence at the middle leg.

Fig. 29 Single-core SCFCL configuration with short-circuited windings

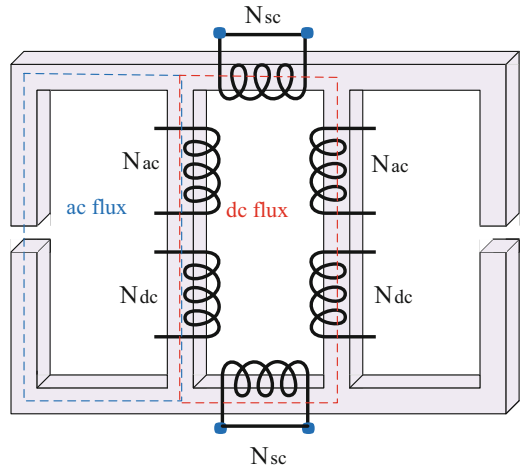
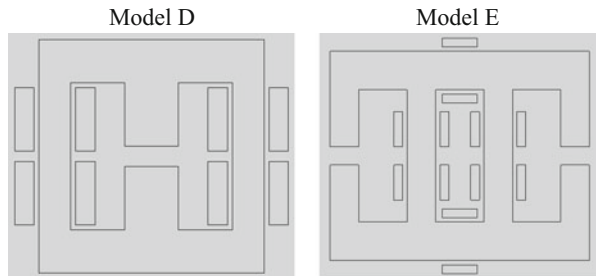


Fig. 30 SCFCL configurations including an inductive saturated core FCL (Model D) and a single-core saturated core FCL with short-circuited windings (Model E)



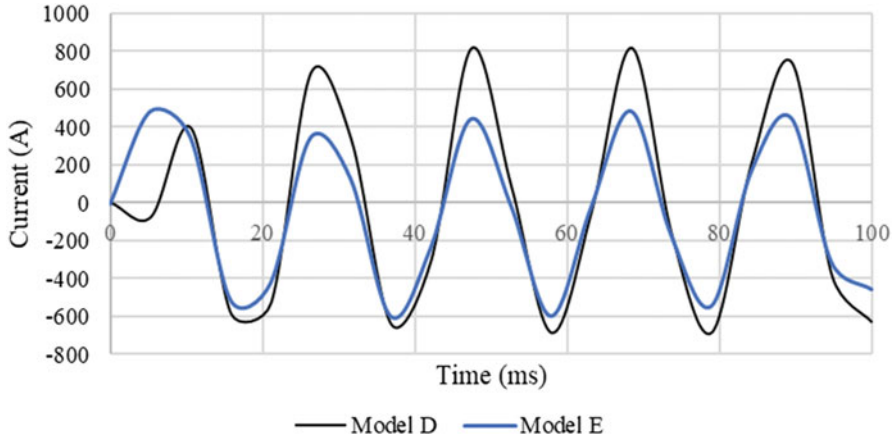


Fig. 31 Current passing through the system with SCFCL in a normal mode

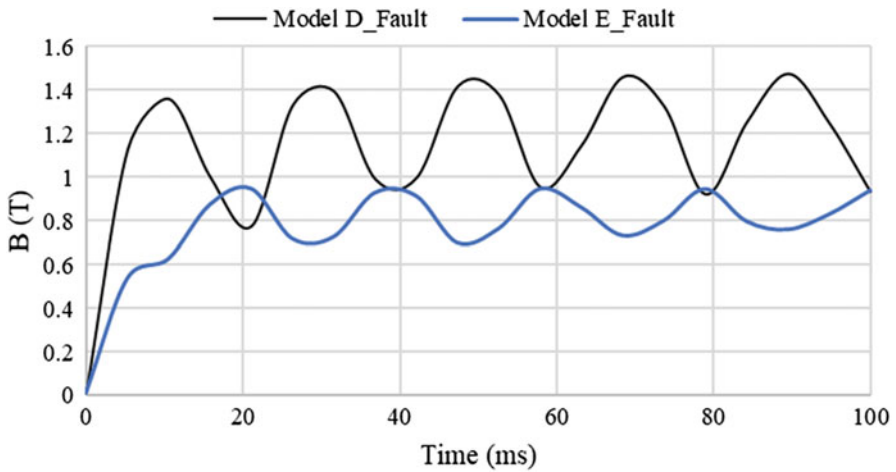


Fig. 32 Flux density of iron core during fault mode for Models D and E

Model D has deeper saturation than model E because the outer legs in model D have dc winding, while in the model E, the dc winding has short-circuited. It causes the iron core to saturate around it later, as shown in Fig. 32, the flux density changes at fault mode for models D and E.

It is possible to show the amount of current in the fault mode for models D and E which their limitation is even less than the nominal current, due to the more voltage drop. Figure 33 observes higher current amplitude than Fig. 31. These structures have a slight effect on reducing the fault in comparison with configurations introduced in previous section and have more material consuming.

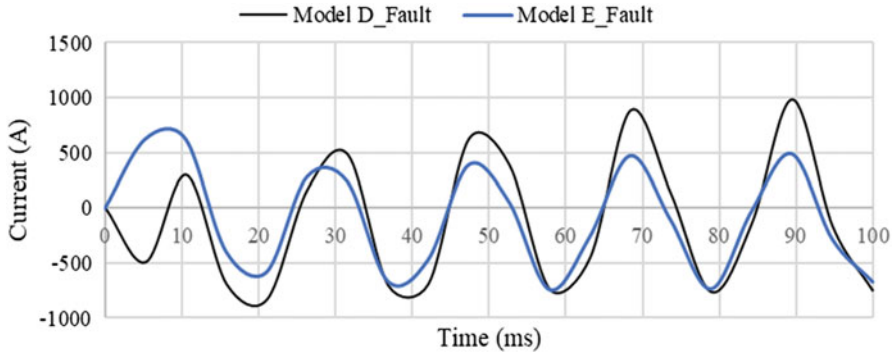


Fig. 33 Current passing through during fault condition with SCFCL

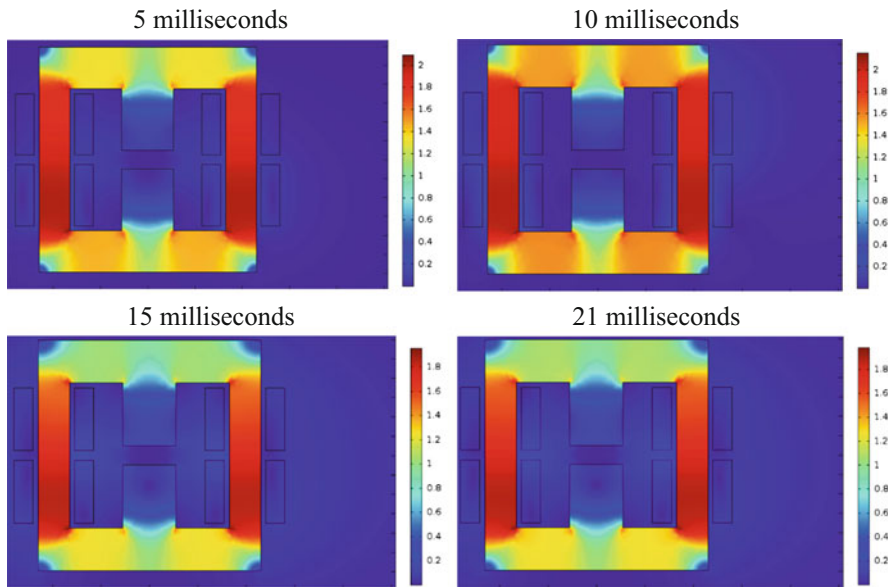


Fig. 34 Flux density distribution for Model D during normal mode

Now, we want to evaluate the flux density distribution in Model D, which are in Figs. 34 and 35 for different times in normal and fault states. By comparing the above two states of flux density distribution, because of the occurrence of a fault, two outer legs gradually deviate from the saturation state, so the flux density is greater than the fault state in the normal mode. It should also be noted that we must apply much dc current to dc winding to fully enter the saturation zone at the beginning of the design; the analogical diagram for two normal and fault modes for model D is shown for 100 milliseconds (Fig. 36).

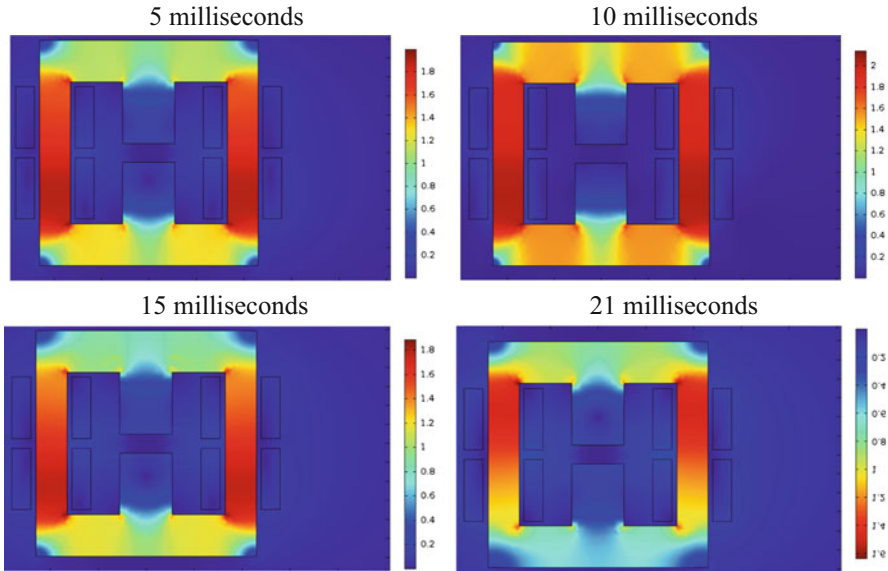


Fig. 35 Flux density distribution for Model D during fault mode

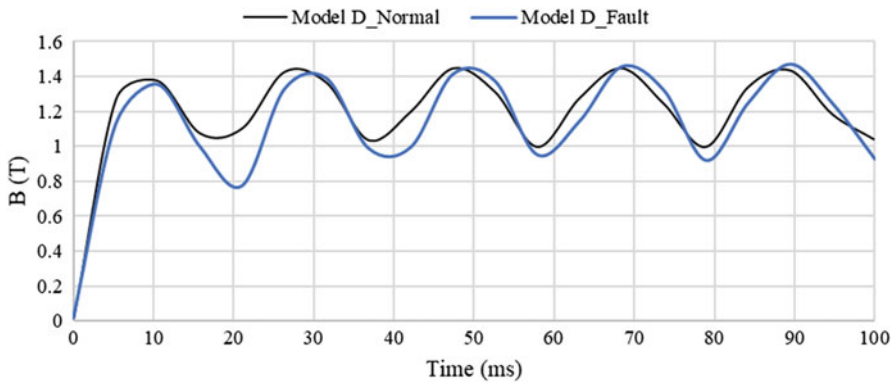


Fig. 36 Flux density for Model D during normal and fault operations

It is also possible to provide a flux density distribution for Model E, which is as follows (Fig. 37).

As it can be perceived, the middle legs are not deeply saturated from the beginning because of the presence of short-circuit windings at the top and bottom of the core, and a large dc current must be applied to the winding to achieve this. The middle legs become gradually saturated over time, and the flux slowly disperses at the surface of the iron core, with the middle legs alternating between saturated and unsaturated modes. There is a summary of proposed configurations and their specifications in Table 3.

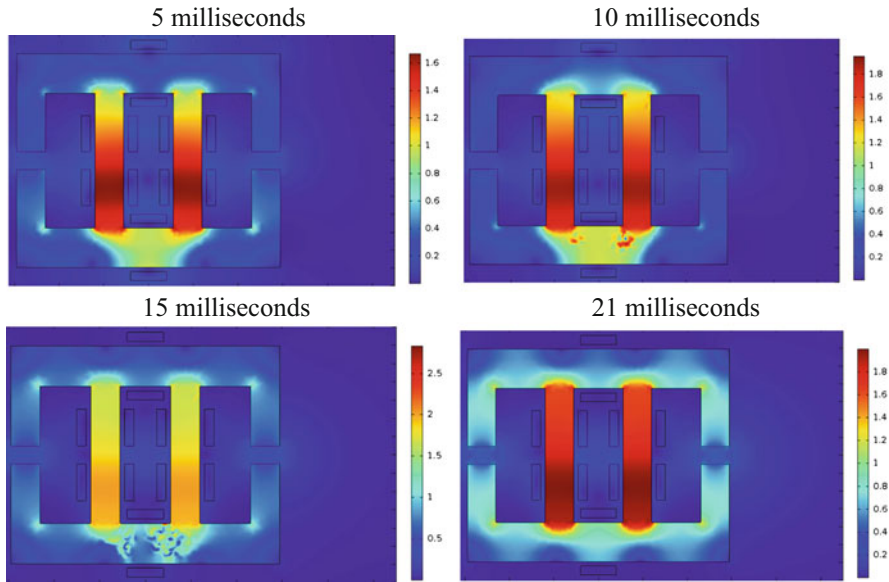
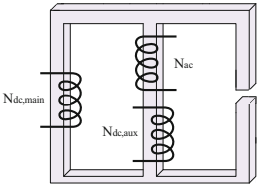
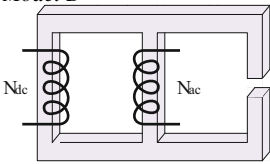
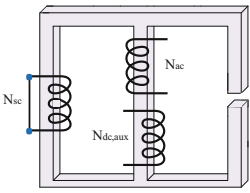
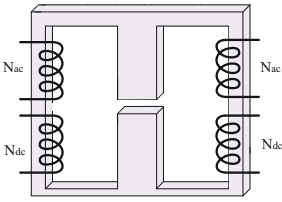
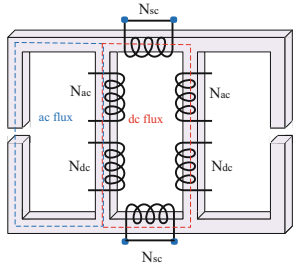


Fig. 37 Flux density distribution for Model E during normal operation

10 Conclusion

Nowadays, fault current limiters can have considerable effects on any failure or outage in power systems. FCLs are very helpful to postpone the replacement of power devices and they take an important role in the mitigation of fault impacts on a power grid. Saturated-core FCLs can be attractive because of saturation features and prompt changes of flux between the different parts of an iron core. Suitable designs of this type of FCLs in terms of material, volume and type of winding placement can be helpful for industrial engineers to utilize an efficient configuration regarding their applicability. Also, this device can remarkably reduce the vulnerability of a power grid. This chapter presents an analysis of different configurations of SCFCLs in which their designs are relied on the number of windings, windings' positions and other factors. Various parameters of this protective device including electric current, magnetic flux density and magnetic field strength are assessed and compared. A numerical analysis with finite element method is carried out to provide comprehensive information related to SCFCLs to demonstrate the variables' changes during normal operation or fault mode comprehensively.

Table 3 Summary of proposed SCFCL configurations

SCFCL configuration	Design specifications
<p><i>Model A</i></p> 	<p>Every phase has two cores Partial magnetic separation of dc & ac fluxes An air gap in side leg voltage is induced in dc winding FCL impedance is declined during normal conditions</p>
<p><i>Model B</i></p> 	<p>Every phase has two cores There is no voltage induced 100% magnetic separation of dc & ac fluxes An air gap in sidelong leg There is no deep saturation in the middle leg because of one ac winding FCL impedance is increased during normal conditions</p>
<p><i>Model C</i></p> 	<p>Every phase has two cores Partial magnetic separation of dc & ac fluxes An air gap in sidelong leg volume of winding material is mitigated because of short-circuited dc winding</p>
<p><i>Model D</i></p> 	<p>Existence of an air gap in middle leg Partial magnetic separation of dc & ac fluxes single phase inductive SCFCL (every phase has a core) Conduction of ac flux across the leg with air gap is sufficient</p>
<p><i>Model E</i></p> 	<p>Partial magnetic separation of dc & ac fluxes single phase inductive SCFCL (every phase has a core) changes in flux distribution because of winding positions</p>

References

1. Naphade V, Ghate V, Dhole G (2021) Experimental analysis of saturated core fault current limiter performance at different fault inception angles with varying DC bias. *Int J Electr Power Energy Syst* 130:106943
2. Jia Y et al (2017) Numerical simulation and analysis of a saturated-core-type superconducting fault current limiter. *IEEE Trans Appl Supercond* 27(4):1–5
3. Zhao Y et al (2014) Performance analysis of flux-lock type SFCL influenced by characteristics of two coils. In: 2014 IEEE PES General Meeting| Conference & Exposition, pp 1–5
4. Zhou H, Yuan J, Chen F (2020) Hybrid-material based saturated core FCL in HVDC system: modeling, analyzing and performance testing. *IEEE Trans Ind Electron*
5. Yuan J et al (2020) Optimized design method of permanent magnets saturated core fault current limiters for HVDC applications. *IEEE Trans Power Deliv* 36(2):721–730
6. Zhou H et al (2019) Performance investigation on a novel high inductance changing ratio MMC-based direct current system saturated core FCL. *IEEE Trans Power Deliv* 35(3): 1502–1514
7. Liu Y et al (2021) Design of a multifunction novel flexible fault current limiter for AC distribution network. *PLoS One* 16(4):e0245956
8. Wei L et al (2020) Limiting mechanism and equivalent analytical model of a bridge-type saturated core fault current limiter. *Electr Power Syst Res* 180:106134
9. Ouali S, Cherkaoui A (2020) Integration of fault current limiters in electric power systems: a review. *IEEE Syst J*
10. Alam MS et al (2018) Fault current limiters in power systems: a comprehensive review. *Energies* 11(5):1025
11. Zhang X, Zhang Y (2019) A viable approach for limiting fault currents in electric networks. *IEEE Trans Electr Electron Eng* 14(4):556–560
12. Li B et al (2019) Current-limiting characteristics of saturated iron-core fault current limiters in VSC-HVDC systems based on electromagnetic energy conversion mechanism. *J Mod Power Syst Clean Energy* 7(2):412–421
13. Shen H et al (2018) Three-phase saturated-core fault current limiter. *Energies* 11(12):3471
14. Safaei A et al (2020) A survey on fault current limiters: development and technical aspects. *Int J Electr Power Energy Syst* 118:105729
15. Shen H et al (2018) Study of a new structure of three-phase saturated-core fault current limiter. In: 2018 International Conference on Smart Grid and Clean Energy Technologies (ICSGCE), pp 239–243
16. Wei L et al (2018) Performance investigation and optimization of a novel hybrid saturated-core fault-current limiter considering the leakage effect. *Energies* 11(1):61
17. Yuan J et al (2018) A novel concept of fault current limiter based on saturable core in high voltage DC transmission system. *AIP Adv* 8(5):56636
18. Baferani MA et al (2018) A novel arrangement for improving three phase saturated-core fault current limiter (SCFCL). In: 2018 IEEE Texas Power and Energy Conference, pp 1–6
19. Ruiz HS et al (2014) Resistive-type superconducting fault current limiters: concepts, materials, and numerical modeling. *IEEE Trans Appl Supercond* 25(3):1–5
20. Tan YX et al (2015) Resistive type superconducting fault current limiter and current flowing time. In: 2015 IEEE International Conference on Applied Superconductivity and Electromagnetic Devices (ASEMD), pp 290–291
21. Chen B et al (2016) Parameter design and performance investigation of a novel bridge-type saturated core fault current limiter. *IEEE Trans Power Deliv* 32(2):1049–1057
22. Commins PA, Moscrop JW (2012) Three phase saturated core fault current limiter performance with a floating neutral. In: 2012 IEEE Electrical Power and Energy Conference, pp 249–254
23. Linden J et al (2019) Design optimization of a permanent-magnet saturated-core fault-current limiter. *Energies* 12(10):1823

24. Linden J et al (2020) Phase-coupling effects in three-phase inductive fault-current limiter based on permanent magnets. *IEEE Trans Magn* 56(2):1–7
25. Commins PA, Moscrop JW (2012) Analytical nonlinear reluctance model of a single-phase saturated core fault current limiter. *IEEE Trans Power Deliv* 28(1):450–457
26. Cvoric D et al (2009) New saturable-core fault current limiter topology with reduced core size. In: 2009 IEEE 6th International Power Electronics and Motion Control Conference, pp 920–926
27. Cvoric D et al (2016) 3D nonlinear transient field-circuit modeling of inductive fault current limiters. *Int J Numer Model Electron Networks, Devices Fields* 29(2):354–360
28. Cvoric D et al (2008) Comparison of the four configurations of the inductive fault current limiter. In: 2008 IEEE Power Electronics Specialists Conference, pp 3967–3973
29. Branco PJC et al (2010) Proposal for an RMS thermoelectric model for a resistive-type superconducting fault current limiter (SFCL). *Electr Power Syst Res* 80(10):1229–1239
30. Yamaguchi H et al (2004) Characteristics analysis of transformer type superconducting fault current limiter. *IEEE Trans Appl Supercond* 14(2):815–818
31. Han T-H et al (2018) Fault current limiting characteristics of transformer-type superconducting fault current limiter due to winding direction of additional circuit. *IEEE Trans Appl Supercond* 28(3):1–6
32. Badakhshan M (2018) Flux-lock type of superconducting fault current limiters: a comprehensive review. *Phys C Supercond Appl* 547:51–54
33. Lim SH (2011) Analysis on current limiting characteristics of a flux-lock type SFCL with two triggering current levels. *Phys C Supercond Appl* 471(21–22):1354–1357
34. Kim J-S et al (2010) Study on protection coordination of a flux-lock type SFCL with over-current relay. *IEEE Trans Appl Supercond* 20(3):1159–1163
35. Tripathi PM, Chatterjee K (2021) Real-time implementation of ring based saturated core fault current limiter to improve fault ride through capability of DFIG system. *Int J Electr Power Energy Syst* 131:107040
36. Zhou H et al (2020) Inductive fault current limiters in VSC-HVDC systems: a review. *IEEE Access* 8:38185–38197
37. Cvoric D et al (2009) Guidelines for 2D/3D FE transient modeling of inductive saturable-core fault current limiters. In: 2009 International Conference on Electric Power and Energy Conversion Systems (EPECS), pp 1–6
38. Gunawardana SM et al (2016) Transient modeling of saturated core fault current limiters. *IEEE Trans Power Deliv* 31(5):2008–2017
39. Nikulshin Y et al (2016) Saturated core fault current limiters in a live grid. *IEEE Trans Appl Supercond* 26(3):1–4
40. Baimel D, Chowdhury N, Belikov J, Levron Y (2021) New type of bridge fault current limiter with reduced power losses for transient stability improvement of DFIG wind farm. *Electr Power Syst Res* 197:107293
41. Yuan J et al (2020) Saturated-core fault current limiters for AC power systems: towards reliable, economical and better performance application. *High Volt* 5(4):416–424
42. Pirhadi A, Shayan H, Bina MT (2020) Design of an unsaturated core-based fault current limiter to tackle unsymmetrical faults. *Electr Power Syst Res* 187:106482
43. Pellicchia A et al (2016) Development of a saturated core fault current limiter with open magnetic cores and magnesium diboride saturating coils. *IEEE Trans Appl Supercond* 27(4):1–7
44. Vilhena N et al (2018) A design methodology for the optimization of three-phase SFCL of saturated cores type. *IEEE Trans Appl Supercond* 28(4):1–5

Optimized Settings of Over Current Relays in Electric Power Systems



Abdelmonem Draz, Mahmoud Elkholy, and Attia El-Fergany

1 Introduction

Protection relays are the brain of the protection scheme that detect the fault based on its nature and then initiate a tripping command to the Circuit Breaker (CB) to isolate the fault. To promote the protection scheme performance, the operation of these relays should achieve a set of requirements. Reliability, sensitivity, redundancy, and selectivity are deemed as the basic attributes that prevail in a well-performed protection scheme. In this context, the most implemented protection type in power systems whether it is radial or meshed, low or medium voltage network is the Over Current (OC) protection. In addition to its simple operation, it has various Characteristics (CCCs) according to the desired application. OC protection is achieved in low voltage distribution networks using fuses and CB with built-in trip unit. This trip unit may be a thermo-magnetic type or electronic type to increase the adjustability in settings range [1].

Over Current Relays (OCRs) are considered as the main protector against OC in medium-voltage distribution networks. They have diverse CCCs like instantaneous, definite time, and inverse type that facilitate their coordination process. OCR with instantaneous CCCs operates without any deliberated time lag, whilst the definite time CCCs trips at an adjustable but fixed time independent of the current magnitude [2]. However, these CCCs limit the cascade protection levels, unlike the inverse type, which assures the coordination flexibility. Accordingly, OCRs have mainly three settings: the current pickup which represents the limit value above which the tripping zone of the relay starts. Moreover, the time dial and the Time Current Characteristic (TCC) type are the additional settings that control the inverse degree

A. Draz · M. Elkholy · A. El-Fergany (✉)
Electrical Power and Machines Department, Zagazig University, Zagazig, Egypt
e-mail: el_fergany@zu.edu.eg

Table 1 Constant values for diverse standardized operating curves

Standard	TCC type	a	β	γ
IEC	NI	0.14000	0.02000	0.00000
IEC	VI	13.50000	1.00000	0.00000
IEC	EI	80.00000	2.00000	0.00000
IEC	LI	120.00000	1.00000	0.00000
UK	Rectifier	45900.00000	5.60000	0.00000
IEEE	MI	0.05150	0.02000	0.11400
IEEE	VI	19.61000	2.00000	0.49100
IEEE	EI	28.20000	2.00000	0.12170
US-CO8	Inverse	5.95000	2.00000	0.18000
US-CO2	SI	0.16758	0.02000	0.11858
ANSI	Inverse	8.93410	2.09380	0.17966
ANSI	SI	0.26630	1.29690	0.03393
ANSI	LI	5.61430	-1.00000	2.18592
ANSI	MI	0.01030	0.02000	0.02280
ANSI	VI	3.92200	2.00000	0.09820
ANSI	EI	5.64000	2.00000	0.02434
ANSI	DI	0.47970	1.56250	0.21359

between the current and the tripping time. Hereinafter, the governing equation that estimates the relay OT (OT) (t_{ri}) as a function of its settings and the fault current (I_f) passing through it is as described in (1) [1, 2].

$$t_{ri} = \left(\frac{a}{\left(\frac{I_f}{I_{pu}}\right)^\beta - 1} + \gamma \right) T_D \quad (1)$$

where: I_{pu} is the current pickup, T_D is the time dial setting, I_f is the magnitude of the actual I_f , and a , β , and γ are constants which their values vary with the selected standard TCC type as declared in Table 1. Figure 1a, b illustrate samples of some standardized operating curves carefully chosen from IEC 60255-3 [1] and ANSI/IEEE C37.112 [3].

Plain OCR is used in radial networks and requires only a current signal from the current transformer. Conversely, Directional OCR (DOCR) is implemented in meshed networks to minimize the system outage by initiating a tripping command only if the fault occurs in its forward tripping zone. Therefore, DOCR requires an additional voltage signal from the voltage transformer to create a reference polarized vector differentiating between forward and reverse faults [2].

The correct consequence of operation between DOCRs to guarantee the minimum outage of power systems is called selectivity, discrimination, or coordination. This process is one of the aspects that governs the protection scheme performance and therefore it shall be optimized. The first line of defense against the faults is called the main Protective Device (PD) while the backup one operates if the main fails to initiate a tripping command. Coordination Time Margin (CTM) is

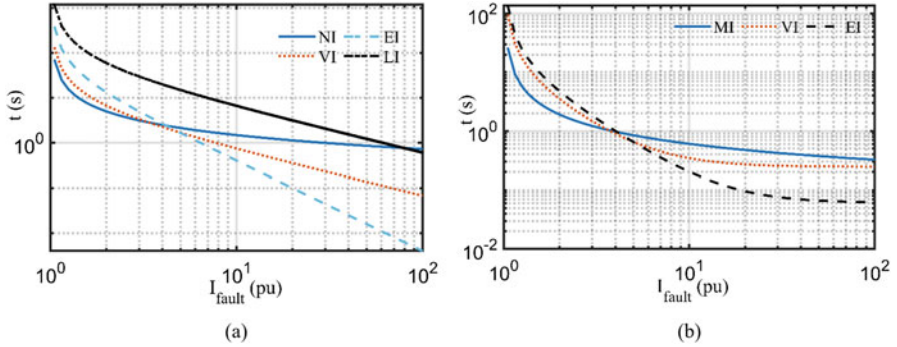


Fig. 1 Samples of IEC and ANSI/IEEE standardized tripping curves. (a) IEC curves. (b) IEEE curves

the time gap between the secondary and the main PDs at the same fault location. The coordination process can be classified into two main categories: absolute coordination and relative coordination [2].

2 Coordination Methods

2.1 Absolute Coordination

The relay operation is instantaneous without any intentional time delay and independent of the operation of other relays in their protected zones. Differential and restricted earth fault relays follow this behavior.

2.2 Relative Coordination

The operation of the PD can be instantaneous or with a time delay and depends on other PDs in other protected zones. This behavior can be found in the protection against over currents and earth faults.

3 Methods of Relative Coordination

3.1 Current Type Selectivity

It depends on the I_f magnitude and its value gets larger when closer to the supply. So, PDs are set to operate for a certain value of I_f and therefore this type of selectivity is also partial.

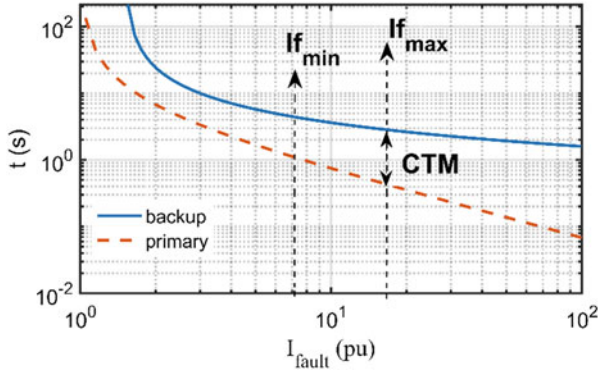


Fig. 2 Full selectivity between M/B relay pairs

3.2 Time Type Selectivity

It depends on the time graded between PDs from downstream to the upstream with Definite Time (DT) CCCS. Though, the number of discrimination levels is limited to avoid the larger OT of the PD installed in the network upstream.

3.3 Time Current Type Selectivity

It is the most recommended method used with OCRs in medium-voltage distribution networks, and it can be used also with low-voltage PDs. It combines the principles of the previous two types by selecting the suitable TCCs of the Main/Backup (M/B) relay pairs, as revealed in Fig. 2. It can be noted that the full selectivity is fulfilled between the M/B relay pairs by ensuring that there is no intersection between the minimum and maximum fault values.

3.4 Energy Type Selectivity

It can only be achieved between Low Voltage CBs (LVCBs) of the same manufacturer. Its performance depends on the fact that the let through energy associated with the downstream LVCB required to trip is lower than the associated value of the upstream LVCB. Consequently, the results are presented in real laboratory tests coordination tables documented by the LVCBs supplier.

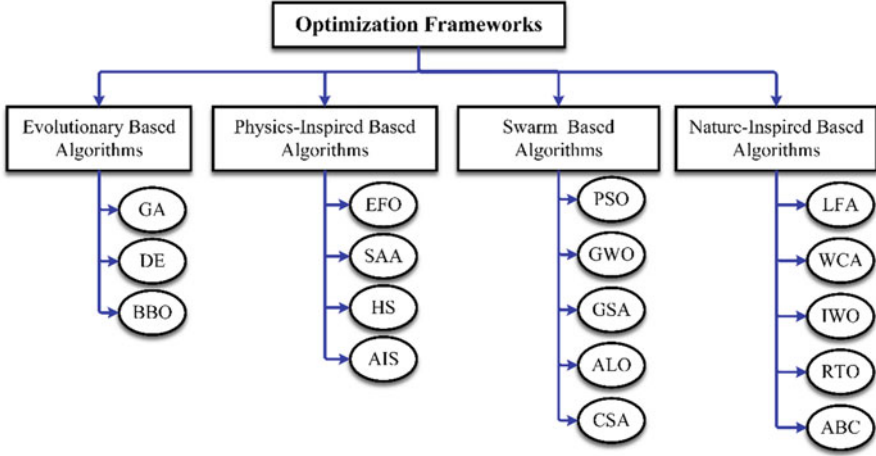


Fig. 3 Optimization algorithms classification for DOCRs coordination

4 OCRs Coordination Process Formulation

The coordination process can be represented as a nonconvex and nonlinear constrained optimization problem. In this context, optimized settings of OCRs are attained using a specified Objective Function (OF) incorporating various collection of constraints. The OF can be formulated by lessening the Total OT (TOT) of the main and/or the backup relays and also with different styles discussed later in this chapter. Regarding optimizing the coordination dilemma in meshed networks, the formulation of all possible M/B relay pairs and their associated I_f values is a prerequisite. In earlier days, many attempts have been dedicated to solve this problem using LP, NLP, and mixed-integer NLP techniques. However, due to the technology advancement, the competition between metaheuristic algorithms with various natures to obtain the global optimal solution is still in process. Figure 3 shows the classification of the optimization algorithms coped with DOCRs coordination model, as illustrated in [2].

5 Objective Function and Its Associated Constraints

The simplified OF that has been tackled by most of the researchers is illustrated through (2) which minimizes the TOT of the main relays [4].

$$OF = \sum_{i=1}^N t_{ri} \quad (2)$$

where: i is the relay counter, N is the total number of DOCRs in the tested network. The OF is subjected to the coming constraints:

5.1 Model Basic Constraints

The basic constraints that should be fulfilled to obtain satisfactory feasible results are described in Eqs. (3)–(6). Moreover, there are additional novel constraints inserted into the optimization model for conceiving some power system issues like transient stability and arc-flash incident energy.

5.2 Boundary Constraints

The attained optimized settings (i.e., I_{pu} and T_D) of DOCRs shall be bounded between minimum and maximum values for feasible results [2, 4].

$$T_{Di,\min} \leq T_{Di} \leq T_{Di,\max} \quad (3)$$

In this regard, the time dial setting is bounded between minimum ($T_{Di,\min}$) and maximum ($T_{Di,\max}$) value, as found in (3) elaborated in the commercial relay settings range. It is worth mentioning that the T_D has continuous values in digital relays while it has discrete values in electromechanical relays and is called Time Setting Multiplier.

$$I_{pui,\min} \leq I_{pui} \leq I_{pui,\max} \quad (4)$$

$$I_{pui,\min} \geq OLF \times I_{load,\max} \quad (5)$$

$$I_{pui,\max} \leq SF \times I_{fault,\min} \quad (6)$$

The philosophy of selecting the I_{pu} of the relay is illustrated in (4)–(6) where $I_{pui,\min}$, $I_{pui,\max}$ are the min/max limits of the I_{pu} of i th relay, respectively. In order to allow the system to operate at 100% of its capacity, $I_{pui,\min}$ shall be higher than the maximum loading current ($I_{load,\max}$) by a certain value greater than one called the Over Loading Factor (OLF). In this context, $I_{pui,\max}$ shall be less than the minimum I_f ($I_{fault,\min}$) by a certain value smaller than one called Safety Factor (SF) to assure that the OCR will trip in the minimum fault conditions as well. Based on the recommended practices, OLF is ranged between 1.25 and 2 while SF is ranged between 0.8 and 0.9.

5.3 Operating Constraints

The correct operating sequence of PDs is fulfilled as defined in (7) and (8) whereas t_{bri} , and t_{pri} stand for the OTs of backup and main PD, respectively.

$$\Delta t_j = t_{\text{bri}} - t_{\text{pri}} \quad (7)$$

$$\text{CTM}_{\text{min},j} \leq \Delta t_j \leq \text{CTM}_{\text{max},j} \quad (8)$$

Moreover, the discrimination time Δt_j between the M/B relay pair at the same fault location should have a positive value bounded between minimum ($\text{CTM}_{\text{min},j}$) and maximum ($\text{CTM}_{\text{max},j}$) values of the CTM.

The applicability of the attained relay settings is completed when t_{pri} is higher than the specific minimum value of the relay OT ($t_{\text{min},i}$) stamped in the relay data sheet, as illustrated in (9). It is worth to mention that the relay would trip in the least possible OT by activating the instantaneous CCCs.

$$t_{\text{pri}} \geq t_{\text{min},i} \quad (9)$$

Hereinafter, optimization models with diverse concepts for DOCRS coordination are discussed.

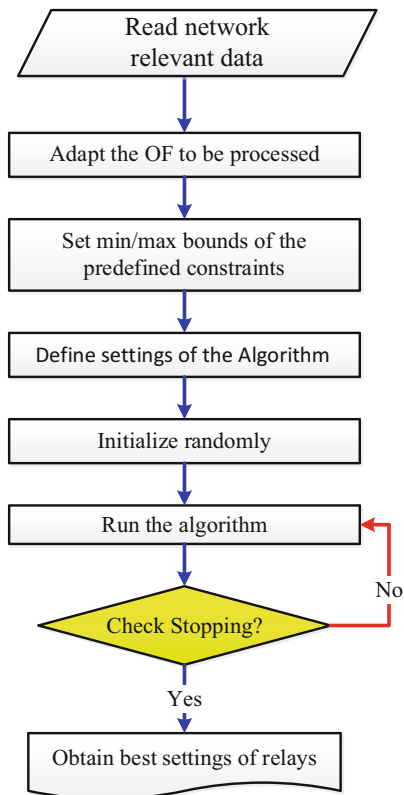
6 Various Optimization Frameworks for DOCRs Coordination

6.1 Optimal DOCRs Coordination Using Optimization Algorithms

Metaheuristic algorithms have become the most powerful approaches for solving the power systems optimization aspects. They are united in the operating principles but differ in the operating technique. Figure 4 demonstrates the basic general steps for defining DOCRs optimization problem using different population-based algorithms [2]. As it is clear that the optimization model starts with defining the input data, like the relay pairs and I_f values proceeding with the OF formulation, then, setting the min/max boundaries of the model constraints, defining the algorithm control parameters, and finally running the model.

Various algorithms diverted in nature have been investigated for the optimal process of DOCRs coordination like the stochastic fractal search algorithm [4]. A new optimizer called opposition-based class toppler optimization is implemented in [5], which is an amended version of the traditional CTO. Furthermore, a hybrid technique is employed in [6] between the gradient-based optimizer and the adaptive differential evolution based on the technique of the linear population size reduction

Fig. 4 Generic steps of DOCRs coordination optimization



to enhance the optimization process in finding the best results. In addition, some amendments have been integrated into the basic Water Cycle Approach (WCA) as disclosed in [7] to realize the equilibrium between the phases of exploration and exploitation. In this context, an improved firefly algorithm [8] and enhanced GWO [9] are presented to promote the convergence rate by lessening the computational time, especially in on-line applications.

Since the hybridization technique manifests its superiority for solving this optimized problem, a hybrid GWO-WO approach is proposed in [10]. Moreover, the fuzzy logic decision-making tool is integrated with the multi-objective GWO in [11] to obtain the best solution among various optimized ones. The Slime Mould Optimizer (SMO) proposed in [12] is considered as one of the latest algorithms applied in this problem and proves its superiority over the other optimizers. Some of the results obtained by the SMO over a standard test case network will be discussed later in this chapter.

6.2 *DOCRs Coordination With and Without Distributed Generators*

Basically, DGs can be classified into two main types; Inverter-Operated DGs (IODGs) and Synchronous-Operated DGs (SODGs). SODGs increase remarkably the I_f level at the installation location unlike the IODGs that are classified as fault restrictors that limit the level of the I_f from one to two per unit [13]. Afterward, various sizes and location of DGs along with preserving the optimal coordination are addressed [14] and solved using the GA. The researchers [15, 16] investigate the penetration of the Renewable Energy Resources (RERs) on the coordination process. Moreover, connecting and disconnecting states of RERs with several operating modes are examined in [16] and solved using the Random Walk GWO technique.

It is recognized that Fault Current Limiters (FCLs) are deployed in distribution networks to mitigate the effect of DGs penetration on DOCRs coordination. Therefore, a multi-objective approach is presented in [17] for maximizing the mitigation impact of FCLs and minimizing their cost by determining their optimal location with their associated impedance values. A novel attempt is dedicated in [18] using variable locations and sizes of DGs for optimal relay coordination based on constraints reduction technique.

6.3 *Optimal Coordination of DOCRs Coordination in Microgrids*

Microgrids (MGs) have two operating modes; islanded and grid-connected mode that has a profound effect on short circuit level. Many attempts have been presented in the literature for optimum sizing of FCLs besides attaining the optimal coordination of protection relays. In this context, a hybrid approach based on cuckoo search algorithm and LP is investigated [19] preserving the optimal coordination in both operating styles of MGs. The coordination of DOCRs in smart grids is discussed [20] by optimizing the operating CCCs to maintain the network stability in the case of transient conditions. Moreover, a comprehensive review for the MGs protection is revealed [21] using the architecture of AC, DC, and hybrid MGs. The calculation of T_D based on the single phase to earth fault computations [22] in addition to optimizing the coordination process in wind farms for various fault types [23] are represented as new thoughts in MGs protection.

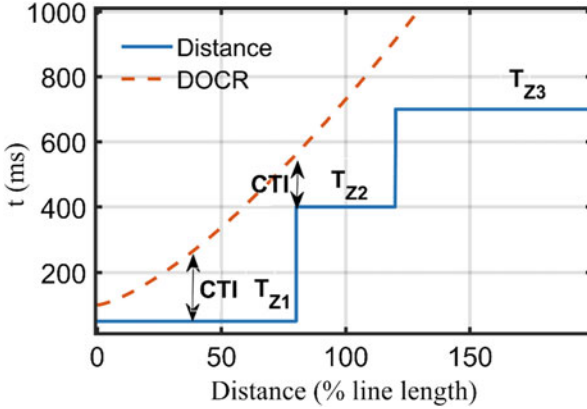


Fig. 5 Hybrid coordination between distance and DOCRs

6.4 Mixed Discrimination Between Impedance and DOCRs

DOCRs can be deemed as the secondary protection for impedance relays in subtransmission systems [24]. Therefore, the discrimination between distance and DOCRs has become a target for the protection engineers, as shown in Fig. 5 to boost the protection scheme performance. In addition, novel DOCRs operating CCCs formulated by an inverse type accompanied by inverse or definite type is deployed in [24] to eliminate the miscoordinations.

6.5 DOCRs Coordination with Dual Setting CCCs

This optimization concept relies on activating the DOCRs reverse direction with separate settings of forward direction as represented in (10) and (11). Both directions have inverse CCCs as depicted in Fig. 6, and their OTs shall be optimized simultaneously in the optimization model [25].

$$t_{fwri} = \left(\frac{a_{fw}}{\left(\frac{I_f}{I_{pufw}} \right)^{\beta_{fw}} - 1} + \gamma_{fw} \right) T_{Dfw} \quad (10)$$

$$t_{rvri} = \left(\frac{a_{rv}}{\left(\frac{I_f}{I_{purv}} \right)^{\beta_{rv}} - 1} + \gamma_{rv} \right) T_{Drv} \quad (11)$$

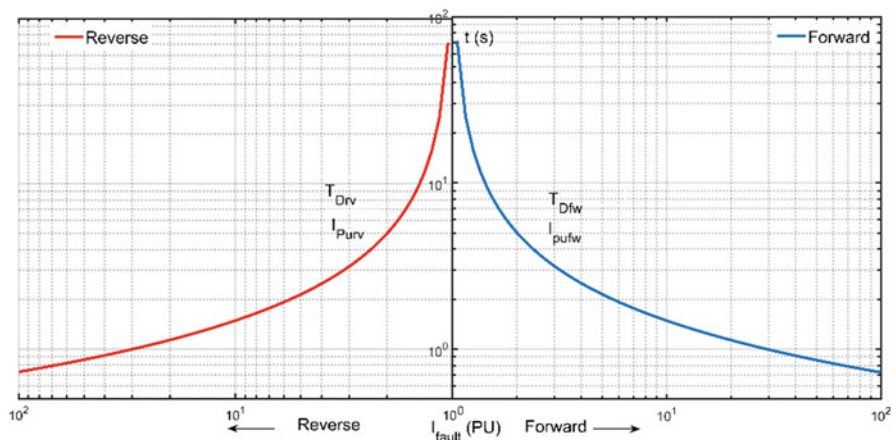


Fig. 6 DOCR with dual operating CCCs

In addition, multiple fault locations approach with nonstandard operating CCCs have been investigated in [26] for better OF solutions. A hybrid communication infrastructure between distance and dual setting DOCRs has been implemented in [27] for N-1 contingency analysis. This model performance is evaluated over the IEEE 14-bus and solved using Chaotic PSO by optimizing the coefficients of both tripping equations.

6.6 Optimal Coordination Using Various, User Defined, and Nonstandard Tripping CCCS

Some researchers insert the DOCR operating curve into the optimization model besides I_{pu} and T_D , as is the case in [28] for better results. However, the optimization of the operating equation parameter (γ) in [29] assures a fast-tripping protection scheme, achieving a notable reduction in the TOT. The deployment of nonstandard CCCs for optimal DOCRs coordination with various DGs types in [30] manifests that it is a good selected approach for this problem. Furthermore, additional parameters optimization in [31] increase the coordination flexibility considering also DGs stability.

6.7 Optimal Coordination of DOCRs with Stability Constraint

In this model, the obtained relay OT shall be less than the Critical Clearing Time (CCT) which represents the stability threshold. In other words, CCT of each relay

feeder is determined first before going into the optimization model, and if the relay violates this constraint, it is equipped with instantaneous CCCs [32]. The implementation of hybrid protection CCCs composed of inverse and definite time curves as in [33] ensures that there is no intersection between the DG CCT and the relay curves. In this regard, the doubly inverse CCCs deployed in [34] have preserved this constraint especially in the high levels of I_f conditions.

6.8 Adaptive DOCRs Coordination

The online or adaptive coordination of DOCRs depends on online assessments of network parameters and then magnitudes of I_f to set the OCRs properly. The relays settings are readjusted according to network configuration and operating conditions to fulfill the full adaptive protection scheme. Fuzzy logic adaptive technique is proposed in [35] using two OCRs tripping unit: the first one is instantaneous, while the second one is a current-voltage-based inverse CCC. Moreover, due to network topology changes, sensitivity study is performed for miscoordination elimination in [36]. It has been solved using a multi-objective GWO to minimize the TOT concurrently while preserving the selectivity constraints.

6.9 Various Novel DOCRs Optimization Frameworks

The implementation of a new DOCRs OF incorporated with the arc flash hazard analysis in [37] is a novel attempt at simulating the actual network conditions. The value of the incident energy produced by the arc should be limited beyond 40 Cal/cm². Therefore, the relay settings shall achieve this concept in addition to the selectivity criterion.

The dynamic model of OCR is exploited in [38] to deal with the transient I_f resulting from the induction motors conversion into generators during fault conditions. Consequently, GA is dedicated to solving this issue to avoid the false operation of OCRs during these transient conditions.

As it was discussed before, there are many optimization frameworks proposed in the literature. However, the progress of this research point is not over yet. Hereinafter, the performance of a new meta-heuristic based framework, namely the SMO is tested over a standard test bench network. Moreover, some results regarding the relay settings and the M/B relays OTs will also be presented.

7 Procedures of the SMO

SMO depends on the natural oscillations of the slime moulds [39]. Its optimal convergence behavior is inspired from the positive and negative feedback production

process by adapting its weighting parameters in the search agent [12]. The search technique of the SMO relies on the dynamic adjusting of the search patterns based on the foodstuff provenience quality. SMO will use the region search restricted method if the quality of the food is high, and vice versa, it will leave the food stuff to scout about other sources if the quality is low [39].

SMO initiates its optimization strategy from the smell in the free air to startup the food approaching stage. This process is bounded between min/max limits that have been represented in our case as the DOCRs optimal settings.

$$\overrightarrow{Y}(t+1) = \begin{cases} \overrightarrow{Y}_b(t) + \vec{v}b \cdot (\vec{W} \cdot \overrightarrow{Y}_1(t) - \overrightarrow{Y}_2(t)), & r < p \\ \vec{v}c \cdot \overrightarrow{Y}(t), & r \geq p \end{cases} \quad (12)$$

The contraction of the slime moulds is represented in (12) where $\overrightarrow{Y}(t+1)$ is the new solution at iteration $(t+1)$ and $\overrightarrow{Y}(t)$ is the previous solution. The vector $\vec{v}b$ changes inside a range as expressed in (13) where a is an adaptive number calculated through (14). In addition, p is computed from (15), where $F(i)$ denotes the fitness value of \overrightarrow{Y} and BF is the best obtained fitness value through all iterations. \overrightarrow{Y}_b is the individual location with the highest smell concentration founded and $\overrightarrow{Y}_1(t)$, $\overrightarrow{Y}_2(t)$ are individuals selected haphazardly from the slime moulds. \vec{W} is the weight of the slime mould and the vector $\vec{v}c$ decays linearly from 1 to 0.

$$\vec{v}b = [-a, a] \quad (13)$$

$$a = \tan h^{-1} \left(- \left(\frac{t}{\max_t} \right) + 1 \right) \quad (14)$$

$$p = \tan h |F(i) - BF|, i \in \text{pop} \quad (15)$$

In our optimization model, $F(i)$ is the OF value which is expressed in (2). The vector \overrightarrow{Y} contains the decision variables set; I_{pu} , T_D , and TCC type where I_{pu} and T_D are considered as continuous variables but the TCC type is a discrete one.

$$\overrightarrow{W}(\text{smell_index}(i)) = \begin{cases} 1 + r \cdot \log \left(\frac{bf - F(i)}{bf - wf} + 1 \right), & \text{condition} \\ 1 - r \cdot \log \left(\frac{bf - F(i)}{bf - wf} + 1 \right), & \text{others} \end{cases} \quad (16)$$

$$\text{smell_index} = \text{sort}(F) \quad (17)$$

\vec{W} is calculated from (16) where: r is a random value between 0 and 1, smell_index in (17) is an allusion of the ascending order sorted OF values. The condition mentioned in (16) signifies that $F(i)$ ranks the first half of population.

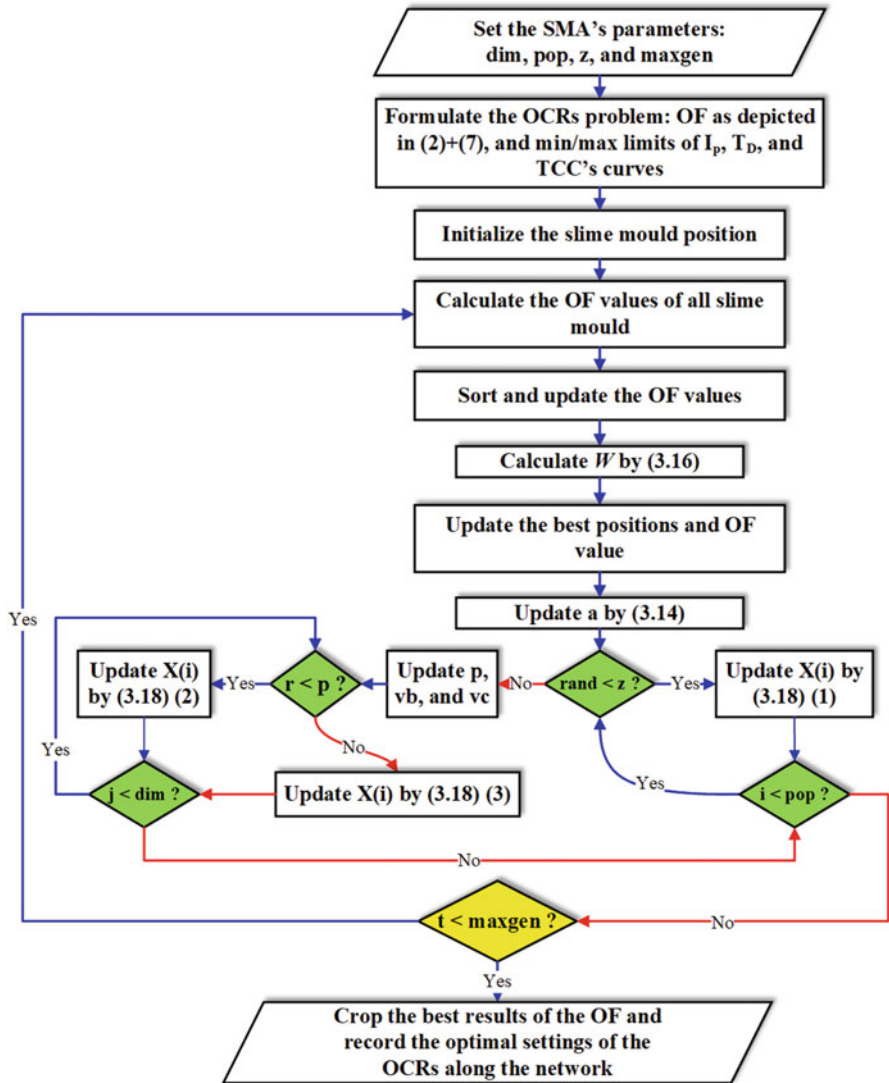


Fig. 7 SMO flow chart

$$\vec{Y}^* = \begin{cases} \text{rand} \cdot (\text{HB} - \text{LB}) + \text{LB}, \text{rand} < z \\ \vec{Y}_b(t) + \vec{v}b \cdot (\vec{W} \cdot \vec{Y}_1(t) - \vec{Y}_2(t)), r < p \\ \vec{v}c \cdot \vec{Y}(t), r \geq p \end{cases} \quad (18)$$

As it is disclosed in (18), the location of the slime mould is updated to simulate the process of contracting of the venous tissue structure, where HB and LB are the higher and lower limits of the search space, respectively. Furthermore, Fig. 7

illustrates the general procedures and the mathematical formula of the SMO which are depicted in a flow chart.

8 Optimized Simulation Results Using the SMO

In this section, the performance of one of the latest optimization algorithms, called SMO for optimal coordination of DOCRs is validated over a standard test network. The simulation results are carried out on the IEEE 8-bus test case that is shown in Fig. 8.

This network composes of 14 DOCRs with 20 M/B relay pairs, 2 generators, 2 distribution transformers, and 7 lines. SMO' optimization model is executed on the IEEE 8-bus network and its data regarding the I_f levels of the M/B relay pairs is organized in Table 2 using 2 scenarios.

In both scenarios, the current pickup ranges between 1 and 1.5 of the full load current, while the CTM ranges between 0.2 s and 0.4 s. SMO's control parameters are finally adapted with these values; pop of 100, maxgen of 500 for scenario 1 and pop of 500, maxgen of 1000 for scenario 2. Scenario 1 optimizes only the I_{pu} and T_D considering fixed NI IEC curve with min/max borders of T_D ; 0.05 s and 1.1 s respectively.

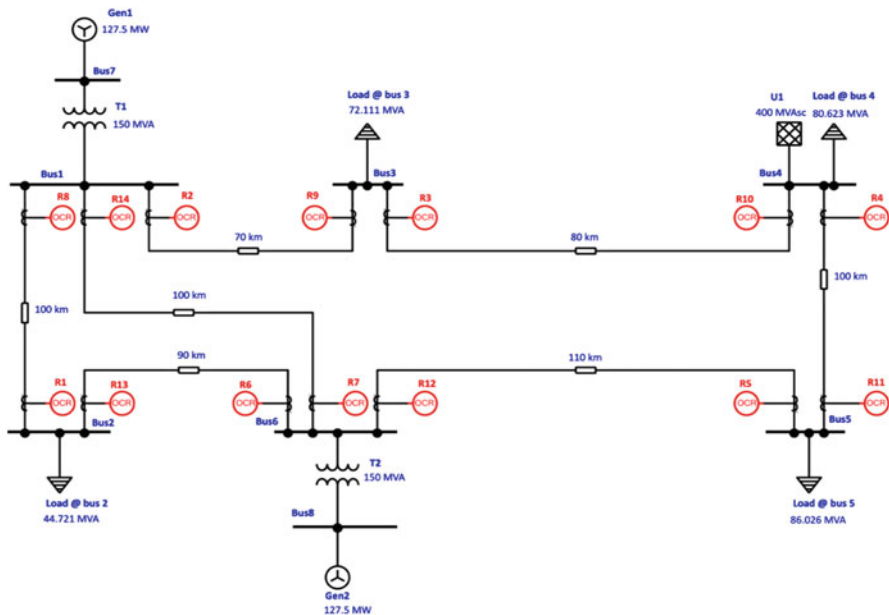


Fig. 8 IEEE 8-bus SLD

Table 2 Values of I_f passing through M/B relay pairs of the IEEE 8-bus network

M/B relay pair		3-phase fault		M/B relay pair		3-phase fault	
P	B	$I_{fp}(kA)$	$I_{fb}(kA)$	P	B	$I_{fp}(kA)$	$I_{fb}(kA)$
1	6	3.232	3.232	8	7	6.093	1.890
2	1	5.924	0.996	8	9	6.093	1.165
2	7	5.924	1.890	9	10	2.484	2.484
3	2	3.556	3.556	10	11	3.883	2.344
4	3	3.783	2.244	11	12	3.707	3.707
5	4	2.401	2.401	12	13	5.899	0.987
6	5	6.109	1.197	12	14	5.899	1.874
6	14	6.109	1.874	13	8	2.991	2.991
7	5	5.223	1.197	14	1	5.199	0.996
7	13	5.223	0.987	14	9	5.199	1.165

Table 3 Optimal settings of DOCRs for scenario 1

Relay ID	I_{pu} (A)	T_D (s)
1	505.3102	0.0593
2	860.9713	0.1144
3	719.5230	0.0822
4	964.2285	0.0593
5	608.2902	0.0500
6	527.7516	0.1122
7	765.8928	0.0791
8	648.5658	0.0909
9	496.5965	0.0588
10	682.9216	0.0846
11	808.8769	0.0823
12	681.5794	0.1409
13	579.2346	0.0500
14	992.9214	0.0595
TOT (s)	4.2694	

However, the problem gets more sophisticated in scenario 2 by optimizing the TCC type among the IEC and IEEE curves (discrete variables) with lower limit of the relay OT of 50 ms by activating the instantaneous tripping zone. It is worth mentioning that the lower limit of T_D is extended to 0.01 s as a common feature in most of the digital relays.

Table 3 lists the optimal values of DOCRs settings using the SMO-based tool for scenario 1. Then, the 42 optimal decision variables regarding the optimization process for scenario 2 are arranged in Table 4 using the SMO and the WCA. It is so clear that the selection of the EI IEC curve is the best choice for obtaining the minimum possible value of the TOT for scenario 2.

Table 5 announces the OTs of M/B pairs and their associated CTM values for both scenarios using SMO with no violations in the selectivity constraints. The

Table 4 Optimal settings of DOCRs for scenario 2 using SMO and WCA

Relay ID	SMO					WCA				
	I _{pu} (A)	T _D (s)	TCC			I _{pu} (A)	T _D (s)	TCC		
			Curve	IEC	IEEE			Curve	IEC	IEEE
1		0.0165	VI	✓	✗	599.4924	0.0655	MI	✗	✓
2	666.3377	0.1084	EI	✓	✗	666.0021	0.2873	EI	✗	✓
3	500.1689	0.0708	EI	✓	✗	612.5918	0.1311	EI	✗	✓
4	732.9210	0.0308	EI	✓	✗	865.7538	0.0675	EI	✗	✓
5	599.3812	0.0100	EI	✓	✗	474.8792	0.0730	EI	✗	✓
6	680.8342	0.0673	EI	✓	✗	458.0000	0.4384	EI	✗	✓
7	541.1628	0.0576	EI	✓	✗	541.0000	0.1582	MI	✗	✓
8	576.5103	0.0810	EI	✓	✗	458.2596	0.1300	EI	✓	✗
9	450.0009	0.0202	EI	✓	✗	450.0000	0.0512	EI	✗	✓
10	499.4759	0.0756	EI	✓	✗	613.0267	0.0577	VI	✓	✗
11	595.8515	0.0546	EI	✓	✗	801.7960	0.1124	VI	✗	✓
12	464.9698	0.2474	EI	✓	✗	458.0006	0.6498	EI	✗	✓
13	505.8599	0.0468	VI	✗	✓	534.6851	0.0475	EI	✗	✓
14	743.9991	0.0364	VI	✓	✗	808.7483	0.0609	EI	✗	✓
TOT (s)			1.1294					1.6107		

Table 5 OTs of M/B relay pairs using SMO

M/B relay pair		Scenario 1			Scenario 2		
P	B	t _{pr} (s)	t _{br} (s)	CTM (s)	t _{pr} (s)	t _{br} (s)	CTM (s)
1	6	0.2197	0.4256	0.2059	0.0499	0.2502	0.2002
2	1	0.4072	0.6080	0.2007	0.1111	0.3267	0.2156
2	7	0.4072	0.6073	0.2001	0.1111	0.4117	0.3006
3	2	0.3543	0.5566	0.2023	0.1142	0.3156	0.2013
4	3	0.2998	0.5000	0.2002	0.0963	0.2959	0.1996
5	4	0.2515	0.4512	0.1998	0.0532	0.2536	0.2004
6	5	0.3129	0.5137	0.2007	0.0678	0.2677	0.2000
6	14	0.3129	0.6510	0.3381	0.0678	0.3232	0.2554
7	5	0.2828	0.5137	0.2308	0.0500	0.2677	0.2177
7	13	0.2828	0.6532	0.3704	0.0500	0.3500	0.3000
8	7	0.2778	0.6073	0.3295	0.0585	0.4117	0.3532
8	9	0.2778	0.4786	0.2008	0.0585	0.2838	0.2253
9	10	0.2516	0.4527	0.2011	0.0549	0.2549	0.2000
10	11	0.3349	0.5357	0.2008	0.1018	0.3020	0.2003
11	12	0.3727	0.5726	0.1999	0.1160	0.3164	0.2004
12	13	0.4472	0.6532	0.2060	0.1237	0.3500	0.2263
12	14	0.4472	0.6510	0.2038	0.1237	0.3232	0.1995
13	8	0.2097	0.4100	0.2003	0.0500	0.2500	0.2000
14	1	0.2472	0.6080	0.3608	0.0820	0.3267	0.2447
14	9	0.2472	0.4786	0.2314	0.0820	0.2838	0.2018
Σ		6.2444	10.9280	4.6834	1.6225	6.1648	4.5423

SMO achieves to obtain an OF equal to 4.2694 s and 1.1294 s for scenarios 1 and 2, respectively. It also can be observed that SMO attains better OF than WCA by accomplishing 29.9% reduction in the TOT of the main relays. Moreover, SMO reaches the optimum solution in 43.4 s in scenario 1 and 403.1 s in scenario 2. Further demonstration and results analysis will be found in details in [12].

9 Conclusions

This chapter proposes the basic concepts and terminologies of over current protection in distribution networks. Also, various types of selectivity based on its principles are clustered, and the reader will note their compatible applications. Time current selectivity and energy selectivity are the most competent techniques in distribution networks due to their lack of limitations. Moreover, it offers the optimized formulation of DOCRs coordination problem with the model boundary and operating constraints. Since this optimization process is a highly constrained one, more effort is dedicated for solving it using the latest metaheuristic algorithms. These optimization algorithms offer the possibility of obtaining the best solutions without trapping into local minima in addition to its fast convergence rate. Furthermore, some researchers augment this problem by developing new approaches like the mixed coordination between DOCRs and distance relays and DOCRs dual setting concept. Also, the effect of DGs penetration on DOCRs coordination, optimal coordination in MGs, online coordination, and transient stability constraint approach are discussed. For each approach, the reader can find the merits, demerits, restrictions, and suitable applications. Finally, one of the latest optimizers is interrogated for an optimization model of DOCRs in a standard test case. SMO manifests that it is an efficient and delicate tool for solving this dilemma without any violations. However, the progress in this research point is still on track, and the researchers will also develop new optimization frameworks in the future.

References


1. Gers JM, Holmes EJ (2011) Protection of electricity distribution networks, IET Power and Energy Series 65, USA, 3rd edn ISBN 978-1-84919-224-8
2. Draz A, Elkholy MM, El-Fergany AA (2021. (in press)) Soft computing methods for attaining the protective device coordination including renewable energies: review and prospective. Arch Computat Methods Eng. <https://doi.org/10.1007/s11831-021-09534-5>
3. C37.112-2018. IEEE Standard for Inverse-Time Characteristics Equations for Overcurrent Relays
4. El-Fergany AA, Hasanien HM (2017) Optimized settings of directional overcurrent relays in meshed power networks using stochastic fractal search algorithm. Int Trans Electr Energy Syst 27(11):e2395. <https://doi.org/10.1002/etep.2395>

5. Choudhary PK, Das DK (2021) Optimal coordination of over-current relay in a power distribution network using opposition-based learning fractional order class topper optimization (OBL-FOCTO) algorithm. *Appl Soft Comput* 113:107916. <https://doi.org/10.1016/j.asoc.2021.107916>
6. Rizk-Allah RM, El-Fergany AA (2021) Effective coordination settings for directional overcurrent relay using hybrid gradient-based optimizer. *Appl Soft Comput* 112:107748. <https://doi.org/10.1016/j.asoc.2021.107748>
7. Korashy A, Kamel S, Youssef A-R, Jurado F (2019) Modified water cycle algorithm for optimal direction overcurrent relays coordination. *Appl Soft Comput* 74:10–25. <https://doi.org/10.1016/j.asoc.2018.10.020>
8. Khurshaid T, Wadood A, Farkoush SG, Kim C-H, Jiangtao Y, Rhee S-B (2019) Improved firefly algorithm for the optimal coordination of directional overcurrent relays. *IEEE Access* 7:78503–78514. <https://doi.org/10.1109/ACCESS.2019.2922426>
9. Kamel S, Korashy A, Youssef A-R, Jurado F (2020) Development and application of an efficient optimizer for optimal coordination of directional overcurrent relays. *Neural Comput Applic* 32:8561–8583. <https://doi.org/10.1007/s00521-019-04361-z>
10. Korashy A, Kamel S, Jurado F, Youssef A-R (2019) Hybrid whale optimization algorithm and grey wolf optimizer algorithm for optimal coordination of direction overcurrent relays. *Electr Power Compon Syst* 47:644–658. <https://doi.org/10.1080/15325008.2019.1602687>
11. Korashy A, Kamel S, Nasrat L, Jurado F (2020) Developed multi-objective grey wolf optimizer with fuzzy logic decision-making tool for direction overcurrent relays coordination. *Soft Comput* 24:13305–13317. <https://doi.org/10.1007/s00500-020-04745-7>
12. Draz A, Elkholy MM, El-Fergany AA (2021) Slime mould algorithm constrained by the relay OT for optimal coordination of directional overcurrent relays using multiple standardized tripping curves. *Neural Comput Applic* 33(18):11875–11887. <https://doi.org/10.1007/s00521-021-05879-x>
13. Shabani M, Karimi A (2018) A robust approach for coordination of directional overcurrent relays in active radial and meshed distribution networks considering uncertainties. *Int Trans Electr Energy Syst* 28(5):e2532. <https://doi.org/10.1002/etep.2532>
14. Yazdanejadi A, Jannati J, Farsadi M (2017) A new formulation for coordination of directional overcurrent relays in interconnected networks for better miscoordination suppression. *Trans Electr Electron Mater* 18(3):169–175. <https://doi.org/10.4313/TEEM.2017.18.3.169>
15. Shrivastava A, Saini DK, Pandit M (2019) Relay co-ordination optimization for integrated solar photo-voltaic power distribution grid. *Cogent Eng* 6(1):1612601. <https://doi.org/10.1080/23311916.2019.1612601>
16. Gupta S, Deep K (2019) Optimal coordination of overcurrent relays using improved leadership-based grey wolf optimizer. *Arab J Sci Eng* 45:2081–2091. <https://doi.org/10.1007/s13369-019-04025-z>
17. Gouda EA, Amer A, Elmitwally A (2021) Sustained coordination of devices in a two-layer protection scheme for DGs-integrated distribution network considering system dynamics. *IEEE Access* 9:111865–111878. <https://doi.org/10.1109/ACCESS.2021.3103824>
18. Ekta Purwar DN, Vishwakarma SP, Singh. (2019) A novel constraints reduction based optimal relay coordination method considering variable operational status of distribution system with DGs. *IEEE Trans Smart Grid* 10(1):889–898. <https://doi.org/10.1109/TSG.2017.2754399>
19. Dehghanpour E, Karegar HK, Kheirollahi R, Soleymani T (2018) Optimal coordination of directional overcurrent relays in microgrids by using cuckoo-linear optimization algorithm and fault current limiter. *IEEE Trans Smart Grid* 9(2):1365–1375. <https://doi.org/10.1109/TSG.2016.2587725>
20. Narimani A, Hashemi-Dezaki H (2021) Optimal stability-oriented protection coordination of smart grid's directional overcurrent relays based on optimized tripping characteristics in double-inverse model using high-set relay. *Electr Power Energy Syst* 133. <https://doi.org/10.1016/j.ijepes.2021.107249>
21. Dagar A, Gupta P, Niranjana V (2021) Microgrid protection: a comprehensive review. *Renew Sust Energy Rev* 149. <https://doi.org/10.1016/j.rser.2021.111401>

22. Rezaei N, Uddin MN, Amin IK, Othman ML, Marsadek M (2019) Genetic algorithm-based optimization of overcurrent relay coordination for improved protection of DFIG operated wind farms. *IEEE Trans Ind Appl* 55(6):5727–5736. <https://doi.org/10.1109/TIA.2019.2939244>
23. El-Naily N, Saad SM, Mohamed FA (2020) Novel approach for optimum coordination of overcurrent relays to enhance microgrid earth fault protection scheme. *Sustain Cities Soc* 54:102006. <https://doi.org/10.1016/j.scs.2019.102006>
24. Yazdaninejadi A, Nazarpour D, Talavat V (2018) Coordination of mixed distance and directional overcurrent relays: miscoordination elimination by utilizing dual characteristics for DOCRs. *Int Trans Electr Energy Syst* 29(3):e2762. <https://doi.org/10.1002/etep.2762>
25. Yazdaninejadi A, Nazarpour D, Golshannavaz S (2017) Dual-setting directional over-current relays: an optimal coordination in multiple source meshed distribution networks. *Electr Power Energy Syst* 86:163–176. <https://doi.org/10.1016/j.ijepes.2016.10.004>
26. Yazdaninejadi A, Golshannavaz S, Nazarpour D, Teimourzadeh S, Aminifar F (2019) Dual-setting directional overcurrent relays for protecting automated distribution networks. *IEEE Trans Ind Inf* 15(2):730–740. <https://doi.org/10.1109/TII.2018.2821175>
27. Yazdaninejadi A, Talavat V, Golshannavaz S (2020) A dynamic objective function for communication-based relaying: increasing the controllability of relays settings considering N-1 contingencies. *Electr Power Energy Syst* 116. <https://doi.org/10.1016/j.ijepes.2019.105555>
28. El-Fergany AA, Hasanien HM (2019) Water cycle algorithm for optimal overcurrent relays coordination in electric power systems. *Soft Comput* 23:12761–12778. <https://doi.org/10.1007/s00500-019-03826-6>
29. Yazdaninejadi A, Naderi MS, Gharehpetian GB, Talavat V (2018) Protection coordination of directional overcurrent relays: new time current characteristic and objective function. *IET Gener Transm Distrib* 12(1):190–199. <https://doi.org/10.1049/iet-gtd.2017.0574>
30. El-Naily N, Saad SM, Hussein T, Mohamed FA (2019) A novel constraint and non-standard characteristics for optimal over-current relays coordination to enhance microgrid protection scheme. *IET Gener Transm Distrib* 13(6):780–793. <https://doi.org/10.1049/iet-gtd.2018.5021>
31. Yazdaninejadi A, Nazarpour D, Golshannavaz S (2020) Sustainable electrification in critical infrastructure: variable characteristics for overcurrent protection considering DG stability. *Sustain Cities Soc* 54:102022. <https://doi.org/10.1016/j.scs.2020.102022>
32. Mosavi SMA, Kejadi TA, Javadi H (2016) Optimal setting of directional over-current relays in distribution networks considering transient stability. *Int Trans Electr Energy Syst* 26(1):122–133. <https://doi.org/10.1002/etep.2072>
33. Aghdam TS, Karegar HK, Zeineldin HH (2018) Transient stability constrained protection coordination for distribution systems with DG. *IEEE Trans Smart Grid* 9(6):5733–5741. <https://doi.org/10.1109/TSG.2017.2695378>
34. Aghdam TS, Karegar HK, Zeineldin HH (2019) Optimal coordination of double-inverse overcurrent relays for stable operation of DGs. *IEEE Trans Ind Inf* 15(1):183–192. <https://doi.org/10.1109/TII.2018.2808264>
35. Momesso AEC, Wellington MS, Bernardes EN, Asada. (2019) Fuzzy adaptive setting for time-current-voltage based overcurrent relays in distribution systems. *Electr Power Energy Syst* 108:135–144. <https://doi.org/10.1016/j.ijepes.2018.12.035>
36. Gutierrez EH, Conde A, Shih MY, Fernandez E (2019) Execution time enhancement of DOCR coordination algorithms for on-line application. *Electr Power Syst Res* 170:1–12. <https://doi.org/10.1016/j.epsr.2019.01.004>
37. El-Fergany A (2016) Optimal directional digital overcurrent relays coordination and arc-flash hazard assessments in meshed networks. *Int Trans Electr Energy Syst* 26(1):134–154. <https://doi.org/10.1002/etep.2073>
38. Maleki MG, Chabanloo RM, Farrokhifar M (2020) Accurate coordination method based on dynamic model of overcurrent relay for industrial power networks taking contribution of induction motors into account. *IET Gener Transm Distrib* 14(4):645–655. <https://doi.org/10.1049/iet-gtd.2019.0325>
39. Li S, Chen H, Wang M, Heidari AA, Mirjalili S (2020) Slime mould algorithm: a new method for stochastic optimization. *Future Gener Comput Syst* 111:300–323. <https://doi.org/10.1016/j.future.2020.03.055>

Optimal Allocation of Active and Reactive Power Compensators and Voltage Regulators in Modern Distribution Systems



Heba M. Elaraby, Ahmed M. Ibrahim, Muhyaddin Rawa, Essam El-Din Abou El-Zahab, and Shady H. E. Abdel Aleem 

1 Introduction

Renewable energy technology has become the most critical technology in energy feeding systems in most countries to reduce dependence on energy production from traditional fossil fuels. These days, the mature renewable-based technologies are wind turbines, solar, fuel cells, small hydropower, oceans (waves and tides), biomass, and geothermal systems. These technologies have enhanced energy security, affected electricity price fluctuations, reduced gas emissions, and reduced congestion of transmission lines while providing enhanced voltage stability potential to electricity grids. A distributed generator (DG) can be a renewable or non-renewable source and can be networked (grid-connected) or act as a stand-alone

H. M. Elaraby

Electrical Power Department, Faculty of Engineering, Cairo University, Giza, Egypt

Electrical Engineering Department, The Higher Institute for Engineering and Technology, Fifth Settlement, New Cairo, Egypt

A. M. Ibrahim · E. E.-D. A. El-Zahab

Electrical Power Department, Faculty of Engineering, Cairo University, Giza, Egypt

M. Rawa

Center of Research Excellence in Renewable Energy and Power Systems, King Abdulaziz University, Jeddah, Saudi Arabia

Department of Electrical and Computer Engineering, Faculty of Engineering, King Abdulaziz University, Jeddah, Saudi Arabia

S. H. E. Abdel Aleem (✉)

Electrical Engineering and Electronics Department, Valley High Institute of Engineering and Technology, Science Valley Academy, Qalyubia, Egypt

e-mail: engyshady@ieee.org

system. Due to their low investment costs and small sizes, DGs are imperative in modern energy system planning [1].

DGs can be classified as follows [2, 3]: (i) technology basis: they can be categorized into renewable (non-fossil fuel-based) and nonrenewable (fossil fuel-based), (ii) generated power basis: they can be categorized into DGs that generate alternating current (AC) power (wind turbines, microturbines (MTs), and others) and DGs that generate direct current (DC) power (fuel cells (FCs), solar photo-voltaics (PV), and others), (iii) supply duration basis: they can be categorized into long duration-based, moderate duration-based, and short duration-based DGs, (iv) capacity basis: they can be categorized into micro decentralized DGs (1 W – 5 kW), small decentralized/centralized DGs (5 kW – 5 MW), medium DGs (5–50 MW) and are almost centralized, and large DGs (50–300 MW) and are centralized, (v) grid interface basis: they can be categorized into inverter-based DGs include PV systems, wind turbine generators (Type 3–Type 5), FCs cells, and MTs, and non-inverter-based DGs which include mini-hydro synchronous and induction generators (Type 1 and Type 2 wind turbines), (vi) power flow model basis: the DGs’ output power can be either set to constant power factor (PF) for small decentralized DGs, and the bus at which the DG is connected is modeled as a PQ bus in power flow studies, or to be set to constant voltage for large centralized DGs, and the bus at which the DG is connected is modeled as a PV bus in power flow studies, and (vii) power delivering capability basis in which DGs can only deliver active power at unity PF (e.g., PV, MTs, and FCs). However, according to the current grid codes, PV systems have to provide reactive power, or deliver only reactive power at zero PF (e.g., synchronous compensators), or to deliver active power but consume reactive power (the reactive power Q is $-ve$), and the PF value is between $[0,1]$. Induction generators are used in Type 1 and Type 2 wind turbines. Doubly-fed induction generators are used in Type 3 wind turbines and synchronous generators are used in Types 4 and 5. DG classifications are explored in Fig. 1 [1, 4].

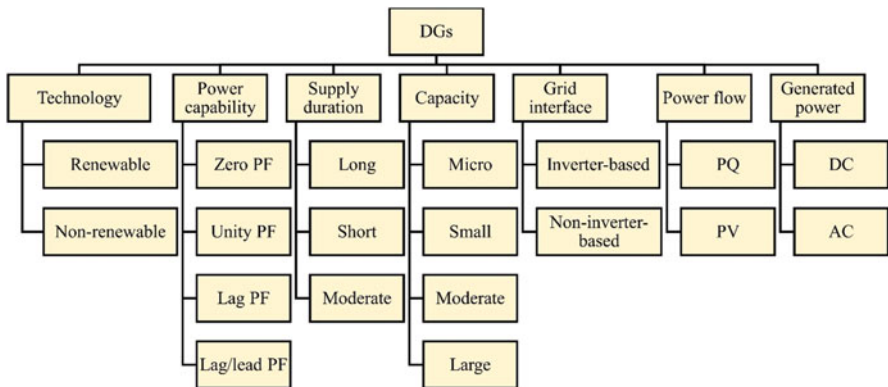


Fig. 1 Classification of DGs

The integration of DGs into RDSs significantly affects the flow of energy and voltage conditions at customers and utility equipment. These effects may be either positive or negative, depending on the distribution systems case and the operating characteristics of DGs [5, 6]. Generally, the positive effects on RDSs have been termed – the supporting benefits – and are bordered as follows [7–9]: active and reactive power loss reduction, reliability enhancement, quality of power (QoP) improvement, voltage stability (VS) enhancement, steady-state voltage profile support, capacity release (transmission and distribution capacities alike), postponements of new or reinforced transmission and distribution infrastructure, easy fitting and connection, and cost reduction. In some cases, integrating DGs at nonoptimal locations with nonoptimal sizes can result in high power losses, system instability, and a boom in operational costs due to poor efficiency and high losses. In addition, the increased renewables penetration increases energy security by expanding (mixing) energy resources, advances self-sufficiency, and boosts flexibility for system operators. Some studies have shown that the presence of DGs that use power electronic-based converters may cause major QoP, overvoltage, overloading, and protection problems, as shown in Fig. 2 that present the recent investigated renewables hosting capacity (HC) problems [6], or simply, the problems that may occur due to nonoptimal DGs allocation.

In the literature, many authors have discussed the use of different technologies to augment the performance of RDSs. The most effective techniques are system reinforcement/reconfiguration or integration of RDSs with DGs, SCBs, VRs, and sometimes their combination. However, most of the authors were much more

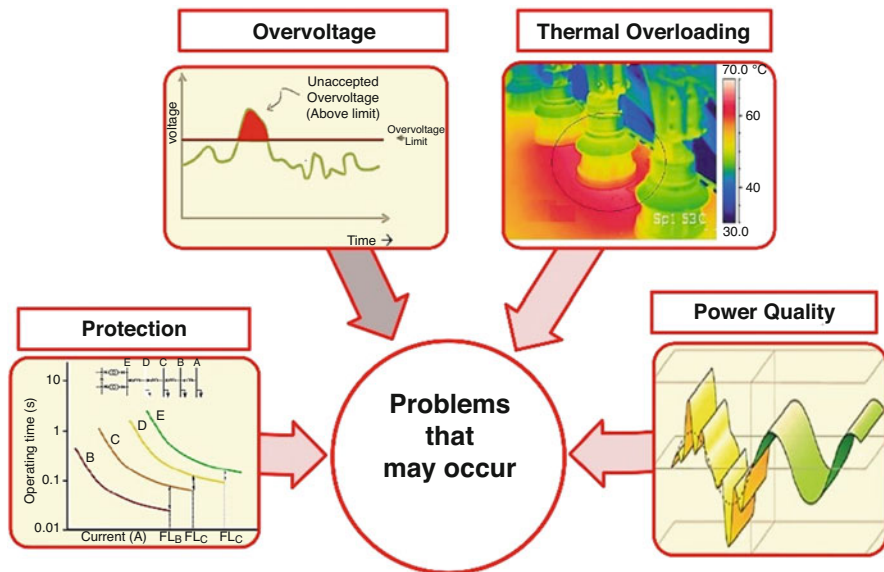


Fig. 2 Major problems that can occur with non-suitable DG ratings or locations

attentive to solving the optimal allocation problems of DGs or SCBs, either simultaneously or individually.

Khatod et al. in [10] used an evolutionary programming algorithm for power loss reduction and voltage profile improvement using optimally allocated DGs in RDSs. In [11], Muttaqi et al. presented an analytical (mathematical-based) approach that depends on algebraic equations to solve the optimal allocation problem of DGs to retain the RDSs' bus voltages within the specified permissible bounds. In [12], Ghanbari et al. applied particle swarm optimization to find DGs' size and optimal location in RDSs to minimize costs and reduce power losses. In [13], Ismael et al. used the crow search algorithm to allocate three DG types in RDS using a loss sensitivity index to choose the most candidate nodes for DG placement. In [14], Abdel-Mawgoud et al. employed a salp swarm algorithm to fit DGs to reduce energy losses in RDSs, while accounting for annual load growth. However, an economic cost model was not formulated in work.

Regarding SCBs allocation in the literature, many optimization procedures, such as particle swarm optimization [15], convex quadratic relaxations for mixed-integer nonlinear programs [16], differential evolution (DE) [17] and fuzzy-DE [18], ETAP tool [19], genetic algorithms [20] and others [21, 22], have been independently functioned for stand-alone SCBs allocation issues. However, it was evidenced that synchronized optimal allocation of SCBs and DGs in RDSs can accomplish better outcomes [23]. At the beginning of solving the problem, few researchers have focused on their simultaneous solution, but later this tendency becomes much more prominent.

In [24], Moradi et al. used a hybrid genetic-imperialist-competitive algorithm to solve the optimal allocation problem of DGs and SCBs to increase power loss reduction capability and enhance voltage regulation and voltage stability (VS).

In [25], Rahmani-Andebili resolved the same problem by employing genetic algorithms in RDSs from a distribution company's viewpoint to minimize total costs. In [26], Muthukumar and Jayalalitha presented a hybridization between harmony search and particle artificial bee colony algorithms to enhance VS and reduce losses by finding the optimal DGs and SCBs locations in RDSs. In [27], Yazdavar et al. determined the candidate sizes, places, and types of DGs and SCBs, in the planning phase in isolated microgrids (μ Gs) with the presence of nonlinear harmonic loads. In [28], Elattar et al. used an improved Manta-ray foraging optimization algorithm to synchronize DGs and SCBs in RDSs to diminish the unexploited consumed energy while satisfying the consumers' requirements. In [29], Kumar et al. joined the firefly and the backtracking algorithms to solve the DGs and SCBs allocation problem to diminish power loss and enhance the steady-state voltage profiles of the nodes in RDSs. In [30], Gampa and Das proposed a two-level multi-objective (MO) fuzzy-based grasshopper optimization procedure for allocating SCBs, DGs, and electric vehicle (EV) charging stations in RDSs, taking into account different technical QoP performance metrics. A genetic algorithm was also employed by Das et al. in [31] to distribute DGs and SCBs on the system relying on advancing voltage profile, reducing the current taken from the grid, and diminishing the power losses and annualized consumed energy.

Moreover, in [32], Almabsout et al. employed an enhanced GA to obtain optimal DGs and SCBs in small, medium, and large RDSs to diminish voltage deviation and power losses. In [33], Shaheen and El-Sehiemy introduced an optimally-coordinated allocation problem of DGs, SCBs, and VRs in RDSs and offered its solution using an adopted grey wolf algorithm. The results in that work confirmed that the used algorithm outperformed the other investigated algorithms regarding power losses, loading capacity, and voltage deviation reduction. Due to enlarged nonlinear loads usage and inverter-based DGs that cause harmonic distortion in RDSs, in [17], Milovanovich et al. allocated inverter-based DGs and SCBs using an improved hybrid particle-swarm-gravity-search algorithm to reduce energy losses.

Regarding VRs, the authors in [34] presented a computerized algorithm for optimal voltage control with VRs to reduce the cost of investing and the cost of energy losses. Also, in [35], a procedure for optimal sizing and siting of VRs has been presented to improve voltage profiles in RDSs. Other works introduced solutions for the optimal allocation of DGs or SCBs separately. Also, the optimal synchronization issue of DGs and VRs was explained in [36–38] and others for power loss minimization, voltage profile control, and VS enhancement. Finally, multi-agents (DGs, SCBs/SVC, or VRs) allocation to improve RDSs performance were presented in [33, 39], accounting for different QoP metrics using ETAP, MATLAB, GAMS [25], and others. However, economic considerations were not usually taken into account.

To sum up, improving the performance of RDSs is a primary target for power system operators. Besides, energy resource limitations and cost-effective electricity distribution to the consumers encourage engineers, distribution system operators, and researchers to investigate increasing the efficiency of electric power distribution systems. Fortunately, many technologies can effectively make such improvements. Active and reactive power compensators such as DGs and SCBs are examples of compensators that can effectively improve modern RDSs. VRs can also help these compensators function better in a much more effective techno-economic manner in RDSs and effectively enhance voltage profiles and load stability and reduce voltage deviations from the acceptable values. Unfortunately, rising project investment may result if uneconomic facilities or expensive technologies are used to reduce electric losses significantly. Therefore, economic considerations related to the installed network equipment should be considered. Also, it is clear from previous studies that no particular optimization method has proved to be the most appropriate method in the synchronized allocation of DGs, VRs, and SCBs objectives, and no guarantee of global solutions for different systems is evidenced.

Finally, to go over the main points, one can find that the standard objective functions in the allocation problem of active and reactive power conditioners and VRs are (i) power/energy loss reduction, (ii) voltage profile enhancement or voltage regulation adjustment or voltage deviation minimization, (iii) VS improvement, (iv) loading capacity/overloading minimization, (v) investment and operating cost minimization, (vi) power factor (PF) maximization, (vii) reducing the purchased apparent power from the electric utility/releasing the transformer capacity, and (viii) harmonic distortion mitigation. These different areas are explored in Fig. 3. Besides,

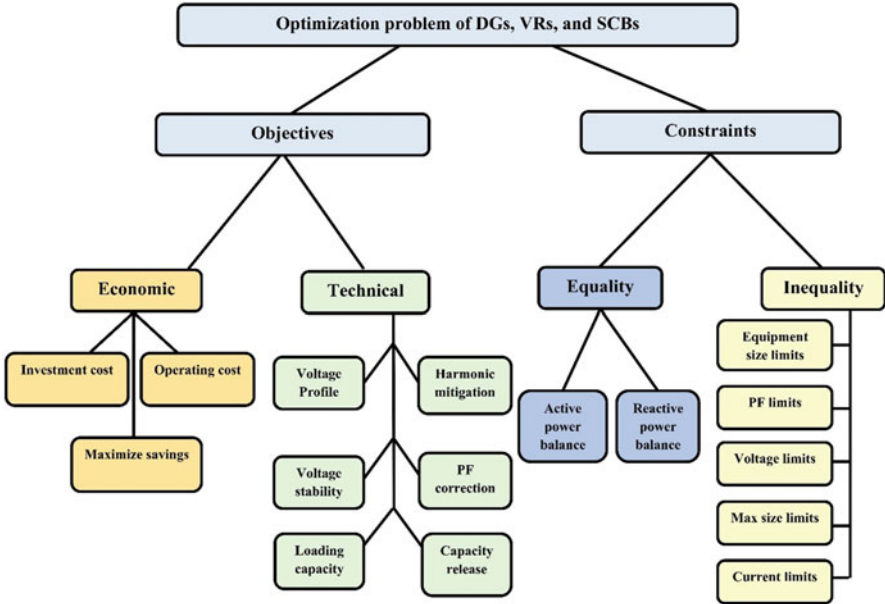


Fig. 3 Typical objectives and constraints used in DGs, VRs, and SCBs allocation

the typical constraints commonly considered (equality and inequality constraints) are explored in the figure. It should be noted that the harmonic mitigation goal is considered in case the loads are nonlinear harmonics-generating loads.

At the local level, to encounter the increasing load growth and hurrying too much to higher levels of mixed variable renewable energy sources (VRESs) integration, Egypt has established a promising energy strategy until 2035 to spread the power generation mix among fossil fuel-based plants. Therefore, improving the quality of power (QoP) performance levels of RDSs has become an authoritative area for system operators to host the ambitious number of renewables. In 2035, the growth of electricity demand will be satisfied in the “most likely” scenario by a combination of coal (48%), nuclear (8%), gas/oil-fired plants (22%), hydro (3%), wind (13%), photovoltaic (PV) (4%), and concentrated solar power (2%) [40]. However, Egypt faces abundant challenges – renewal of the existing deteriorated power generation plants, upgrade and development of transmission networks, dealing with the technical and nontechnical losses, pushing direction to use to the automated substation systems rather than the manual traditional operated substations, refining the energy laws to be more attractive for foreign investments, and the high spinning reserve that needs either interconnection with other countries or exporting electric energy to near countries.

In 2020, an increase in demand for investment in renewable energy was seen for both wind and solar energy projects. Many renewable energy projects have been implemented in Egypt to target 20% of the total energy produced in 2022. Egypt’s total installed renewable energy capacity is 3.7 GW, including 2.8 GW of hydropower and about 0.9 GW of solar and wind power. In addition, the Egyptian

Table 1 Energy potential in Egypt by 2022 and 2035 [40]

Generation technology		In 2022 (short-term scenario)		In 2035 (long-term scenario)	
		Total share (%)	Share of each type (%)	Total share (%)	Share of each type (%)
Thermal power plants		80.00		55.00	
Renewable energy	Hydropower	20.00	6.00	42.00	2.00
	Solar energy		2.00		25.00
	Wind energy		12.00		15.00
	Nuclear energy	0.00	0.00	3.00	3.00

government has set renewable energy targets of 20% of the electricity mix by 2022 and 42% by 2035, as presented in Table 1 [40]. Egypt recommends key measures to accelerate renewables hosting [40] – power and energy sector strategies update to follow the rising benefits of renewable energy; biomass energy promotion in future energy strategy updates; reformation of the current market framework to improve project finance sources; universalization of regulations and explanation of institutional roles and responsibilities for wind and solar energy development; promotion of renewables and ensuring their financial viability; risk mitigation by proper solutions; the accomplishment of comprehensive measurement campaigns for solar and wind powers; and development of a dominant plan to boost local manufacturing capabilities to create a local renewable energy industry.

Accordingly, in this work, the well-known whale optimization algorithm (WOA) is applied in this work to allocate DGs, SCBs, and VRs in a realistic 37-bus distribution system in Egypt to minimize power losses while conforming with several linear and nonlinear constraints. A cost-benefit analysis of the optimization problem is made in terms of – investment and running costs of the compensators used, saving gained from the power loss reduction, and benefits from decreasing the power to be purchased from the grid, reducing voltage deviations and overloading, and enhancing VS. Three loading scenarios are considered in this work – light, shoulder, and peak levels of load demand. The numerical findings obtained show a noteworthy techno-economic improvement of the QoP performance level of the RDS and approve the efficiency and economic benefits of the proposed solutions compared to other solutions in the literature. Figure 4 displays a visualization of the compensators/considerations investigated in this work.

The rest of the chapter is arranged as follows: Sect. 2 presents the VS definition and the formulation used in this work. The VR model and its mathematical formulation are given in Sect. 3. Section 4 presents the load flow method used with and without the engaged VRs. Section 5 introduces the optimization problem and is investigated in detail. Section 6 explores the applied optimization method (WOA). Section 7 explores the metrics and indices used to qualify the performance of the system. Section 8 explores the system under study. Section 9 shows the results obtained, and their discussions are presented in the same section. Lastly, conclusions and future works are given in Sect. 10.

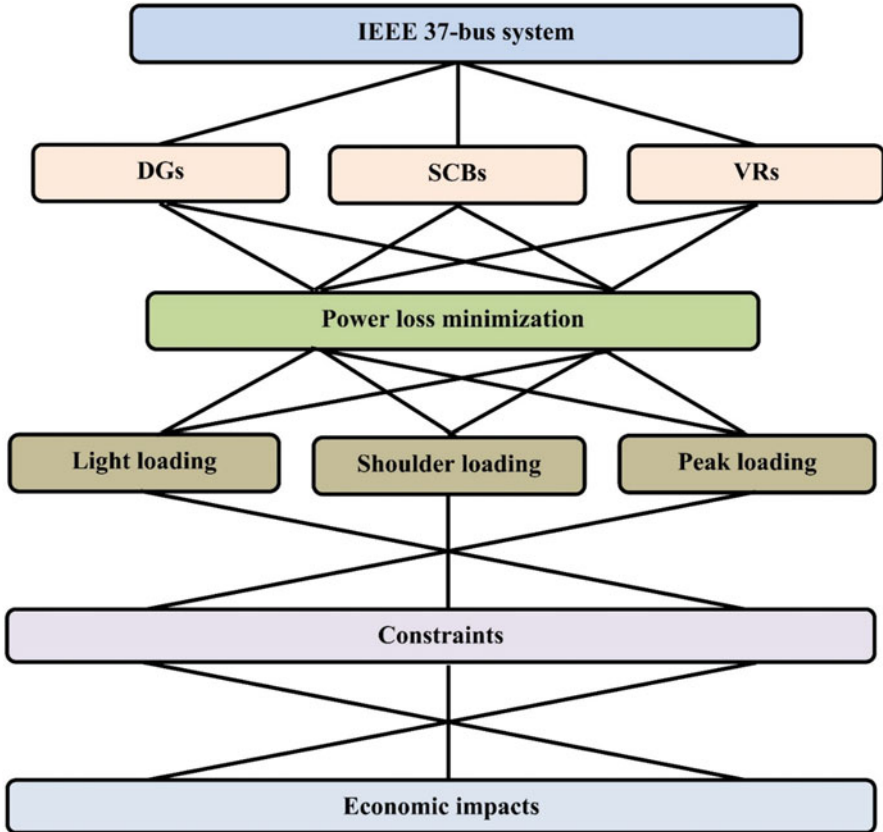


Fig. 4 Visualization of the compensators/considerations investigated in this work

2 Voltage Stability Analysis

Voltage stability (VS) analysis evaluates unstable or weak areas of electrical power systems that may endanger load growth due to unpredicted voltage collapse, and this means that operative VS analysis is essential in power system planning (PSP) and longstanding operability. In this regard, the authors in [41] proposed a voltage sensitivity analysis method that computes a metric at each bus to recognize the most sensitive bus for voltage collapse. The index is derived from a bi-quadratic expression usually employed in optimal power flow (OPF) algorithms [42].

For the explanatory distribution system model shown in Fig. 5. The quadratic expression relating the voltage magnitude at the sending and receiving nodes of a branch and power (active and reactive) at the receiving end is given as follows:

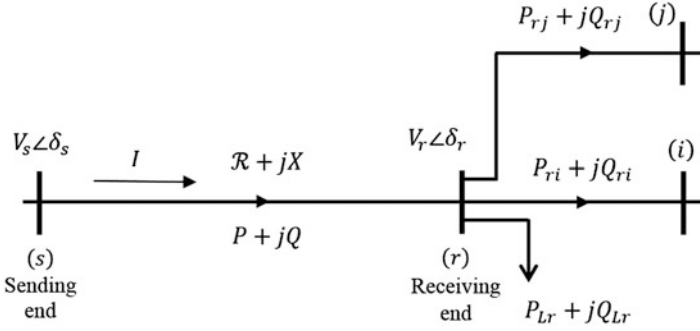


Fig. 5 Demonstrative distribution system model used in derivations

The line current (I) is stated as:

$$I = \frac{P - jQ}{V_r^*} \quad (1)$$

The sending-end voltage (V_s) is expressed as:

$$V_s = V_r + I (R + jX) \quad (2)$$

Combining these Eqs. (1) and (2), one can get the following:

$$V_s^2 = V_r^2 + 2(RP + XQ) + (R^2 + X^2) \left[\frac{P^2 + Q^2}{V_r^2} \right] \quad (3)$$

where V_s , V_r , $R + jX$, and $P + jQ$ denote the sending-end voltage, the receiving-end voltage, the impedance of the line, and the transferred active and reactive power, respectively.

Multiplying Eq. (3) by (V_r^2) will lead to the well-known expression in Eq. (4):

$$\begin{aligned} V_r^2 V_s^2 &= V_r^4 + 2(RP + XQ) V_r^2 + (R^2 + X^2) (P^2 + Q^2) \\ \Rightarrow V_r^4 - [V_s^2 - 2(RP + XQ)] V_r^2 + [(R^2 + X^2) (P^2 + Q^2)] &= 0 \quad (4) \\ \Rightarrow a V_r^4 - b V_r^2 + c &= 0 \end{aligned}$$

so that:

$$\begin{aligned} a &= 1 \\ b &= V_s^2 - 2(RP + XQ) \\ c &= (R^2 + X^2) (P^2 + Q^2) \end{aligned} \quad (5)$$

It is clear from (5) that the solution of the equation will provide four roots, and only the maximum positive roots are the feasible solutions that will give the V_r values. Thus:

$$V_r = \frac{1}{\sqrt{2}} \sqrt{\left(b + \left(\sqrt{b^2 - 4c}\right)\right)} \quad (6)$$

The critical loading point or voltage instability or collapse will not be reached if Eq. (7) is satisfied.

$$\begin{aligned} b^2 - 4c &\geq 0 \\ \Rightarrow [V_s^2 - 2(RP + XQ)]^2 - 4(R^2 + X^2)(P^2 + Q^2) &\geq 0 \end{aligned} \quad (7)$$

This will lead to the following:

$$V_s^4 - 4(PX - QR)^2 - 4V_s^2(PR + QX) \geq 0 \quad (8)$$

The voltage stability index (VSI) can be expressed as follows:

$$VSI_{bus} = V_s^4 - 4(PX - QR)^2 - 4V_s^2(PR + QX), \forall bus \quad (9)$$

The low values of VSI_{bus} correspond to a much higher possibility of voltage instability or extreme voltage collapse, as illustrated in Fig. 6. Voltage collapse (VC) is

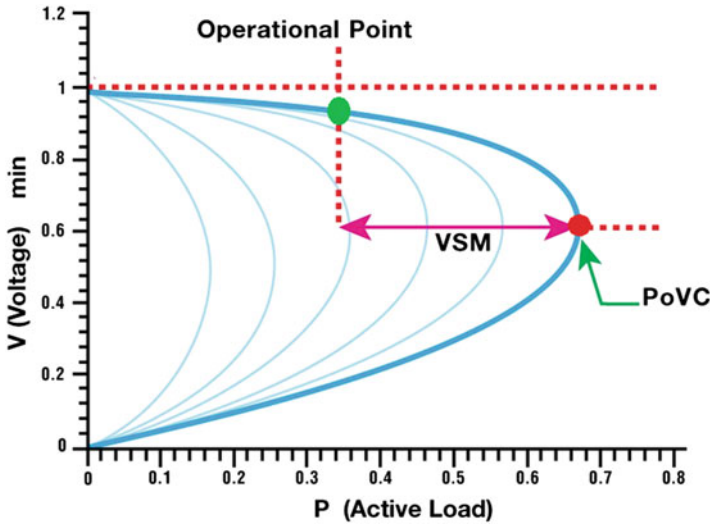


Fig. 6 Illustration of the VSM concept on an illustrative PV curve from ETAP voltage stability software

becomes much more probable when the power system operates with an insufficient VS margin (VSM) in at least one bus. *VSM* is the distance between the current operating point and the collapse point (PoVC). Periodic studies must be performed to decide if the grid is susceptible to VC and find proper solutions to avoid it, predominantly, under heavily loaded conditions.

3 Voltage Regulators

Supplying every customer with a voltage within acceptable limits is an essential distribution feeder requirement; thus, the voltages should be regulated. VR is one of the most common ways used. An automatic VR comprises an autotransformer and a load tap shifting mechanism that tolerates handling the tap location, in which the output voltage can be adjusted by varying the tap location through changing the winding (series-winding of the autotransformer).

The control circuit, known as the line drop compensator, governs the tap location [43]. Step VRs can be connected as Type A or Type B connections, reported in ANSI/IEEE C57.15 standard series [44] that classifies the voltage ranges in these types. However, Type B-VR is more common. Figure 7 illustrates a schematic diagram of a step VR in the raise position [45].

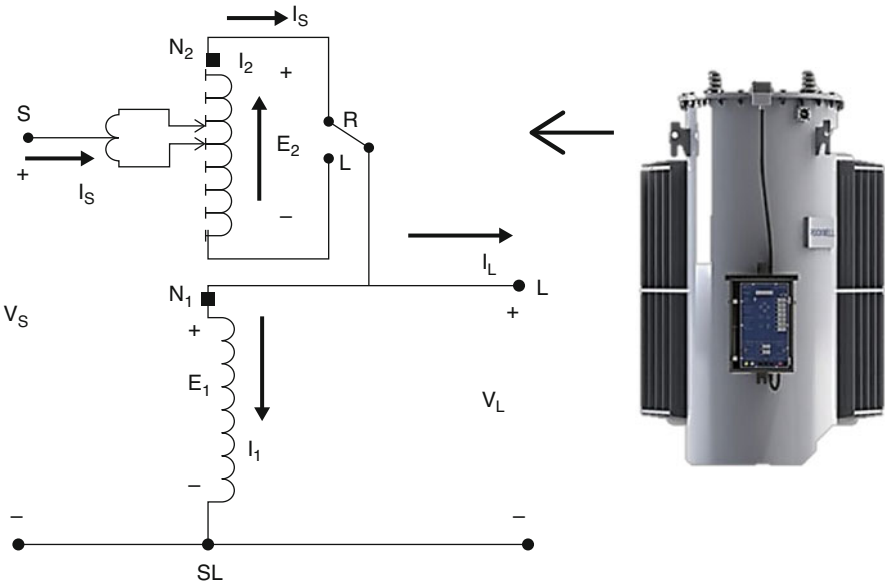


Fig. 7 Diagram of a step VR, Type B

A standard step VR comprises a reversing switch that allows the voltage to be regulated in a range of $\pm 10\%$ of the rated voltage, up and down. Characteristically, the voltage is stepped in 8, 16, or 32 steps. The 32-step is the most common in substations (16 in the up-voltage raise position and 16 in the down-voltage lower position). Each step change is equivalent to a 0.00625 per unit change in the voltage (each change in tap changes the voltage by $(5/8)\%$ or 0.00626 per unit to give the $\pm 10\%$ of the rated voltage). VRs may connect as Y or Δ or open Δ for a three-phase system. Bandwidth is always set so that the taps are only changed when the voltage is out of the bandwidth. It is specified by minimum and maximum regulation voltage (set to $\pm 1\%$ of the nominal voltage) to bound the number of changes of the tapping.

The mathematical description of a phase VR is formulated as follows:

$$V_S = a_R V_L, I_L = a_R I_S \quad (10)$$

where V_S denotes the supply voltage, V_L denotes the load voltage, and a_R denotes the effective VR ratio, which can be defined in terms of the transformer turns ratio as follows:

$$a_R = \begin{cases} 1 - \frac{N_2}{N_1}, & \text{raise position} \\ 1 + \frac{N_2}{N_1}, & \text{lower position} \end{cases} \quad (11)$$

Additionally, the effective regulator ratio can be defined in terms of the tap position (TP) as follows:

$$a_R = \begin{cases} 1 - (0.00625 \times \text{TP}), & \text{raise position} \\ 1 + (0.00625 \times \text{TP}), & \text{lower position} \end{cases} \quad (12)$$

One can refer to [45] to find more details on VRs and control circuits.

4 Optimal Power Flow (OPF)

Due to the RDSs topology, the OPF-based matrices presented in [46] were used in work done in this chapter. It relies on three matrices – the bus-injection-to-branch-current matrix, designated as [BIBC], the branch-current-to-bus-voltage matrix, specified as [BCBV], and their multiplication matrix [CV] to solve the OPF problem. This matrices method is effective and efficient in solving OPF in RDSs. First of all, let us define an illustrative nine-bus RDS, shown in Fig. 8. BC_i represents the i th branch current, and I_i represents the i th bus injection current, where i represents the bus number. At each i , one can compute the complex apparent load power (S_i), as follows:

$$S_i = P_i + jQ_i, \forall i \in n \quad (13)$$

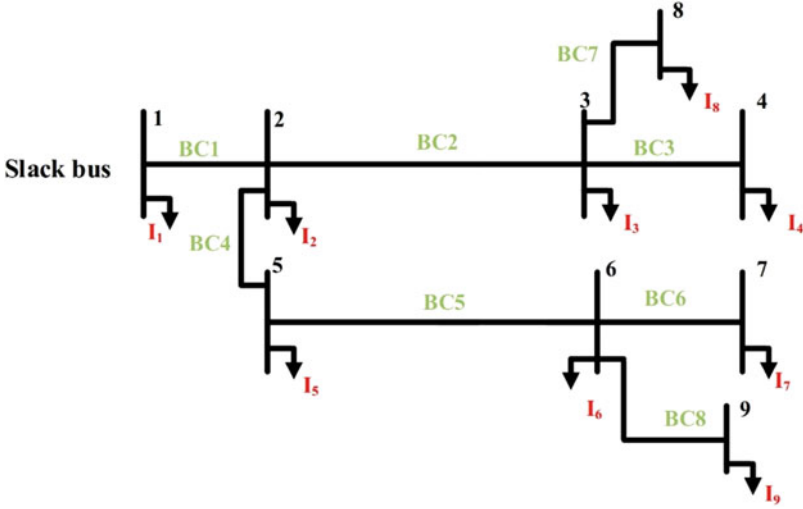


Fig. 8 A simple nine-bus RDS

where P_i and Q_i denote the active and reactive load power at bus i , respectively, and n represents the total bus number, i.e., $n = 9$. The current injection at iteration (itr) is specified using P_i , Q_i , and the i th bus voltage, V_i , as follows:

$$I_i^{itr} = \left(\frac{P_i + jQ_i}{V_i^{itr}} \right)^*, \forall i \in n, \forall itr \in itr_{max} \quad (14)$$

The iteration number (itr) should be less than or equal to the maximum iteration number specified (itr_{max}), i.e., $itr \leq itr_{max}$. Hereafter, using Eq. (14), equivalent bus current injections are obtained. Further, the branch currents can be computed from Kirchhoff's current law applied to RDS, as shown in Eq. (15). Then, one can formulate the relation between the branch and load currents and put it in the matrix form, as follows:

$$\begin{aligned} BC_8 &= I_9 \\ BC_7 &= I_8 \\ BC_6 &= I_7 \\ BC_5 &= I_6 + BC_6 + BC_8 = I_6 + I_7 + I_9 \\ BC_4 &= I_5 + BC_5 = I_5 + I_6 + I_7 + I_9 \\ BC_3 &= I_4 \\ BC_2 &= I_3 + BC_3 + BC_7 = I_3 + I_4 + I_8 \\ BC_1 &= I_2 + BC_2 + BC_4 = I_2 + I_3 + I_4 + I_5 + I_6 + I_7 + I_8 + I_9 \end{aligned} \quad (15)$$

$$\begin{bmatrix} BC_1 \\ BC_2 \\ BC_3 \\ BC_4 \\ BC_5 \\ BC_6 \\ BC_7 \\ BC_8 \end{bmatrix} = \begin{bmatrix} 1 & 1 & 1 & 1 & 1 & 1 & 1 & 1 & 1 \\ 0 & 1 & 1 & 0 & 0 & 0 & 1 & 0 & 0 \\ 0 & 0 & 1 & 0 & 0 & 0 & 0 & 0 & 0 \\ 0 & 0 & 0 & 1 & 1 & 1 & 0 & 1 & 0 \\ 0 & 0 & 0 & 0 & 1 & 1 & 0 & 1 & 0 \\ 0 & 0 & 0 & 0 & 0 & 1 & 0 & 0 & 0 \\ 0 & 0 & 0 & 0 & 0 & 0 & 1 & 0 & 0 \\ 0 & 0 & 0 & 0 & 0 & 0 & 0 & 1 & 0 \end{bmatrix} \times \begin{bmatrix} I_2 \\ I_3 \\ I_4 \\ I_5 \\ I_6 \\ I_7 \\ I_8 \\ I_9 \end{bmatrix} \quad (16)$$

Equation (16) can be generalized to be in terms of [BIBC], as follows:

$$[BC] = [BIBC] \times [I] \quad (17)$$

The i th bus voltage can be obtained from Kirchoff's voltage law applied to RDS; as follows:

$$\begin{aligned} cV_2 &= V_1 - BC_1 Z_{12} \\ V_3 &= V_2 - BC_2 Z_{23} = V_1 - BC_1 Z_{12} - BC_2 Z_{23} \\ V_4 &= V_3 - BC_3 Z_{34} = V_1 - BC_1 Z_{12} - BC_2 Z_{23} - BC_3 Z_{34} \\ V_5 &= V_2 - BC_4 Z_{25} = V_1 - BC_1 Z_{12} - BC_4 Z_{25} \\ V_6 &= V_5 - BC_5 Z_{56} = V_1 - BC_1 Z_{12} - BC_4 Z_{25} - BC_5 Z_{56} \\ V_7 &= V_6 - BC_6 Z_{67} = V_1 - BC_1 Z_{12} - BC_4 Z_{25} - BC_5 Z_{56} - BC_6 Z_{67} \\ V_8 &= V_3 - BC_7 Z_{38} = V_1 - BC_1 Z_{12} - BC_2 Z_{23} - BC_7 Z_{38} \\ V_9 &= V_6 - BC_8 Z_{69} = V_1 - BC_1 Z_{12} - BC_4 Z_{25} - BC_5 Z_{56} - BC_8 Z_{69} \end{aligned} \quad (18)$$

Z_{ij} denotes the impedance between buses i and j . From Eq. (18), V_i is formulated in terms of BCs, Z_{ij} , and the slack bus or substation voltage (V_1). Therefore, the connection between BCs and V_{is} can be stated as follows:

$$\begin{bmatrix} V_2 \\ V_3 \\ V_4 \\ V_5 \\ V_6 \\ V_7 \\ V_8 \\ V_9 \end{bmatrix} = \begin{bmatrix} V_1 \\ V_1 \\ V_1 \\ V_1 \\ V_1 \\ V_1 \\ V_1 \\ V_1 \end{bmatrix} - \begin{bmatrix} Z_{12} & 0 & 0 & 0 & 0 & 0 & 0 & 0 & 0 \\ Z_{12} & Z_{23} & 0 & 0 & 0 & 0 & 0 & 0 & 0 \\ Z_{12} & Z_{23} & Z_{34} & 0 & 0 & 0 & 0 & 0 & 0 \\ Z_{12} & 0 & 0 & Z_{25} & 0 & 0 & 0 & 0 & 0 \\ Z_{12} & 0 & 0 & Z_{25} & Z_{56} & 0 & 0 & 0 & 0 \\ Z_{12} & 0 & 0 & Z_{25} & Z_{56} & Z_{67} & 0 & 0 & 0 \\ Z_{12} & Z_{23} & 0 & 0 & 0 & 0 & Z_{38} & 0 & 0 \\ Z_{12} & 0 & 0 & Z_{25} & Z_{56} & 0 & 0 & 0 & Z_{69} \end{bmatrix} \times \begin{bmatrix} BC_1 \\ BC_2 \\ BC_3 \\ BC_4 \\ BC_5 \\ BC_6 \\ BC_7 \\ BC_8 \end{bmatrix} \quad (19)$$

Consequently, the voltage drops (ΔV) between each bus V_i and the slack bus V_1 is given as follows:

$$\begin{bmatrix} V_1 \\ V_1 \\ V_1 \\ V_1 \\ V_1 \\ V_1 \\ V_1 \\ V_1 \\ V_1 \end{bmatrix} - \begin{bmatrix} V_2 \\ V_3 \\ V_4 \\ V_5 \\ V_6 \\ V_7 \\ V_8 \\ V_9 \end{bmatrix} = \begin{bmatrix} Z_{12} & 0 & 0 & 0 & 0 & 0 & 0 & 0 & 0 \\ Z_{12} & Z_{23} & 0 & 0 & 0 & 0 & 0 & 0 & 0 \\ Z_{12} & Z_{23} & Z_{34} & 0 & 0 & 0 & 0 & 0 & 0 \\ Z_{12} & 0 & 0 & Z_{25} & 0 & 0 & 0 & 0 & 0 \\ Z_{12} & 0 & 0 & Z_{25} & Z_{56} & 0 & 0 & 0 & 0 \\ Z_{12} & 0 & 0 & Z_{25} & Z_{56} & Z_{67} & 0 & 0 & 0 \\ Z_{12} & Z_{23} & 0 & 0 & 0 & 0 & Z_{38} & 0 & 0 \\ Z_{12} & 0 & 0 & Z_{25} & Z_{56} & 0 & 0 & 0 & Z_{69} \end{bmatrix} \times \begin{bmatrix} BC_1 \\ BC_2 \\ BC_3 \\ BC_4 \\ BC_5 \\ BC_6 \\ BC_7 \\ BC_8 \end{bmatrix} \quad (20)$$

Equation (20) can be generalized to be in terms of [BCBV], as follows:

$$[\Delta V] = [BCBV] \times [BC] \quad (21)$$

Combining Eqs. (17) and (21), the relationship between I_{is} and V_{is} can be expressed as follows:

$$[\Delta V] = [BCBV] \times [BC] = [BCBV] \times [BIBC] \times [I] \quad (22)$$

$$[\Delta V] = [CV] \times [I] \quad (23)$$

[CV] is a multiplication matrix of [BCBV] and [BIBC] matrices. The dimension of [BIBC] is $m \times (n-1)$, where m is the number of branches, and the size of [BCBV] is $(n-1) \times m$. [CV] is given as follows:

$$[CV] = [BCBV] \times [BIBC] \quad (24)$$

The OPF solution for RDS can be obtained by solving the following equations iteratively, at $\text{itr} \in \text{itr}_{\max}$; thus:

$$I_i^{\text{itr}} = \left(\frac{P_i + jQ_i}{V_i^{\text{itr}}} \right)^*, \forall i \in n, \forall \text{itr} \in \text{itr}_{\max} \quad (25)$$

$$\Delta V_i^{\text{itr}+1} = [CV] \times I_i^{\text{itr}}, \forall i \in n, \forall \text{itr} \in \text{itr}_{\max} \quad (26)$$

$$V_i^{\text{itr}+1} = V_i^{\text{itr}} + \Delta V_i^{\text{itr}+1}, \forall i \in n, \forall \text{itr} \in \text{itr}_{\max} \quad (27)$$

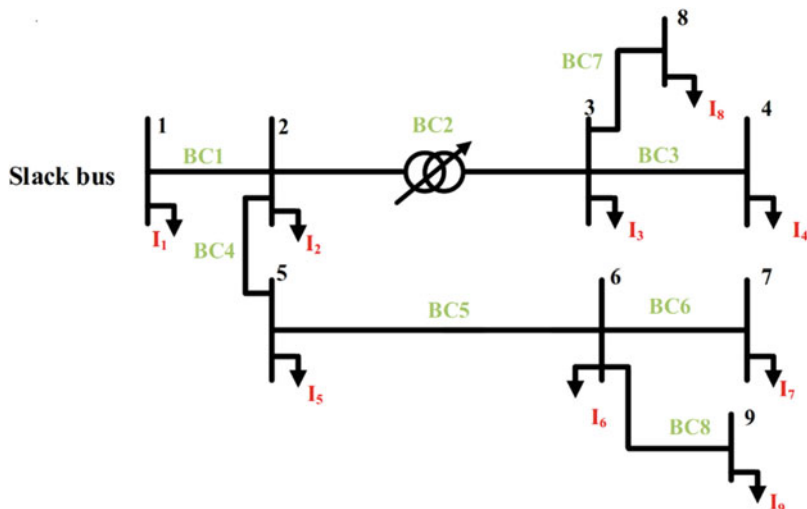


Fig. 9 Adopted nine-bus RDS with VR included in the system

A modified mathematical-based OPF technique for RDSs with VRs embedded in the system is presented to provide the load flow and VR's optimum tap setting as quickly as possible.

To demonstrate the updated OPF procedure, the nine-bus RDS is modified to include a VR between bus #2 and bus #3, as shown in Fig. 9.

One can formulate the branch and load currents and put them in matrix form, as follows:

$$\begin{aligned}
 BC_8 &= I_9 \\
 BC_7 &= I_8 \\
 BC_6 &= I_7 \\
 BC_5 &= I_6 + BC_6 + BC_8 = I_6 + I_7 + I_9 \\
 BC_4 &= I_5 + BC_5 = I_5 + I_6 + I_7 + I_9 \\
 BC_3 &= I_4 \\
 BC_2 &= \frac{I_3}{a_R} + \frac{BC_3}{a_R} + \frac{BC_7}{a_R} = \frac{I_3}{a_R} + \frac{I_4}{a_R} + \frac{I_8}{a_R} \\
 BC_1 &= I_2 + BC_2 + BC_4 = I_2 + \frac{I_3}{a_R} + \frac{I_4}{a_R} + I_5 + I_6 + I_7 + \frac{I_8}{a_R} + I_9
 \end{aligned} \tag{28}$$

Then;

$$\begin{bmatrix} BC_1 \\ BC_2 \\ BC_3 \\ BC_4 \\ BC_5 \\ BC_6 \\ BC_7 \\ BC_8 \end{bmatrix} = \begin{bmatrix} 1 & \frac{1}{a_R} & \frac{1}{a_R} & 1 & 1 & 1 & \frac{1}{a_R} & 1 \\ 0 & \frac{1}{a_R} & \frac{1}{a_R} & 0 & 0 & 0 & \frac{1}{a_R} & 0 \\ 0 & 0 & 1 & 0 & 0 & 0 & 0 & 0 \\ 0 & 0 & 0 & 1 & 1 & 1 & 0 & 1 \\ 0 & 0 & 0 & 0 & 1 & 1 & 0 & 1 \\ 0 & 0 & 0 & 0 & 0 & 1 & 0 & 0 \\ 0 & 0 & 0 & 0 & 0 & 0 & 1 & 0 \\ 0 & 0 & 0 & 0 & 0 & 0 & 0 & 1 \end{bmatrix} \times \begin{bmatrix} I_2 \\ I_3 \\ I_4 \\ I_5 \\ I_6 \\ I_7 \\ I_8 \\ I_9 \end{bmatrix} \tag{29}$$

Also, the *i*th bus voltage equations and the branch current relations can be written as follows:

$$\begin{aligned}
 V_2 &= V_1 - BC_1 Z_{12} \\
 V_3 &= \left(\frac{V_2 - BC_2 Z_{23}}{a_R} \right) = \frac{V_1 - BC_1 Z_{12} - BC_2 Z_{23}}{a_R} \\
 V_4 &= V_3 - BC_3 Z_{34} = \frac{V_1 - BC_1 Z_{12} - BC_2 Z_{23}}{a_R} - BC_3 Z_{34} \\
 V_5 &= V_2 - BC_4 Z_{25} = V_1 - BC_1 Z_{12} - BC_4 Z_{25} \\
 V_6 &= V_5 - BC_5 Z_{56} = V_1 - BC_1 Z_{12} - BC_4 Z_{25} - BC_5 Z_{56} \\
 V_7 &= V_6 - BC_6 Z_{67} = V_1 - BC_1 Z_{12} - BC_4 Z_{25} - BC_5 Z_{56} - BC_6 Z_{67} \\
 V_8 &= V_3 - BC_7 Z_{38} = \frac{V_1 - BC_1 Z_{12} - BC_2 Z_{23}}{a_R} - BC_7 Z_{38} \\
 V_9 &= V_6 - BC_8 Z_{69} = V_1 - BC_1 Z_{12} - BC_4 Z_{25} - BC_5 Z_{56} - BC_8 Z_{69}
 \end{aligned} \tag{30}$$

$$\begin{bmatrix} V_2 \\ V_3 \\ V_4 \\ V_5 \\ V_6 \\ V_7 \\ V_8 \\ V_9 \end{bmatrix} = \begin{bmatrix} V_1 \\ V_1 / a_R \\ V_1 / a_R \\ V_1 \\ V_1 \\ V_1 \\ V_1 / a_R \\ V_1 \end{bmatrix} - [BCBV] \times \begin{bmatrix} BC_1 \\ BC_2 \\ BC_3 \\ BC_4 \\ BC_5 \\ BC_6 \\ BC_7 \\ BC_8 \end{bmatrix} \tag{31}$$

so that:

$$[\text{BCBV}] = \begin{bmatrix} Z_{12} & 0 & 0 & 0 & 0 & 0 & 0 & 0 \\ Z_{12}/a_R & Z_{23}/a_R & 0 & 0 & 0 & 0 & 0 & 0 \\ Z_{12}/a_R & Z_{23}/a_R & Z_{34} & 0 & 0 & 0 & 0 & 0 \\ Z_{12} & 0 & 0 & Z_{25} & 0 & 0 & 0 & 0 \\ Z_{12} & 0 & 0 & Z_{25} & Z_{56} & 0 & 0 & 0 \\ Z_{12} & 0 & 0 & Z_{25} & Z_{56} & Z_{67} & 0 & 0 \\ Z_{12}/a_R & Z_{23}/a_R & 0 & 0 & 0 & 0 & Z_{38} & 0 \\ Z_{12} & 0 & 0 & Z_{25} & Z_{56} & 0 & 0 & Z_{69} \end{bmatrix} \quad (32)$$

Accordingly, one has to perform the OPF without VRs included. One VR is added to the system between two buses, and the minimum and maximum regulation voltage values are identified, a_R is initially set to 1 and TP_{old} is set to 0. If the voltage at the VR bus exceeds the maximum regulation voltage, then Eq. (33) is applied to lower the voltage.

$$\begin{aligned} \text{TP}_{\text{change}} &= \frac{V_{\text{VR}} - V_{\text{max}}}{0.00625}, \\ \text{TP}_{\text{new}} &= \text{TP}_{\text{old}} - \text{TP}_{\text{change}}, \forall \text{TP} = \{1, 2, \dots, 16\} \\ a_R &= 1 + 0.00625 (\text{TP}_{\text{new}}) \end{aligned} \quad (33)$$

Otherwise, Eq. (34) is used to raise the voltage if the voltage at the VR bus is lower than the minimum voltage value.

$$\begin{aligned} \text{TP}_{\text{change}} &= \frac{V_{\text{min}} - V_{\text{VR}}}{0.00625}, \\ \text{TP}_{\text{new}} &= \text{TP}_{\text{old}} + \text{TP}_{\text{change}}, \forall \text{TP} = \{1, 2, \dots, 16\} \\ a_R &= 1 - 0.00625 (\text{TP}_{\text{new}}) \end{aligned} \quad (34)$$

Iteratively, this will be repeated until no change occurs in the tap; $\text{TP}_{\text{new}} = \text{TP}_{\text{old}}$. Consequently, the procedure will be recurrent for all VRs connected to the system.

5 Formulation of the Problem

The objective function (f) formulated in this work minimizes the total active power losses ($P_{\text{loss,tot}}$) given in Eq. (35) in three equally weighted loading scenarios – light (Lig), shoulder (Sh), and peak (Pk) levels of load demand. k_1 , k_2 , and k_3 are the weighting factors of the loading scenarios.

$$f = \min_h P_{\text{loss,tot}} = \min_h (k_1 P_{\text{loss}}(\text{lig}) + k_2 P_{\text{loss}}(\text{Sh}) + k_3 P_{\text{loss}}(\text{Pk})), h = 8760 \quad (35)$$

Lig represents 60% of the peak loading level of hours, Sh represents 80% of the peak loading, and Pk represents 100%. Each of them occurs for 2920 hours per year. At that time, f subjects to a different set of constraints – equality power flow constraints represented by Eqs. (36) and (37), DGs size limits represented by (38), DGs penetration represented by (39), PF limits represented by (40), SCBs size represented by (41), the h th branch current thermal limits represented by (42), and the h th allowable voltage boundaries, represented by (43). The suffix min denotes the minimum value of the variable/parameter, while max denotes the maximum value of the variable/parameter.

$$P_{\text{grid}} + \sum_{g=1}^{N_{\text{DG}}} P_{\text{DG}}(g) = \sum_{i=1}^n P_{\text{d}}(i) + \sum_{\text{br}=1}^{N_{\text{br}}} P_{\text{loss}}(\text{br}), \forall g \in N_{\text{DG}}, \forall \text{br} \in N_{\text{br}}, \forall i \in n \quad (36)$$

$$Q_{\text{grid}} + \sum_{c=1}^{N_{\text{SCB}}} Q_{\text{SCB}}(c) = \sum_{i=1}^n Q_{\text{d}}(i) + \sum_{\text{br}=1}^{N_{\text{br}}} Q_{\text{loss}}(\text{br}), \forall c \in N_{\text{SCB}}, \forall \text{br} \in N_{\text{br}}, \forall i \in n \quad (37)$$

where P_{grid} and Q_{grid} denote the grid' active and reactive power, respectively, P_{loss} and Q_{loss} denote the active and reactive power losses, respectively, and $P_{\text{d}}(i)$ and $Q_{\text{d}}(i)$ denote the i th real and reactive power demand. N_{br} denotes the total number of branches, and n denotes the number of buses in the power system. N_{DG} and N_{SCB} denote the total number of DGs and SCBs, respectively, P_{DG} denotes the DG's active power, and Q_{SCB} denotes the SCB's reactive power.

$$P_{\text{DG}}(g) \leq P_{\text{DG}}(g)_{\text{max}}, \forall g \in N_{\text{DG}} \quad (38)$$

$$\sum_{g=1}^{N_{\text{DG}}} P_{\text{DG}}(g) \leq \alpha \sum_{i=1}^n P_{\text{d}}(i), \forall g \in N_{\text{DG}} \quad (39)$$

In Eq. (39), α represents a percentage of the demand power in which the maximum permissible DG penetration is determined when one constraint violates the limit.

$$0.85 \text{ lag} \leq \text{PF} \leq 1 \quad (40)$$

$$Q_{\text{SCB}}(c) \leq Q_{\text{SCB}}(c)_{\text{max}}, \forall c \in N_{\text{SCB}} \quad (41)$$

$$I_{br,h} \leq I_{\max,br}, \forall br \in N_{br}, \forall h \quad (42)$$

$$V_i^{\min} \leq V_{i,h} \leq V_i^{\max}, \forall i \in n, \forall h \quad (43)$$

6 Whale Optimization Algorithm (WOA)

Nature-inspired metaheuristic algorithms (NIMHAs) have amazingly solved complex engineering problems. In this realm, WOA is a population-based NIMHA settled by Mirjalili and Lewis in 2016, and it was grounded on imitating the pursuing behavior of a specific kind of the seven whale types called the humpback whale (HW) [47]. Whales, the largest mammals in the world, are brilliant emotional creatures. Whales have cells similar to those found in humans in their brains, so-called spindle cells, responsible for emotional actions, judgment, and social behaviors in general. The hunting method of HWs is termed the net-bubble feeding method (NBFM). HWs select to catch small fishes (as prey) near the surface [48].

When HW notices its prey, it dives about 12 m down and then begins to make spiral bubbles around the prey. The prey is afraid to cross these bubbles, which appear as a trap. Hence, HW swims up to the surface and collects its trapped prey, as illustrated in Fig. 10.

The NBFM of the HW is mathematically modeled in three phases – encircling preys, NBFM as the exploitation (EXPL) phase, and the exploration (EXPR) phase. The EXPL is also divided into the shrink mechanism and the spiral position's update [47].

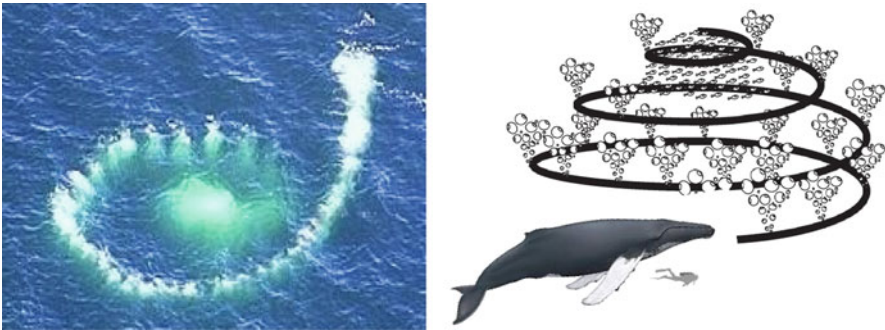


Fig. 10 Net-bubble trap of the HWs during hunting

6.1 Encircling Stage

HWs can recognize and surround the prey's location. Since the optimal design position in the search space is unknown, the WOA considers the current search factor as the target prey (or solution) or close to the optimal one.

After the best search representative is defined, other search representatives try to update their location toward the best search representative, as represented by the following equations: t denotes the current iteration, $t + 1$ denotes the subsequent iteration to t , X^* denotes the position vector of the best solution obtained. It is iteratively updated until the best value is obtained or the maximum iterations number, t_{\max} , is reached and \vec{X} denotes the position vector. $||$ indicates the absolute value (abs), and \cdot means multiplication.

$$\vec{D} = \left| \vec{C} \cdot \vec{X}^*(t) - \vec{X}(t) \right| \quad (44)$$

$$\vec{X}(t + 1) = \vec{X}^*(t) - \vec{A} \cdot \vec{D} \quad (45)$$

The vectors \vec{A} and \vec{C} are formulated as follows:

$$\vec{A} = 2(\vec{a} \cdot \vec{r}) - \vec{a} \quad (46)$$

$$\vec{C} = 2\vec{r} \quad (47)$$

where \vec{a} is promoted to linearly decrease from 2 to 0 to characterize the spiral bubbles over the iterations and \vec{r} denotes a random vector that ranges between $[0,1]$. \vec{D} denotes the abs difference between the obtained solutions.

6.1.1 Bubble-Net Hunting Stage

Shrink Mechanism

This mechanism is realized by decreasing \vec{a} shown in Eq. (46) from 2 to 0. This, in turn, decreases \vec{A} 's value in a random manner in $[-a, a]$. Figure 11 illustrates the possible positions of random HW's at (X, Y) toward the prey at (X^*, Y^*) , keeping that $(0 \leq A \leq 1)$.

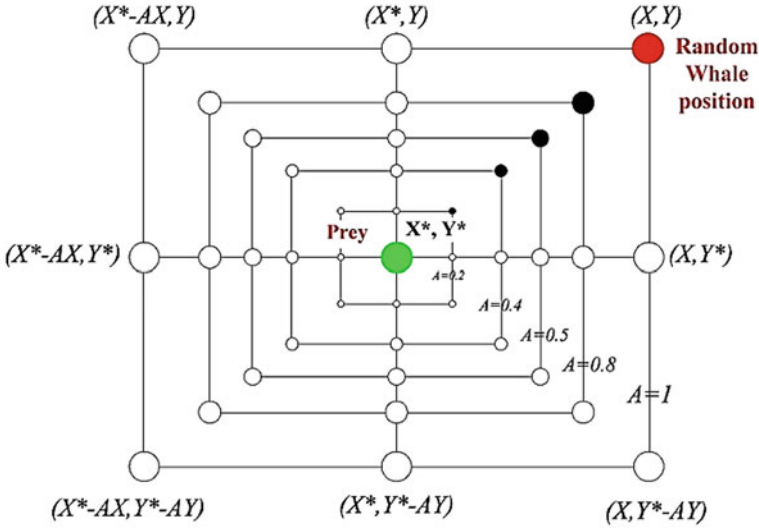


Fig. 11 Illustration of the shrink mechanism

Spiral Update (Helix-Based Movement)

The distance between the HW at (X, Y) and the prey at (X^*, Y^*) is computed first. At that point, a spiral mechanism is created between the HW's and prey's positions to imitate a helix-based movement as explored in Fig. 12.

$$\vec{X}(t + 1) = \vec{D}' \cdot e^{sl} \cdot \cos(2\pi l) + \vec{X}^*(t) \tag{48}$$

$$\vec{D}'_i = \left| \vec{X}^*(t) - \vec{X}(t) \right| \tag{49}$$

where \vec{D}'_i denotes the distance between an i th HW and the prey, s represents the shape of the logarithmic spiral, l is a random number in $[-1, 1]$.

The HWs swim around the prey using the shrink mechanism or along a spiral-shaped path. Mathematically, a 50% probability is assumed in the optimization process to choose either shrinking or spiral moving toward the prey in updating the HWs' position. Thus;

$$\vec{X}(t + 1) = \begin{cases} \vec{X}^*(t) - \vec{A} \cdot \vec{D} & \forall p_r < 0.5 \\ \vec{X}(t + 1) = \vec{D}' \cdot e^{sl} \cdot \cos(2\pi l) + \vec{X}^*(t) & \forall p_r \geq 0.5 \end{cases} \tag{50}$$

where p_r denotes a random number in $[0, 1]$.

Fig. 12 Illustration of the spiral update mechanism

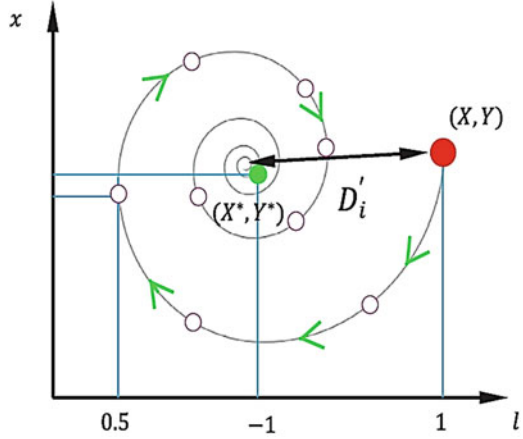


Table 2 The values of the parameters used

Parameter	Value
Number of search agents	30
\vec{a}	Linearly decreases from 2 to 0
Maximum number of iterations	2000

6.1.2 Exploration (EXPR) Stage

The vector \vec{A} with random values greater than 1 or less than -1 , $|\vec{A}| > 1$, was employed to force search agents to move far away from a reference HW to avoid interactions between them during hunting. Besides, the HWs (search agents) search for the best prey (global solution) randomly and change their positions according to the position of other HWs. To consider this randomness, Eqs. (44) and (45) are updated after replacing X^* with \vec{X}_{rand} , where \vec{X}_{rand} is a random position vector (a random HW) chosen from the population. as follows:

$$\vec{D} = \left| \vec{C} \cdot \vec{X}_{rand}(t) - \vec{X}(t) \right| \tag{51}$$

$$\vec{X}(t + 1) = \vec{X}_{rand}(t) - \vec{A} \cdot \vec{D} \tag{52}$$

To recap, the WOA parameters used in this work are given in Table 2, and the WOA’s flowchart is shown in Fig. 13.

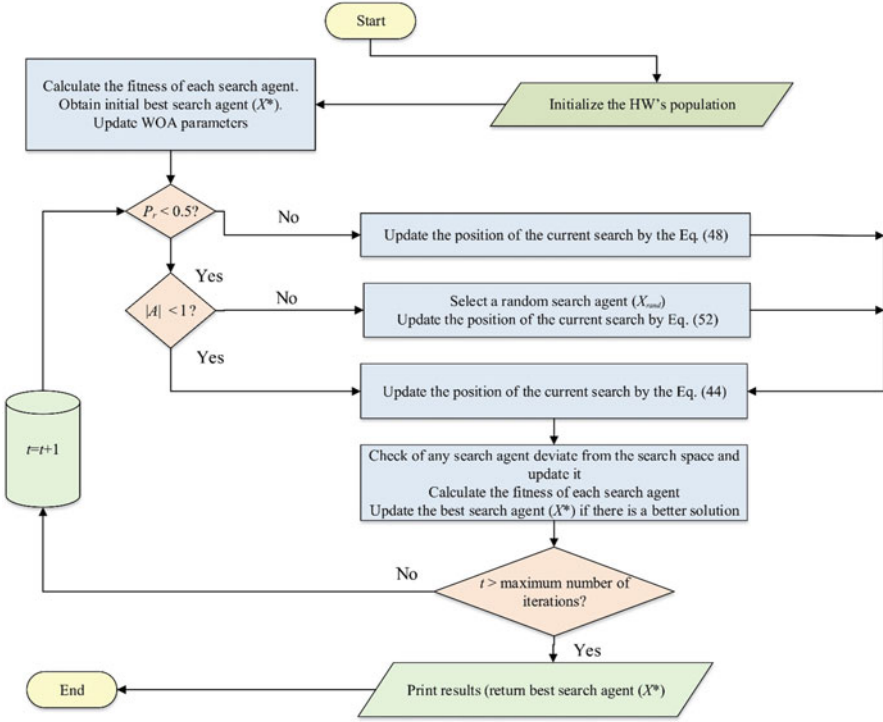


Fig. 13 Flowchart for WOA

7 Qualification of the Performance of the System

The different metrics and indices used to qualify the studied system's performance and determine the economic benefits are presented in this section.

7.1 Technical Indices

Reduction in the Active Energy Loss Benefits (TI_P)

The difference in the active energy loss values before and after compensation, \$/year, is formulated in (53), where R_1 represents the tariff rate of the energy (\$/kWh), and s denotes the scenario number. R_1 equals \$0.06/kWh as given in [33, 49].

$$TI_P = \sum_{s=1}^{s=3} \left[R_1 h \left(P_{\text{loss},s}^{\text{before}} - P_{\text{loss},s}^{\text{after}} \right) \right], s \in \{\text{Lig}, \text{Sh}, \text{Pk}\} \quad (53)$$

Reduction in the Apparent Power Purchased from the Grid (TI_S)

The change in the contracted apparent power (S_{grid}) values before and after compensation, \$/year, is formulated in (54), where R_2 represents the tariff rate of the apparent power (\$/kVAh) and is set to \$0.06/kWh [33, 49].

$$TI_S = \sum_{s=1}^{s=3} \left[R_2 \left(S_{grid,s}^{before} - S_{grid,s}^{after} \right) \right], s \in \{\text{Lig, Sh, Pk}\} \quad (54)$$

Enhancement of the Voltage Profile (TI_{VD})

The voltage profile enhancement is formulated by calculating the sum of the absolute values of the squared voltage of each bus deviated from one per unit at the peak loading level, as given in Eq. (55) [50]. The enhancement is determined by comparing the obtained index value with the corresponding value in the uncompensated system.

$$TI_{VD} = \sum_{i=1}^n (1 - V_i)^2, \forall i \in n, s = \text{Pk} \quad (55)$$

Enhancement of the Loading Capacity (TI_{LC})

The loading capacity of the branch currents is formulated by determining the maximum branch current, as given in Eq. (56), where $I_{max,br}$ is the maximum branch current allowed to flow.

$$TI_{LC} = \max \left(\frac{I_{br}}{I_{max,br}} \right), \forall br \in N_{br}, s = \text{Pk} \quad (56)$$

Voltage Stability Improvement (TI_{VS})

The VS enhancement is formulated by determining the minimum VSI calculated at all buses [31], as given in Eq. (57) and comparing its value with the uncompensated case.

$$TI_{VS} = \min [VSI_{bus}] = V_i^4 - 4(PX - QR)^2 - 4V_i^2 (PR + QX), \forall i \in n \quad (57)$$

7.2 Economic Indices

DGs Costs (EI_{DG})

EI_{DG} (\$/year) is formulated as given in (58), where R_{DG} represents DGs' operation and maintenance costs. RF_{DG} denotes the capital recovery factors of DGs used to convert the present value cost to annualized cost. R_{DG} is set to \$5/W [33].

$$EI_{DG} = R_{DG} \times RF_{DG} \sum_{g=1}^{N_{DG}} P_{DG}(g) \quad (58)$$

SCBs Costs (EI_{SCB})

EI_{SCB} (\$/year) is formulated as given in (59), where R_{SCB} represents SCBs' operation costs, C_{SCB} means SCBs' investment costs, and RF_{SCB} denotes SCBs' capital recovery factors. R_{SCB} and C_{SCB} are set to 30 \$/kvar and \$1000, respectively [33].

$$EI_{SCB} = R_{SCB} \left[C_{SCB} + RF_{SCB} \sum_{c=1}^{N_{SCB}} Q_{SCB}(c) \right] \quad (59)$$

VRs Costs (EI_{VR})

EI_{VR} (\$/year) is formulated in (60), where RF_{VR} represents VRs' investment and operation costs. RF_{SCB} denotes the capital recovery factors of SCBs. R_0 is the VR's cost (\$) that relies on the current rating of the VR (I_{VR}). For instance, R_0 equals \$38,000 for 100 A, \$44,800 for 150 A, \$50,600 for 200 A, \$58,100 for 250 A, \$64,700 for 300 A, \$70,300 for 350 A, and \$77,900 for 400 A [33].

$$EI_{VR} = RF_{VR} \times R_0(I_{VR}) \quad (60)$$

A generalized expression of the recovery factors of the different compensators (RF_c) is expressed in (61), where I is the interest rate (7%) and Y is the operation number of years of the compensator – 20 years for the DGs, 10 years for the SCBs, and 15 years for the VRs.

$$RF_c = \frac{I(1+I)^Y}{(1+I)^Y - 1}, \forall c = \{DG, SCB, VR\} \quad (61)$$

Returned Funds from Savings (EI_{SAV})

Finally, the returned funds or savings are expressed in Eq. (62) as the difference between benefits and costs.

$$EI_{SAV} = [TI_P + TI_S] - [EI_{DG} + EI_{SCB} + EI_{VR}] \quad (62)$$

EI_{SAV} is calculated while considering the three Lig, Sh, and Pk levels.

8 System Studied

Figure 14 explores the studied radial distribution system in Menoufia, Egypt. It comprises 37 buses supplied from 11 kV–50 Hz substation to feed 31 loads. P_d is 4.8019 MW, and the Q_d is 2.9759 MVar. The base MVA and voltage are set to

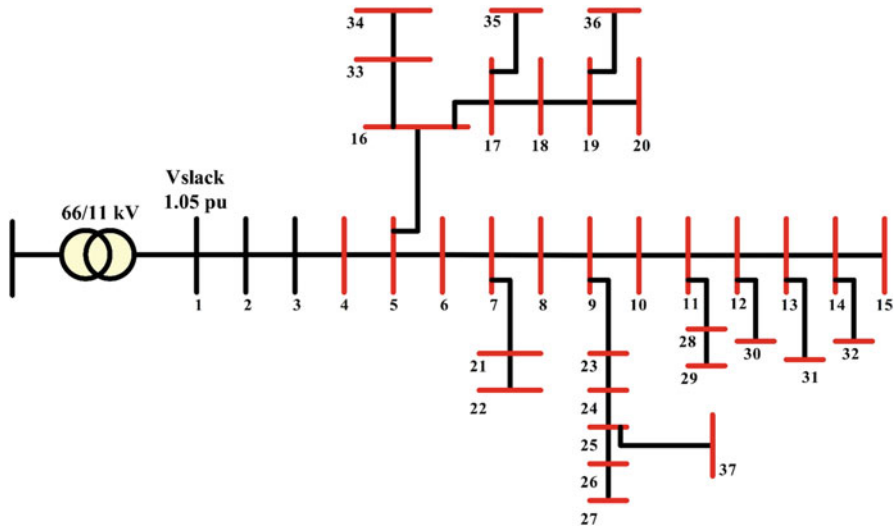


Fig. 14 Line diagram of the 37-bus radial distribution system studied

Table 3 Line data of the 37-bus system

br	From <i>i</i>	To <i>j</i>	I_{max} (A)	R (Ω)	X (Ω)	br	From <i>i</i>	To <i>j</i>	I_{max} (A)	R (Ω)	X (Ω)
1	1	2	788.00	0.0349	0.0493	19	19	20	183.70	0.4004	0.1540
2	2	3	788.00	0.1862	0.2629	20	7	21	183.70	0.8425	0.3240
3	3	4	788.00	1.2891	1.8201	21	21	22	183.70	0.2086	0.0802
4	4	5	788.00	1.1640	1.6434	22	9	23	183.70	1.4015	0.5389
5	5	6	367.50	0.0776	0.1096	23	23	24	183.70	0.5005	0.1925
6	6	7	367.50	0.0466	0.0657	24	24	25	183.70	0.5798	0.2230
7	7	8	367.50	0.0388	0.0548	25	25	26	183.70	0.6006	0.2310
8	8	9	367.50	0.1263	0.1534	26	26	27	183.70	0.4004	0.1540
9	9	10	367.50	0.1240	0.0893	27	11	28	183.70	0.9009	0.3465
10	10	11	367.50	0.2066	0.1489	28	28	29	183.70	1.1011	0.4235
11	11	12	367.50	0.1240	0.0893	29	12	30	183.70	0.2066	0.1489
12	12	13	367.50	0.1269	0.0914	30	13	31	183.70	0.2252	0.0866
13	13	14	367.50	0.0901	0.0649	31	14	32	183.70	0.4371	0.1681
14	14	15	367.50	0.2587	0.1864	32	16	33	183.70	0.1668	0.0642
15	5	16	183.70	0.7007	0.2695	33	33	34	183.70	0.4755	0.1829
16	16	17	183.70	0.2002	0.0770	34	17	35	183.70	0.6006	0.2310
17	17	18	183.70	0.7007	0.2695	35	19	36	183.70	1.1011	0.4235
18	18	19	183.70	0.9009	0.3465	36	25	37	183.70	0.5005	0.1925

1 MVA and 11 kV, respectively. The complete system data are presented in Tables 3 and 4 [33]. All the buses given in red indicate a violation of the voltage limits (less than 0.9 pu), and this shows that the investigated electrical system is a deteriorated system that suffers from a low voltage profile, such that the minimum voltage is

Table 4 Load data of the 37-bus system at the three different loading levels

Bus i	Pk		Sh		Lig	
	P_i (kW)	Q_i (kVAr)	P_i (kW)	Q_i (kVAr)	P_i (kW)	Q_i (kVAr)
1	0	0	0	0	0	0
2	0	0	0	0	0	0
3	21.2003	13.1388	16.9602	10.511	12.7202	7.88328
4	10.6002	6.5694	8.48016	5.25552	6.36012	3.94164
5	117.7795	72.9932	94.2236	58.3946	70.6677	43.7959
6	255.5814	158.3951	204.465	126.716	153.349	95.0371
7	127.2018	78.8326	101.761	63.0661	76.3211	47.2996
8	0	0	0	0	0	0
9	0	0	0	0	0	0
10	138.9798	86.1319	111.184	68.9055	83.3879	51.6791
11	181.3804	112.4095	145.104	89.9276	108.828	67.4457
12	152.5244	94.5261	122.02	75.6209	91.5146	56.7157
13	0	0	0	0	0	0
14	221.4254	137.2271	177.14	109.782	132.855	82.3363
15	241.4479	149.6360	193.158	119.709	144.869	89.7816
16	42.4006	26.2775	33.9205	21.022	25.4404	15.7665
17	144.8687	89.7816	115.895	71.8253	86.9212	53.869
18	26.5004	16.4235	21.2003	13.1388	15.9002	9.8541
19	41.8117	25.9126	33.4494	20.7301	25.087	15.5476
20	66.5454	41.2411	53.2363	32.9929	39.9272	24.7447
21	325.0713	201.4611	260.057	161.169	195.043	120.877
22	214.9475	133.2125	171.958	106.57	128.969	79.9275
23	113.0683	70.0734	90.4546	56.0587	67.841	42.044
24	121.9017	75.5479	97.5214	60.4383	73.141	45.3287
25	175.4914	108.7598	140.393	87.0078	105.295	65.2559
26	94.2236	58.3945	75.3789	46.7156	56.5342	35.0367
27	118.3684	73.3581	94.6947	58.6865	71.021	44.0149
28	299.1598	185.4026	239.328	148.322	179.496	111.242
29	215.5364	133.5775	172.429	106.862	129.322	80.1465
30	0	0	0	0	0	0
31	241.4479	149.6360	193.158	119.709	144.869	89.7816
32	267.9483	166.0594	214.359	132.848	160.769	99.6356
33	276.1928	171.1689	220.954	136.935	165.716	102.701
34	106.0015	65.6938	84.8012	52.555	63.6009	39.4163
35	256.7592	159.1251	205.407	127.3	154.056	95.4751
36	10.6002	6.5694	8.48016	5.25552	6.36012	3.94164
37	174.9025	108.3948	139.922	86.7158	104.942	65.0369

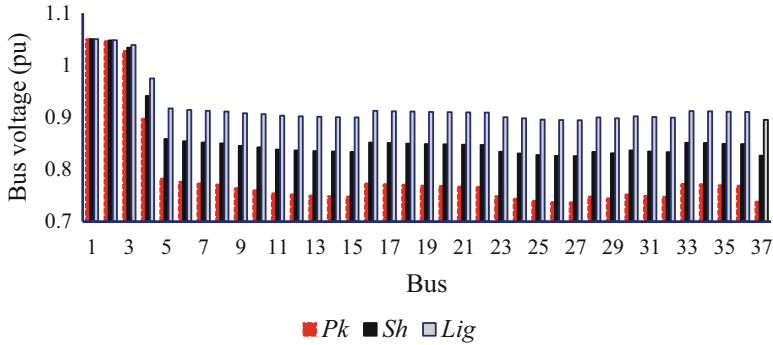


Fig. 15 Uncompensated voltage profile of the studied system at the three loading levels

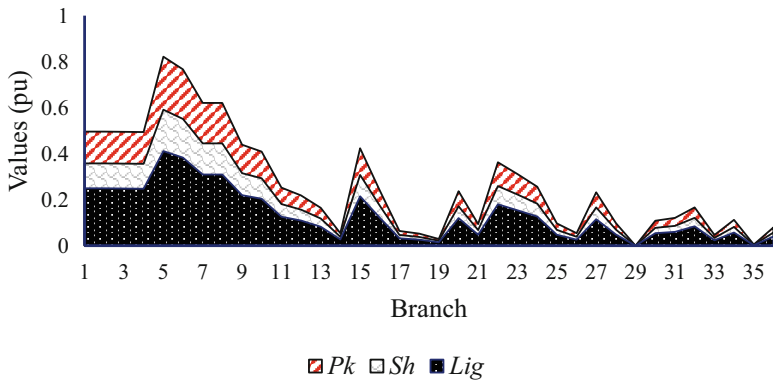


Fig. 16 Loading capacity of the branches of the studied system at the three loading levels

measured at bus #27 and equals 0.7371 pu. Also, the 37-bus system suffers from very high-apparent power losses (higher than 1 MW for active power losses and 1.8 MVar for reactive power losses in the period of the maximum demand). The slack bus voltage is set to 1.05 pu.

The 37-bus system has three different loading levels, Lig, Sh, and Pk, each of which continues for 2920 hours (i.e., 8760/3 hours) as mentioned before.

The voltage magnitudes of the 37 buses are explored in Fig. 15 at the three loading levels before compensation. Figure 16 explores the loading capacity of the branches at the three loading levels. Noticeably, the system undergoes poor voltage regulation, highly active and reactive power losses, and expected current problems, principally at the Pk level. The insufficient voltage is caused because the system includes long branches (around 13 km for branches 3–4 and 4–5). These branches will be considered candidate locations to allocate VRs.

The technical QoP indices used are presented in Table 5 for the uncompensated 37-bus system in which P_{loss} (kW), Q_{loss} (kVar), S_{grid} (MVA), minimum (V_{min})

Table 5 Results of the uncompensated 37-bus studied system

QoP metric		Loading levels					
		Lig		Sh		Pk	
P_{loss} (kW)		343.1828		707.4094		1361.7	
Q_{loss} (kVAr)		463.8976		956.0957		1839.9	
S_{grid} (MVA)		3.9312		5.6414		7.8213	
V_{min} (pu)	Bus	0.8946	27	0.8259	27	0.7371	27
V_{max} (pu)	Bus	1.05	1	1.05	1	1.05	1
Loading capacity (%)		41.12		59.10		82.15	
Minimum VSI (pu)		0.6406		0.4652		0.2952	

voltage magnitude (pu) and its bus number, loading capacity of the branches in percentage, and the minimum VSI are calculated at the three loading levels.

9 Results and Discussions

The decision variables of the problem formulated are the DGs and SCBs – locations and sizes and the tapping of the VR. One to three DGs, $1 \leq N_{\text{DG}} \leq 3$, can connect to the system. Also, one to eight SCBs can connect to the system ($N_{\text{SCB}} \leq 8$). The probable locations of DGs and SCBs are specified as integer variables between 2 and 37 (bus #2 to bus #37). DG sizes are expressed as continuous variables that range between 0 kW and 5 MW. SCBs sizes are considered as discrete variables ranging between 0 and 1200 kVAr. SCBs size is deemed to be in steps of 150 kVAr. The maximum number of SCBs and DGs to be located is 12 (8 SCBs and 3 DGs, in addition to one VR with two variables (location and size)). The VR cost and the current capacity are taken from [29].

Six cases are investigated – Case #1: DGs allocation, Case #2: SCBs allocation, Case #3: DGs/SCBs coordination, Case #4: DGs/VRs coordination, Case #5: SCBs/VRs coordination, and Case #6: DGs/SCBs/VRs coordination. The results of the six cases are reported in the following subsections, and a comparison between them is given. It should be noted that the number of populations is 30, and 2000 iterations are set. The sizes, locations, and tap settings of the VRs obtained in the various cases are tabulated in Table 6. Table 7 shows the objective function values obtained and the time needed to reach them in all cases investigated.

It is evident that the lowest objective function was achieved when f_6 – DGs/SCBs/VRs – was used (17.208 MW), followed by f_3 – DGs/SCBs – (51.279 MW). This means that coordinating the compensators is necessary to achieve good results. On the other side, the worst objective function was performed when f_2 – SCBs – was used (475.472 MW). However, f_6 needs considerable computation time to be executed (33.78 minutes) compared with the other objective functions.

Tables 8, 9, and 10 show the compensated bus voltage values at the different cases investigated in the three scenarios (Lig, Sh, Pk), respectively. As is obvious,

Table 6 Sizes, locations and tap settings of the VRs obtained in the various cases

Case #1	DGs	Size (kW)	1316.6872, 2084.5915, 709.5161
		Location (bus)	13, 5, 25
Case #2	SCBs	Size (kVAr)	750, 600, 1200, 150, 900, 150, 150
		Location (bus)	26, 10, 8, 15, 5, 11, 2
Case #3	DGs	Size (kW)	100, 3571.50, 100
		Location (bus)	25, 9, 13
	SCBs	Size (kVAr)	300, 150, 750, 150, 750, 450, 600
		Location (bus)	2, 20, 5, 29, 23, 14, 2
Case #4	DGs	Size (kW)	1859.204, 1121.695, 2212.0772
		Location (bus)	2, 12, 7
	VRs	Location (bus)	Between buses 3 and 4
		Tapping (Lig, Sh, Pk)	-2, 2, 13
Case #5	SCBs	Size (kVAr)	450, 900, 450, 750, 300, 300, 300
		Location (bus)	3, 12, 2, 6, 25, 2, 2
	VRs	Location (bus)	Between buses 3 and 4
		Tapping (Lig, Sh, Pk)	0, 10, 16
Case #6	DGs	Size (kW)	478.3795, 2182.7499, 730.6741
		Location (bus)	18, 11, 8
	SCBs	Size (kVAr)	300, 450, 450, 300, 300, 450, 300
		Location (bus)	14, 2, 7, 11, 15, 8, 17
	VRs	Location (bus)	Between buses 3 and 4
		Tapping (Lig, Sh, Pk)	-9, -7, -4

Table 7 Objective function values and the time needed to attain them

Cases	#1	#2	#3	#4	#5	#6
<i>f</i> (MW)	187.680	475.472	51.279	91.342	203.636	17.208
<i>Time</i> (s)	232.043	313.000	260.030	11,948.911	19,465.457	2,026.202

the voltage profiles have been enhanced at the three loading scenarios and thereby meet the permissible limits (among all cases, the lowest voltage value is 0.9 pu in the peak loading).

Tables 11, 12, and 13 show the compensated branch current values at the different cases investigated in the three scenarios, respectively. Compared with the I_{max} values given in Table 3, the current values have been reduced at the three loading scenarios and are lower than the maximum branch current values.

Table 14 shows the technical performance metrics calculated in all cases under study. Regarding the active power loss reduction (kW), the best reduction value obtained was in Case #3 as 2258.462 kW in DGs/SCBs coordination, followed by 2251.906 in DGs/SCBs/VRs coordination. This means that minimizing the power loss as an objective function is not the best choice, as maximizing the benefits can achieve better results.

Table 8 Bus voltage values at the different cases investigated, Lig

Cases							Cases						
Bus	#1	#2	#3	#4	#5	#6	Bus	#1	#2	#3	#4	#5	#6
1	1.05	1.05	1.05	1.05	1.05	1.05	20	1.01	1.04	1.09	0.98	0.98	1.02
2	1.05	1.05	1.05	1.05	1.05	1.05	21	1.01	1.05	1.09	0.99	0.98	1.01
3	1.05	1.05	1.05	1.05	1.05	1.05	22	1.01	1.05	1.09	0.99	0.98	1.01
4	1.03	1.05	1.08	1.01	1.01	1.01	23	1.02	1.05	1.10	0.98	0.98	1.01
5	1.02	1.05	1.09	0.99	0.99	1.02	24	1.02	1.05	1.10	0.98	0.97	1.01
6	1.02	1.05	1.10	0.99	0.98	1.02	25	1.02	1.04	1.10	0.98	0.97	1.01
7	1.02	1.05	1.10	0.99	0.98	1.02	26	1.02	1.05	1.09	0.98	0.97	1.01
8	1.02	1.05	1.10	0.99	0.98	1.02	27	1.02	1.05	1.09	0.97	0.97	1.01
9	1.02	1.05	1.10	0.99	0.98	1.02	28	1.01	1.04	1.09	0.98	0.98	1.02
10	1.02	1.05	1.10	0.99	0.98	1.02	29	1.01	1.04	1.09	0.98	0.97	1.02
11	1.02	1.05	1.10	0.99	0.98	1.02	30	1.02	1.05	1.10	0.99	0.98	1.02
12	1.02	1.05	1.10	0.99	0.98	1.02	31	1.02	1.04	1.10	0.98	0.98	1.02
13	1.02	1.04	1.10	0.98	0.98	1.02	32	1.01	1.04	1.10	0.98	0.98	1.02
14	1.02	1.04	1.10	0.98	0.98	1.02	33	1.01	1.04	1.09	0.99	0.98	1.02
15	1.01	1.04	1.10	0.98	0.98	1.02	34	1.01	1.04	1.09	0.99	0.98	1.01
16	1.02	1.05	1.09	0.99	0.98	1.02	35	1.01	1.04	1.09	0.98	0.98	1.01
17	1.01	1.04	1.09	0.99	0.98	1.02	36	1.01	1.04	1.09	0.98	0.98	1.02
18	1.01	1.04	1.09	0.98	0.98	1.02	37	1.02	1.04	1.09	0.98	0.97	1.01
19	1.01	1.04	1.09	0.98	0.98	1.02							

Table 9 Bus voltage values at the different cases investigated, Sh

Cases							Cases						
Bus	#1	#2	#3	#4	#5	#6	Bus	#1	#2	#3	#4	#5	#6
1	1.05	1.05	1.05	1.05	1.05	1.05	20	0.97	0.98	1.05	0.94	1.00	0.99
2	1.05	1.05	1.05	1.05	1.05	1.05	21	0.97	0.99	1.05	0.94	1.00	0.98
3	1.04	1.04	1.05	1.04	1.04	1.05	22	0.97	0.99	1.05	0.94	1.00	0.98
4	1.01	1.01	1.05	0.99	1.05	1.00	23	0.97	0.98	1.05	0.93	0.99	0.98
5	0.98	0.99	1.05	0.95	1.01	0.99	24	0.97	0.98	1.05	0.93	0.99	0.97
6	0.98	0.99	1.05	0.95	1.01	0.99	25	0.97	0.98	1.05	0.92	0.99	0.97
7	0.97	0.99	1.05	0.94	1.01	0.99	26	0.97	0.98	1.04	0.92	0.99	0.97
8	0.97	0.99	1.05	0.94	1.01	0.99	27	0.97	0.98	1.04	0.92	0.99	0.97
9	0.97	0.99	1.05	0.94	1.00	0.99	28	0.97	0.98	1.05	0.93	0.99	0.98
10	0.97	0.99	1.05	0.94	1.00	0.99	29	0.96	0.98	1.05	0.93	0.99	0.98
11	0.97	0.98	1.05	0.94	1.00	0.99	30	0.97	0.98	1.05	0.94	1.00	0.99
12	0.97	0.98	1.05	0.94	1.00	0.99	31	0.97	0.98	1.05	0.94	1.00	0.99
13	0.97	0.98	1.05	0.94	1.00	0.99	32	0.97	0.98	1.05	0.93	1.00	0.98
14	0.97	0.98	1.05	0.94	1.00	0.99	33	0.97	0.99	1.05	0.94	1.00	0.98
15	0.97	0.98	1.05	0.93	1.00	0.99	34	0.97	0.99	1.05	0.94	1.00	0.98
16	0.97	0.99	1.05	0.94	1.00	0.98	35	0.97	0.98	1.04	0.94	1.00	0.98
17	0.97	0.99	1.05	0.94	1.00	0.98	36	0.97	0.98	1.04	0.94	1.00	0.99
18	0.97	0.99	1.05	0.94	1.00	0.99	37	0.97	0.98	1.04	0.92	0.99	0.97
19	0.97	0.98	1.05	0.94	1.00	0.99							

Table 10 Bus voltage values at the different cases investigated, Pk

Cases							Cases						
Bus	#1	#2	#3	#4	#5	#6	Bus	#1	#2	#3	#4	#5	#6
1	1.05	1.05	1.05	1.05	1.05	1.05	20	0.92	0.91	1.00	0.99	0.99	0.96
2	1.05	1.05	1.05	1.05	1.05	1.05	21	0.92	0.92	1.00	1.00	0.99	0.95
3	1.04	1.04	1.05	1.04	1.04	1.04	22	0.92	0.91	1.00	1.00	0.99	0.95
4	0.98	0.98	1.02	1.06	1.06	0.99	23	0.92	0.91	1.00	0.98	0.98	0.94
5	0.93	0.92	1.00	1.00	1.00	0.96	24	0.92	0.90	0.99	0.98	0.98	0.94
6	0.93	0.92	1.00	1.00	1.00	0.96	25	0.92	0.90	0.99	0.98	0.97	0.94
7	0.93	0.92	1.00	1.00	0.99	0.96	26	0.92	0.90	0.99	0.98	0.97	0.93
8	0.93	0.92	1.00	1.00	0.99	0.96	27	0.92	0.90	0.99	0.97	0.97	0.93
9	0.92	0.92	1.00	1.00	0.99	0.96	28	0.91	0.90	0.99	0.99	0.98	0.95
10	0.92	0.91	1.00	0.99	0.99	0.96	29	0.91	0.90	0.99	0.98	0.98	0.95
11	0.92	0.91	1.00	0.99	0.98	0.96	30	0.92	0.91	1.00	0.99	0.98	0.95
12	0.92	0.91	1.00	0.99	0.98	0.95	31	0.92	0.91	1.00	0.99	0.98	0.95
13	0.92	0.91	1.00	0.99	0.98	0.95	32	0.92	0.90	0.99	0.99	0.98	0.95
14	0.92	0.90	1.00	0.99	0.98	0.95	33	0.92	0.92	1.00	1.00	0.99	0.95
15	0.92	0.90	0.99	0.99	0.98	0.95	34	0.92	0.92	1.00	1.00	0.99	0.95
16	0.92	0.92	1.00	1.00	0.99	0.96	35	0.92	0.91	1.00	0.99	0.99	0.95
17	0.92	0.92	1.00	1.00	0.99	0.96	36	0.92	0.91	1.00	0.99	0.99	0.96
18	0.92	0.91	1.00	0.99	0.99	0.96	37	0.92	0.90	0.99	0.98	0.97	0.93
19	0.92	0.91	1.00	0.99	0.99	0.96							

Regarding the reactive power loss reduction (kVAr), the best reduction value obtained was in Case #3 as 3112.182 kVAr in DGs/SCBs coordination, followed by 3098.964 kVAr in DGs/SCBs/VRs coordination. However, in terms of the capacity release in MVA, the best value obtained was in Case #6 as 14.233 MVA in DGs/SCBs/VRs coordination, followed by 13.163 MVA in DGs/SCBs coordination.

At $s = Pk$, the VSI values are improved when any of the six cases are applied. However, it is also clear that a significant improvement is obtained when both DGs/SCBs and DGs/VRs are connected to the system. So, Cases #3 and #4 have had a better impact on VS than others. Besides, at $s = Pk$, the best TI_{VD} and TI_{LC} were obtained while employing Case #3.

Table 15 shows the economic performance metrics calculated in all cases under study. The best EI_{SAV} was obtained in Case #3 (10.4488 million \$/year), while a no saving case was observed in Case #4 (-0.6989 million \$/year). It was expected that the economic performance metrics would be low in cases including VRs because of their added capital costs.

Finally, Table 16 explores the active power loss values calculated on heavy demands using different algorithms in the literature, such as particle swarm, grey wolf, sine cosine, and the proposed whale algorithm. The results validate the effectiveness and the superiority of the proposed algorithm in solving the formulated problem.

Table 11 Branch currents values at the different cases investigated. Lig

Cases Branch	#1	#2	#3	#4	#5	#6	Cases Branch	#1	#2	#3	#4	#5	#6
	1	111.70	190.50	101.51	146.14	170.80		49.86	19	2.43	2.36	7.63	2.51
2	111.70	186.10	59.93	96.88	155.39	30.70	20	19.73	19.11	18.30	20.28	20.41	19.72
3	111.68	185.77	60.65	96.62	154.22	31.44	21	7.85	7.61	7.29	8.07	8.13	7.85
4	111.69	185.62	61.00	97.70	153.88	33.60	22	19.37	35.71	34.23	30.28	25.86	29.32
5	71.63	141.72	74.98	93.86	121.56	43.88	23	20.21	35.15	19.27	26.00	22.25	25.18
6	66.07	138.85	83.02	95.52	110.83	53.18	24	21.96	35.07	15.19	21.39	18.68	20.71
7	56.41	133.98	104.49	61.91	89.33	67.12	25	7.73	37.73	7.20	8.08	8.11	7.82
8	56.41	92.16	104.49	61.91	89.33	27.06	26	4.31	4.20	4.01	4.50	4.52	4.36
9	38.44	60.47	51.56	39.00	63.64	52.67	27	18.85	18.29	14.83	19.42	19.57	18.72
10	36.91	57.69	47.61	36.16	59.59	57.44	28	7.90	7.66	7.83	8.14	8.20	7.85
11	39.57	36.27	28.16	32.57	43.34	36.31	29	0.00	0.00	0.00	0.00	0.00	0.00
12	42.23	30.98	24.69	36.60	36.90	32.93	30	8.81	8.57	8.16	9.09	9.16	8.76
13	26.68	22.72	24.63	27.52	27.74	28.97	31	9.78	9.51	9.06	10.09	10.18	9.73
14	8.81	8.17	8.17	9.09	9.17	13.67	32	13.96	13.55	12.99	14.37	14.45	13.95
15	35.50	34.47	29.45	36.54	36.75	6.10	33	3.87	3.76	3.60	3.99	4.01	3.87
16	20.00	19.42	15.87	20.58	20.70	9.44	34	9.39	9.11	8.73	9.66	9.72	9.37
17	5.32	5.17	7.31	5.48	5.51	20.36	35	0.39	0.38	0.36	0.40	0.40	0.39
18	4.35	4.22	7.31	4.48	4.50	4.33	36	6.36	6.21	5.92	6.64	6.67	6.43

Table 12 Branch currents values at the different cases investigated, Sh

Cases Branch	#1	#2	#3	#4	#5	#6	Cases		#1	#2	#3	#4	#5	#6
							Branch	#6						
1	129.43	217.56	53.91	142.81	214.50	24.84	19	19	3.39	3.34	7.09	3.41	3.28	3.34
2	129.43	216.03	6.30	134.53	212.98	29.83	20	20	27.49	27.03	25.45	27.59	26.62	27.15
3	128.94	215.29	6.07	133.81	215.92	28.84	21	21	10.94	10.76	10.13	10.98	10.60	10.81
4	128.71	214.93	6.01	131.77	201.96	29.58	22	22	21.75	38.49	34.55	41.39	34.25	40.58
5	110.86	165.19	43.92	101.40	155.07	5.12	23	23	20.33	35.83	28.22	35.56	29.15	34.85
6	100.02	157.11	51.69	97.58	146.95	8.56	24	24	20.57	33.83	22.50	29.25	23.90	28.67
7	74.86	139.34	77.35	95.72	116.86	36.89	25	25	10.82	34.16	10.06	11.05	10.62	10.83
8	74.86	118.95	77.35	95.72	116.86	26.67	26	26	6.03	5.97	5.60	6.15	5.91	6.03
9	54.51	84.05	75.19	58.43	82.75	32.86	27	27	26.36	25.97	21.16	26.51	25.58	25.87
10	49.62	84.62	69.08	52.63	76.82	38.38	28	28	11.05	10.89	9.12	11.11	10.72	10.84
11	37.69	53.00	40.19	32.71	50.63	47.96	29	29	0.00	0.00	0.00	0.00	0.00	0.00
12	39.12	45.40	33.97	49.95	48.24	41.79	30	30	12.31	12.16	11.38	12.40	11.97	12.10
13	37.28	33.41	30.03	37.55	36.26	33.29	31	31	13.68	13.51	12.64	13.77	13.30	13.44
14	12.32	10.42	11.39	12.41	11.98	13.76	32	32	19.43	19.14	18.05	19.53	18.82	19.20
15	49.44	48.71	42.18	49.68	47.89	19.01	33	33	5.39	5.31	5.01	5.42	5.22	5.33
16	27.85	27.44	22.65	27.99	26.98	2.33	34	34	13.08	12.88	12.14	13.14	12.66	12.90
17	7.41	7.30	7.44	7.45	7.18	19.64	35	35	0.54	0.53	0.50	0.54	0.52	0.53
18	6.06	5.97	7.11	6.09	5.87	5.96	36	36	8.90	8.83	8.27	9.09	8.73	8.91

Table 13 Branch currents values at the different cases investigated, Pk

Cases Branch	#1	#2	#3	#4	#5	#6	Cases Branch	#1	#2	#3	#4	#5	#6
	1	174.54	276.32	56.07	169.72	274.99		83.30	19	4.46	4.50	6.66	4.14
2	174.54	277.32	68.36	191.89	284.67	96.17	20	36.20	36.43	33.40	33.50	33.72	35.02
3	173.61	276.17	67.11	190.80	290.71	94.93	21	14.41	14.51	13.30	13.34	13.43	13.94
4	173.13	275.59	66.48	174.77	261.04	96.64	22	28.78	47.05	39.24	50.42	44.52	52.61
5	161.33	213.02	50.33	122.67	197.93	56.51	23	24.34	41.41	38.29	43.32	37.75	45.21
6	145.71	198.79	45.08	112.88	190.76	40.23	24	21.64	36.20	30.74	35.64	30.62	37.19
7	106.72	164.10	55.42	126.36	151.09	27.89	25	14.33	30.43	13.27	13.47	13.52	14.06
8	106.72	161.63	55.42	126.36	151.09	59.58	26	7.98	8.12	7.39	7.50	7.53	7.83
9	78.91	116.88	103.45	78.52	106.67	25.01	27	34.86	35.21	28.68	32.27	32.52	33.48
10	71.00	117.41	95.13	70.68	98.64	26.04	28	14.62	14.77	11.43	13.53	13.64	14.04
11	41.39	73.27	55.68	37.05	60.94	62.59	29	0.00	0.00	0.00	0.00	0.00	0.00
12	39.70	62.93	46.79	60.81	61.31	53.72	30	16.26	16.47	14.98	15.09	15.21	15.66
13	49.27	46.56	38.58	45.72	46.09	40.62	31	18.08	18.31	16.65	16.77	16.91	17.40
14	16.28	14.10	14.99	15.10	15.23	14.92	32	25.56	25.76	23.67	23.69	23.82	24.73
15	65.05	65.57	56.51	60.29	60.62	32.68	33	7.09	7.15	6.57	6.57	6.61	6.86
16	36.66	36.95	30.55	33.97	34.16	5.29	34	17.21	17.35	15.93	15.95	16.04	16.63
17	9.76	9.83	8.27	9.04	9.09	18.91	35	0.71	0.72	0.66	0.66	0.66	0.69
18	7.98	8.04	7.41	7.39	7.44	7.69	36	11.78	12.00	10.91	11.07	11.12	11.55

Table 14 Technical performance metrics calculated in all cases under study

Cases	Scenario	Base case	#1	#2	#3	#4	#5	#6
P_{loss} (kW)	Lig	343.2	115.2296	311.4027	51.5445	96.5471	215.955	23.7434
	Sh	707.4	159.2406	421.3609	26.5525	177.2899	394.6647	27.7864
	Pk	1361.7	288.5721	693.6539	75.741	96.5471	686.5978	108.8639
Q_{loss} (kVAr)	Lig	463.9	151.3254	418.1321	59.0815	122.0755	289.9842	21.013
	Sh	956.1	206.3696	563.7286	16.4286	223.6043	531.9385	19.21
	Pk	1839.9	375.7626	928.5421	72.208	418.4663	928.0445	120.7133
S_{grid} (MVA)	Lig	3.9312	2.2345	3.811	2.0308	2.9235	3.417	0.9975
	Sh	5.6414	2.5893	4.3524	1.0784	2.8569	4.291	0.497
	Pk	7.8213	3.4918	5.5278	1.1217	3.3953	5.5011	1.6664
$P_{\text{loss,tot}}$ (kW)		2412.3	563.0423	1426.418	153.838	370.3841	1297.218	160.3937
$Q_{\text{loss,tot}}$ (kVAr)		3259.9	733.4576	1910.403	147.7181	764.1461	1749.967	160.9363
$S_{\text{grid,tot}}$ (MVA)		17.3939	8.3156	13.6912	4.2309	9.1757	13.2091	3.1609
TlVS	Lig	0.6406	1	1	1	0.8561	0.7828	0.947
	Sh	0.4652	0.861	0.9141	1	0.7694	0.8894	0.8573
	Pk	0.2952	0.6859	0.6563	0.9564	0.87	0.7762	0.7601
Active power loss reduction (kW)			1849.258	985.8825	2258.462	2041.916	1115.083	2251.906
Reactive power loss reduction (kVAr)			2526.442	1349.497	3112.182	2495.754	1509.933	3098.964
Capacity release (MVA)			9.0783	3.7027	13.163	8.2182	4.1848	14.233
TlVD ($s = \text{Pk}$)			0.1739	0.2162	0.0085	0.0149	0.0201	0.0881
TlLC ($s = \text{Pk}$)			0.8218	0.5796	0.1976	0.3438	0.5386	0.2864

Table 15 Economic performance metrics calculated in all cases under study

Cases	#1	#2	#3	#4	#5	#6
Costs						
El _{DG} (million \$/year)	1.9401	0	1.7800	2.4509	0	1.6008
El _{SCB} (million \$/year)	0	0.0168	0.0136	0	0.0149	0.0110
El _{VR} (million \$/year)	0	0	0	0.0056	0.0071	0.0042
Benefits (TI _P + TI _S) (million \$/year)	11.4550	10.3620	12.2424	1.7576	0.9285	2.8882
El _{SAV} (million \$/year)	9.5149	10.3452	10.4488	-0.6989	0.9065	1.2721

Table 16 Active power loss calculated on heavy demands using different algorithms in the literature

$P_{loss, peak}$ (kW)	Algorithm	Ref.	Compensator		
			DGs	SCBs	VRs
288.5721	Whale	Proposed	✓	×	×
693.6539			×	✓	×
75.741			✓	✓	×
96.5471			✓	×	✓
686.5978			×	✓	✓
108.8639			✓	✓	✓
740.32	Particle swarm	[49]	×	✓	×
302.74			✓	×	×
1122.15			×	×	✓
438.29			✓	✓	✓
134.4	Grey wolf	[33]	✓	✓	×
341.00			✓	×	×
580.3			×	✓	×
413.4			✓	×	✓
340.9671	Sine cosine	Proposed	✓	×	×
699.4165			×	✓	×
216.6044			✓	✓	×

10 Conclusions

Integration of active and reactive power compensators into power networks should be arranged not to pose problems in these systems but to enjoy the benefits and avoid the issues. To do this, finding the optimal location and size of these compensators in a system is necessary. Economically speaking, the rising project investment may result if uneconomic facilities or expensive technologies are used to reduce electric losses significantly. Also, high investment expenses limit renewables-based technologies to generate electricity, but these costs decline over days. Therefore, economic considerations related to the installed network equipment should be considered. In this regard, the well-known WOA is applied in this work to allocate DGs, SCBs, and VRs in a realistic 37-bus distribution system to minimize power

losses while conforming with several linear and nonlinear constraints. A cost-benefit analysis of the optimization problem is presented in terms of – investment and running costs of the compensators used; saving gained from the power loss reduction and benefits from decreasing the power to be purchased from the grid; reducing voltage deviations and overloading; and enhancing VS. Three loading scenarios are addressed in this work – Lig, Sh, and Pk levels of load demand. The numerical findings obtained show a noteworthy techno-economic improvement of the QoP performance level of the RDS and approve the efficiency and economic benefits of the proposed solutions compared to other solutions in the literature.

The main remarks that have been concluded during this research work are that the proposed coordination of DGs/SCBs and DGs/SCBs/VRs can effectively enhance the QoP levels to comply with the Egyptian practice code limits. They showed efficient savings results, particularly when considering techno-economic aspects together. They showed acceptable steady-state voltage profiles that comply with the standard limits and considerable power loss reduction in addition to the released capacity of the power distribution transformer. The coordination of active and reactive power conditioners showed that the best performance metrics values were obtained using the optimal coordination of DGs/SCBs and DGs/SCBs/VRs. However, it was also clear that a significant improvement was obtained when DGs/SCBs were connected to the system, leading to better impacts. The benefits of adding VRs will advance if higher loading levels are investigated but on the economic advantages side.

Finally, the results confirm that WOA is a powerful optimization tool in convergence and exploration-exploitation balance. Also, it is well applicable to solve more complex engineering problems. However, it should be noted that no optimization algorithm can solve all problems, but one algorithm can solve a particular problem much more efficiently.

Future works will address combining the investigated objective functions and formulating the problem as a multi-objective optimization problem under uncertain conditions and parameters variations. Also, the allocation of fault current limiters and battery energy storage technologies shall investigate their impacts on the system's performance while considering the potential load growth/higher loading levels. Finally, recent metaheuristic optimization techniques can solve the optimization problem with more practical probabilistic considerations.

References

1. Bansal R (2017) Handbook of distributed generation. Springer International Publishing, Cham
2. Masoum MAS, Fuchs EF (2015) Power quality in power systems and electrical machines. Elsevier Academic Press, Cambridge, MA
3. Diaaeldin I, Abdel Aleem S, El-Rafei A, Abdelaziz A, Zobaa AF (2019) Optimal network reconfiguration in active distribution networks with soft open points and distributed generation. *Energies* 12(21):4172. <https://doi.org/10.3390/en12214172>
4. El-Khattam W, Salama MMA (2004) Distributed generation technologies, definitions and benefits. *Electr Power Syst Res* 71(2):119–128. <https://doi.org/10.1016/j.epsr.2004.01.006>

5. Diaaeldin IM, Abdel Aleem SHE, El-Rafei A, Abdelaziz AY, Zobaa AF (2020) Hosting capacity maximization based on optimal reconfiguration of distribution networks with optimized soft open point operation. In: *Hosting capacity for smart power grids*. Springer, Cham, pp 179–193.
6. Ismael SM, Abdel Aleem SHE, Abdelaziz AY, Zobaa AF (2019) State-of-the-art of hosting capacity in modern power systems with distributed generation. In: *Renewable energy*, vol 130. Elsevier, pp 1002–1020
7. Wei X, Qiu X, Xu J, Li X (2010) Reactive power optimization in smart grid with wind power generator. In: *2010 Asia-Pacific power and energy engineering conference*, pp 1–4
8. Li L, Zeng X, Zhang P (2008) Wind farms reactive power optimization using genetic/tabu hybrid algorithm. In: *2008 international conference on intelligent computation technology and automation (ICICTA)*, vol 1, pp 1272–1276
9. Ardizzon G, Cavazzini G, Pavesi G (2014) A new generation of small hydro and pumped-hydro power plants: advances and future challenges. *Renew Sust Energy Rev* 31:746–761
10. Khatod DK, Pant V, Sharma J (2012) Evolutionary programming based optimal placement of renewable distributed generators. *IEEE Trans Power Syst* 28(2):683–695
11. Muttaqi KM, Le ADT, Negnevitsky M, Ledwich G (2014) An algebraic approach for determination of DG parameters to support voltage profiles in radial distribution networks. *IEEE Trans Smart Grid* 5(3):1351–1360
12. Ghanbari N, Mokhtari H, Bhattacharya S (2018) Optimal distributed generation allocation and sizing for minimizing losses and cost function. In: *2018 IEEE industry applications society annual meeting (IAS)*, pp 1–6
13. Ismael SM, Aleem SHEA, Abdelaziz AY (2018) Optimal sizing and placement of distributed generation in Egyptian radial distribution systems using crow search algorithm. In: *Proceedings of 2018 International Conference on Innovative Trends in Computer Engineering, ITCE 2018*, vol 2018-March, pp 332–337. <https://doi.org/10.1109/ITCE.2018.8316646>
14. Abdel-mawgoud H, Kamel S, Yu J, Jurado F (2019) Hybrid Salp swarm algorithm for integrating renewable distributed energy resources in distribution systems considering annual load growth. *J King Saud Univ Inf Sci* 34:1381. <https://doi.org/10.1016/j.jksuci.2019.08.011>
15. Kim T, Lee Y, Lee B, Song H, Kim T (2009) Optimal capacitor placement considering voltage stability margin based on improved PSO algorithm. In: *2009 15th international conference on intelligent system applications to power systems, ISAP '09*, pp 1–5. <https://doi.org/10.1109/ISAP.2009.5352890>
16. Hijazi H, Coffrin C, Van Hentenryck P (2017) Convex quadratic relaxations for mixed-integer nonlinear programs in power systems. *Math Program Comput* 9(3):321–367. <https://doi.org/10.1007/s12532-016-0112-z>
17. Shaheen AM, El-Sehiemy RA, Farrag SM (2019) A reactive power planning procedure considering iterative identification of VAR candidate buses. *Neural Comput Appl* 31(3):653–674
18. Kannan SM, Renuga P, Kalyani S, Muthukumaran E (2011) Optimal capacitor placement and sizing using fuzzy-DE and fuzzy-MAPSO methods. *Appl Soft Comput J* 11(8):4997–5005. <https://doi.org/10.1016/j.asoc.2011.05.058>
19. Kumar A, Bhatia RS (2015) Optimal capacitor placement in radial distribution system. *India Int Conf Power Electron IICPE 2015(4)*:630–637. <https://doi.org/10.1109/IICPE.2014.7115763>
20. Delfanti M, Granelli GP, Marannino P, Montagna M (2000) Optimal capacitor placement using deterministic and genetic algorithms. *IEEE Trans Power Syst* 15(3):1041–1046. <https://doi.org/10.1109/59.871731>
21. Park JY, Sohn JM, Park JK (2009) Optimal capacitor allocation in a distribution system considering operation costs. *IEEE Trans Power Syst* 24(1):462–468. <https://doi.org/10.1109/TPWRS.2008.2009489>
22. Ng HN, Salama MMA, Chikhani AY (2000) Classification of capacitor allocation techniques. *IEEE Trans Power Deliv* 15(1):387–392. <https://doi.org/10.1109/61.847278>
23. Diaaeldin I, Aleem SA, El-Rafei A, Abdelaziz A, Zobaa AF (2019) Optimal network reconfiguration in active distribution networks with soft open points and distributed generation. *Energies* 12(21):4172. <https://doi.org/10.3390/en12214172>

24. Moradi MH, Zeinalzadeh A, Mohammadi Y, Abedini M (2014) An efficient hybrid method for solving the optimal siting and sizing problem of DG and shunt capacitor banks simultaneously based on imperialist competitive algorithm and genetic algorithm. *Int J Electr Power Energy Syst* 54:101–111. <https://doi.org/10.1016/j.ijepes.2013.06.023>
25. Rahmani-Andebili M (2016) Simultaneous placement of DG and capacitor in distribution network. *Electr Power Syst Res* 131:1–10. <https://doi.org/10.1016/j.epsr.2015.09.014>
26. Muthukumar K, Jayalalitha S (2016) Optimal placement and sizing of distributed generators and shunt capacitors for power loss minimization in radial distribution networks using hybrid heuristic search optimization technique. *Int J Electr Power Energy Syst* 78:299–319. <https://doi.org/10.1016/j.ijepes.2015.11.019>
27. Yazdavar AH, Shaaban MF, El-Saadany EF, Salama MMA, Zeineldin HH (2020) Optimal planning of distributed generators and shunt capacitors in isolated microgrids with nonlinear loads. *IEEE Trans Sustain Energy* 11(4):2732–2744
28. Elattar EE, Shaheen AM, El-Sayed AM, El-Sehiemy RA, Ginidi AR (2021) Optimal operation of automated distribution networks based-MRFO algorithm. *IEEE Access* 9:19586–19601
29. Kumar Injeti S, Shareef SM, Kumar TV (2018) Optimal allocation of DGs and capacitor banks in radial distribution systems. *Distrib Gener Altern Energy J* 33(3):6–34
30. Gampa SR, Das D (2019) Simultaneous optimal allocation and sizing of distributed generations and shunt capacitors in distribution networks using fuzzy GA methodology. *J Electr Syst Inf Technol* 6(1):1–18
31. Das S, Das D, Patra A (2019) Operation of distribution network with optimal placement and sizing of dispatchable DGs and shunt capacitors. *Renew Sust Energ Rev* 113:109219. <https://doi.org/10.1016/j.rser.2019.06.026>
32. Almabsout EA, El-Sehiemy RA, An ONU, Bayat O (2020) A hybrid local search-genetic algorithm for simultaneous placement of DG units and shunt capacitors in radial distribution systems. *IEEE Access* 8:54465–54481. <https://doi.org/10.1109/ACCESS.2020.2981406>
33. Shaheen AM, El-Sehiemy RA (2020) Optimal coordinated allocation of distributed generation units/capacitor banks/voltage regulators by EGWA. *IEEE Syst J* 12:373. <https://doi.org/10.1109/JSYST.2015.2491966>
34. Safigianni AS, Salis GJ (2000) Optimum voltage regulator placement in a radial power distribution network. *IEEE Trans Power Syst* 15(2):879–886
35. Dolli SA, Jangamshetti SH (2012) Modeling and optimal placement of voltage regulator for a radial system. In: 2012 international conference on power, signals, controls and computation, pp 1–6
36. Jabbari M, Niknam T, Hosseinpour H (2011) Multi-objective fuzzy adaptive PSO for placement of AVR's considering DG's. In: 2011 IEEE power engineering and automation conference, vol 2, pp 403–406
37. Ranamuka D, Agalgaonkar AP, Muttaqi KM (2016) Examining the interactions between DG units and voltage regulating devices for effective voltage control in distribution systems. *IEEE Trans Ind Appl* 53(2):1485–1496
38. Ghanegaonkar SP, Pande VN (2015) Coordinated optimal placement of distributed generation and voltage regulator by multi-objective efficient PSO algorithm. In: 2015 IEEE workshop on computational intelligence: theories, applications and future directions (WCI), pp 1–6
39. Rakočević S, Čalasan M, Abdel Aleem SHE (2021) Smart and coordinated allocation of static VAR compensators, shunt capacitors and distributed generators in power systems toward power loss minimization. *Energy Sources, Part A Recover Util Environ Eff*:1–19. <https://doi.org/10.1080/15567036.2021.1930289>
40. International Renewable Energy Agency (2021) Renewable energy Outlook
41. Chakravorty M, Das D (2001) Voltage stability analysis of radial distribution networks. *Int J Electr Power Energy Syst* 23(2):129–135
42. Dobson I et al (2002) Voltage stability assessment: concepts, practices and tools. *IEEE Power Eng Soc Power Syst Stab Subcomm Spec Publ* 11:21–22
43. Kersting WH (2018) Distribution system modeling and analysis. CRC Press, Boca Raton

44. Gallego LA, Padilha-Feltrin A (2008) Voltage regulator modeling for the three-phase power flow in distribution networks. In: 2008 IEEE/PES transmission and distribution conference and exposition: Latin America, T and D-LA, pp 1–6. <https://doi.org/10.1109/TDC-LA.2008.4641843>
45. Kersting WH (2009) The modeling and application of step voltage regulators. In: 2009 IEEE/PES power systems conference and exposition, PSCE 2009, pp 1–8. <https://doi.org/10.1109/PSCE.2009.4840004>
46. Teng J-H (2003) A direct approach for distribution system load flow solutions. *IEEE Trans Power Deliv* 18(3):882–887
47. Mirjalili S, Lewis A (2016) The whale optimization algorithm. *Adv Eng Softw* 95:51–67. <https://doi.org/10.1016/j.advengsoft.2016.01.008>
48. Ismael SM, Abdel Aleem SHE, Abdelaziz AY (2019) Optimal conductor selection in radial distribution systems using whale optimization algorithm. *J Eng Sci Technol* 14(1):87–107
49. Elsayed AM, Mishref MM, Farrag SM (2018) Distribution system performance enhancement (Egyptian distribution system real case study). *Int Trans Electr Energy Syst* 28(6):e2545
50. Diaaeldin I et al (2019) Optimal network reconfiguration in active distribution networks with soft open points and distributed generation. *Energies* 12(21):4172. <https://doi.org/10.3390/en12214172>

Analysis of Impacts of Multiple Renewable Energy Sources and D-STATCOM Devices on Distribution Networks



R. Satish, K. Vaisakh, and Almoataz Y. Abdelaziz

1 Introduction

The grid interfacing of distributed generation (DG) is specified by the IEEE-1547 [1] standards. In [2], to improve the characteristics of convergence, a novel PV bus representation is incorporated into the proposed Newton-Rapson power flow method. This method is based on current injection, and the representation of nonlinear current injections is done based on rectangular coordination. The installation of shunt capacitors at suitable locations will support the Q to the system, thereby reducing the power loss of the system along with increased equipment usage and stopping equipment's early aging. In [3], a Cuckoo search optimization method is used to distribute shunt capacitors along RDN and the designed objective function diminishes the network losses and enhances the voltage profile and power factor. Authors of [4] propose a flower pollination algorithm to allocate and size the capacitors optimally in different distribution networks. In [5], the author proposes an optimum solution to allocate the DG and shunt capacitor banks in RDN. Authors of [6] investigate the improvement in quality of voltage in low-voltage distribution networks using single-phase PV inverters. Authors of [7] propose a novel algorithm to size and place the RES optimally in distribution networks. In [8], various algorithms for optimization are developed by modifying the big bang big crunch method for realization of virtual power plant. These algorithms are designed to handle the energy in distribution networks to minimize the amount of energy

R. Satish
Department of EEE, ANITS, Visakhapatnam, India

K. Vaisakh
Department of EE, AUCE (A), Visakhapatnam, India

A. Y. Abdelaziz (✉)
Future University in Egypt, Cairo, Egypt

purchased on the grid. In [9], optimization algorithm is discussed for planning, allocation, and sizing of DGs in distribution networks.

The compensation of Q through the distribution flexible AC transmission system (DFACTS) such as D-STATCOM can further improve the power quality of the network. The harmonic pollution, noise, and pollution issues are less in D-STATCOM device, unlike traditional Q compensation devices such as shunt or series capacitors. In [10], a probabilistic technique for allocating the D-STATCOM optimally by taking into account the correlation among the uncertain variables is presented. Authors of [11] propose an optimum control algorithm for the three-phase D-STATCOM. It compensates harmonics along with the compensation of Q in three-phase linear and nonlinear loads. In [12], the key effects of connecting DG to a grid and the STATCOM's role in reducing the adverse effects to make DG fully usable are presented. As a result, a control strategy for STATCOM is proposed on the basis of direct power control to illustrate the influence of this unit on the power system quality. In [13], to minimize the P loss in distribution networks, a GA-based optimization is proposed for the DG, STATCOM and hybrid vehicle integrations. In [14–16], three-phase DPFA are proposed by developing bus number and branch number matrices with the integration of RES and D-STATCOM device in unbalanced distribution networks.

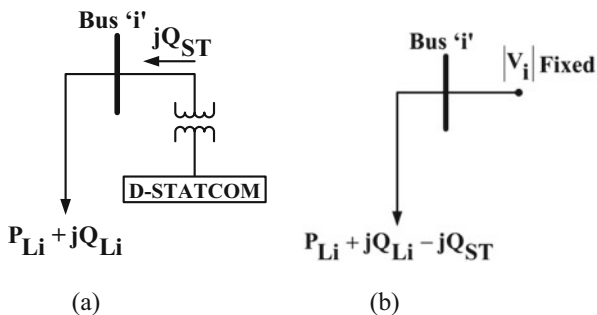
This chapter proposes a novel DPFA for analyzing the impacts of integrations of RES and D-STATCOM device in RDN using the developed BNM and BRNM matrices in this chapter. The BNM stores the bus number information of newly split segments of RDN, and BRNM stores the branch number information of newly split segments of RDN. These segments were split by using the radial topology in RDN. Fundamentals such as KCL and KVL are used in this algorithm and, therefore, it is easy to comprehend. The locations of RES and D-STATCOM device are selected by using the voltage stability index (VSI) value. The rest of the chapter is convened in the following order: Modeling of RES and D-STATCOM is presented in Sect. 2. In Sect. 3, VSI is discussed. Section 4 describes the development algorithm for BNM and BRNM matrices. Section 5 discuss the DPFA with RES and D-STATCOM device integrations. Various test results and discussions on 15-bus and 69-bus RDN are presented in Sect. 6. The conclusions of this chapter are discussed in Sect. 7.

2 RES and D-STATCOM Device Modeling

2.1 RES

There are three ways for the integration of RES to the distribution networks. The first one uses synchronous generators (SGs) or induction generators (IGs). The second one uses IGs in combinations power electronic converters (PECs). The third one uses only PECs. The SG can be modeled as PQ bus, or PV bus, or static voltage characteristic model (SVC) based on the control on its excitation system [17]

Fig. 1 (a) The connection of D-STATCOM to a bus and (b) D-STATCOM modeling



for DPFA. The IG can be modeled as PQ bus or SVC for DPFA [18]. If the interfacing of RES happens through IG in combination with PECs or only through PECs then it is modeled as PV bus [18] or PQ bus [19] for DPFA based on control on converter circuit. In [14], the various types of RES available with the grid integration methodologies and appropriate modeling for DPFA are presented.

2.2 D-STATCOM

In DPFA, the D-STATCOM is generally considered as shunt compensator for Q power. The Q injection of D-STATCOM can be adjusted by itself to regulate its magnitude of voltage at D-STATCOM bus.

Figure 1 illustrates the connection of D-STATCOM's connection to a bus and its modeling for DPFA. It should be noted from Fig. 1b that the prescribed Q load at a bus and D-STATCOM's Q output are combined. So that, the magnitude of voltage at bus is varied with respect to Q . It is absolutely a PV bus with output P as zero of D-STATCOM [20]. The D-STATCOM losses including its connection are assumed to be neglected for this model.

3 Voltage Stability Index

The VSI suggested in [21] is employed in this chapter to recognize the bus that is under the margin of its voltage collapse. According to this, the bus with minimum VSI value is under the fringe for collapse in voltage. Consider two buses in a system as shown in Fig. 2.

The VSI at bus "j" is given with Eq. (1).

$$VSI(j) = |V_j|^4 - 4((P_k \cdot X_{jk}) - (Q_k \cdot R_{jk}))^2 - 4((P_k \cdot R_{jk}) + (Q_k \cdot X_{jk})) |V_j|^2 \tag{1}$$

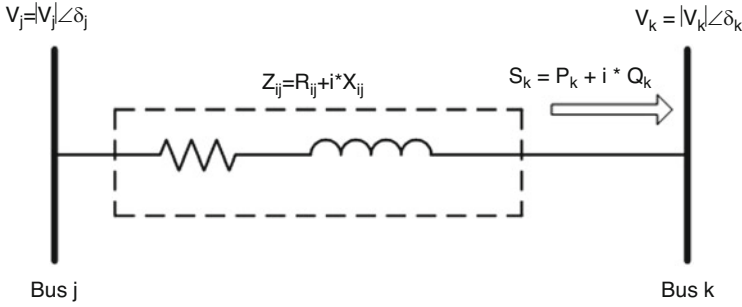


Fig. 2 Sample two buses in a RDN

For steady functioning of the RDN,

$$VSI(j) \geq 0 \quad \forall \quad j = 2, 3 \dots N.$$

Where, N : Total bus numbers.

4 Methodology for Developing BNM and BRNM

A methodical numbering to the buses and branches in RDN improves the performance of DPFA and it also saves memory. In [22], the numbering scheme presented is utilized in this method. The following steps illustrate the procedure to write the MATLAB code to split the RDN into several segments as represented in Fig. 3.

1. For the sample RDN shown in Fig. 3, the three arrays called the branch number (BRN) array and the corresponding sending end bus (SEB) array and receiving end bus (REB) array are constructed as follows:

$$BRN = [1, 2, 3, 4, 5, 6, 7, 8, 9, 10, 11, 12, 13, 14, 15, 16, 17, 18, 19, 20].$$

$$SEB = [1, 2, 3, 4, 5, 6, 7, 8, 9, 10, 3, 12, 13, 14, 15, 6, 17, 18, 19, 20].$$

$$REB = [2, 3, 4, 5, 6, 7, 8, 9, 10, 11, 12, 13, 14, 15, 16, 17, 18, 19, 20, 21]$$

2. Begin with $BRN = 1$ and identify the REB of this BRN (i.e., bus-2) and identify how many times this 2 is repeated in SEB row. In SEB row, this 2 appears for one time. This indicates that, bus-2 is SEB for only one branch. Fill these REB 2 and BRN 1 as first row and first column elements in BNM and BRNM, respectively. Now increase the column number by one.
3. Increase the BRN (i.e., $BRN = 2$), read the REB of BRN, i.e., 3. Then check for the appearance of 3 in SEB row. The bus 3 appears for two times. That means from the bus 3, two branches are leaving. Then fill these REB 3 and BRN 2 in to the BNM and BRNM as the first row and present column elements. Name

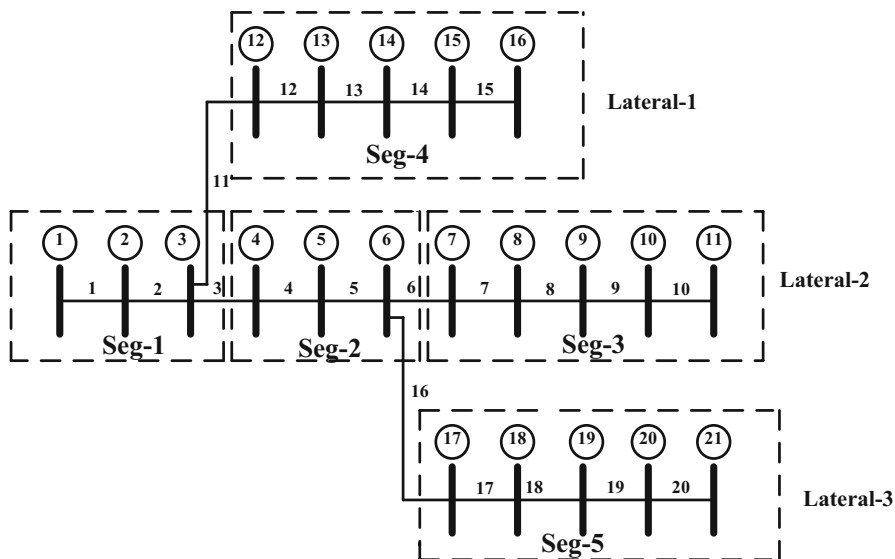


Fig. 3 Split segments for the sample RDN

this row as segment-1. Now the row number is increased by one and the column number is set to one.

- Similarly, increase the BRN, read the REB of BRN, and check for the appearance of this REB in SEB row. If it appears once, then fill this REB and BRN values as the present row and present column elements in BNM and BRNM respectively and now column number is increased by one and step 4 is to be repeated. If it does not appear at all or more than once in SEB row, then fill the corresponding REB and BRN values as present row and present column elements, and identify this row as a segment. Then the row number is increased by one and the column number is set to one. And repeat step 4.

Repeat the above steps until the BRN value reaches to 20. At the end, BNM and BRNM are constructed as below.

BNM =	2	3	0	0	0	→ Segment-1
	4	5	6	0	0	→ Segment-2
	7	8	9	10	11	→ Segment-3
	12	13	14	15	16	→ Segment-4
	17	18	19	20	21	→ Segment-5

$$\mathbf{BRNM} = \begin{array}{|c|c|c|c|c|} \hline 1 & 2 & 0 & 0 & 0 \\ \hline 3 & 4 & 5 & 0 & 0 \\ \hline 6 & 7 & 8 & 9 & 10 \\ \hline 11 & 12 & 13 & 14 & 15 \\ \hline 16 & 17 & 18 & 19 & 20 \\ \hline \end{array} \begin{array}{l} \rightarrow \text{Segment-1} \\ \rightarrow \text{Segment-2} \\ \rightarrow \text{Segment-3} \\ \rightarrow \text{Segment-4} \\ \rightarrow \text{Segment-5} \end{array}$$

5 Distribution Power Flow Algorithm for RDN with RES and D-STATCOM

Figures 4 and 5 help in explaining the DPFA. In Fig. 4, the last segment (segment-5) with its buses and branches is shown. In Fig. 5, the first segment with its buses and branches is shown. The following steps illustrate the detailed iterative procedure.

1. Read the system data and construct BNM and BRNM for the given RDN.
2. Set the outside iteration (γ) and inside iteration (*itr*) numbers as 1.
3. Set all the bus voltages in RDN equal to sub-station bus voltage.
4. Based on type of load, find the load currents at all buses.
5. Select the last segment (segment-5) in BNM and collect the current at bus-21 as given in Eq. (2). Now select the last segment (segment-5) in BRNM and find the current in branch-20 using Eq. (3).

$$I_{21} = I_{L21} \tag{2}$$

$$I_{20-21} = I_{21} \tag{3}$$

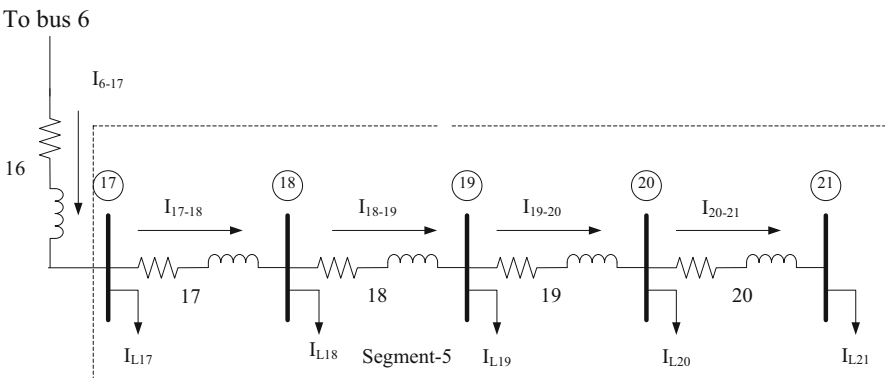


Fig. 4 Segment-4 taken from Fig. 3

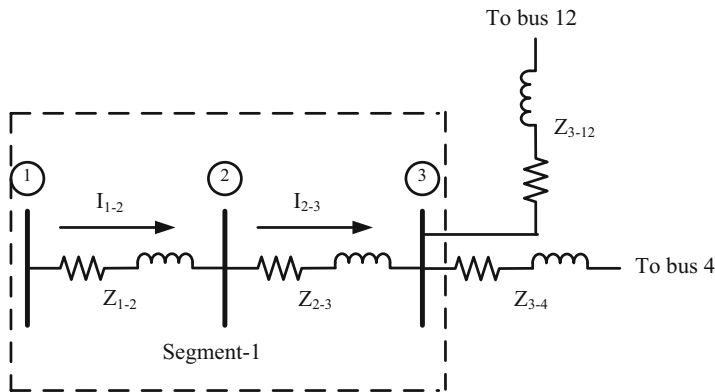


Fig. 5 Segment-1 taken from Fig. 3

Where, I_{L21} is the load current at bus-21.

Now, move to bus-20 in segment-5 in BNM and collect the bus current at this bus by applying KCL as given in Eq. (4). Move to branch-19 in segment-5 in BRNM and find the current branch as given in Eq. (5).

$$I_{20} = I_{20-21} + I_{L20} \tag{4}$$

$$I_{18-22} = I_{22} \tag{5}$$

Likewise, collect the currents in all buses in segment-5 in BNM and find the currents in all branches in segment-5 in BRNM.

6. Now move to segment-4 in BNM and BRNM and repeat the procedure explained in step-5 to find the bus current and branch currents. Likewise, move up to segment-1.
7. Now start with segment-1 in BNM and find the bus-2 voltage using Eq. (6).

$$V_2 = V_1 - (Z_{1-2} \bullet I_{1-2}) \tag{6}$$

Where, Z_{1-2} is the impedance of branch-1.

Similarly, find the bus voltages at all buses in segment-1.

8. Likewise, move up to the segment-5 in BNM by finding the voltages at all buses.
9. Now check for the convergence of obtained voltage solution at the end of first iteration using Eq. (7). If the convergence is not attained, repeat the steps 4–8.

$$\left| V_i^{\text{itr}} - V_i^{\text{itr}-1} \right| \leq \varepsilon \quad (7)$$

10. With the converged solution and using Eq. (1), find the VSI at all buses.
11. Select the rating and model of RES and D-STATCOM device for outside γ^{th} iteration. The location of these devices is selected based on VSI values at different buses.
12. If the bus at which RES is connected is modeled as PQ bus, then the current injection by RES at this bus is evaluated by using Eq. (8).

$$I_{\text{PQ}}^\gamma = \text{conj} \left(\frac{S_{\text{PQ}}}{V_{\text{PQ}}} \right) \quad (8)$$

13. If at a bus D-STATCOM or RES with PV model is available, then find the mismatches in voltages at all PV buses using Eq. (9).

$$\Delta V^\gamma = \left| V^{(\text{sp})} \right| - \left| V^{(\text{cal})} \right|^\gamma \quad (9)$$

14. If the voltage mismatch at PV bus is not below the specified tolerance, then find the required incremental current injection to maintain the specified voltage at PV bus using Eq. (10).

$$[\Delta I_{\text{PV}}]^\gamma = [Z_{\text{PV}}]^{-1} \bullet [\Delta V]^\gamma \quad (10)$$

The calculation procedure for $[Z_{\text{PV}}]$ matrix is presented in [23].

15. If unlimited Q generation is available at PV buses, then reactive current injections at PV buses is obtained using Eq. (11). And then find the incremental Q injection at PV bus $\Delta Q_{\text{PV}}^\gamma$.

$$\Delta I_{\text{PV}}^\gamma = |\Delta I_{\text{PV}}|^\gamma (\cos(90^\circ + \delta_{v,\text{PV}}) + j \bullet \sin(90^\circ + \delta_{v,\text{PV}})) \quad (11)$$

Where, δ_{vj} is the voltage angle at the PV bus.

16. The Q generation needed at PV bus γ^{th} iteration is obtained using Eq. (12).

$$Q_{\text{PV}}^\gamma = Q_{\text{PV}}^{\gamma-1} + \Delta Q_{\text{PV}}^\gamma \quad (12)$$

17. Now find the complex power generation at PV bus using Eq. (13). And then find the current injection at PV bus using Eq. (14).

$$S_{PV}^{\gamma} = P_{PV} + j \bullet Q_{PV}^{\gamma} \quad (13)$$

$$I_{PV}^{\gamma} = \text{conj} \left(\frac{S_{PV}^{\gamma}}{V_{PV}} \right) \quad (14)$$

18. If limited Q generation is available at PV buses, then check the Q limits.
 If $Q_{Gen,min} \leq Q_{PV}^{\gamma} \leq Q_{Gen,max}$ then set $Q_{PV}^{\gamma} = Q_{PV}^{\gamma}$.
 If $Q_{PV}^{\gamma} \leq Q_{Gen,min}$ then set $Q_{PV}^{\gamma} = Q_{Gen,min}$.
 If $Q_{PV}^{\gamma} \geq Q_{Gen,max}$ then set $Q_{PV}^{\gamma} = Q_{Gen,max}$.
 With the obtained Q generation and specified P generation, find the complex power generation at PV bus using Eq. (13). And obtain the current injection at PV bus using Eq. (14).
19. With the obtained current injections at PQ and PV buses, repeat from step 2 by increasing the outside iteration number by 1 until the mismatch in voltages at all PV buses is within the specified tolerance value.

The flowchart for the DPFA is shown in Fig. 6.

6 Test Results and Discussions

6.1 15-Bus RDN

6.1.1 15-Bus RDN Without RES and D-STATCOM

Figure 7 shows the 15-bus existing rural RDN. In [24], the line data and load data of the network are presented. 11 kV and 1000 kVA are selected as base values. The convergence tolerance for inside and outside iterations is selected as 0.001. The solution obtained from the proposed DPFA is presented in Table 1 in comparison with solution presented in [24]. It is found that the maximum error in voltage magnitudes is 0.00005, which is of negligible value. Therefore, the proposed DPFA is very accurate. The proposed DPFA is converged after four iterations. From Table 1, the VSI minimum value is 0.7959 at bus-13. The P and Q losses are obtained as 61.7911 kW and 57.2945kVAR, respectively, which are accurate with loss presented in [24].

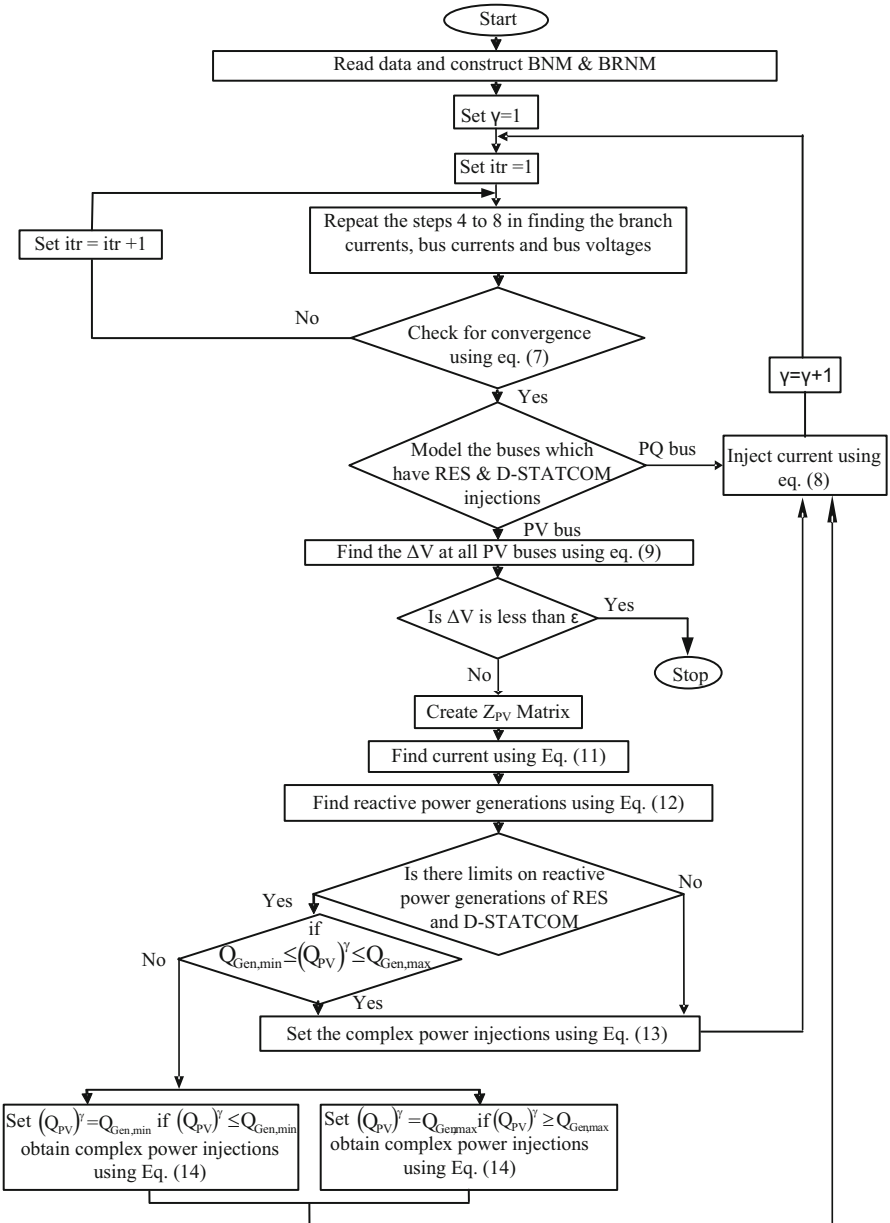


Fig. 6 Flowchart for DPFA with RES and D-STATCOM

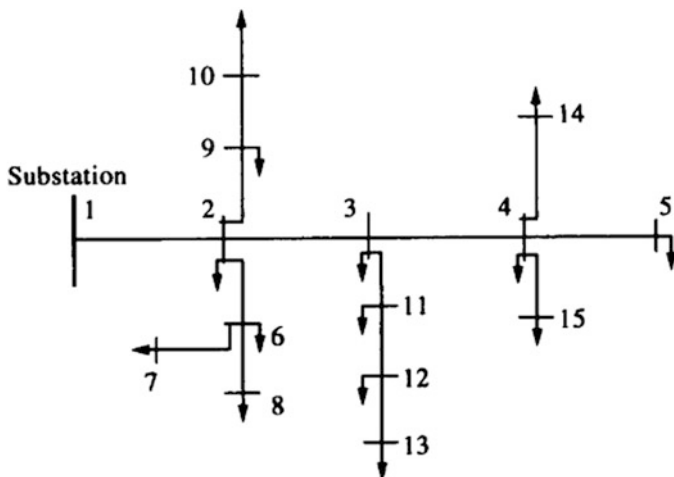


Fig. 7 15-bus existing rural RDN

Table 1 Distribution power flow result for 15-bus RDN

Bus no.	Obtained $ V _{p.u}$	Obtained voltage angles in Deg.	$ V _{p.u}$ [24]	Error in $ V $	VSI
1	1.0000	0	1.00000	0	1.0000
2	0.9713	0.0319	0.97128	-0.00002	0.8884
3	0.9567	0.0493	0.95667	-0.00003	0.8372
4	0.9509	0.0565	0.95090	0	0.8176
5	0.9499	0.0686	0.94992	0.00002	0.8142
6	0.9582	0.1893	0.95823	0.00002	0.8428
7	0.9560	0.2166	0.95601	0.00001	0.8353
8	0.9570	0.2050	0.95695	-0.00005	0.8386
9	0.9680	0.0719	0.96797	-0.00003	0.8779
10	0.9669	0.0849	0.96690	0	0.8740
11	0.9500	0.1315	0.94995	-0.00005	0.8143
12	0.9458	0.1824	0.94583	0.00003	0.8003
13	0.9445	0.1986	0.94452	0.00002	0.7959
14	0.9486	0.0848	0.94861	0.00001	0.8097
15	0.9484	0.0869	0.94844	0.00004	0.8092

6.1.2 Case Studies on 15-Bus RDN

The rating, location, and modeling of RES and D-STATCOM device for various test studies are presented in Table 2, and the obtained voltage solution for these test studies is presented in Table 3.

Table 2 Test studies on 15-bus RDN

Test study	Device	Location	Rating	Bus modeling
Test-1	Single-phase RES	Bus-13	$P = 400 \text{ kW}, Q = 300 \text{ kVAR}$	PQ
Test-2	Single-phase RES	Bus-13	$P = 400 \text{ kW}, Q = 300 \text{ kVAR}$	PQ
Test-3	Single-phase RES	Bus-15	$P = 200 \text{ kW}$ $96.86 \leq Q \leq 535.28 \text{ kVAR}$	PV
	Single-phase RES	Bus-13	$P = 400 \text{ kW}, Q = 300 \text{ kVAR}$	PQ
	Single-phase D-STATCOM	Bus-15	$P = 0 \text{ kW}$ $100 \leq Q \leq 300 \text{ kVAR}$	PV

Table 3 Obtained voltage solution of different test studies on 15-bus RDN

Bus No.	Test-1 $ V _{p.u}$	Test-2 $ V _{p.u}$	Test-3 $ V _{p.u}$
1	1.0000	1.0000	1.0000
2	0.9796	0.9880	0.9830
3	0.9720	0.9877	0.9785
4	0.9664	0.9872	0.9750
5	0.9654	0.9863	0.9740
6	0.9666	0.9752	0.9702
7	0.9644	0.9730	0.9680
8	0.9654	0.9739	0.9689
9	0.9763	0.9848	0.9798
10	0.9752	0.9837	0.9787
11	0.9746	0.9902	0.9810
12	0.9829	0.9984	0.9893
13	0.9917	1.0071	0.9981
14	0.9641	0.9850	0.9727
15	0.9639	0.9905	0.9746

6.1.3 Discussion on 15-Bus RDN

Figure 8 compares the voltage profiles without RES and D-STATCOM device integrations and voltage profiles obtained from the test studies on 15-bus RDN. It is observed that there is improvement in voltage profiles with respect to the voltage profile obtained without RES and D-STATCOM integrations. The voltage profile in Test-2, in which two RES are integrated, is more than all other test results. Figure 9 compares the minimum value of voltage on 15-bus RDN for different test studies. From Fig. 9, it is observed in Test-2 that the minimum value of voltage on 15-bus RDN is 0.973 p.u which is more than other test studies. Figure 10 compares the P and Q loss on the network for different test studies, and it is observed that the P and Q loss are found to be 29.59 kW and 16.82 kVAR, respectively, in Test-2, which are less than the loss obtained in other test studies.

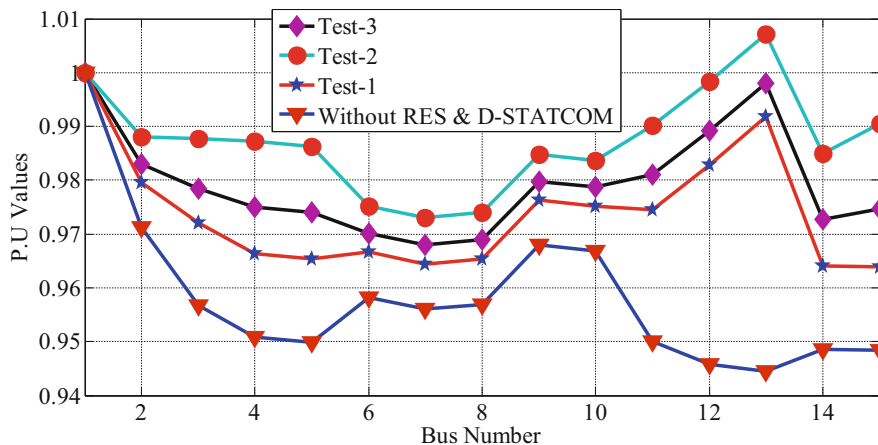


Fig. 8 Voltage profile comparison for different test studies on 15-bus RDN

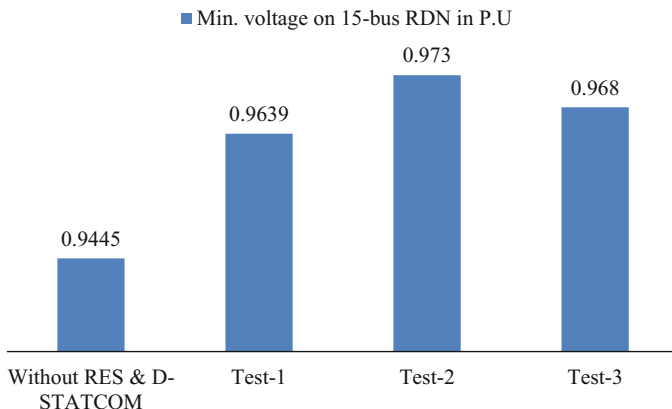


Fig. 9 Comparison of min. Voltage for different test studies on 15-bus RDN

6.2 69-Bus RDN

6.2.1 69-Bus RDN Without RES and D-STATCOM

Figure 11 shows the 69-bus RDN, and its line data and load data is presented in [21]. 12.66 kV and 100 kVA are selected as the base values for the system. The convergence tolerance for inside and outside iterations is selected as 0.001. The obtained power flow solution is presented in Table 4. The proposed DPFA has taken four iterations to get this converged solution. From Table 4, the VSI minimum value is 0.6833 at bus-65. The P and Q losses are obtained as 224.97 kW and 102.15 kVAR respectively.

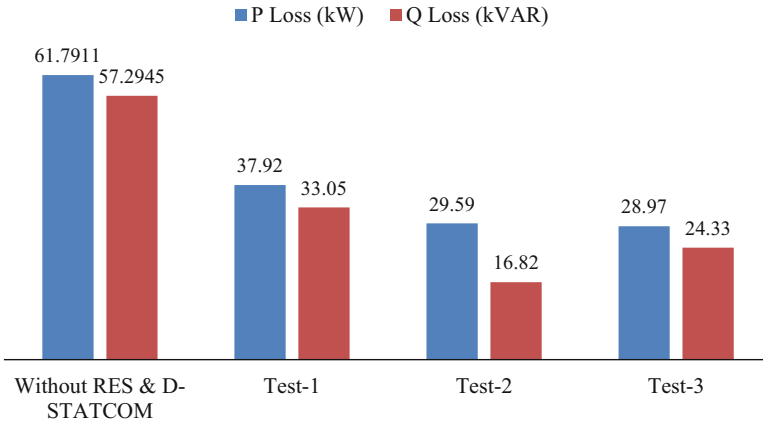


Fig. 10 Comparison of power loss for different test studies on 15-bus RDN

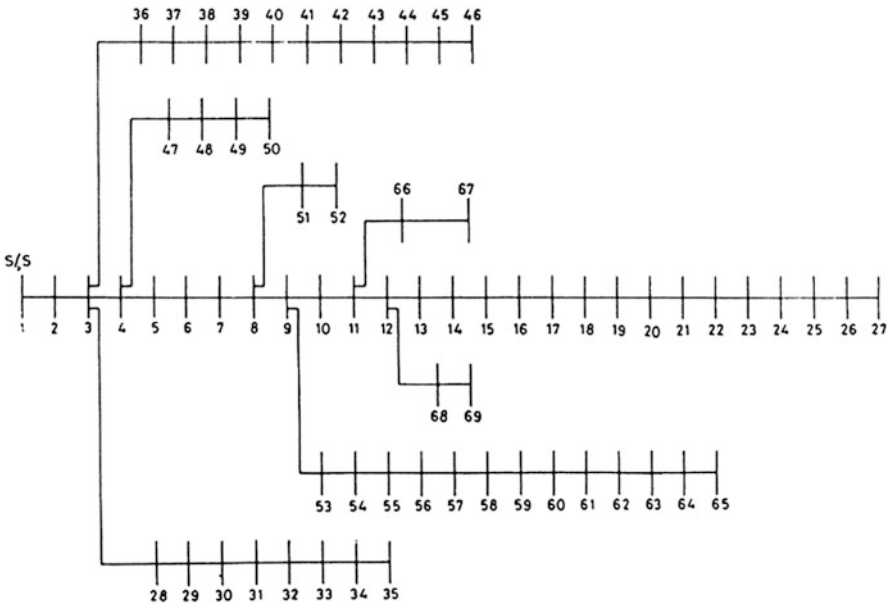


Fig. 11 69-bus RDN

6.2.2 Test Studies on 69-Bus RDN

Table 5 presents the device location, its rating, and modeling for different test studies on 69-bus RDN. Table 6 presents the obtained voltage solution for these test studies. Figure 12 compares the voltage profile without RES and D-STATCOM device integrations and voltage profiles for different test studies on 69-bus RDN.

Table 4 Obtained voltage solution for 69-bus RDN

Bus no.	$ V_{p,u} \angle \text{deg}$	VSI	Bus No.	$ V_{p,u} \angle \text{deg}$	VSI
1	1.0000 \angle 0°	1.0000	36	0.9999 \angle -0.0030°	0.9997
2	1.0000 \angle -0.0012°	0.9999	37	0.9997 \angle -0.0094°	0.9990
3	0.9999 \angle -0.0025°	0.9997	38	0.9996 \angle -0.0118°	0.9984
4	0.9998 \angle -0.0059°	0.9994	39	0.9995 \angle -0.0125°	0.9982
5	0.9990 \angle -0.0185°	0.9961	40	0.9995 \angle -0.0125°	0.9982
6	0.9901 \angle 0.0493°	0.9608	41	0.9988 \angle -0.0235°	0.9954
7	0.9808 \angle 0.1211°	0.9252	42	0.9986 \angle -0.0281°	0.9942
8	0.9786 \angle 0.1383°	0.9170	43	0.9985 \angle -0.0288°	0.9941
9	0.9774 \angle 0.1472°	0.9128	44	0.9985 \angle -0.0289°	0.9940
10	0.9724 \angle 0.2320°	0.8942	45	0.9984 \angle -0.0307°	0.9936
11	0.9713 \angle 0.2508°	0.8902	46	0.9984 \angle -0.0307°	0.9936
12	0.9682 \angle 0.3036°	0.8786	47	0.9998 \angle -0.0077°	0.9992
13	0.9653 \angle 0.3501°	0.8681	48	0.9985 \angle -0.0525°	0.9942
14	0.9624 \angle 0.3963°	0.8577	49	0.9947 \angle -0.1916°	0.9789
15	0.9595 \angle 0.4423°	0.8475	50	0.9942 \angle -0.2114°	0.9768
16	0.9590 \angle 0.4508°	0.8456	51	0.9785 \angle 0.1386°	0.9169
17	0.9581 \angle 0.4650°	0.8425	52	0.9785 \angle 0.1388°	0.9169
18	0.9581 \angle 0.4651°	0.8425	53	0.9747 \angle 0.1691°	0.9024
19	0.9576 \angle 0.4736°	0.8409	54	0.9714 \angle 0.1947°	0.8904
20	0.9573 \angle 0.4792°	0.8398	55	0.9669 \angle 0.2303°	0.8741
21	0.9568 \angle 0.4880°	0.8381	56	0.9626 \angle 0.2652°	0.8585
22	0.9568 \angle 0.4882°	0.8381	57	0.9401 \angle 0.6618°	0.7801
23	0.9567 \angle 0.4895°	0.8379	58	0.9290 \angle 0.8643°	0.7447
24	0.9566 \angle 0.4924°	0.8373	59	0.9248 \angle 0.9453°	0.7313
25	0.9564 \angle 0.4956°	0.8367	60	0.9197 \angle 1.0498°	0.7155
26	0.9563 \angle 0.4969°	0.8365	61	0.9123 \angle 1.1188°	0.6927
27	0.9563 \angle 0.4972°	0.8364	62	0.9121 \angle 1.1216°	0.6920
28	0.9999 \angle -0.0027°	0.9997	63	0.9117 \angle 1.1252°	0.6908
29	0.9999 \angle -0.0053°	0.9994	64	0.9098 \angle 1.1431°	0.6850
30	0.9997 \angle -0.0032°	0.9989	65	0.9092 \angle 1.1484°	0.6833
31	0.9997 \angle -0.0028°	0.9988	66	0.9713 \angle 0.2519°	0.8900
32	0.9996 \angle -0.0009°	0.9984	67	0.9713 \angle 0.2519°	0.8900
33	0.9993 \angle 0.0035°	0.9974	68	0.9678 \angle 0.3097°	0.8775
34	0.9990 \angle 0.0094°	0.9961	69	0.9678 \angle 0.3097°	0.8775
35	0.9989 \angle 0.0104°	0.9958	-		

6.2.3 Discussion on 69-Bus RDN

Figure 13 compares the minimum value of voltage on 69-bus RDN for different test studies. From Fig. 13, it is observed in Test-2 that the minimum value of voltage on 69-bu RDN is 0.9365 p.u, which is more than that obtained in other test studies. Figure 14 compares the P and Q loss on the network for different test studies, and

Table 5 Test studies on 69-bus RDN

Test study	Device	Location	Rating	Bus modeling
Test-1	Single-phase RES	Bus-65	$P = 400 \text{ kW}, Q = 300 \text{ kVAR}$	PQ
Test-3	Single-phase RES	Bus-27	$P = 200 \text{ kW}$ $96.86 \leq Q \leq 535.28 \text{ kVAR}$	PV
	Single-phase RES	Bus-65	$P = 400 \text{ kW}, Q = 300 \text{ kVAR}$	PQ
	Single-phase D-STATCOM	Bus-27	$P = 0 \text{ kW}$ $100 \leq Q \leq 300 \text{ kVAR}$	PV

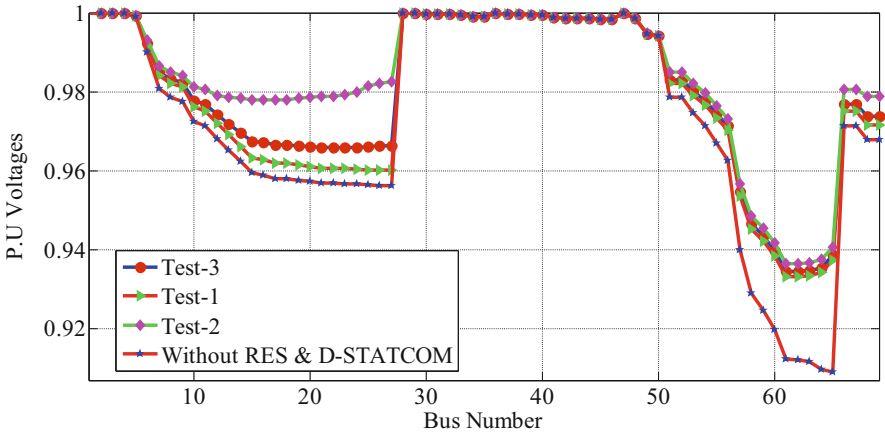


Fig. 12 Voltage profile comparison for different test studies on 69-bus RDN

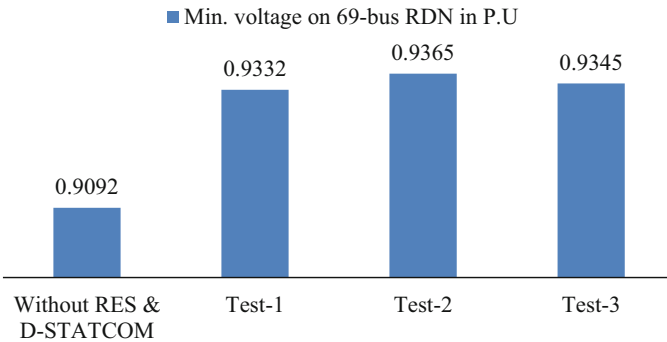


Fig. 13 Comparison of min. Voltage for different test studies on 69-bus RDN

it is observed that, the P and Q loss are found to be 122.19 kW and 57.16 kVAR, respectively, in Test-2, which are less than the loss obtained in other test studies.

Table 6 Obtained voltage solution of different test studies on 69-bus RDN

Bus No.	Test-1 $ V _{p.u}$	Test-2 $ V _{p.u}$	Test-3 $ V _{p.u}$
1	1.0000	1.0000	1.0000
2	1.0000	1.0000	1.0000
3	0.9999	1.0000	0.9999
4	0.9999	0.9999	0.9999
5	0.9992	0.9993	0.9992
6	0.9917	0.9930	0.9922
7	0.9840	0.9865	0.9849
8	0.9822	0.9850	0.9831
9	0.9812	0.9842	0.9823
10	0.9763	0.9812	0.9778
11	0.9752	0.9805	0.9768
12	0.9720	0.9791	0.9742
13	0.9691	0.9787	0.9719
14	0.9662	0.9783	0.9697
15	0.9633	0.9780	0.9675
16	0.9628	0.9780	0.9671
17	0.9619	0.9780	0.9665
18	0.9619	0.9780	0.9665
19	0.9615	0.9783	0.9662
20	0.9612	0.9785	0.9661
21	0.9607	0.9789	0.9658
22	0.9607	0.9789	0.9658
23	0.9606	0.9792	0.9658
24	0.9605	0.9799	0.9659
25	0.9603	0.9815	0.9662
26	0.9602	0.9822	0.9663
27	0.9602	0.9826	0.9664
28	0.9999	0.9999	0.9999
29	0.9999	0.9999	0.9999
30	0.9997	0.9998	0.9997
31	0.9997	0.9997	0.9997
32	0.9996	0.9996	0.9996
33	0.9994	0.9994	0.9994
34	0.9990	0.9990	0.9990
35	0.9990	0.9990	0.9990
36	0.9999	0.9999	0.9999
37	0.9998	0.9998	0.9998
38	0.9996	0.9996	0.9996
39	0.9996	0.9996	0.9996
40	0.9995	0.9996	0.9996
41	0.9989	0.9989	0.9989
42	0.9986	0.9986	0.9986
43	0.9985	0.9985	0.9985
44	0.9985	0.9985	0.9985

(continued)

Table 6 (continued)

Bus No.	Test-1 $ V _{p.u}$	Test-2 $ V _{p.u}$	Test-3 $ V _{p.u}$
45	0.9984	0.9984	0.9984
46	0.9984	0.9984	0.9984
47	0.9998	0.9998	0.9998
48	0.9986	0.9986	0.9986
49	0.9947	0.9947	0.9947
50	0.9942	0.9942	0.9942
51	0.9821	0.9849	0.9831
52	0.9821	0.9849	0.9831
53	0.9792	0.9821	0.9802
54	0.9767	0.9797	0.9778
55	0.9734	0.9764	0.9745
56	0.9702	0.9732	0.9713
57	0.9536	0.9567	0.9547
58	0.9454	0.9486	0.9466
59	0.9422	0.9454	0.9434
60	0.9386	0.9418	0.9398
61	0.9332	0.9365	0.9345
62	0.9333	0.9366	0.9346
63	0.9334	0.9367	0.9347
64	0.9342	0.9375	0.9355
65	0.9375	0.9408	0.9387
66	0.9751	0.9805	0.9768
67	0.9751	0.9805	0.9768
68	0.9717	0.9788	0.9738
69	0.9717	0.9788	0.9738

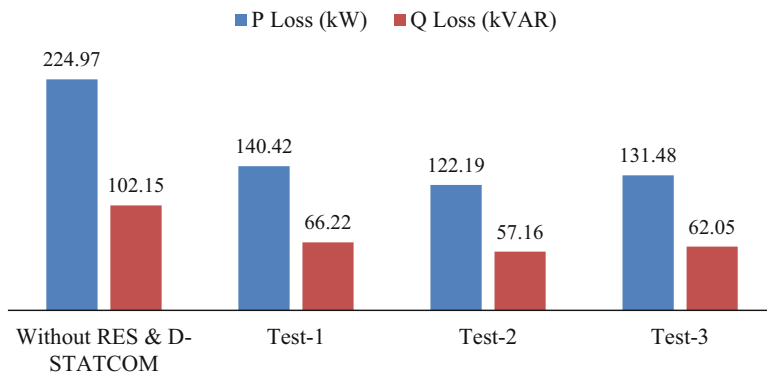


Fig. 14 Comparison of power loss for different test studies on 69-bus RDN

7 Conclusions

The proposed DPFA in this chapter handles the various models of RES and D-STATCOM devices. This DPFA uses BNM and BRNM for its implementation. These matrices can give the way to proceed with finding the bus currents, branch currents, and bus voltages. The power flow solution of the proposed DPFA is tested on 15-bus RDN for its accuracy. The results were exact compared to the literature. The results of the test studies on 15-bus and 69-bus RDN show that the integrations of RES and D-STATCOM devices on the network can improve the voltage profile and reduce the P and Q loss of the network.

References

1. IEEE Standard for Interconnecting Distributed Resources with Electric Power Systems (2003) IEEE Standard 1547–2003, pp. 1–16
2. Kumar A, Jha BK, Singh D, Misra RK (2020) A new current injection based power flow formulation. *Electr Power Compon Syst*:1–13
3. El-Fergany A, Abdelaziz AY (2013) Cuckoo search-based algorithm for optimal shunt capacitor allocations in distribution networks. *Elect Power Compon Syst* 41(16):1567–1581
4. Abdelaziz AY, Ali ES, Abd Elazim SM (2016) Flower pollination algorithm for optimal capacitor placement and sizing in distribution systems. *Electr Power Compon Syst* 44(5):544–555
5. Balu K, Mukherjee V (2020) Siting and sizing of distributed generation and shunt capacitor banks in radial distribution system using constriction factor particle swarm optimization. *Electr Power Compon Syst*:1–14
6. Zeraati M, Josep MEHG, Guerrero M (2019) Voltage quality improvement in low voltage distribution networks using reactive power capability of single-phase PV inverters. *IEEE Trans Smart Grid* 10(5):5057–5065
7. Arabi Nowdeh S, Faraji Davoodkhani I, Hadidian Moghaddam MJ, Seifi Najmi E, Abdelaziz AY, Ahmadi A, Razavi SE, Gandoman FH (2019) Fuzzy multi-objective placement of renewable energy sources in distribution system with objective of loss reduction and reliability improvement using a novel hybrid method. *Appl Soft Comput J* 77:761–779
8. Othman MM, Hegazy YG, Abdelaziz AY (2017) Electrical energy management in unbalanced distribution networks using virtual power plant concept. *Electr Power Syst Res* 145:157–165
9. Abdelaziz AY, Hegazy YG, El-Khattam W, Othman MM (2015) Optimal planning of distributed generators in distribution networks using modified firefly method. *Electr Power Compon Syst* 43(3):320–333
10. Rezaeian-Marjani S, Galvani S, Talavat V, Farhadi-Kangarlu M (2020) Optimal allocation of D-STATCOM in distribution networks including correlated renewable energy sources. *Electr Power Energy Syst* 122:1–14
11. Patel SK, Arya SR, Maurya R (2019) Optimal step LMS-based control algorithm for DSTATCOM in distribution system. *Electr Power Compon Syst*:1–17
12. Sayahi K, Kadri A, Bacha F, Marzougui H (2020) Implementation of a D-STATCOM control strategy based on direct power control method for grid connected wind turbine. *Electr Power Energy Syst* 121:1–14
13. Singh B, Singh S (2019) GA-based optimization for integration of DGs, STATCOM and PHEVs in distribution systems. *Energy Rep* 5:84–103

14. Satish R, Kantarao P, Vaisakh K (2021) A new algorithm for impacts of multiple DGs and D-STATCOM in unbalanced radial distribution networks. *Int J Renew Energy Technol* 12:221–242
15. Satish R, Vaisakh K, Abdelaziz AY, El-Shahat A (2021) A novel three-phase power flow algorithm for evaluation of impact of renewable energy sources and D-STATCOM device in unbalanced radial distribution networks. *Energies* 14:6152
16. Satish R, Vaisakh K, Abdelaziz AY, El-Shahat A (2021) A novel three-phase harmonic power flow algorithm for unbalanced radial distribution networks with the presence of D-STATCOM devices. *Electronics* 10:2663
17. Chen H, Chen J, Shi D, Duan X (2006) Power flow study and voltage stability analysis for distribution systems with distributed generation. *IEEE Power Eng Soc General Meet*:1–8
18. Naka S, Genji T, Fukuyama Y (2001) Practical equipment models for fast distribution power flow considering interconnection of distributed generators. *Power Eng Soc Summer Meet Conf Proc*:1007–1012
19. Nehrir H, Wang C, Shaw SR (2006) Fuel cells: promising devices for distributed generation. *IEEE Power Energy Mag* 4(1):47–53
20. Gotham DJ, Heydt GT (1998) Power flow control and power flow studies for systems with FACTS devices. *IEEE Trans Power Syst* 13(1):60–65
21. Charkravoty M, Das D (2001) Voltage stability analysis of radial distribution networks. *Electr Power Energy Syst* 23:129–135
22. Das D, Nagi HS, Kothari DP (1994) Novel method of solving radial distribution networks. *IEE Proc Gener Transm Distrib* 141(4):291–298
23. Cheng CS, Shirmohammadi D (1995) A three-phase power flow method for real-time distribution system analysis. *IEEE Trans Power Syst* 10(2):671–679
24. Das D, Kothari DP, Kalam A (1995) Simple and efficient method for load flow solution of radial distribution systems. *Electr Power Energy Syst* 17(5):335–346

A Convex Formulation for Hosting Capacity Analysis in Power Distribution Networks



Alejandro Garcés  and José Maria Yusta

1 Introduction

Renewable resources are becoming increasingly important in modern power systems. The enormous interest in this technology is motivated by concerns about global warming and the cost of fossil fuels, including natural gas. However, the high penetration of renewable resources creates new challenges for power systems operators. For example, solar photovoltaic systems may introduce overvoltages during high radiation and low-demand hours. This phenomenon limits the penetration of renewable generation in power distribution networks and microgrids, which necessitates a hosting capacity assessment study. This study determines the amount of solar photovoltaic generation that can be hosted on a grid at a given time without adversely impacting safety, power quality, reliability, or other operational features [1]. Although the idea may be extended to other renewable generations, this chapter only focuses on power distribution networks and microgrids with solar generation.

Different phenomena may be studied when assessing hosting capacity; for example, high penetration of solar generation can produce transient stability and undamped oscillation modes due to the low inertia and the interaction of controls in power electronic converters. This problem is known as transient hosting capacity.

A. Garcés (✉)

Department of Electric Power Engineering, Universidad Tecnológica de Pereira, Pereira, Colombia

e-mail: alejandrogarcés@utp.edu.co

J. M. Yusta

Department of Electric Power Engineering, Universidad de Zaragoza, Zaragoza, Spain

e-mail: jmyusta@unizar.es

However, the most common problem relates to overvoltages in a stationary state; therefore, the concept is mainly defined as the maximum amount of generated power that a network can host without creating overvoltages and maintaining operational limits on the distribution lines.

Overvoltage problems have been observed in Germany, Australia, and the USA as reported in [2]. Grid codes in countries with incipient solar energy penetration must be conservative to avoid these problems. For example, in Colombia, the maximum amount of solar energy in a primary feeder has been defined as half of the minimum load of the feeder [3]. This conservative limit is driven by a simplified method of assessing the hosting capacity and not by the physical constraints of the grid. Such restrictive limits reduce the potential integration of more renewable energy and impede the fight against climate change, despite the high potential of solar generation in tropical countries. A suitable assessment of hosting capacity is thus essential to increase the penetration of renewable energy [4].

Optimization models usually consider a dc model of the power flow equations. However, the hosting capacity must include voltages and reactive power in order to identify possible overvoltage problems [5]. In addition, the model must accurately describe systems with a high r/x relation, as is common in power distribution networks [6]. The non-convex nature of power flow equations makes the problem complicated and reduces the likelihood of a global optimum, a sine-qua-non condition for any modern application.

On the other hand, a hosting capacity analysis requires one to consider the stochastic nature of solar radiation and power demand [7]. Thus, Monte Carlo simulation is the most common approach for modeling hosting capacity in power distribution networks [8]. This method generates many scenarios to which a power flow analysis is then applied. As power flow is a nonlinear problem, there is no guarantee of convergence in all these scenarios [9]. In addition, the high number of scenarios makes the method cumbersome for everyday operation. Risk assessment tools have also been proposed to solve the problem [10]. However, like Monte Carlo methods, these tools require the generation of multiple scenarios. Heuristic and metaheuristic methods may be a suitable alternative, although there is no guarantee of global optimality or convergence [11, 12].

The problem of hosting capacity is closely related to other problems, such as the distributed generation placement in power distribution grids, the optimal operation of renewable energy sources, the reconfiguration of primary feeders, and the control of energy storage devices [13]. These optimization problems impact both the hosting capacity problem and the planning and operation of power distribution networks. However, a simple but accurate model is required to measure the hosting capacity of a power distribution network before including the optimization as mentioned above models.

This chapter presents a deterministic convex model to assess the hosting capacity of power distribution networks and microgrids. The nonlinear, non-convex equations related to the power flow are approximated by complex linearization. Exponential models of the loads are considered, and their equations are also approximated using the same complex linearization method. This approach guarantees an

affine model on the complex set and allows one to estimate the magnitude of the voltage and the reactive power of each power electronic converter. The model is generalizable to radial and meshed networks. Furthermore, the model considers both the unity power factor and optimal reactive power operation. The model is compared to conventional Monte Carlo simulation and conventional power flow calculations to determine its accuracy and robustness against variations in solar radiation and demand.

The rest of the chapter is organized as follows: Sect. 2 presents the basic nonlinear and non-convex model, including loads, photovoltaic units, and the grid. The two possible objective functions are also presented in that section. Next, the complex linearization is presented in Sect. 3, which describes the proposed convex model. Numerical results are included in Sect. 4, comparing conventional Monte Carlo simulation and conventional power flow. Finally, conclusions are given in Sect. 5, followed by relevant references.

2 General Models for Hosting Capacity

2.1 Nomenclature

The following variables, sets, and operators are used along this chapter:

s_k	Apparent power in each node k
v_k	Voltage in each node k
y_{km}	Entry km of the nodal admittance matrix
Y	Nodal admittance matrix
\mathbb{C}	Set of complex numbers
\mathbb{R}	Set of real numbers
\circ	Hadamard product
$(\cdot)^*$	Complex conjugate
α_k	Exponential model of the load k
s_{L_k}	Nominal power of the load k
s_{G_k}	Power generated at node k
ζ	Growth of solar generation in the proportional growth approach

2.2 Problem Definition

A primary feeder in a power distribution network may have one or several photovoltaic units along its circuit. A small number of these units may be beneficial for the grid; however, as the number of photovoltaic units increases, as do the voltage profiles, ultimately reaching unacceptably high values. A hosting capacity analysis determines the maximum amount of photovoltaic generation the grid can

host without jeopardizing its normal operational voltage. The system departs from a basic configuration, and new photovoltaic units are incorporated. This growth of photovoltaic generation may be done in different ways, and its impact on the grid may be measured with different metrics, leading to different optimization models.

In this work, photovoltaic generation growth is achieved in two different ways, namely proportional growth and maximum hypervolume. For the former, there is a given configuration of photovoltaic units along the nodes of the network, and new units are connected in the same proportion. The location of the photovoltaic units is known, and new units are placed at the same nodes as the existing units. The proportion of the power is also known a priori, that is, if one photovoltaic system doubles its capacity, the other units will also double their capacity. In the case of maximum hypervolume, the location and proportion of photovoltaic units along the feeder are unknown. The objective function must therefore be oriented to accommodate the maximum amount of photovoltaic generation regardless of the location.

Constraints of the problem include the conventional power flow equations, the loads' exponential model, and the converters' capacity. The following sections present the main aspects of the model.

2.3 Objective Function

As previously mentioned, two objective functions are considered: proportional growth and maximum hypervolume. For proportional growth, the objective is to maximize a real variable ζ that represents the proportional growth of each photovoltaic unit, as described in Eq. (1):

$$\max \zeta \quad (1)$$

The power generation at each node of the system increases by the same proportion ζ . Conversely, the second objective function increases the total generation of the grid, regardless of the existing configuration. Therefore, power generation can grow in different proportions, and the objective is to maximize generation. This generation can be measured using the hypervolume of the hypercube formed in the space of the generated power, defined as Eq. (2):

$$\max \prod \text{real}(S_G) \quad (2)$$

The following example elucidates this objective function.

Example 1 Figure 1 depicts a simple power distribution network with two photovoltaic units connected at Nodes 2 and 3. In this system, the maximum capacity of PV2 is 40 MW and the maximum capacity of PV3 is 5 MW. In a proportional growth model, the power generation in each node can be increased by a factor ζ

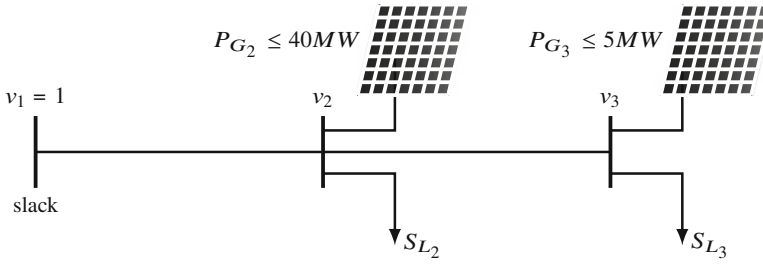


Fig. 1 Example of small distribution network with two photovoltaic systems

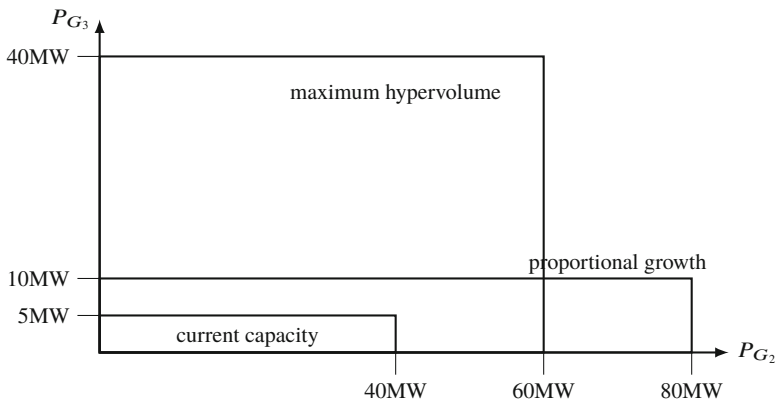


Fig. 2 Two possible objective functions related to the maximum amount of photovoltaic generation for a system with two units

in each PV system. For example, for $\zeta = 2$, the capacity of PV2 would become 80 MW, and that of PV3, 10 MW.

The second objective function increases the amount of PV generation, regardless of the initial configuration of the system. For the system in Fig. 1, this rise in generation would increase the area $P_{G_2} \times P_{G_3}$. This concept can be generalized as volume in a system with three PV systems and so forth. Thus, hypervolume represents the general case. Figure 2 depicts the effect of each objective function. The total power generated by the photovoltaic units is higher in the maximum hypervolume function than in the proportional growth function; however, the proportion is different, since the optimal solution may allocate more generation to Node 2 than Node 3, unlike in the initial configuration of the system. The actual proportion of the generated power will depend on the parameters and the topology of the grid, as will be demonstrated in the results.

2.4 Modeling the Network

In this section and for the rest of the chapter, all variables are in the complex domain unless otherwise specified. The configuration and parameters of the power distribution network are represented by the nodal admittance matrix $Y = [y_{km}] \in \mathbb{C}^{n \times n}$, nodal voltages are represented by the vector $V = [v_k] \in \mathbb{C}^n$ and nodal powers are given by $S = [s_k] \in \mathbb{C}^n$. Other variables are specified in the nomenclature above.

Current balance is defined by Eq. (3), which applies to each node k of the grid, as indicated below:

$$\frac{s_k^*}{v_k^*} = \sum_{m=1}^n y_{km} v_m \quad (3)$$

where s_k is the nodal power at node k , y_{km} is the entry km of the nodal admittance matrix, and n is the number of nodes. A matrix representation is proposed to simplify the analysis, as given in Eq. (4):

$$S^* = V^* \circ (YV) \quad (4)$$

where V^* represents the vector complex conjugate (without transposing) of V and \circ is the Hadamard product (i.e., pointwise multiplication, or the command `.*` in MATLAB). Note that this model is nonlinear and equivalent to conventional representations of the nodal power flow equations. Without loss of generality, the voltage in the slack node is set to $v_{\text{slack}} = 1$ pu; therefore, Eq. (4) is mainly defined for the remaining nodes. The nodal power at each node k is the difference between generation S_G and load S_L , as defined in Eq. (5):

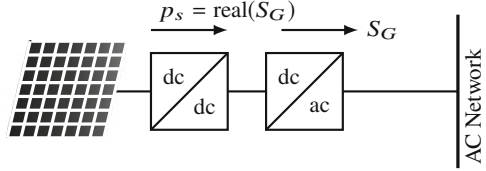
$$s_k = s_{G_k} - s_{L_k} \|v_k\|^{\alpha_k} \quad (5)$$

In this case, loads are represented by an exponential model with $\alpha \in \mathbb{R}$; usually, $\alpha = 2$ for residential loads, $\alpha = 1$ for commercial loads, and $\alpha = 0$ for industrial loads. Nevertheless, the model is general for any real value of α . Note that some entries of S_G and S_L may be zero. Both Eqs. (4) and (5) are nonlinear equality constraints of the optimization model. This type of constraint is not convex and makes the problem highly difficult to solve.

2.5 Modeling Photovoltaic Units

Each photovoltaic unit is equipped with an energy conversion system that integrates the power, generated in dc, into the three-phase ac network, as depicted in Fig. 3. The system consists of a dc/dc converter that extracts the maximum amount of available solar power and a dc/ac converter that integrates the system into the three-phase grid.

Fig. 3 Schematic representation of a solar photovoltaic unit



Both converters use force commutated converter technology that enables rapid control of the generated power (in the case of the dc/dc converter) or the reactive power (in the case of the dc/ac converter). In general, a dc/ac voltage source converter is able to delivery and consume reactive power, according to the control objective. However, apparent power capacity is limited by the maximum current that can support the commutation devices (i.e., the maximum rating of the insulate gate bipolar transistors that constitute the converter). This limit can be represented in terms of the apparent power S_G ; thus, the capacity of the converter may be defined by the nominal power factor ρ , as presented in Eq. (6):

$$\|s_{Gk}\| \leq (1/\rho) \text{real}(s_{Gk}) \tag{6}$$

Figure 2 depicts the set defined by this constraint. A converter with $\rho = 1$ can operate at the unity power factor at nominal solar radiation (i.e., $s_G = p_G + 0j$). However, when the solar radiation decreases, the converter can generate additional reactive power, as long as the apparent power does not exceed the converter’s nominal capacity. The model can consider operation modes in which the converter generates or consume reactive power (Fig. 4).

The power electronic converter may be controlled in different ways. This work assumes vector-oriented control. In this control, the converter is synchronized to the frequency of the grid via a phase-locked loop (PLL). Then, a current control or inner-loop is performed in the 0dq reference frame. This current control allows the system to either maintain maximum current or maintain a current such that the dc link of the capacitor and the power factor ρ is controlled; the latter control is known as outer-loop. More details about the control of the converter can be found in [14].

2.6 Complete Model

The complete optimization model can be formulated once the objective function and the main constraints are defined. Additional constraints include the voltage in the slack node and box constraints related to the voltage, as presented below:

$$v_{\text{slack}} = 1 + j0 \tag{7}$$

$$\|v_k\| \leq v_k^{\text{max}} \tag{8}$$

Fig. 4 Capability of active and reactive power of a power electronic converter

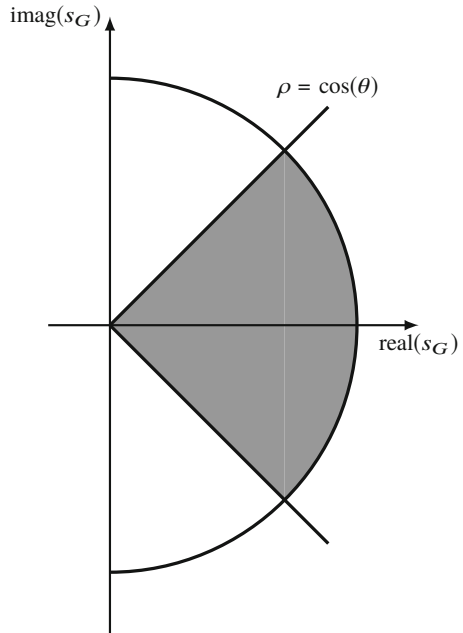


Table 1 Details of the proposed optimization model

Name	Equation	Type
Objective function	(1) for proportional growth or (2) for maximum hypervolume	Eq (1) convex Eq (2) non-convex
Power balance	(4)	Non-convex
Load model	(5)	Non-convex
Power generation	(6)	Convex
Voltage at slack	(7)	Convex
Maximum voltage	(8)	Convex

Table 1 describes the main features of the optimization model. There are non-convex equations both in the objective function and in the constraints. Therefore, several approximations are required to transform this model into a tractable convex optimization problem.

Notice that some constraints are already convex. However, the power balance equation and the load model, as well as the objective function for maximum hypervolume optimization are non-convex.

3 Convexification of the Problem

3.1 Objective Function

In the case of the maximum hypervolume, the objective function is transformed into a convex function using a logarithmic transformation, as described in Eq. (9):

$$\ln \left(\prod \text{real}(S_G) \right) = \sum \ln(\text{real}(S_G)) \tag{9}$$

The following convex equivalent is possible since \ln is both monotone and concave:

$$\min \sum_{\text{node} \neq \text{slack}} -\ln(\text{real}(S_G)) \tag{10}$$

This objective function is convex and completely equivalent to the original objective function (i.e., it is not an approximation but rather a better representation of the same phenomena).

3.2 Complex Linearization

Optimization problems are defined in ordered sets, such as the set of the real or the natural numbers. However, this optimization problem includes equality constraints on the complex domain. Although it is possible to divide the function into real and imaginary parts, it is more convenient to maintain a complex form. Moreover, some programming languages such as MATLAB, Python, or Julia allow one to define models in complex form. Thus, Eqs. (4) and (5) are a compact and straightforward representations of the power flow equations. However, these equations are non-affine, so a linearization is required.

Any complex number may be represented as $z = x + jy$ where $j = \sqrt{-1}$; therefore, a complex function $f : \mathbb{C} \rightarrow \mathbb{C}$ can be also divided into real and imaginary parts, that is, $f(z) = u(x, y) + jv(x, y)$. Complex functions have additional requirements to be analytical (i.e., derivable); in particular, a complex function is analytical if it fulfils the Cauchy–Riemann conditions, presented in Eqs. (11) and (12).

$$\frac{\partial u}{\partial x} = \frac{\partial v}{\partial y} \tag{11}$$

$$\frac{\partial u}{\partial y} = -\frac{\partial v}{\partial x} \tag{12}$$

These conditions imply that the limit, which defines the derivative, may be taken in any direction on the complex plane with the same result. Unfortunately, power flow equations do not fulfill the Cauchy–Riemann conditions, since these equations depend on both the nodal voltages and their conjugates. Therefore, new operators must be defined in order to perform a linearization. These operators, called Wirtinger’s derivative and conjugate Wirtinger’s derivative [15], are defined for a complex function $f(z) = u(x, y) + jv(x, y)$ in Eqs. (13) and (14), respectively:

$$\frac{\partial f}{\partial z} = \frac{1}{2} \left(\frac{\partial u}{\partial x} + \frac{\partial v}{\partial y} \right) + \frac{j}{2} \left(\frac{\partial v}{\partial x} - \frac{\partial u}{\partial y} \right) \quad (13)$$

$$\frac{\partial f}{\partial z^*} = \frac{1}{2} \left(\frac{\partial u}{\partial x} - \frac{\partial v}{\partial y} \right) + \frac{j}{2} \left(\frac{\partial v}{\partial x} + \frac{\partial u}{\partial y} \right) \quad (14)$$

The use of these operators is similar to partial derivatives concerning the variable z and its conjugate z^* . Furthermore, when f is analytical, its Wirtinger’s derivatives degenerate to the standard complex derivative, while its conjugate Wirtinger’s derivative vanishes, as represented in Eqs. (15) and (16) below (see [16] for more details):

$$\frac{\partial f}{\partial z} = f'(z) \quad (15)$$

$$\frac{\partial f}{\partial z^*} = 0 \quad (16)$$

The following example demonstrates the use of the rules of differentiation in Wirtinger’s calculus.

Example 2 Let us consider the following complex function

$$f(z) = 3z + 4z^* - 15zz^* \quad (17)$$

This function is not analytic, which means it does not have derivative in the complex domain. However, it has two Wirtinger’s derivatives, namely:

$$\frac{\partial f}{\partial z} = 3 - 15z^* \quad (18)$$

$$\frac{\partial f}{\partial z^*} = 4 - 15z \quad (19)$$

3.3 Linear Power Flow Equations

One of the main challenges for any optimization model in power system applications is the nonlinear nature of the load flow equations. These equations may be

simplified using convex approximations, such as second-order cone and semidefinite approximations. Another option is to linearize around $1 + j0$ using Wirtinger's calculus, starting with a linearization of Eq. (3), as described in Eq. (20):

$$\Delta s_k^* = \sum_{m=1}^n y_{km} (\Delta v_k^* + \Delta v_m) \quad (20)$$

This equation is written in matrix representation in Eq. (21):

$$\Delta S^* = 1_N \circ Y \Delta V + \Delta V^* \circ Y 1_N \quad (21)$$

where $1_N \in \mathbb{R}^n$ is a vector whose entries are all equal to 1, resulting in Eq. (22):

$$\Delta S^* = Y \Delta V + \text{diag}(Y 1_N) \Delta V^* \quad (22)$$

where

$$\Delta S = S - 1_N \circ Y 1_N \quad (23)$$

$$\Delta V = V - 1_N \quad (24)$$

Then, the linear version of Eq. (3) is given by Eq. (25).

$$S^* = Y V + \text{diag}(Y 1_N) V^* - Y^* 1_N \quad (25)$$

Notice that this linearization differs from the one proposed previously in [17]. Here, the equation is linear in both V and S . Therefore, it can be included directly in the optimization model since it defines an affine space (see [18] for a rigorous definition of affine space in the context of convex optimization).

Equation (5) must also be linearized in order to be included in the convex optimization model. The complex linearization around 1_N is shown in Eqs. (26) and (27):

$$\Delta S = \Delta S_G - \frac{\alpha}{2} \circ S_L \circ (\Delta V + \Delta V^*) \quad (26)$$

$$S = S_G - \frac{\alpha}{2} \circ S_L \circ (V + V^*) + (\alpha - 1) \circ S_L \quad (27)$$

For the sake of completeness, the entire optimization model is presented below for the proportional growth case:

$$\begin{aligned}
& \max \zeta \\
& S^* = YV + \text{diag}(Y1_N) V^* - Y^*1_N \\
& S = S_G - \frac{\alpha}{2} \circ S_L \circ (V + V^*) + (\alpha - 1) \circ S_L \\
& V_{\text{slack}} = 1 + j0 \\
& |V| \leq v_{\text{max}} \\
& |S_G| \leq (1/\rho) \text{ real}(S_G) \quad \forall \text{ node} \neq \text{slack} \\
& \text{real}(S_G) \geq \zeta P_G \quad \forall \text{ node} \neq \text{slack}
\end{aligned} \tag{28}$$

The model of maximum hypervolume is the same, except for the objective function, which is replaced by (10). This model is convex because the objective function is convex, the set of equality constraints are affine and the inequality constraints are convex. The first two constraints determine an affine representation of the power flow equations and the exponential model of the loads. The third constraint gives the value of the voltage in the slack node (again an affine equation). The remaining constraints are inequalities that represent the maximum voltage, maximum reactive power and growth of PV generation, respectively.

In these models, the decision variables are $V, S, S_G \in \mathbb{C}^n$ and $\zeta \in \mathbb{R}$. As discussed at the beginning of this section, the model is represented using complex variables to achieve a compact representation. Notice that the objective(s) function(s) as well as the inequality constraints are functions with images in the real domain. The use of complex numbers enables a compact representation and simplifies its implementation. As is demonstrated in the results, the model can be easily implemented in programming languages such as Python or MATLAB that allow complex variables.

4 Results

4.1 Test System

The medium-voltage benchmark test system presented in [19] was used to demonstrate the use of the proposed model. This system, depicted in Fig. 5, consists of a 20 kV network that supplies a small town and the surrounding rural areas. Parameters of the grid are given in Table 2; parameters of the components at each node are given in Table 3.

The model of the loads was defined using an α that was set to $\alpha = 0$ for industrial loads and to $\alpha = 2$ for household loads. The grid was represented in per unit with $V_{\text{base}} = 20 \text{ kV}$ and $S_{\text{base}} = 10 \text{ MW}$.

Three cases were analyzed. First, the basic model with unit power factor operation is presented. This operation model is the most common in power distribution

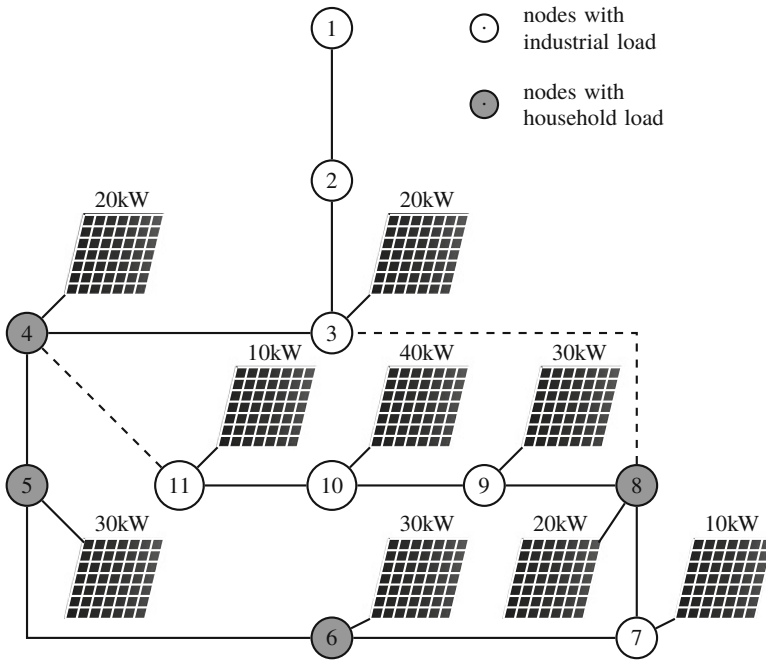


Fig. 5 Medium-voltage rural distribution benchmark network

Table 2 Parameters of the grid

From	To	R (Ω /km)	X (Ω /km)	C (nF/km)	L (km)
1	2	0.579	0.367	9.93	2.82
2	3	0.164	0.113	413	4.42
3	4	0.262	0.121	405	0.61
4	5	0.354	0.129	285	0.56
5	6	0.336	0.126	343	1.54
6	7	0.256	0.130	235	0.24
7	8	0.294	0.123	350	1.67
8	9	0.339	0.130	273	0.32
9	10	0.399	0.133	302	0.77
10	11	0.367	0.133	285	0.33
3	8	0.172	0.115	411	1.30
11	4	0.423	0.134	310	0.49

networks since many grid codes typically demand only unity power factor operation for solar photovoltaic generation. Next, the effect of the power factor is studied by considering different operation modes with generation and/or demand of reactive power. Finally, the effect of the topology of the grid is studied, and the accuracy and robustness of the models are assessed.

Table 3 Parameters of the nodes

Node	P_L (kW)	Q_L (kVAr)	$P_{G(\max)}$ (kW)	Type of load
3	500	250	20	Industrial
4	432	108	20	Household
5	725	182	30	Household
6	550	138	30	Household
7	77	48	10	Industrial
8	588	147	20	Industrial
9	574	356	30	Household
10	68	42	40	Industrial
11	331	120	10	Industrial

The system presents two loops that connect nodes 3–8 and 4–11. Three cases were considered: (i) both lines opened, (ii) line connecting nodes 3–8 closed, and (iii) both lines connecting nodes 3–8 and nodes 4–11 closed.

4.2 Basic Models with Unity Power Factor

The first case, corresponding to a radial system, was evaluated using the model for proportional growth. The system departs from the photovoltaic units shown in Fig. 5. All photovoltaic units are supposed to operate at unity power factor, and the maximum value for the magnitude of the voltage is $v_{\max} = 1.05$ pu. The model was implemented in MATLAB with CVX, a package for specifying and solving convex programs with complex variables [20]. The CPU time was 1.5 s on average on a computer with Intel Core i7-8700 CPU @3.20 GHz. The optimal value of ζ was 53.48. The maximum generated power at each node is depicted in Fig. 6. As expected, the growth in photovoltaic generation was proportional to the base case. For example, Node 10 had the maximum amount of generation and Node 2 remained without generation.

The maximum hypervolume case was also evaluated in the radial system. In this case, the objective function was replaced by Eq. (10) and the constraints remained equal. Here, CPU time was around 5 s (logarithmic functions usually increase calculation time, but here the problem remained tractable). Results are presented in Fig. 7. The algorithm tried to incorporate the greatest amount of photovoltaic generation regardless of the initial configuration of the network. The algorithm naturally tried to implement higher generation at nodes close to the slack node, which reduced the capacity of the nodes at the end of the feeder.

The hosting capacity was next evaluated in a meshed grid. First, the loop created by including the line connecting nodes 3–8 was incorporated. Second, the line connecting nodes 4–11 was also incorporated to form a meshed grid with two loops. The model for proportional growth was used. The results indicated that the meshed

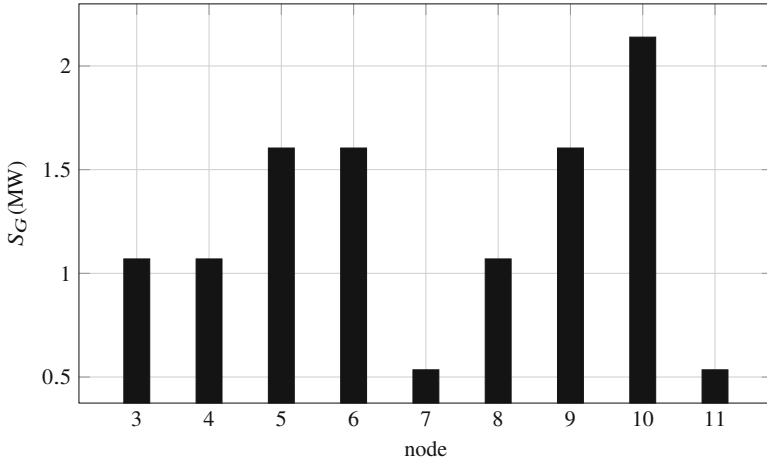


Fig. 6 Hosting capacity in each node of the test system for proportional growth of photovoltaic generation. Lines 3–8 and 4–11 are open

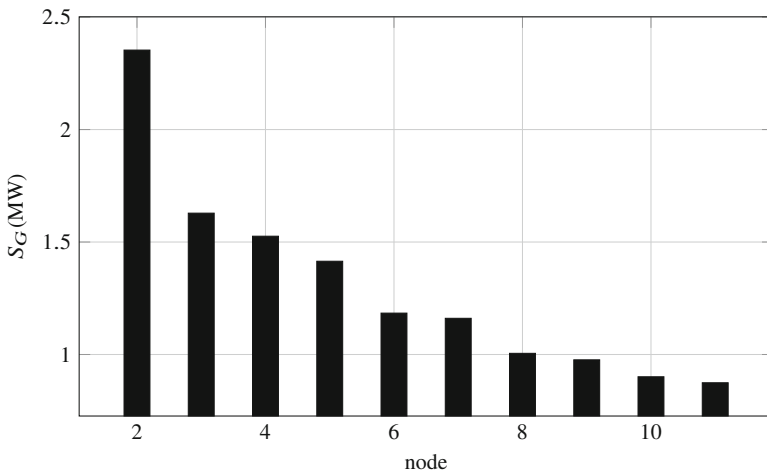


Fig. 7 Hosting capacity in each node of the test system for maximum hypervolume. Lines 3–8 and 4–11 are open

grid has a higher hosting capacity than the radial system. The value of ζ went from $\zeta = 53.48$ in the radial case to $\zeta = 66.25$ for the meshed grid. Results are depicted in Fig. 8. It was clear that the second loop increased the hosting capacity, but this increase was less pronounced than that of the first loop.

The model for maximum hypervolume was also evaluated in the meshed grid, with the results shown in Fig. 9. In this case, the amount of new generation at nodes close to the slack (for example, Node 2) was reduced in order to increase the capacity

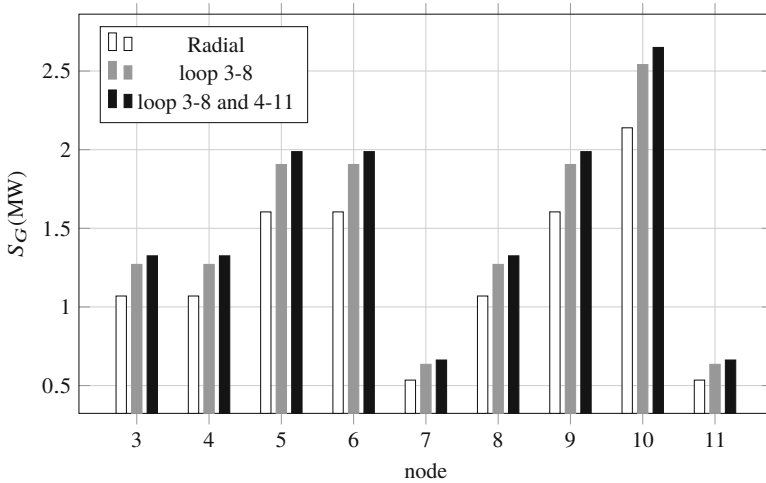


Fig. 8 Hosting capacity in each node of the test system for proportional growth of photovoltaic generation. As the system becomes more meshed, the hosting capacity increases

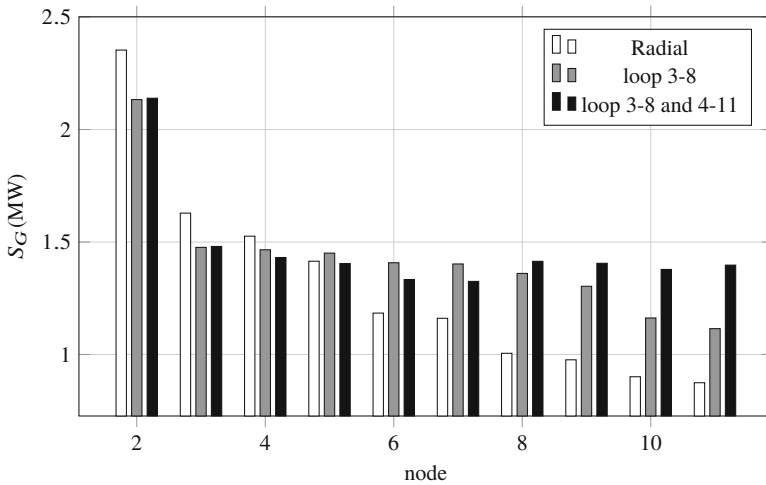


Fig. 9 Hosting capacity in each node for a meshed network and maximum hypervolume

of other nodes (for example, Node 10) that belonged to the new loop. In other words, new loops tended to balance new generation among the nodes of the system.

4.3 Effect of the Power Factor

The model was also evaluated for the case in which the nominal power factor was different from 1, that is, when the converters generated some reactive power to

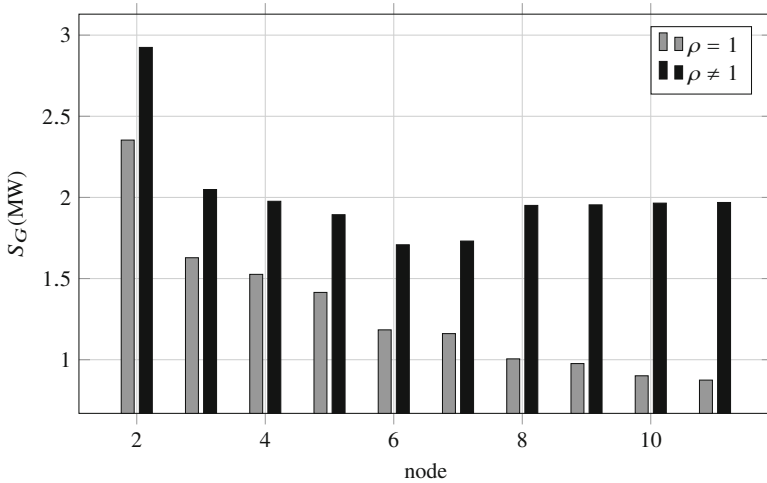


Fig. 10 Hosting capacity in each node for a meshed network and maximum hypervolume with different nominal power factor. A power factor different from 1 can increase the hosting capacity of the network

supply local demands. Results are depicted in Fig. 10 for minimum power factor $\rho = 0.8$ and maximum hypervolume. The hosting capacity increased significantly, especially at terminal nodes, due to the capability of the converters to generate or consume reactive power.

4.4 Robustness and Accuracy of the Model

The proposed model presents two characteristics that require careful analysis. First, the model is an approximation because the power flow equations and the model of the loads are linear approximations of the exact model. Second, the model is deterministic, even though solar radiation and loads are stochastic variables.

In order to evaluate the first characteristic, a load flow calculation was performed on the system at maximum photovoltaic generation. This result was compared to the linearization results. The maximum error in voltage was 3×10^{-4} . Linearization generally leads to an overestimation of the voltage. This is in fact an advantage for the hosting capacity model since the linear model is conservative. Therefore, the proposed model is accurate for the application.

The second aspect (i.e., the stochastic nature of the problem) was evaluated using a Monte Carlo simulation. A total of 1×10^4 random scenarios of solar radiation and demand were evaluated. The maximum voltage in each scenario was stored, and the resulting histogram is presented in Fig. 11. Only nine of these scenarios had maximum voltages that fell within the interval $[1.045-1.051]$ pu (i.e., overvoltage). Therefore, the proposed deterministic model constitutes a robust model for the hosting capacity analysis.

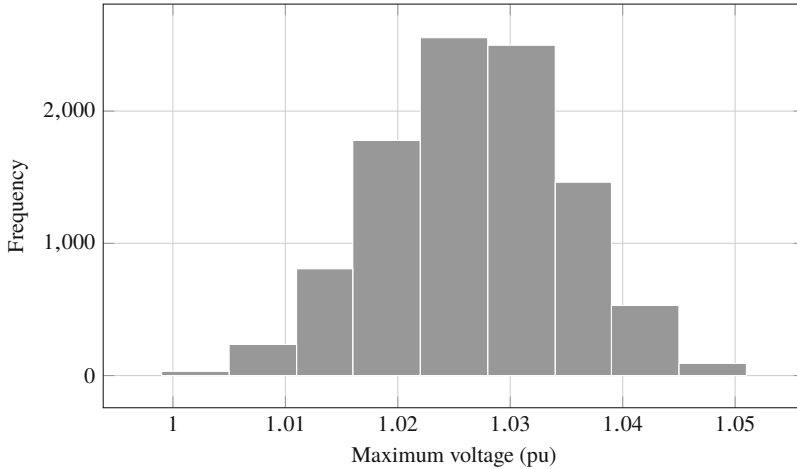


Fig. 11 Results for Monte Carlo simulation considering a maximum penetration given by the convex optimization model. None of the voltages exceeds the maximum value

4.5 MATLAB Implementation

The proposed convex model can be easily implemented in modern languages such as Python or MATLAB that allow matrices of complex variables. The following code was implemented in MATLAB 2019 with the current version of CVX [20].

```

cvx_begin quiet
    variable V(n) complex;
    variable SG(n) complex;
    variable S(n) complex;
    variable zeta;
    minimize sum(-log(real(SG(2:end)))));
    subject to
        conj(S) == Y*V + diag(Y*u) * conj(V) - Y*u;
        S == SG - 0.5*alpha.*SL.*(V+conj(V)) + (alpha-u).*SL;
        V(1) == 1;
        abs(V) <= 1.05;
        abs(SG(2:end)) <= (1/0.8)*real(SG(2:end));
        real(SG(2:end)) >= PG(2:end)*zeta;
cvx_end

```

This code is general for any grid given the nodal admittance matrix Y , the loads of the system S_L , the exponential models α , and the number of nodes n . The slack node is Node 1. The rest of the code is available in [21]. Notice that the code is simple and clean due to the complex representation.

5 Conclusions

A convex optimization model for the hosting capacity analysis in power distribution networks was presented. The model applies complex linearization to both the power flow equations and the exponential models of the loads. The model results were very accurate compared to the complete power flow, with errors less than 1×10^{-4} . A Monte Carlo simulation was used to demonstrate that the optimization model is also robust to variations in loads and solar radiation.

Two objective functions, proportional growth and maximum hypervolume, were considered. In the first model, the photovoltaic generation increases at the same proportion with respect to an initial configuration. The second model determines the maximum photovoltaic generation that can be introduced into the system without affecting the voltage profile. Results indicated that a higher amount of generation was added to the nodes close to the slack for the maximum hypervolume case.

The model considered meshed and radial grids. As expected, meshed grids presented higher hosting capacity than radial grids, but each new loop yielded a lower increment in the hosting capacity than the previous loop. This finding indicates that a weakly meshed grid may sufficiently increase the hosting capacity. For hypervolume maximization, the results were flattened in the meshed case compared to the decreasing characteristic of the radial system.

The hosting capacity was also affected by the minimum power factor available for photovoltaic units. The network could host a higher amount of solar generation when proper reactive power was defined. This implies that a well-designed strategy of optimal power flow and/or tertiary control may increase the hosting capacity in power distribution networks. In general, the result demonstrated that a power distribution network has a higher hosting capacity (in terms of maximum voltage) compared to the conservative limits given by some grid codes.

The proposed model may be used not only to assess but also to increase hosting capacity. The hosting capacity can be improved by different actions, such as adding a new component (e.g., a voltage regulator or a d-statcom). However, the method presented here is based on the use of the power electronic converters required to integrate solar panels, which do not require significant infrastructure upgrades. Thus, these results demonstrate that hosting capacity can be improved by a suitable coordination of the reactive power in power electronic converters.

References

1. Stanfield S, Safdi S, Mihaly S (2017) *Optimizing the grid, a regulator's guide to hosting capacity analyses for distributed energy resources*, 1st edn. IREC, New York
2. Divan D, Kandula P (2016) Increasing solar hosting capacity is the key to sustainability. In: 2016 first international conference on sustainable green buildings and communities (SGBC), pp 1–5
3. CREG (2018) Resolución 030 de 2018. In: Comisión de regulación de energía y gas, vol 30

4. Rawa M, Abusorrah A, Al-Turki Y, Mekhilef S, Mostafa MH, Ali ZM, Aleem SHEA (2020) Optimal allocation and economic analysis of battery energy storage systems: self-consumption rate and hosting capacity enhancement for microgrids with high renewable penetration. *Sustainability* 12(23):10144. <https://www.mdpi.com/2071-1050/12/23/10144>
5. Torquato R, Salles D, Oriente Pereira C, Meira PCM, Freitas W (2018) A comprehensive assessment of PV hosting capacity on low-voltage distribution systems. *IEEE Trans Power Delivery* 33(2):1002–1012
6. Ismael SM, Aleem SH, Abdelaziz AY, Zobaa AF (2019) State-of-the-art of hosting capacity in modern power systems with distributed generation. *Renew Energy* 130:1002–1020. <https://www.sciencedirect.com/science/article/pii/S0960148118307936>
7. Ding F, Mather B (2017) On distributed PV hosting capacity estimation, sensitivity study, and improvement. *IEEE Trans Sustain Energy* 8(3):1010–1020
8. Dubey A, Santoso S (2017) On estimation and sensitivity analysis of distribution circuit's photovoltaic hosting capacity. *IEEE Trans Power Syst* 32(4):2779–2789
9. Ismael SM, Abdel Aleem SHE, Abdelaziz AY, Zobaa AF (2019) Probabilistic hosting capacity enhancement in non-sinusoidal power distribution systems using a hybrid PSO-GSA optimization algorithm. *Energies* 12(6):1018. <https://www.mdpi.com/1996-1073/12/6/1018>
10. Al-Saadi H, Zivanovic R, Al-Sarawi SF (2017) Probabilistic hosting capacity for active distribution networks. *IEEE Trans Indus Inform* 13(5):2519–2532
11. Gensollen N, Horowitz K, Palmintier B, Ding F, Mather B (2019) Beyond hosting capacity: using shortest-path methods to minimize upgrade cost pathways. *IEEE J Photovoltaics* 9(4):1051–1056
12. Diaaeldin IM, Abdel Aleem SHE, El-Rafei A, Abdelaziz AY, Zobaa AF (2020) Enhancement of hosting capacity with soft open points and distribution system reconfiguration: multi-objective bilevel stochastic optimization. *Energies* 13(20):5446. <https://www.mdpi.com/1996-1073/13/20/5446>
13. Zobaa AF, Abdel-Aleem SH, Ismael SM, Ribeiro PF (2020) *Hosting capacity for smart power grids*. Springer, Berlin
14. Teodorescu R, Liserre M, Rodriguez P (2011) *Grid converters for photovoltaic and wind power systems*. IEEE Power Engineering Society, New Jersey: Wiley-Interscience
15. Hunger R (2007) *An introduction to complex differentials and complex differentiability*. Reporte técnico, Technische Universität München, Associate Institute for Signal Processing
16. Fischer R (2005) Appendix A: Wirtinger calculus, in precoding and signal shaping for digital transmission. John Wiley and Sons, pp 405–413. <https://onlinelibrary.wiley.com/doi/abs/10.1002/0471439002.app1>
17. Garcés A (2015) A linear three-phase load flow for power distribution systems. *IEEE Trans Power Syst* PP(99):1–2
18. Nesterov Y (2008) *Introductory lectures on convex programming volume I: basic course*. Springer, Berlin
19. Rudion K, Styczynski Z, Hatziaargyriou N, Papathanassiou S, Strunz K, Ruhle O, Ortho O, Rozel A (2006) Development of benchmarks for low and medium voltage distribution networks with high penetration of dispersed generation. In: *International symposium of modern electric power systems*, vol 1. Wroclaw, Poland
20. Grant M, Boyd S (2014) CVX: Matlab software for disciplined convex programming, version 2.1. <http://cvxr.com/cvx>
21. Garcés A (2020) Matlab exchange. <https://la.mathworks.com/matlabcentral/profile/authors/3009175>

Power Quality in Modern Power Systems: A Case Study in Bosnia and Herzegovina



Mia Lešić Aganović, Tatijana Konjić, Miloš Milovanović, Martin Čalasan,
Ahmed I. Omar, and Shady H. E. Abdel Aleem 

Abbreviations

ANSI	American National Standards Institute
BH	Bosnia and Herzegovina
DG	Distributed generation
DHPF	Decoupled harmonic power flow
EMC	Electromagnetic compatibility
EPRI	Electric Power Research Institute

M. L. Aganović
Electric Power Transmission Company, Operational Area Tuzla, Tuzla, Bosnia and Herzegovina
e-mail: mia.lesic@elprenos.ba

T. Konjić
Faculty of Electrical Engineering, University of Tuzla, Tuzla, Bosnia and Herzegovina

M. Milovanović
Faculty of Technical Sciences, University of Priština in Kosovska Mitrovica, Kosovska Mitrovica, Serbia
e-mail: milos.milovanovic@pr.ac.rs

M. Čalasan (✉)
Faculty of Electrical Engineering, University of Montenegro, Podgorica, Montenegro
e-mail: martinc@ucg.ac.me

A. I. Omar
Electrical Power and Machines Engineering Department, The Higher Institute of Engineering at El-Shorouk City, El-Shorouk Academy, Cairo, Egypt
e-mail: a.omar@sha.edu.eg

S. H. E. Abdel Aleem
Electrical Engineering Department, Valley Higher Institute of Engineering and Technology, Science Valley Academy, Qalyubia, Egypt
e-mail: engyshady@ieee.org

FC	Fuel cells
IEC	International Electrotechnical commissionCommission
IEEE	Institute of Electrical and Electronics Engineers
IHDI	Individual harmonic current distortion
IHDU	Individual harmonic voltage distortion
LV	Low voltage
MPPT	Maximum power point tracker
MT	Micro-turbine
MV	Medium voltage
NEMA	National Electrical Manufacturers Association
NFPA	National Fire Protection Association
NIST	National Institute of Standards and Technology
NOCT	Nominal operating cell temperature
PCC	Point of common coupling
PCU	Power conditioning unit
PF	Power factor
PV	Photovoltaic
STC	Standard test condition
TDD	Total distortion demand
THD	Total harmonic distortion
THDI	Total harmonic current distortion
THDU	Total harmonic voltage distortion
TIF	Telephone influence factor
UL	Underwriters laboratories
WTG	Wind turbine generator

1 Introduction

The need to enhance the amount of installed renewable energy sources (RES) in the entire community's energy balance is getting bigger due to increased environmental consciousness, legislative requirements, and international conventions that demand carbon emissions reduction and energy efficiency enhancement [1, 2]. As a country trying to become a member of the EU, Bosnia and Herzegovina is obliged to follow recommendations related to increasing electricity production from renewable energy sources, all according to applicable EU standards [3]. Due to suitable natural circumstances, solar energy has become one of the most appropriate RESs in Bosnia and Herzegovina [4], following EU norms and current global trends.

Bosnia and Herzegovina's climate is Mediterranean in the south and continental in the north. Global horizontal irradiation in the south areas of Bosnia and Herzegovina is around 1550.5 Wh/m^2 . In the northern areas, irradiation is around 1250 kWh/m^2 , as shown in Fig. 1a [5]. Photovoltaic power potential is shown in Fig. 1b [23]. The amount of sunlight hours each year is important information. The sunlight hours in the nation's southern parts is from 1900 to 2300 h, while

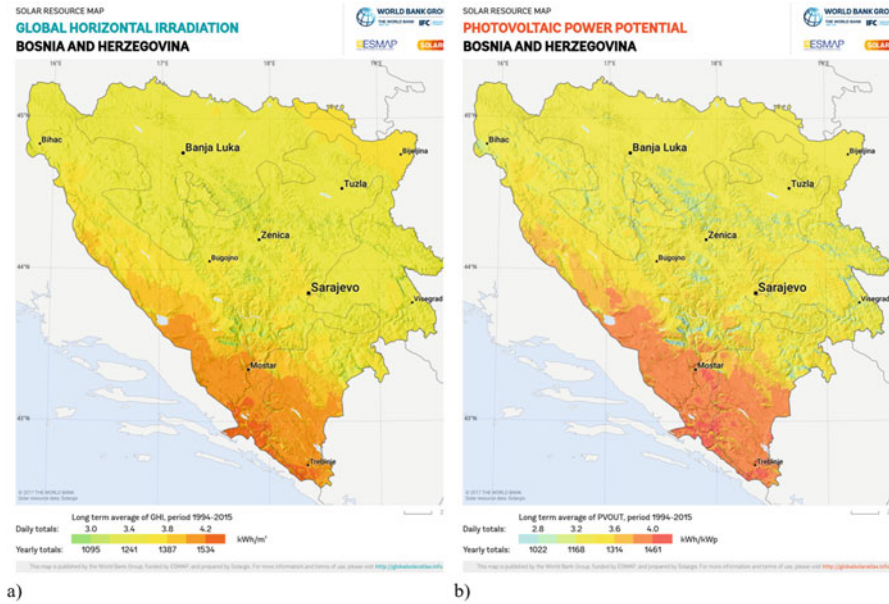


Fig. 1 (a) Global irradiation and (b) PV power potential – Bosnia and Herzegovina [5]

the sunlight hours in the northern parts of the country ranges from 1800 to 2000 h [6]. These statistics may be used to determine how much solar energy is available in a certain location. Solar energy may be employed everywhere, but the peculiarities of the geographical and climatic environment could have a significant influence on total performance, especially when considering the cost [7].

2 Types of Photovoltaic Systems

Photovoltaic (PV) systems are made up of cells that produce electricity from sunlight. Each cell has layers of semi-conducting material. As seen in Fig. 2, when light strikes the cell, an electric field that flows across the layers is created, enabling the flow of electricity. Each cell produces power quantity depending on the intensity of the light. The PV system does not require direct sunshine to work. It may also use reflected sunlight to create power on foggy and rainy days.

PV systems are classified into two categories:

- PV system that is not connected to the networks (*off-grid*) are sometimes referred to stand-alone system.
- A PV system that is directly connected to the networks (*on-grid*) is sometimes referred to as a grid-connected system.

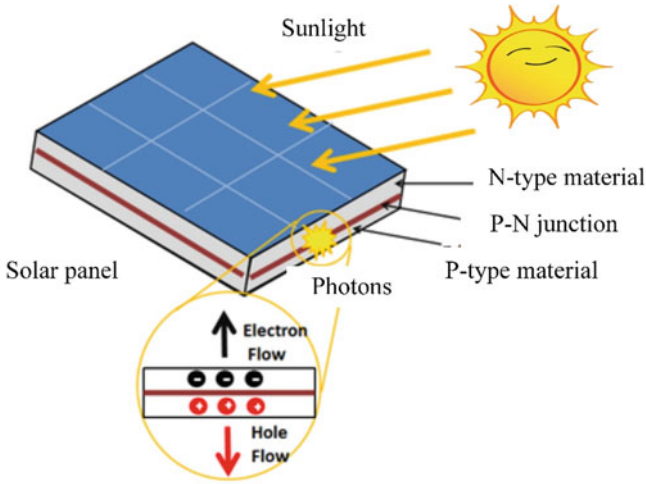


Fig. 2 The PV effect

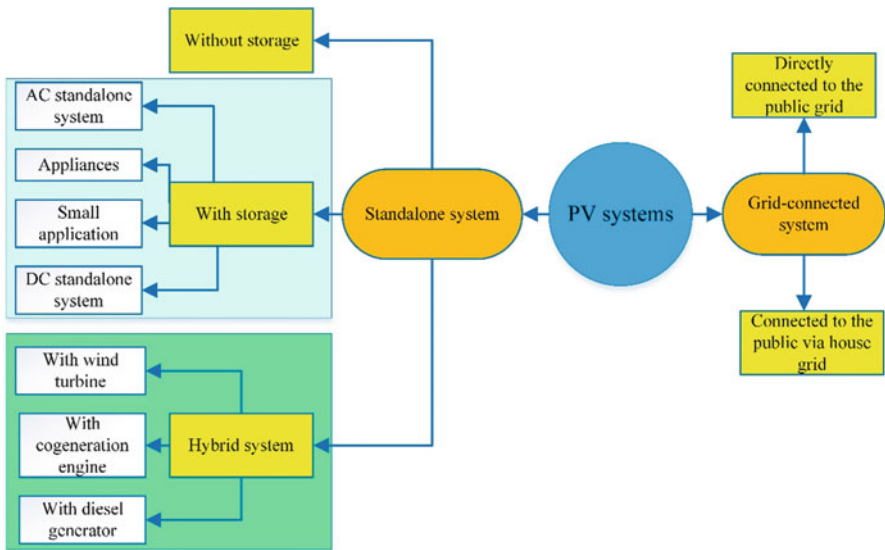


Fig. 3 Types of PV systems

Energy demand and solar energy production are matched in stand-alone PV systems. There is often a case where energy production from solar cells does not always match the energy consumption of linked loads, extra-large devices (batteries) can be commonly employed. A photovoltaic hybrid system is the system combined with other types of generators as it is diesel or wind. The public power grid serves as energy storage in grid-connected PV systems (Fig. 3).

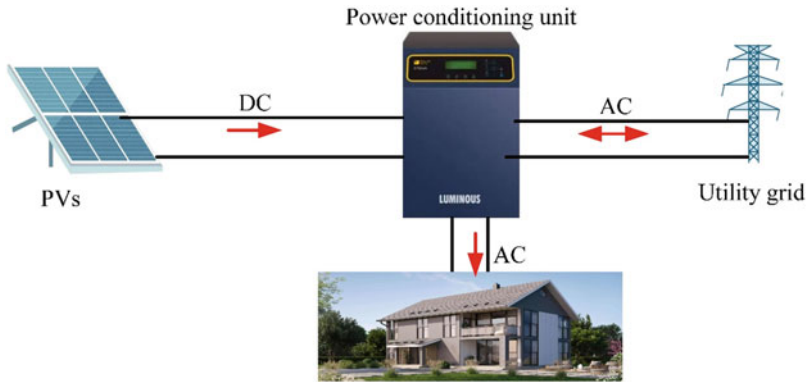


Fig. 4 Simplified grid-connected PV system

Because of market and PV advanced technologies, PV systems are now being installed not only in constructions and their current surroundings but also on free exteriors close to the main networks or in which there is no power utility, forming low, medium, or high voltage connection to the network.

Figure 4 depicts a basic grid-connected system with PVs delivering electricity to a construction. The PV array can be installed on a mast or affixed to the roofs from the outside, or it can be integrated into the building’s shell. Thin-film solar panels and PV shingles employed for glazing provide two functions: electricity and construction, and such a system is known as building-integrated photovoltaics in this instance. Grid-connected photovoltaic systems transmit dc electricity to a power conditioning unit (PCU), which transforms it to ac and distributes it to the construction. If a PV system is insufficient to meet the building’s immediate need, the PCU takes additional energy from the grid, ensuring that demand is met under any circumstances. If there is case where PVs generate more electricity than required, an extra generated amount can be routed back to the grid, theoretically turning the electric metre backwards. As weather changes, the PCU helps photovoltaic to run at its most efficient voltage and current.

Grid-connected PV systems get several advantages:

- Making pollution-free clean energy
- Zero transmission losses
- Consistent source
- Safe source
- Lower maintenance expenses than centralized manufacturing plants have.
- Installing PV systems in big centralized industrial systems is easier and more accessible.
- Installation and commissioning are quick and simple.

Figure 5 shows how PV system is comprised. It has two leads going from each string to combiner enclosure, which comprises blocking diodes, separate sign for

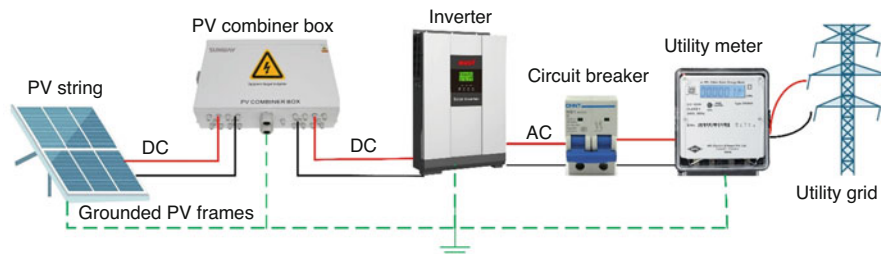


Fig. 5 PV system (grid-connected) with a single inverter's main components

every string, and, in most cases, lightning surge arrestors. A cable of two wires from the combiner enclosure sends dc power to fused arrays disconnect switches, which isolates the PVs from the system in the event of a breakdown. The inverter transfers ac power, generally at 240 V, to the service panel through a breaker. Either residential circuit receives 120-V electricity by connecting each end of the output's inverter to opposing sides of the service panel.

Not shown in the picture are other components that PV systems include, such as a maximum power point tracker (MPPT), a ground-fault circuit interrupter (GFCI) and circuitry to separate the PV system from the grid if the utility power loss occurs. GCFI is used to shut off the system if any current flows to the ground. A single PCU often contains the inverter, other fuses and switches, the MPPT, GCFI, and other different management components.

Inverters are often intended to function with 24-volt modules or serially connected pairs of 12-volt modules. Easy system expansion is possible if the PV systems are connected singly to the inverter. Individual inverters can be linked to solar arrays for PV systems with higher power production connected to the grid. The usage of costly DC wires is decreased to a minimum, resulting in a system that is less costly than one that uses a huge, central inverter.

3 Description of the First Grid-Connected Photovoltaic System in Bosnia and Herzegovina

The first grid-connected solar power system in Bosnia and Herzegovina was put into operation on 19/03/2012. The system can be housed on the roof of a gym in Kalesija, just outside of Tuzla. The system model is presented in Fig. 6, while the real situation is presented in Fig. 7. The photovoltaic system is directly linked to the electrical grid. The "Eko Energija" (*engl. "Eco-Energy"*) company from Kalesija, Bosnia and Herzegovina, has spent around 800,000 KM (approximately 400,000 €) on this photovoltaic system, with a nine-year payback predicted. This solar system has a capacity of 120 kW and is expected to provide 140 MWh of electricity per year. Table 1 provides general information about the photovoltaic system. SMA STP 1500

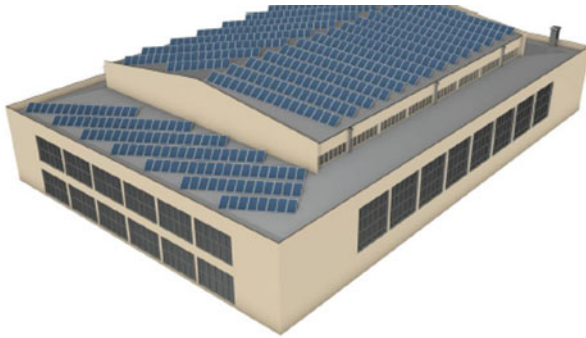


Fig. 6 Model of the PV system on gym rooftop [6]



Fig. 7 Current position of the PV modules

TL-10 type inverter is used to link the system to the network. Table 2 summarizes the inverter's characteristics, whereas Table 3 contains information about the solar modules. The appearance of the inverters and the modules are presented in Fig. 8a, b, respectively.

The PV system monitoring system was created by the Slovenian business Talum, and it allows for continuous monitoring of the system's daily functioning, as illustrated in Fig. 9. The technology employed is real-time data transmission, which provides a wide-range of possibilities for observing, managing, scheduling, maintenance, and failure interference. The RS485 serial bus connects the inverter to the communicator (WEB-BOX), periodically remembering all critical settings. As indicated in Fig. 10, the communicator can be fixed in the switchgear building's communication cabinet. A solar irradiation intensity sensor (sensor enclosure) can be mounted on the building's roof, allowing the system's efficiency to be monitored.

Table 1 Data on Bosnia and Herzegovina's first grid-connected PV system

Basic information	
Investors	EKO ENERGIJA d.o.o. Kalesija, BH
Hired	2012
Contractors	TALUM d.d. Slovenia
Solar Specifications	
Module type	REC 240 PE
Number of modules	520
Module's output power	240 W
Maximum AC power	120 kW
Estimated power production per year	140 MWh
Project Assessment	
Venture capital	800,000 KM (approx. 400,000 €)
Business assist	12 years
Repayment	9 years

Table 2 Inverter's characteristics

Class		SMA STP 15000TL-10
No. of inverters		8
Dimensions		664/690/264 mm
Weight		64 kg
Working temperatures		(-25 – +60) °C
Typology		Transformerless
Maximum DC power		15,340 W
Maximum DC voltage		1000 V
PV voltage range, MPPT		360 V–800 V/600 V
Maximum input current		33 A/11 A
Number of MPPT		2
Efficiency	Maximum	98.21%
	Minimum	97.81%

The SMA Sunny Portal, which offers online plant operating information, connects the system to the Internet. To provide better security, an alarm tool has been placed to send SMS alerts in the case of a breakdown, and it also acts as a point of entry from the outside.

Figure 11 shows the forecast electricity production and array efficiency of the photovoltaic system for the first 25 years. Annual production is shown by the red line, while efficiency is represented by the blue line.

Figure 12a depicts the total power generated by the solar system “Eko Energija” in August, the warmest and sunniest month of the year. The greatest production of 850 kWh was recorded on 13/08/2012. Except for 8th and 11th August, when it rained, the system was quite productive throughout the month since it was very bright and warm. Figure 12b depicts the solar system's entire power output throughout the winter of 2012, in December. On 27 December 2012, the greatest

Table 3 Solar module specification

Solar Module REC 240 PE	
Class	Polycrystalline
Frame colors	Clear
Dimensions	1665/991/38 mm
Area	1.66 m ²
Weight	18 kg
Power rating at STC	240 W
Power rating at PTC	218 W
Power per unit of area at STC	148.61 W/m ²
Peak efficiency	14.56%
No. of cells	60
Maximum current	8.05 A
Maximum voltage	29.91 V
Current of short circuit	8.6 A
Voltage of open circuit	27 V
NOCT	47.9 °C

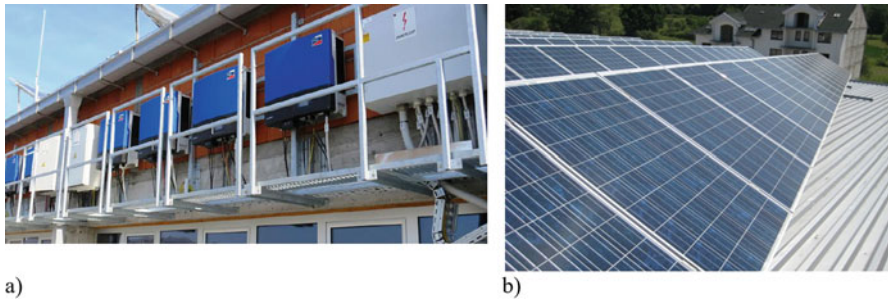


Fig. 8 The PV system: (a) inverters and (b) modules

production of 320 kWh was recorded. The solar inverter was used to create the production diagrams.

4 Power Quality Factors Measurement

The PQ presents an important characteristic for proper power system operation as well as proper customer appliance operation. Voltage frequency and phase synchronization allow the electrical system to perform in its anticipated way with no substantial loss of operation or life span. This refers to the load power as well as the capacity of the load for operating correctly. Electric equipment (or load) might cause failure, fail early, or not work at all if it doesn't have enough power. Low power quality can be reflected in different ways, as well as for a variety of other reasons [8, 9].

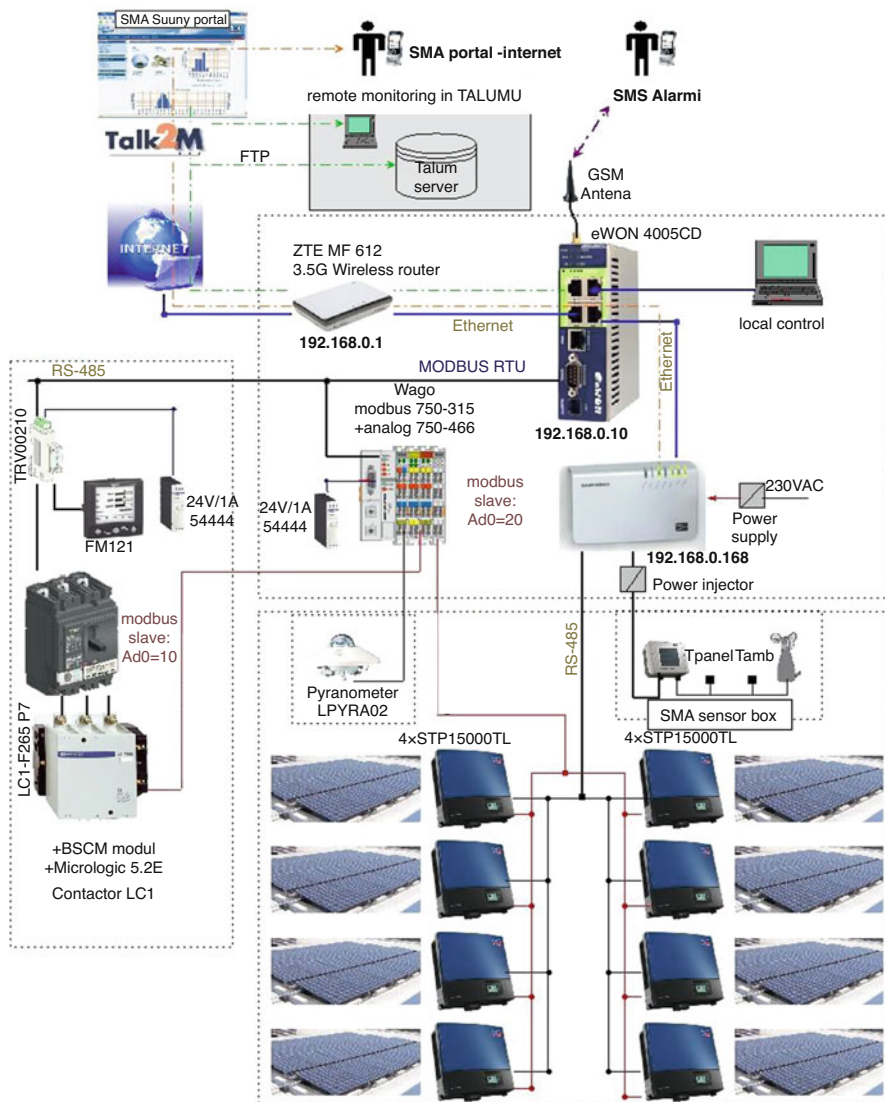


Fig. 9 Control system block diagram

Power quality can be defined as a collection of values for factors such as:

- Continuity in service
- Voltage and current oscillations
- Variation in voltage magnitude
- Harmonic disturbance in waveforms

Fig. 10 Communication cabinet



Under normal operating circumstances, European Standard EN 50160 [10] specifies the major voltage characteristics and their allowable difference range at the consumer's frequent connection in public low and medium voltage distribution networks.

Due to their electronic components, solar systems might have an influence on the power system, so power quality analysis must be measured and surveyed.

Parameters of power quality were checked a few times on the observed PV system during different seasons and weather conditions:

- 20/07/2012–24/07/2012 – summer
- 12/10/2012–17/10/2012 – autumn
- 06/12/2012–13/12/2012 and 28/12/2012–12/01/2013 – winter

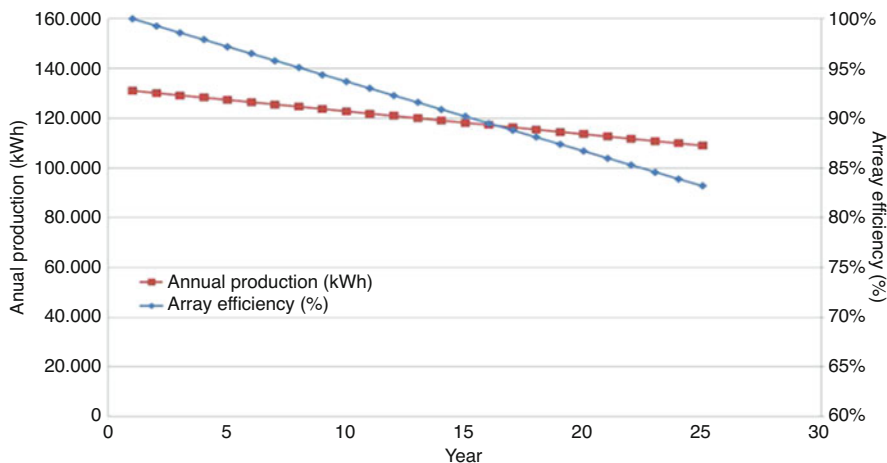
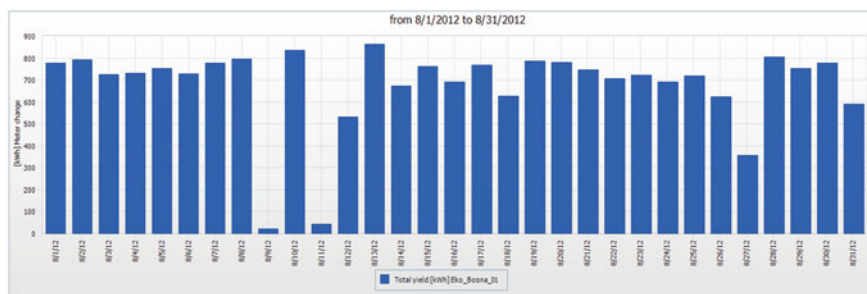
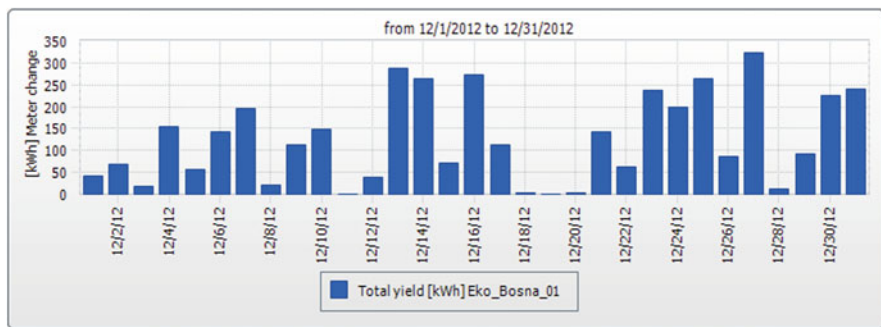


Fig. 11 The electricity production predicted for “Eko Energija” PV system



(a)



(b)

Fig. 12 The PV system electricity production: (a) August 2012 and (b) December 2012

Three-Phase PQ Analyzer – Fluke 434, as shown in Fig. 13, was used to measure power quality parameters. The instrument compares the findings to the EN

Fig. 13 Three-phase PQ analyzer – Fluke 434 [11]

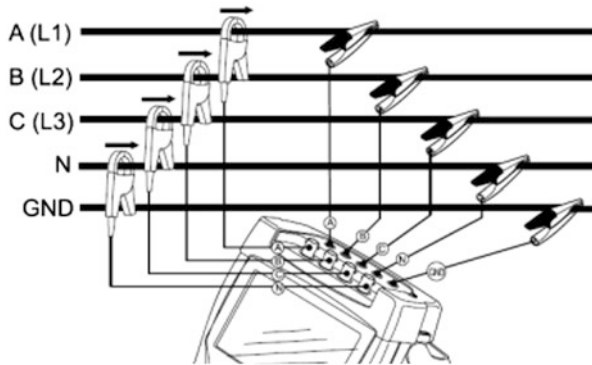


Fig. 14 The test setup

50160:2004 European Standard. Voltage and current waveforms were also recorded under varied weather circumstances, in addition to power quality measures. Figure 14 depicts the instrument’s connection to the three-phase system. Figure 15 depicts the specific configuration of the PV system “Eko Energija” distribution cabinet.

Voltage and current waveforms noted at 14:00:22 on 12/10/2012 are shown in Fig. 16a, b, respectively. It was evident that the voltage profile might be depicted as an almost clear sine wave, even though that was not the issue with the current. The transformerless inverter that links the evaluated PV system to the distribution system must give the system’s optimum operating position on the I-V characteristic. The system’s operational settings are altered throughout the day. The effect of changing the optimal operating position of PV systems is particularly noticeable for appliances without transformers. The inverter contains two appliances that track the MPP, which is why the current waveform is not sine. Because of the overcast



Fig. 15 PQ parameters measurement look on (a) whole cabinet and (b) instruments [12]

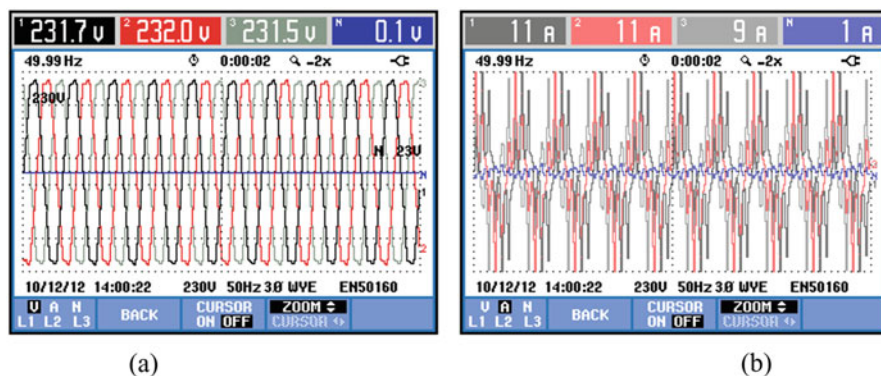


Fig. 16 Waveforms: (a) voltage, (b) current, 12/10/2012 – cloudy weather [13]

weather, there is a minimal quantity of electrical output. On a snowy and overcast day at 16:43:21 on 06/12/2012, the voltage (Fig. 17a) was a very clear sin wave while the current (Fig. 17b) was a small and bad waveform. When the weather is bright, as it was at 13:26:26 on 12/01/2013, the waveform of voltage (Fig. 18a) was similar as in the previous case in December, while the current was higher than in December with quite a good sin wave.

Due to the sunny day, more energy was produced in January than in December. Even though it was a different season, the voltage and current waveforms displayed in Fig. 19a, b on 29/04/2013 are quite similar to those shown in Fig. 18a, b.

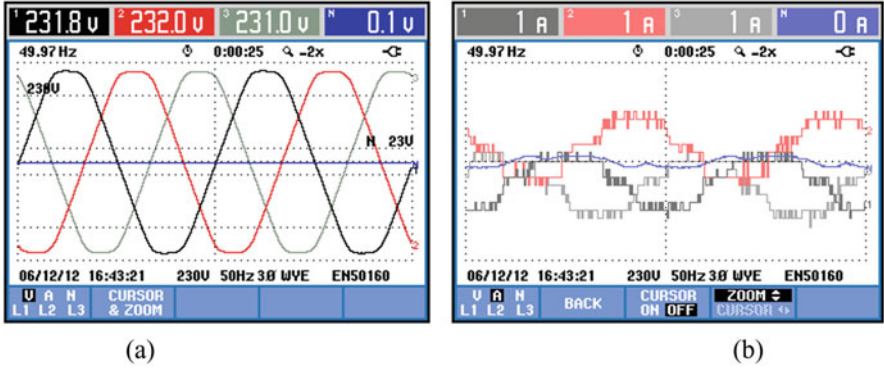


Fig. 17 Waveforms: (a) voltage, (b) current, 06/12/2012 – cloudy [13]

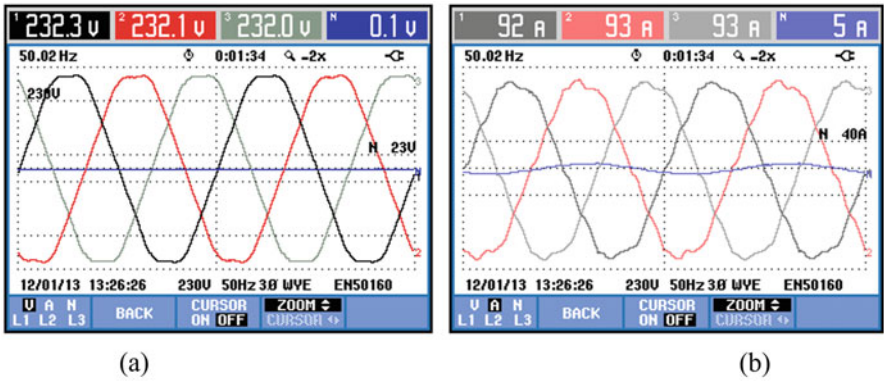


Fig. 18 Waveforms: (a) voltage, (b) current, 12/01/2013 – sunny [13]

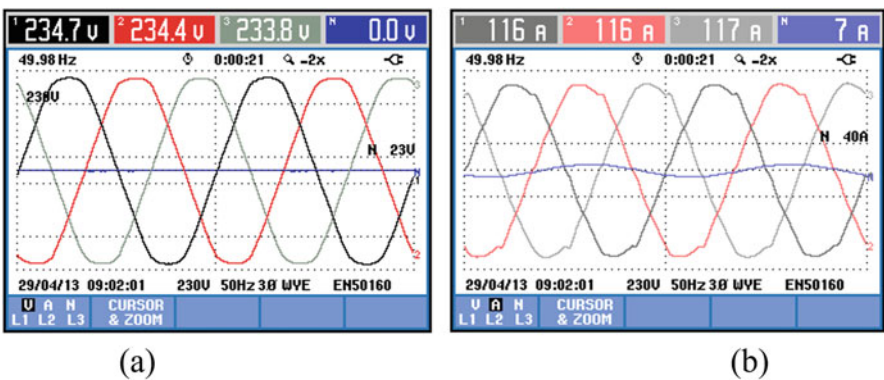


Fig. 19 Waveforms: (a) voltage, (b) current, 29/04/2013 – sunny [13]

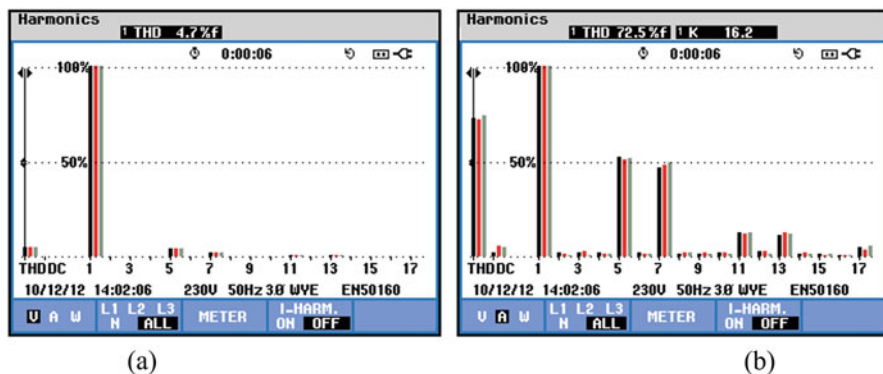


Fig. 20 Harmonic components and *THD*: (a) voltage, (b) current, 12/10/2012 [13]

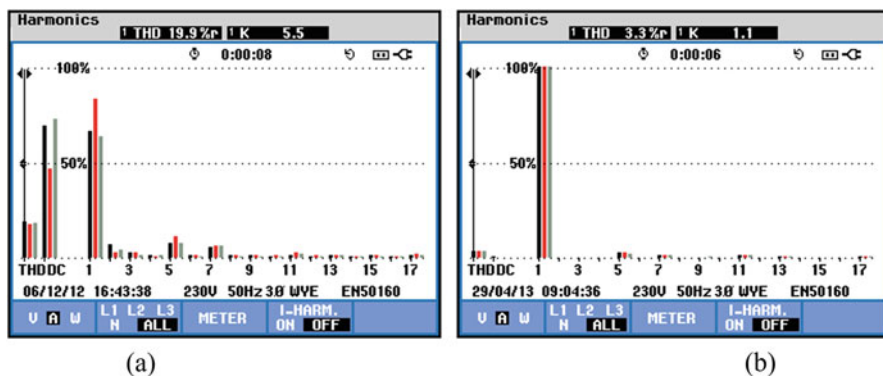


Fig. 21 Harmonic components and *THDI*: (a) 06/12/2012 – cloudy, (b) 29/04/2013 – sunny [13]

It may be inferred that the PV system's productivity is determined by solar irradiation angle rather than outage temperature [13]. The main reason for high production is higher solar radiation during sunny days [14–17]. There is no difference between whether a sunny day occurs during the summer or any other season. On a sunny day in January and April, the current was 92 A (Fig. 18b) and 116 A (Fig. 19b), respectively, while on the cloudy day in October and December, the current was 11 A (Fig. 16b) and 1 A (Fig. 17b), respectively.

On 12/10/2012, voltage harmonic components and *THDU* were measured, and current harmonic components and *THDI* were measured (Fig. 20). The PQ analyzer examines *THDI* and the current harmonic component in accordance with IEC 61000-4-30 guideline [18]. Harmonic components of current are larger than harmonic components of the voltage, although they are even within acceptable limits. The current harmonic components of the “Eko Energija” PV system sent to the distribution grid are shown in Fig. 21a, and the overall harmonic distortion of current is shown in Fig. 21b. Whether the weather is sunny or overcast, harmonic

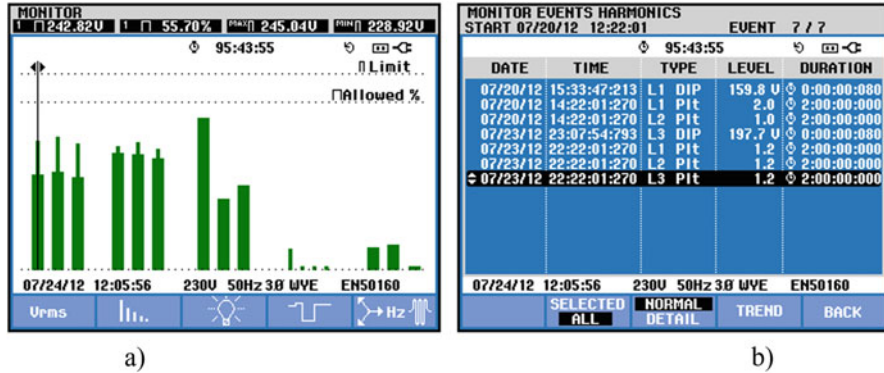


Fig. 22 (a) PQ parameters and (b) Events in accordance with EN 50160, 20/07/2012–24/07/2012 [13]

components were smaller than the permissible by the Standards in each case. Fifth and seventh current harmonics were dominant in both circumstances.

Figure 22a displays the values of power quality characteristics recorded in July 2012 by the PV system “Eko Energija.” The findings are presented in the form of columns and may be matched to the EN 50160:2004 guideline. The first three sets of three columns, from left to right, reflect the efficient value of voltage, harmonics, and flicker for each phase separately. The following columns depict sags, interruptions, fast voltage shifts, imbalance, frequency, and mains signaling, with each bar being added up for all three phases as the factor value goes away from the nominal value and the height of the column changes. Columns are ready to adjust color from green to red if the value of any parameter is larger than the recommended value. The power quality analyzer may also pinpoint when a disturbance occurred, such as a flicker, voltage sags, or swells. Figure 22b depicts the events that happened in relation to PQ. There were two voltage dips and five flickers throughout this testing period; however, the total value for calculating the time of any of these illnesses is not greater than the typically allowed limits.

THD and harmonic components in L1, L2, and L3 are shown in Fig. 23a–c, respectively. THD stands for Total Harmonic Distortion, which is defined as any phase with a THD of less than 8%, which is the maximum allowable value. The fifth and seventh harmonic components, both in Standard permitted values, are dominant harmonic components. Figure 24a–c shows the third, fifth, and seventh harmonic component trends observed from 20/07/2012 to 24/07/2012.

The outcomes of several measurements of PQ parameters are shown in Figs. 25a, b, 26a, b, and 27a, b. No disorders occurred, either from the PV system to the grid or the other way around, through the second and third measurement period, as indicated in Figs. 25b and 26b, respectively. There were eight voltage sags and four flickers during the final test, as shown in Fig. 27b, although neither of these diseases for observed time exceeded typical permitted limits.

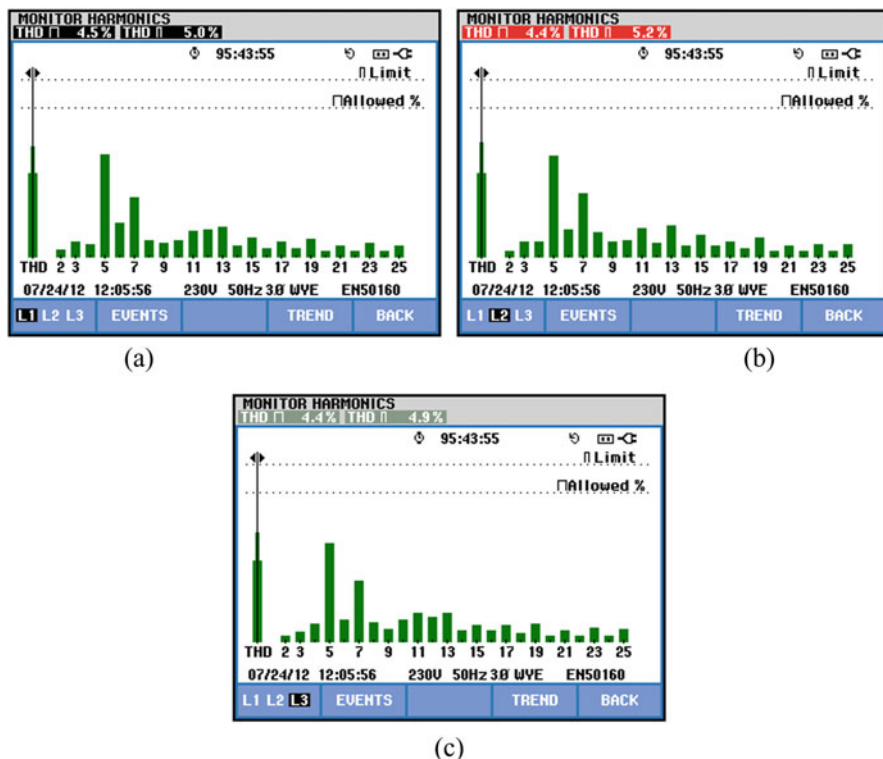


Fig. 23 Harmonic components and *THD*: (a) L1, (b) L2, (c) L3, 20/07/2012–24/07/2012 [14]

THD and harmonic components for L1, L2, and L3 are shown in Fig. 28a–c. *THD* is defined as the percentage of each phase that is less than or equal to 8%, which is the maximum allowable value. In Standard permitted values, the dominant harmonic components are the fifth and seventh. The third, fifth, and seventh harmonic component trends are presented in Fig. 29a–c over the measurement period of 12/10/2012–17/10/2012.

Standard voltage standards are followed by the photovoltaic system. Voltage imbalance is depicted in Fig. 30a, b for 20/07/2012–22/07/2012 and 12/10/2012–17/10/2012, respectively. Voltage imbalance is 0.2% in both situations at its maximum point, which is much below the 2% restriction. Figure 31 shows an example of a measurement report generated by the PQ analyzer program.

After analyzing the outcomes of measuring the PQ implemented in different weather circumstances, it could be settled that “Eko Energija” grid-connected PV system complies with guidelines as defined in EN 50160 guideline regarding point of connection to the distribution grid, and as a result, has no overall negative impact on the grid. Table 4 [14] summarizes the findings of all measurements.

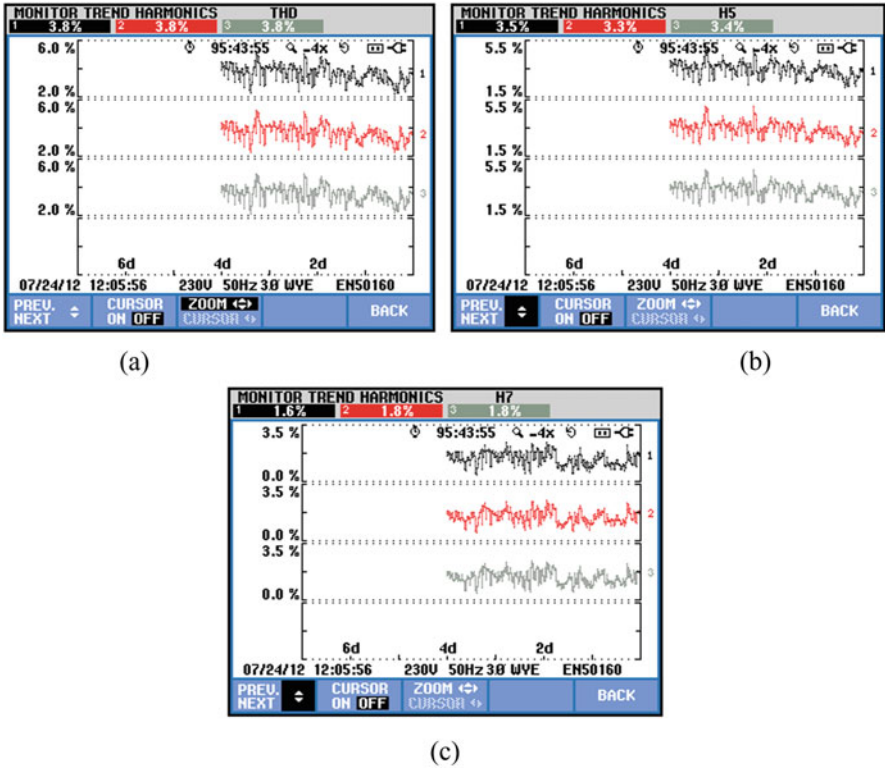


Fig. 24 Harmonic components trend: (a) third, (b) fifth (c), seventh, 20/07/2012–24/07/2012 [14]

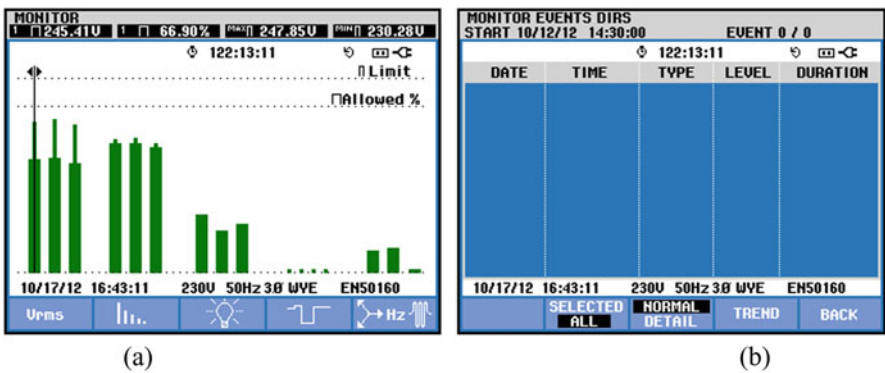


Fig. 25 PQ (a) parameters and (b) events in accordance with EN 50160, 12/10/2012–17/10/2012 [13]

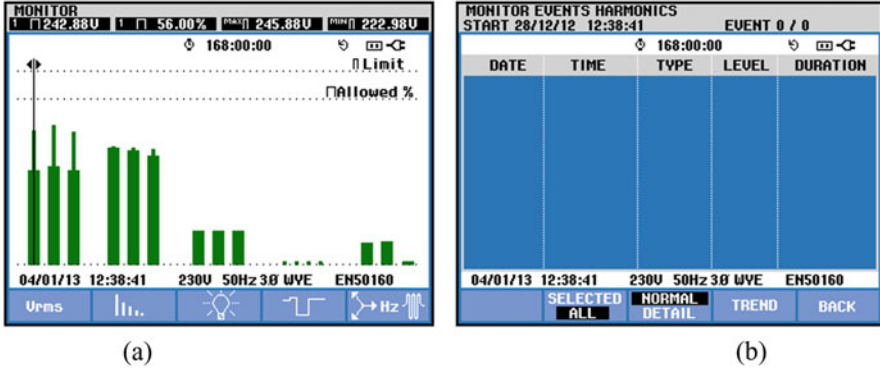


Fig. 26 (a) PQ parameters, (b) PQ events in accordance with EN 50160, 28/12/2012–04/01/2013 [13]

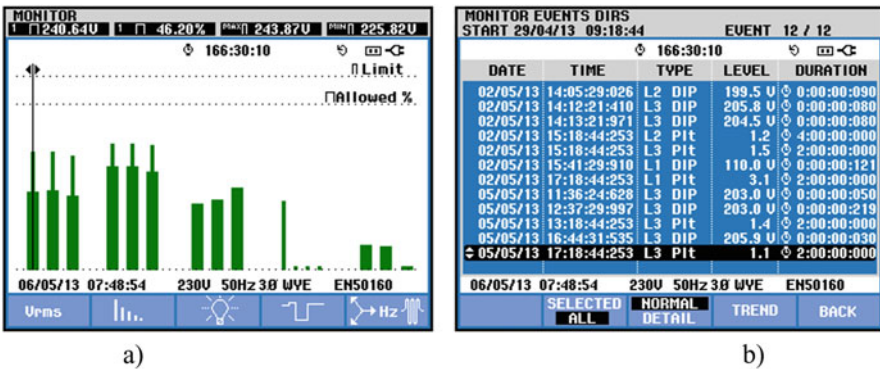


Fig. 27 (a) PQ parameters, (b) PQ events in accordance with EN 50160, 29/04/2013–06/05/2013 [13]

5 Conclusions

European Union standards obligate Bosnia and Herzegovina to improve power output from renewable sources. Photovoltaic systems have been increasingly integrated into Bosnia and Herzegovina’s electrical supply in recent years. In March 2012, Bosnia and Herzegovina commissioned the first solar system with a capacity of 120 kW. The PV system “Eko Energija” was used to assess power quality

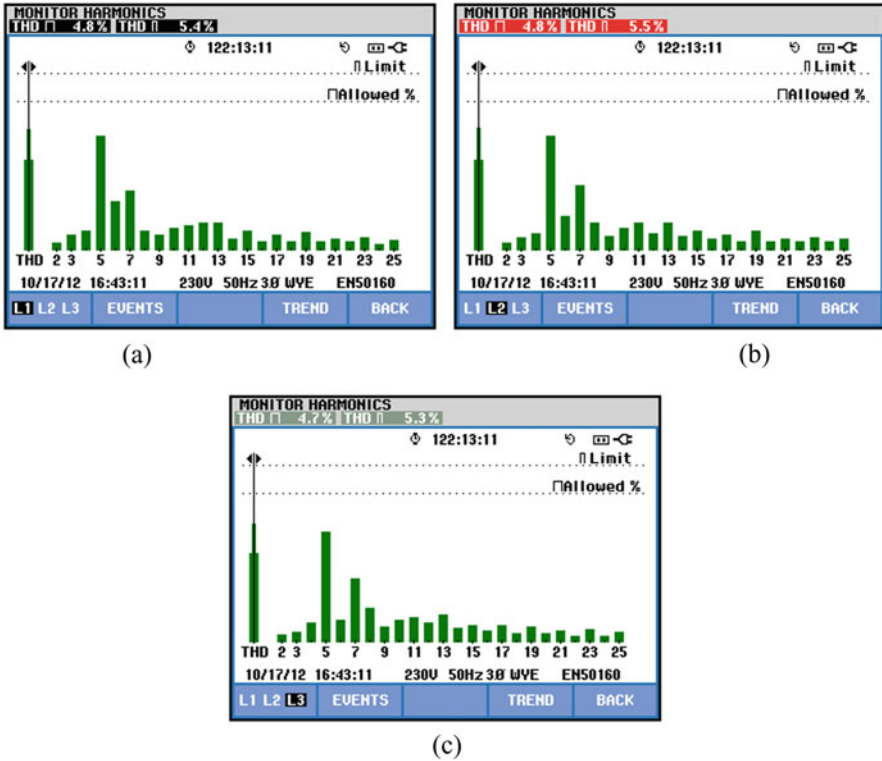


Fig. 28 Harmonic components and THD: (a) L1, (b) L2, (c) L3, 12/10/2012–17/10/2012 [14]

characteristics since photovoltaic systems, and RESs might have an influence on the distribution network’s quality. When the measured values of PQ parameters are compared to the EN 50160 guidelines, it may be determined that the solar system in question completely conforms with the applicable guidelines regarding the connection point to the distribution grid. The PV system produces a varying amount of harmonic components during its operation, all depending on the weather conditions. On the other hand, Harmonic current components are minimal and, in any event, do not surpass the limits set by applicable regulations.

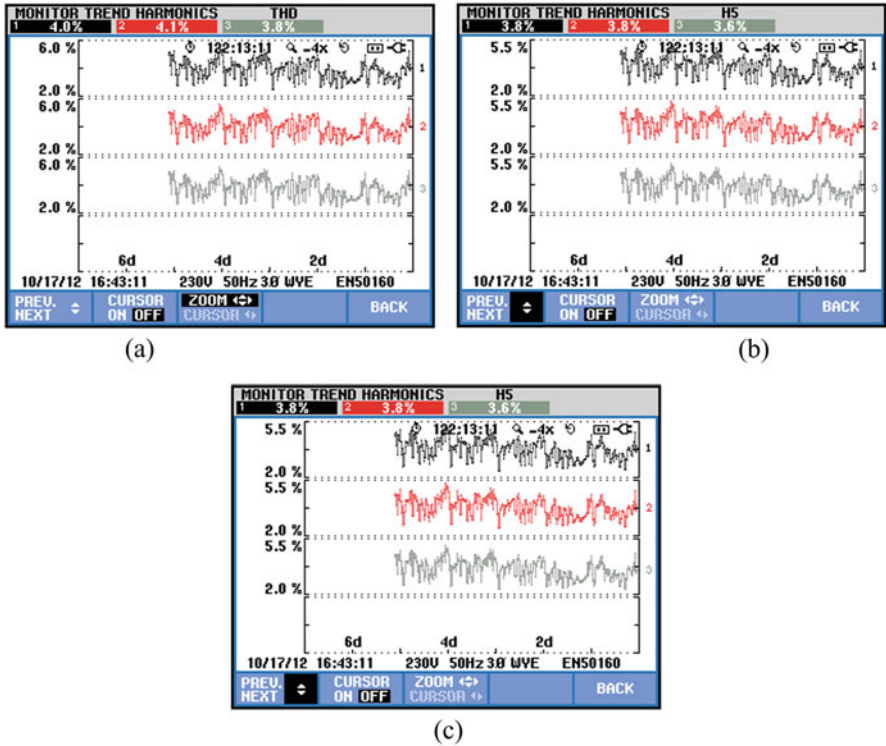


Fig. 29 Harmonic components trend: (a) third, (b) fifth, and (c) seventh, 12/10/2012–17/10/2012 [14]

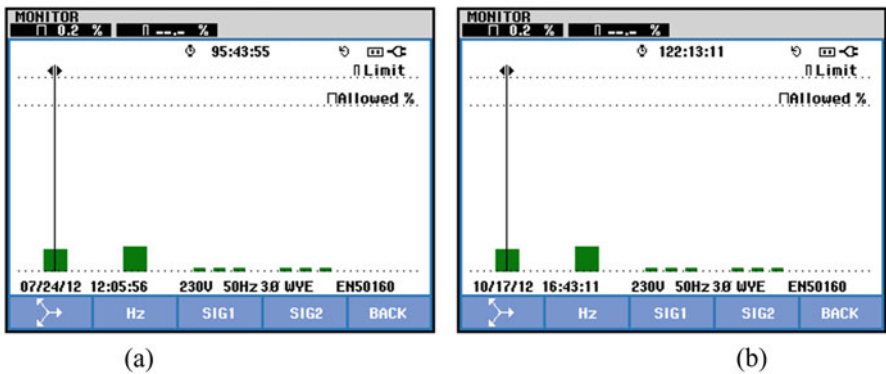


Fig. 30 Voltage imbalance: (a) 20/07/2012–24/07/2012, (b) 10/10/2012–17/10/2012 [14]

Limit Summary:		
RMS	> 207.0 V < 253.0 V	95.0 % of time
THD	< 8 %	100 % of time
Plt	< 1	95.0 % of time
Dip	< 207 V	20 / week
Swell	> 253 V	20 / week
Unb.	< 2 %	95.0 % of time
Hz	> 49.5 Hz < 50.5 Hz	99.5 % of time

Fig. 31 The PQ analyzer package measurement information, 20/07/2012–24/07/2012 [14]

Table 4 Measurement brief

Measuring facility/location	“Eko-Energija” grid-connected PV system, Kalesija, BH	
Instrument	Three-phase PQ analyzer – Fluke 434	EN 50160
1st calibration	20/07/2012–24/07/2012	Fulfill
2nd calibration	12/10/2012–17/10/2012	Fulfill
3rd calibration	06/12/2012–13/12/2012	Fulfill
4th calibration	28/12/2012–01/01/2013	Fulfill
5th calibration	29/04/2013–06/05/2013	Fulfill

References

- Omar AI, Ali ZM, Al-Gabalawy M, Abdel Aleem SHE, Al-Dhaifallah M (2020) Multi-objective *environmental* economic dispatch of an electricity system considering integrated natural gas units and variable renewable energy sources. *Mathematics* 8(7):1100
- Rawa M et al (2021) Economical-technical-environmental operation of power networks with wind-solar-hydropower generation using analytic hierarchy process and improved grey wolf algorithm. *Ain Shams Eng J* 12(3):2717–2734
- European Commission (2010) Energy 2020, a strategy for competitive, sustainable and secure energy. Publication Office of the European Union, Brussels, Belgium
- Vukmir G, Stanišljević L, Cero M et al (2009) Initial national communication of Bosnia and Herzegovina under the United Nations framework convention on climate change (UNFCCC), Banja Luka, Bosnia and Herzegovina
- <https://globalsolaratlas.info/downloads/bosnia-and-herzegovina>, accessed: July 2019
- Verdenik A, Kovačić D, Dobrun T (2012, June) Izgradnja prve solarne elektrane u Bosni i Hercegovini. In: International conference Energa, Tuzla, Bosnia and Herzegovina
- Omar AI, Khattab NM, Abdel Aleem SHE (2022) Optimal strategy for transition into net-zero energy in educational buildings: a case study in El-Shorouk City, Egypt. *Sustain Energy Technol Assessments* 49:101701
- Masters GM (2004) Renewable and efficient electric power systems. John Wiley & Sons Inc., New Jersey, USA

9. Omar AI, Abdel Aleem SHE, El-Zahab EEA, Algablawy M, Ali ZM (2019) An improved approach for robust control of dynamic voltage restorer and power quality enhancement using grasshopper optimization algorithm. *ISA Trans* 95:110–129
10. European standard EN 50160 Voltage characteristics of electricity supplied by public distribution systems, CENELEC TC 8X, 2006
11. Fluke 434/435 Three phase power quality analyzer, Users manual, Everett, Washington, USA, Fluke Corporation, 2006
12. Ahmedić J (2016) Tehnoekonomska analiza pogona fotonaponskih sistema, master thesis, Faculty of Electrical Engineering, University of Sarajevo, Bosnia and Herzegovina
13. Lešić M, Konjić T, Kurtić A, Tomljenović T (2013) Uticaj fotonaponskih sistema na kvalitet električne energije u distributivnoj mreži, Neum, Bosnia and Herzegovina, 11. Savjetovanje BH K Cigre
14. Lešić M, Konjić T (2018) Power quality field measurements on photovoltaic system. In: Hadžikadić M, Avdaković S (eds) *Advanced technologies, systems, and applications II*. IAT 2017. Lecture notes in networks and systems, vol 28. Springer, Cham
15. Zobaa A, Aleem SA Uncertainties in modern power systems, ISBN 978-0-12-820491-7, Elsevier. <https://doi.org/10.1016/C2019-0-01693-7>
16. Omar AI, Ali ZM, Abdel Aleem SHE, El-Zahab EEA, Sharaf AM (2019) A dynamic switched compensation scheme for grid-connected wind energy systems using cuckoo search algorithm. *Int J Energy Convers* 7(2):64–74
17. Omar AI, Sharaf AM, Shady A, Mohamed AA, Essam EZ (2019) Optimal switched compensator for vehicle-to-grid battery chargers using Salp optimization. In: 2019 21st International Middle East Power Systems Conference, MEPCON 2019 – Proceedings, pp 139–144
18. IEEE recommended practices and requirements for harmonic control in electrical power systems. IEEE Std. 519–1992, IEEE New York, 1993

Optimal Coordination of Distributed Generation Units and Shunt Capacitors in Egyptian Distribution System Using Sine-Cosine Optimization Algorithm



Moustafa M. Ahmed, Muhyaddin Rawa, Ahmed M. Ibrahim, Hala M. Abdel Mageed, and Shady H. E. Abdel Aleem 

Abbreviations

AHP	Analytic hierarchy process
CO and CO ₂	Carbon monoxide and carbon dioxide
DGU	Distributed generation unit
EGWA	Enhanced grey wolf algorithm
GA	Genetic algorithm
GOA	Grasshopper optimization algorithm
KCL and KVL	Kirchhoff's current and voltage laws
LF	Load flow
LLL	Light loading level
MLL	Moderate loading level
MO	Multi-objective
NSO	Normalized single-objective
PLL	Peak loading level
PQ	Power quality

M. M. Ahmed
Electrical Power Department, Faculty of Engineering, Cairo University, Giza, Egypt

M. Rawa
Department of Electrical and Computer Engineering, Engineering College, King Abdulaziz University, Jeddah, Saudi Arabia
e-mail: mrawa@kau.edu.sa

A. M. Ibrahim · H. M. Abdel Mageed
National Institute of Standards, Giza, Egypt

S. H. E. Abdel Aleem (✉)
Electrical Engineering and Electronics Department, Valley Higher Institute of Engineering and Technology, Science Valley Academy, Al-Qalyubia, Egypt
e-mail: engyshady@ieee.org

PSO	Particle swarm optimization
RDN	Radial distribution network
SCO	Sine-cosine optimization
SCS	Shunt capacitors
SS	Search space
VRES	Variable renewable energy source
WOA	Whale optimization algorithm
WSAS	Weighted sum average strategy

Nomenclature

[BCBV]	Branch-current-to-bus-voltage matrix
[BIBC]	Bus-injection-to-branch-current matrix
[MM]	Multiplication matrix
ACost _{DG} and ACost _{SC}	Total annualized DGUs and SCs costs (\$/year)
BC_i	i th branch current
C_{SC}	Instalment cost of the SCs
CRF _{DG} and CRF _{SC}	Capital recovery factors of DGUs and SCs
ΔV	Voltage drop
δ	Factor represent the limit of DGUs penetration
F_1^{\max} , F_2^{\max} and F_3^{\max}	Maximum values specified by the designer to normalize the OFs
I_i	i th bus injection current
i	Bus number
i_e and y_e	Interest rate and lifetime of each equipment (e)
$I_{\max,m}$	Maximum allowed branch current
iter	Iteration number
iter _{max}	Maximum iteration number
K_{DG} and K_{SC}	Operation and maintenance costs of DGUs and SCs
LC	Per-unit maximum loading capacity of the branches
LL	Number of hours per loading level
λ	Weighting factor
m	Number of branches
n	Total bus number
N_b	Total number of branches
N_{DG} and N_{SC}	Total number of DGUs and SCs
N_L	Number of the loading levels
OF	Objective function
PF	System power factor
PF _{min} and PF _{max}	Minimum and maximum PF
P_i	Active load power at bus i
Q_i	Reactive load power at bus i
P_{DG} and Q_{SC}	DGUs size (kW) and SCs sizes (kvar)

P_{loss} and Q_{loss}	Active and reactive power loss
P_{utility} and Q_{utility}	Utility active and reactive power
k_1 and k_2	Tariff rate of the energy (\$/kWh) and apparent power (\$/kVAh)
R/X	Resistance-to-reactance ratio
$X_{i,\text{SCO}}^t$ and $X_{i,\text{SCO}}^{t+1}$	Current and the next positions of the i th population at iteration t in SCO
S_i	Complex apparent load at bus i
S_{utility}	Contracted apparent power from the utility
V_1	Slack bus or substation voltage
V_i	i th bus voltage
V_{min} and V_{max}	Minimum and maximum voltage magnitude
Z_{ij}	Impedance between buses i and j

1 Introduction

Several problems face conventional fossil fuel-based technologies. Diminution of fuel resources, fluctuations of global fuel prices, and complexity in fuel transportation, particularly with COVID-19 pandemic issues that the world is facing these days, global warming, and greenhouse gas emissions such as carbon dioxide (CO_2), carbon monoxide (CO), and other hazardous gases that result in terrain and climate change are examples of these problems [1, 2]. This has motivated researchers to find alternatives to replace fossil fuel-based technologies with renewable energy-based technologies and enhance the new technologies' performance [3].

The high penetration of these renewable-based energy generation technologies in conventional unsupported "deteriorated" distribution systems can pose various problems such as overvoltage, harmonic distortion, increased line losses, and increased short-circuit capacities resulting in protection failure [4, 5]. Accordingly, the integration of distributed generation units (DGUs) into power distribution networks should be codified so as not to pose problems in these power systems. Optimal placing and sizing of DGUs will definitely minimize power losses in the network, reduce generation and transmission costs, and diminish harmful emissions. Besides, reactive power flow control by shunt capacitors (SCs) will positively impact the performance of power systems, either to compensate loads or support voltage. Again, finding their optimal location and size in a system is necessary [6].

In addition, the particular topology of radial distribution networks (RDNs), high resistance-to-reactance (R/X) ratios, the misuse and exploitation of these systems, specifically with increased variable renewable energy sources (VRESs) that are added in these networks, increased load demands, and nontechnical losses are leading to a significant decrease in voltage magnitude of some buses in these networks with a rapid increase in energy losses and voltage drop values. Besides, some of the RDN's elements may overload.

In Egypt, to encounter the increasing load growth and hurry too much to higher levels of VRESs production, Egypt has established a promising energy strategy until 2035 to diversify the power generation mix among fossil fuel-based plants. Therefore, improving the power quality (PQ) performance levels of RDNs has become an authoritative goal for system operators to host ambitious renewables.

Many research works have focused on finding either the optimal allocation of SCs or DGUs individually in the literature. However, it was found that their simultaneous optimal allocation in RDNs can result in better results [7]. Few researchers have paid attention to their simultaneous optimization problem. In [8], optimal placement and sizing of DGUs and SCs problems were solved using a hybrid genetic algorithm (GA) and imperialist competitive algorithm to enhance power loss reduction, voltage regulation, and stability. Further, in [9], the same problem was solved using GA in RDN from the point of view of a distribution company to minimize the total cost over the planning period. In [10], a hybridization between harmony search algorithm and particle artificial bee colony algorithm was introduced to obtain the DGUs' and SCs' optimal locations in RDNs to enhance voltage stability and reduce losses. In [11], a two-stage multi-objective fuzzy-based grasshopper optimization algorithm (GOA) based is proposed for allocating SCs, DGUs, and charging stations to charge electric vehicles in RDNs. GA was used again in [12] to allocate DGUs and SCs based on improving voltage, reducing the current drawn from the grid, and minimizing the annualized energy and power losses. In [13], optimal locations of DGUs and SCs were found in three RDNs (33-node, 69-node, and 119-node) based on minimization of active power losses and voltage deviation using an improved GA. In [14], the optimally coordinated allocation problem of DGUs, SCs, and voltage regulators in Egyptian RDN was solved using an enhanced grey wolf algorithm (EGWA). The results obtained indicated that the improved grey wolf algorithm outperformed other algorithms in the literature regarding power losses, loading capacity, and minimum voltage magnitude. Recently, because of the increase of nonlinear loads and inverter-based DGUs that result in harmonic distortion in RDNs, in [15], inverter-based DGUs and SCs were allocated using hybrid particle swarm optimization and gravitational search algorithm for power loss minimization. However, hybrid methods or two-stage methods used are complex-level algorithms, which consume almost double the time to reach a solution [16, 17]. Also, it is clear that no optimization method has been evidenced to be the most suitable method in the simultaneous allocation of DGUs and SCs, and no guarantee is observed for realizing global solutions of the different systems.

In this work, thoughtful coordination of DGUs and SCs in Egyptian RDN is presented to increase resiliency and enhance the reliability of this system. The sine-cosine optimization (SCO) algorithm was used to solve the formulated multi-objective (MO) constrained optimization problem. The various objectives presented in this work aim to reduce the operating costs of the system and investment expenses for the proposed coordinated DGUs and SCs in the system while maximizing the benefits of reducing energy loss and contracted power from the utility, in addition to improving the voltage profile and loading capacity of the system. Three

different loading levels were investigated in this work. Various linear and nonlinear constraints were taken into account. A weighted sum approach using the well-known analytic hierarchy process (AHP) was used to transform the MO problem into a normalized single-objective (NSO) optimization problem.

Numerical calculations and examples supplement the procedure employed in this paper to help explore the article in a straightforward way. It can be helpful to power system studies and engineers interested in optimizing modern power systems with renewables and energy storage technologies [18–21].

The rest of the work is arranged as follows: Sect. 2 presents an illustrative analysis of the used load flow (LF) methodology. Section 3 introduces the formulation of the optimization problem – objectives, constraints, weighted sum-based AHP approach, and the optimization algorithm. Section 4 explores the system under study and its base results calculated before compensation. Section 5 presents the results obtained after compensation via the coordination DGUs and SCs in Egyptian RDNs using SCO. Finally, Sect. 6 presents the conclusions of this study and the possible future work directions.

2 Analysis of the Load Flow (LF) Methodology

Due to the particular topology of radial distribution networks (RDNs), the LF presented in [22] is used for LF analysis. The methodology relies on two matrices, the bus-injection-to-branch-current matrix, denoted as $[BIBC]$, and the branch-current-to-bus-voltage matrix, denoted as $[BCBV]$. A straightforward multiplication matrix $[MM]$ is then formed to get LF solutions. This methodology is often robust, effective, and efficient in solving LF in RDNs. The LF methodology is described clearly in this section using an illustrative 7-bus RDN, shown in Fig. 1. BC_i

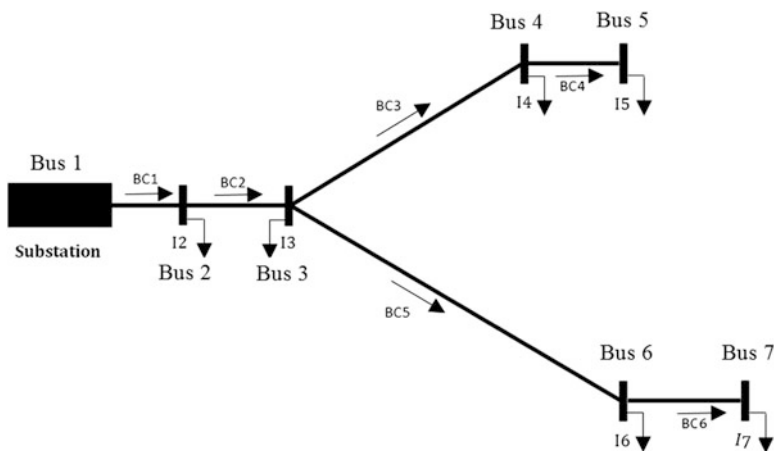


Fig. 1 A simple 7-bus RDN

represents the i th branch current, and I_i represents the i th bus injection current, where i denotes the bus number. At each i , one can calculate the complex apparent load power S_i as follows:

$$S_i = P_i + jQ_i, \forall i \in n \quad (1)$$

where P_i and Q_i denote the active and reactive load power at bus i , respectively, and n denotes the total bus number, i.e., $n = 7$. The current injection at iteration (iter) is specified using P_i , Q_i , and the i th bus voltage, V_i , as follows:

$$I_i^{\text{iter}} = \left(\frac{P_i + jQ_i}{V_i^{\text{iter}}} \right)^*, \forall i \in n, \forall \text{iter} \in \text{iter}_{\text{max}} \quad (2)$$

The iteration number (iter) should be less than or equal to the maximum iteration number specified (iter_{max}). Hence, using Eq. (2), equivalent bus current injections are obtained. Further, the branch currents can be found from Kirchhoff's current law (KCL) applied to RDN; thus:

$$\begin{aligned} \text{BC}_6 &= I_7 \\ \text{BC}_5 &= I_6 + \text{BC}_6 = I_6 + I_7 \\ \text{BC}_4 &= I_5 \\ \text{BC}_3 &= I_4 + \text{BC}_4 = I_4 + I_5 \\ \text{BC}_2 &= I_3 + \text{BC}_3 + \text{BC}_5 = I_3 + I_4 + I_5 + I_6 + I_7 \\ \text{BC}_1 &= I_2 + \text{BC}_2 = I_2 + I_3 + I_4 + I_5 + I_6 + I_7 \end{aligned} \quad (3)$$

Hereafter, one can formulate the relation between the branch and load currents. Putting it in the matrix form, thus:

$$\begin{bmatrix} \text{BC}_1 \\ \text{BC}_2 \\ \text{BC}_3 \\ \text{BC}_4 \\ \text{BC}_5 \\ \text{BC}_6 \end{bmatrix} = \begin{bmatrix} 1 & 1 & 1 & 1 & 1 & 1 \\ 0 & 1 & 1 & 1 & 1 & 1 \\ 0 & 0 & 1 & 1 & 0 & 0 \\ 0 & 0 & 0 & 1 & 0 & 0 \\ 0 & 0 & 0 & 0 & 1 & 1 \\ 0 & 0 & 0 & 0 & 0 & 1 \end{bmatrix} \times \begin{bmatrix} I_2 \\ I_3 \\ I_4 \\ I_5 \\ I_6 \\ I_7 \end{bmatrix} \quad (4)$$

Equation (4) can be generalized to be in terms of [BIBC], as follows:

$$[\text{BC}] = [\text{BIBC}] \times [I] \quad (5)$$

The i th bus voltage can be obtained from Kirchhoff's voltage law (KVL) applied to RDN; thus:

$$\begin{aligned}
V_2 &= V_1 - BC_1 Z_{12} \\
V_3 &= V_2 - BC_2 Z_{23} = V_1 - BC_1 Z_{12} - BC_2 Z_{23} \\
V_4 &= V_3 - BC_3 Z_{34} = V_1 - BC_1 Z_{12} - BC_2 Z_{23} - BC_3 Z_{34} \\
V_5 &= V_4 - BC_4 Z_{45} = V_1 - BC_1 Z_{12} - BC_2 Z_{23} - BC_3 Z_{34} - BC_4 Z_{45} \\
V_6 &= V_3 - BC_5 Z_{36} = V_1 - BC_1 Z_{12} - BC_2 Z_{23} - BC_5 Z_{36} \\
V_7 &= V_6 - BC_6 Z_{67} = V_1 - BC_1 Z_{12} - BC_2 Z_{23} - BC_5 Z_{36} - BC_6 Z_{67}
\end{aligned} \tag{6}$$

Z_{ij} denotes the impedance between buses i and j . From Eq. (6), V_i is formulated in terms of BCs , Z_{ij} , and the slack bus or substation voltage (V_1).

Therefore, the connection between BCs and V_{is} can be expressed as follows:

$$\begin{bmatrix} V_2 \\ V_3 \\ V_4 \\ V_5 \\ V_6 \\ V_7 \end{bmatrix} = \begin{bmatrix} V_1 \\ V_1 \\ V_1 \\ V_1 \\ V_1 \\ V_1 \end{bmatrix} - \begin{bmatrix} Z_{12} & 0 & 0 & 0 & 0 & 0 \\ Z_{12} & Z_{23} & 0 & 0 & 0 & 0 \\ Z_{12} & Z_{23} & Z_{34} & 0 & 0 & 0 \\ Z_{12} & Z_{23} & Z_{34} & Z_{45} & 0 & 0 \\ Z_{12} & Z_{23} & 0 & 0 & Z_{36} & 0 \\ Z_{12} & Z_{23} & 0 & 0 & Z_{36} & Z_{67} \end{bmatrix} \times \begin{bmatrix} BC_1 \\ BC_2 \\ BC_3 \\ BC_4 \\ BC_5 \\ BC_6 \end{bmatrix} \tag{7}$$

Consequently, the voltage drop ΔV from each bus V_i to the slack bus V_1 can be obtained as follows:

$$\begin{bmatrix} V_1 \\ V_1 \\ V_1 \\ V_1 \\ V_1 \\ V_1 \end{bmatrix} - \begin{bmatrix} V_2 \\ V_3 \\ V_4 \\ V_5 \\ V_6 \\ V_7 \end{bmatrix} = \begin{bmatrix} Z_{12} & 0 & 0 & 0 & 0 & 0 \\ Z_{12} & Z_{23} & 0 & 0 & 0 & 0 \\ Z_{12} & Z_{23} & Z_{34} & 0 & 0 & 0 \\ Z_{12} & Z_{23} & Z_{34} & Z_{45} & 0 & 0 \\ Z_{12} & Z_{23} & 0 & 0 & Z_{36} & 0 \\ Z_{12} & Z_{23} & 0 & 0 & Z_{36} & Z_{67} \end{bmatrix} \times \begin{bmatrix} BC_1 \\ BC_2 \\ BC_3 \\ BC_4 \\ BC_5 \\ BC_6 \end{bmatrix} \tag{8}$$

Equation (8) can be generalized to be in terms of $[BCBV]$, as follows:

$$[\Delta V] = [BCBV] \times [BC] \tag{9}$$

Combining Eqs. (5) and (9), the relationship between I_{is} and V_{is} can be expressed as follows:

$$[\Delta V] = [BCBV] \times [BC] = [BCBV] \times [BIBC] \times [I] \tag{10}$$

$$[\Delta V] = [MM] \times [I] \tag{11}$$

so that $[MM]$ is a multiplication matrix of $[BCBV]$ and $[BIBC]$ matrices. The dimension of $[BIBC]$ is $m \times (n - 1)$, where m is the number of branches, and the dimension of $[BCBV]$ is $(n - 1) \times m$. $[MM]$ is given as follows:

$$[MM] = [BCBV] \times [BIBC] \quad (12)$$

The LF solution for RDN can be obtained by solving the following equations iteratively, at $\text{iter} \in \text{iter}_{\max}$; thus:

$$I_i^{\text{iter}} = \left(\frac{P_i + jQ_i}{V_i^{\text{iter}}} \right)^*, \forall i \in n, \forall \text{iter} \in \text{iter}_{\max} \quad (13)$$

$$\Delta V_i^{\text{iter}+1} = [MM] \times I_i^{\text{iter}}, \forall i \in n, \forall \text{iter} \in \text{iter}_{\max} \quad (14)$$

$$V_i^{\text{iter}+1} = V_i^{\text{iter}} + \Delta V_i^{\text{iter}+1}, \forall i \in n, \forall \text{iter} \in \text{iter}_{\max} \quad (15)$$

The flowchart that explores the LF procedure is illustrated in Fig. 2.

3 Formulation of the Optimization Problem

This section presents the formulated problem of the smart coordination of DGUs and SCs in Egyptian RDN. The formulated problem is a multi-objective (MO) constrained optimization problem. The various objectives presented in this work aim to reduce the operating costs of the system and investment expenses for the proposed coordinated DGUs and SCs in the system while maximizing the benefits of reducing energy loss and contracted power from the utility, in addition to improving the voltage profile and loading capacity of the system. Various linear and nonlinear constraints were taken into account. A weighted sum approach using the well-known analytic hierarchy process (AHP) was used to transform the MO problem into a normalized single-objective (NSO) optimization problem.

3.1 Objective Functions

There are three different min-max objective functions (OFs) formulated as follows:

$$\text{OFs} = \begin{cases} F_1 = \min f_1 - \max f_2 \\ F_2 = \min f_3 \\ F_3 = \min f_4 \end{cases} \quad (16)$$

so that f_1 represents the annualized SCs and DGUs costs (\$/year), f_2 represents the annualized savings due to the benefits gained from SCs and DGUs allocation (\$/year), f_3 represents the enhancement of the voltage profile by reducing voltage

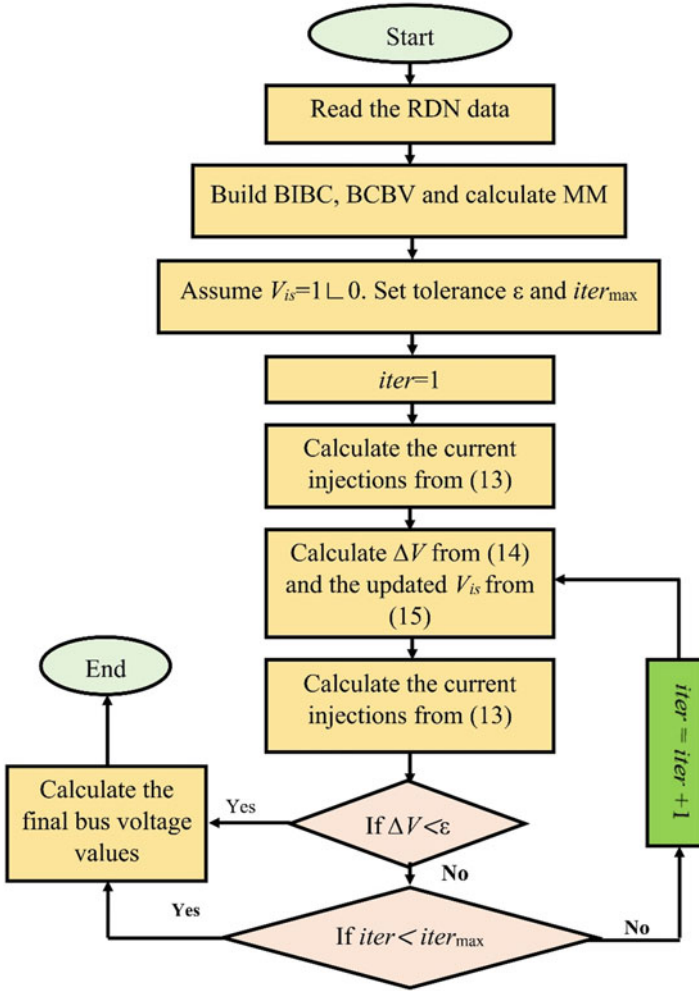


Fig. 2 Illustration of the LF procedure

deviation from the allowable values, and f_4 represents the enhancement in the loading capacity of the branches due to the minimization of the current flowing through them. These sub-objectives are defined as follows:

$$f_1 = ACost_{DG} + ACost_{SC} = \left[K_{DG} CRF_{DG} \sum_{b=1}^{N_{DG}} P_{DG}(b) \right] + CRF_{SC} \left[C_{SC} + \sum_{g=1}^{N_{SC}} K_{SC} Q_{SC}(g) \right] \quad (17)$$

where K_{DG} and K_{SC} denote the operation and maintenance costs of DGUs and SCs, respectively. CRF_{DG} and CRF_{SC} denote the capital recovery factors of DGUs and

SCs used to convert the present value cost to annualized cost due to the different lifetimes, interest rates, and references of these features [23]. N_{DG} and N_{SC} denote the total number of DGUs and SCs, respectively. C_{SC} represents the installment cost of the SCs. P_{DG} and Q_{SC} represent DGUs (kW) and the SCs (kvar) sizes. Also, $ACost_{DG}$ and $ACost_{SC}$ represent the total annualized DGUs and SCs costs (\$/year). CRF of DGUs and SCs are calculated as follows:

$$CRF = \frac{i_e(1+i_e)^{y_e}}{(1+i_e)^{y_e} - 1} \quad (18)$$

where i_e and y_e represent the interest rate and lifetime of each equipment (e), so that, $e = DGU$ or SC .

$$f_2 = \sum_{L=1}^{N_L} LL \left[\left(k_1 \left(P_{\text{loss}}^{\text{before}} - P_{\text{loss}}^{\text{after}} \right) \right) + \left(k_2 \left(S_{\text{utility}}^{\text{before}} - S_{\text{utility}}^{\text{after}} \right) \right) \right] \quad (19)$$

The gained annualized techno-economic benefits are formulated by the reduction in the value of the active power loss (P_{loss}) and reduction in the contracted apparent power (S_{utility}) from the utility after compensation with SCs and DGs. These benefits are mathematically represented in (19) while considering three loading levels – light, moderate, and peak. k_1 and k_2 represent the tariff rate of the energy (\$/kWh) and apparent power (\$/kVAh), respectively. LL denotes the number of hours per loading level (h). N_L represents the number of the loading levels – light, moderate, and peak [14]. Accordingly, F_1 (\$/year) is defined as the annualized difference between f_1 and f_2 , as described in Eq. (20).

$$F_1 = f_1 - f_2 \quad (20)$$

F_2 represents the voltage profile enhancement by reducing voltage deviation from the allowable values at the highest loading level (peak), as given in Eq. (21) [24].

$$F_2 = \min f_3 = \sum_{i=1}^n (1 - V_i)^2, \forall i \in n \quad (21)$$

F_3 represents the enhancement in the loading capacity of the branch currents due to the minimization of the current flowing through the branches, as given in Eq. (22), where $I_{\text{max},m}$ is the maximum allowed branch current [25], and N_b is the total number of branches.

$$F_3 = \min f_4 = \min \left[\max \left(\frac{I_m}{I_{\text{max},m}} \right) \right], \forall m \in N_b \quad (22)$$

3.2 Constraints

The *OFs* are subjected to the following six inequality constrained groups – DGUs size (G_1), penetration of DGUs (G_2), power factor limits (G_3), SCs size (G_4), voltage magnitude limits (G_5), and branch current magnitude limits (G_6), in addition to the conventional power balance equality constraints. The suffix “max” and the suffix “min” refer to the maximum and minimum values of a parameter specified by the operator.

3.2.1 Inequality Constrained Groups

$$\begin{aligned}
 G_1 & \{ P_{DG}(b) \leq P_{DG}(b)_{\max}, \forall b \in N_{DG} , \\
 G_2 & \left\{ \sum_{b=1}^{N_{DG}} P_{DG}(b) \leq \delta \sum_{i=1}^n P_i , \right. \\
 G_3 & \{ PF_{\min} \leq PF \leq PF_{\max} , \\
 G_4 & \{ Q_{SC}(g) \leq Q_{SC}(g)_{\max} , \forall g \in N_{SC}, \\
 G_5 & \left\{ V_{i,L}^{\min} \leq V_{i,L} \leq V_{i,L}^{\max} , \forall i \in n, \forall L \in N_L, \right. \\
 G_6 & \left. \{ I_{m,L} \leq I_{\max,m,L} , \forall m \in N_b, \forall L \in N_L. \right.
 \end{aligned} \tag{23}$$

G_1 shows that the DGU size should not exceed the maximum size limit, while G_2 shows that the penetration of DGUs should be limited by the factor (δ) to avoid any overvoltage or other related issues in the system [5]. In other words, it refers to the hosting capacity limit of the system, in which δ should be less than 1. PF is the system power factor. PF_{\min} is the minimum lagging PF (set to 0.85) and PF_{\max} is the maximum PF (set to unity). Also, G_4 shows that the SC size should not exceed the maximum size limit. Both G_5 and G_6 show the bus voltage and branch current boundaries, respectively, for each L .

3.2.2 Equality Constrained Groups

Equality constraints that guarantee the balance of active and reactive power should be met at each L , as follows:

$$P_{\text{utility}} + \sum_{b=1}^{N_{DG}} P_{DG}(b) = \sum_{i=1}^n P_i + \sum_{m=1}^{N_b} P_{\text{loss}}(m) \tag{24}$$

$$Q_{\text{utility}} + \sum_{g=1}^{N_{\text{SC}}} Q_{\text{SC}}(g) = \sum_{i=1}^n Q_i + \sum_{m=1}^{N_b} Q_{\text{loss}}(m) \quad (25)$$

where P_{utility} and Q_{utility} are the utility active and reactive power, respectively, Q_{loss} is the reactive power loss, and summation of P_{is} and Q_{is} denote the real and imaginary power demand.

In this work, $K_{\text{DG}} = \$5000/\text{kW}$, $K_{\text{SC}} = \$30,000/\text{MVAr}$, and $C_{\text{SC}} = \$1000$, in addition, i_e is set to 7%. The lifetime of DGUs and SCs are assumed to be 20 and 10 years, respectively. The size of SCs is expressed in a 150 kVAr step. k_1 and k_2 are set to $\$0.06/\text{kWh}$ and $\$0.06/\text{kVAh}$, respectively, as mentioned in [14], to enable the comparison of the results with the literature. It should be noted that the average energy price in medium-voltage applications in Egypt is almost 1 LE/kWh in agricultural areas (irrigation) and 1.15 LE/kWh in other applications. Also, a fixed demand rate of 60 LE/kW/month is added to the Egyptian tariff for this type of application.

3.3 Analytical Hierarchy Process (AHP)

AHP is one of the most used methods in decision-making because of its clarity, simplicity, and flexibility, which permits assessing and ranking several alternatives based on the operator's preference to help determine which choice should be favored or ranked first [26, 27]. It relies on the pairwise comparison strategy, which depends on a meaningful scale ranging from 1 to 9 [28]. Scale#1 reveals the equality criterion. Scale#3 shows a marginally higher significant measure compared to the other one (moderate importance). Scale#5 designates that one measure is more important than the other, Scale#7 suggests that one measure is much more significant than the other, and finally, Scale#9 means that one criterion is most important than the others (extreme importance) [29].

In this work, a weighted sum average strategy (WSAS) using the AHP is employed to convert the MO problem into an NSO one. Mathematically, the normalization procedure is combined with the WSAS to scale the objectives on the same base, as follows:

$$\text{OF} = \lambda_1 \frac{F_1}{F_1^{\max}} + \lambda_2 \frac{F_2}{F_2^{\max}} + \lambda_3 \frac{F_3}{F_3^{\max}} \quad (26)$$

where F_1^{\max} , F_2^{\max} and F_3^{\max} denote the maximum values specified by the designer to normalize the first, second, and third OFs. They are set to 1000, 1, and 1, respectively [14]. α denotes the weighting factor. Thus:

$$\sum_{s=1}^s \lambda_s = 1, \lambda_1 + \lambda_2 + \lambda_3 = 1. \quad (27)$$

The AHP is employed to rank the three values based on the following decision matrix given in Eq. (28).

$$\lambda = \begin{bmatrix} 1 & \lambda_{12} & \lambda_{13} \\ \lambda_{21} & 1 & \lambda_{23} \\ \lambda_{31} & \lambda_{32} & 1 \end{bmatrix} = \begin{bmatrix} 1 & 3 & 7 \\ 1/3 & 1 & 3 \\ 1/7 & 1/3 & 1 \end{bmatrix} \quad (28)$$

The pairwise comparison weights (α_{12} , α_{13} and α_{23}) were set to 3, 7, and 3, respectively, to indicate the relative importance of economic benefits compared to the technical advantages, it should be noted that the technical requirements must be satisfied via the constraints to allow its further comparison with the financial drives.

For each OF, the following expression (SUM_m) is calculated.

$$SUM_j = \sum_{s=1}^s \lambda_{js}, s, j = \{1, 2, 3\} \quad (29)$$

For instance, $SUM_1 = 1 + 3 + 7$, $SUM_2 = (1/3+1 + 3)$, and $SUM_3 = (1/3+1/7+1)$. Finally, the three values of each OF can be determined as follows:

$$\lambda_j = \frac{SUM_j}{\sum_{s=1}^s SUM_s}, s, j = \{1, 2, 3\} \quad (30)$$

Based on (30), the three α values are calculated as follows: $\lambda = \begin{cases} \lambda_1 = 0.6544 \\ \lambda_2 = 0.2578 \\ \lambda_3 = 0.0879 \end{cases}$.

3.4 Sine-Cosine Optimization (SCO) Algorithm

This sub-section presents the description of the employed meta-heuristic optimization technique. The method described in this work is the sine-cosine optimization (SCO) algorithm. S. Mirjalili developed SCO in 2016 [30] as a population-based algorithm that suggests several initial random candidate solutions, then fluctuating them around the best solution using a mathematical model based on the sine and cosine functions.

Theoretically, the SCO algorithm can determine the global solutions of different engineering problems because it generates a set of random solutions that intrinsically benefit from the high potential of exploration and local optima avoidance [31]. Then it smoothly transits from exploration to exploitation in a flexible range using its sine and cosine functions. The search space (SS) is efficiently explored when the sine and cosine functions return a value >1 or < -1 (exploration). On the other side, when the functions return a value between -1 and 1 , the promising areas in

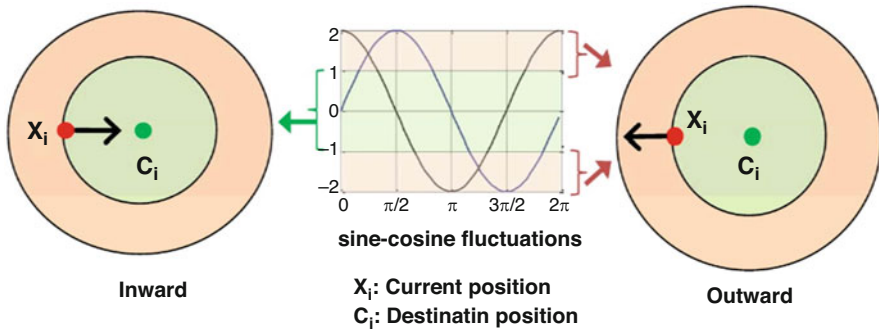


Fig. 3 Illustration of the SCO' adaptive trajectory

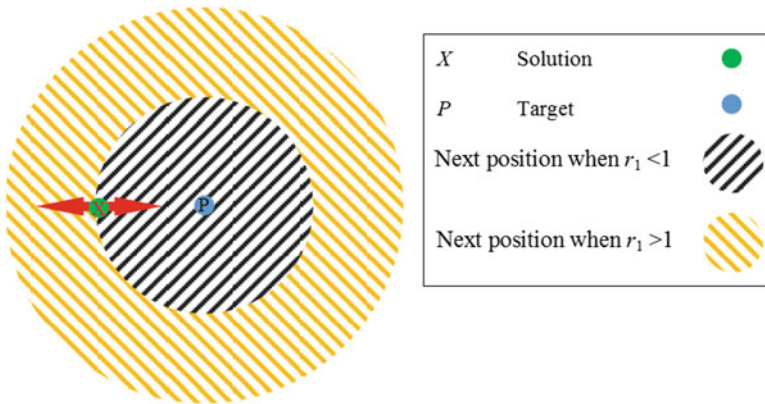


Fig. 4 Variation of r_1 and its impact on the SCO movement

SS are exploited (exploitation). Figure 3 illustrates this adaptive exploration and exploitation transition based on the returned values [32].

The best solution could be updated in SCO as shown in Eq. (31) [30], where $X_{i,SCO}^t$ and $X_{i,SCO}^{t+1}$ represent the current and the next positions of the i th population at iteration t .

$$X_{i,SCO}^{t+1} = \begin{cases} X_{i,SCO}^t + r_1 \times \sin(r_2) \times \left| r_3 P_{i,SCO}^t - X_{i,SCO}^t \right| & \text{if } r_4 \leq 0.5 \\ X_{i,SCO}^t + r_1 \times \cos(r_2) \times \left| r_3 P_{i,SCO}^t - X_{i,SCO}^t \right| & \text{otherwise.} \end{cases} \quad (31)$$

Four control parameters defined in the SCO are r_1 , r_2 , r_3 , and r_4 . r_1 expresses the area of the following position between the target position and the current solution. r_2 describes the solution's random motion and direction, and it ranges between $[0, 2\pi]$. r_3 represents the adaption of the target solution (emphasis ($r_3 > 1$) and de-emphasis ($r_3 < 1$) stages). r_4 is responsible for switching the sine and cosine functions among the algorithm as given in (31). Figure 4 shows the

impact of r_1 on the algorithm movement, in which the solution directs toward the target if $r_1 < 1$ [30].

4 The Egyptian Studied RDN

Figure 5 shows the Egyptian studied RDN (known as Tala_Menoufia system). This rural network comprises 37 buses, 31 loads fed from 11 kV, 50 Hz substation. The total active power demand is 4.8019 MW, and the total reactive power demand is 2.9759 MVar (loadings). The base MVA is set to 1.

The system is a nonrelaxed practical system that suffers from a poor voltage profile (the minimum voltage is measured at bus 27 and equals 0.7371 pu) and high-power losses (higher than 1 MW and 1.8 MVar in the increased loading intervals). The slack bus voltage is set to 1.05 pu. The complete system data are tabulated in Table 1 [33].

The voltage magnitudes of the system buses at the three loading intervals before compensation – light 60% loading (LLL), moderate 80% loading (MLL), and peak 100% loading (PLL) – are illustrated in Fig. 6. It is clear that this RDN suffers from a considerably poor voltage profile, particularly at bus number 27.

The PQ metrics used are given in Table 2 for the uncompensated system in the three loading levels, in which P_{loss} (kW), Q_{loss} (kVar), $S_{utility}$ (MVA), minimum (V_{min}) and maximum (V_{max}) voltage magnitudes (pu) and their buses' number, and

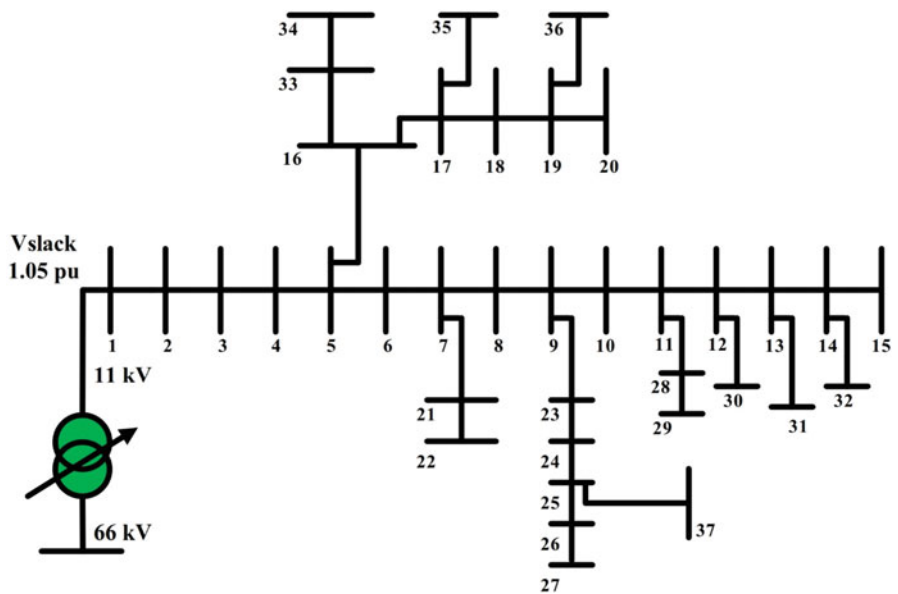


Fig. 5 The Egyptian studied RDN

Table 1 The Egyptian studied RDN

Branch m	From bus i	To bus j	I_{\max} (A)	R (Ω)	X (Ω)	Bus i	P_i (kW)	Q_i (kVAr)
1	1	2	788.00	0.0349	0.0493	1	0	0
2	2	3	788.00	0.1862	0.2629	2	0	0
3	3	4	788.00	1.2891	1.8201	3	21.2003	13.1388
4	4	5	788.00	1.1640	1.6434	4	10.6002	6.5694
5	5	6	367.50	0.0776	0.1096	5	117.7795	72.9932
6	6	7	367.50	0.0466	0.0657	6	255.5814	158.3951
7	7	8	367.50	0.0388	0.0548	7	127.2018	78.8326
8	8	9	367.50	0.1263	0.1534	8	0	0
9	9	10	367.50	0.1240	0.0893	9	0	0
10	10	11	367.50	0.2066	0.1489	10	138.9798	86.1319
11	11	12	367.50	0.1240	0.0893	11	181.3804	112.4095
12	12	13	367.50	0.1269	0.0914	12	152.5244	94.5261
13	13	14	367.50	0.0901	0.0649	13	0	0
14	14	15	367.50	0.2587	0.1864	14	221.4254	137.2271
15	5	16	183.70	0.7007	0.2695	15	241.4479	149.6360
16	16	17	183.70	0.2002	0.0770	16	42.4006	26.2775
17	17	18	183.70	0.7007	0.2695	17	144.8687	89.7816
18	18	19	183.70	0.9009	0.3465	18	26.5004	16.4235
19	19	20	183.70	0.4004	0.1540	19	41.8117	25.9126
20	7	21	183.70	0.8425	0.3240	20	66.5454	41.2411
21	21	22	183.70	0.2086	0.0802	21	325.0713	201.4611
22	9	23	183.70	1.4015	0.5389	22	214.9475	133.2125
23	23	24	183.70	0.5005	0.1925	23	113.0683	70.0734
24	24	25	183.70	0.5798	0.2230	24	121.9017	75.5479
25	25	26	183.70	0.6006	0.2310	25	175.4914	108.7598
26	26	27	183.70	0.4004	0.1540	26	94.2236	58.3945
27	11	28	183.70	0.9009	0.3465	27	118.3684	73.3581
28	28	29	183.70	1.1011	0.4235	28	299.1598	185.4026
29	12	30	183.70	0.2066	0.1489	29	215.5364	133.5775
30	13	31	183.70	0.2252	0.0866	30	0	0
31	14	32	183.70	0.4371	0.1681	31	241.4479	149.6360
32	16	33	183.70	0.1668	0.0642	32	267.9483	166.0594
33	33	34	183.70	0.4755	0.1829	33	276.1928	171.1689
34	17	35	183.70	0.6006	0.2310	34	106.0015	65.6938
35	19	36	183.70	1.1011	0.4235	35	256.7592	159.1251
36	25	37	183.70	0.5005	0.1925	36	10.6002	6.5694
						37	174.9025	108.3948

the per-unit maximum loading capacity of the branches (LC) (pu) are the used metrics. Figure 7 shows the LC of the branches at the three loading levels.

Obviously, the studied RDN suffers from high active and reactive losses, poor voltage profile, and expected current problems.

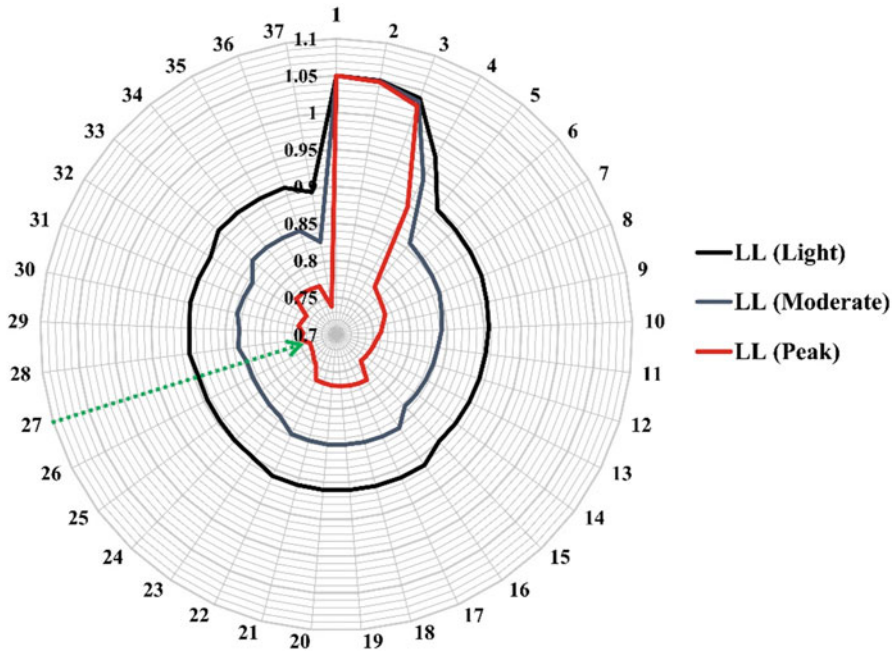


Fig. 6 Voltage profile of the studied RDN before compensation

Table 2 Results obtained for the uncompensated Egyptian studied RDN

PQ metric	Loading levels		
	LLL	MLL	PLL
P_{loss} (kW)	343.1828	707.4094	1361.7
Q_{loss} (kVAr)	463.8976	956.0957	1839.9
$S_{utility}$ (MVA)	3.9312	5.6414	7.8213
V_{min} (pu)@bus	0.8946@27	0.8259@27	0.7371@27
V_{max} (pu)@bus	1.05@1	1.05@1	1.05@1
LC (pu)	0.4112	0.591	0.8215

5 Numerical Results and Discussion

The decision variables of the problem formulated are the DGUs and SCs – sizes and locations (for both). Up to three DGUs are permitted in the solution ($N_{DG} \leq 3$). The possible places of DGUs and SCs are treated as integer numbers (integer variables) ranging from bus 2 to 37. The sizes of DGUs are treated in a continuous manner (continuous variables) in the range between 0 and 3000 kW. The sizes of SCs are treated in a discrete manner (discrete variables) in the range between 0 and 1200 kVAr. Up to three SCs are permitted in the solution ($N_{SC} \leq 8$).

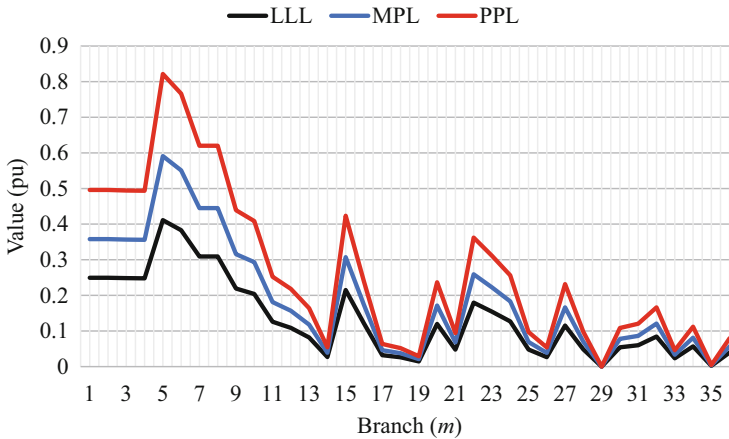


Fig. 7 LC of the branches at the three loading levels

Three scenarios were investigated – Scenario 1: DGUs allocation with no SCs connection, Scenario 2: SCs allocation with no DGUs connection, and Scenario 3: simultaneous allocation of SCs and DGUs. The results obtained from the three scenarios are given in the following subsections.

5.1 Results of Scenario 1

In this scenario, the number of dimensions is 6, the number of populations is 30, and 5000 iterations are allowed. The magnitudes of the six decision variables obtained from the optimization and the corresponding PQ metrics are given in Table 3 for the compensated system in the three loading levels. Figure 8 shows the voltage profile of the studied RDN before and after compensation using DGUs, and Fig. 9 shows the LC of the branches at the three loading levels after compensation using DGUs.

It was evident from Table 3 and Fig. 9 that the LC values are reduced after compensation compared to the case before the settlement of DGUs. The maximum LC value was considerably reduced from 0.8215 at the peak loading level to only 0.3631.

As shown in Fig. 8, the voltage profile has been improved, and the minimum and maximum voltage values are within the permissible limits at the three loading conditions. The OF value is -0.04932195 , which indicates that a saving will be achieved compared to the system with no DGUs and the values obtained using EGWA (-0.0345) and particle swarm optimization (PSO) (-0.0303), reported in [14]. Figure 10 shows the convergence curve of the SCO generated in less than 2 minutes.

Table 3 Results obtained for the compensated Egyptian studied RDN: Scenario 1

DGUs	Size (kW)	1904.0840, 1198.7348, 372.9161		
	Location (buses)	14, 37, 29		
PQ metric	Loading levels			
		LLL	MLL	PLL
P_{loss} (kW)	121.3005	185.5703	340.9671	
Q_{loss} (kVAr)	139.3105	227.6544	439.3923	
S_{utility} (MVA)	1.9821	2.6660	3.8003	
V_{min} (pu)@bus	0.9985@20	0.9536@20	0.9031@20	
V_{max} (pu)@bus	1.05@1	1.05@1	1.05@1	
LC (pu)	0.3062	0.3116	0.3631	
OF (proposed)	−0.0493			
OF obtained using EGWA [14]	−0.0345			
OF obtained using PSO [14]	−0.0303			
Time elapsed (s)	109.767443			

5.2 Results of Scenario 2

In this scenario, the number of dimensions is 14, the number of populations is 30, and 5000 iterations are allowed. The magnitudes of the 14 decision variables obtained from the optimization and the corresponding PQ metrics are given in Table 4 for the compensated system for the three loading levels. Figure 11 shows the voltage profile of the studied RDN before and after compensation using SCs, and Fig. 12 shows the LC of the branches at the three loading levels after compensation using SCs.

It was evident from Table 4 and Fig. 11 that the LC values are reduced after compensation compared to the case before the settlement of SCs. The maximum LC value was considerably reduced from 0.8215 at the peak loading level to only 0.5898. As shown in Fig. 12, the voltage profile has been improved, and the minimum and maximum voltage values are within the permissible limits at the three loading conditions. The *OF* value is −0.4112, which indicates that a saving will be achieved compared to the system with no SCs and the values obtained using EGWA (−0.3742), PSO (−0.3242), and whale optimization algorithm (WOA) (−0.3196), reported in [14]. Figure 13 shows the convergence curve of the SCO generated in less than one minute and a half.

5.3 Results of Scenario 3

In this scenario, the number of dimensions is 20, the number of populations is 30, and 5000 iterations are allowed. The magnitudes of the 20 decision variables obtained from the optimization and the corresponding PQ metrics are given in Table

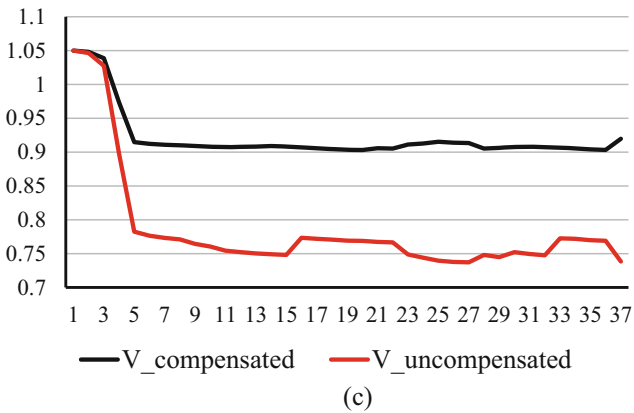
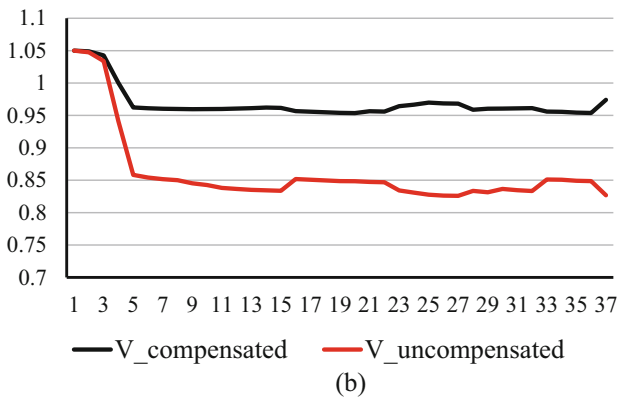
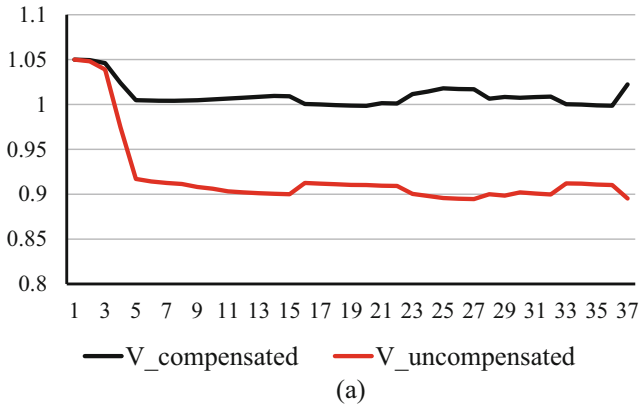


Fig. 8 Voltage profile of the studied RDN before and after compensation, Scenario 1. (a) LLL. (b) MLL. (c) PLL

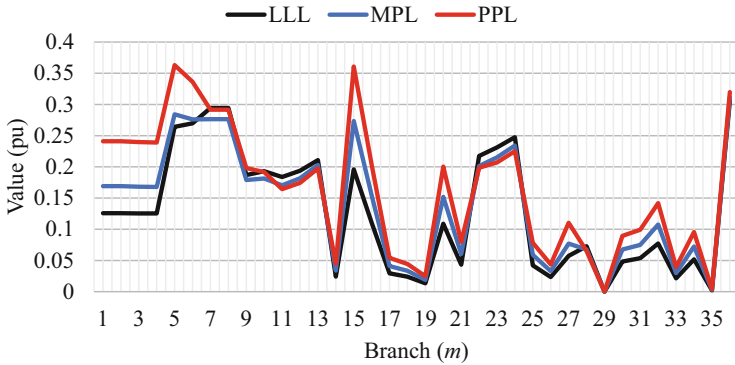


Fig. 9 LC of the branches at the three loading levels, Scenario 1

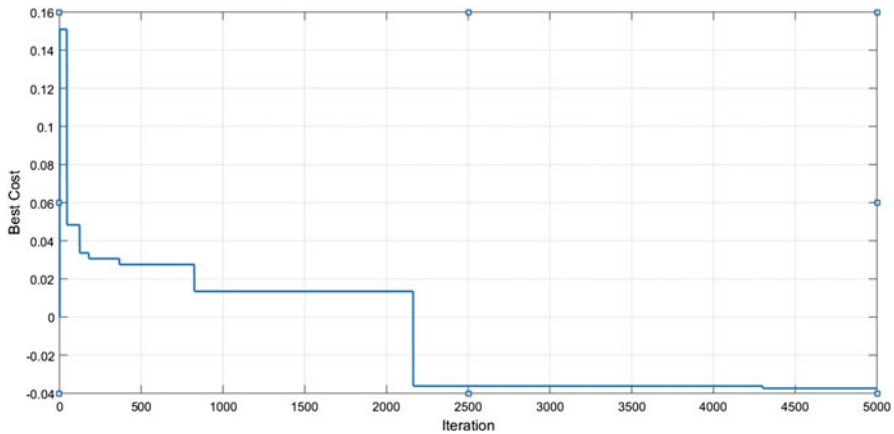


Fig. 10 Convergence curve of SCO, Scenario 1

5 for the compensated system for the three loading levels. Figure 14 shows the voltage profile of the studied RDN before and after compensation using both DGUs and SCs, and Fig. 15 shows the LC of the branches at the three loading levels after compensation using DGUs and SCs.

It was evident from Table 5 and Fig. 14 that the LC values are reduced after compensation compared to the case before the settlement of DGUs and SCs. The maximum LC value was considerably reduced from 0.8215 at the peak loading level to only 0.3469. As shown in Fig. 15, the voltage profile has been improved, and the minimum and maximum voltage values are within the permissible limits at the three loading conditions.

The OF value is -0.8163 , which indicates that a saving will be achieved compared to the system with no DGUs and SCs and the values obtained using EGWA (-0.7823), PSO (-0.7994), and whale optimization algorithm (WOA)

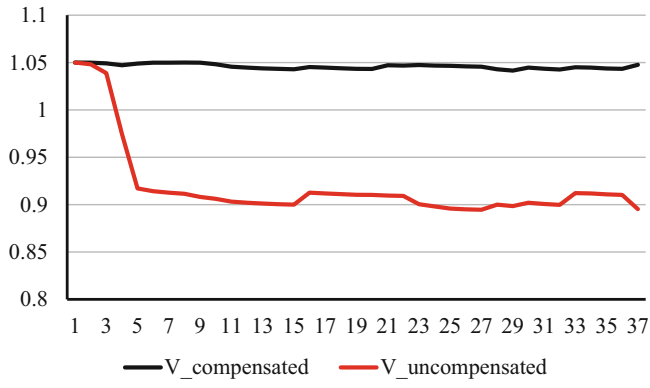
Table 4 Results obtained for the compensated Egyptian studied RDN: Scenario 2

SCs	Size (kVAr)	1100, 450, 150, 1200,1050		
	Location (buses)	37, 8, 33, 9, 6		
PQ metric	Loading levels			
		LLL	MLL	PLL
P_{loss} (kW)		320.2098	428.6557	699.4165
Q_{loss} (kVAr)		425.2305	569.7199	933.4909
S_{utility} (MVA)		3.7312	4.3291	5.5542
V_{min} (pu)@bus		1.0415@29	0.9775@29	0.9006@29
V_{max} (pu)@bus		1.05@1	1.05@1	1.05@1
LC (pu)		0.4642	0.4923	0.5898
OF (proposed)		−0.4112		
OF obtained using EGWA [14]		−0.3742		
OF obtained using PSO [14]		−0.3242		
OF obtained using WOA [14]		−0.3196		
Time elapsed (s)		89.999		

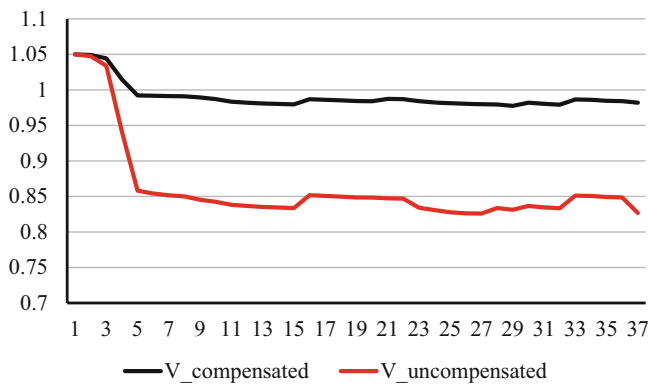
(−0.7693), reported in [14]. Figure 16 shows the convergence curve of the SCO generated in about 81 seconds.

6 Conclusions

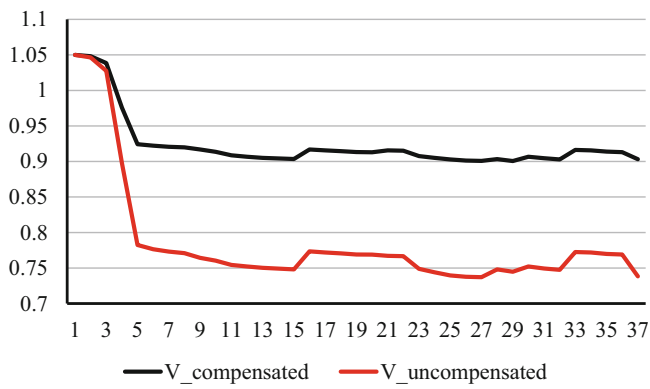
In this work, smart coordination of DGUs and SCs in Egyptian RDN is presented to increase resiliency and enhance the reliability of this system. SCO algorithm was used to solve the formulated MO problem. Three different loading levels were investigated. Three scenarios were investigated – Scenario 1: DGUs allocation with no SCs connection, Scenario 2: SCs allocation with no DGUs connection, and Scenario 3: simultaneous allocation of SCs and DGUs. The results obtained show a significant techno-economic enhancement of the PQ performance level of the system. Analyzing the presented results, it was apparent that the best OF (−0.8163) value was obtained using the optimal coordination of DGUs and SCs. Also, the lowest accepted total active and reactive power losses were obtained in the same case (302.2073 kW and 343.9133 kVAr) compared to the total active and reactive power losses obtained in Scenario 2 (1448.282 kW and 1928.4413 kVAr) and Scenario 3 (647.8379 kW and 806.3572 kVAr). Besides, the proposed SCO outperformed the other algorithms (PSO, EGWA, and WOA) presented in the literature to solve the problem.



(a)



(b)



(c)

Fig. 11 Voltage profile of the studied RDN before and after compensation, Scenario 2. (a) LLL. (b) MLL. (c) PLL

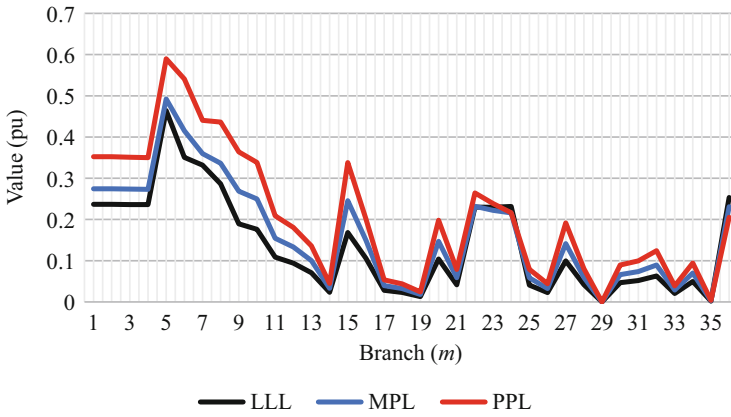


Fig. 12 LC of the branches at the three loading levels, Scenario 2

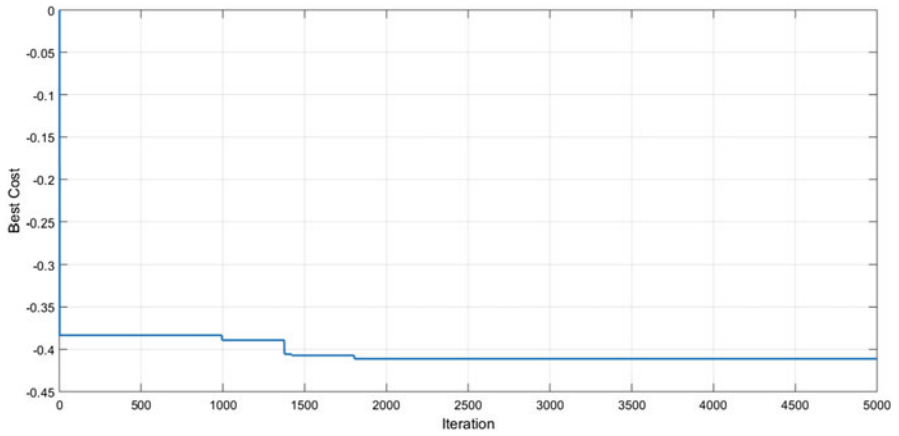


Fig. 13 Convergence curve of SCO, Scenario 2

Table 5 Results obtained for the compensated Egyptian studied RDN: Scenario 3

DGUs	Size (kW)	2613.327, 100		
	Location (buses)	10, 7		
SCs	Size (kVAr)	600, 150, 150, 1200, 150		
	Location (buses)	2, 13, 31, 7, 37		
PQ metric		Loading levels		
		LLL	MLL	PLL
P_{loss} (kW)		17.1767	68.4262	216.6044
Q_{loss} (kVAr)		10.8571	71.5669	261.4893
S_{utility} (MVA)		0.6998	1.2051	2.5560
V_{min} (pu)@bus		1.0385@27	0.9855@27	0.9254@27
V_{max} (pu)@bus		1.0502@2	1.0500@1	1.0500@1
LC (pu)		0.2025	0.2626	0.3469
OF (proposed)		-0.8163		
OF obtained using EGWA [14]		-0.7823		
OF obtained using PSO [14]		-0.7994		
OF obtained using WOA [14]		-0.7693		
Time elapsed (s)		80.234		

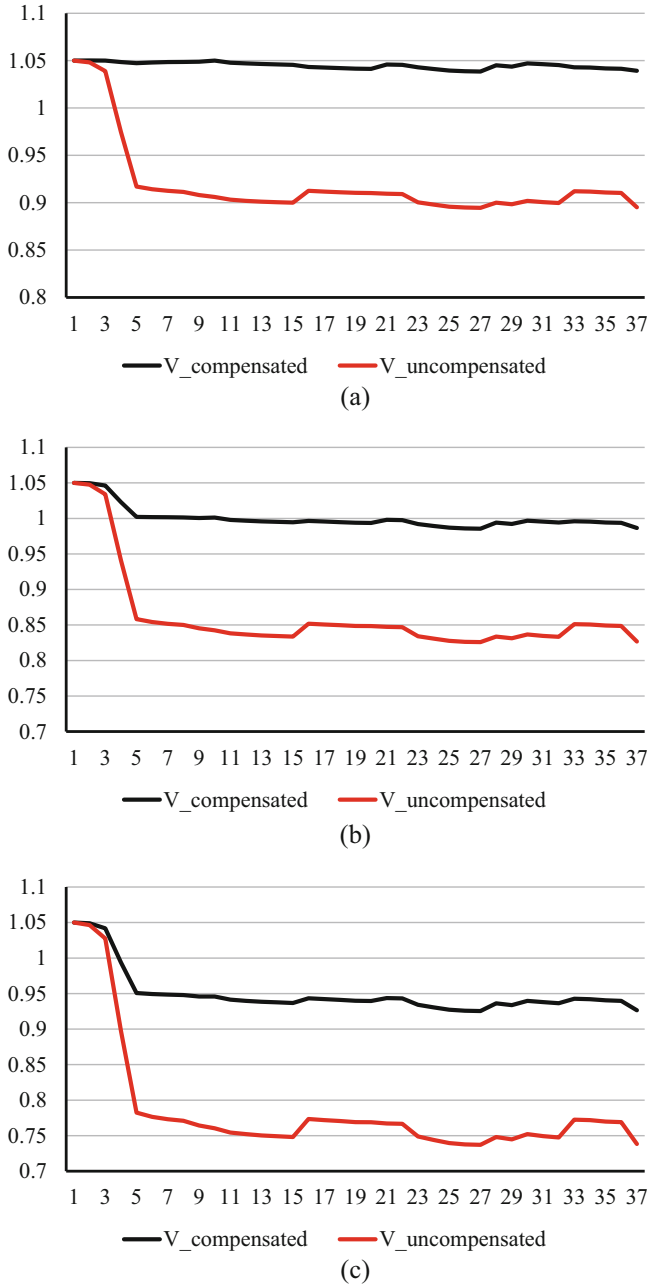


Fig. 14 Voltage profile of the studied RDN before and after compensation, Scenario 3. (a) LLL. (b) MLL. (c) PLL

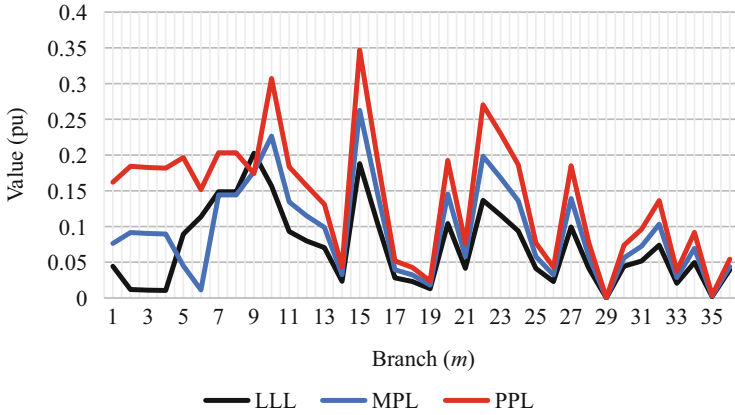


Fig. 15 LC of the branches at the three loading levels, Scenario 3

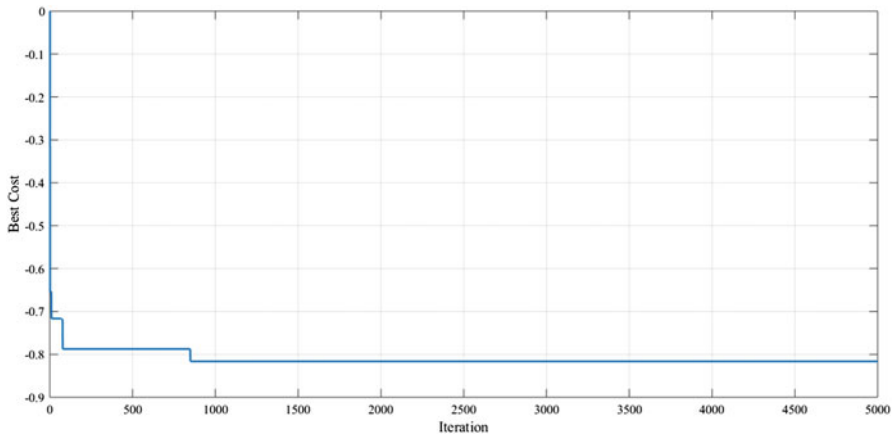


Fig. 16 Convergence curve of SCO, Scenario 3

Our future research will examine the impact of energy storage systems on system performance and their effects on voltage profiles and power loss values. Further, the combined allocation effects of energy storage devices, DGUs, and SCs will be investigated.

References

1. Eshra NM, Zobaa AF, Abdel Aleem SHE (2021) Assessment of mini and micro hydropower potential in Egypt: Multi-criteria analysis. *Energy Reports* 7: 81–94
2. Mousa AGE, Abdel Aleem SHE, Ibrahim AM (2016) Mathematical analysis of maximum power points and currents based maximum power point tracking in solar photovoltaic system: a solar powered water pump application. *Int Rev Electr Eng* 11:97–108. <https://doi.org/10.15866/iree.v11i1.8137>

3. Rozlan MBM, Zobaa AF, Abdel Aleem SHE (2011) The optimisation of stand-alone hybrid renewable energy systems using HOMER. *Int Rev Electr Eng* 6:1802–1810
4. Zulpo RS, Leborgne RC, Bretas AS (2014) Optimal location and sizing of distributed generation based on power losses and voltage deviation. In: 2014 IEEE PES Transm. Distrib. Conf. Expo. Am. (PES T&D-LA). IEEE, pp 1–5
5. Ismael SM, Aleem SHEA, Abdelaziz AY, Zobaa AF (2019) Probabilistic hosting capacity enhancement in non-sinusoidal power distribution systems using a hybrid PSO-GSA optimization algorithm. *Energies* 12:185–217, Elsevier. <https://doi.org/10.3390/en12061018>
6. Mahmoud K, Lehtonen M (2021) Direct approach for optimal allocation of multiple capacitors in distribution systems using novel analytical closed-form expressions. *Electr Eng* 103:245–256
7. Diaaeldin I, Aleem SA, El-Rafei A, Abdelaziz A, Zobaa AF (2019) Optimal network reconfiguration in active distribution networks with soft open points and distributed generation. *Energies* 12:4172. <https://doi.org/10.3390/en12214172>
8. Moradi MH, Zeinalzadeh A, Mohammadi Y, Abedini M (2014) An efficient hybrid method for solving the optimal siting and sizing problem of DG and shunt capacitor banks simultaneously based on imperialist competitive algorithm and genetic algorithm. *Int J Electr Power Energy Syst* 54:101–111. <https://doi.org/10.1016/j.ijepes.2013.06.023>
9. Rahmani-Andebili M (2016) Simultaneous placement of DG and capacitor in distribution network. *Electr Power Syst Res* 131:1–10. <https://doi.org/10.1016/j.epsr.2015.09.014>
10. Muthukumar K, Jayalalitha S (2016) Optimal placement and sizing of distributed generators and shunt capacitors for power loss minimization in radial distribution networks using hybrid heuristic search optimization technique. *Int J Electr Power Energy Syst* 78:299–319. <https://doi.org/10.1016/j.ijepes.2015.11.019>
11. Gampa SR, Das D (2019) Simultaneous optimal allocation and sizing of distributed generations and shunt capacitors in distribution networks using fuzzy GA methodology. *J Electr Syst Inf Technol* 6:1–18
12. Das S, Das D, Patra A (2019) Operation of distribution network with optimal placement and sizing of dispatchable DGs and shunt capacitors. *Renew Sust Energy Rev* 113:109219. <https://doi.org/10.1016/j.rser.2019.06.026>
13. Almabsout EA, El-Sehiemy RA, An ONU, Bayat O (2020) A hybrid local search-genetic algorithm for simultaneous placement of DG units and shunt capacitors in radial distribution systems. *IEEE Access* 8:54465–54481. <https://doi.org/10.1109/ACCESS.2020.2981406>
14. Shaheen AM, El-Sehiemy RA (2020) Optimal coordinated allocation of distributed generation units/capacitor banks/voltage regulators by EGWA. *IEEE Syst J* 15:257
15. Milovanović M, Tasić D, Radosavljević J, Perović B (2020) Optimal placement and sizing of inverter-based distributed generation units and shunt capacitors in distorted distribution systems using a hybrid phasor particle swarm optimization and gravitational search algorithm. *Electr Power Components Syst* 48:543–557
16. Zobaa AF, Aleem SHEA, Abdelaziz AY (2018) Classical and recent aspects of power system optimization. <https://doi.org/10.1016/C2016-0-03379-X>
17. Čalasan M, Abdel Aleem SHE, Zobaa AF (2020) On the root mean square error (RMSE) calculation for parameter estimation of photovoltaic models: a novel exact analytical solution based on Lambert W function. *Energy Convers Manag* 210:112716. <https://doi.org/10.1016/j.enconman.2020.112716>
18. Čalasan M, Micev M, Djurovic Ž, Mageed HMA (2020) Artificial ecosystem-based optimization for optimal tuning of robust PID controllers in AVR systems with limited value of excitation voltage. *Int J Electr Eng Educ*:0020720920940605
19. Carew N, Warnock W, Bayindir R, Hossain E, Rakin AS (2020) Analysis of pumped hydroelectric energy storage for large-scale wind energy integration. *Int J Electr Eng Educ*:0020720920928456
20. Pramila V, Chandramohan S (2021) Intelligent energy scheduling in a microgrid with custom power devices. *Int J Electr Eng Educ* 58:572–589

21. Mostafa MH, Aleem SHEA, Ali SG, Abdelaziz AY, Ribeiro PF, Ali ZM (2020) Robust energy management and economic analysis of microgrids considering different battery characteristics. *IEEE Access* 8:54751–54775. <https://doi.org/10.1109/ACCESS.2020.2981697>
22. Teng J-H (2003) A direct approach for distribution system load flow solutions. *IEEE Trans Power Deliv* 18:882–887
23. Aleem SHEA, Elmathana MT, Zobaa AF (2013) Different design approaches of shunt passive harmonic filters based on IEEE Std. 519-1992 and IEEE Std. 18-2002. *Recent Patents Electr Electron Eng* 6:68–75, Elsevier. <https://doi.org/10.2174/2213111611306010009>
24. Diaaeldin I, Abdel Aleem S, El-Rafei A, Abdelaziz A, Zobaa AFAF, Aleem SA et al (2019) Optimal network reconfiguration in active distribution networks with soft open points and distributed generation. *Energies* 12:4172. <https://doi.org/10.3390/en12214172>
25. Ismael SM, Abdel Aleem SHE, Abdelaziz AY, Zobaa AF (2018) Practical considerations for optimal conductor reinforcement and hosting capacity enhancement in radial distribution systems. *IEEE Access* 6:27268–27277, Elsevier. <https://doi.org/10.1109/ACCESS.2018.2835165>
26. Saaty RW (1987) The analytic hierarchy process-what it is and how it is used. *Math Model* 9:161–176. [https://doi.org/10.1016/0270-0255\(87\)90473-8](https://doi.org/10.1016/0270-0255(87)90473-8)
27. Moutinho L, Hutcheson G, Beynon MJ (2014) Analytic hierarchy process. *SAGE Dict. Quant. Manag. Res.*, 1 Oliver’s Yard, 55 City Road, London EC1Y 1SP United Kingdom. SAGE Publications Ltd, pp 9–12. <https://doi.org/10.4135/9781446251119.n3>
28. Rawa M, Abusorrah A, Bassi H, Mekhilef S, Ali ZM, Aleem SHEA et al (2021) Economical-technical-environmental operation of power networks with wind-solar-hydropower generation using analytic hierarchy process and improved grey wolf algorithm. *Ain Shams Eng J* 12:2717
29. Abdel Aleem SHE, Zobaa AF, Abdel Mageed HM (2015) Assessment of energy credits for the enhancement of the Egyptian green pyramid rating system. *Energy Policy* 87:407–416. <https://doi.org/10.1016/j.enpol.2015.09.033>
30. Mirjalili S (2016) SCA: a sine cosine algorithm for solving optimization problems. *Knowledge-Based Syst* 96:120–133. <https://doi.org/10.1016/j.knsys.2015.12.022>
31. Rizk-Allah RM, Mageed HMA, El-Sehiemy RA, Aleem SHEA, El Shahat A (2017) A new sine cosine optimization algorithm for solving combined non-convex economic and emission power dispatch problems. *Int J Energy Convers* 5:180–192. <https://doi.org/10.15866/irecon.v5i6.14291>
32. Ismael SM, Aleem SHEA, Abdelaziz AY (2018) Optimal selection of conductors in Egyptian radial distribution systems using sine-cosine optimization algorithm. In: 2017 19th International Middle-East Power System Conference MEPCON 2017 - Proceedings, vol 2018, pp 103–107. <https://doi.org/10.1109/MEPCON.2017.8301170>
33. Elsayed AM, Mishref MM, Farrag SM (2018) Distribution system performance enhancement (Egyptian distribution system real case study). *Int Trans Electr Energy Syst* 28:e2545

Power Quality Enhancement of Balanced/Unbalanced Distribution Systems Using Metaheuristic Optimizations



Ahmad Eid

1 Introduction

1.1 Necessary Background on Power Quality

According to IEEE standard 115-2019 [1], Power Quality (PQ) refers to a large variety of electromagnetic phenomena that characterize voltage and current at a particular time and place on the power system. The increasing usage of electronic devices that might create or be susceptible to electromagnetic disturbances has increased interest in PQ over several years. These electromagnetic disturbances may come from different noise sources, such as harmonics, voltage fluctuation, voltage sag/swell/imbalance, power frequency variations, DC in AC networks, or magnetic/electric fields. There are many different types of harmonic current sources in power systems, but the most frequent ones include switched-mode power supply, static VAR systems, and distributed generation inverters.

The harmonic contents are usually measured using the Total Harmonic Distortion (THD), Individual Harmonic Distortion (IHD), and Total Demand Distortion (TDD) of the voltage and current at the PCC. The existence of harmonics in power systems causes severe quality problems, such as amplifying harmonic levels from series and parallel resonances, reducing the operation efficiency of electricity utilization, aging and deterioration of insulations, and malfunctioning of some system devices. With existing harmonics in distribution systems, the current through the feeders or cables increases, and consequently, the heating of the cable rises with a possibility of tripping protection devices. The circulation of triple harmonics causes extra heating in the neutral conductors of the system and may cause parallel resonance on installed

A. Eid (✉)

Department of Electrical Engineering, Faculty of Engineering, Aswan University, Aswan, Egypt
e-mail: ahmadeid@aswu.edu.eg

filter capacitors, causing heating, aging, and destruction. Moreover, when harmonic currents pass through the transformer winding, it causes overheating of the winding and insulation loss, reducing efficiency, and taking the transformer to saturation regions. The same problems may happen with a transformer as the circulation of harmonic currents can happen to the operating motors and generators of the grid besides the difficulty of their synchronization to the utility.

1.2 Literature Review

Many utilities are now promoting their electric system to integrate independent renewable resources such as distributed generations (DG). Nevertheless, depending on the DG operational characteristics and the distribution network, installing the DG into the distribution system might have both positive or negative influences [2]. DG can be beneficial provided the system's operational attitude and feeder design fulfill the fundamental requirements. The impact of DG on PQ [3] depends on the type of DG, its interfaces to the system, the size of the DG unit, and its total capacity relative to the system. Depending on the DG type or the power converter technology, a DG unit linked to a distribution system might contribute to its harmonic distortion [4]. Depending on the connection technology of the DG with the distribution systems, the DG unit can be either inverter-based or non-inverter-based type. The inverter-based DG (IBDG) units exemplify the photovoltaic (PV) generators, wind turbine generators, fuel cell, or battery energy storage resources. In contrast, the non-inverter-based DG units represent the small microturbines connected to synchronous generators. The connection of such IBDG units into distribution systems affects the grid technically and economically, turns it into an active system, and may increase the harmonic content in the system [5, 6]. It is vital that DG is appropriately allocated in distribution systems to prevent power distribution degradation services [7].

The issues and challenges aforementioned above about the PQ of power systems encourage researchers to find ways and techniques to enhance the overall operation of power systems [8]. The presence of harmonics in the distribution system can lead to excessive loss, overheating, and destruction of system equipment. The harmonic levels of the distribution system may surpass the specified limitations because of the widespread power electronic equipment and nonlinear loads inside the distribution system [9]. Therefore, in distribution systems, the harmonic reduction becomes more attractive to reduce distortion and improve system performance [10, 11]. The authors of [12] have proposed installing an inductive hybrid unified power quality conditioner (UPQC) to achieve the bidirectional PQ improvement for the medium-voltage supply of a park with the help of passive and active filters. A similar study of designing a UPQC with a Kalman filter is proposed in [13], to improve the PQ of three-phase distribution networks, where the bat algorithm (BA) is adopted for proportional-integral (PI) parameter estimation. Passive filters are applied [14, 15] to reduce harmonics and enhance small distribution systems. A custom power device

is suggested [16] to compensate the harmonic currents in the smart grid with the assistance of the meters of the grid and enhance the PQ of the system using particle swarm optimization (PSO). To reduce the THD, power loss, and filter cost, the authors [3] applied the water cycle algorithm (WCA) to optimally locate IBDG units and single-tuned passive filters in distribution systems. Ant lion optimization (ALO) algorithm [17] is used to optimize the controller gains during off-grid operation wind-based microgrid system. For the PQ assessment of distorted distribution power networks in the presence of IBDG units, an analytical hierarchy procedure (AHP) is proposed [18]. The study took the voltage profile/sag/imbalance and harmonics into consideration.

The distribution synchronous static-compensator (DSTATCOM) [19] is applied in distribution systems with existing linear and nonlinear loads through a neural network-oriented control for PQ improvement. Active power filters (APF) are adopted to mitigate harmonics and regulate the voltage profile of distribution power systems [5, 20]. APF and static var compensator (SVC) are combined [21] to enhance the PQ of distribution systems equipped with arc furnaces. The APF and SVC modified the power factor and balanced the three-phase currents of the system. A comprehensive review of PQ primary and secondary controls for hybrid microgrids is contrived in [22]. A hybrid particle swarm optimization-grey wolf optimization (PSO-GWO) and PI controller [23] are utilized to control an APF that provides reactive power and harmonic compensations under different loading circumstances. Detailed mathematical models of PQ disturbances and indices are investigated and analyzed [24] using compressed sensing and deep convolution artificial neural networks (ANN). A D-STATCOM with an optimal tuned PID controller using the grasshopper optimization algorithm (GOA) is concocted [25] to improve the overall dynamic performance and PQ of microgrids. A hybrid passive filter, consisting of shunt and series filters, is proposed in [26] to mitigate the harmonics of currents and voltages of power systems to acceptable limits. The effects of harmonics on PQ and efficiency of distribution systems are investigated in [27], adopting the modeling of nonlinear residential, commercial, and office loads and estimating energy losses due to these harmonics. The reactive power capability [28] is adopted for voltage control of unbalanced three-phase distribution systems equipped with PV sources using fuzzy logic control. On the other hand, for enhancement of voltage stability of distribution systems is proposed using continuous power-flow based on secant predictor technique [29] under different loading scenarios and 50% PV penetration.

Further, due to the uneconomic solution of the APFs, single-tuned passive harmonic filters remain, due to their efficiency and cost benefits, one of the most prevalent methods for harmonic reduction. Depending on the low impedance of filters at specific harmonics, the single-tuned passive filter traps the harmonic to the ground and prevents it from propagating through the network [30]. The nondominated sorting genetic algorithm for optimizing passive filters is proposed [31] in a multi-objective problem to minimize the annual cost and maximize the power quality of distribution systems. A complete design methodology of a C-type passive filter is conceived in [32] to reduce the harmonics and dampen resonance in

balanced distribution systems with a frequency-impedance index. For mining power distribution systems [33], large passive filters are designed for harmonic reductions of 12-pulse cyclo-converters and nonlinear loads. A distributed harmonic filter [34] is formulated to work with residential distribution systems in randomly selected places. An ANN algorithm is adopted to design a passive filter in [35] to improve the power factor and eliminate the harmonics of distribution systems. An efficient LCL filter is developed and proposed [36] for renewable energy systems to reduce the cost and weight of passive filters and increase the robustness and stability of the power electronics converter. A damped high-pass filter [37] has been devised to reduce harmonics and avoid detrimental resonance with the system impedance. The approach significantly reduces filtering and spacing costs for multipulse systems.

1.3 Motivation

As demonstrated in the previous literature study, the harmonic distortion in distribution systems can negatively influence the power quality of distribution systems equipped with nonlinear loads and inverter-based renewable energy sources. It is necessary to reduce the harmonics inside the system to acceptable levels recommended by the standards. In this regard, the newly published Bald Eagle Search (BES) optimization algorithm is adopted in two different phases to enhance the power quality of distribution systems. In the first phase, the BES algorithm optimizes DG units to minimize the power loss and reduce the unbalance between the three-phase voltages of unbalanced distribution systems. In the second phase of the study, the BES algorithm optimally chooses the sizes and sites of inverter-based distributed generation (IBDG) units and passive filters of balanced distribution systems equipped with nonlinear loads to reduce the harmonics to acceptable limits. In this case, in addition to harmonic emissions from non-linear loads, the harmonic spectrums of IBDGs in the distribution system are examined. The standard Forward/Backward Sweep Method (FBSM) harmonic load flow solves first phase of the study. Different case studies with and without the designed passive filters are applied and compared, achieving many technical and economic objectives such as minimizing the power loss, reducing the THD, and voltage/current unbalance factors of distribution systems.

2 Modeling of Unbalanced Distribution Systems (UDS)

The distribution systems can be generally divided into balanced and unbalanced systems. The balanced distribution systems (BDS) usually are three-phase systems with equal loads and similar cable or feeder impedance per meter. In contrast, unbalanced distribution systems (UDS) have different loads and/or different cable/feeder impedances per phase. Moreover, the UDS may be a single-, two-, or three-

phase system, and it may also contain mutual coupling between its phases, which should be considered when it exists. Another difficulty added to the UDS is the impossibility of solving it as a single-phase system instead of solving the whole three-phase system to consider the mutual coupling between phases, besides the type of connection of the load (delta or star). The different components of the UDS are modeled and applied into FBSM as follows:

2.1 Modeling of Line Branches

The pi-model will be used to depict distribution lines or cables. The model consists of a series impedance and a shunt admittance, as shown in Fig. 1. The four-wire branches with 4×4 matrices are simply converted to 3×3 matrices using Kron reduction [37, 38]. If one or two phases are not found, their self impedances or mutual coupling will be zeros. The relationship between the buses k, j is described as:

$$\begin{bmatrix} V_{ak} - V_{aj} \\ V_{bk} - V_{bj} \\ V_{ck} - V_{cj} \end{bmatrix} = \begin{bmatrix} Z_{aa} & Z_{ab} & Z_{ac} \\ Z_{ba} & Z_{bb} & Z_{bc} \\ Z_{ca} & Z_{cb} & Z_{cc} \end{bmatrix} \times \begin{bmatrix} I_a \\ I_b \\ I_c \end{bmatrix} \tag{1}$$

where V_{ak}, V_{bk}, V_{ck} are the phase voltages at bus k ; the corresponding phase voltages at bus j are V_{aj}, V_{bj}, V_{cj} ; Z_{aa}, Z_{bb}, Z_{cc} represent the self-impedance of the three lines, while the impedances with different subscripts represent the mutual impedance between the corresponding lines; I_a, I_b, I_c are the branch or line currents; Y_{abc} is the shunt admittance at each bus, and Ic_{abc}^k, Ic_{abc}^j are the capacitive currents at buses k, j , respectively due to shunt admittance.

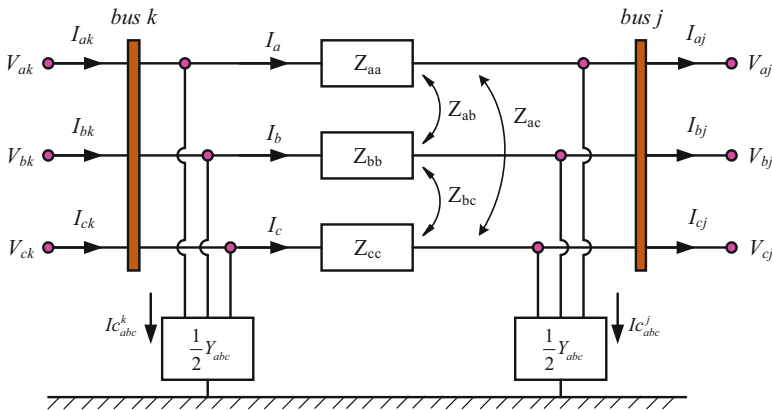


Fig. 1 Representation of a three-phase branch with mutual coupling and shunt capacitance

The values of impedance matrix components rely upon the material, size, and geometric placement of conductors in the space. The shunt currents of the admittance, which is usually susceptance (B), are calculated from the bus voltages as:

$$\begin{bmatrix} I_c^k \\ I_c^k \\ I_c^k \end{bmatrix} = \frac{1}{2} \begin{bmatrix} Y_{aa} & Y_{ab} & Y_{ac} \\ Y_{ba} & Y_{bb} & Y_{bc} \\ Y_{ca} & Y_{cb} & Y_{cc} \end{bmatrix} \times \begin{bmatrix} V_{ak} \\ V_{bk} \\ V_{ck} \end{bmatrix} \quad (2)$$

where the matrix Y represents the admittance matrix of the branch. If the coupling between the phase is neglected and admittance is only equal to the susceptance, the above equation becomes:

$$\begin{bmatrix} I_c^k \\ I_c^k \\ I_c^k \end{bmatrix} = j \frac{1}{2} \begin{bmatrix} B_a & 0 & 0 \\ 0 & B_b & 0 \\ 0 & 0 & B_c \end{bmatrix} \times \begin{bmatrix} V_{ak} \\ V_{bk} \\ V_{ck} \end{bmatrix} \quad (3)$$

Similar equations can be written for the capacitive currents at bus j as:

$$\begin{bmatrix} I_c^j \\ I_c^j \\ I_c^j \end{bmatrix} = j \frac{1}{2} \begin{bmatrix} B_a & 0 & 0 \\ 0 & B_b & 0 \\ 0 & 0 & B_c \end{bmatrix} \times \begin{bmatrix} V_{aj} \\ V_{bj} \\ V_{cj} \end{bmatrix} \quad (4)$$

2.2 Load Modeling

For dynamic distribution system operations, dynamic models for the load should be considered [28, 38], where time-based governing equations are built for the system components and used for transient stability analysis, as an example. On the other hand, when the distribution systems work in a steady-state or quasi-static mode, the loads are constant during each period and are called static loads. Different loads are described as follows.

2.2.1 Constant Real and Reactive Power (CP) Load

With CP load, the three phases could be connected either as star or delta with fixed values of complex power. Thus initially, the complex power is given as:

$$S_{a,b,c} = P_{a,b,c} + jQ_{a,b,c} \quad (5)$$

where the subscripts indicate the same equation for the three phases a, b, c, in this case, the initial currents drawn by the star-connected load are:

$$\begin{bmatrix} I_{La} \\ I_{Lb} \\ I_{Lc} \end{bmatrix} = \begin{bmatrix} (S_a / V_{an})^* \\ (S_b / V_{bn})^* \\ (S_c / V_{cn})^* \end{bmatrix} \quad (6)$$

where I_{La} , I_{Lb} , I_{Lc} are the load current per phase, V_{an} , V_{bn} , V_{cn} are phase to neutral voltage. For delta-connected load, phase currents are calculated from the line voltages and the corresponding apparent power of each phase as:

$$\begin{bmatrix} I_{Lab} \\ I_{Lbc} \\ I_{Lca} \end{bmatrix} = \begin{bmatrix} (S_{ab} / V_{ab})^* \\ (S_{bc} / V_{bc})^* \\ (S_{ca} / V_{ca})^* \end{bmatrix} \quad (7)$$

The line currents drawn by this load are then calculated from the phase counterparts as follows:

$$\begin{bmatrix} I_{La} \\ I_{Lb} \\ I_{Lc} \end{bmatrix} = \begin{bmatrix} 1 & 0 & -1 \\ -1 & 1 & 0 \\ 0 & -1 & 1 \end{bmatrix} \times \begin{bmatrix} I_{Lab} \\ I_{Lbc} \\ I_{Lca} \end{bmatrix} \quad (8)$$

During the load flow solution, voltages are updated with each iteration, and hence, the load currents are also updated while the apparent power is constant.

2.2.2 Constant Impedance (CZ) Load

In this type of load, the load impedance is constant during the load flow solution. For star-connected load, the impedance is calculated from the apparent power of load and rated phase voltage of the system as:

$$\begin{bmatrix} Z_a \\ Z_b \\ Z_c \end{bmatrix} = \begin{bmatrix} |V_{an}^r|^2 / (S_a)^* \\ |V_{bn}^r|^2 / (S_b)^* \\ |V_{cn}^r|^2 / (S_c)^* \end{bmatrix} \quad (9)$$

where V_{an}^r , V_{bn}^r , V_{cn}^r are the rated phase voltages of the distribution system. Thus the load impedance is kept constant during the solution period. The drawn current by the CZ load per phase is calculated from:

$$\begin{bmatrix} I_{La} \\ I_{Lb} \\ I_{Lc} \end{bmatrix} = \begin{bmatrix} V_{an} / Z_a \\ V_{bn} / Z_b \\ V_{cn} / Z_c \end{bmatrix} \quad (10)$$

Note that the load current changes with changing of the phase voltages during the iterations process. For delta-connected load, the impedances are calculated from:

$$\begin{bmatrix} Z_{ab} \\ Z_{bc} \\ Z_{ca} \end{bmatrix} = \begin{bmatrix} |V_{ab}^r|^2 / (S_{ab})^* \\ |V_{bc}^r|^2 / (S_{bc})^* \\ |V_{ca}^r|^2 / (S_{ca})^* \end{bmatrix} \quad (11)$$

where V_{ab}^r , V_{bc}^r , V_{ca}^r are the rated line voltages of the distribution system. The phase currents are given as:

$$\begin{bmatrix} I_{Lab} \\ I_{Lbc} \\ I_{Lca} \end{bmatrix} = \begin{bmatrix} V_{ab} / Z_{ab} \\ V_{bc} / Z_{bc} \\ V_{ca} / Z_{ca} \end{bmatrix} \quad (12)$$

The drawn line currents are then calculated using (8).

2.2.3 Constant Current (CI) Load

In CI load, the current amplitude is kept constant and calculated from the apparent power of the load and rated voltage values. Thus, for star-connected load, the current magnitudes are:

$$\begin{bmatrix} |I_{La}| \\ |I_{Lb}| \\ |I_{Lc}| \end{bmatrix} = \begin{bmatrix} |(S_a / V_{an}^r)^*| \\ |(S_b / V_{bn}^r)^*| \\ |(S_c / V_{cn}^r)^*| \end{bmatrix} \quad (13)$$

For delta-connected load, the current magnitudes are:

$$\begin{bmatrix} |I_{Lab}| \\ |I_{Lbc}| \\ |I_{Lca}| \end{bmatrix} = \begin{bmatrix} |(S_{ab} / V_{ab}^r)^*| \\ |(S_{bc} / V_{bc}^r)^*| \\ |(S_{ca} / V_{ca}^r)^*| \end{bmatrix} \quad (14)$$

For calculating the line currents, Eq. (8) is applied. It is worth mentioning that although the current magnitudes are constants during load flow solution, their phase angles change with changing the voltage phases with iterations. During the iteration process, the angles of the three-phase currents are calculated using the same procedure but taking the bus voltages instead of the rated voltages while keeping the magnitudes without changing.

2.2.4 Capacitor Banks

When a capacitor bank is connected to a system, it can be modeled as a constant impedance or constant admittance load. The admittance of the capacitor bank is modeled in terms of nominal reactive power for star-connection as:

$$\begin{bmatrix} Y_a^c \\ Y_b^c \\ Y_c^c \end{bmatrix} = j \times \begin{bmatrix} B_a^c \\ B_b^c \\ B_c^c \end{bmatrix} = j \times \begin{bmatrix} Q_a^c / |V_{an}^r|^2 \\ Q_b^c / |V_{bn}^r|^2 \\ Q_c^c / |V_{cn}^r|^2 \end{bmatrix} \quad (15)$$

where Y_a^c, Y_b^c, Y_c^c are the admittance of the capacitor bank, and B_a^c, B_b^c, B_c^c are its corresponding susceptance per phase; Q_a^c, Q_b^c, Q_c^c are the rating reactive power of each phase.

The currents of the capacitor bank can be calculated as:

$$\begin{bmatrix} I_{c_a}^c \\ I_{c_b}^c \\ I_{c_c}^c \end{bmatrix} = j \times \begin{bmatrix} B_a & 0 & 0 \\ 0 & B_b & 0 \\ 0 & 0 & B_c \end{bmatrix} \times \begin{bmatrix} V_{an} \\ V_{bn} \\ V_{cn} \end{bmatrix} \quad (16)$$

where $I_{c_a}^c, I_{c_b}^c, I_{c_c}^c$ are the capacitance current per phase. For delta-connection, the capacitive currents are calculated based on the line voltages instead of the phase values, as:

$$\begin{bmatrix} I_{c_{ab}}^c \\ I_{c_{bc}}^c \\ I_{c_{ca}}^c \end{bmatrix} = j \times \begin{bmatrix} B_{ab} & 0 & 0 \\ 0 & B_{bc} & 0 \\ 0 & 0 & B_{ca} \end{bmatrix} \times \begin{bmatrix} V_{ab} \\ V_{bc} \\ V_{ca} \end{bmatrix} \quad (17)$$

When calculating the line currents, (8) is applied. Note that the capacitor currents vary with the voltage of the bus they connected to it. The phase susceptance is calculated from the nominal reactive power and the nominal line voltage.

3 Harmonic Load Flow Analysis

Newton-Raphson has effectively handled the challenge of well-conditioned power systems using rapidly decoupled power fluid solution techniques. Nevertheless, these approaches can fail or have difficulties with distribution network operations [2, 39]. Considering IBDG and nonlinear loads in distribution networks, power flow techniques with appropriate robustness and convergence characteristics need to be used. The FBSM approach [40] is a robust method used in distribution systems with harmonic load flow. In this case, the distribution system should be modeled to cover all considered harmonics of the IBDG and nonlinear loads. Thus, the system should be modeled as passive elements and harmonic current sources. The CP load is expressed using the resistance-inductance combination for linear loads. On the other hand, the nonlinear loads are expressed as harmonic current sources. For each existing harmonic, a constant current is injected into the system with appropriate magnitude and phase. The FBSM runs as before in two steps. In the first forward step, the linear, nonlinear, and IBDG currents are calculated at each harmonic order, starting from the farthest bus and moving toward the slack bus. The

second backward step calculates the voltages starting from the slack bus and moving towards the ends of the feeders. The modeling of all components for harmonic FBSM load flow is discussed as follows.

3.1 Linear Loads

The linear load with specified constant active power and reactive power is modeled as a parallel combination [41] of resistance and inductive reactance as:

$$Z_L^{(h)} = \frac{R_L(hX_L)^2 + j(hX_L)R_L^2}{R_L^2 + (hX_L)^2} \quad (18)$$

where $Z_L^{(h)}$ is the harmonic load impedance; h is the harmonic order; R_L, X_L are the resistance and reactance at the fundamental frequency and calculated from the load power as:

$$R_L^k = V_k^2 / P_{IL}^k \quad (19)$$

$$X_L^k = V_k^2 / Q_{IL}^k \quad (20)$$

where R_L^k, X_L^k are the resistance and reactance of the load calculated at the nominal voltage V_k at any bus, k and the linear load have real and reactive power of P_{IL}^k, Q_{IL}^k at the same bus k .

The current of a linear load at any bus k , is calculated as:

$$I_{IL,k}^{(h)} = V_k^{(h)} / Z_L^{(h)} \quad (21)$$

It should be pointed out that the voltages are calculated at the base load of the system, without any harmonics or DG units, using standard FBSM load flow. The reactive part of the impedance load increases with increasing harmonic frequency, which reduces harmonic currents.

3.2 Nonlinear Loads

The nonlinear loads are modeled as shunt currents at fundamental and other h^{th} harmonic orders from the specified active and reactive powers at any bus k , as follows [39]:

$$I_{\text{nL},k}^{(1)} = \left[\left(P_{\text{nL}}^k + j Q_{\text{nL}}^k \right) / V_k^{(1)} \right]^* \quad (22)$$

$$I_{\text{nL},k}^{(h)} = r(h) \times I_{\text{nL},k}^{(1)} \quad (23)$$

where P_{nL}^k , Q_{nL}^k are the active and reactive powers of the nonlinear load at bus, k ; $V_k^{(1)}$, $I_k^{(1)}$ are the fundamental voltage (of the bus at which it is connected), and the current of the nonlinear load; $I_k^{(h)}$ is the h^{th} harmonic current component; $r(h)$ is the ratio of the harmonic currents to the fundamental value.

3.3 Branch Impedance

The distribution systems usually have a known branch impedance matrix of the normal load at the fundamental frequency operation (without harmonics included). For harmonic load flow, this impedance is modified to include the effects of the harmonic frequencies. The reactive part of the branch impedance is affected by higher frequencies as [41]:

$$Z_{\text{B}}^{(h)} = R_{\text{B}} + jh \times X_{\text{LB}} \quad (24)$$

where $Z_{\text{B}}^{(h)}$ is the branch series impedance connected between any two buses; R_{B} , X_{LB} are the resistance and inductive reactance of the branch impedance at the fundamental frequency.

The shunt admittance of the branch is modified to [42]:

$$Y_{\text{B}}^{(h)} = jh \times X_{\text{CB}} \quad (25)$$

where X_{CB} is the fundamental capacitive reactance of the branch admittance. If the skin effect is taken into consideration [42], the resistance of the overhead lines is modified to:

$$R_{\text{B}}^{(h)} = R_{\text{B}} \times \left(1 + \frac{0.646 \times h^2}{192 + 0.518 \times h^2} \right) \quad (26)$$

While for the underground cables [42], it is corrected to:

$$R_{\text{B}}^{(h)} = R_{\text{B}} \times \left(0.187 + 0.532 \times \sqrt{h} \right) \quad (27)$$

3.4 Transformers

A simple representation of a transformer is a series resistance with an inductance that is a function of harmonics when saturation and capacitance are neglected for harmonic calculations as [41]:

$$Z_T^{(h)} = R_T + jh \times X_T \quad (28)$$

where Z_T^h is the transformer impedance at any harmonic, h ; R_T , X_T are, respectively, the resistance and inductive reactance at the fundamental frequency.

3.5 DG Units

When the DG units are turbine-generator types (non-inverter-based) without any power electronics interfaces, they can be modeled as a current source injecting power into the distribution system at the fundamental frequency only. The current of the non-inverter-based DG is calculated from its specific power and the nominal bus voltage connected to it as:

$$I_{DG,k}^{(1)} = -\left[\left(P_{DG}^k + jQ_{DG}^k\right) / V_k^{(1)}\right]^* \quad (29)$$

$$I_{DG,k}^{(h)} = 0 \quad (30)$$

where $I_{DG,k}^{(1)}$, $I_{DG,k}^{(h)}$ are the fundamental and harmonic currents of the DG unit; P_{DG}^k , Q_{DG}^k are the real and reactive power of the DG; $V_k^{(1)}$ is the fundamental voltage of bus k to which the DG is connected. The negative sign represents the current reference direction of the DG. On the other hand, the IBDG units are modeled in the same way as non-inverter-based DG except for the harmonic currents as:

$$I_{DG,k}^{(h)} = r(h) \times I_{DG,k}^{(1)} \quad (31)$$

3.6 Passive Harmonic Filters

The passive shunt harmonic filter (PHF) consists of combinations of inductance and capacitance tuned to a specific harmonic frequency, where it provides a low-impedance path to the harmonic current. Initially, the capacitance of the filter C_F is estimated from the required reactive power (Q_c), generated from the BES algorithm

as [43]:

$$C_F = \frac{Q_c}{m\omega V_{Ln}} \quad (32)$$

where m is the branches of the filter ($m = 3$ for a three-phase system); ω is the radian frequency of the supply; V_{Ln} is the fundamental voltage across the filter.

The inductor (L_F) required to trap the specific harmonic current is calculated from the filter capacitance:

$$L_F = \frac{1}{h^2\omega^2 C_F} \quad (33)$$

The series resistance of the filter, including the internal coil resistance and any other design value, is calculated from:

$$R_F = \frac{h \times \omega L_F}{Q_f} = \frac{\sqrt{L_F/C_F}}{Q_f} \quad (34)$$

where Q_f is the quality factor of the filter, generally with a range of $10 < Q_f < 100$ for single-tuned filters [43].

The total impedance of the PHF is calculated from:

$$Z_F^{(h)} = R_F + jh \left(\omega L_F - \frac{1}{\omega C_F} \right) \quad (35)$$

The current drawn by the PHF at any bus k can be calculated as:

$$I_{F,k}^{(h)} = V_k^{(h)} / Z_F^{(h)} \quad (36)$$

4 Problem Mathematical Formulations

As discussed earlier in this chapter, the PQ of distribution systems is relieved in two directions. In the first direction, the PQ of distribution systems is enhanced by decreasing the unbalance factor and keeping it as small as possible while the load is modeled as CP type. On the other hand, the reductions of the THD with accompanied harmonic load flow are performed in the second direction. The BES algorithm is adopted to optimally size and site the DG and PHF devices for both cases. These two targets and directions are formulated as follows:

4.1 Case I: PQ of UDS Without Consideration of Harmonics

In this case study, the main objectives are to reduce the power loss and unbalance-factor (UF) and TVD of unbalanced distribution systems (UDS) loaded by CP loads by optimal allocation of DG units. The DG is considered a non-inverter-based type, and nonlinear loads are not considered. The system is solved using the standard FBSM load flow.

The UDSs have different currents passing through their feeders. Thus, the power loss of any branch (P_{branch}) and reactive power loss located between two successive buses without mutual coupling between the phases are calculated as:

$$P_{\text{branch}} = \sum_{k=a,b,c} I_k^2 \times R_k \quad (37)$$

$$Q_{\text{branch}} = \sum_{k=a,b,c} I_k^2 \times X_k \quad (38)$$

where I_k is the per phase current; R_k , X_k is the per phase resistance and inductive reactance; $k = a, b, c$.

When the mutual coupling between the three phases exists, the branch power and reactive losses should be calculated from the difference between the apparent powers at the sending and receiving ends of the same branch. For a branch connected between buses i, j , the losses are:

$$P_{\text{branch}} = \Re \left[\sum_{k=a,b,c} \left(V_k^i \times (I_k^i)^* - V_k^j \times (I_k^j)^* \right) \right] \quad (39)$$

$$Q_{\text{branch}} = \Im \left[\sum_{k=a,b,c} \left(V_k^i \times (I_k^i)^* - V_k^j \times (I_k^j)^* \right) \right] \quad (40)$$

The total losses of the system depend on the number of branches (N_R):

$$P_{\text{Loss}} = \sum_{k=1}^{N_R} P_{\text{branch},k} \quad (41)$$

$$Q_{\text{Loss}} = \sum_{k=1}^{N_R} Q_{\text{branch},k} \quad (42)$$

The voltage unbalance factor at any bus k [28] is calculated from:

$$\text{UF}^k = \frac{\max \left[\left(V_a^k - V_{\text{avg}}^k \right), \left(V_b^k - V_{\text{avg}}^k \right), \left(V_c^k - V_{\text{avg}}^k \right) \right]}{V_{\text{avg}}^k} \quad (43)$$

The UF of the system is considered as the maximum unbalance generated at all buses of the system:

$$UF = \max \left(\left\{ UF^k, k = 1, 2, \dots, N_B \right\} \right) \quad (44)$$

where N_B is the system number of buses.

The total voltage deviation per phase (TVD $_{\varnothing}$) is calculated separately for each phase as:

$$TVD_{\varnothing} = \sum_{k=1}^{N_B} |(1 - V_k)| \quad (45)$$

The TVD of the system is taken as the maximum deviation out of three phases:

$$TVD = \max \left(\{TVD_{\varnothing}, \varnothing = a, b, c\} \right) \quad (46)$$

The considered objectives functions considered for UDS and optimized by BES algorithm are:

$$\begin{aligned} f_{\text{obj},1} &= \min (P_{\text{Loss}}) \\ f_{\text{obj},2} &= \min (UF) \\ f_{\text{obj},3} &= \min (TVD) \end{aligned} \quad (47)$$

4.2 Case II: PQ of BDS with Consideration of Harmonics

This section provides the performance design of balanced distribution systems (BDS) equipped with nonlinear load, IBDG units, and passive harmonic filters. The nonlinear loads are considered harmonic current sources, where the fundamental currents are estimated from their power and the nominal voltage value of the bus to which they are connected. The other harmonic currents are calculated as a percentage of the fundamental current. On the other hand, the linear loads are treated as a parallel combination of resistance and inductive reactance calculated from their specific power. The IBDG units are also considered harmonic currents, where the BES algorithm estimates the optimal power values. Their fundamental currents are calculated based on the estimated power and the bus voltages. The higher-frequency currents of the IBDG are calculated from the fundamental current.

The fundamental and harmonic components of the voltages and currents of the BDS can be found by the FBSM load flow, considering each harmonic as a case study and implementing the superposition technique to calculate the performance parameters such as the total system losses, TVD, and THD. In the forward step, the currents of the linear, nonlinear loads, PHF, and IBDG are calculated. The branch currents are then estimated using KCL, starting from the farthest bus and moving

towards the slack bus. Noting that the harmonic currents of the nonlinear loads and IBDG are constants during the iteration process of the FBSM load flow. At any iteration, the current of a branch i can be calculated as the sum of all shunt currents connected at the receiving end bus and the currents of successive branches:

$$I_i^{(h)} = I_{\text{IL},i}^{(h)} + I_{\text{nL},i}^{(h)} - I_{\text{DG},i}^{(h)} + I_{\text{F},i}^{(h)} + \sum_{\substack{m \neq i \\ m \in Mb}} I_m^{(h)};$$

$$i = N_{\text{R}}, N_{\text{R}} - 1, \dots, 1 \quad (48)$$

where $I_i^{(h)}$ is the harmonic current of branch i at any iteration; $I_{\text{IL},i}^{(h)}$ is the harmonic current of linear load; $I_{\text{nL},i}^{(h)}$ is the harmonic current of nonlinear load; $I_{\text{DG},i}^{(h)}$ is the harmonic current of IBDG units injected into the system; $I_{\text{F},i}^{(h)}$ is the harmonic current of the PHF; $I_m^{(h)}$ is the branch current connected to the branch i ; Mb is the number of branches connected to branch i .

In the backward step, the voltage drops of the branches and voltages of all buses can be calculated from the previous branch currents using KVL. The harmonic voltage at bus $k + 1$ can be calculated from the preceding harmonic voltage of bus k as:

$$V_{k+1}^{(h)} = V_k^{(h)} - I_i^{(h)} \times Z_i^{(h)} \quad (49)$$

where $Z_i^{(h)}$ is the branch impedance between the buses $k, k + 1$.

The power losses of BDSs are calculated as the sum of all branch losses at all frequencies as follows:

$$P_{\text{Loss}} = 3 \times \sum_{k=1}^{N_{\text{R}}} \sum_{h=1}^{h_{\text{max}}} \left(I_k^2 \times R_k \right)_h \quad (50)$$

$$Q_{\text{Loss}} = 3 \times \sum_{k=1}^{N_{\text{R}}} \sum_{h=1}^{h_{\text{max}}} \left(I_k^2 \times X_k \right)_h \quad (51)$$

where R_k, X_k are the resistance and reactance of the branch k ; I_k is the branch current; the constant three is applied for three-phase systems; h_{max} is the maximum considered harmonic order.

The THD is calculated at all buses for all harmonic frequencies as follows:

$$\text{THD} = \max \left(\sum_{k=1}^{N_{\text{B}}} \left[\frac{1}{V_{1,k}} \times \sqrt{\sum_{h=2}^{h_{\text{max}}} V_{k,h}^2} \right] \right) \quad (52)$$

where $V_{1,k}$ is the fundamental voltage of bus k ; $V_{k,h}$ is the voltage at bus k for harmonic frequency h .

The voltage profile enhancement can be expressed using the TVD, which can be estimated as:

$$\text{TVD} = \sum_{k=1}^{N_B} \left| \left(1 - \sqrt{\sum_{h=1}^{h_{\max}} V_{k,h}} \right) \right| \quad (53)$$

The objectives functions considered for BDS and optimized by BES algorithm are:

$$f_{\text{obj},1} = \min (P_{\text{Loss}})$$

$$f_{\text{obj},2} = \min (\text{THD}) \quad (54)$$

5 Outline of the Bald Eagle Search (BES) Algorithm

The bald eagle search (BES) algorithm [44] is a metaheuristic optimization algorithm inspired by nature that refers to the hunting technique or sophisticated social behavior of bald eagles in pursuit of fish. Bald eagles are a chance-oriented forgers and the most of them pick fish (living or dead), especially salmon, as the primate meal. The BES algorithm imitates the bald eagle's behavior in hunting its prey. The hunting process is divided into three stages, as shown in Fig. 2.

1. Select stage:

During the chosen stage, the bald eagles identify and select the optimal place in the selected search area (in relation to the amount of food) for the prey. This process can be represented mathematically as [44]:

$$X_{\text{new},i} = X_{\text{best}} + \alpha \times r \times (X_{\text{mean}} - X_i) \quad (55)$$

where α , r are a control parameter takes a value of 1.5–2, and a random number [0 1], respectively; X_{best} , X_{mean} , $X_{\text{new},i}$ are the best position so far (of the previous step), the average of all particles positions, and the new position of a particle i , respectively.

2. Search stage:

Bald eagles look for prey in the chosen search region and travel in a spiral to speed up the search in the searching stage. The new position is identified as [44]:

$$X_{\text{new},i} = X_i + \delta(i) \times (X_i - X_{i+1}) + \gamma(i) \times (X_i - X_{\text{mean}}) \quad (56)$$

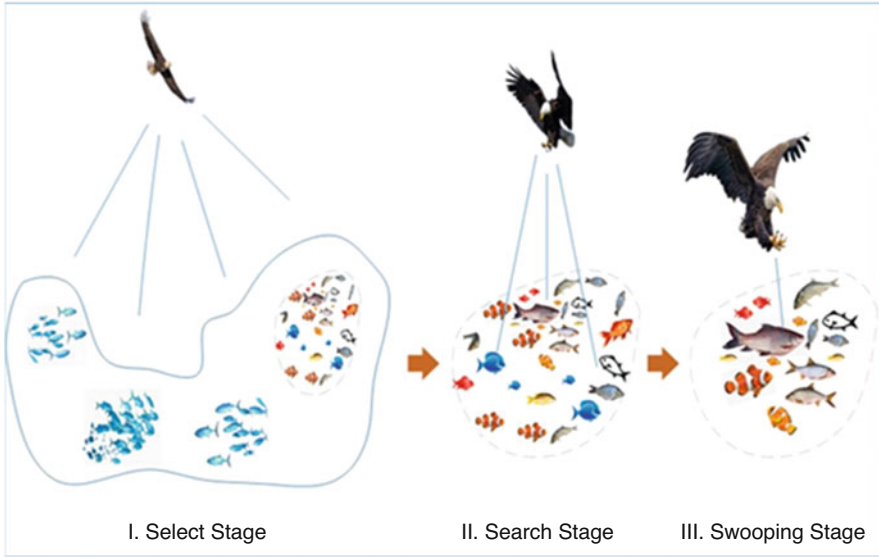


Fig. 2 The behavior of bald eagles during the three stages of hunting prey

$$\gamma(i) = \gamma_1(i) / \max(|\gamma_1|), \delta(i) = \delta_1(i) / \max(|\delta_1|) \quad (57)$$

$$\gamma_1(i) = r(i) \times \sin(\theta(i)), \delta_1(i) = r(i) \times \cos(\theta(i)) \quad (58)$$

$$\theta(i) = a\pi \times \text{rand}, r(i) = \theta(i) + \mu \times \text{rand} \quad (59)$$

where a is a parameter (5–10); μ is another parameter (0.5–2);

3. Swooping stage:

Bald eagles swoop from the best location in the search space to their prey during the swooping stage. Everything also goes to the best place. This moving is expressed as follows [44]:

$$X_{\text{new},i} = \text{rand} \times X_{\text{best}} + \gamma_1(i) \times (X_i - c_1 \times X_{\text{mean}}) + \delta_1(i) \times (X_i - c_2 \times X_{\text{best}}) \quad (60)$$

$$\gamma_1(i) = \gamma_2(i) / \max(|\gamma_2|), \delta_1(i) = \delta_2(i) / \max(|\delta_2|) \quad (61)$$

$$\gamma_2(i) = r(i) \times \sinh(\theta(i)), \delta_2(i) = r(i) \times \cosh(\theta(i)) \quad (62)$$

$$r(i) = \theta(i) = a\pi \times \text{rand} \tag{63}$$

where $c_1, c_2 \in [1, 2]$. The hunting stages of the BES algorithm are outlined in Fig. 2.

6 Simulation Results and Discussions

The simulation part will be broadly divided into two sections to cover the PQ enhancement of unbalanced (UDS) and balanced (BDS) distribution systems. The PQ of UDS will be studied on the IEEE 10-bus and IEEE 37-bus systems. On the other hand, the PQ analysis of BDS with nonlinear loads and IVBD units using harmonic load flow will be on the 69-bus and 118-bus distribution systems.

6.1 Case I: PQ of Unbalanced Distribution Systems

The solution of the UDS is performed using the standard FBSM, with the modeling of system components outlined in Sect. 3. The PQ of the distribution systems is achieved by the optimal allocation of DG units using the BES algorithm. Two UDSs are used as test systems: the 8.66 kV10-bus, as shown in Fig. 3, and the 4.8 kV 37-bus system, as shown in Fig. 4. The 10-bus UDS [28, 45] is an unbalanced system with single-, two-, and three-phase branches and loads with mutual coupling branch impedances. The total load of the system is 825 kW, 475 kVar, where phase A represents more than 50% of the total load. The 37-bus UDS has a very unbalanced load with a total of 2457 kW, 1201 kVar. A delta configuration of ungrounded loads characterizes the system, with some nodes that are not loaded at all. The two systems are simulated to check the provided modeling techniques, and their solutions are compared to the solutions provided in the literature.

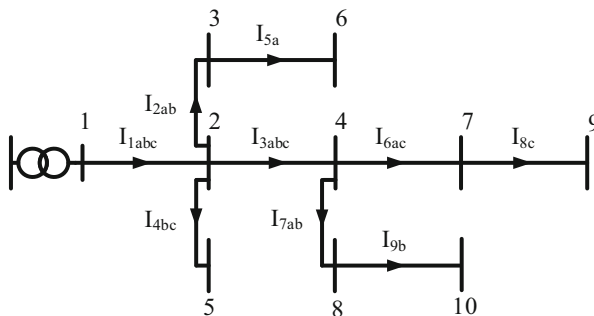


Fig. 3 The 10-bus unbalanced distribution system layout

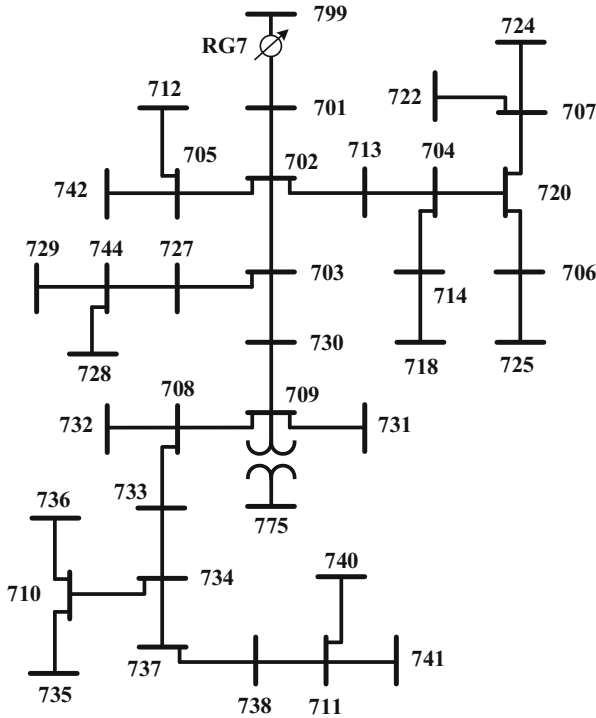


Fig. 4 The 37-bus unbalanced distribution system layout

6.1.1 Base Case Solution

In this section, the two UDSs are simulated and solved using standard FBSM load flow without DG integrations to check the precision of the modeling method discussed before. The performance of the two systems for the base case is listed in Table 1. As can be noticed, the maximum mismatch for the 10-bus UDS is 0.2539 V for phase B, while it is 0.2693 V for the same phase for the 37-bus UDS. These values indicate very small mismatches and acceptable modeling techniques. The power losses per phase and the total losses are also indicated in the table. As the A-phase of the 10-bus UDS is heavily loaded, the power loss of it is much higher than the other two phases, B and C. The total losses are 28.96 kW and 42.58 kVar. The TVD per phase is maximum for phase A due to the big load, and the average of the TVD (TVD_{av}) is 0.1911 pu, and the unbalance factor of the voltage (UF_v) and current (UF_i) are 3.75% and 74.30%, respectively. The UF_i is significantly large due to the big unbalance between the three phases (Phase A represents more than 50% of the total load). This large unbalance affects the operation of the transformer and supply and causes many problems for other loads connected to the same grid.

Table 1 Base case performance of the 10-bus and 37-bus UDSs

Parameter	10-bus			37-bus		
	Phase A	Phase B	Phase C	Phase A	Phase B	Phase C
V_{\min} (pu)	0.9190	0.9815	0.9671	0.9981	0.9950	0.9847
V_{\max} (pu)	1.0	1.0	0.9864	1.0437	1.0250	1.0345
Mismatch (V)	0.2054	0.2539	0.1955	0.2386	0.2693	0.2389
P_{Loss}/φ (kW)	24.7486	0.6533	3.5543	26.6690	13.8037	20.0871
P_{Loss} (kW)	28.9562			60.5598		
Q_{Loss}/φ (kVar)	37.4840	3.3682	1.7326	18.7678	17.7342	9.9517
Q_{Loss} (kVar)	42.5849			46.4538		
TVD/ φ (pu)	0.4039	0.0603	0.1090	0.5438	0.1645	0.2972
TVD _{av} (pu)	0.1911			0.3352		
UF _v (%)	3.7543			1.3068		
UF _i (%)	74.3015			16.7749		

Moreover, the unbalance causes more losses, motor failure, a decrease in life cycles, and relay malfunctions.

The performance of the 37-bus UDS is quite different. The active and reactive losses per phase and total values are represented in the table. As noticed, the active loss of phases A and C are near each other, while phase B is quite small. For reactive loss, phases A, B are similar, and phase C is smaller than them. This indicates current unbalance in the system through the branches. The P_{Loss} and Q_{Loss} reaches 60.56 kW and 46.45 kVar, respectively. The TVD is maximum for phase A with a value of 0.544 pu with a TVD_{av} of 0.3352 pu while the UF_v and UF_i are 1.31% and 16.77%, respectively. Although the voltage unbalance factor is acceptable [46], the current unbalance factor is higher than the standards.

6.1.2 Single-Objective Optimization (SOO)

The BES algorithm is adopted here to optimally determine the sizes and sites of DG units in order to reduce the objective functions regarding the power loss, unbalance factors, and TVD. Due to the large unbalance between the three phases of the studied systems, especially the 10-bus UDS, the optimization algorithm is solved such that every phase is optimized separately. The BES algorithm optimizes three DG units simultaneously, one for each phase of the system, and so the locations may be at different buses. The DG units are assumed to work at the unity power factor. The simulation study includes the following cases to reduce the following objectives:

- The total loss of the systems ($f_{\text{obj}} = P_{\text{Loss}}$)
- The average TVD of voltages ($f_{\text{obj}} = \text{TVD}_{\text{av}}$)
- The voltage unbalance factor ($f_{\text{obj}} = \text{UF}_v$)
- The current unbalance factor ($f_{\text{obj}} = \text{UF}_i$)

Table 2 System performance with minimizing P_{Loss} and TVD_{av}

Objective/parameter	$f_{obj} = P_{Loss}$		$f_{obj} = TVD_{av}$	
	10-bus	37-bus	10-bus	37-bus
DG sizes (kW) $\left\{ \begin{array}{l} a \\ b \\ c \end{array} \right.$	357.64 (4)	345.54 (33)	450.0 (7)	109.65 (1)
	200.00 (2)	489.05 (11)	200.0 (8)	109.97 (37)
	122.61 (4)	649.75 (28)	156.81 (4)	40.12 (1)
V_{min} (pu) $\left\{ \begin{array}{l} a \\ b \\ c \end{array} \right.$	0.9373	1.0275	0.9399	0.9980
	0.9807	1.0056	0.9933	0.9962
	0.9864	1.0146	0.9929	0.9890
V_{max} (pu) $\left\{ \begin{array}{l} a \\ b \\ c \end{array} \right.$	1.0	1.0437	1.0000	1.0437
	1.0	1.0250	1.0032	1.0250
	1.0	1.0345	1.0005	1.0345
P_{Loss} (kW)	14.08	20.93	20.79	56.27
Q_{Loss} (kVar)	18.70	9.74	25.24	42.49
TVD_{av} (pu)	0.12	0.02	0.08	0.01
UF _v (%)	2.20	1.36	1.90	1.22
UF _i (%)	89.36	12.46	92.25	17.37

Table 3 System performance with minimizing UF_v and UF_i

Objective Parameter	$f_{obj} = UF_v$		$f_{obj} = UF_i$	
	10-bus	37-bus	10-bus	37-bus
DG sizes (kW) $\left\{ \begin{array}{l} a \\ b \\ c \end{array} \right.$	450.0 (4)	697.04 (24)	450.0 (4)	20.00 (37)
	200.0 (10)	341.86 (9)	15.43 (1)	150.17 (2)
	175.0 (8)	907.71 (17)	58.22 (1)	526.01 (37)
V_{min} (pu) $\left\{ \begin{array}{l} a \\ b \\ c \end{array} \right.$	0.9433	0.9973	0.9396	1.0178
	0.9897	0.9989	0.9649	0.9944
	0.9763	0.9878	0.9832	1.0103
V_{max} (pu) $\left\{ \begin{array}{l} a \\ b \\ c \end{array} \right.$	1.0000	1.0437	1.0	1.0437
	1.0336	1.0250	1.0	1.0250
	1.0000	1.0345	1.0	1.0345
P_{Loss} (kW)	23.82	52.30	17.79	36.88
Q_{Loss} (kVar)	26.76	38.42	26.05	24.49
TVD_{av} (pu)	0.113	0.006	0.14	0.012
UF _v (%)	0.84	0.91	1.49	1.83
UF _i (%)	53.63	23.46	29.34	0.04

Implementing the described models of the 10-bus and 37-bus UDS, the BES algorithm optimizes the different DG units of the three phases separately and determines their sizes and locations in order to achieve the listed objective functions independently. The performance of the two systems when optimizing the P_{Loss} , and TVD_{av} are listed in Table 2, while Table 3 shows their performance when optimizing the UF_v and UF_i using the BES algorithm in SOO operations, respectively. Each table shows the DG sizes, their locations, minimum voltages (V_{min}) and maximum

voltages (V_{\max}) for each phase, and the other objective functions besides the total reactive power loss (Q_{Loss}). When the BES algorithm optimizes the DG units to reduce P_{Loss} , the active and reactive losses are reduced by 51.37%, and 56.09%, and by 65.44%, 79.03% for the 10-bus and 37-bus systems, respectively. At the same time, the TVD_{av} , UFv are also reduced by 37.21%, 41.40% for the 10-bus system, while the TVD_{av} is reduced by 94.03% and UFv is increased by 4.07% for the 37-bus system. Regarding the UFi is increased by 20.27% and reduced by 25.72% for the 10-bus and 37-bus systems, respectively. The corresponding voltage profiles of the 10-bus and 37-bus UDSs are shown in Figs. 5 and 6, respectively, for simulation case studies as well as for the base case. The minimum voltages of each system are improved by allocating the DG units into the UDSs. The corresponding voltage profiles of this case are shown in Figs. 5b and 6b.

When the BES algorithm optimizes the problem to reduce the average TVD (TVD_{av}), the systems show better performance compared to the base case. The lower values of the TVD_{av} indicate the bus voltages are near to the reference voltage. The optimal DG allocation reduces the TVD_{av} by 58.14% and 97.02% for the 10-bus and 37-bus systems, respectively. Moreover, the power losses (P_{Loss} , Q_{Loss}) are reduced by 28.20%, 40.73%, and 7.08%, 8.53% for the two systems in the same order. The related voltage profiles of this case are shown in Figs. 5c and 6c.

The BES algorithm optimizes three DG units in the same way to reduce the third objective function (UFv). The UFv should be as small as possible for its deterministic effects on the systems and loads. The BES algorithm reduces the UFv by 77.63% and 30.36% compared to the base case for the 10-bus and 37-bus UDSs, respectively. Simultaneously, the power losses P_{Loss} , Q_{Loss} are reduced by 17.74%, 37.16%, and 13.64%, 17.29%, for the two systems, respectively. Concurrently, the TVD_{av} is reduced by 40.87% and 98.21% for the same systems. The analogous voltage profiles for this case study are shown in Figs. 5d and 6d, respectively, for the two considered systems. As it can be seen, the three phases at each bus are getting closer.

Due to the conflicting nature of the objective functions, we can notice that the UFi may increase or decrease depending on the case study and distribution system. It is very important to balance the currents in the three phases of any distribution system. If the currents in the phases are equal, they lead to the equal cross-sectional area required for the wires and equal power losses for each phase. If the currents become equal, then the system may be transferred to a balanced one. The BES algorithm optimizes the size and sites of the DG units to reduce the UFi to the lowest possible value. The UFi is reduced by 60.51% and 99.76%, respectively, for the 10-bus and 37-bus UDSs. The three-phase currents in the 37-bus UDS are nearly equal. Accompanying with the reduction of the UFi , the power losses are also decreased by 38.56%, 38.83%, and 39.10%, 47.28% for the two systems. Contemporaneous values of TVD_{av} are lessened by 26.74% and 96.42% for the 10-bus and 37-bus UDSs, respectively. The voltage profiles after optimizing the UFi are shown in Figs. 5e and 6e, respectively, for the two systems in the same order. The obtained results emphasize improving the PQ of the distribution systems by optimally allocating different DG units using the BES algorithm.

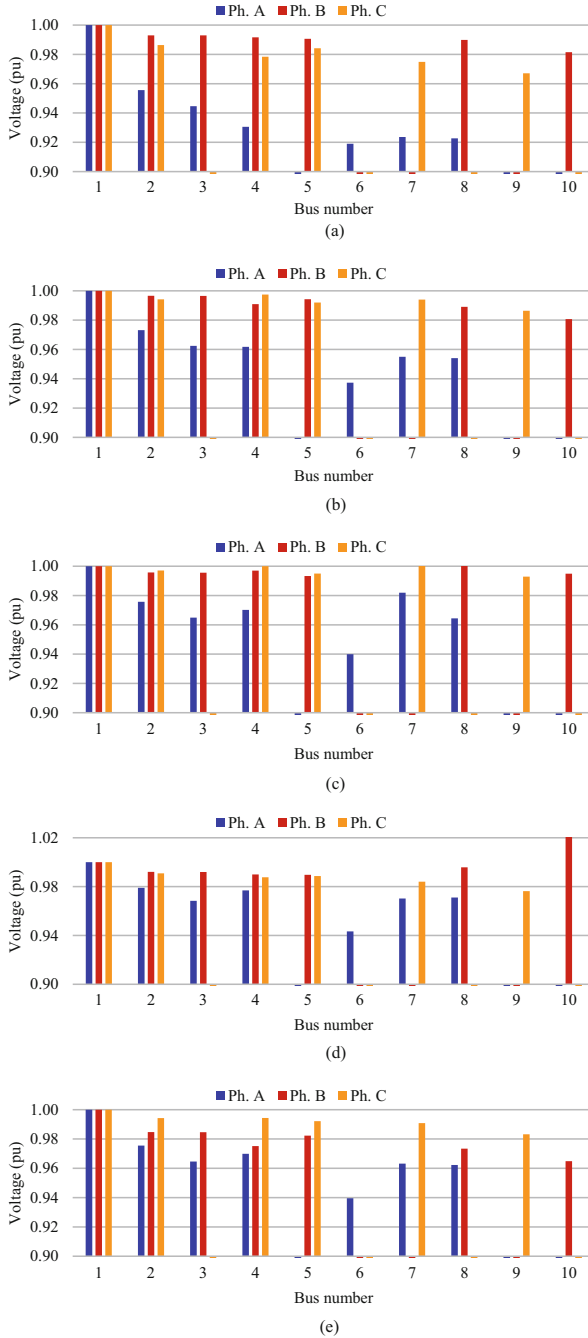


Fig. 5 Voltage profile of the 10-bus UDS under different operating conditions. **(a)** Voltage profile for the base case. **(b)** Voltage profile for objective = P_{Loss} . **(c)** Voltage profile for objective = TVD_{av} . **(d)** Voltage profile for objective = UF_v . **(e)** Voltage profile for objective = UF_i

Fig. 6 Voltage profile of the 37-bus UDS under different operating conditions. **(a)** Voltage profile for the base case. **(b)** Voltage profile for objective = P_{Loss} . **(c)** Voltage profile for objective = TVD_{av} . **(d)** Voltage profile for objective = UF_v . **(e)** Voltage profile for objective = UF_i

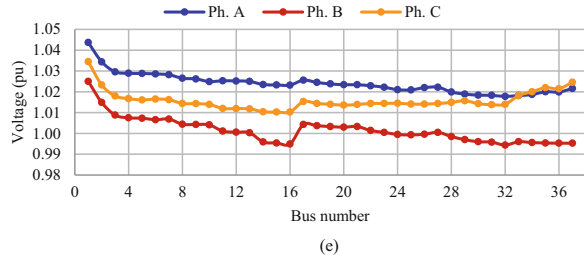
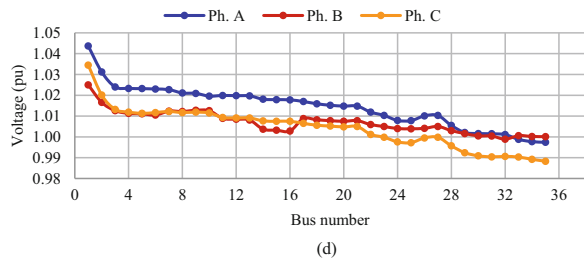
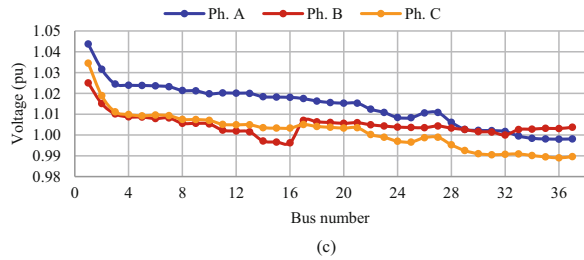
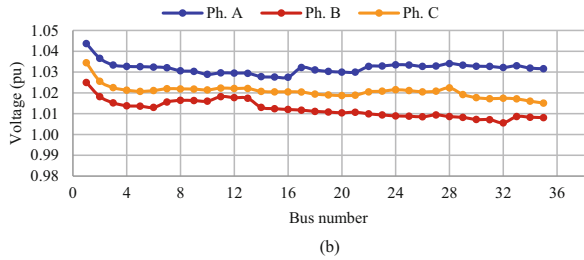
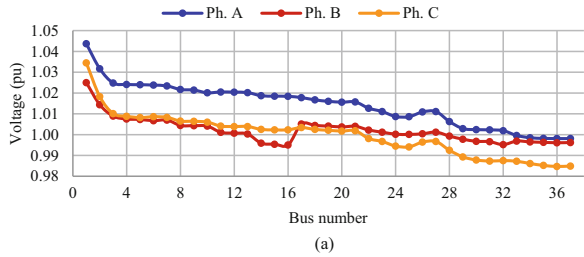


Table 4 System performance with MOO

System/parameters	10-bus			37-bus		
	Base	MOO	Δf (%)	Base	MOO	Δf (%)
DG sizes (kW) $\left\{ \begin{array}{l} a \\ b \\ c \end{array} \right.$	–	434.46 (4) 159.33 (1) 18.98 (6)	–	–	197.89 (34) 326.27 (15) 688.91 (28)	–
V_{\min} (pu) $\left\{ \begin{array}{l} a \\ b \\ c \end{array} \right.$	0.9190 0.9815 0.9671	0.9390 0.9854 0.9826	2.18 0.04 1.60	0.9981 0.9950 0.9847	1.0258 1.0003 1.0154	2.78 0.53 3.12
V_{\max} (pu) $\left\{ \begin{array}{l} a \\ b \\ c \end{array} \right.$	1.0 1.0 0.9864	1.0 1.0 1.0	0.0 0.0 1.38	1.0437 1.0250 0.9847	1.0437 1.0250 1.0345	0.0 0.0 5.06
P_{Loss} (kW)	28.96	17.56	39.35	60.56	27.06	55.31
Q_{Loss} (kVar)	42.58	25.41	40.33	46.45	16.51	64.46
TVD _{av} (pu)	0.191	0.137	28.41	0.335	0.012	96.36
UF _v (%)	3.75	1.47	60.79	1.31	1.20	8.03
UF _i (%)	74.30	29.46	60.35	16.77	0.009	99.95

6.1.3 Multi-Objective Optimization (MOO)

Unbalanced distribution systems are simulated and solved as MOO problems, with the total objective function representing all of the objectives. The aggregated sum technique is used here to build the objective function. The sharing of each objective can vary depending on the system operating conditions or preferences of the operator. In this study, the sharing of the individual objectives is the same and equal to 25%. Thus:

$$f_{\text{MOO}} = \omega_1 P_{\text{Loss}} + \omega_2 \text{TVD}_{\text{av}} + \omega_3 \text{UF}_v + \omega_4 \text{UF}_i \quad (64)$$

where the weight coefficients are:

$$\omega_1 + \omega_2 + \omega_3 + \omega_4 = 1.0 \quad (65)$$

The system performance, in this case, will be a compromised situation between the extreme situations of optimization of each objective individually. The two systems' 10-bus and 37-bus UDSs are optimized with the BES algorithm using the same modeling approach and load flow as previously by allocating a DG unit for each phase of the system. The MOO results obtained for the two systems are listed in Table 4. As can be noticed from Table 4, all the individual objective functions are enhanced and improved overall system performance. The parameter Δf represents the percentage change of the variable parameters and objectives comparing the MOO with the base case for the two distribution systems. The maximum voltages are increased with some phases but still less than the standard value of 1.05 pu.

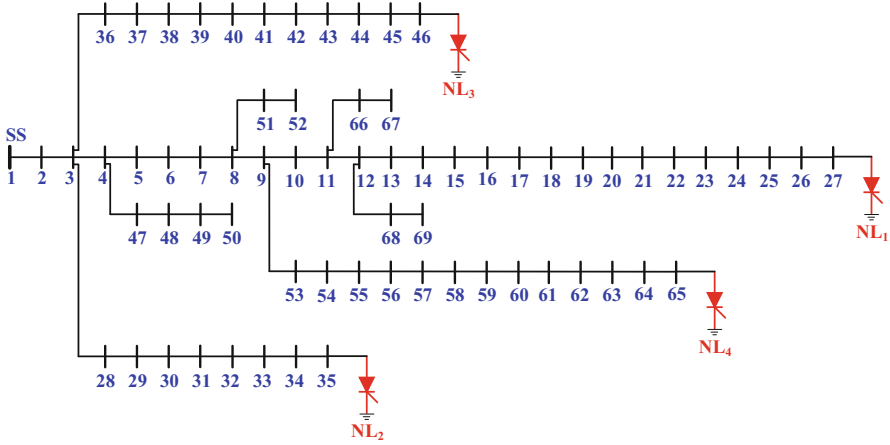


Fig. 7 IEEE 69-bus distribution system with added nonlinear loads

6.2 Case II: PQ of Distribution Systems Considering Harmonics

The second phase of the PQ of distribution systems includes harmonics generated from the nonlinear load connected to them and from the IBDG units. In this study, four similar nonlinear loads (NL₁-NL₄) are connected to the IEEE 69-bus BDS, as shown in Fig. 7. The NL loads are located at the far ends of the main branches to harmonize the whole system (buses 27, 35, 46, and 65). The total NL loads represent 30% of the actual load and are distributed equally between the four locations. These NL loads represent a six-pulse inverter, and they are modeled by current sources injecting harmonics into the system, according to Table 5. The BES algorithm optimizes a MOO problem to reduce the power loss and the THD of the system. In this case, the objective is:

$$f_{MOO} = \omega_1 P_{Loss} + \omega_2 THD \tag{66}$$

where P_{Loss} is the sum of the fundamental and harmonic losses and weighting factors are equal ($\omega_1 = \omega_2 = 0.5$).

It is worth mentioning that the two objective functions are normalized to be used in the final MOO to their values before adding the IBDG and HPF. The study takes three scenarios besides the base case, as follows:

- Scenario A: optimization of HPF
- Scenario B: optimization of two IBDG units
- Scenario C: optimization of HPF and two IBDG units

Table 5 Harmonic spectrum of NL loads and IBDG units [4]

Nonlinear load		IBDG	
Harmonic order	Magnitude (%)	Harmonic order	Magnitude (%)
1	100	1	100
5	68.3	5	38.4
7	47.8	7	11.41
11	20	11	10.8
13	6.1	13	7.3
17	4.2	17	5.4

Table 6 Performance of the 69-bus at different scenarios

Case	V_{\min} (pu)	V_{\max} (pu)	P_{Loss} (kW)	Q_{Loss} (kVar)	TVD (pu)	THD (%)
Base	0.8621	1.0	798.2941	645.3436	3.2776	17.1077
Scenario A	0.9047	1.0	269.1727	149.5126	2.1418	4.8595
Scenario B	0.9292	1.0	130.9398	81.6880	1.2192	2.3025
Scenario C	0.9577	1.0	87.4122	72.2643	0.9587	3.1633

Table 7 Optimized parameters of the HPF

Case	Q_C (kVar)	Site	Q_f	h_f	C_F (μF)	L_F (mH)	R_F (Ω)
Scenario A	1215.22	61	50	5	20.1116	7.1396	0.0119
Scenario C	800.469	64	50	5	13.2476	10.8389	0.5721

6.2.1 Scenario A: Optimization of a Harmonic Power Filter (HPF)

The 69-bus system is modeled for harmonic FBSM load flow equipped with the four nonlinear loads. The BES algorithm optimizes the capacity of the HPF (Q_C), its location, and the harmonic order (h_f) to be tuned to reduce the MOO problem. The filter currents are calculated at all harmonics using Ohm's law. In contrast, at the tuned harmonic order, the current is calculated using Thevenin's equivalent to prevent the resonance between the filter capacitance and the system [3]. Inserting the HPF into the system reduces the THD from 17.11% to 4.86%, as listed in Table 6. The BES algorithm optimizes the filter capacity to 1215.22 kVar and its location at bus number 61 with a tuned harmonic frequency of $h_f = 5$. The other parameters of the optimized HPF are listed in Table 7. Adding the HPF enhances the PQ of the 69-bus system. The power loss reduces to 269.17 kW compared to the 798.29 kW of the base case. Reductions of 66.28% and 76.83% are achieved to active and reactive power losses, respectively. The minimum voltage of the system has been improved from 0.8621 pu to 0.9047 pu with a percentage increase of 4.94%. On the other hand, the TVD and THD are reduced by 34.65% and 71.59%, respectively. The voltage THD values at each bus system are shown in Fig. 8, where the THD is reduced at all buses and meets the standard.

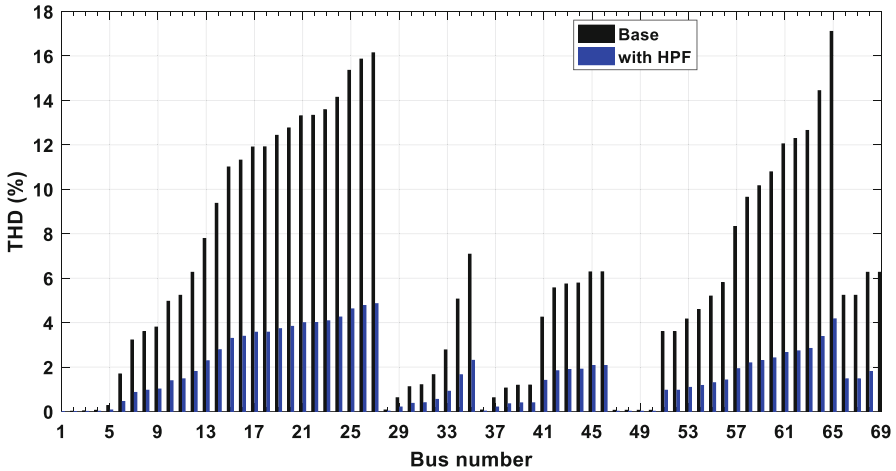


Fig. 8 THD values of the 69-bus system with HPF compared to the base case

Table 8 Optimized parameters of the IBDG units

	IBDG 1			IBDG 2		
Case	Size (kW)	Site	PF	Size (kW)	Site	PF
Scenario B	811.34	61	0.8309	618.05	27	0.8228
Scenario C	1192.00	61	0.8985	1061.72	69	0.9203

6.2.2 Scenario B: Optimization of Two IBDG Units

In this scenario, the polluted 69-bus BDS is simulated using the harmonic FBSM load flow while integrated with two IBDG units operating at OPF. The BES algorithm determines the optimal sizes and sites of the two IBDG in order to minimize the MOO problem (reducing the power loss and THD). The performance parameters are listed in Table 6 for this scenario. Both objective functions are reduced by integrating two IBDG units due to their effects in raising the bus voltages and reducing the system losses. Consequently, the minimum voltage is raised from 0.8621 to 0.9292 pu achieving an increase of 7.78%, while the losses are reduced to 130.94 kW and 81.69 kVar for the active and reactive losses, respectively. The TVD and THD are reduced by 62.80% and 86.54%, respectively. The parameters of the optimized IBDG units are listed in Table 8, and the THD distribution is shown in Fig. 9. The THD at each bus is much reduced compared to the base case.

6.2.3 Scenario C: Optimization of Two IBDG Units and HPF

Here the BES algorithm optimizes the two IBDG and HPF altogether in order to reduce the objective functions of power loss and THD. In this case, both advantages

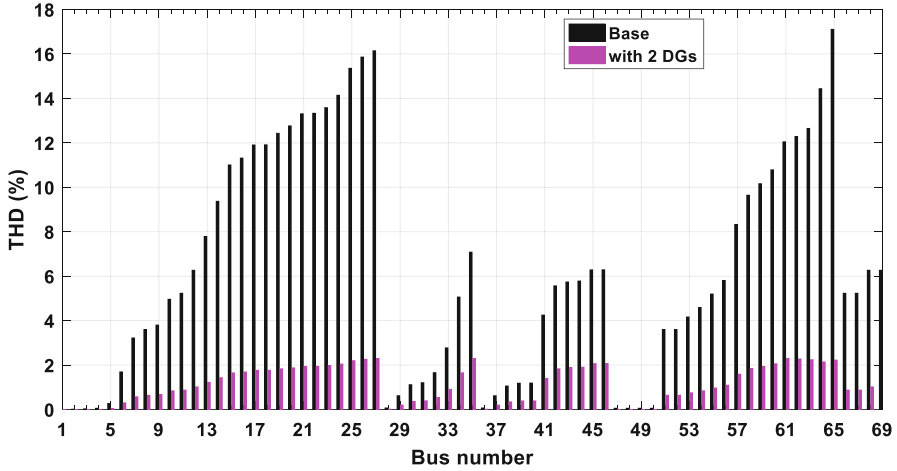


Fig. 9 THD values of the 69-bus system with 2 IBDG units compared to the base case

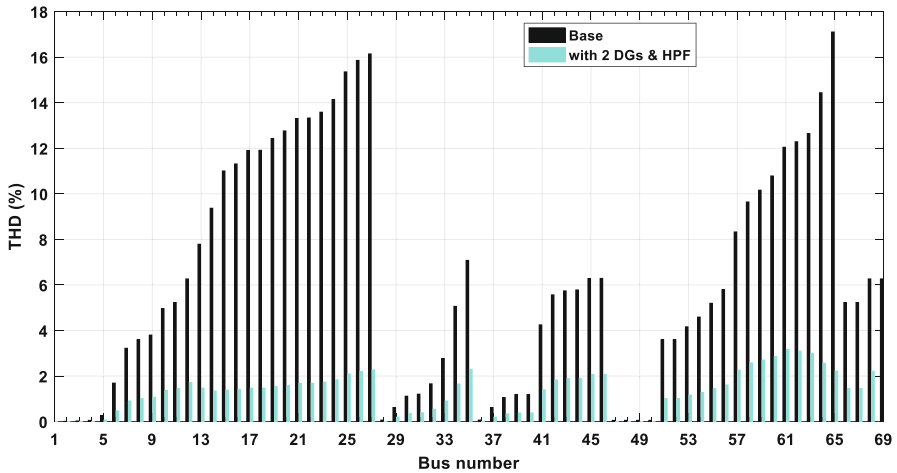


Fig. 10 THD values of the 69-bus system with 2 IBDG units and HPF compared to the base case

of previous cases are attained. The IBDG raises the voltages and reduces the losses, while the HPF reduces the THD of the system. The minimum voltage is raised to 0.9577 pu as listed in Table 6 with the rest of the performance parameters. The active and reactive losses are reduced by 89.05% and 88.80%, respectively. The TVD and THD are minimized by 70.75% and 81.51%, respectively. The optimized parameters of the HPF are listed in Table 7, while the parameters of the two IBDG units are listed in Table 8. The THD distribution at all system buses is shown in Fig. 10, with a remarkable decrease in the values compared to the base case.

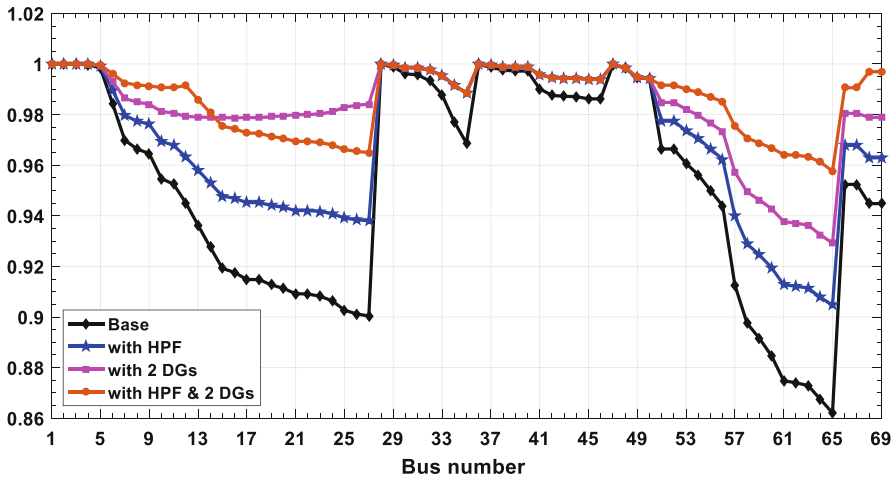


Fig. 11 The rms voltage of the 69-bus system at different scenarios

The voltage distribution for all scenarios is shown in Fig. 11 with the base case. As can be seen, the voltage is improved by each scenario. In the meantime, in scenario C, the most significant improvement is achieved.

7 Conclusions

The chapter proposes two different analysis techniques to solve either balanced or unbalanced distribution systems. In both cases, the Forward/Backward sweep method is adopted appropriately to suit the specified solution. In the first part of the work, the unbalanced distribution systems are solved and optimized to enhance their power quality (PQ) by installing DG units into the system. The BES algorithm minimizes the power loss, TVD, and the unbalance factors of the studied distribution systems to meet the specific standards. The study included both single-objective and multi-objective optimizations. On the other side of the study, a balanced distribution system is modeled and solved using the harmonic load flow to consider the nonlinear and inverter-based DG (IBDG) units harmonics. The BES algorithm is ruled to optimize the system with and without a harmonic power filter to reduce loss and harmonic contents. The THD and harmonic contents are lowered to meet the specified standards with the proposed optimization methodology. Two IBDG units are optimally allocated to the system in different scenarios where the system performance is compared and the voltage profiles are improved. It is confirmed that the BES algorithm is capable of enhancing the PQ of balanced and unbalanced distribution. The simulation results also showed that the approach

presented effectively identifies the optimal design, number, and place of the single-toned filter and IBDG units.

References

1. IEEE Power and Energy Society (2009) IEEE recommended practice for monitoring electric power quality, vol 1995
2. Kumawat M, Gupta N, Jain N, Bansal RC (2018) Optimal planning of distributed energy resources in harmonics polluted distribution system. *Swarm Evol Comput* 39(July 2017):99–113
3. Abbas AS et al (2021) Optimal harmonic mitigation in distribution systems with inverter based distributed generation. *Appl Sci* 11(2):1–16
4. Abdul kadir AF, Mohamed A, Shareef H, Wanik MZC (2013) Optimal placement and sizing of distributed generations in distribution systems for minimizing losses and THDv using evolutionary programming. *Turk J Electr Eng Comput Sci* 21(Suppl 2):2269–2282
5. Guest E, Jensen KH, Rasmussen TW (2020) Mitigation of harmonic voltage amplification in offshore wind power plants by wind turbines with embedded active filters. *IEEE Trans Sustain Energy* 11(2):785–794
6. Eid A (2014) Utility integration of PV-wind-fuel cell hybrid distributed generation systems under variable load demands. *Int J Electr Power Energy Syst* 62:689–699
7. Eid A, Kamel S, Korashy A, Khurshaid T (2020) An enhanced artificial ecosystem-based optimization for optimal allocation of multiple distributed generations. *IEEE Access* 8:178493–178513
8. Eid A, El-Kishky H, Abdel-Salam M, El-Mohandes MT (2010) On power quality of variable-speed constant-frequency aircraft electric power systems. *IEEE Trans Power Deliv* 25(1):55–65
9. Terriche Y et al (2021) Effective controls of fixed capacitor-thyristor controlled reactors for power quality improvement in shipboard microgrids. *IEEE Trans Ind Appl* 57(3):2838–2849
10. Eid A, Abdel-Fadil R, Abdel-Salam M (2017) Performance and power quality improvements of MEA power distribution systems using model predictive control. *Int Rev Aerosp Eng* 10(1):31–41
11. Elphick S, Gosbell V, Smith V, Perera S, Ciuffo P, Drury G (2017) Methods for harmonic analysis and reporting in future grid applications. *IEEE Trans Power Deliv* 32(2):989–995
12. Yu J, Xu Y, Li Y, Liu Q (2020) An inductive hybrid UPQC for power quality management in premium-power-supply-required applications. *IEEE Access* 8:113342–113354
13. Alam SJ, Arya SR (2020) Control of UPQC based on steady state linear Kalman filter for compensation of power quality problems. *Chinese J Electr Eng* 6(2):52–65
14. Eid A, El-Kishky H, Abdel-Salam M, El-Mohandes T (2008) Constant frequency aircraft electric power systems with harmonic reduction. In: *IECON proceedings (industrial electronics conference)*
15. Eid A, Abdel-Salam M, El-Kishky H, El-Mohandes T (2009) Simulation and transient analysis of conventional and advanced aircraft electric power systems with harmonics mitigation. *Electr Power Syst Res* 79(4):660–668
16. Moghbel M, Masoum MAS, Fereidouni A, Deilami S (2018) Optimal sizing, siting and operation of custom power devices with STATCOM and APLC functions for real-time reactive power and network voltage quality control of smart grid. *IEEE Trans Smart Grid* 9(6):5564–5575
17. Amritha K, Rajagopal V, Raju KN, Arya SR (2020) Ant lion algorithm for optimized controller gains for power quality enrichment of off-grid wind power harnessing units. *Chinese J Electr Eng* 6(3):85–97

18. Bajaj M, Singh AK, Alowaidi M, Sharma NK, Sharma SK, Mishra S (2020) Power quality assessment of distorted distribution networks incorporating renewable distributed generation systems based on the analytic hierarchy process. *IEEE Access* 8:145713–145737
19. Arya SR, Niwas R, Bhalla KK, Singh B, Chandra A, Al-Haddad K (2015) Power quality improvement in isolated distributed power generating system using DSTATCOM. *IEEE Trans Ind Appl* 51(6):4766–4774
20. Eid A, Abdel-Salam M, El-Kishky H, El-Mohandes T (2009) Active power filters for harmonics cancellation in conventional and advanced aircraft electric power systems. *Electr Power Syst Res* 79(1):80–88
21. Liu YW, Rau SH, Wu CJ, Lee WJ (2018) Improvement of power quality by using advanced reactive power compensation. *IEEE Trans Ind Appl* 54(1):18–24
22. Nejabatkhah F, Li YW, Tian H (2019) Power quality control of smart hybrid AC/DC microgrids: an overview. *IEEE Access* 7:52295–52318
23. Mishra AK, Das SR, Ray PK, Mallick RK, Mohanty A, Mishra DK (2020) PSO-GWO optimized fractional order PID based hybrid shunt active power filter for power quality improvements. *IEEE Access* 8:74497–74512
24. Wang J, Xu Z, Che Y (2019) Power quality disturbance classification based on compressed sensing and deep convolution neural networks. *IEEE Access* 7:78336–78346
25. Elmetwaly AH, Eldesouky AA, Sallam AA (2020) An adaptive D-FACTS for power quality enhancement in an isolated microgrid. *IEEE Access* 8:57923–57942
26. Zobaa AF, Abdel Aleem SHE (2014) A new approach for harmonic distortion minimization in power systems supplying nonlinear loads. *IEEE Trans Ind Inf* 10(2):1401–1412
27. Ghorbani MJ, Mokhtari H (2015) Impact of harmonics on power quality and losses in power distribution systems. *Int J Electr Comput Eng* 5(1):166–174
28. Eid A, Abdel-Akher M (2017) Voltage control of unbalanced three-phase networks using reactive power capability of distributed single-phase PV generators. *Int Trans Electr Energy Syst* 27(11):e2394
29. Aly M, Eid A, Abdel-Akher M (2013) Advanced modeling of photovoltaic energy systems for accurate voltage stability assessment of distribution systems. *Adv Sci Lett* 19(5):1353
30. Das JC (2015) Power system harmonics and passive filter designs. *Power Syst Harmon Passiv Filter Des*: 1–844
31. Cabral Leite J, Pérez Abril I, Santos Azevedo MS (2017) Capacitor and passive filter placement in distribution systems by nondominated sorting genetic algorithm-II. *Electr Power Syst Res* 143:482–489
32. Abdel Aleem SHE, Zobaa AF (2017) Optimal C-type filter for harmonics mitigation and resonance damping in industrial distribution systems. *Electr Eng* 99(1):107–118
33. Moran L, Albistur CA, Burgos R (2016) Multimega VAR passive filters for mining applications: practical limitations and technical considerations. *IEEE Trans Ind Appl* 52(6):5310–5317
34. Bagheri P, Xu W, Ding T (2016) A distributed filtering scheme to mitigate harmonics in residential distribution systems. *IEEE Trans Power Deliv* 31(2):648–656
35. Iqbal M et al (2021) Neural networks based shunt hybrid active power filter for harmonic elimination. *IEEE Access* 9:69913–69925
36. Solatalkaran D, Zare F, Saha TK, Sharma R (2020) A novel approach in filter design for grid-connected inverters used in renewable energy systems. *IEEE Trans Sustain Energy* 11(1):154–164
37. Kersting WH (1999) A new approach to modeling three-phase transformer connections. *IEEE Trans Ind Appl* 35(1):169–175
38. Eid A, Abdel-Akher M (2018) Modeling and simulation of unbalanced distribution systems for time-domain analysis under different operating conditions. In: 2017 19th International Middle East Power Systems Conference MEPCON 2017 - Proceedings, vol. 2018-Febru, no. December, pp 477–483
39. Abdelsalam AA, Zidan AA, El-Saadany EF (2015) Optimal DG allocation in radial distribution systems with high penetration of non-linear loads. *Electr Power Compon Syst* 43(13):1487–1497

40. Teng JH, Chang CY (2007) Backward/forward sweep-based harmonic analysis method for distribution systems. *IEEE Trans Power Deliv* 22(3):1665–1672
41. Milovanović M, Radosavljević J, Perović B (2020) A backward/forward sweep power flow method for harmonic polluted radial distribution systems with distributed generation units. *Int Trans Electr Energy Syst* 30(5):1–17
42. Milovanović M, Radosavljević J, Perović B, Dragičević M (2019) Power flow in radial distribution systems in the presence of harmonics. *IJEEC - Int J Electr Eng Comput* 2(1):10–19
43. Kazmierkowski MP (2015) Power quality: problems and mitigation techniques [Book News]. 9(2):62
44. Alsattar HA, Zaidan AA, Zaidan BB (2020) Novel meta-heuristic bald eagle search optimisation algorithm. *Artif Intell Rev* 53(3):2237–2264
45. Ramos ER, Gómez Expósito A, Cordero GÁ (2004) Quasi-coupled three-phase radial load flow. *IEEE Trans Power Syst* 19(2):776–781
46. Abdel Aleem S, Almoataz AY, Zobaa AF, Bansal RC (2020) Decision making applications in modern power systems. Academic Press 2019

Knowledge Discovery in Database Process Used to Analyze Voltage THD of a Computer Factory



Edson Farias de Oliveira, Ítalo Rodrigo Soares Silva, Ricardo Silva Parente, Paulo Oliveira Siqueira Junior, Manoel Henrique Reis Nascimento, Jandecy Cabral Leite, and David Barbosa de Alencar

1 Introduction

Rodriguez-Guerrero et al. (2017) state that the analysis of disturbances related to the Power Quality (PQ) in the Electric Power System (EPS) (Baggini 2008; Dugan et al. 2004; Afonso and Martins 2005) has been becoming increasingly relevant as a result of the increase of events and disturbances in the electrical network and that according to Kahle (2016) is due to the significant increase of more modern and efficient electronic equipment. Among the most worrying disturbances are the harmonic disturbances, as stated by Arrillaga and Watson (2004) and Bollen and Gu (2006), cited in most studies in this area of knowledge and caused by the increasing use of equipment based on electronic converters. For Iagar et al. (2014), the proliferation of this equipment is in domestic and commercial applications such as computers, monitors, laptops, electronic lamps, etc.

In recent decades, state De Araújo et al. (2015) and Granados-Lieberman et al. (2011), the interest in developing new methods for accurate measurement of PQ indicators has increased considerably. In Brazil, the National Agency of Electric Energy (ANEEL) has been working on the standardization of PQ indicators and has developed procedures, such as module 8 of the Distribution Procedures (PRODIST) (Aneel 2012, 2016), which presents among the main objectives to ensure that distribution systems operate with safety, efficiency, quality, and reliability, however, there are still no penalties for consumers who generate harmonic currents in the ESS and, as stated by Matos et al. (2016), it is necessary to create legal means that

E. F. de Oliveira (✉) · Í. R. S. Silva · R. S. Parente · P. O. S. Junior · M. H. R. Nascimento · J. C. Leite · D. B. de Alencar
Institute of Technology and Education Galileo from Amazon (ITEGAM), Manaus, Amazonas, Brazil
e-mail: jandecy.cabral@itegam.org.br; italo.silva@itegam.org.br

provide sanctions to those responsible for generating above-permitted currents, and the procedures for identifying the sources of harmonic distortions are nonexistent.

This chapter aims to contribute by presenting a procedure based on the Knowledge Discovery in Database (KDD) process to help identify the main sources of voltage total harmonic distortion (THD) at the Point of Common Coupling (PCC) of a computer factory. To apply the methodology, computational intelligence and data mining techniques were used to analyze the data collected by PQ meters strategically installed in the plant's PCC and in the main loads, with the purpose of identifying the contribution of each load in the voltage THD in the PCC. The proposed methodology begins by analyzing the layout of the plant and the loads for the installation of the PQ meters, followed by the application of the KDD process that includes the procedures of data collection, selection, cleaning, integration, transformation and reduction, mining, interpretation, and evaluation. In the data mining step (Hand et al. 2001; Hand 1997), the Decision Tree (Breiman et al. 1984; Gehrke et al. 1999, 2000) and Naïve Bayes techniques (Cabena et al. 1998) were applied with the testing of several algorithms to find the ones that presented the best results for this type of application and if this methodology is applied to identify the main sources of harmonic distortion (Grossman and Domingos 2004; Hall and Frank 2008). As a contribution, different data balancing indexes, training, and testing in different scenarios were also tested (Cowell 1999).

2 Materials and Methods

2.1 The KDD Process

The term KDD comes from Knowledge Discovery in Databases and refers to a broad process of discovering knowledge from a database, as stated by Nogueira et al. 2014; Nogueira et al. 2015a, b and Oliveira et al. 2017). For Fayyad et al. (1996) and Piatetsky-Shapiro and Frawley (1991), the KDD process encompasses, in its nature, the areas of machine learning, pattern recognition, neural networks, databases, statistics, artificial intelligence, and data visualization.

For Fayyad et al. (1996) and Roiger (2017), technically, the KDD process can be divided into five phases: selection, preprocessing, transformation, data mining, and interpretation, as per Fig. 1.

2.2 Application of the KDD Process

The KDD process was applied through the following steps:

1. Choose an industry for application.
2. Define the research environment.

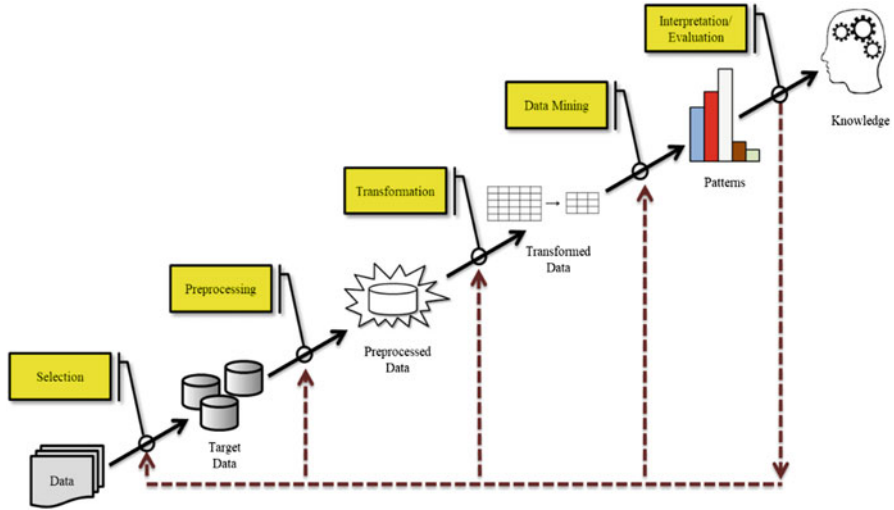


Fig. 1 KDD process. (Adapted from Fayyad et al. (1996))

3. Define the collection points.
4. Select the PQ analyzers.
5. Define the collection period.
6. Collect the data.
7. Execute the KDD process.
 - (a) Select the data.
 - (b) Perform data cleansing.
 - (c) Integrate the data.
 - (d) Transform the data.
 - (e) Reduce the data.
 - (f) Mine the data.
 - (i) Apply the Decision Tree technique.
 - (ii) Apply the Naïve Bayes technique.
 - (g) Interpret and evaluate the data.
8. Analyze and discuss the results.
 - (a) Redo step 7 in all 3 shifts (T0, T1, and T2).
 - (b) Redo step 7 with different percentages of training and testing (30/70, 50/50, and 70/30).
 - (c) Redo step 7 with different percentages of class balancing (100%, 200%, 300%, 1000%, and 2000%).
9. Complete the process.

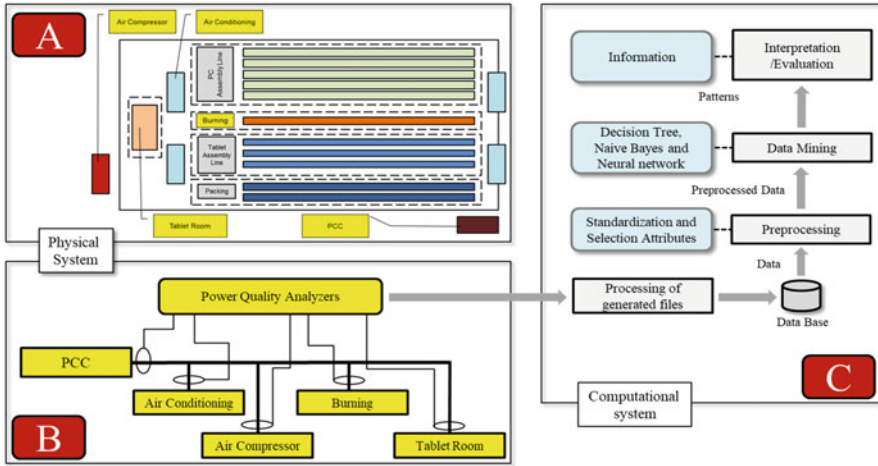


Fig. 2 Layout of the plant (A), the installation of the Power Quality Analyzers (B) and the KDD process (C). (Oliveira et al. 2017)

2.3 Computer Factory Analysis

To apply the methodology with the KDD Process, a factory of technology products such as desktops, notebooks, netbooks, cell phones, and TVs, among others, was selected.

In the development of the methodology, the physical and computational systems were used, as shown in Fig. 2. Figure 2 (A and B) presents the physical system, with the layout in Fig. 2 (A) and the PQ meters in Fig. 2 (B). In Fig. 2 (C), we have the computational system, represented by the KDD process.

The physical system, shown in Fig. 2 (A), is composed of:

- *PC Assembly Lines* are composed of five production lines, where the first two assemble desktops have a total power of 15 kW each and the last three assemble notebooks and netbooks have a power of 3 kW each, totaling 39 kW.
- *Burning* is a line designed to perform stress tests on desktop, notebook, netbook, and tablet products, where the products are turned on in this line and stay on for an average of 2 h running stress software for the detection of possible malfunctions. On average, 480 desktops and 720 notebooks/netbooks, totaling 167 kW.
- *Tablet Assembly Lines* consist of three tablet assembly lines with a total power of 2.5 kW.
- *PCCKaging Lines* are two lines where the PCCKaging process of all products that passed the tests and inspections takes place.
- *Tablet Assembly Room* are two lines in cells destined to the assembly of corporate tablets. The assembly room has an infrastructure with 10 laser printers of 445 W

each, 4 electronic scales of 6 W each, 17 computers of 300 W each, 25 LED tube lamps of 19 W each, and 140 tablets in production of 8 W each, totaling 11 kW in the tablet production room.

- *Air Conditioners* are four pieces of refrigeration equipment positioned between the beginning and end of the assembly lines. Each air conditioner has a power of 52 kW, totaling 208 kW of power for cooling the production unit.

The external part of the physical system, shown in Fig. 2 (A), is composed of:

- *Air Compressor Room* where there is one air compressor with an average power of 55 kW and two 18 kW pumps, totaling 91 kW. The pumps and compressors work during production hours to produce compressed air for the lines and equipment of the production unit and to pump water from the artesian well to the water tower.
- *A step-down* substation that receives the 13,800 V power from the utility. It has three step-down transformers from 13.8 kV to 220 V/127 V, being a 300 kVA transformer to feed the office building, a 1000 kVA transformer to feed the production unit and another 1000 kVA as a backup. It also has a generator group of 105 kVA for the building and another of 450 kVA for the production unit.

2.4 Application

The choice of a computer manufacturing company was due to the inexistence of real data related to harmonic distortions in computer factories, as well as the recommendations to the CBEMA-ITIC curve and INTEL procedures, because the vast majority are distributed nonlinear loads as shown in Table 1.

Table 1 Data collection points

Collection point	Point characteristic	Period of operation
PCC	It has a distribution transformer: Capacity: 1000 kVA Primary voltage: 220 V Secondary voltage: 127 V	24 h per day
Ar conditioning	It has four central air conditioner: 2 compressors of 15 TR (52 kW) each one	5:30 AM – 1:30 AM on weekdays
Air compressors	Capacity: 125 HP	5:30 AM – 1:30 AM on weekdays
Burning	Capacity: 1200 computers per shift	24 h per day
Tablet production unit	Capacity: 140 tablets under teste, 17 computers, 4 electronic scales, and 10 printers	24 h per day

Table 2 Shifts

Shift	Home	End
T1 (First)	6 h	15 h 48
T2 (Second)	15 h 48	1 h 10
T0 (Empty)	1 h 10	6 h

Table 3 Tables for the collection points

Location	Description
GLVSB	General low voltage SwitchBoard (220 V/127 V) located in the substation
AR conditioning	SwitchBoard for 4 air conditioning centers
Compressors	SwitchBoard for compressor room and water pump
<i>Burning</i>	SwitchBoard for the notebook test line
<i>Tablet</i>	SwitchBoard for the tablet assembly room

The air conditioning and the air compressors are only on during production hours, and the other loads are on 24 h. The distribution of times in the shifts is shown in Table 2.

2.4.1 Collection Points

The objective of this chapter is to present the analysis of the data collected from the PQ analyzers installed according to Fig. 2 (A).

The collection points were installed in the General Frames as shown in Table 3.

2.4.2 PQ Analyzers

The PQ meter selected for data collection was HIOKI's PW3198 Power Quality Analyzer, as shown in Fig. 3. This is a power quality analyzer for monitoring and recording power supply anomalies, allowing their causes to be quickly investigated, and for assessing power supply problems such as voltage dips, flicker, harmonics, and other electrical problems.

2.4.3 Period of Data Collection

Data collection took place from 06/03/14 to 06/11/2014, according to Fig. 4.

As noted, from 1:45 pm on June 3 to 4:32 pm on June 5, the contribution of the measurement of all points collected takes place. With the exclusion of the Air Compressor point, the collection is extended and runs from 1:20 pm on June 3 to 10:10 am on June 11. All PQ Analyzers were removed on June 11th.



Fig. 3 PW3198 PQ Analyzer (HIOKI)

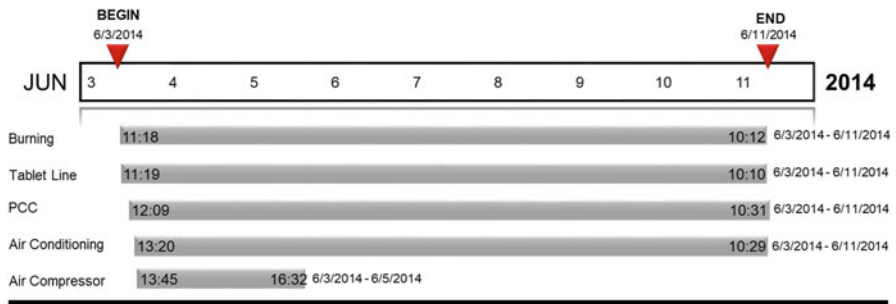


Fig. 4 Collection period

2.4.4 Collected Data

For the PQ meter used, data was collected via SD card and transferred to a computer as a preparatory step for the KDD process.

2.4.5 Executing the KDD Process

This chapter applies all phases of the KDD process as described in Sect. 2.1 and are described in the following topics.

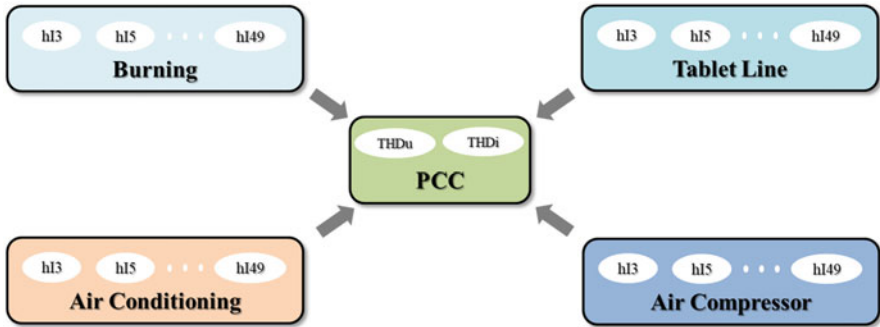


Fig. 5 Impact on the PCC THDu due to the individual contribution of each current harmonic

KDD Process: Data Selection

As shown in Fig. 5, the importance of this phase was to evaluate the impact on the PCC voltage THD due to the individual contribution of each current harmonic of the main installed loads.

The PQA-HiVIEW PRO 9624-50 software was used for the analysis and the following items were selected:

- RMS voltage (U).
- RMS current (I).
- THDv (U-THD).
- THDi (I-THD).
- Harmonic Current (odd up to order 49).
- Harmonic Voltage (odd up to order 49).

Conversion to CSV format and selected items are shown in Fig. 6.

KDD Process: Pre-processing: Cleaned and Integrated Collected Data

Figure 7 presents the structure used to organize and adjust the collected data. Only the initial data of all blocks are presented in Table 4, due to the size of the file.

The data structure for each collection point is represented as below:

- *ID*: Identifier of the record.
- *Date*: Date of data collection.
- *Time*: Time of data collection.
- *RMS U RST*: RMS voltage data for phases R, S, and T.
- *RMS I RST*: RMS current data for phases R, S, and T.
- *THDU RST*: Total Harmonic Distortion of voltage for phases R, S, and T.
- *HI 1-49 RST*: Harmonic of the 1st to 49th order current for phases R, S, and T.

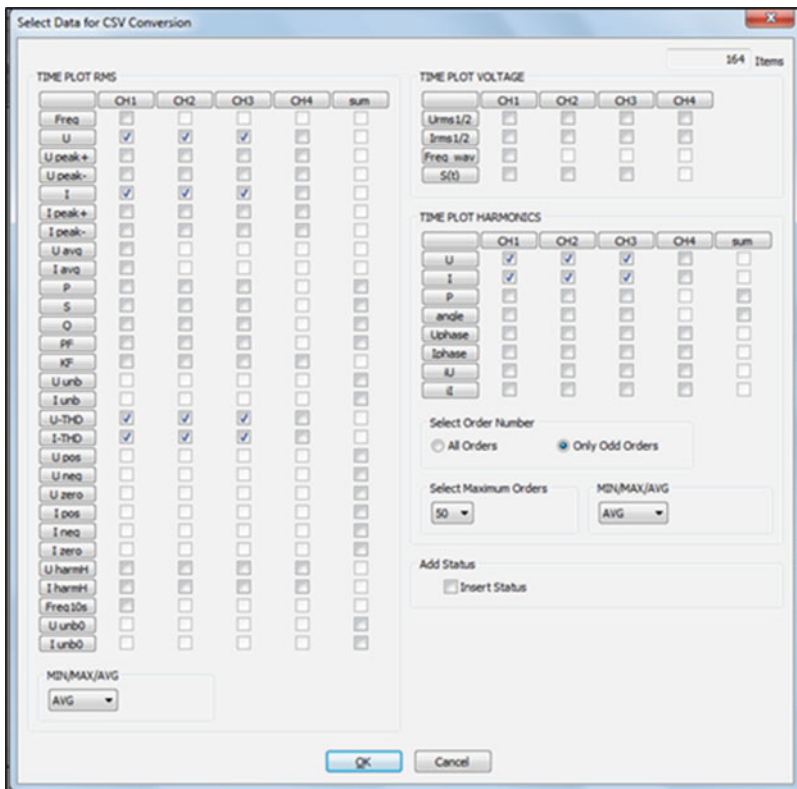


Fig. 6 Selection screen of the PQA-HiVIEW PRO 9624-50 Software

ID	Date	Time	RMS U RST	RMS I RST	THD U RST	H I 1-49 RST	H U 1-49 RST
----	------	------	--------------	--------------	--------------	-----------------	-----------------

Fig. 7 Structure of the collected data

- *H U 1-49 RST*: Harmonic of the voltage from 1st to 49th order for phases R, S, and T.

Data Cleaning

A total of 17,070,240 items of collected data were analyzed and the proposed actions for cleaning them are presented in Table 5.

To apply the actions, the data were converted into a database and scripts in SQL language were applied to clean the data using the Postgresql Tool. The cleaned data are shown in Table 6.

Table 4 Collected data in CSV format

Id	Date	Time	RMS U R	RMS U S	RMS U T	RMS I R	RMS I S	RMS I T
1	3-Jun-14	1:20:00 PM	128.03E+0	127.20E+0	126.72E+0	0.267E+3	0.231E+3	0.219E+3
2	3-Jun-14	1:21:00 PM	128.37E+0	127.53E+0	127.03E+0	0.175E+3	0.150E+3	0.141E+3
3	3-Jun-14	1:22:00 PM	128.55E+0	127.73E+0	127.19E+0	0.174E+3	0.150E+3	0.140E+3
4	3-Jun-14	1:23:00 PM	128.43E+0	127.57E+0	127.03E+0	0.175E+3	0.150E+3	0.140E+3
5	3-Jun-14	1:24:00 PM	128.49E+0	127.64E+0	127.17E+0	0.174E+3	0.151E+3	0.141E+3
6	3-Jun-14	1:25:00 PM	128.75E+0	127.93E+0	127.54E+0	0.175E+3	0.151E+3	0.142E+3
7	3-Jun-14	1:26:00 PM	128.36E+0	127.50E+0	127.13E+0	0.175E+3	0.151E+3	0.142E+3
8	3-Jun-14	1:27:00 PM	128.45E+0	127.55E+0	27.16E+0	0.175E+3	0.151E+3	0.142E+3
9	3-Jun-14	1:28:00 PM	128.58E+0	127.67E+0	127.27E+0	0.176E+3	0.151E+3	0.143E+3
10	3-Jun-14	1:29:00 PM	128.53E+0	127.61E+0	127.17E+0	0.175E+3	0.150E+3	0.142E+3
11	3-Jun-14	1:30:00 PM	128.73E+0	127.85E+0	127.41E+0	0.176E+3	0.151E+3	0.143E+3
12	3-Jun-14	1:31:00 PM	128.66E+0	127.79E+0	127.37E+0	0.175E+3	0.152E+3	0.142E+3
13	3-Jun-14	1:32:00 PM	128.75E+0	27.87E+0	127.42E+0	0.176E+3	0.152E+3	0.142E+3

Table 5 Cleaning actions for the collected data

Point	Sampling rate	Lines	Columns	Total data	Analysis
<i>Burning</i>	1 minute	9871.00	165.00	1,628,715.00	The current harmonic values must be converted to levels, since the equipment has been configured for percentages. All voltage, current, total harmonic distortion (THD) and harmonic values must be converted from scientific notation to normal
Tablet room	1 minute	9872.00	165.00	1,628,880.00	Current values should be divided by 1000 to adjust the tip used. All voltage, current, THD, and harmonic values should be converted from scientific notation to normal
PCC	1 minute	11,423.00	165.00	1,884,795.00	The current values should be divided by 1000 to adjust the probe used. All voltage, current, THD, and harmonic values should be converted from scientific notation to normal
Conditioners of air	1 minute	11,350.00	165.00	1,872,750.00	All voltage, current, THD, and harmonic values should be converted from scientific notation to normal
Air compressors	3 seconds	60,940.00	165.00	10,055,100.00	All voltage, current, THD, and harmonic values should be converted from scientific notation to normal

Table 6 Cleaned data after applying the scripts

Id	Date	Time	RMS U R	RMS U S	RMS U T	RMS I R	RMS I S	RMS I T
1	3-Jun-14	1:20:00 PM	128.03	127.20	126.72	267.00	231.00	219.00
2	3-Jun-14	1:21:00 PM	128.37	127.53	127.03	175.00	150.00	141.00
3	3-Jun-14	1:22:00 PM	128.55	127.73	127.19	174.00	150.00	140.00
4	3-Jun-14	1:23:00 PM	128.43	127.57	127.03	175.00	150.00	140.00
5	3-Jun-14	1:24:00 PM	128.49	127.64	127.17	174.00	151.00	141.00
6	3-Jun-14	1:25:00 PM	128.75	127.93	127.54	175.00	151.00	142.00
7	3-Jun-14	1:26:00 PM	128.36	127.50	127.13	175.00	151.00	142.00
8	3-Jun-14	1:27:00 PM	128.45	127.55	127.16	175.00	151.00	142.00
9	3-Jun-14	1:28:00 PM	128.58	127.67	127.27	176.00	151.00	143.00
10	3-Jun-14	1:29:00 PM	128.53	127.61	127.17	175.00	150.00	142.00
11	3-Jun-14	1:29:00 PM	128.73	127.85	127.41	176.00	151.00	143.00



Fig. 8 Structure of the integrated data

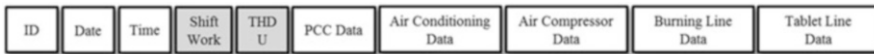


Fig. 9 Structure of the transformed data

Data Integration

Figure 8 presents the structure with the integrated data, considering the phase separation of current and voltage and the synchronization of the date and time between the data, as shown in Table 7.

KDD Process: Transforming Data

Transforming numeric values to categories for some collected data is necessary for data mining preparation. For the transformation of THDv data, as shown in Table 8, Leite (2013) and the standards (IEEE 519-1992, Revision 2014) that establish limits for harmonic distortion of current and voltage in distribution networks were used as references. Transmission networks for low voltage systems and Schneider-Electric (2005) that establish normal (NORM), risk (RISK) and critical (CRIT) ranges for THDv.

Based on preliminary analyses, the data were divided into shifts, as shown in Table 9.

Figure 9 presents the structure of the new data format, with the addition of information from Tables 8 and 9.

Table 7 Integrated data

Id	Date	Time	PCC data THDv	Air conditioning data 3rd harmonic current air_hi_a_3	Air conditioning data 5th harmonic current air_hi_a_5	Air conditioning data 7th harmonic current air_hi_a_7	Air conditioning data 9th harmonic current air_hi_a_9
43	3-Jun-14	2:27:00 PM	2.08	5.20	2.30	1.80	0.90
44	3-Jun-14	2:28:00 PM	2.15	5.20	2.30	1.90	0.90
45	3-Jun-14	2:29:00 PM	2.18	5.20	2.40	1.90	0.90
46	3-Jun-14	2:30:00 PM	2.15	5.10	2.40	1.80	0.80
47	3-Jun-14	2:31:00 PM	2.16	5.20	2.40	1.90	0.70
48	3-Jun-14	2:32:00 PM	2.13	5.20	2.40	1.80	0.70
49	3-Jun-14	2:33:00 PM	2.10	5.20	2.40	1.80	0.70
50	3-Jun-14	2:34:00 PM	2.16	5.20	2.40	1.90	0.80
51	3-Jun-14	2:35:00 PM	2.18	5.20	2.50	1.90	0.80

Table 8 Range of values for THD_v – Leite (2013), IEEE 519-1992/Revision 2014 e Schneider (2005)

Status	THD _v
<i>NORM</i>	<5%
<i>RISK</i>	>5% and < 8%
<i>CRIT</i>	>8%

Table 9 Shift categorization

Status	Schedule
T1	Hour >= '06:00' & hour <= '15:48'
T2	Hour > '15:48' & hour <= '23:59' OU Hour >= '00:00' & hour <= '01:10'
T0	Hour > '01:10' & hour < '06:00'

Table 10 Discarded data

PCC	Total harmonic distortion of current (THDi) RMS voltage RMS current Fundamental voltage Fundamental current Voltage harmonics of order 17 to 49 Current harmonics of order 17 to 49
Loads: Burning Tablet room Air conditioners Air compressors	RMS voltage RMS current Voltage total harmonic distortion (THD _v) Current total harmonic distortion (THDi) Fundamental voltage Fundamental current Voltage harmonics of order 17 to 49

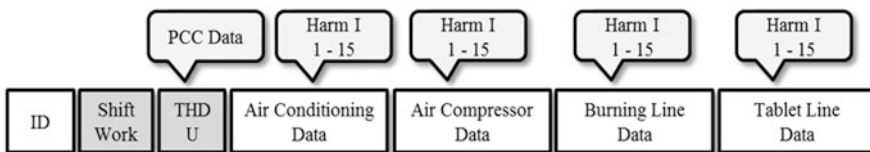


Fig. 10 Structure of the reduced data

KDD Process: Data Reduction

In the data reduction phase, because the literature shows impact up to the 15th harmonic component, harmonic components above the 15th and other data were discarded as presented in Table 10.

The structure with the reduced data is shown in Fig. 10.

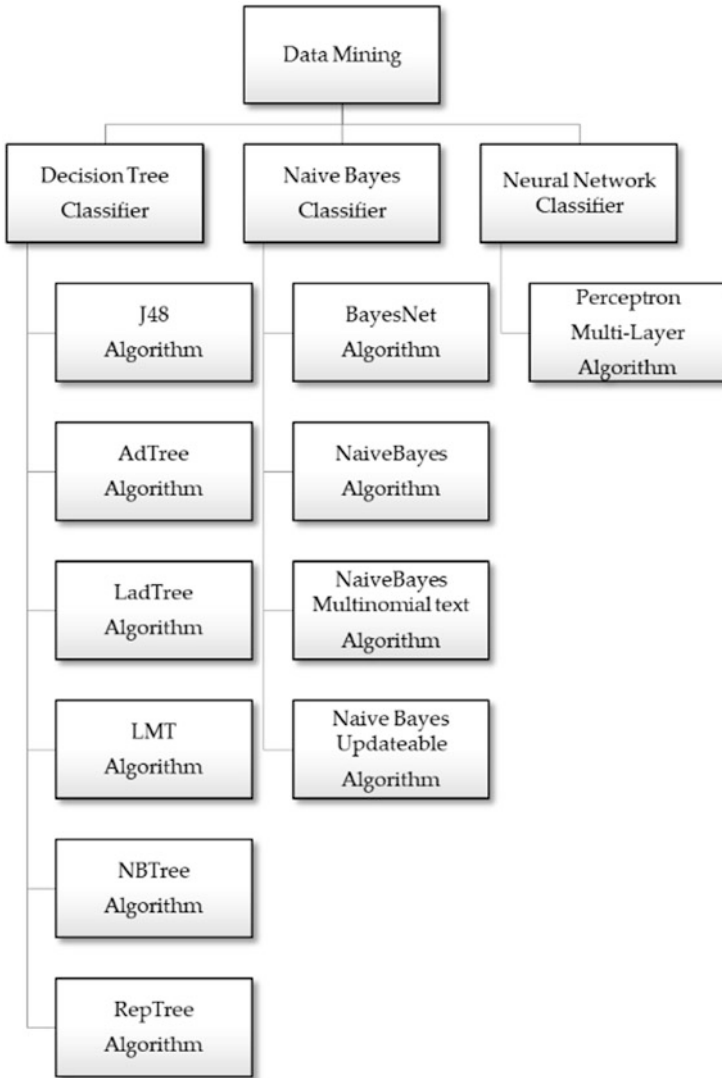


Fig. 11 Data Mining Algorithms

KDD Process: Data Mining

For data mining, version 3.7.13 of WEKA software (2015) and version 6.5.02 of Rapid Miner Studio Basic (2015) were used, and the Decision Tree classifiers with 7 algorithms and Naïve Bayes with 4 algorithms were chosen, according to Fig. 11.

KDD Process: Data Interpretation and Evaluation

For validation purposes, the data was evaluated with different types of algorithms and the result presented in a comparative way, for the Decision Tree classifier (Mahela and Shaik 2017; Oliveira et al. 2017; Ozgonenel et al. 2012; Rodríguez et al. 2013) and Naïve Bayes classifier (Langley et al. 1992; Langley and Sage 1994; Niedermayer 2008; Zhang 2004) through two data mining software: WEKA and Rapid Miner (Hall et al. 2009).

Considering the dynamism of the KDD process and the possibility of returning to previous steps, analyses were performed with different scenarios to ensure the balancing of classes, in this action, the technique used was SMOTE as a synthetic oversampling technique with different adjustment values. For the same purpose, it was also evaluated using different percentages for separating the data into training and test sets.

To further identify, validate, and compare the results, analyses were performed with the data separated into shift groups. Considering that the air compressor load does not have great relevance for analysis, its collected data were excluded and, as a consequence, there was an increase in the number of days and data to be evaluated.

2.4.6 Final Considerations

The factory chosen for the application of the methodology presents very interesting characteristics due to the concentration of a large number of computer products such as notebooks, desktops, and tablets simultaneously connected without interruption. Another important characteristic is the other analyzed loads that work only during the production period. This data is important to direct the analysis of the data and understand the behavior of the loads that most impacted the THD of the PCC.

3 Results

Five PQ Analyzers collected 17,070,240 data, which were submitted to several stages of the KDD process, and in data mining, the Decision Tree classifier was used, applied in different scenarios and for this, the WEKA software was used without applying a filter for class balancing and with the cross-validation test option with folds set to 10.

The consolidated data shows 3028 instances, of which 2902 are classified as NORM and 126 as RISC, as shown in Fig. 12.

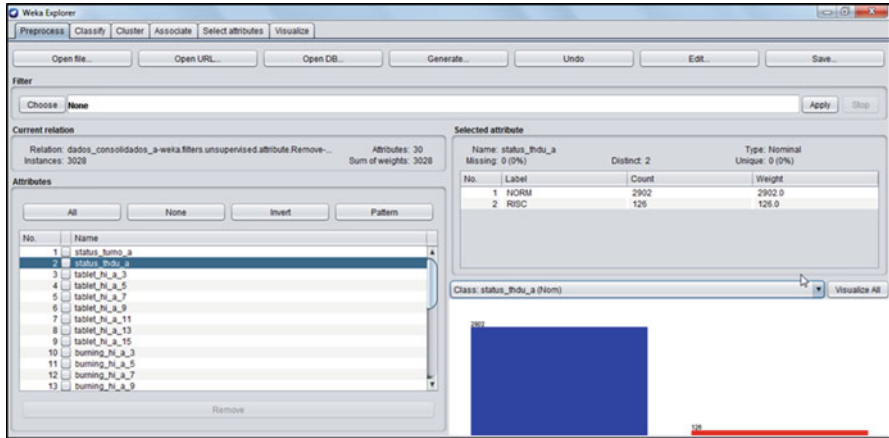


Fig. 12 General data consolidated in WEKA software

Table 11 Results of the Decision Tree classifier algorithms of the WEKA software

Algorithm	Correctly sorted instances	Incorrectly sorted instances	ROC area	False positives	False negatives
J48	99.9009%	0.0991%	1.000	3	0
NBTREE	99.8349%	0.1651%	1.000	2	3
LADTREE	99.8018%	0.1982%	1.000	4	2
ADTREE	99.7358%	0.2642%	1.000	5	3
LMT	99.7358%	0.2642%	1.000	4	4
REPTREE	99.1744%	0.8256%	0.961	14	11

3.1 Result with the Decision Tree Classifier in the WEKA Software

3.1.1 Decision Tree Analysis with General Data, Without Class Balancing, with Cross-Validation on Ten Folds, and with the J48, NBTREE, LADTREE, ADTREE, LMT, and REPTREE Algorithms

Data mining was used with WEKA software, using the Decision Tree classifier with several algorithms and choosing the option of testing with ten folds in the cross-validation technique to identify the most relevant result based on the metrics Correctly Classified Instances, Incorrectly Classified Instances, ROC Area, False Positives, and False Negatives as per Table 11.

Algorithm J48 presented the most significant result, as presented in Table 11, due to the items Correctly Classified Instances, Incorrectly Classified Instances, ROC Area, False Positive, and False Negative. The result indicated the seventh

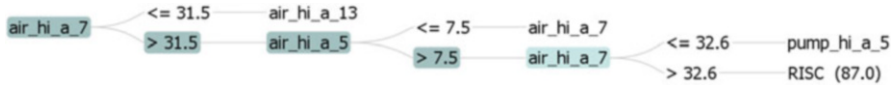


Fig. 13 Result with J48 algorithm on THDv with total data

Table 12 Results with J48 algorithm on THDv and THDi

Algorithm	Correctly sorted instances	Incorrectly sorted instances	ROC area	False positives	False negatives
J48 – THDv	99.9009%	0.0991%	1.000	3	0
J48 – THDi	99.9670%	0.0330%	0.999	0	1

Table 13 Result with J48 algorithm on THDv during the T0 shift

Algorithm	Correctly sorted instances	Incorrectly sorted instances	ROC area	False positives	False negatives
J48 – THDv-Total	99.9009%	0.0991%	1.000	3	0
J48 – THDv-T1	THDv Normal – no result				
J48 – THDv-T2	THDv Normal – no result				
J48 – THDv-T0	99.6422%	0.3578%	0.998	2	0

harmonic current component of the Air Conditioners point as the most impactful and the evidence is presented in Fig. 13.

In Fig. 10, it is shown that if the seventh harmonic of the air conditioning plants is greater than 31.5% and the fifth harmonic of current of the air conditioning plants is greater than 7.5%, then the THDv will enter the risk condition in 87 cases out of the total 126, considering the data set collected during the measurement campaign period.

The J48 algorithm was then used to perform the analyses with THDv and THDi according to Table 12.

3.1.2 Decision Tree Analysis with Data from Each Shift, Without Class Balancing, with Cross-Validation on Ten Folds, and with the J48 Algorithm

Considering the collection of data from June 3 to June 5, in all shifts, the results indicated that the greatest impact was the seventh harmonic component of the air conditioning point current. To validate and prove the sanity of the analysis, the database was divided into three and organized by shifts: T0, T1, and T2.

Figures 14 and 15 show that it was not possible to execute the Decision Tree for the data from shifts T1 and T2, as a result of all THDv values being classified as normal.

In Shift 0, the result is presented in Table 13, considering the THDv.

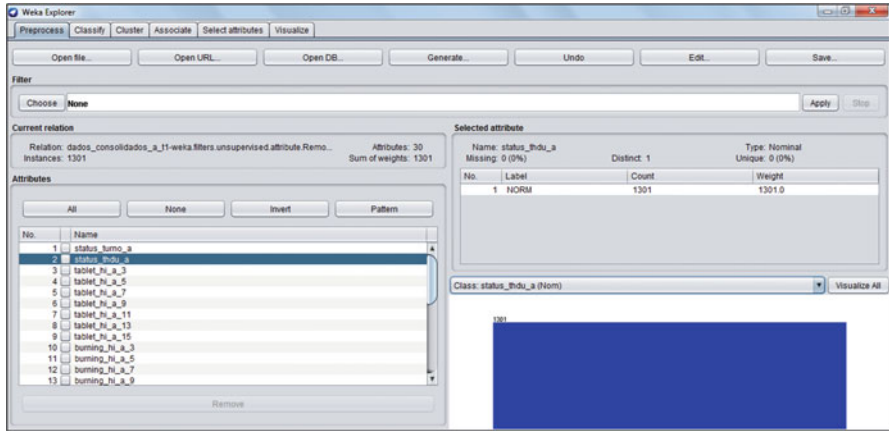


Fig. 14 Result, at shift T1, with J48 algorithm on THDv

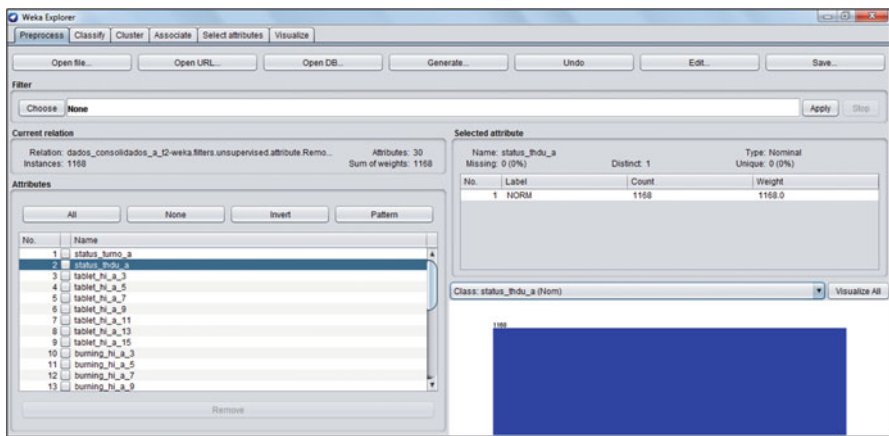


Fig. 15 Result, on shift T2, with J48 algorithm on THDv

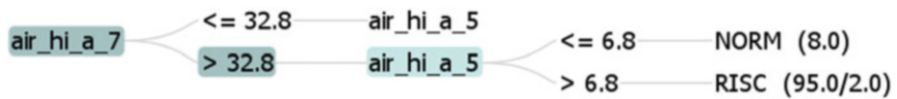


Fig. 16 Decision Tree for Shift T0

The result of the Decision Tree with data from shift T0, shown in Fig. 16, shows that the greatest impact is from the seventh current harmonic at the Air Conditioning point and it is possible to consider that the previous analyses are correct.

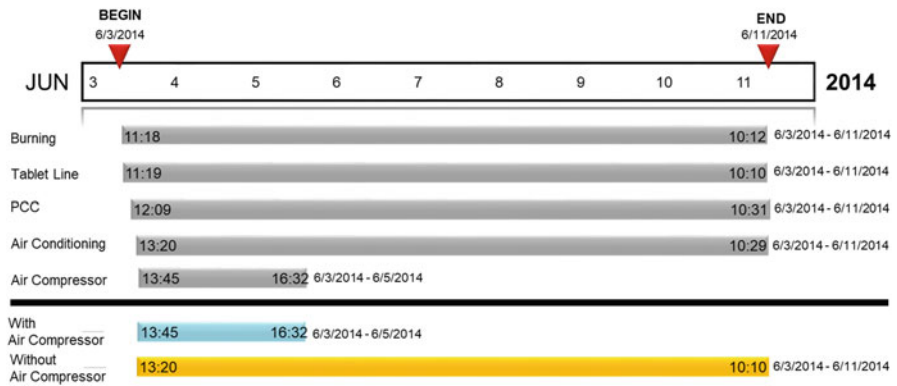


Fig. 17 Data collected with COMPRESSORS and without COMPRESSORS

Table 14 Result with J48 algorithm on THDv with and without air compressors

Algorithm	Correctly sorted instances	Incorrectly sorted instances	ROC area	False positives	False negatives
J48 – THDv with compressors	99.9009%	0.0991%	1.000	3	0
J48 – THDv without compressors	99.9281%	0.0719%	1.000	2	5

Decision Tree Analysis with General Data Without the Air Compressor Point, Without Class Balancing, with Cross-Validation on Ten Folds, and with the J48 Algorithm

Considering that the Air Compressors point was not impacting the results and with the purpose of increasing the number of days analyzed, a database was created discarding the data from the Air Compressors point with all shifts as can be seen in Fig. 17.

The proposed strategy, as shown in Table 14, increased the number of lines from 3028 to 9741, without affecting the quality of the analysis, as there was an increase in the workload from 51 to 179 h.

Summary of Decision Tree Analyses Without Class Balancing, with Cross-Validation on Ten Folds, and with the J48 Algorithm

The summary of the results, with the J48 algorithm applied in the Decision Tree technique, is presented in Table 15.

Table 15 Summary of results with J48 algorithm on THDv

Scenario	Load	Shift	Impacted
1	All loads: 03/06–05/06	All shifts	7th harmonic component of current air conditioners
2	All loads: 03/06–05/06	t1 only	Unable to run, because THDv was normal
3	All loads: 03/06–05/06	t2 only	Unable to run, because THDv was normal
4	All loads: 03/06–05/06	t0 only	7th harmonic component of current air conditioners
5	No compressors: 03/06–11/06	All shifts	7th harmonic component of current air conditioners
6	No compressors: 03/06–11/06	t1 only	Unable to run, because THDv was normal
7	No compressors: 03/06–11/06	t2 only	7th harmonic component of current air conditioners
8	No compressors: 03/06–11/06	t0 only	7th harmonic component of current air conditioners

Scenarios from 1 to 4 represent the analyses with all the data collected and applied to the steps of the KDD process, being scenario 1 the analysis with all the data and scenarios 2, 3, and 4 the analyses with the shifts T0, T1, and T3.

Scenarios 5 to 8 represent the analyses performed with the data collected at the air compressor point and applied to the KDD process steps, scenario 5 being the analysis with all the data and scenarios 6, 7, and 8 the analyses with the T0, T1, and T3 shifts.

In all the analyzed hypotheses, considering the data collected, the greatest impact that leads to the risk of the THD Voltage in the PCC is due to the seventh harmonic component of the current at the Air Conditioning point and at the time of the T0 shift.

Decision Tree Analysis with General Data, Without Class Balancing, with Cross-Validation at 10, 50, 100, and 1000 Folds, and with the J48 Algorithm

For the consistency analysis, the overall data with 3028 instances, 2902 being NORM classified and 126 RISC classified, they were subjected to different numbers of folds with the cross-validation technique and for comparison of the result and the accuracy of each. The result is presented in Table 16 and Fig. 18.

The result of Table 16 and Fig. 18 showed that the most impactful current harmonic component on the input THDv is the seventh and that the metrics in all scenarios are very similar. Figure 18 presents the Decision Tree for all scenarios using cross-validation, i.e., the result was exactly the same for folds 10, 50, 100,

Table 16 Comparison of cross-validation analysis with folds 10, 50, 100, and 1000

Metrics	Folds 10	Folds 50	Folds 100	Folds 1000
VP	2892	2890	2889	2891
VN	114	111	112	113
FP	12	15	14	13
FN	10	12	13	11
Accuracy	99.3%	99.1%	99.1%	99.2%
DV _T Sensitivity	99.7%	99.6%	99.6%	99.6%
TF _P Recall	9.5%	11.9%	11.1%	10.3%
TV _N Specificity	90.5%	88.1%	88.9%	89.7%
TF _N	0.3%	0.4%	0.4%	0.4%
VP _P Precision	99.6%	99.5%	99.5%	99.6%
VP _N	91.9%	90.2%	89.6%	91.1%
Gmean	95.0%	93.7%	94.1%	94.5%
ROC area	0.980	0.958	0.962	0.967
Result	7th harmonic component of the current of the air conditioners			

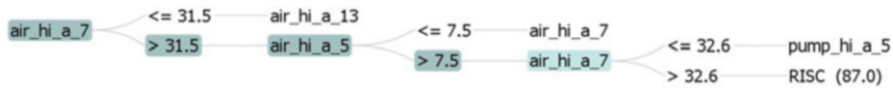


Fig. 18 Decision tree for the condition without balancing and with cross-validation

and 100. It is worth noting that the previous analyses were done with folds 10, i.e., the folds did not affect the decision tree results.

Decision Tree Analysis with General Data, Without Class Balancing, with Training and Testing Rates of 30/70%, 50/50%, and 70/30%, and with the J48 Algorithm

Table 17 shows the results for different training and testing rate scenarios. This way the True Positive-VP data are being reduced, as they correspond to the percentage of the test set, so at a 30/70 rate, the VP value corresponds to 70% of the data set, at a 50/50 rate, it corresponds to 50% of the data set, and at a 70/30 rate, it corresponds to only 30% of the data set.

The data in Table 17 shows that the metrics improve with increasing training percentage and that in the 70/30 condition, the indicators are better than the cross-validation. It also shows that the result is exactly the same as the cross-validation, and the Decision Tree shown in Fig. 18 is the same for the three training and testing rate conditions.

Table 17 Comparison between analysis with training and test rates of 30/70, 50/50, and 70/30

Metrics	Cross-validation Folds 10	Rate 30/70	Rate 50/50	Rate 70/30
VP	2892	2020	1436	855
VN	114	65	58	47
FP	12	26	18	4
FN	10	9	2	2
Accuracy	99.3%	98.3%	98.7%	99.3%
DV _T Sensitivity	99.7%	99.6%	99.9%	99.8%
TF _P Recall	9.5%	28.6%	23.7%	7.8%
TV _N Specificity	90.5%	71.4%	76.3%	92.2%
TF _N	0.3%	0.4%	0.1%	0.2%
VP _P Precision	99.6%	98.7%	98.8%	99.5%
VP _N	91.9%	87.8%	96.7%	95.9%
<i>Gmean</i>	95.0%	84.3%	87.3%	95.9%
ROC <i>area</i>	0.980	0.903	0.856	0.961
Result	7th harmonic component of the current of the air conditioners			

Decision Tree Analysis with General Data with Class Balancing and with Different Training and Testing Rates

The use of class balancing techniques is key to improving the performance of data mining techniques. As in the original data, the distribution between NORM instances with 2902 and RISC instances with 126 demonstrates that there is a very large unbalance since NORM represents 95.8% of the data and RISC only 4.2%.

To balance the data seeking to improve performance the SMOTE filter was applied, which is framed as a synthetic oversampling technique. For the analyses, different oversampling percentages were applied to the original data corresponding to 100%, 200%, 300%, 1000%, and 2000% in different training and test rate analyses as presented in Table 18.

It can be seen that the metrics tend to improve as the data is balanced. The results of the Decision Trees are similar and indicate, as evidenced in Figs. 19 and 20, that the main impact is the seventh harmonic current component of the Air Conditioners.

The differences between Figs. 19 and 20 are the rate of the fifth harmonic current component of the Air Plants changing from 7.5% to 7.2% and the RISC value changing from 87.0 to 183.0 cases.

The only difference between Figs. 20 and 21 is the RISC value that changes from 183.0 to 278.0 cases.

The results presented in Figs. 21 and 22 are similar, considering that the greatest impact is the seventh harmonic current component of the Air Conditioning point, whereas in Fig. 21 it is 31.5% and in Fig. 22 it is 31.6%. Another point of similarity is the fifth harmonic component of the Air Conditioning current, where in Fig. 21 it is 7.2% and in Fig. 22 it is 7.0%, with the risk in Fig. 21 being 278 and in Fig. 22 at 356.

Table 18 Comparison of general data between balancing analysis with SMOTE

Instances	Original	SMOTE 100%	SMOTE 200%	SMOTE 300%	SMOTE 1000%	SMOTE 2000%
Total	3028	3154	3280	3406	4288	5548
NORM	2902	2902	2902	2902	2902	2902
RISC	126	252	378	504	1386	2646
%	95.8/4.2	92.0/8.0	88.4/11.6	85.2/14.8	67.7/32.3	52.3/47.7
% training/testing = 30/70						
VP	2020	2029	2034	2021	2016	1998
VN	65	155	240	334	948	1854
FP	26	18	14	19	15	7
FN	9	6	8	10	23	25
Accuracy	98.3%	98.9%	99.0%	98.8%	98.7%	99.2%
TV _P Sensitivity	99.6%	99.7%	99.6%	99.5%	98.9%	98.8%
TF _P Recall	28.6%	10.4%	5.5%	5.4%	1.6%	0.4%
TV _N Specificity	71.4%	89.6%	94.5%	94.6%	98.4%	99.6%
TF _N	0.4%	0.3%	0.4%	0.5%	1.1%	1.2%
VP _P Precision	98.7%	99.1%	99.3%	99.1%	99.3%	99.7%
VP _N	87.8%	96.3%	96.8%	97.1%	97.6%	98.7%
G _{mean}	84.3%	94.5%	97.0%	97.0%	98.7%	99.2%
ROC area	0.903	0.931	0.961	0.974	0.988	0.995

% training/testing = 50/50									
VP	1436	1448	1446	1440	1444	1401			
VN	58	115	173	251	679	1349			
FP	18	7	9	9	8	9			
FN	2	7	12	3	13	15			
Accuracy	98.7%	99.1%	98.7%	99.3%	99.0%	99.1%			
TV _P Sensitivity	99.9%	99.5%	99.2%	99.8%	99.1%	98.9%			
TF _P Recall	23.7%	5.7%	4.9%	3.5%	1.2%	0.7%			
TV _N Specificity	76.3%	94.3%	95.1%	96.5%	98.8%	99.3%			
TF _N	0.1%	0.5%	0.8%	0.2%	0.9%	1.1%			
VP _P Precision	98.8%	99.5%	99.4%	99.4%	99.4%	99.4%			
VP _N	96.7%	94.3%	93.5%	98.8%	98.1%	98.9%			
Gmean	87.3%	96.9%	97.1%	98.2%	99.0%	99.1%			
ROC area	0.856	0.970	0.996	0.986	0.987	0.995			
% training/testing = 70/30									
VP	855	862	878	869	858	851			
VN	47	65	101	145	413	800			
FP	4	15	0	3	7	5			
FN	2	4	5	5	8	8			
Accuracy	99.3%	98.0%	99.5%	99.2%	98.8%	99.2%			
TV _P Sensitivity	99.8%	99.5%	99.4%	99.4%	99.1%	99.1%			
TF _P Recall	7.8%	18.8%	0.0%	2.0%	1.7%	0.6%			
TV _N Specificity	92.2%	81.3%	100.0%	98.0%	98.3%	99.4%			
TF _N	0.2%	0.5%	0.6%	0.6%	0.9%	0.9%			
VP _P Precision	99.5%	98.3%	100.0%	99.7%	99.2%	99.4%			
VP _N	95.9%	94.2%	95.3%	96.7%	98.1%	99.0%			
Gmean	95.9%	89.9%	99.7%	98.7%	98.7%	99.2%			
ROC area	0.961	0.869	0.997	0.992	0.987	0.994			

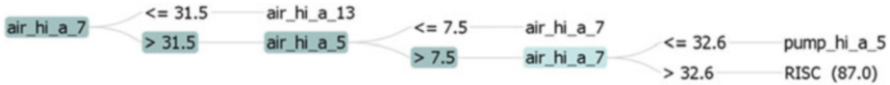


Fig. 19 Decision Tree with 70/30 training and no balancing

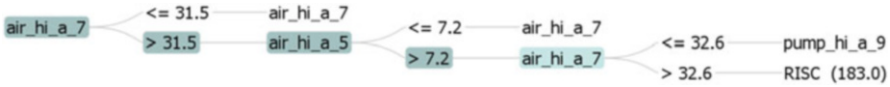


Fig. 20 Decision Tree with 70/30 training and with 100% SMOTE balancing

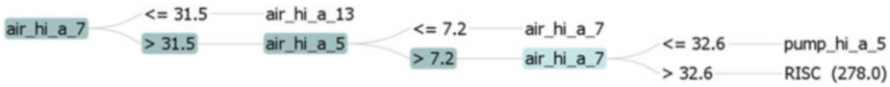


Fig. 21 Decision Tree with 70/30 training and with 200% SMOTE balancing

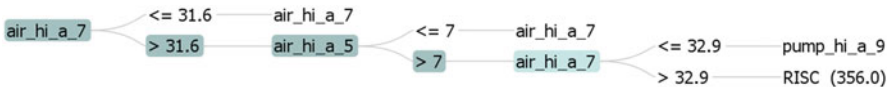


Fig. 22 Decision Tree with 70/30 training and with SMOTE 300% balancing

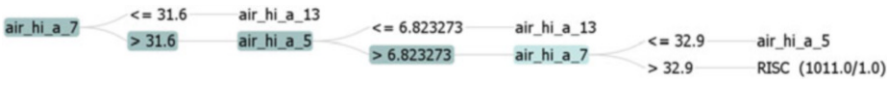


Fig. 23 Decision Tree with 70/30 training and with SMOTE 1000% balancing



Fig. 24 Decision Tree with 70/30 training and with SMOTE 2000% balancing

The differences between Figs. 22 and 23 are the index of the fifth harmonic component of the Air Plants current that changes from 7.0% to 6.823273% and the RISC value that changes from 356.0 to 1011.0/1.0 cases, considering the collected data.

With the SMOTE configuration with 2000%, the Decision Tree shown in Fig. 24 already presents a larger number of branches and the thirteenth harmonic component of the Air Plants current and the seventh harmonic component of the Burning current appear.

Table 19 Results of the Naïve Bayes classifier algorithms of the WEKA software

Algorithm	Correctly sorted instances	Incorrectly sorted instances	ROC area	False positives	False negatives
BAYESNET	89.6962%	10.3038%	0.996	312	0
NAÏVE BAYES	92.4373%	7.5627%	0.984	229	0
NAÏVE BAYES MULTINOMIAL TEXT	95.8388%	4.1612%	0.500	0	126
NAÏVE BAYES UPDATEABLE	92.4373%	7.5627%	0.984	229	0

3.1.3 Result with Naïve Bayes Classifier in WEKA Software

This section will discuss the use of the Naïve Bayes classifier with the main scenarios used in the previous sections of this chapter.

General Data Analysis with Naïve Bayes, Without Class Balancing, with Cross-Validation on Ten Folds, and with the BAYESNET, NAÏVE BAYES, NAÏVE BAYES MULTINOMIAL TEXT, and NAÏVE BAYES UPDATEABLE Algorithms

In the analysis with the Naïve Bayes classifier in WEKA software, several algorithms were used, and the test option was set with 10 folds in the cross-validation technique to identify the most significant result based on the metrics Correctly Classified Instances, Incorrectly Classified Instances, ROC Area, False Positives, and False Negatives as per Table 19.

Table 19 evidences that the NAÏVE BAYES and NAÏVE BAYES UPDATEABLE algorithms presented the most significant results due to the items Correctly Classified Instances, Incorrectly Classified Instances, ROC Area, False Positive, and False Negative. As evidenced in Fig. 25, the biggest impactor is the seventh harmonic current component of the Air Conditioning point.

In Fig. 25, the area containing the distributions for each instance can be seen, where the blue points are those classified as normal (NORM) and the red ones are those classified as at risk (RISC). Thus, it is observed that the ones with the highest concentrations are the fifth and seventh harmonic current components at the Air-Conditioning point. In the larger area of Fig. 25, it is shown the numerical value of the seventh current harmonic according to the X:air_hi_a_7 (Num) axis against the parametric value according to the Y:status_thdu_a (Nom) axis, thus indicating that the highest concentration is around the maximum value of 38.7%.

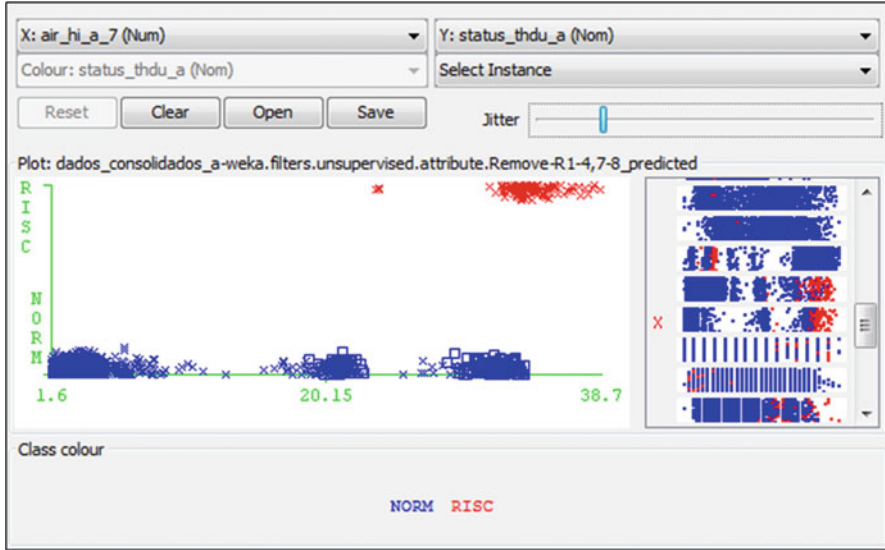


Fig. 25 Naïve Bayes result without balancing and with 10 folds with cross-validation

General Data Analysis with Naïve Bayes, with Class Balancing, and with Different Training and Testing Rates

Similar to the analysis with the Decision Tree classifier, Table 20 presents the data from using the SMOTE filter with the same values applied in the analyses with the Decision Tree classifier and the same training and testing rates (Langley and Sage 1994).

Unlike the analyses with the Decision Tree, the most significant metrics were in the SMOTE 100% condition with training rate 30/70 and SMOTE 2000% condition with training rate 70/30. The results with the Naïve Bayes classifier remain very similar and also indicate the seventh harmonic current component of the Air Conditioners as the main impactor as seen in Figs. 26, 27, 28, 29, 30, and 31.

3.2 Validation of Results

Maximum and minimum values of the third to fifth harmonic current components, among the data collected from each load, as shown in Table 21, were used to validate the results.

According to the data in Table 21, it is observed that the seventh harmonic current component of the Air Conditioning point is the highest value (38.70), followed by the fifth harmonic current component of the Burnnig point with 36.18 and the third current harmonic component of the Burnnig point with 31.74.

Table 20 Comparison of general data between balancing analysis with SMOTE on the Naive Bayes classifier

Instances	Original	SMOTE 100%	SMOTE 200%	SMOTE 300%	SMOTE 1000%	SMOTE 2000%
Total	3028	3154	3280	3406	4288	5548
NORM	2902	2902	2902	2902	2902	2902
RISC	126	252	378	504	1386	2646
%	95.8/4.2	92.0/8.0	88.4/11.6	85.2/14.8	67.7/32.3	52.3/47.7
% training/testing = 30/70						
VP	1886	1930	1883	1834	1858	1826
VN	91	173	254	351	963	1859
FP	0	0	0	2	0	2
FN	143	105	159	197	181	197
Accuracy	93.3%	95.2%	93.1%	91.7%	94.0%	94.9%
TV _P Sensitivity	93.0%	94.8%	92.2%	90.3%	91.1%	90.3%
TF _P Recall	0.0%	0.0%	0.0%	0.6%	0.0%	0.1%
TV _N Specificity	100.0%	100.0%	100.0%	99.4%	100.0%	99.9%
TF _N	7.0%	5.2%	7.8%	9.7%	8.9%	9.7%
VP _P Precision	100.0%	100.0%	100.0%	99.9%	100.0%	99.9%
VP _N	38.9%	62.2%	61.5%	64.1%	84.2%	90.4%
G _{mean}	96.4%	97.4%	96.0%	94.8%	95.5%	95.0%
ROC area	0.987	0.987	0.983	0.984	0.983	0.980

(continued)

Table 20 (continued)

Instances	Original	SMOTE 100%	SMOTE 200%	SMOTE 300%	SMOTE 1000%	SMOTE 2000%
% training/testing = 50/50						
VP	1358	1347	1336	1296	1321	1289
VN	76	121	181	258	685	1354
FP	0	1	1	2	2	4
FN	80	108	122	147	136	127
Accuracy	94.7%	93.1%	92.5%	91.3%	93.6%	95.3%
TVpSensitivity	94.4%	92.6%	91.6%	89.8%	90.7%	91.0%
TFpRecall	0.0%	0.8%	0.5%	0.8%	0.3%	0.3%
TVNSpecificity	100.0%	99.2%	99.5%	99.2%	99.7%	99.7%
TFN	5.6%	7.4%	8.4%	10.2%	9.3%	9.0%
VPpPrecision	100.0%	99.9%	99.9%	99.8%	99.8%	99.7%
VPN	48.7%	52.8%	59.7%	63.7%	83.4%	91.4%
Gmean	97.2%	95.8%	95.5%	94.4%	95.1%	95.3%
ROC area	0.987	0.980	0.981	0.982	0.981	0.978
% training/testing = 70/30						
VP	820	810	811	785	790	785
VN	51	80	101	146	419	804
FP	0	0	0	2	1	1
FN	37	56	72	89	76	74
Accuracy	95.9%	94.1%	92.7%	91.1%	94.0%	95.5%
TVpSensitivity	95.7%	93.5%	91.8%	89.8%	91.2%	91.4%
TFpRecall	0.0%	0.0%	0.0%	1.4%	0.2%	0.1%
TVNSpecificity	100.0%	100.0%	100.0%	98.6%	99.8%	99.9%
TFN	4.3%	6.5%	8.2%	10.2%	8.8%	8.6%
VPpPrecision	100.0%	100.0%	100.0%	99.7%	99.9%	99.9%
VPN	58.0%	58.8%	58.4%	62.1%	84.6%	91.6%
Gmean	97.8%	96.7%	95.8%	94.1%	95.4%	95.5%
ROC area	0.992	0.984	0.985	0.979	0.981	0.980



Fig. 26 Naïve Bayes with 70/30 training and no balancing

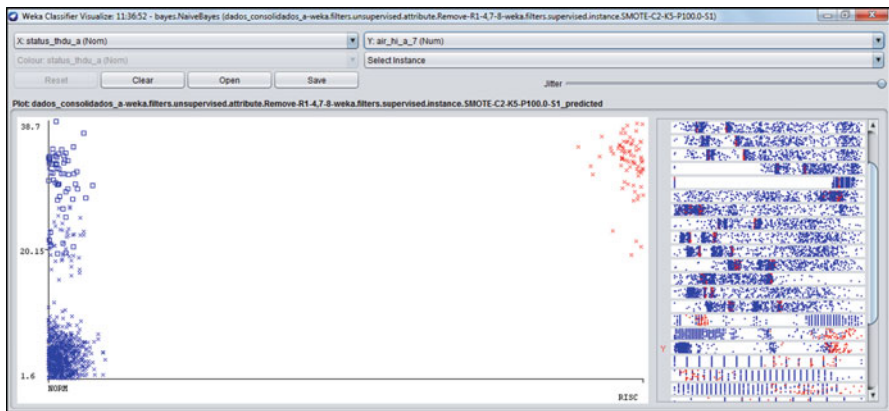


Fig. 27 Naïve Bayes with 70/30 training and with SMOTE 100% balancing

3.3 Discussion of Results

The results found demonstrate the applicability of the KDD process with data mining techniques to analyze the impact of harmonic components on the THD Voltage in the PCC in computer manufacturing companies or similar. It also shows that, in the specific case study, the seventh harmonic current component is the main impact, to lead to the risk condition, the THD Voltage of the PCC of a computer industry and that the same occurs in the T0 shift, which covers the period from 1:10 am to 6:00 am.

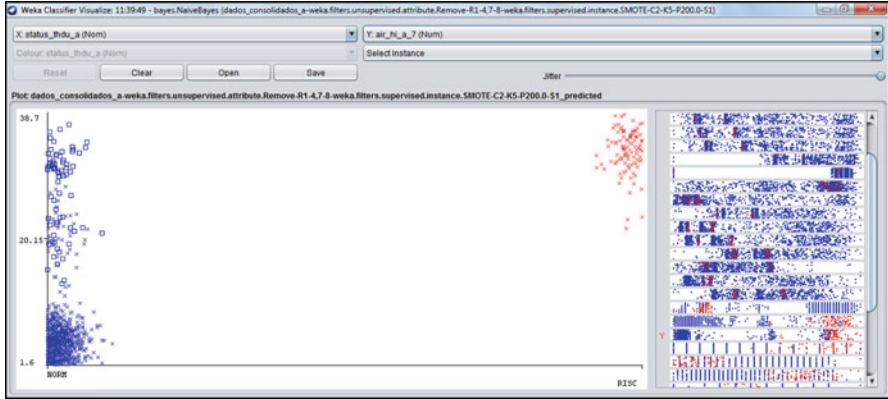


Fig. 28 Naïve Bayes with 70/30 training and SMOTE 200% balancing

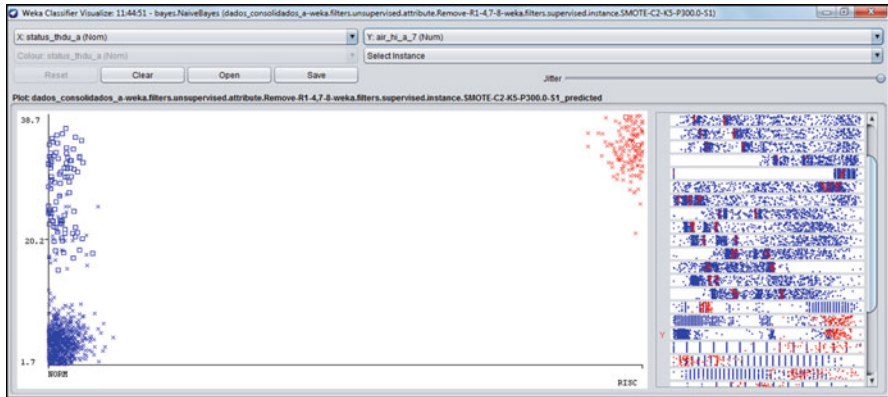


Fig. 29 Naïve Bayes with 70/30 training and with SMOTE 300% balancing



Fig. 30 Naïve Bayes with 70/30 training and with SMOTE 1000% balancing

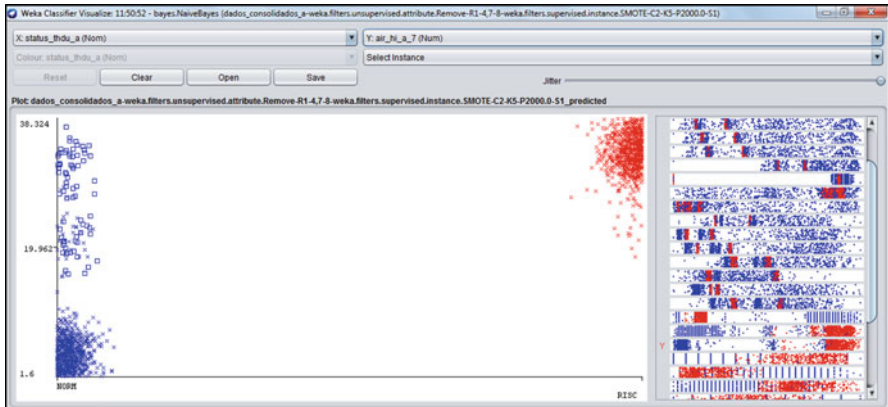


Fig. 31 Naïve Bayes with 70/30 training and with SMOTE 2000% balancing

Table 21 Valores mínimos e máximos considerando as correntes harmônicas ímpares (3ª a 15ª)

Collection points	Number of registrations	3ª harmonic component of current		5ª harmonic component of current		7ª harmonic component of current		9ª harmonic component of current		11ª harmonic component of current		13ª harmonic component of current		15ª harmonic component of current	
		Min	Max	Min	Max	Min	Max	Min	Max	Min	Max	Min	Max	Min	Max
Burning	9966	2.69	31.74	16.50	36.18	13.90	24.03	0.90	7.09	0.09	4.10	2.09	5.78	0.57	3.40
Air conditioners	11,350	0.30	6.60	0.20	9.40	1.60	38.70	0.20	1.70	0.20	3.40	0.60	5.30	0.50	1.80
Air compressors	60,940	0.00	6.40	0.00	12.10	0.10	14.80	0.00	0.80	0.00	1.00	0.00	0.40	0.00	0.30
Tablet room	11,350	1.62	5.98	1.31	4.77	1.13	3.48	0.00	2.23	0.00	1.18	0.00	0.00	0.00	0.00

References

1. Afonso J, Martins J (2005) Qualidade da energia eléctrica
2. Aneel (2012) Nota Técnica, nº 0083 /2012-SRD/ANEEL. Processo: 48500.002798/2012-61.12 Junho
3. Aneel (2016) Módulo 8 – Procedimentos de Distribuição de Energia Elétrica no Sistema Elétrico Nacional – PRODIST. Revisão 8
4. Arrillaga J, Watson N (2004) Power system harmonics. John Wiley & Sons. ISBN-13: 978-0470851296
5. Baggini A (2008) Handbook of power quality. John Wiley & Sons. Print ISBN: 9780470065617 |Online ISBN: 9780470754245 | <https://doi.org/10.1002/9780470754245>
6. Bollen M, Gu I (2006) Signal processing of power quality disturbances. John Wiley & Sons. ISBN-13 978-0-471-73168-9
7. Breiman L et al (1984) Classification and regression trees. CRC Press. ISBN-13: 978-0412048418
8. Cabena P et al (1998) Discovering data mining: from concept to implementation. Prentice Hall. ISBN-13: 978-0137439805
9. Cowell R (1999) Advanced inference in Bayesian networks, Learning in graphical models
10. De Araújo, V. et al. Dedicated hardware implementation of a high precision power quality meter. In: Instrumentation and measurement technology conference (I2MTC), 2015 IEEE international. IEEE, 2015. p. 393–398
11. Dugan R, McGranaghan M, Beaty, H (2004). Electrical power systems quality. McGraw-Hill. ISBN 0-07- 430-018031-8 1996
12. Fayyad U, Piatetsky-Shapiro G, Smyth P (1996) From data mining to knowledge discovery in databases. *AI Mag* 17(3):37
13. Gehrke J et al (1999) Boast- optimistic decision tree construction. In: ACM SIGMOD record. ACM, pp 169–180
14. Gehrke J, Ramakrishnan R, Ganti V (2000) RainForest—a framework for fast decision tree construction of large datasets. *Data Min Knowl Disc* 4(2):127–162
15. Granados-Lieberman D et al (2011) Techniques and methodologies for power quality analysis and disturbances classification in power systems: a review. *IET Gener Transm Distrib* 5(4):519–529
16. Grossman D, Domingos P (2004) Learning Bayesian maximizing conditional likelihood. In: Proceedings on machine learning, p. 46–57
17. Hall M, Frank E (2008) Combining Naïve Bayes and decision tables. In: 2008 FLAIRS Conference - AAAI
18. Hall M et al (2009) The WEKA data mining software: an update. *ACM SIGKDD explorations newsletter* 11(1):10–18
19. Hand D (1997) Construction and assessment of classification rules. Wiley
20. Hand D, Mannila H, Smyth P (2001) Principles of data mining. MIT Press
21. Iagar A, Popa G, Dinis C (2014) The influence of home nonlinear electric equipment operating modes on power quality. *WSEAS Trans Syst* 13:357–367
22. IEEE Recommended Practices and Requirements for Harmonic Control in Electrical Power Systems (2014) IEEE Std. 519–2014 (Revision of IEEE Std 519–1992), IEEE New York
23. Kahle K (2016) Power converters and power quality. arXiv preprint arXiv:1607.01556
24. Langley P, Sage S (1994) Induction of selective Bayesian classifiers. In: Proceedings of the tenth international conference on uncertainty in artificial intelligence. Morgan Kaufmann Publishers Inc., pp 399–406
25. Langley P et al (1992) An analysis of Bayesian classifiers. In: Proceedings of the 10th National Conference on Artificial Intelligence, San Jose, 1992, pp 223–228
26. Leite J (2013) Projeto multicritério de filtros harmônicos passivos para instalações industriais utilizando técnicas de inteligência computacional. Tese de Doutorado. Universidade Federal do Pará

27. Mahela O, Shaik A (2017) Recognition of power quality disturbances using S-transform based ruled decision tree and fuzzy C-means clustering classifiers. *Appl Soft Comput* 59:243–257
28. Matos E et al (2016) Análise não paramétrica para identificação de fontes de distorções harmônicas em sistemas de energia elétrica: um estudo aplicado no campus universitário do Guamá da Universidade Federal do Pará. Tese de Doutorado. Universidade Federal do Pará
29. Niedermayer D (2008) An introduction to Bayesian networks and their contemporary applications. In: *Innovations in Bayesian networks*, pp 117–130. Springer. ISBN 978-3-540-85065-6
30. Nogueira R et al (2014) Análisis de los Impactos Armónicos en la Industria de la Electrónica utilizando Árboles De Decisión. CIIC - CUJAE, CUBA. (Trabalhos completos publicados em anais de congressos)
31. Nogueira R et al (2015a) Harmonic impact analysis coming from the manufacturing processes of a eletroeletronic industry using KDD and decision trees. *J Eng Technol Ind Appl - JETIA, Manaus-Amazonas*:80–87
32. Nogueira R et al (2015b) Análise dos impactos harmônicos em uma indústria de manufatura de eletroeletrônicos utilizando árvores de decisão. Dissertação de Mestrado. Universidade Federal do Pará
33. Oliveira E et al (2017) Voltage THD analysis using knowledge discovery in databases with a decision tree classifier. *IEEE Access* 6:1177–1188
34. Ozgonenel O, Thomas D, Yalcin T(2012) Superiority of decision tree classifier on complicated cases for power system protection
35. Piatetsky-Shapiro G, Frawley W (1991) *Knowledge discovery in databases*. AAAI, Cambridge, MA
36. Rodríguez A et al (2013) A decision tree and S-transform based approach for power quality disturbances classification. In: *Power engineering, energy and electrical drives (POWERENG), 2013 fourth international conference on*. IEEE, pp 1093–1097
37. Rodriguez-Guerrero M et al (2017) A novel methodology for modeling waveforms for power quality disturbance analysis. *Electr Power Syst Res* 143:14–24
38. Roiger R (2017) *Data mining: a tutorial-based primer*. CRC Press. ISBN-13 978-1498763974
39. Schneider-Electric (2005) *Qualidade de Energia-Harmônicas*. In: *Workshop de Instalações Elétricas de Baixa Tensão*
40. Zhang H (2004) The optimality of Naïve Bayes. In: *2004 FLAIRS Conference - AAAI*

Optimization of Economic and Environmental Dispatch Using Bio-inspired Computer Metaheuristics



Manoel Henrique Reis Nascimento, Jandecy Cabral Leite,
Alexandra Amaro de Lima, Edson Farias de Oliveira,
Ítalo Rodrigo Soares da Silva, Ricardo Silva Parente,
Jorge Laureano Moya Rodríguez, and Paulo Oliveira Siqueira Junior

1 Introduction

The use of fossil fuels has a strong influence in global power generation, and in recent decades the world has been confronted with a scarcity of electricity, mainly because of industrial development. Nevertheless, there is a great deal of pressure to reduce the use of such power generation, especially by increased environmental protection laws. This has brought the need to search for more efficient methods that make use of the most competitive fossil fuels in technical, economic, and environmental terms.

Owing to serious environmental impacts and growing global energy demand, traditional economic load distribution with the sole purpose of reducing energy generation costs has been insufficient to meet national strategic requirements for energy conservation and pollutant reduction. There is a growing need to find a method of power generation that can reduce energy consumption and pollutant emissions (Li 2021).

The scarcity of energy resources has led to the search for renewable sources of energy, especially in underdeveloped countries. The benefits of renewable energy consumption having less impact on the environment led to the search for new energy generation alternatives, diversifying the sources of global energy generation (Destek 2016).

M. H. R. Nascimento (✉) · J. C. Leite · A. A. de Lima · E. F. de Oliveira · Í. R. S. da Silva ·
R. S. Parente · J. L. M. Rodríguez · P. O. S. Junior
Institute of Technology and Education Galileo of the Amazon (ITEGAM), Manaus, Amazonas,
Brazil
e-mail: jandecy.cabral@itegam.org.br; italo.silva@itegam.org.br

The development of more efficient power generation systems has involved a constant search for objects by several nations, not only concerned with the generation of energy to meet its growing demand but also by power generation that causes less pollution, with reductions in emission levels of greenhouse gases.

At the same time, the fast depletion of fossil fuels, the alarming rate of increase in pollution levels of the Earth's atmosphere, the increasing impact of global warming, and the strict laws of pollution imposed in some countries have generated an extra stimulus for exploration and evaluation of alternative fuels for internal combustion engines (Abedin et al. 2013).

The increase in global environmental awareness has led many researchers to consider emissions in the Economic Dispatch problem. Emissions of hazardous and harmful pollutants such as sulfur dioxide (SO₂), nitrogen oxide (NO_x), carbon monoxide (CO_x), and carbon dioxide (CO₂) have given rise to widespread calls for utilities to develop ways to reduce these pollutants (Nwulu and Xia 2015). As environmental issues, particularly climate change, become more and more important, the requirements relating to the consumption and production of electricity have been increasingly demanding to comply with certain international standards. Nationally, Brazilian legislation limits the level of pollutant gas emissions into the atmosphere, arising from the production of energy in thermoelectric plants, with fines and other punishments (CONAMA 2006).

With the development of the global economy and the growing demand for energy, people are increasingly aware of the coordinated development between human beings and the environment. Among them, pollution caused by thermal energy generation represents the largest proportion, which makes more and more people pay attention to environmental pollution caused by pollutant emissions from thermoelectric plants. The economic and environmental dispatch (EED) problem of energy is an important optimization problem in the operation of the power system (Xin-Gang et al. 2020). Thus, optimizing the use of internal combustion engines (ICEs), making them more efficient and consequently reducing their emissions of polluting gases, will bring a significant reduction in the environmental impacts arising from the production of energy in thermoelectric systems.

During the period 1999 to 2013, rural electrification programs brought access to electricity to 16 million inhabitants in Brazil. Even so, around 155,000 rural families remain without access to electricity in the Amazon region, living in very isolated communities that cannot be served by the expansion of the existing national grid and interconnected system. To supply electricity to these communities, off-grid generation using diesel fuel has traditionally been the only option considered (Sánchez et al. 2015).

Allied to this context, because of the large industrial production capacity in the North and in particular the Industrial Pole of Manaus/AM, where over 90% of its energy is derived from thermoelectric power plants (TPPs) it becomes necessary to use computational tools that enable managers and specialists of these TPPs to make decisions about optimizing fuel consumption, maintenance of generators, energy production, energy efficiency, and reduction in pollution levels.

In the classic ED problem, the generation of power from fossil fuels such as coal, oil, and gas releases a large amount of atmospheric emissions, represented by polluting gases, such as sulfur oxides (SO_x), NO_x, CO₂, and some particles. Electricity generation from fossil fuels is exacerbating the atmospheric pollution, which has become one of the most important concerns in recent years. Therefore, besides moving toward generating electricity from clean and renewable energies, pollutant emissions released by traditional generation units should also be considered in the generation scheduling of the system (Rezaie et al. 2019).

Some optimization methods such as those described in Sakhivel et al. (2021), who propose a new multi-objective squirrel search algorithm to solve the combined economic and environmental power dispatch problem, a new metaheuristic technique based on a genetic algorithm (GA), adaptive strategy, and two constraint handling repair mechanisms (Postolov and Iliev 2022), the chaotic whale optimization algorithm (Paul et al. 2020), the moth swarm algorithm (Ajayi and Heymann 2021), the EED of integrated regional energy systems considering an integrated demand response (He et al. 2020), and the solution of economic and environmental power dispatch problem of an electrical power system with the Broyden Fletcher Goldfarb Shanno based on the augmented Lagrangian algorithm (Talbi et al. 2020), are also used to solve the economic dispatch optimization problem. Methods based on mathematical approaches have also been developed to provide a faster solution (Palanichamy and Srikrishna 1991; Palanichamy and Babu 2002). The multi-objective evolutionary algorithms (MOEAs) (Carrano et al. 2014; Ruiz et al. 2015) were applied to solve the economic load dispatch problem.

Ajayi and Heymann (2021) proposed an improved sailfish optimization algorithm to deal with the problems of high operation costs and large pollution emissions in hybrid dynamic economic emission dispatch of the power system. In Li (2021) multi-objective optimization of space adaptive division for environmental economic dispatch is presented.

Li et al. (2021) proposed an improved tunicate swarm algorithm to solve and optimize the dynamic economic emission dispatch problem. Liu et al. (2021) also proposed a novel approach based on the enhanced moth–flame optimization algorithm.

This chapter presents a new proposed solution for economic and environmental dispatch, which includes the shutdown of generators with higher fuel consumption, implemented by nondominated sorting genetic algorithms (NSGA) II and III, which are appropriate for solving the problem optimization of EED in TPPs. Such implementation is characterized by incorporating some innovations, such as the reduction of fuel costs and polluting gas emissions.

2 Theoretical Framework

2.1 *Economic and Environmental Dispatch*

In recent years, environmental issues and energy have attracted considerable attention; most of the energy being used is from the combustion of fossil fuels, which simultaneously release significant amounts of heat and waste (Du et al. 2015).

The growing global awareness of the effects of environmental pollution caused by the production of energy in thermoelectric plants has been pressing the authorities to create legislation that limits the levels of pollutant emissions, which makes it a crucial issue to be considered in the economic dispatch.

The shifts in fossil-fuel use result in rapid and large decreases in both CO₂ and non-CO₂ emissions, with CO₂ from fossil sources and sulfur dioxide (SO₂, which is largely co-emitted) decreasing by around 75–85% by 2050 in most scenarios (Shindell and Smith 2019).

The typical EED problem can be formulated as a multi-objective optimization problem (MOOP) that involves simultaneously minimizing emission and fuel costs under conventional ramp rate constraints, load limitations, etc. (Ghasemi et al. 2015).

The purpose of the EED is to estimate the optimal quality portion of power generated by each generator, minimizing fuel cost and pollutant emission levels simultaneously, maintaining satisfactory load demand, in addition to meeting operational restrictions (Nwulu and Xia 2015).

However, it is realized that conventional techniques become very laborious when dealing with increasingly complex EED problems, and are further limited by their lack of robustness and efficiency in a number of practical applications.

Several methods have been used to represent emission levels. A summary of environmental/economic dispatch algorithms dating back to 1970 using conventional optimization methods has been provided, the environmentally constrained economic dispatch problem is solved using the Hopfield Neural Network method, in which the energy function of the network contains both the objective function and equality and inequality constraints. Also, the emission is inserted as a constraint and the problem was solved using the neural network (Abou El Ela et al. 2010).

A price penalty factor to solve the problem of the EED, combining the functions of emission and fuel costs in a single objective function was proposed by Gopalakrishnan and Krishnan (2012).

The solution to the EED was the use of a genetic algorithm with arithmetic crossing, which was proposed by Yalcinoz and Altun (2002).

Several strategies to reduce the atmospheric emissions have been proposed and discussed. These include installation of pollutant cleaning equipment, switching to low emission fuels, replacement of the aged fuel burners with cleaner ones, and emission dispatching. The first three options require installation of new and/or modification of existing equipment, which involves considerable capital outlay; hence, they can be considered long-term options (Abou El Ela et al. 2010). On

the other hand, the EED optimization option is an attractive short-term alternative where emissions must be minimized, in addition to the objective of reducing fuel costs. Thus, the EED problem can be treated as a multicriteria optimization problem with nonmeasurable and contradictory goals.

Further, the problem has been reduced to a single-objective problem by treating the emission as a constraint. This formulation, however, has severe difficulty in obtaining the trade-off relations between cost and emission (Hota et al. 2010).

Nevertheless, many mathematical assumptions have to be considered to simplify the problem. Furthermore, this approach does not give any information about the compensation of those involved. One of the most intuitive ways of obtaining a single unique solution for multi-objective optimization is the weighted sum method (WSM). In this approach, the MOOP are converted into a scalar preference function using a linear weighted sum function (Augusto et al. 2012).

An important aspect of the WSM is that a set of non-inferior solutions (or Pareto optimal solutions) can be obtained by varying the weights. Unfortunately, this technique requires several runs, as many times as needed for the number of Pareto optimal solutions. Furthermore, an optimal solution of the Pareto front cannot be used for nonconvex problems. To avoid this difficulty, the ϵ -restriction technique optimizes the objective function with greater importance and considers the other objectives with less relevance for some levels of permissions (Yokoyama et al. 1988; Ying-Tung et al. 1994). The most obvious weaknesses of this approach are the computational cost and the tendency to find weakly nondominated solutions.

To solve the EED-Dynamic problem, three versions of the differential harmonic search algorithm are proposed in the literature, namely: the chaotic differential harmony search algorithm, the self-adaptive differential harmony search algorithm, and the chaotic self-adaptive differential harmony search algorithm (Arul et al. 2015).

The typical EED problem can be formulated as a multi-criteria optimization model, with at least two conflicting objectives, namely, fuel cost and pollutant emissions. This problem can be formulated as described in the following sections.

2.1.1 Objective 1: Minimizing Fuel Cost

The generator cost curves are represented by quadratic functions $F(P_i)$. The problem of minimizing the total cost (\$/h) of fuel can be represented as follows, original Eq. (1) adapted from Farhan Tabassum et al. (2021):

$$\text{Minimize } F = \sum_{i=1}^n f_i (P_i) \tag{1}$$

$$f_i (P_i) = a_i + b_i P_i + c_i P_i^2 \text{ (\$/h)} \tag{2}$$

where a_i , b_i and c_i are the cost coefficients of the generator i_{th} and P_i is the real power of the generator i_{th} .

2.1.2 Objective 2: Minimization of Pollutant Emissions

The most important emissions considered in the power generation industry because of their effects on the environment are sulfur dioxide (SO₂) and nitrogen oxide (NO_x). These emissions can be modeled using functions that associate the emissions with the energy production for each unit. Sulfur dioxide emissions are dependent on fuel consumption and they take the same form as the cost functions of fuels used in economic dispatch. NO_x emissions are more difficult to model as they come from different sources and their production is associated with several factors, such as boiler temperature and air content (Wang and Singh 2007).

The total ton/h of pollutant emissions $E(P_i)$ from the atmosphere such as sulfur dioxide, SO₂ and nitrogen oxide NO_x, caused by the burning of fuel in the generating units, can be expressed as in Eq. (3) adapted from Ajayi and Heymann (2021):

$$\text{Minimize } E = \sum_{i=1}^n f_i(P_i) \quad (3)$$

$$f_i(P_i) = \alpha_i + \beta_i P_i + \gamma_i P_i^3 \text{ (ton/h)} \quad (4)$$

where α_i , β_i and γ_i are the characteristic coefficients of the generator i_{th} emissions. As restrictions for solving the problem, the same restrictions as for EED are considered.

In summary, the objective of EED optimization is to minimize $F(P_i)$ and $E(P_i)$ simultaneously, subject to system constraints. The basic particle swarm algorithm is revised and expanded to address the multi-objective case. The proposed algorithm proves to be effective, as the solutions obtained have some superior characteristics compared with other approaches, including weighted aggregation and MOEA. In addition, the proposed approach addresses MOOPs more efficiently, as it is able to obtain a manageable set of nondominated solutions in a single solution (Wang and Singh 2007). With increasing interest in environmental pollution, traditional ED, which ignores pollutant emissions from fossil fuels used by thermal power plants, no longer meets the needs. Therefore, the EED, as an alternative, has become more attractive because it considers pollutant emissions as well as economic advantages (Aydin et al. 2014). The solution of the EED problem comprises some important evaluation criteria such as fuel cost, environmental impact, and loss of total active power. Thus, the EED problem is a multi-objective mathematical problem in which conflicting objectives are optimized simultaneously (Aydin et al. 2014).

In the general literature, the EED problem can be solved through three approaches. In the first one, the emission amount is calculated as a constant within

the allowed limits. However, it is very difficult to formulate trade-off relationships between fuel cost and emissions. As an example of this approach, the EED problem was solved with the Davidon–Fletcher–Powell method apud (Aydin et al. 2014), with the amount of emission taken as a constant within the allowed limits.

In a second approach, emission reduction is considered beyond cost minimization. In this case, the optimization problem for multiple goals in solving the EED problem is converted into a single goal optimization problem that considers only one goal at a time, or the linear combination of the two goals. In the literature, this type of optimization problem was solved by algorithms such as the genetic algorithm, the ED algorithm, the particle swarm optimization algorithm, the artificial bee colony (ABC) algorithm, the fast successive linear programming algorithm, the evolutionary computation algorithms, the hybrid bacterial foraging Nelder–Mead algorithm, the optimization algorithm based on biogeography with hybrid differential evolution, the analytical solution, the Newton–Raphson method, the gravitational opposition-based search algorithm, and the first-order gradient method (Aydin et al. 2014).

Finally, in a third approach, simultaneously contradictory objectives are evaluated together in solving the EED problem. Both fuel cost and emissions are minimized together. In the literature, as an example of such an approach, the optimization problem was solved using methods such as multi-objective mathematical programming, a formulation based on the fast ε -constraint approach, algorithms such as nondominated bacterial foraging classification and fuzzy domain-based bacterial foraging (Aydin et al. 2014).

A combination of the ED problem and the NO_x emission problem in a single-objective optimization problem can be solved using the WSM (Aydin et al. 2014).

The transformation from the MOOP to the single objective problem using the appropriate transformations is called scaling. The WSM is one of the oldest and most common scaling methods. The method is mainly suitable for convex problems. More than one objective function is scaled using this method, multiplying them with positive weights added to them. In this way, the MOOP is transformed into a single-objective optimization problem. After that, both algorithms, the ABC and the incremental ABC, with dynamic population size, are used to solve the converted problem (Aydin et al. 2014).

2.2 Brazilian Environmental Regulation

In Brazil, the regulation of the limits of atmospheric emissions are determined by the National Council for the Environment – CONAMA, which in the use of the powers conferred on it by Law No. 6.938, of 31 August 1981, regulated by Decree No. 99,274, of 6 July 1990, in view of the provisions of its Internal Regulation and considering the provisions of resolution CONAMA No. 5, of 15 June 1989, the National Air Pollution Control Program – PRONAR (CONAMA 2006) is established.

Table 1 Classification of fuels according to their physical state

Turbine by fuel type	NO _x ^a (as NO ₂)	CO ^a	SO _x ^a (as SO ₂)	MP ^a
Natural gas	50	65	NA	NA
Liquid fuel	135	NA.	200	50

Source: CONAMA (2006)

^aThe results must be expressed in the concentration unit mg/Nm³, on a dry basis and 3% excess oxygen

NA not applicable

According to the emission limits of atmospheric pollutants, from gas turbines for electricity generation, defined by PRONAR (CONAMA 2006):

1. The emission limits for atmospheric pollutants generated by turbines for the generation of electric energy, powered by natural gas or liquid fuels, in a simple cycle or a combined cycle, without supplementary burning, with electrical power above 100 MW, are defined here. When the total sum of electricity generation per project exceeds 100 MW, the limits established here are also required for each turbine individually, regardless of its generation capacity.
2. For the application of this Annex, the following definition of the term must be considered: gas turbines – equipment that converts part of the energy contained in the fuel into mechanical energy, by means of the axial rotation of an axis, which activates an electric generator.
3. The following emission limits are established for air pollutants generated in electricity generation processes by gas turbines (Table 1).
 - (a) The limits established for turbines powered by liquid fuel also apply to turbines powered by natural gas, when they use liquid fuel in emergency situations or in the case of shortages.
 - (b) In performance testing of new equipment, compliance with the established limits must be verified under full load conditions.
 - (c) In periodic assessment, compliance with the established limits may be verified under typical operating conditions, at the discretion of the licensing environmental agency.
4. When carrying out the sampling, activities or sources that emit pollutants must have the necessary structure and/or direct determination of pollutants in ducts and chimneys, in accordance with a standardized methodology or equivalent accepted by the licensing environmental agency.
5. In the event of two or more sources whose final launch is carried out in a common duct or chimney, measurements must be made individually. When it is impossible to carry out individual measurements, in accordance with the standardized or equivalent methodology accepted by the licensing environmental agency, these may be carried out in the common duct or chimney and the emission limits must be individually weighted with the respective nominal thermal powers of the sources in question.

6. The release of gaseous effluents into the atmosphere must be carried out through ducts or chimneys, whose design must take into account the buildings surrounding the polluting source and the established air quality standards.
7. Owing to the local characteristics of the area of influence of the polluting source on air quality, the licensing environmental agency may establish more restrictive emission limits, including considering the alternative of using fuels with less polluting potential.

2.3 Thermal Plants

2.3.1 The Diesel Engine

The diesel engine remains the most efficient liquid fuel burning unit yet conceived and has demonstrated its reliability for mass transport and power generation units. Thus, the proper and efficient functioning of a diesel engine is an important objective, especially for marine and industrial applications (i.e., power generation) (Hountalas et al. 2014).

Additionally, it should be considered that the modularity of the equipment of a TPP operating on a diesel cycle allows for a short assembly time and a minimum space for construction, in addition to excellent load flexibility. There are numerous applications for motor generator sets, ranging from the production of a few kilowatts to hundreds of megawatts, for isolated or interconnected generation purposes, propulsion, or as generators to support power outages.

2.3.2 Internal Combustion Engines

Few inventions have had such a large impact on society, the economy, and the environment as the alternative ICEs, and these engines are commonly used for the propulsion of mobile systems. Internal combustion is advantageous in mobile scenarios, as it can provide a close relationship between weight and power (Deligiannis and Manesis 2006).

These engines are also used in industrial applications such as oil and gas production, compression, quarrying, recycling, and electric power generation. Their extensive use derives from the fact that they can work with a variety of fuels at a wide range of speeds and with variable loads (Deligiannis and Manesis 2006).

2.3.3 Basic Types of Alternative Engines

Spark ignition engines are engines in which ignition is ordinarily triggered by an electrical spark whereas in compression ignition (CI) engines ignition ordinarily takes place without the need for an electrical spark or a surface heated by an external

source of energy. These engines have received a great deal of attention in recent years owing to their low emissions and great efficiency (Nikhil et al. 2010).

The two main types of internal combustion engines are spark ignition (SI) engines, where the fuel is ignited by a spark, and CI engines, where the increase in temperature and pressure during compression is enough to provoke the spontaneous ignition of the fuel (Deligiannis and Manesis 2006).

2.3.4 Energy Generation Process with Combustion Engines

Combined heat and power (CHP) systems allow one of the best ways of consuming fossil fuels efficiently. These systems emit less pollution than separate production of the same amount of power and heat, and, owing to their significant savings and environmental benefits, there is a growing trend toward using them in the power generation industry (Abusoglu and Kanoglu 2009; Meybodi and Behnia 2011). ICEs are widely used as the main engine of cogeneration systems.

The preferred fuel of SI engines for power generation is natural gas. IC engines, which are most commonly diesel engines, operate primarily on this fuel. Alternatively, both gas engines and diesel engines can be configured to run on other fuels (Meybodi and Behnia 2011). Cogeneration systems based on internal combustion engines have been studied in recent years. As an example, the model developed to design and evaluate cogeneration systems for residential use can be highlighted and there is a growing trend toward using these systems in the power generation industry (Meybodi and Behnia 2011; Muccillo and Gimelli 2014).

2.3.5 Energy Resources

In the generation of thermoelectric energy, the term source of energy input is directly associated with the term fuel, which is defined as a substance that, when chemically combined with an oxidizing compound, generates an exothermic reaction releasing large amounts of heat (Lora and Nascimento 2004).

A classification of fuels, according to their physical state, is presented in Table 2.

The energy resources available for the generation of electrical energy from fossil fuels are directly related to this classification, and in this sense it is possible to work with gas, steam, combined cycle, generation systems, etc.

Gas Turbine

The main device of the combined cycle TPPs is the gas turbine, a technology originating from the development of jet propulsion turbines, developed for military and civil aircraft, where the fuel is kerosene.

Table 2 Classification of fuels according to their physical state

Combustible	Physical state
Solid	Mineral coal
	Charcoal
	Schist
	Peat
	Firewood
	Agribusiness waste agroindustry
Liquid	Gasoline
	Kerosene
	Diesel
	Fuel oils
Gaseous	Natural gas
	Liquefied petroleum gas
	Biogas

Source: Lora and Nascimento (2004)

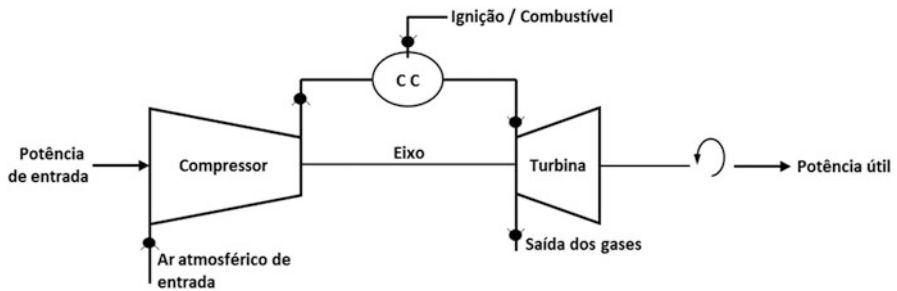


Fig. 1 Main components of a gas turbine. (Source: Lora and Nascimento (2004))

In TPPs, the most frequently used fuel is natural gas, although there is almost always the possibility of operating with a second fuel, such as diesel oil, for example, to avoid interruptions in the case of gas supply problems.

Three main components can be distinguished in a gas turbine:

- The compressor
- The combustion chamber (CC)
- The turbine itself

Figure 1 illustrates the three main components of a gas turbine.

The turbine is a mechanical drive source for both the compressor and the electric generator. In the case of a gas turbine, it basically consists of a compressor with its respective air intake section, a combustion system, and an expansion turbine associated with the exhaust gas section.

However, the turbine can be operated in an isolated way (simple cycle), as in aircraft; its thermal efficiency is low, and about 64% of the heat generated by burning the fuel is lost in the exhaust gases. Additionally, the increase in thermal efficiency can be achieved by raising temperatures and inlet pressures, but this would greatly

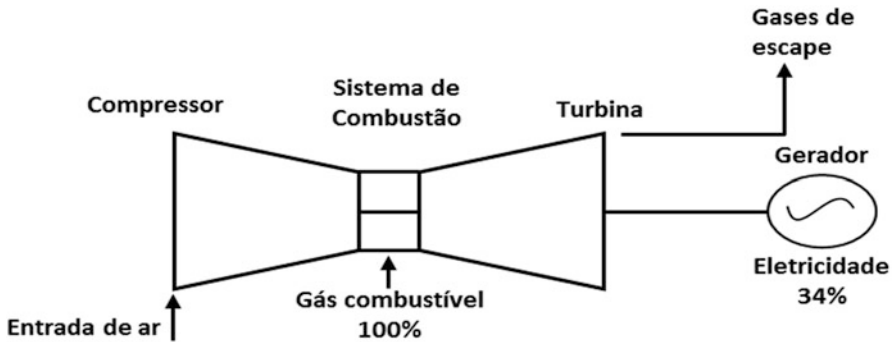


Fig. 2 Single-cycle gas turbine. (Source: Lora and Nascimento (2004))

increase the cost of construction and maintenance of the process equipment, making the project unfeasible.

In Fig. 2, a characteristic arrangement of a simple cycle gas turbine is presented, showing the input and output energy distribution.

In addition, gas turbines are excellent in the production of electric energy in a simple cycle or cogeneration, especially when using natural gas instead of liquid fuels. Furthermore, when natural gas is used as fuel, the emissions of atmospheric pollutants, such as NO_x, SO₂, and CO_x, are very low. At the same time, liquid fuels are known to cause maintenance problems owing to the presence of chemical elements and salts that can accelerate the corrosion of components present in the CC, and in the path of hot gases.

Heat Recovery Boiler

One of the main elements of combined cycle plants is a steam generator capable of recovering part of the heat emitted by the gases generated during the exhaust of the gas turbines. This steam generator or boiler is known by the acronym HRSG, which stands for heat recovery steam generator. Through the use of an HRSG, the thermal efficiency is substantially increased (as shown in Fig. 3), as the steam produced by it drives the turbine, with no need to burn additional fuel.

Cogeneration

Cogeneration systems are used in situations where electricity and heat are needed.

As CHP systems involve the production of thermal energy in the form of steam or hot water or electricity, the efficiency of energy production can be increased from current levels ranging from 35% to 55% in conventional power plants, can exceed by more 90% in cogeneration systems (Abusoglu and Kanoglu 2009).

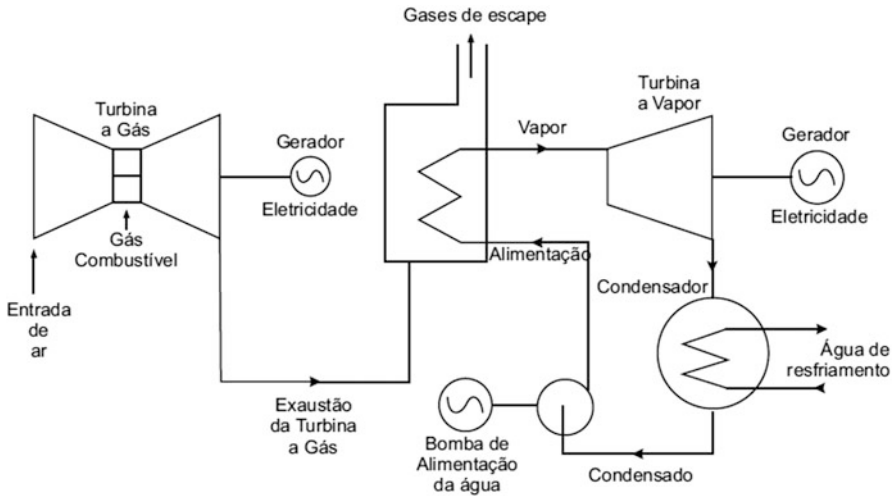


Fig. 3 Heat recovery boiler. (Source: Lora and Nascimento (2004))

The cogeneration process with an internal combustion engine is connected to an electric generator and to heat exchangers in water jackets and exhaust gas for heat recovery. Heat and power plants combined with internal combustion engines are widely used because of their cost, effectiveness, mobility, and high efficiency ratio (Abusoglu and Kanoglu 2009).

Combined heat and power systems allow fossil fuels to be consumed efficiently. These systems emit less pollution than separately producing the same amount of electricity and heat.

2.3.6 Thermo-economics

Thermo-economic analysis has great academic relevance, allowing the simultaneous assessment of technological, thermodynamic, economic, and financial aspects; therefore, it provides more solid results in decision making (Dincer and Cengel 2001).

The application of thermo-economics for industrial installations consists of determining the product (useful effect) and its cost in fuel (set of energy goods or materials consumed) and expenses (capital investments, operation, maintenance, etc.), evaluated in terms of its energy content. The energy-economic optimization implies obtaining the minimum total unit cost related to the product, that is, it consists in the gradual implementation of a development project, according to a plan that leads to a minimum total unit cost of the product. An important problem to be solved with the means provided by thermo-economics refers to the

macroeconomic decision on the most advantageous destination for the investment of financial resources available for the development of the energy industry (Dincer and Cengel 2001; Wall and Gong 2001; Abusoglu and Kanoglu 2009). Advantages of the thermo-economic analysis method are that:

- Thermo-economics allows, unlike other methods, the use of technical, energy, and financial resources to be optimized; giving companies greater competitiveness, taking into account the scarcity of resources and the need to produce more with less and at the lowest possible cost.
- Thermo-economy makes it possible to calculate the real energy cost in each of the flows involved in the process, and only the knowledge of the true costs will make it possible to rationalize finite resources.
- Thermo-economics, based on a property such as exergy, is able to classify all physical fluids according to their essence (their quality). This fact unites all the streams into a single type and can be treated in this way, not only for its content, but also for its quality.
- Thermo-economics allows the quantification and identification of the causes of irreversibilities in systems conceived by humans. By quantifying them in energy units, thermo-economics manages to change qualities into something measurable, mathematically treatable, and with the possibility of being submitted for scientific discussion.

3 Optimization Techniques

3.1 Multi-objective Optimization

Applications studied in practice usually involve the simultaneous optimization of multiple goals, which are generally nonmeasurable and conflict with each other. The purposes of multi-objective problems in mathematical programming are based on optimizing different objective functions, subject to a set of system constraints (Vahidinasab and Jadid 2008).

Multi-objective optimization, also called multicriteria optimization or vector optimization, has been defined as finding a vector with decision variables that satisfy the constraints by assigning feasible values to all objective functions (Atashkari et al. 2007). In the absence of any preferential information, a nondominated set of solutions is obtained, rather than a single optimal solution. These optimal solutions are called Pareto optimal solutions (Panigrahi et al. 2010; Alberto et al. 2014).

In this context, Pareto dominance is a vector $U = [u_1, u_2, \dots, u_k] \in R^k$, which is dominant to a vector $V = [v_1, v_2, \dots, v_k] \in R^k$ (represented by $U < V$) if and only if $\forall i \in \{1, 2, \dots, k\}, u_i \leq v_i \exists j \in \{1, 2, \dots, k\} : u_j < v_j$. In other words, there is at least one u_j , which is smaller than v_j , whereas the rest of the u 's are less than or equal to their counterparts' v 's (Atashkari et al. 2007).

Many optimization problems involve multiple goals. A MOOP) can be mathematically formulated as in Eq. (5) (Zhou et al. 2011):

$$\begin{aligned} &\text{Minimize } F(x) = (f_1(x), \dots, f_m(x))^T, \\ &\text{and } x \in \Omega \end{aligned} \tag{5}$$

where Ω is the decision space and $x \in \Omega$ is a decision vector. $F(x)$ consists of m objective functions $f_i: \Omega \rightarrow R, i = 1, \dots, m$, where R^m is the objective space.

In Eq. (5) there are conflicts between the objectives to be minimized. The improvement of one objective can lead to the deterioration of the other. Thus, a single solution that can optimize all objectives at the same time does not exist, but rather a set of tradeoff solutions, called Pareto optimal solutions, which are important for decision making (Zhou et al. 2011).

Mathematically, the general MOOP is to find the vector \vec{x} that satisfies the m inequality constraints and p equality constraints and that optimizes the objective function vector Eq. (6) (Vahidinasab and Jadid 2008):

$$\begin{aligned} &\text{Minimize } \vec{F}(\vec{x}) \\ &\text{as } \vec{h}(\vec{x}) = \vec{0} \\ &\text{and } \vec{g}(\vec{x}) \leq \vec{0}, \end{aligned} \tag{6}$$

where $\vec{x} \in R^n, \vec{F}(\vec{x}) \in R^m, \vec{h}(\vec{x}) \in R^p, \vec{g}(\vec{x}) \in R^q$.

Equality and inequality constraints define a limited subarea for finding the ideal solution, which is called a viable area. Any point in this area thus defines a viable solution.

Owing to the nature of conflicting goals, an ideal solution that simultaneously optimizes all criteria is often not achievable. Therefore, it is often preferable to give a set of solutions rather than a single solution for this type of optimization problem. These solutions are called efficient solutions or Pareto optimalities, which are solutions that cannot be improved in an objective function without deteriorating performance in at least one of the other objectives (Vahidinasab and Jadid 2008).

A general MOOP can be expressed by Eq. (7). It is assumed that there are k objective functions that will be minimized.

$$\text{Min } F(X) = (f_1(X), f_2(X), \dots, f_k(X))^T \quad X \in S \tag{7}$$

The general form of problem F is nonlinear and multimodal, and S can be defined by nonlinear constraints containing both continuous and discrete decision variables.

Definition 1 (Dominated).

Vector y will be dominated by vector w , if Eq. (8):

$$\forall i \in (1, 2, \dots, k) : f_i(w) \leq f_i(y) \text{ e } \exists j \in (1, 2, \dots, k) : f_j(w) < f_j(y) \tag{8}$$

Definition 2 (Pareto optimality).

Vector $X \in S$ is an Pareto optimal solution if and only if there is no vector $Y \in S$, where Eq. (9):

$$F(Y) = (f_1(Y), f_2(Y), \dots, f_k(Y)) \text{ dominates } F(X) = (f_1(X), f_2(X), \dots, f_k(X)). \tag{9}$$

The space ρ in R^k is known as the Pareto optimal frontier, being formed by the objective vectors of Pareto optimal solutions. Obviously, any solution, if possible to define, must belong to the Pareto optimal. Other terminologies such as nondominated or efficient solutions are also used in the literature instead of Pareto optimal solutions (Gitizadeh and Aghaei 2014).

A dot $X^* \in \Omega$ (where Ω is a viable region in R^n), is said to be Pareto optimal with respect to all $X \in \Omega$ if and only if $F(X^*) < F(X)$. Alternatively, it can be easily updated as Eq. (10):

$$\forall i \in \{1, 2, \dots, k\}, \forall X \in \Omega - \{X^*\} f_i(X^*) \leq f_i(X) \wedge \exists j \in \{1, 2, \dots, k\} : f_j(X^*) < f_j(X) \tag{10}$$

In other words, the solution X^* is declared as a Pareto optimal (minimum), if no other solution can be found to dominate X^* using the Pareto dominance definition (Atashkari et al. 2007). A graphical representation of this concept is illustrated in Fig. 4.

In Fig. 4, f_1^* and f_2^* are used to designate the corresponding individual minima of each objective function, and the solution is defined as utopian $F^* = (f_1^*, f_2^*)^T$. Note that, for the case of k objective functions, $f_1^*, f_2^*, \dots, f_k^*$ will be used to designate the individual minima of each objective function and the solution is

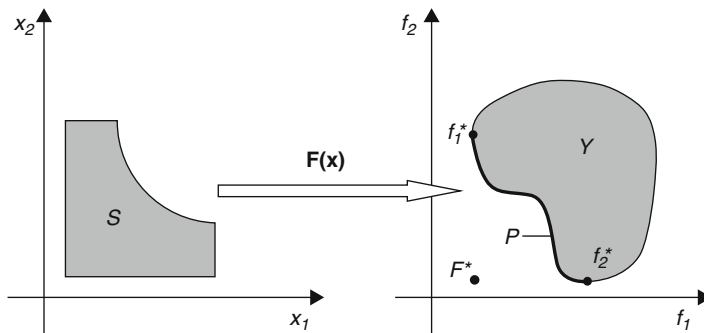


Fig. 4 Parameter/solution and Pareto surface, for a two-dimensional problem. (Source: Gitizadeh and Aghaei (2014))

utopian $F^* = (f_1^*, f_2^*, \dots, f_k^*)^T$. As F^* simultaneously minimizes all goals, this is an ideal solution that is rarely feasible (Gitizadeh and Aghaei 2014).

For a given MOP the Pareto front PT^* is a set of objective function vectors that are obtained using the decision variable vectors in the Pareto series P^* , which corresponds to $PT^* = F(X) = (f_1(X), f_2(X), \dots, f_k(X)) : X \in P^*$. In other words, the Pareto front is a set of objective function vectors mapped from P^* (Atashkari et al. 2007).

3.2 Multi-objective Optimization and Pareto Optimal Solutions

A single-purpose optimization problem can be formulated as the expression given by Eq. (11) (Idoumghar et al. 2013; Taghdisian et al. 2015; Castro 2015):

$$\min_{x \in S} f(x) \tag{11}$$

where f is a scalar function and S is a group of constraints that can be defined as Eq. (12).

$$S = \{x \in R^m : h(x) = 0, g(x) \geq 0\}. \tag{12}$$

Multi-objective optimization, on the other hand, can be written in mathematical terms as in Eq. (13).

$$\min [f_1(x), f_2(x), \dots, f_n(x)] \quad x \in S, \tag{13}$$

where $n > 1$ and S is the group of previously defined constraints. The space called the “objective space” contains the vector with the various objectives and the space reached contains the image of the entire group considered suitable for the aptitude function F . Such space is defined in Eq. (14) (Caramia and Dell’olmo 2008; Ghane-Kanafi and Khorram 2015; Castro 2015):

$$C = \{y \in R^n : y = f(x), x \in S\}. \tag{14}$$

The concept of “optimal” scalar does not apply directly to a multi-objective optimization group. Instead of a scalar number indicating “optimal,” the multi-objective solution introduces the concept “Pareto optimal.”

The concept consists in the fact that the entire vector $x^* \in S$ is considered to be contained in the Pareto optimal of a multi-objective problem if and only if all the vectors $x \in S$ have a value greater than or equal to the vector x^* , and by minus one x^* is less than one of the objective functions f_i , where $i = 1, 2, \dots, n$.

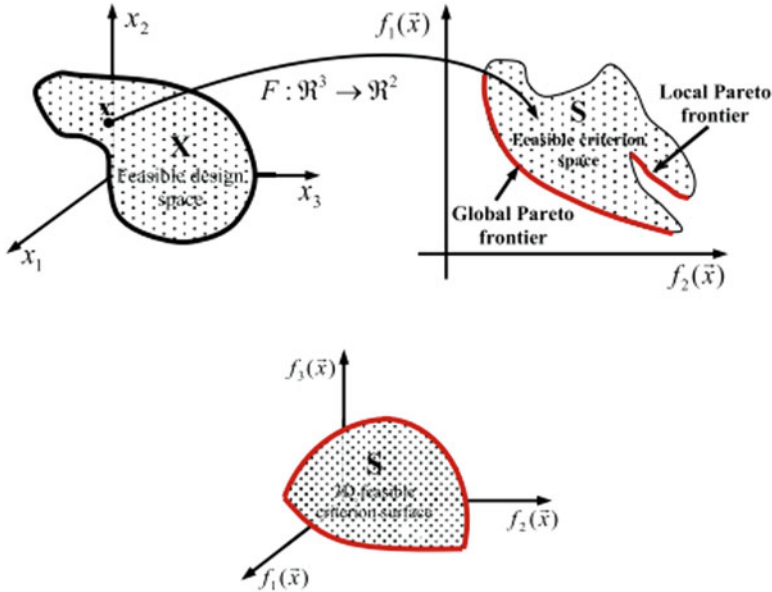


Fig. 5 General concept of the Pareto curve. (Source: adapted from Taghdisian et al. (2015))

The one that contains all the efficient solutions is known as the Pareto front, Pareto curve, or Pareto surface. The shape of Pareto’s figure indicates the nature of exchanges between the objective functions (Caramia and Dell’olmo 2008; Gitizadeh and Aghaei 2014; Castro 2015).

Figure 5 shows a viable decision space and Pareto front for a multi-objective problem with two or three goals. These points are known as nondominated or non-inferior points.

At the top of Fig. 5, the viable decision space and the Pareto front for the problem with two goals are shown. At the bottom, a Pareto 3D surface for an optimization problem with three goals is shown.

In Fig. 6, the Pareto set is visualized by four possible combinations of the two types of objectives.

3.3 Multi-objective Optimization Problem Solving Techniques

In certain cases, Pareto curves cannot be efficiently computed. Although in theory it is possible to find exactly all the points, it is possible that there might be problems of exponential size. For these there are approximation methods that are frequently used. However, the approximation is often not a secondary choice for the decision maker. In fact, there are many real-life problems from which it is very difficult for the decision maker to obtain all the information to formulate these problems

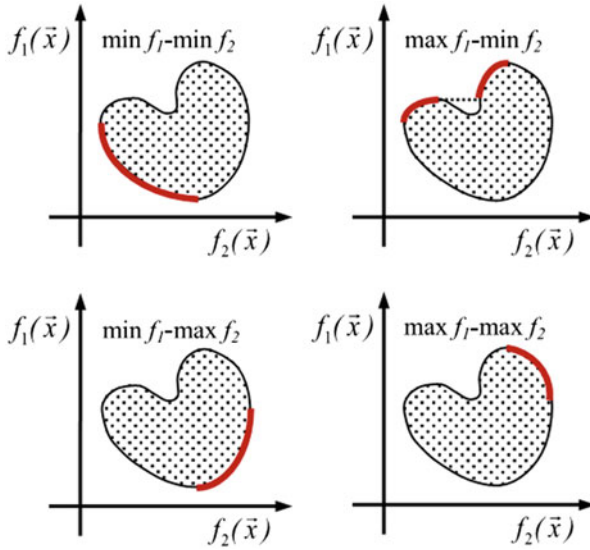


Fig. 6 Set of Pareto combinations for two purposes. (Source: Caramia and Dell’olmo (2008))

correctly. Considering that decision makers tend to understand more about the problem once some preliminary solutions are presented, having some approximate solutions can help the expert in his task (Bazgan et al. 2013; Mirjalili and Lewis 2015; Castro 2015).

Approximation techniques usually have varied goals such as: representing a group of graphical solutions that can be converted to numbers (convex multi-objective problems); representation of a group of graphic solutions where only some Pareto curves can be represented numerically (nonlinear multi-objective problems); representation of a group of graphical solutions where every efficient group of solutions cannot be represented numerically (discrete multi-objective problems) (Castro 2015).

3.3.1 Scalar Transformation Technique

Classically, a multi-objective optimization model can be scaled or transferred to a single objective optimization problem. Two simple methods of this approach are: the WSM and the weighted product method (WPM). In the first method, the composite function is generated by pre-multiplying each goal by a weight provided by the user (Eq. 15), whereas in the last method the composition of the function is generated by multiplying the goals with a given power by the user (Eq. 16). The weights and potencies referred to generally represent the paradigm preference in multicriteria optimization (Taghdisian et al. 2015; Ghane-Kanafi and Khorram 2015):

$$\text{minimize } F_{\text{eq}}(\vec{x}) = \sum_{i=1}^k w_i f_i(\vec{x}), \quad (15)$$

$$\text{minimize } F_{\text{eq}}(\vec{x}) = \prod_{i=1}^k [f_i(\vec{x})]^{w_i}. \quad (16)$$

Also, in Eqs. (15) and (16) w_i is a vector of weights (or powers), normally defined by decision makers. Both methods have their advantages and limitations. For example, although WSM is the simplest and probably the most widely used approach, selecting appropriate values for weighting factors is still another milestone for the decision system (Ghane-Kanafi and Khorram 2015; Caramia and Dell'olmo 2008).

In the case of WPM, potentiating by increasing the nonlinearities in the composition of the function prevents the widespread use of this method. This is the case where classical solvers are used; otherwise evolutionary optimizers can handle nonlinearities very skillfully.

A multi-objective problem is usually solved by combining several objectives into a single scalar objective function. This technique is called weighted sum or scalar transformation method. In more detail, the WSM positively minimizes the related weighted sum of the objective functions, as in Eq. (17) (Caramia and Dell'olmo 2008; Ghane-Kanafi and Khorram 2015; Castro 2015):

$$\begin{aligned} \min \sum_{i=1}^n \gamma_i \cdot f_i(x) \\ \sum_{i=1}^n \gamma_i = 1 \\ \gamma_i > 0, i = 1, \dots, n \\ x \in S, \end{aligned} \quad (17)$$

which represents a new optimization of only one objective function. The function $P_s(\gamma)$ can be assigned to this new name of the weighted sum.

It is possible to prove that by minimizing the single-objective function $P(\gamma)$ an efficient solution to the original multi-objective problem is found, because the image of this function belongs to the Pareto curve. In particular, if the weighted vector γ has all its elements greater than zero, then the minimization converges to the constrained Pareto optimal region ($P(\gamma)$); in contrast, if at least one element of γ is equal to zero, then the minimization converges to the optimal weak Pareto region. There is no a priori relationship between the weighted vector γ and the solution of the vector, and it is up to the decision maker to determine the appropriate coefficients, although the coefficient is not directly related to the importance of the objective functions. In addition, the decision maker is not aware of which coefficients are appropriate to satisfactorily obtain the solution. Bearing this in mind, it can also be said that the task of developing a heuristic to assist the decision maker is significantly difficult because it must start from the concept of initializing the

search with certain coefficients and interacting with the weighted vectors to reach a certain Pareto curve region (Antczak 2011; Ghane-Kanafi and Khorram 2015; Castro 2015).

As the creation of a weighted vector leads to only one point on the Pareto curve, performing several optimizations requires a great deal of processing power and a high computational cost. However, it is up to the technical specialist to determine which different combinations of coefficients should be considered so that a good part of the Pareto front can be represented (Ghane-Kanafi and Khorram 2015). In addition to the high computational cost, the scalar transformation method also has two technical deficiencies, which are explained below (Castro 2015):

- The relationship between the objective function coefficients and the Pareto curve is such that a uniform distribution of the coefficients, in general, does not reproduce a uniform distribution on the Pareto curve. This can be seen from the fact that some points are grouped in some parts of the Pareto front whereas some parts (sometimes the most significant ones) are not reproduced.
- The nonconvex parts of the Pareto group cannot be reached by combining the convex minimization of the objective functions. To illustrate, we consider a geometric interpolation of the WSM in two dimensions, when $n = 2$. In a two-dimensional space the objective function can be expressed as in Eq. (18):

$$y = \gamma_1 \cdot f_1(x) + \gamma_2 \cdot f_2(x), \tag{18}$$

where

$$f_2(x) = -\frac{\gamma_1 \cdot f_1(x)}{\gamma_2} + \frac{y}{\gamma_2}. \tag{19}$$

The minimization of $\gamma \cdot f(x)$ in the WSM can be interpreted as the attempt to find the value of y such that the line whose slope is determined by $-\frac{\gamma_1}{\gamma_2}$ is tangent to the C region. Obviously, by changing the coefficient parameters it is possible to reach different points contained in the Pareto front. If the Pareto curve is convex, there is a greater possibility of calculating such points for different vectors of y (as can be seen in Fig. 7).

Similarly, when the curve is nonconvex there is a group of points that cannot be reached by any combinations of the weighted vector γ (as shown in Fig. 8).

According to Geoffrion apud (Caramia and Dell'olmo 2008), the necessary and sufficient conditions for convexity cases are:

- If a group of solutions S is convex and the n objectives of f_i are convex in S , where x^* is considered an optimal Pareto restricted solution, if and only if there exists a $\gamma \in R^n$ such that x^* is an optimal solution of the problem $P_r(\gamma)$;

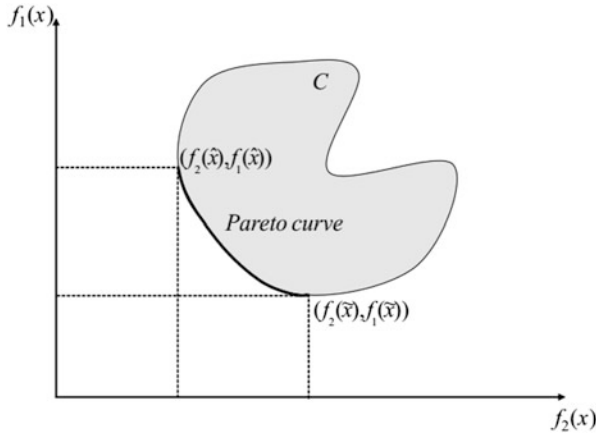


Fig. 7 Geometric representation of the weighted sum in the case of the convex Pareto curve. (Source: Caramia and Dell’olmo (2008))

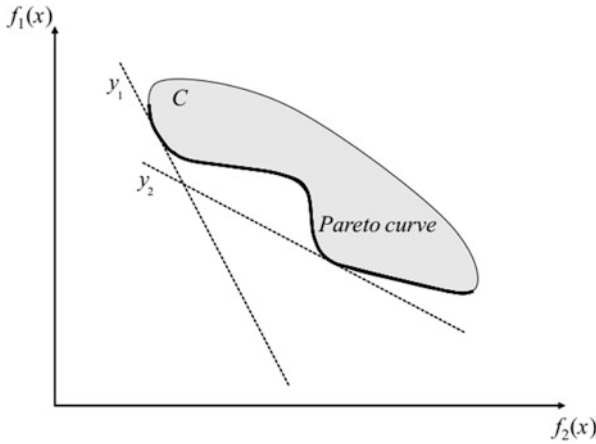


Fig. 8 Geometric representation of the weighted sum, nonconvex Pareto curve. (Source: Caramia and Dell’olmo (2008))

- Likewise: if a group of solutions S is convex and the n objectives of f_i are convex in S , where x^* is considered a weak Pareto optimal solution if and only if there exists a $\gamma \in R^n$ such that x^* is an optimal solution of the $P_f(\gamma)$ problem.

If the convexity hypothesis is not satisfied, only the necessary conditions will remain valid, that is, the optimal solutions of $P_r(\gamma)$ and $P_f(\gamma)$ are respectively the restricted and weak Pareto optimality (Caramia and Dell’olmo 2008; Antczak 2011; Ghane-Kanafi and Khorram 2015; Castro 2015).

4 Methods of EED Optimization

The approach described below includes a breakdown of the heuristic methods used to optimize the EED considered in this section.

4.1 *Heuristic Methods*

A heuristic method is a set of practical rules derived from experience. There is no definitive proof of its veracity, but the heuristic technique is expected to work most but not all of the time. A heuristic will help us to find good solutions, but not necessarily great ones. To apply heuristic rules, several metaheuristic techniques were developed.

A metaheuristic is a set of concepts that can be used to define heuristic methods that can be applied to a wide range of different problems. In other words, a metaheuristic can be seen as a general algorithmic framework that can be applied to different optimization problems with relatively few modifications to adapt it to a specific problem (Silva and Silva 2014).

Modern metaheuristic algorithms are a promising alternative for solving complex ED and EED optimization problems (Basu 2014b). In the following sections, the computational intelligence techniques applied in this chapter are described in detail.

4.2 *Nondominated Sorting Genetic Algorithm*

In their research, Fonseca and Fleming exposed the procedure for ranking solutions based on a dominance level system known as the nondominated genetic classification algorithm (NSGA), which was implemented in its entirety (Srinivas and Deb 1993; Fonseca and Fleming 1995).

The NSGA varies from the simple genetic algorithm only in how the selection operator works. The crossover and mutation operators remain the same (Srinivas and Deb 1993; Coello 1999).

Before selection is performed, the population is classified based on the nondomination of an individual. Nondominated individuals present in the population are first identified from the current population. Then, all these individuals are admitted to constitute the first nondominated front of the population and a high standard aptitude score is assigned.

Sharing is achieved by performing the selection operation using a reduction in fitness values, which are obtained by dividing an individual's initial fitness value by an amount proportional to the number of individuals around him. This causes multiple ideal points of coexistence in the population. After sharing, nondominated

individuals are temporarily ignored when processing the rest of the population in the same way to identify individuals for the second nondominated front.

This new set of points is then assigned a new default fitness value that is kept lower than the previous front's minimum shared fitness value. This process is continued until the entire population is classified on various fronts. The population is then reproduced according to the fitness values. Because individuals on the first front have a maximum aptitude score, they always receive more copies than the rest of the population.

This was the intention to look for nondominated regions or Pareto optimal fronts. This results in a rapid convergence of population toward nondominated regions in this region. By emphasizing nondominated points, the NSGA is processing the schemas that represent Pareto optimal regions.

The efficiency of the NSGA lies in the way in which multiple goals are reduced to a standard fitness function using the nondominated classification procedure (Srinivas and Deb 1993).

Another aspect of the method is that virtually any number of goals can be solved. Both minimization and maximization problems can also be handled by this algorithm. The only place that requires a change for the two cases above is in the way in which nondominated points are identified (Srinivas and Deb 1993).

4.3 The Elitist Nondominated Sorting Genetic Algorithm II

The Elitist Nondominated Sorting Genetic Algorithm II (NSGA-II) is one of the most frequently used algorithms for solving MOOPs (Deb et al. 2002, Golchha and Qureshi 2015).

Furthermore, the NSGA-II differs from the NSGA in that it uses a faster screening procedure, an elitist preservation approach, and a parameter for the segment operator (Golchha and Qureshi 2015). The functioning of the NSGA-II is shown in Fig. 9:

(a) Initial Population

Initially, a random parent population is created. The population is ordered on the basis of nondomination. Each solution is assigned an aptitude equal to its nondomination level (1 is the best level). Thus, fitness minimization is assumed. Tournament selection, recombination, and mutation operators are used to create a descendant population of size N (Kalaivani et al. 2013).

The population is initialized based on the problem range and constraints, if any, and this population is initialized and sorted based on nondomination.

(b) Selection

In the original NSGA-II binary tournament selection (BTS) is used, where a tournament is played between two solutions and the best one is selected for the crossing. Two other solutions are taken again and another opening in the crossover

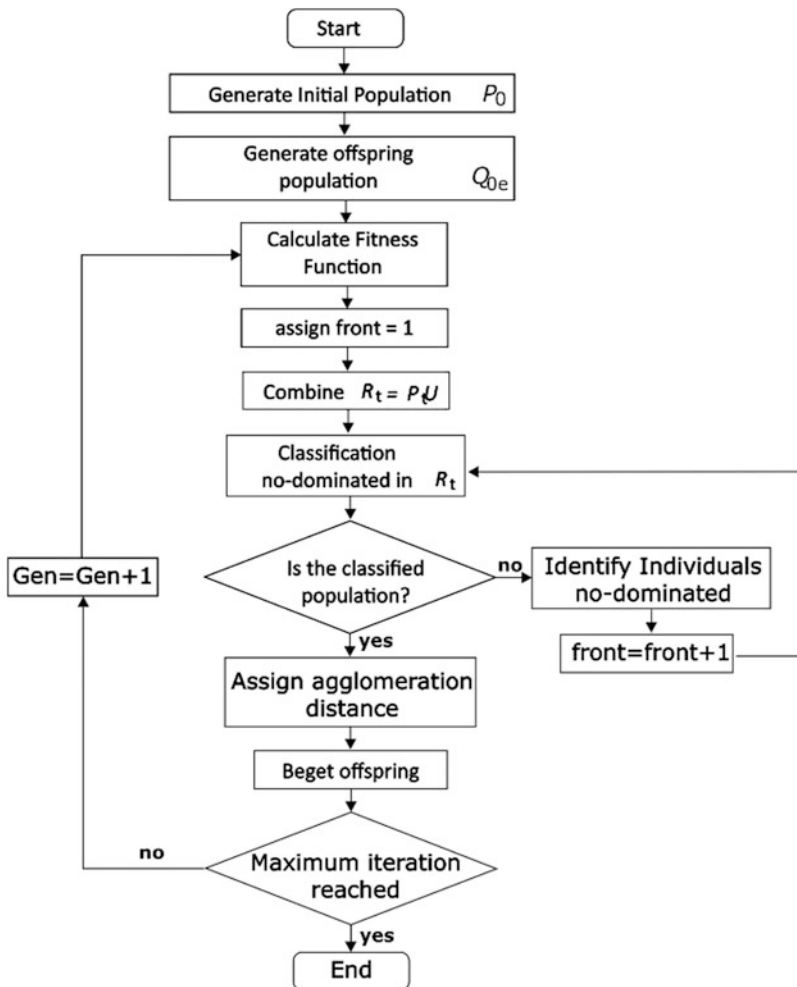


Fig. 9 Operation of the NSGA-II. (Source: Adapted from Golchha and Qureshi (2015))

association is filled. It is carried out in such a way that each solution can participate in exactly two tournaments (Golchha and Qureshi 2015).

(c) **Crossover**

In NSGA-II simulated binary crossover is used, which works with two parent solutions and generates two offspring. The following step-by-step procedure is described (Golchha and Qureshi 2015):

- Step 1: Choose a random number $u_i \in [0, 1]$;
- Step 2: Calculate using Eq. (20);
- Step 3: Calculate descending using Eq. (21).

The mathematical formulation can be described as follows:

$$\beta_{qi} = \begin{cases} (2u_i)^{\frac{1}{n_c+1}} & \text{if } u_i \leq 0,5; \\ \left(\frac{1}{2(1-u_i)}\right)^{\frac{1}{n_c+1}} & \text{other cases.} \end{cases} \tag{20}$$

$$\begin{aligned} X_i^{(1,t+1)} &= 0,5 \left[(1 + \beta_{qi}) X_i^{(1,t)} + (1 - \beta_{qi}) X_i^{(2,t)} \right], \\ X_i^{(2,t+1)} &= 0,5 \left[(1 - \beta_{qi}) X_i^{(1,t)} + (1 + \beta_{qi}) X_i^{(2,t)} \right], \end{aligned} \tag{21}$$

where:

- u_i : A random number such that $u_i \in [0, 1]$;
- n_c : Distribution index (non-negative real number);
- $X_i^{(1,t)}$ & $X_i^{(2,t)}$: Parent solutions;
- $X_i^{(1,t+1)}$ & $X_i^{(2,t+1)}$: Descendants' solutions.

(d) Mutation

Polynomial mutation is used, which transforms each solution separately, that is, a parent solution gives offspring after being mutated. The mathematical formulation can be described as in Eq. (22) (Golchha and Qureshi 2015):

$$y_i^{(1,t+1)} = \left(y_i^{(1,t+1)} + X_i^{(U)} - X_i^{(L)} \right) \bar{\delta}_1 \tag{22}$$

and:

$$\bar{\delta}_1 = \begin{cases} (2r_i)^{1/(n_m+1)} - 1, & \text{se } r_i < 0,5, \\ 1 - [2(1-r_i)]^{1/(n_m+1)}, & \text{se } r_i \geq 0,5, \end{cases} \tag{23}$$

where:

- r_i : A random number such that $u_i \in [0, 1]$;
- n_m : Distribution index (non-negative real number);
- $X_i^{(1,t+1)}$: Mother solution;
- $X_i^{(U)}$: Upper limit of parent solution;
- $X_i^{(L)}$: Lower limit of parent solution;
- $y_i^{(1,t+1)}$: Descendants' solutions.

(e) Cluster Tournament Selection

To obtain an estimate of the density of solutions close to a particular solution i in the population, we take the average of the two solutions on both sides of solution i together with each of the objectives. This quantity d_i is the Cluster Distance. The

following algorithm is used to calculate the agglomeration distance of each point in set \mathcal{F} (Golchha and Qureshi 2015).

Assignment procedure: Agglomeration-Selection ($\mathcal{F}, < c$)

Step 1: Consider the number of solutions in \mathcal{F} as $l = |\mathcal{F}|$. For each i in the set, first assign $d_i = 0$.

Step 2: For each objective function $m = 1, 2, \dots, M$, rank the set in worst order of f_m . Find the vector of ranking indexes $I_m = \text{Selection}(f_m, >)$.

Step 3: For $m = 1, 2, \dots, M$, allocate a great deal of distance to cutting-edge solutions, $d_{I_1^m} = \infty$, and for all other solutions $j = 2$ para $(l - 1)$ calculate Eq. (24):

$$d_{I_j^m} = d_{I_j^m} + \frac{f_m^{(I_{j+1}^m)} - f_m^{(I_{j-1}^m)}}{f_m^{\max} - f_m^{\min}} \tag{24}$$

The NSGA-II presents an improved technique for maintaining the diversity of solutions, proposing a method of clustering the classification distance. However, in its process, the classification technique remained unchanged from its previous version. (Suksonghong et al. 2014).

In the NSGA-II, all individuals are classified into matched populations (parents and descendants) based on the Pareto dominance relationship and then classified into several layers based on which an individual is located. On each front, the individuals are arranged in decreasing order of magnitude of the agglomeration distance value. In the BTS process, the algorithm first selects an individual positioned on a better nondominated front. In cases where individuals with an identical front are compared, the tournament selection operator chooses the winner based on the value of the agglomeration distance (Suksonghong et al. 2014).

The NSGA-II elitist strategy considers all combinations of nondominated population solutions as solution candidates for the next generation. If the number of nondominated solutions is less than the population size, they are all kept as the latest generation solutions. Otherwise, candidates for the next generation are selected using the agglomeration distance criterion. This criterion has the advantage of maintaining the diversity of solutions in the population in order to avoid premature convergence (Suksonghong et al. 2014; Liu et al. 2015).

4.4 Multi-objective NSGA-III

The basic architecture of the NSGA-III Multi-objective proposal is like that of the NSGA-II, being different in its selection structure. However, in contrast to the NSGA-II, to ensure diversity among individuals in the population, the NSGA-III is aided by the provision and adaptation of an updated number of reference points in

a well-distributed manner. In the NSGA-III, the agglomeration band operator was replaced by (Deb and Jain 2014):

(a) **Classification of the population at nondominated levels**

In the NSGAIII, the procedure for identifying nondominated fronts is the usual dominance principle (Gitizadeh and Aghaei 2014). All members of the tier 1 population, from the undominated front, are included first S_l . And if $|S_l| = N$, no further changes are required and the following generation starts with $P_{l+1} = S_l$. For $|S_l| > N$, individuals of the fronts from 1 to $l - 1$ are already selected, that is, $P_{l+1} = \cup_{i=1}^{l-1} F_i$, and the rest of the members of the population are chosen from the last F_l front F_l (Deb and Jain 2014).

(b) **Determining Benchmarks on a Hyper-plane**

The NSGAIII uses a predefined set of reference points to ensure diversity in obtained solutions. The chosen reference points can be predefined in a structured way or preferably provided by the user. In the absence of any preference information, any structured placement of predefined reference points can be adopted. A systematic approach that places points on a normalized hyper-plane of $(M - 1)$ single dimensional unit, which is equally inclined to all objective axes and has an intercept of one on each axis. If p divisions are considered along each objective, the total number of reference points (H) in a M -objective problem is given by Eq. (25) (Deb and Jain 2014).

$$H = \binom{M + p - 1}{p} \quad (25)$$

In a problem with three objectives $M = 3$, reference points are created in a triangle with the vertex at $(1, 0, 0)$, $(0, 1, 0)$, and $(0, 0, 1)$. If four divisions are selected ($p = 4$) for each objective axis like $H = \binom{3+4-1}{4}$, 15 waypoints are created; these waypoints are shown in Fig. 10. For the NSGA-III, in addition to solutions to highlight the nondominated, the population members who are in some way associated with each of these reference points are emphasized. Because the above reference points are created, normalized, and widely distributed across the hyper-plane, the obtained solutions are also likely to be widely distributed on or near the Pareto front. In the case of a user-supplied preferred set of reference points, ideally, the user should be able to mark points on the normalized hyper-plane or indicate any H , M -dimensional vectors for the purpose. The proposed algorithm is likely to find solutions close to the Pareto optimal corresponding to the reference points provided, thus allowing this method to be used more for a combined application of decision-making and multi-objective optimization (Deb and Jain 2014).

(c) **Adaptive Normalization of Population Members**

First, the population ideal point S_l is defined by specifying a minimum value z_i^{\min} for each objective function $i = 1, 2, \dots, M$ within $\cup_{T=0}^l$ and getting an optimal

Fig. 10 Fifteen-point structure of reference for a three-objective problem in a normalized plane for $p = 4$. (Source: Deb and Jain (2014))

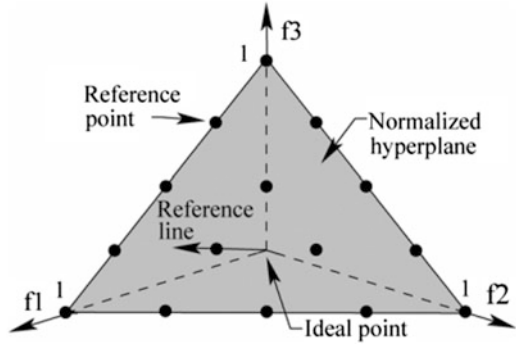
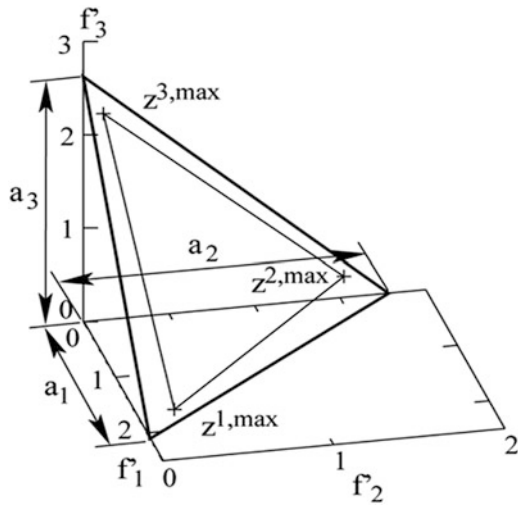


Fig. 11 Procedure for calculating intercept and then forming the extreme point hyper-plane for a three-purpose problem. (Source: Deb and Jain (2014))



point in $\bar{z} = (z_1^{\min}, z_2^{\min}, \dots, z_M^{\min})$. Each objective value of S_t is then obtained by subtracting the objective $f_i(x)$ by z_i^{\min} for the ideal translation point S_t to become a zero vector. This objective is defined as $f'_i(x) = f_i(x) - z_i^{\min}$. After that, the extreme point z_i^{\max} on each objective axis (i_{th}) is found within the search space ($x \in S_t$), which corresponds to the scalarization function $f'_i(x)$ and a vector of weight near the objective axis i_{th} minimum. These extreme M vectors are then used to constitute an M -dimension hyper-plane. The intercept of the i_{th} objective axis and the linear hyper-plane can then be calculated (Fig. 11). The objective function can then be normalized as in Eq. (26) (Deb and Jain 2014):

$$f_i^n(x) = \frac{f'_i(x)}{a_i}, \text{ para } i = 1, 2, \dots, M. \tag{26}$$

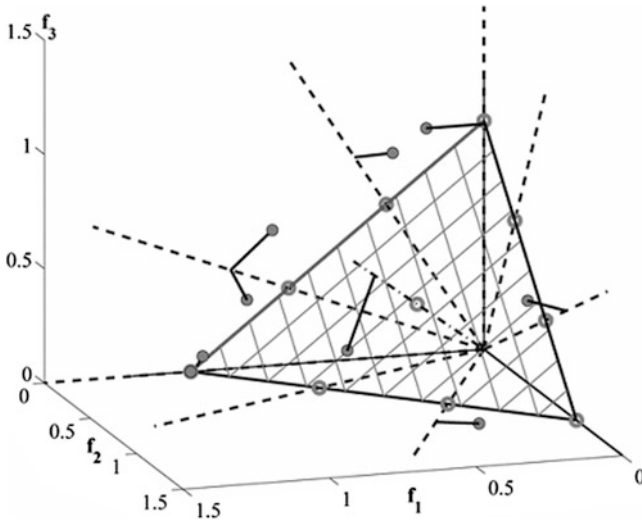


Fig. 12 Association between individuals in the population and their reference points. (Source: Deb and Jain (2014))

Note that the intercept on each normalized objective axis is now at $f_i^n = 1$, and a hyper-plane built with these intercept points will do $\sum_{i=1}^M f_i^n = 1$.

(d) Association Operation

After normalizing each goal adaptively based on the extent of members of S_t in the goal space, each population member must be associated with a reference point. For this purpose, a reference line corresponding to each reference point on the hyper-plane is defined, joining the reference point with the origin. The perpendicular distance of each of the members of the population S_t is calculated from each of the reference lines.

The reference point whose reference line is closest to a population member in the normalized objective space is considered to be associated with the population member. This is illustrated in Fig. 12 (Deb and Jain 2014).

(e) Operation Niche Preservation

It is worth noting that a landmark may have one or more population members associated with it, or it does not need to have any population members associated with it. The number of population members of $P_{t+1} = S_t / F_l$ that are associated with each reference point is counted. This niche count is denoted as p_j for the i_{th} reference point i_{th} . A new niche preservation operation is designed as follows. First, identify the reference point set $J_{mim} = \{j : \arg\min_j p_j\}$ having minimum p_j . In the case of several of these reference points, one ($\bar{j} \in J_{mim}$) is selected randomly (Deb and Jain 2014).

If $p_j = 0$ (means that there is no member P_{t+1} associated with the reference point), there can be two scenarios with \bar{j} in set F_l . First, there exists one or more individuals in front F_l that are associated with the reference point \bar{j} , in this case, the one having the shortest perpendicular distance from the reference line is added to P_{t+1} . The count $p_{\bar{j}}$ for reference point \bar{j} is then incremented by one. Second, the front F_l has no individual related to the reference point \bar{j} . Therefore, the reference point is excluded from the current generation.

If $p_j > 1$ (means that there is already a individual associated with the reference point in S_t / F_l), an individual is randomly selected; if there is any individual from the front F_l that is associated with the reference point \bar{j} , then it is added to P_{t+1} . Then, p_j is increased by one. After updating the counts, the procedure is repeated up to K times, filling all the spaces in the population P_{t+1} (Deb and Jain 2014).

(f) Genetic Operations to Create Descendant Population (Offspring)

After forming P_{t+1} , it is then used to create a new descendant population Q_{t+1} , by applying the usual genetic operators. In NSGA-III, it has already performed a careful elitist selection of solutions and tried to maintain diversity among solutions, emphasizing solutions closer to the reference line of each reference point. Furthermore, for a computationally low cost, we have a set of values to the N close to H , thus hoping to evolve an individual from the population close to the Pareto front. For all these reasons, no NSGA-III playback operation is used to deal with problems that have only box constraints. The population Q_{t+1} is created using the traditional crossover and mutation operators, randomly selecting the parents of P_{t+1} (Deb and Jain 2014).

(g) NSGAIII Least Parameters Property

As with the NSGA-II, the NSGA-III does not require the creation of new parameters beyond those already defined in the GA, for example, the size of the population, crossover, and mutation probabilities. The number of reference points H are not parameters of the algorithm, as they are related to the defined number of exchange points. The population size N is dependent on H , like $N \approx H$. The location of the reference points is dependent on the defined parameters that the user is interested in achieving in the obtained solutions (Deb and Jain 2014).

5 Methodology for New EED Optimization Solution

5.1 Introduction

The new solution proposed for the EED optimization problem contemplates the shutdown of generators with higher fuel costs at the time of optimization to meet a certain power demand. In this solution, the incremental fuel cost and power losses are considered.

Table 3 Characteristic data of plant generators

Generator	c_i (\$/MW ²)	b_i (\$/MW)	a_i (\$)	P_{\min} (MW)	P_{\max} (MW)
UG1	0.007	7	240	0.66	3.35
UG2	0.0095	10	200	0.9	3.7
UG3	0.009	8.5	220	0.8	3.6
UG4	0.009	11	200	0.66	3.35
UG5	0.008	10.5	220	0.72	3.45
UG6	0.0075	12	120	0.66	2.97
UG7	0.0075	14	130	0.88	3.5
UG8	0.0075	14	130	0.754	3.33
UG9	0.0075	14	130	0.9	3.9
UG10	0.0075	14	130	0.56	2.95

Source: Nascimento et al. (2016)

The study was carried out in the electric power generation sector with data from a thermoelectric power plant (with ICES) at the Manaus Industrial Pole and compared with a test system from the Institute of Electrical and Electronics Engineers (IEEE).

For the treatment and analysis of the data, the computational tool MATLAB version r2016b was used, microcomputer, Intel i7 processor, with 8 GB of RAM, for the implementation of the various computational methods used (NSGA-II and NSGA-III) to validate the proposed methodology.

5.2 Operating Parameters of the TPP Case Study

In particular, the TPP (case study) works with a fixed demand of power to be generated, which is less than its maximum generation capacity, allowing the shutdown of generators with higher fuel consumption without compromising their operation. The reference plant selected for the case study is composed of ten generators, named (UG1 to UG10), as shown in Table 3. In the first column, the number of generating units is presented, in the second, third, and fourth there are the coefficients a_i , b_i , e c_i and in the last two, the minimum and maximum power of each generating unit are shown.

These data were obtained from measurements carried out in the field, with the consumption record for different percentages of power of each generator (60, 70, 80, 90 and 100%), and their coefficients specified through a regression method with help from software *CurveExpert*.

The loss coefficients (B_i) are given by a square matrix of size $n \times n$, described in Table 4, where n is the number of generators and all values are multiplied by 10^{-7} .

The loss coefficients (B_i) were obtained using Kron's method (Wang and Singh 2007).

Table 4 Loss coefficients B_i

n	c1	c2	c3	c4	c5	c6	c7	c8	c9	c10
UG1	0.14	0.17	0.15	0.19	0.26	0.22	0.34	0.38	0.43	0.45
UG2	0.17	0.6	0.13	0.16	0.15	0.2	0.23	0.56	0.23	0.51
UG3	0.15	0.13	0.65	0.17	0.24	0.19	0.25	0.38	0.43	0.45
UG4	0.19	0.16	0.17	0.71	0.3	0.25	0.43	0.56	0.23	0.51
UG5	0.26	0.15	0.24	0.3	0.69	0.32	0.18	0.37	0.42	0.48
UG6	0.22	0.2	0.19	0.25	0.32	0.85	0.97	0.55	0.27	0.58
UG7	0.22	0.2	0.19	0.25	0.32	0.85	0.67	0.38	0.43	0.45
UG8	0.19	0.7	0.13	0.18	0.16	0.21	0.28	0.56	0.23	0.51
UG9	0.26	0.15	0.24	0.3	0.69	0.32	0.18	0.37	0.42	0.48
UG10	0.15	0.13	0.65	0.17	0.24	0.19	0.25	0.38	0.43	0.45

Source: Nascimento et al. (2016)

Table 5 General emission coefficients – case study

Generator	$\alpha_i(\text{g/m}^3)$	$\beta_i(\text{g/m}^3)$	$\gamma_i(\text{g/m}^3)$
UG1	4.59	-884.13	112,047.21
UG2	5.28	-871.68	105,511.36
UG3	3.41	-581.35	96,795.36
UG4	0.87	-263.50	86,264.93
UG5	0.23	-198.77	84,132.86
UG6	1.88	-444.28	92,565.64
UG7	0.87	-302.81	88,329.64
UG8	2.96	-654.92	102,614.29
UG9	3.44	-712.03	104,626.14
UG10	3.38	-716.90	104,892.86

Source: Authors (2016)

In Table 5, the general emission coefficients are presented. The first column shows the number of generating units, the second, third, and fourth show the emission coefficients α_i , β_i e γ_i of each generating unit.

5.3 Operating Parameters of the TPP Test System – NSGA-II

To validate the robustness of the solution using the technique proposed in this chapter, a comparison was made with a Test System (Basu 2008) that contains ten thermal generating units, named (PG1 to PG10), with the characteristics shown in Table 6. In the first column, there is the number of generating units, in the second, third, fourth, fifth, and sixth are the fuel cost coefficients c_i , b_i , a_i , d_i , and e_i and in the last two columns are the minimum power and maximum of each generating unit (Table 6).

Table 6 Characteristic data of the test system generators – NSGA-II

Generator	c_i (\$/MW) ² h	b_i (\$/MWh)	a_i (\$/h)	d_i (\$/h)	e_i (rad/MW)	P_{\min} (MW)	P_{\max} (MW)
PG1	0.1524	38.5397	786.7988	450	0.041	150	470
PG2	0.1058	46.1591	451.3251	600	0.036	135	470
PG3	0.028	40.3965	1049.9977	320	0.028	73	340
PG4	0.0354	38.3055	1243.5311	260	0.052	60	300
PG5	0.0211	36.3278	1658.5696	280	0.063	73	243
PG6	0.0179	38.2704	1356.6592	310	0.048	57	160
PG7	0.0121	36.5104	1450.7045	300	0.086	20	130
PG8	0.0121	36.5104	1450.7045	340	0.082	47	120
PG9	0.109	39.5804	1455.6056	270	0.098	20	80
PG10	0.1295	40.5407	1469.4026	380	0.094	10	55

Source: Basu (2008)

Table 7 General emission coefficients test system – NSGA-II

Generator	α_i (lb/h)	β_i (lb/Mwh)	γ_i (lb/Mw) ² h)	η_i (lb/h)	δ_i (l/Mwh)
PG1	0.0312	-2.4444	103.3908	0.5035	0.0207
PG2	0.0312	-2.4444	103.3908	0.5035	0.0207
PG3	0.0509	-4.0695	300.3910	0.4968	0.0202
PG4	0.0509	-4.0695	300.3910	0.4968	0.0202
PG5	0.0344	-3.8132	320.0006	0.4972	0.02
PG6	0.0344	-3.8132	320.0006	0.4972	0.02
PG7	0.0465	-3.9023	330.0056	0.5163	0.0214
PG8	0.0465	-3.9023	330.0056	0.5163	0.0214
PG9	0.0465	-3.9524	350.0056	0.5475	0.0234
PG10	0.047	-3.9864	360.0012	0.5475	0.0234

Source: Basu (2008)

In Table 7, the general emission coefficients are presented. In the first column is the number of generating units, in the second, third, fourth, fifth, and sixth are the emission coefficients α_i , β_i , γ_i , η_i , and δ_i of each generating unit.

The loss coefficients (B) are given by a square matrix of size $n \times n$, multiplied by 10^{-4} , presented in Table 8, where n is the number of generators.

5.4 Operating Parameters of the TPP Test System – NSGA-III

To validate the robustness of the solution using the technique proposed in this work, a comparison was performed with a test system (Dhillon and Jain 2011) that contains six thermal generating units, named (PG1 to PG6), with the characteristics presented in Table 9. In the first column is the number of generating units, in the second, third, and fourth are the fuel cost coefficients c_i , b_i , and a_i , and in the last two columns are the minimum and maximum power of each generating unit.

Table 8 Test system loss coefficients – NSGA-II

n	11	12	13	14	15	16	17	18	19	1 10
PG1	0.49	0.14	0.15	0.15	0.16	0.17	0.17	0.18	0.19	0.20
PG2	0.14	0.45	0.16	0.16	0.17	0.15	0.15	0.16	0.18	0.18
PG3	0.15	0.16	0.39	0.10	0.12	0.12	0.14	0.14	0.16	0.16
PG4	0.15	0.16	0.10	0.40	0.14	0.10	0.11	0.12	0.14	0.15
PG5	0.16	0.17	0.12	0.14	0.35	0.11	0.13	0.13	0.15	0.16
PG6	0.17	0.15	0.12	0.10	0.11	0.36	0.12	0.12	0.14	0.15
PG7	0.17	0.15	0.14	0.11	0.13	0.12	0.38	0.16	0.16	0.18
PG8	0.18	0.16	0.14	0.12	0.13	0.12	0.16	0.40	0.15	0.16
PG9	0.19	0.18	0.16	0.14	0.15	0.14	0.16	0.15	0.42	0.19
PG10	0.20	0.18	0.16	0.15	0.16	0.15	0.18	0.16	0.19	0.44

Source: Basu (2008)

Table 9 Characteristic data of the test system generators – NSGA-III

Generator	c_i (\$/MW) ² h	b_i (\$/MWh)	a_i (\$/h)	P_{min} (MW)	P_{max} (MW)
PG1	0.002035	8.43205	85.6348	100	250.00
PG2	0.003866	6.41031	303.778	50	230.00
PG3	0.002182	7.4289	847.1484	200	500.00
PG4	0.001345	8.3154	274.2241	85	265.00
PG5	0.002162	7.42289	847.1484	200	500.00
PG6	0.005963	6.91559	202.0258	200	490.00

Source: Dhillon and Jain (2011)

Table 10 NOx emission coefficients test system – NSGA-III

Generator	c_{Ni}	b_{Ni}	a_{Ni}
PG1	0.006323	-0.38128	80.9019
PG2	0.006483	-0.79027	28.8249
PG3	0.003174	-1.36061	324.1775
PG4	0.006732	-2.39928	610.2535
PG5	0.003174	-1.36061	324.1775
PG6	0.006181	-0.39077	50.3808

Source: Dhillon and Jain (2011)

In Table 10, the NOx emission coefficients are presented. In the first column, there is the number of generating units, in the second, third, and fourth are the emission coefficients a_{Ni} , b_{Ni} , and c_{Ni} of each generating unit.

In Table 11, the COx emission coefficients are presented. In the first column is the number of generating units, in the second, third and fourth are the emission coefficients a_{Ci} , b_{Ci} , and e_{Ci} of each generating unit.

The loss coefficients (B) are given by a square matrix of size $n \times n$, presented in Table 12, where n is the number of generators.

Table 11 COx emission coefficients test system – NSGA-III

Generator	c_{Ci}	b_{Ci}	a_{Ci}
PG1	0.265110	-61.02	5080.148
PG2	0.140053	-29.95	3824.77
PG3	0.105929	-9.55	1342.851
PG4	0.106409	-12.74	1819.625
PG5	0.105929	-9.55	1342.851
PG6	0.403144	-121.98	11,381.07

Source: Dhillon and Jain (2011)

Table 12 Test system loss coefficients – NSGA-III

n	l1	l2	l3	l4	l5	l6
PG1	0.00020	0.00001	0.00002	0.00001	0.00000	-0.00003
PG2	0.00001	0.00030	-0.00002	0.00000	0.00001	0.00001
PG3	0.00002	-0.00002	0.00010	-0.00001	0.00001	0.00001
PG4	0.00001	0.00000	-0.00001	0.00015	0.00001	0.00005
PG5	0.00000	0.00001	0.00001	0.00001	0.00025	0.00002
PG6	-0.00003	0.00001	0.00001	0.00005	0.00002	0.00021

Fonte: Dhillon and Jain (2011)

5.5 Mathematical Formulation for the EED Problem Case Study

The classical mathematical formulation for the total fuel cost function is given by Eq. (27): (Barisal and Prusty 2015; Behera et al. 2015; Elattar 2015; Aragón et al. 2015).

$$\text{Minimize TC} = \sum_{i=1}^n F_i (P_i), \tag{27}$$

where n is the number of generating units in the system, P_i is the power capacity of each generating unit (in MW), F_i is the fuel cost for each generating unit (in R\$/h), and TC is the total cost of fuel (in R\$/h).

In this work, F_i is considered as a simplified cost function, expressed as a single quadratic function described in Eq. (28) (Nascimento et al. 2016):

$$F_i (P_i) = c_i P_i^2 + b_i P_i + a_i \left(\frac{\$}{h} \right), \tag{28}$$

where a_i , b_i and c_i are the fuel consumption cost coefficients of the i_{th} unit.

In addition to minimizing the total cost of fuel, the programming considered the fulfillment of the following equality and inequality constraints:

- Power balance constraint: the total generated power P_i must equal the required power demand P_D . It is defined as Eq. (29):

$$\sum_{i=1}^N P_i = P_D. \tag{29}$$

- Operating limit restrictions: thermal units have physical limits on the maximum and minimum power that can generate Eq. (30):

$$P_{\text{mini}} \leq P_i \leq P_{\text{maxi}}, \tag{30}$$

where P_{mini} and P_{maxi} are the minimum and maximum power of the i_{th} unit respectively.

- Power balance, with transmission loss: some energy systems include the loss of the P_L transmission network; thus, Eq. (29) is replaced by Eq. (31) (Nascimento et al. 2016):

$$\sum_{i=1}^N P_i = P_D + P_L. \tag{31}$$

This is:

$$\sum_{i=1}^N P_i - P_D - P_L = 0, \tag{32}$$

where P_L are the transmission losses, P_D is the power demand, and P_i is the power of each i_{th} unit respectively.

The P_L value was calculated as a function of transmission losses of each unit, which uses a matrix of loss coefficients B , a vector $B0$ and a value $B00$ (Eq. 33) (Nascimento et al. 2016):

$$P_L = \sum_{i=1}^N \sum_{j=i}^N P_i B_{ij} P_j + \sum_{i=i}^N B0_i P_i + B00. \tag{33}$$

- Prohibited operating zones: restrict the operation of generating units, owing to steam; valve-operating conditions; and shaft-bearing vibrations, restrictions (Eq. 34):

$$\begin{cases} P_{\min i} \leq P_i \leq P_{i,1}^l \\ P_{i,j1}^u \leq P_i \leq P_{i,j}^l, & j = 2, 3, \dots, nj, \\ P_{i,nj}^u \leq P_i \leq P_{\max i} \end{cases} \quad (34)$$

where n_j is the number of prohibited zones in the i_{th} unit, $P_{i,j}^l$ and $P_{i,j}^u$ are the lower and upper limits of the forbidden zone.

- Restricting inequality in terms of fuel supply.

At each interval, the amount of fuel supplied to all units must be less than or equal to the fuel supplied by the seller, that is, the fuel supplied to each unit, at each interval, must be within its lower limit F_i^{\min} and its limit upper F_i^{\max} , so the restriction (Eq. 35) (Basu 2014a):

$$F_i^{\min} \leq F_{im} \leq F_i^{\max}, i \in N, m \in M, \quad (35)$$

where F_{im} : fuel supplied to generator i in interval m ; F_i^{\min} : minimum amount of fuel supplied to generator i ; F_i^{\max} : maximum amount of fuel supplied to generator i .

- Inequality constraint in terms of fuel storage limits.

The fuel storage limit of each unit in each interval must be within its lower limit V_{\min} and the upper limit V_{\max} , so the restriction (Eqs. 36 and 37) (Basu 2014a):

$$V_{\min} \leq V_{im} \leq V_{\max}, \quad (36)$$

$$V_{im} = V_{(m-1)} + F_{im} - t_m [\eta_i + \delta_i P_i + \mu_i P_i^2] \quad i \in N, m \in M, \quad (37)$$

where, η_i , δ_i , and μ_i are the coefficients of the fuel consumption of each generating unit and t_m is the duration of the sub-interval m .

- Constraint (Eq. 38) of inequality in terms of power demand limits:

$$\sum_{i=1}^n P_{\min} \leq P^D \leq \sum_{i=1}^n P_{\max} \quad (38)$$

The incremental fuel cost method: by optimal dispatch, it is assumed that the incremental cost for each unit is described as in Eq. (39) (Dike et al. 2013):

$$\frac{\partial F_1}{\partial P_1} = \frac{\partial F_2}{\partial P_2} = \dots = \frac{\partial F_m}{\partial P_m}, \quad (39)$$

$$\frac{\partial F_i}{\partial P_i} = \lambda, \quad (40)$$

where, λ is the incremental cost.

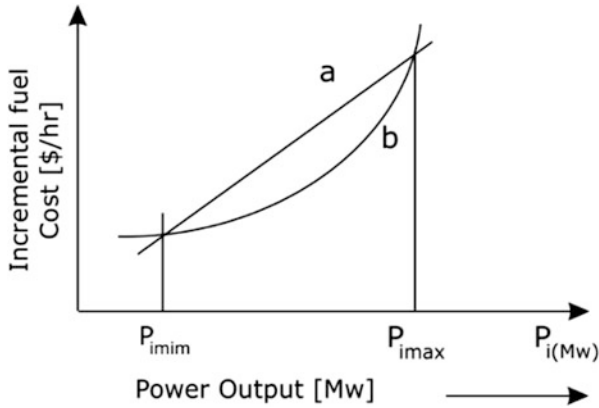


Fig. 13 Incremental fuel cost curve. (Source: Nascimento et al. (2016))

The optimal condition from Eq. (40) reduces to Eq. (41):

$$\frac{\partial F_i}{\partial P_i} = b_i + 2c_i P_i, \tag{41}$$

$$\lambda = b_i + 2c_i P_i, \tag{42}$$

where λ is the incremental cost of fuel.

The incremental fuel cost curve is shown in Fig. 13. **a** corresponds to the values of the different points on the actual incremental cost curve and **b** are the values of the points on the approximate (linear) curve for the incremental cost. P_i is the total power generation (Dhamanda et al. 2013).

For load dispatch purposes the cost is generally approximated to one or more quadratic segments; thus, the fuel cost curve in active power generation assumes a quadratic shape.

From Eq. (42) the power generated in the unit can be obtained as in Eq. (43) (Dike et al. 2013):

$$P_i = \frac{\lambda - b_i}{2c_i}. \tag{43}$$

Furthermore, the optimal condition, Eq. (40), becomes Eq. (44):

$$\frac{\partial F_i}{\partial P_i} + \lambda \frac{\partial P_L}{\partial P_i} = \lambda, \tag{44}$$

$$\frac{\partial P_L}{\partial P_i} = 2 \sum_{j=1}^n B_{ij} P_j + B_{0i}, \quad (45)$$

where $\frac{\partial P_L}{\partial P_i}$ is the incremental loss of the generating unit i .

Inserting Eqs. (41) and (45) into Eq. (44), one obtains Eq. (46) (Dike et al. 2013):

$$b_i + 2c_i P_i + 2\lambda \sum_{j=1}^n B_{ij} P_j + B_{0i} \lambda = \lambda. \quad (46)$$

From Eq. (46), the power generated in unit i can be described as in Eq. (47):

$$P_i = \frac{\lambda(1 - B_{0i}) - b_i - 2\lambda \sum_{j=1}^n B_{ij} P_j}{2(c_i + \lambda B_{ii})}. \quad (47)$$

It can be simplified as in Eq. (48):

$$P_i = \frac{\lambda - b_i}{2(c_i + B_{ii})}. \quad (48)$$

To calculate the levels of general emissions, the quadratic equation (Eq. 49) was used, from the analysis of measurement data, and its specified coefficients by means of a regression method with the aid of CurveExpert Software.

$$Eg_i(P_i) = \sum_{i=1}^n \alpha_i P_i^2 + \beta_i P_i + \gamma_i \quad (\text{gm}^3/\text{h}), \quad (49)$$

where α_i, β_i e γ_i are the general emission coefficients; n is the number of generating units in the system; P_i is the power capacity of each generating unit (in MW); and $Eg_i(P_i)$ is the total emissions in cubic molar grams per hour (gm^3/h).

To calculate the NO_x emission levels, the quadratic equation (Eq. 50) was used, from the analysis of measurement data, and its specified coefficients through a regression method with the aid of CurveExpert Software.

$$\text{NO}_{x_i}(P_i) = \sum_{i=1}^n \alpha n_i P_i^2 + \beta n_i P_i + \gamma n_i \quad (\text{gm}^3/\text{h}), \quad (50)$$

where $\alpha n_i, \beta n_i$ e γn_i are the emission coefficients of NO_x; n is the number of generating units in the system; P_i is the power capacity of each generating unit (in MW); and $\text{NO}_{x_i}(P_i)$ is the total emissions of NO_x (in gm^3/h).

To calculate the levels of CO₂ emissions, the quadratic equation (Eq. 51) was used, from the analysis of measurement data, and its specified coefficients by means of a regression method with the aid of CurveExpert Software.

$$CO_{2i}(P_i) = \sum_{i=1}^n \alpha c_i P_i^2 + \beta c_i P_i + \gamma c_i \left(\frac{gm^3}{h} \right), \tag{51}$$

where $\alpha c_i, \beta c_i$ e γc_i are the CO₂ emission coefficients; n is the number of generating units in the system; P_i is the power capacity of each generating unit (in MW); and $CO_{2i}(P_i)$ is the total CO₂ emissions (in gm³/h).

5.6 Mathematical Formulation for the EED – Test System – NSGA-II

For the test system, the mathematical formulation adopted for the function of the total fuel cost, considering the valve-point effect, is considered, given by Eq. (52) (Basu 2008):

$$f_1 = \sum_{i=1}^n \left[a_i + b_i P_i + c_i P_i^2 |d_i \sin \{e_i (P_{i,\min} - P_i)\} | \right], \tag{52}$$

where:

$a_i, b_i, c_i, d_i,$ and e_i are the fuel consumption coefficients;
 n is the number of test system generating units for the NSGA-II;
 P_i is the power capacity of each generating unit (in MW);
 f_1 is the total cost (in \$/h).

For the general emissions of pollutants into the atmosphere, considering the emissions of sulfur oxide (SOx), nitrogen oxide (NOx), and carbon dioxide (CO₂), a quadratic equation and an exponential function given by Eq. (53) (Basu 2008):

$$f_2 = \sum_{i=1}^n \left[\alpha_i + \beta_i P_i + \gamma_i P_i^2 + \eta_i \exp(\delta_i P_i) \right] \text{ lb/h}, \tag{53}$$

where:

$\alpha_i, \beta_i, \gamma_i, \eta_i,$ and δ_i are the emission coefficients;
 n is the number of test system generating units for the NSGA-II;
 P_i is the power capacity of each generating unit (in MW);
 f_2 is the total emissions (in lb/h).

5.7 Mathematical Formulation for the EED – Test System – NSGA-III

For NSGA-III the mathematical formulation adopted for the total fuel cost function is given by Eq. (54) (Dhillon and Jain 2011):

$$F_{FC} = \min \sum_{i=1}^n \left(a_i + b_i P_i + c_i P_i^2 \right) \frac{\$}{h}, \quad (54)$$

where:

a_i , b_i , and c_i are the fuel consumption coefficients;
 n is the number of test system generating units for the NSGA-III;
 P_i is the power capacity of each generating unit (in MW);
 F_{FC} is the total fuel cost (in \$/h).

For the calculation of NOx pollutant emissions in the atmosphere, a quadratic equation is given by Eq. (55) (Dhillon and Jain 2011):

$$F_{NX} = \min \sum_{i=1}^n \left(a_{Ni} + b_{Ni} P_i + c_{Ni} P_i^2 \right) \text{ kg/h}, \quad (55)$$

where:

a_{ni} , b_{ni} , and c_{ni} are the emission coefficients of NOx;
 n is the number of test system generating units for the NSGA-III;
 P_i is the power capacity of each generating unit (in MW);
 F_{NX} is the total NOx emissions (in kg/h).

For the calculation of COx pollutant emissions in the atmosphere, a quadratic equation given by Eq. (56) is considered (Dhillon and Jain 2011):

$$F_{CX} = \min \sum_{i=1}^n \left(a_{Ci} + b_{Ci} P_i + c_{Ci} P_i^2 \right) \frac{\text{kg}}{h}, \quad (56)$$

where:

a_{ci} , b_{ci} , and c_{ci} are the emission coefficients of COx;
 n is the number of test system generating units for the NSGA-III;
 P_i is the power capacity of each generating unit (in MW);
 F_{CX} is the total emissions of COx (in kg/h).

5.8 Optimization of EED by NSGA-II – Case Study

In Table 13a and 13b, the results of the case study are presented, from a point on the Pareto border, after the execution of the NSGA-II.

Average run time: 8.41459 s for the classic solution, 13.39859 s for the new solution that turns off the generators with the highest fuel cost, and 13.23760 s for the new solution that turns off the most polluting generators.

The solution report presents the input parameters for running the algorithm, such as: total power demand P^D ; minimum and maximum power capacity of the PPT; total and fuel costs of each generating unit and the total power losses P_L .

The minimum number of generators with the lowest fuel cost is selected to meet the total need for active power demand P^D and the optimal output power P_i of each generating unit is specified. The generators with the highest fuel cost (UG1, UG3, and UG5) are turned off at the time of optimization.

In Fig. 14, the comparative graph of the optimal output power of each generator is visualized, between the classic solution and the new proposed solution, turning off the generators with the highest fuel cost (R. Cost) or turning off the most polluting generators (R. Emissions), implemented with NSGA-II for the case study.

In Fig. 15, the comparative graph of the fuel cost of each generator is visualized, between the classic solution and the new proposed solution, turning off the generators with the higher fuel cost (R. Cost) or turning off the most polluting generators (R. Emissions), implemented with NSGA-II for the case study.

In Fig. 16, the comparative graph of emissions of each generator is visualized, between the classic solution and the new proposed solution, turning off the generators with the highest fuel cost (R. Cost) or turning off the most polluting generators (R. Emissions), implemented with NSGA-II for the case study.

In this analysis, the EED operational optimization problem was solved considering the incremental cost and implemented with the NSGA-II, contemplating the shutdown of generators with the highest fuel cost. The results, with the new solution turning off generators with higher fuel costs, showed a reduction of 32.27% in the total cost of fuel and a reduction of 30.29% in emissions, compared with the classic solution that distributes the generation of fuel power between all generators, not

Table 13a NSGA II – Parameters using NSGA II – case study

EED parameters using NSGA II – Solutions:			
NSGA II – Classic solution		NSGA II – Solution turning off the most costly generators	NSGA II – Solution turning off the most polluting generators
Total of P^D :	20 MW	20 MW	20 MW
Minimum power:	0.56 MW	0.56 MW	0.66 MW
Maximum power:	3.9 MW	3.9 MW	3.9 MW
Total of P^L :	0.053 MW	0.046 MW	0.39 MW

Source: Authors (2016)

Table 13b NSGA II – Exit results – case study

	Power P_i (MW)	Cost (R\$)	Emissions (g/m ³)	Power P_i (MW)	Cost (R\$)	Emissions (g/m ³)	Power P_i (MW)	Cost (R\$)	Emissions (g/m ³)
UG1	3.254	262.85	109,218.98	0.000	0.00	0.00	0.000	0.00	0.00
UG2	3.164	231.73	102,806.61	3.614	236.27	102,429.73	0.000	0.00	0.00
UG3	2.197	238.72	95,534.43	0.000	0.00	0.00	3.600	250.72	94,746.72
UG4	0.660	207.26	86,091.40	2.526	227.85	85,604.79	2.184	224.07	85,693.52
UG5	0.721	227.57	83,989.74	0.000	0.00	0.00	2.087	241.95	83,719.03
UG6	1.364	136.38	91,963.23	3.096	157.22	91,208.31	2.610	151.38	91,418.68
UG7	2.137	159.95	87,686.52	2.316	162.46	87,633.05	2.730	168.27	87,509.54
UG8	2.923	170.99	100,725.23	3.212	175.04	100,541.51	3.330	176.70	100,466.25
UG9	1.793	155.12	103,360.85	3.064	172.96	102,476.90	3.858	184.12	101,930.35
UG10	1.969	157.59	103,494.47	2.219	161.10	103,318.89	0.000	0.00	0.00
Total	20.18	1948.17	964,871.4	20.04	1292.90	673,213.2	20.39	1397.21	645,484.1

Source: Authors (2016)

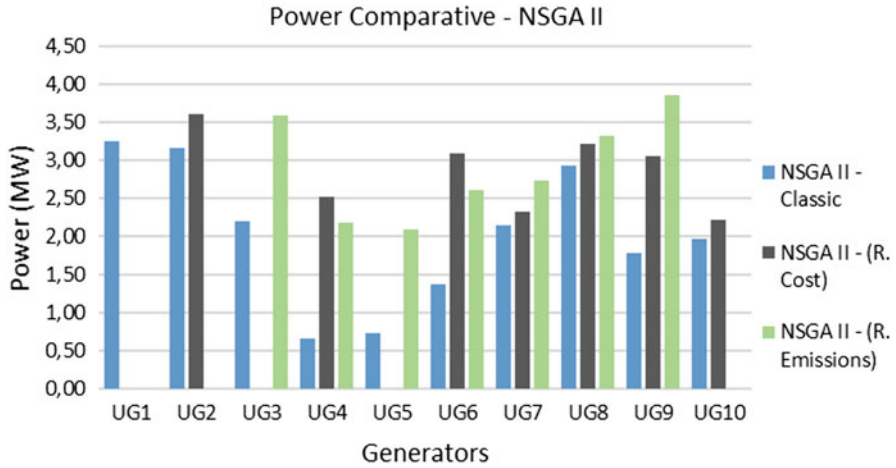


Fig. 14 Power comparative graph, NSGA-II – case study. (Source: Authors (2016))

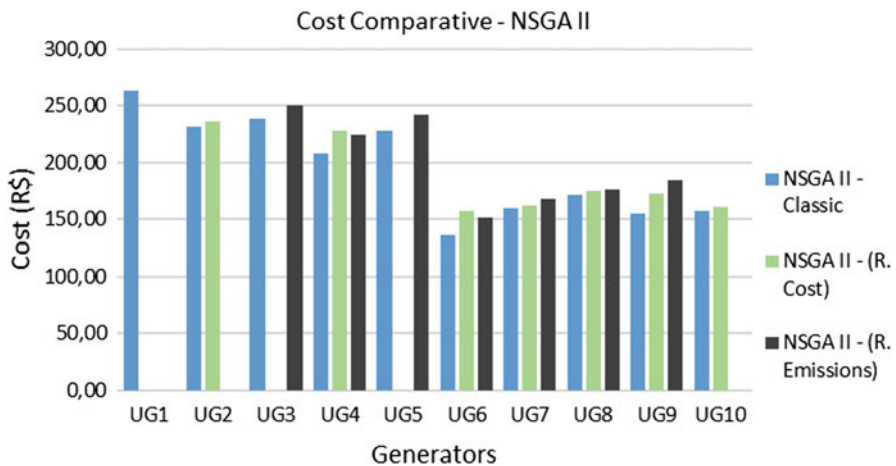


Fig. 15 Cost comparative chart, NSGA-II – case study. (Source: Authors (2016))

contemplating their shutdown with the highest fuel cost. By opting for the shutdown of the most polluting generators, a 28.26% reduction in the total fuel cost is obtained and a 33.10% reduction in emissions compared with the classic solution.

In Fig. 17, the Pareto front graphic is visualized for the classical solution implemented with NSGA-II for the case study.

Figure 18 shows the Pareto front graph for the new solution that turns off generators with higher fuel costs, implemented with NSGA-II for the case study.

In Fig. 19, the Pareto front graph is visualized for the new solution that turns off generators with the highest rate of emissions, implemented with NSGA-II for the case study.

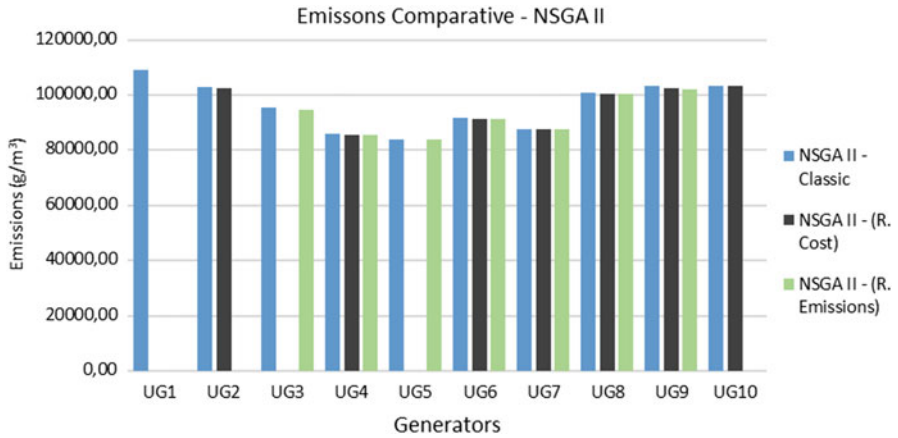


Fig. 16 Comparative emissions chart, NSGA-II – case study. (Source: Authors (2016))

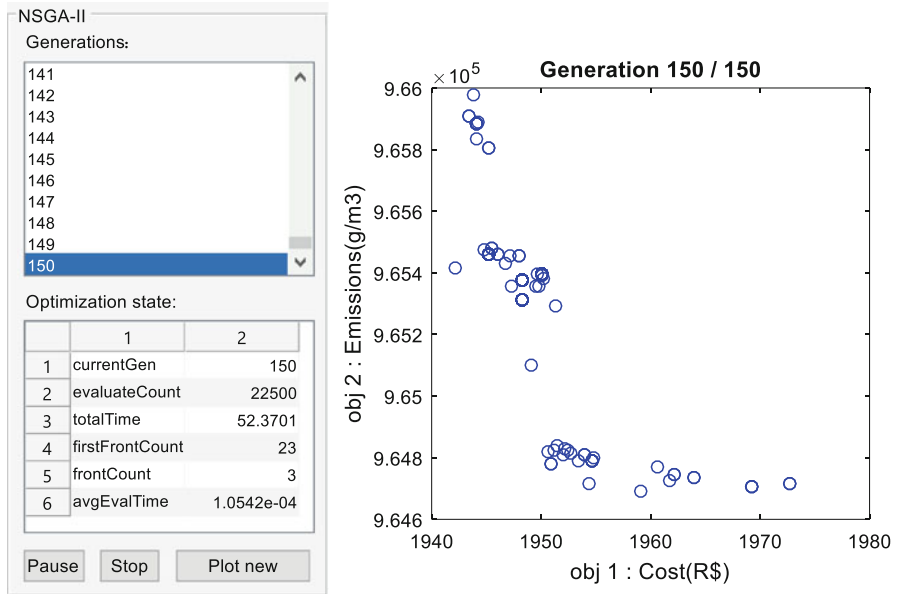


Fig. 17 Pareto front of the classic solution, NSGA-II – case study. (Source: Authors (2016))

5.9 NSGA-II Comparative with Test System

In Table 14a and 14b, the comparative results with the test system of Basu (2008) are presented for the EED optimization problem, and compared with the new solution, which contemplates the shutdown of generators with a higher fuel cost implemented with the NSGA-II.

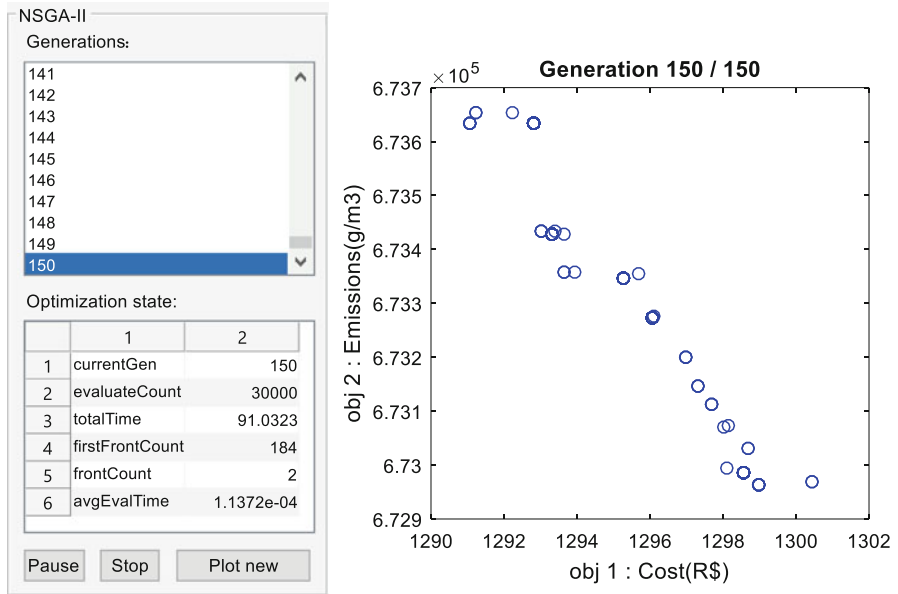


Fig. 18 Pareto front of cost reduction, NSGA-II – case study. (Source: Authors (2016))

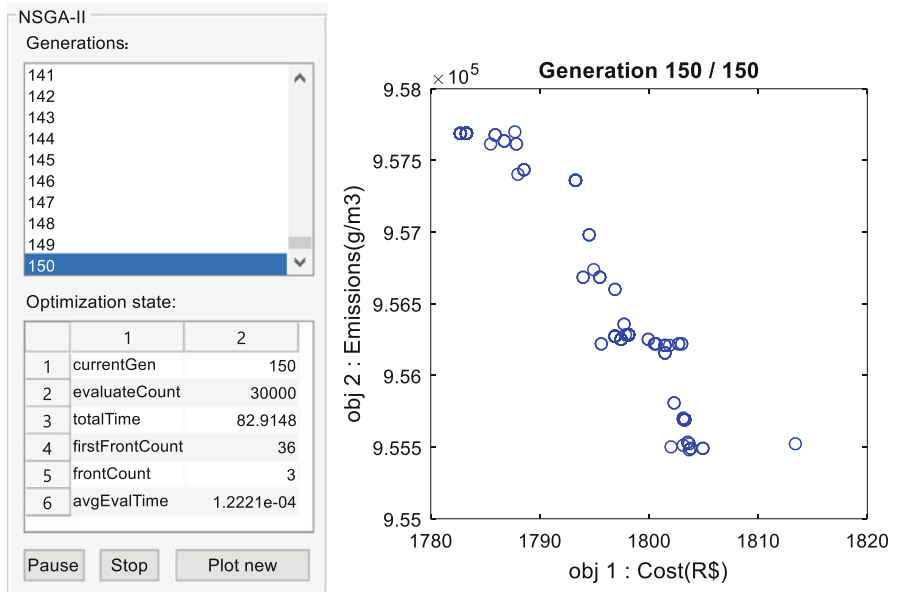


Fig. 19 Pareto front for emission reduction, NSGA-II – case study. (Source: Authors (2016))

The solution report presents the input parameters to run the algorithm, such as total power demand P^D ; minimum and maximum power capacity of the PPT; total and fuel costs of each generating unit, and the total power losses P_L .

The minimum number of generators with the lowest fuel cost is selected to meet the total need for active power demand P^D and the optimal output power P_i of each generating unit is specified. The generators with the highest fuel cost (PG1, PG2, PG9, and PG10) are turned off at the time of optimization.

In Fig. 20, the comparative graph of the optimal output power of each generator is visualized, between the classic solution of Basu (2008) and the new proposed solution, turning off the generators with higher fuel costs (R. Cost) or turning off the most polluting generators (R. Emissions), implemented with NSGA-II for the test system.

In Fig. 21, the comparative graph of fuel cost of each generator is visualized, between the classic solution of Basu (2008) and the new proposed solution, turning off the generators with higher fuel cost (R. Cost) or turning off the most polluting generators (R. Emissions), implemented with NSGA-II for the test system.

In Fig. 22, the comparative graph of emissions of each generator is displayed, between the classic solution of Basu (2008) and the new proposed solution, turning off generators with higher fuel costs (R. Cost) or turning off more polluting generators (R. Emissions), implemented with NSGA-II for the test system.

In this analysis, the EED operational optimization problem was solved considering the incremental cost and implemented with the NSGA-II, contemplating the shutdown of generators with the highest fuel cost. The results, with the new solution turning off the generators with the highest fuel cost, showed a reduction of 22.44% in the total cost of fuel and a reduction of 32.53% in emissions, compared with the classic solution that distributes the generation of fuel power between all generators, not contemplating their shutdown with the highest fuel cost.

By opting for the shutdown of the most polluting generators, there is a 19.72% increase in the total fuel cost and an 81.96% reduction in emissions compared with the classic solution. In Fig. 23, the Pareto front graphic is visualized for the classical solution implemented with NSGA-II for the test system.

Figure 24 shows the Pareto front graph for the new solution that turns off generators with higher fuel costs, implemented with NSGA-II for the test system.

Table 14a Parameters using for the Test System – NSGA-II

EED parameters using NSGA II – Solutions:			
NSGA II – Classic solution (BASU, 2008)		NSGA II – Solution turning off the most costly generators	NSGA II – Solution turning off the most polluting generators
Total of P^D :	1036 MW	1036 MW	1036 MW
Minimum power:	10 MW	10 MW	10 MW
Maximum power:	470 MW	470 MW	470 MW
Total of P^L :	19.69 MW	19.32 MW	11.72 MW

Source: Authors (2016)

Table 14b Comparison of results for the test system – NSGA-II

	Power P_i (MW)	Cost (R\$)	Emissions (lb)/h	Power P_i (MW)	Cost (R\$)	Emissions (lb)/h	Power P_i (MW)	Cost (R\$)	Emissions (lb)/h
PG1	167.63	11,826.83	586.49	0.00	0.00	0.00	149.95	9993.58	449.62
PG2	192.66	13,796.89	817.74	0.00	0.00	0.00	231.08	16,954.71	1264.75
PG3	214.35	11,228.38	1804.39	0.00	0.00	0.00	115.55	6389.04	514.91
PG4	100.83	5686.96	411.33	294.07	15,669.08	3694.01	46.07	3255.80	222.20
PG5	146.31	7704.34	507.79	242.87	11,994.28	1487.03	120.20	6376.93	364.19
PG6	56.89	3593.32	215.95	159.90	8235.89	602.00	242.57	11,846.63	1482.80
PG7	55.55	3541.43	258.42	124.31	6307.91	570.86	142.27	7155.96	726.86
PG8	53.37	3603.25	255.80	116.83	6061.14	515.08	0.00	0.00	0.00
PG9	32.63	3118.43	271.72	62.35	4575.32	286.69	0.00	0.00	0.00
PG10	35.48	3328.83	278.98	54.99	4426.91	284.90	0.00	0.00	0.00
Total	1055.69	67,428.67	5408.62	1055.32	57,270.54	7440.57	1047.7	61,972.64	5025.33

Source: Authors (2016)

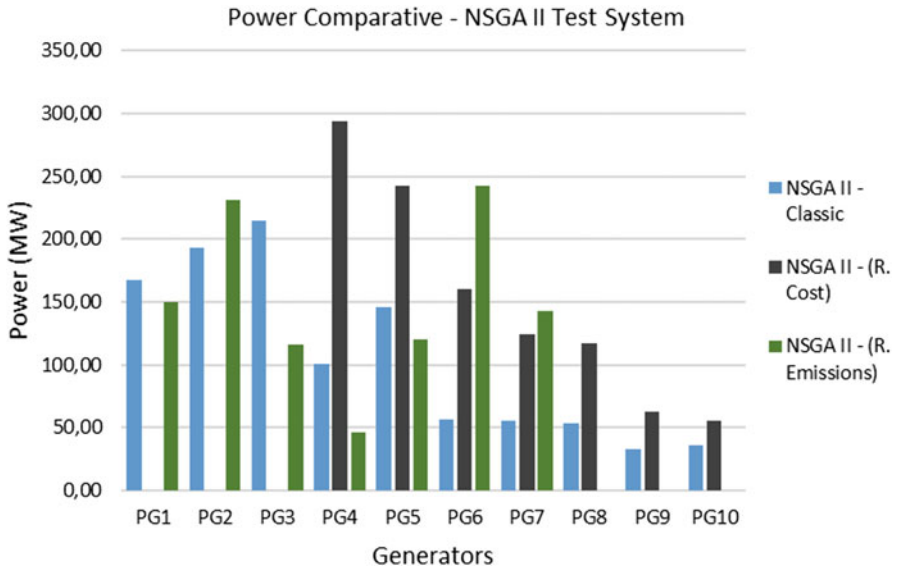


Fig. 20 Power comparative graph, NSGA-II – test system. (Source: Authors (2016))

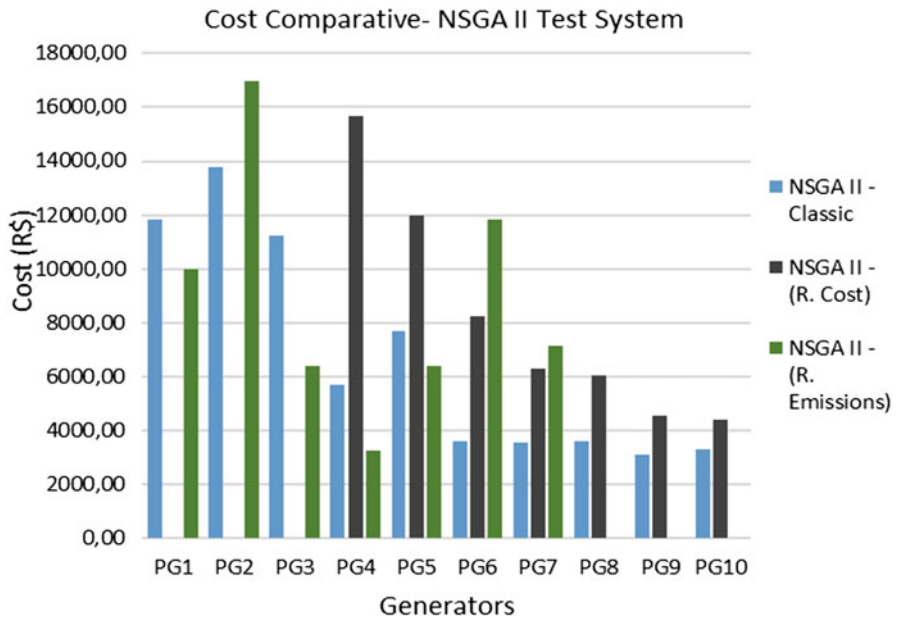


Fig. 21 Cost comparative chart, NSGA-II – test system. (Source: Authors (2016))

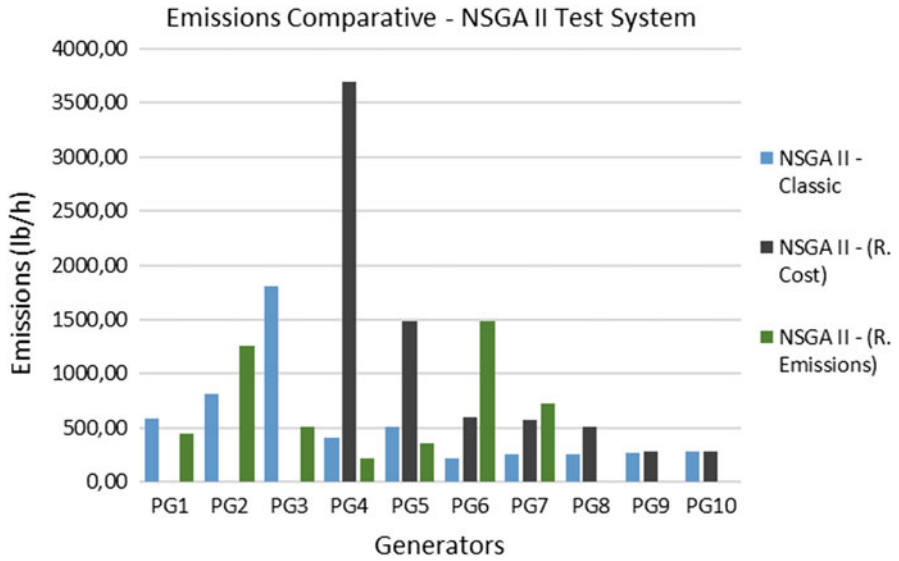


Fig. 22 Comparative emissions chart, NSGA-II – test system. (Source: Authors (2016))

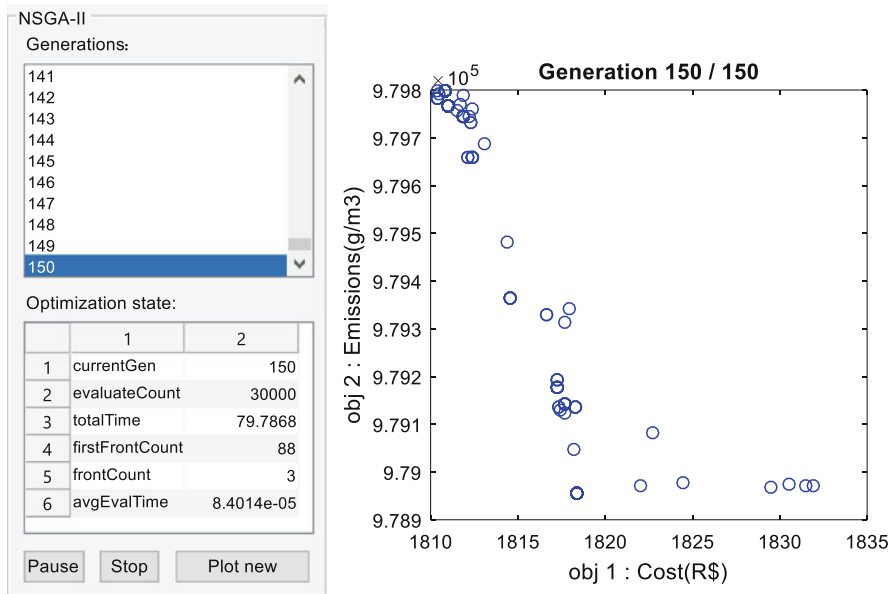


Fig. 23 Pareto front of the classic solution, NSGA-II – test system. (Source: Authors (2016))

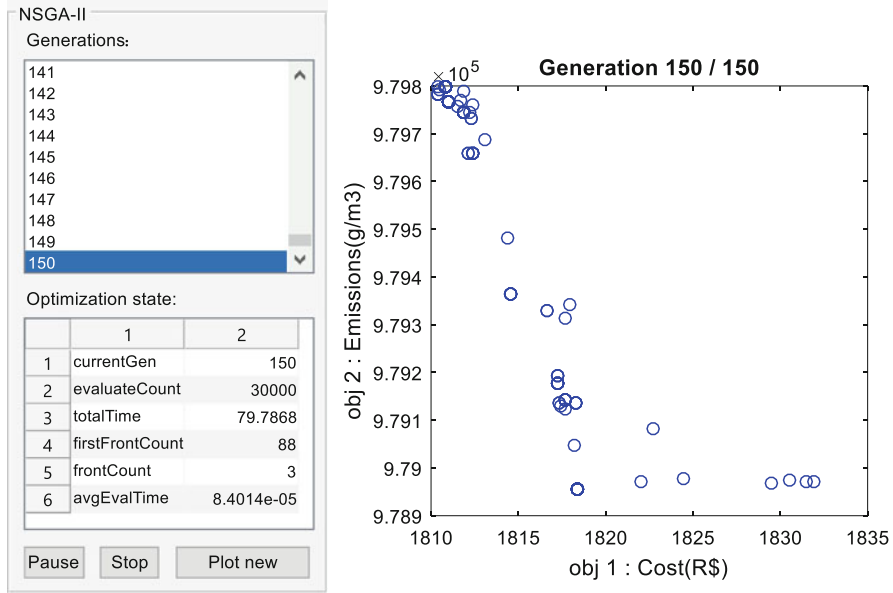


Fig. 24 Pareto front of cost reduction, NSGA-II – test system. (Source: Author (2016))

Table 15 Parameters. NSGA-III – case study

EED parameters using NSGA-III				
Solutions:	P^D	P_{imin} (M)	P_{imax} (M)	P_L
Classic	20 MW	0.56 MW	3.9 MW	0.3 MW
Turning off generators at higher cost (R\$)	20 MW	0.56 MW	3.9 MW	0.19 MW
Turning off generators with higher emissions of NOx	20 MW	0.56 MW	3.7 MW	0.21 MW
Turning off generators with higher emissions of CO ₂	20 MW	0.66 MW	3.9 MW	0.28 MW

Source: Authors (2016)

5.10 Optimization of EED by NSGA-III – Case Study

Table 15 shows the operating parameters of the NSGA-III for the case study.

Average execution time is 15.4435 s for the classic solution, 12.8941 s for the new solution that turns off generators with higher fuel costs, 12.6606 s for the new solution that turns off generators with higher NOx emissions, and 14.1847 s for the new solution that shuts down generators with higher CO₂ emissions.

The solution report presents the input parameters to run the algorithm, such as total power demand P^D ; minimum and maximum power capacity of the PPT; total and fuel costs of each generating unit and the total power losses P_L .

Table 16 Optimal power output results. NSGA-III – case study

Optimal output power of each generating unit				
Solution:				
	Classic	R. Cost	R. NOx	R. CO ₂
	Power:			
	P_i (MW)	P_i (MW)	P_i (MW)	P_i (MW)
UG1	2.99	0	0	0
UG2	3.03	3.40	3.48	0
UG3	2.18	0	3.44	3.33
UG4	1.20	2.42	2.52	2.42
UG5	1.22	0	2.42	2.53
UG6	1.47	2.80	2.89	2.58
UG7	1.43	2.42	2.93	2.53
UG8	2.16	2.90	0	3.07
UG9	2.59	3.61	0	3.71
UG10	2.00	2.64	2.54	0
Total	20.2800	20.1919	20.2199	20.1691

Source: Authors (2016)

In Table 16, the results of the optimal output power P_i of each generating unit are presented, comparing the classic solution with the new solution that turns off generators with higher fuel consumption (R. Cost) or with higher NOx emissions (R. NOx) or with a higher rate of CO₂ emissions (R. CO₂), after the execution of the NSGA-III for the case study.

The classic solution that uses all generators to meet the need for active power demand P^D was the one with the greatest power loss. In Fig. 26, the optimal output power comparative graph displays the P_i of each generator, between the classic solution and the new proposed solution implemented with NSGA-III for the case study (Fig. 25).

Table 14b shows the results of total costs (R\$) for each generating unit, comparing the classic solution with the new solution that turns off generators with higher fuel consumption (R. Cost) or with a higher rate of emissions. NOx (R. NOx) or with a higher rate of CO₂ emissions (R. CO₂), after the execution of NSGA-III for the case study (Table 17).

The minimum number of generators with the lowest fuel cost is selected to meet the active power demand P^D and the optimal output power P_i of each generating unit is specified. The generators with the highest costs (UG1, UG3, and UG5) are turned off at the time of optimization. The solution that turns off the generators with the highest fuel costs showed a reduction of 33.45%, compared with the classic solution that uses all generators to meet the need for active power demand P^D . In Fig. 26, the comparative graph of fuel cost for each generator is visualized, between the classic solution and the new proposed solution implemented with NSGA-III for the case study.

Table 18 shows the results of total NOx emissions for each generating unit, comparing the classic solution with the new solution that turns off generators with

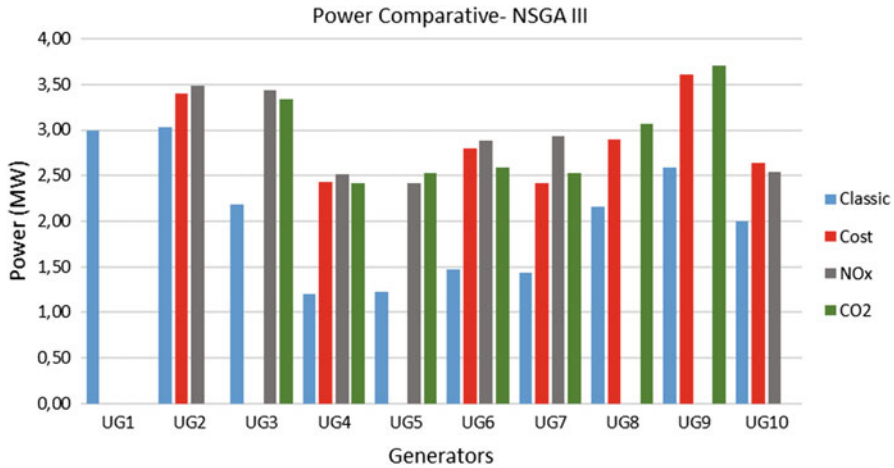


Fig. 25 Power comparison chart, NSGA-III – case study. (Source: Author (2016))

Table 17 Results of total costs (R\$). NSGA-III – case study

Total costs (R\$) of each generating unit				
Solution:				
	Classic	R. Cost	R. NOx	R. CO ₂
	Cost:			
	(R\$)	(R\$)	(R\$)	(R\$)
UG1	261.01	0.00	0.00	0.00
UG2	230.42	234.09	234.93	0.00
UG3	238.57	0.00	249.35	248.44
UG4	213.26	226.72	227.78	226.67
UG5	232.85	0.00	245.45	246.59
UG6	137.66	153.69	154.74	151.07
UG7	150.00	163.89	171.05	165.46
UG8	160.33	170.62	0.00	172.98
UG9	166.32	180.61	0.00	182.02
UG10	157.97	167.06	165.60	0.00
Total	1948.39	1296.69	1448.92	1393.23

Source: Authors (2016)

higher fuel consumption (R. Cost) or with higher NOx emissions rate (R. NOx) or with a higher rate of CO₂ emissions (R. CO₂), after the execution of the NSGA-III for the case study.

The minimum number of generators with the lowest NOx emission rates was selected to meet the total demand for active power P^D . The generators with the highest NOx emission rates (UG1, UG8, and UG9) are turned off at the time of optimization.

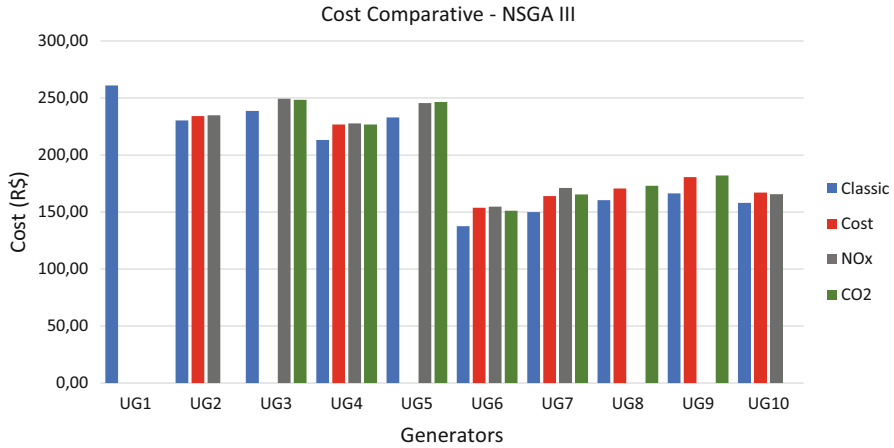


Fig. 26 Fuel cost comparison chart, NSGA-III – case study. (Source: Authors (2016))

Table 18 NOx emission results. NSGA-III – case study

NOx emissions from each generating unit				
Solutions:				
	Classic	R. Cost	R. NOx	R. CO ₂
Emissions of the NOx:				
	(g/m ³)	(g/m ³)	(g/m ³)	(g/m ³)
UG1	484.93	0.00	0.00	0.00
UG2	260.37	259.25	259.00	0.00
UG3	175.88	0.00	172.95	173.20
UG4	310.19	305.50	305.13	305.51
UG5	230.02	0.00	227.28	227.04
UG6	171.94	170.84	170.77	171.02
UG7	328.27	322.48	319.53	321.83
UG8	328.35	323.56	0.00	322.47
UG9	411.41	402.54	0.00	401.67
UG10	189.04	187.80	188.00	0.00
Total	2890.41	1971.97	1642.66	1922.74

Source: Author (2016)

The solution that turns off generators with the highest levels of NOx emissions presented a reduction of 43.17%, compared with the classic solution that uses all generators to meet the demand for active power P^D .

In Fig. 27, the comparative graph of NOx emissions for each generator is visualized, between the classic solution and the new proposed solution implemented with NSGA-III for the case study.

Table 19 shows the results of total CO₂ emissions for each generating unit, comparing the classic solution with the new solution that turns off generators with higher fuel consumption (R. Cost) or with higher NOx emissions rate (R. NOx) or

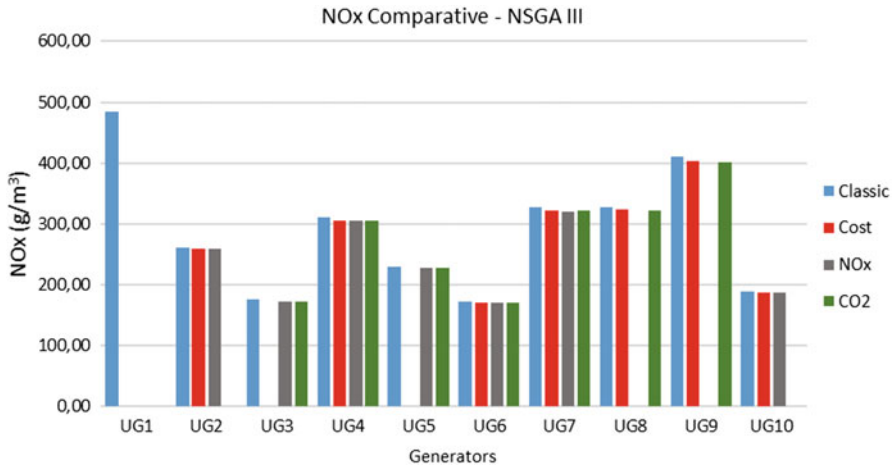


Fig. 27 Comparative chart of NOx emissions, NSGA-III – case study. (Source: Authors (2016))

Table 19 Results of CO₂ emissions. NSGA-III – case study

CO ₂ emissions from each generating unit				
Solutions:				
	Classic	R. Cost	R. NOx	R. CO ₂
Emissions of the CO ₂ :				
	(g/m ³)	(g/m ³)	(g/m ³)	(g/m ³)
UG1	108,958.09	0.00	0.00	0.00
UG2	102,935.57	10,2628.49	102,558.39	0.00
UG3	95,368.80	0.00	94,662.42	94,721.83
UG4	85,638.73	85,325.69	85,301.14	85,326.83
UG5	85,633.98	0.00	85,326.93	85,299.45
UG6	91,744.77	91,164.68	91,126.91	91,259.17
UG7	87,570.79	87,280.08	87,130.95	87,247.32
UG8	100,882.60	100,418.17	0.00	100,312.30
UG9	102,705.28	102,001.58	0.00	101,932.72
UG10	103,119.60	102,668.77	102,741.04	0.00
Total	964,558.21	671,487.46	648,847.78	646,099.64

Source: Authors (2016)

with a higher rate of CO₂ emissions (R. CO₂), after the execution of the NSGA-III for the case study.

The minimum number of generators with the lowest CO₂ emissions is selected to meet the total demand for active power P^D . The generators with the highest CO₂ emission rates (UG1, UG2, and UG10) are switched off at the time of optimization.

The solution that turns off generators with the highest levels of CO₂ emissions presented a reduction of 33.02%, compared with the classic solution that uses all generators to meet the demand for active power P^D .

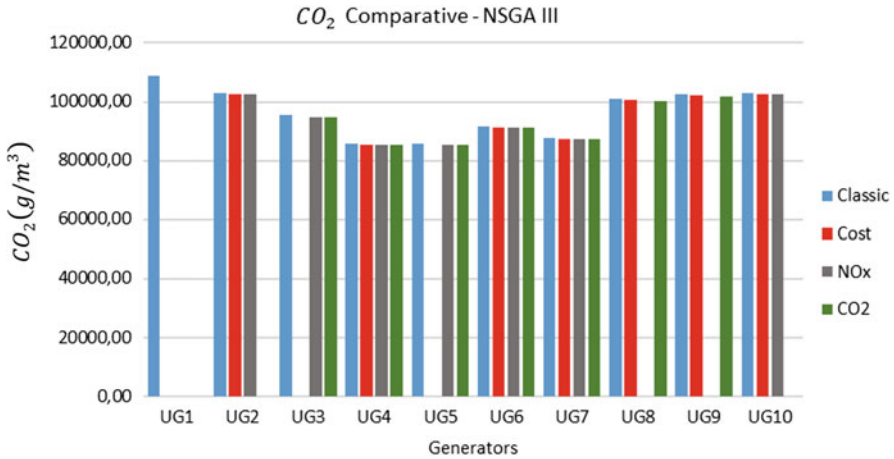


Fig. 28 Comparative chart of CO₂ emissions, NSGA-III – case study. (Source: Authors (2016))

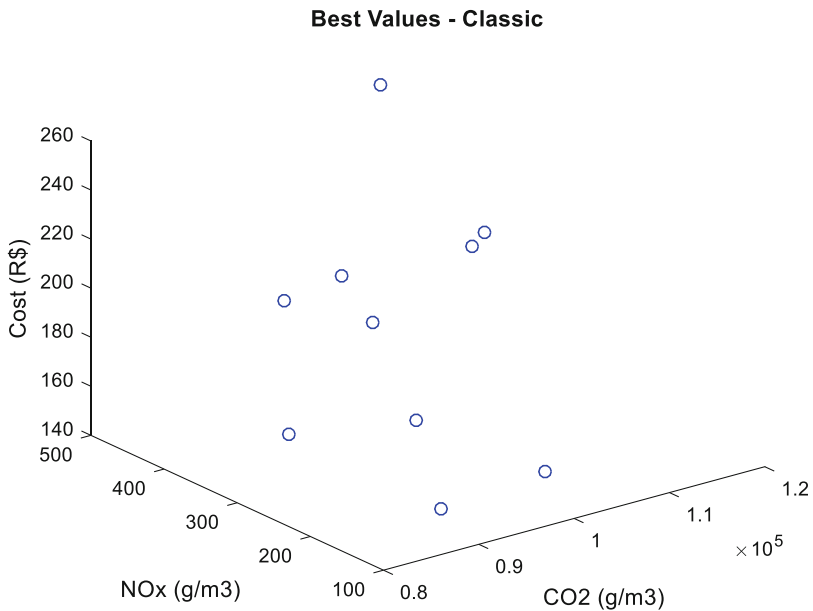


Fig. 29 Best individuals for the classic solution, NSGA-III – case study. (Source: Authors (2016))

In Fig. 28, the comparative graph of CO₂ emissions for each generator is visualized, between the classic solution and the new proposed solution implemented with NSGA-III for the case study.

In Fig. 29, the graph of the best individuals for the classic solution implemented with NSGA-III for the case study is visualized.

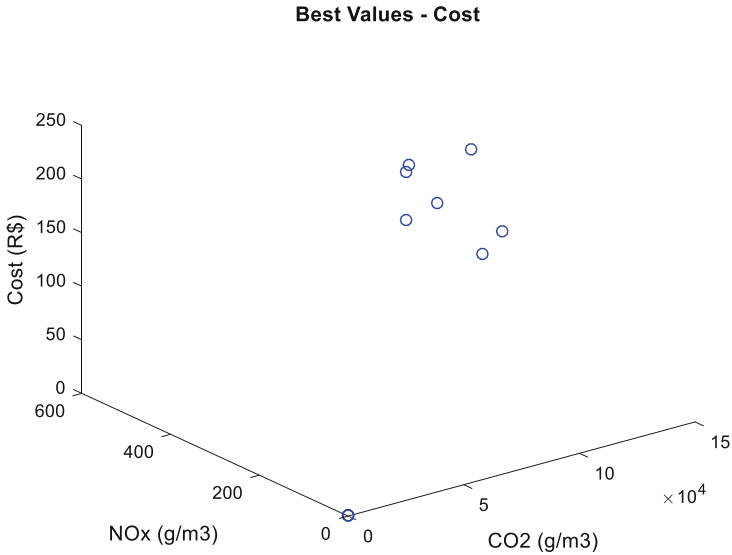


Fig. 30 Best individuals for cost reduction, NSGA-III – case study. (Source: Authors (2016))

Figure 30 shows the graph of the best individuals for the solution that turns off the generators with the highest fuel cost, implemented with NSGA-III for the case study.

In Fig. 31, the graph of the best individuals for the solution that turns off the generators with the highest CO₂ emission index is visualized, implemented with NSGA-III for the case study.

Figure 32 shows the graph of the best individuals for the solution that turns off the generators with the highest NO_x emission rate, implemented with NSGA-III for the case study.

5.11 NSGA-III Comparison with Test System

In Table 20, the operating parameters of the NSGA-III are presented for the test system.

The average execution time is 10.312 s for the classic solution, 14.4588 s for the new solution that turns off generators with higher fuel costs, 15.6611 s for the new solution that turns off generators with the highest rate of NO_x emissions, and 9.1874 s for the new solution that shuts down generators with the highest CO₂ emissions.

In Table 21, the results of the optimal output power P_i of each generating unit are presented, comparing the classic solution with the new solution that turns off generators with higher fuel consumption (R. Cost), with higher NO_x emissions (R.

Best Values - CO2

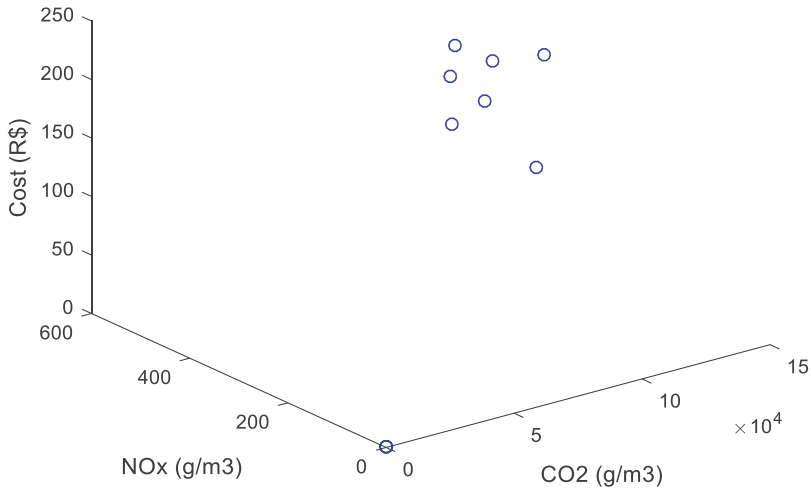


Fig. 31 Best individuals for CO₂ reduction, NSGA-III – case study. (Source: Authors (2016))

Best Values - NOx

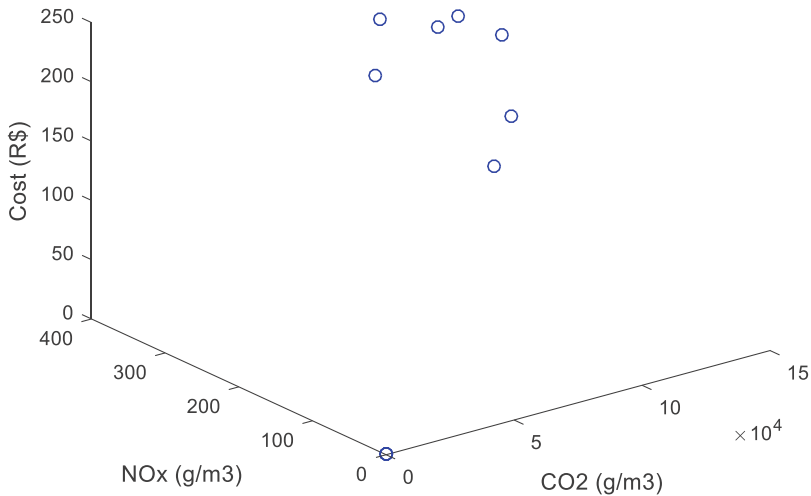


Fig. 32 Best individuals for NO_x reduction, NSGA-III – case study. (Source: Authors (2016))

Table 20 Economic and environmental dispatch (EED) parameters. NSGA-III – test system

EED parameters using NSGA-III				
Solutions:	P^D	$P_{i\min}(M)$	$P_{i\max}(M)$	P_L
Classic	1500 MW	50 MW	500 MW	0.72 MW
Turning off generators with the highest cost (R\$)	1500 MW	50 MW	500 MW	1.05 MW
Turning off generators with higher NOx emissions	1500 MW	50 MW	500 MW	0.78 MW
Turning off generators with higher CO ₂ emissions	1500 MW	50 MW	500 MW	0.20 MW

Source: Authors (2016)

Table 21 Optimal power output result. NSGA-III – test system

Optimal output power of each generating unit				
	Solution:			
	Classic	R. Cost	R. NOx	R. COx
	Power:			
	P_i (MW)	P_i (MW)	P_i (MW)	P_i (MW)
PG1	183.91	226.90	199.77	246.76
PG2	179.89	221.35	204.86	0.00
PG3	326.16	0	432.42	496.95
PG4	209.67	252.01	240.35	262.93
PG5	346.81	472.19	423.37	493.57
PG6	254.29	328.60	0	0
Total	1500.7295	1501.0481	1500.7760	1500.2018

Source: Authors (2016)

NOx), or with a higher rate of COx emissions (R. COx), after the execution of the NSGA-III for the test system.

The new solution, which includes the shutdown of generators with higher fuel consumption, was the one with the greatest power loss.

In Fig. 33, the comparative graph of the optimal output power P_i of each generator is visualized, between the classic solution and the new proposed solution implemented with NSGA-III for the test system.

Table 22 shows the results of total costs (R\$) for each generating unit, comparing the classic solution with the new solution that turns off generators with higher fuel consumption (R. Cost) or with higher fuel emissions. NOx (R. NOx) or with a higher rate of COx emissions (R. COx), after running the NSGA-III for the test system.

The minimum number of generators with the lowest fuel costs is selected to meet the total demand for active power P^D . The generator with the highest cost (PG3) is turned off at the time of optimization.

The solution that turns off the generators with the highest fuel costs showed a reduction of 3.16%, compared with the classic solution that uses all generators to meet the need for active power demand P^D . In their work, Dhillon and Jain (2011), obtain a total fuel cost of \$17,520.30 using NSGA-II. The new solution proposed in

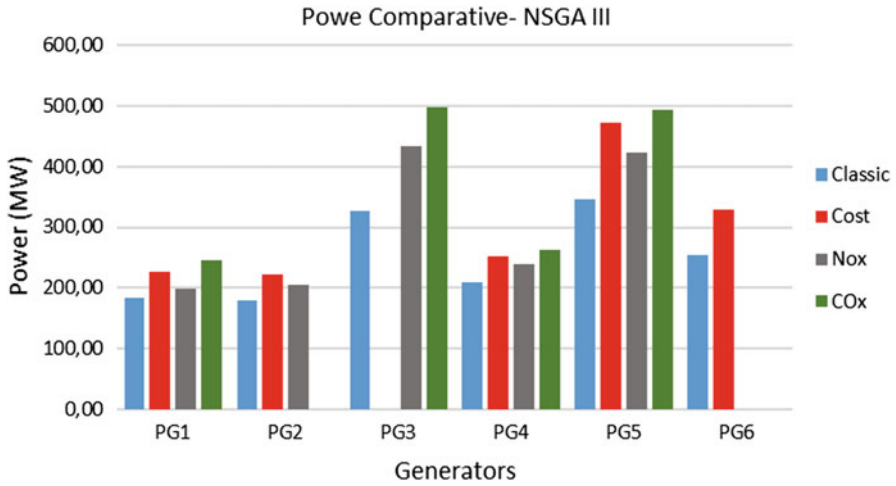


Fig. 33 Power comparative chart, NSGA-III – test system. (Source: Authors (2016))

Table 22 Results of total costs (R\$). NSGA-III – test system

Total costs (R\$) of each generating unit				
	Solution:			
	Classic	R. Cost	R. NOx	R. CO ₂
	Courses:			
	(R\$)	(R\$)	(R\$)	(R\$)
PG1	1705.20	2103.64	1851.33	2290.25
PG2	1582.02	1912.12	1779.26	0.00
PG3	3502.32	0.00	4467.59	5077.77
PG4	2076.84	2455.17	2350.55	2553.54
PG5	3681.52	4834.20	4377.28	5037.53
PG6	2346.14	3118.39	0.00	0.00
Total	14,894.05	14,423.52	14,826.00	14,959.10

Source: Authors (2016)

this chapter presents a reduction of 17.68% in the total fuel cost compared with this result (Dhillon and Jain 2011).

In Fig. 34, the comparative graph of fuel costs for each generator is displayed, between the classic solution and the new proposed solution implemented with NSGA-III for the test system.

Table 23, presented the results of total NOx emissions for each generating unit, comparing the classic solution with the new solution that turns off generators with higher fuel consumption (R. Cost) or with higher NOx emissions rates (R. NOx) or with a higher rate of COx emissions (R. COx), after the execution of the NSGA-III for the test system. left

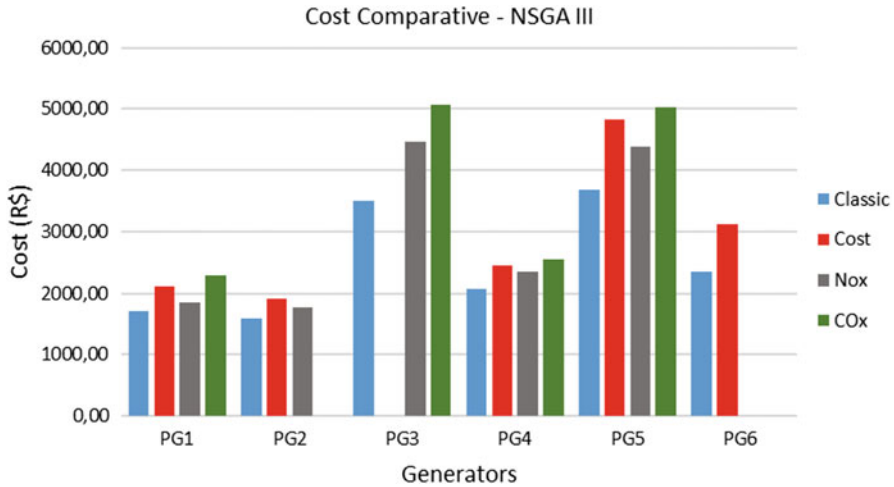


Fig. 34 Fuel cost comparative chart, NSGA-III – test system. (Source: Authors (2016))

Table 23 NOx emission results. NSGA-III – test system

NOx emissions from each generating unit				
	Solutions:			
	Classic	R. Cost	R. NOx	R. COx
	Emissions of NOx:			
	(kg/h)	(kg/h)	(kg/h)	(kg/h)
PG1	224.64	319.92	1851.33	371.83
PG2	96.45	171.54	1779.26	0.00
PG3	218.06	0.00	4467.59	431.87
PG4	403.15	433.15	2350.55	444.80
PG5	234.06	389.39	4377.28	425.84
PG6	350.69	589.39	0.00	0.00
Total	1527.05	1903.40	14,826.00	1674.34

Source: Authors (2016)

The minimum number of generators with the lowest NOx emission rates is selected to meet the total demand for active power P^D . The generator with the highest NOx emission rate (PG3) is turned off at the time of optimization.

The solution that turns off generators with the highest NOx emission rates showed a reduction of 4.07%, compared with the classic solution that uses all generators to meet the need for active power demand P^D .

In their work, Dhillon and Jain (2011) obtain total NOx emissions of 1805.34 kg using NSGA-II (Dhillon and Jain 2011). The new solution proposed in this chapter, presents a reduction of 18.86% in total NOx emissions in relation to this result.

In Fig. 35, the comparative graph of NOx emissions for each generator is displayed, between the classic solution and the new proposed solution implemented with NSGA-III for the test system.

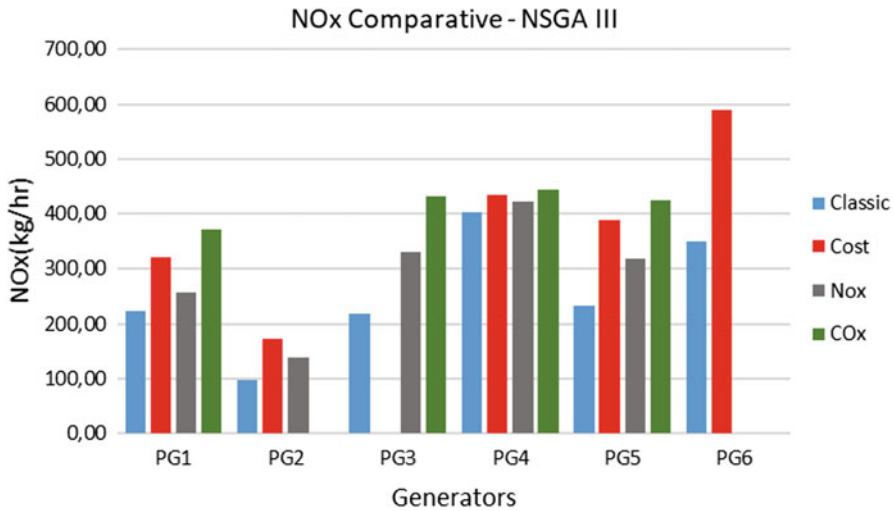


Fig. 35 Comparative chart of NOx emissions, NSGA-III – test system. (Source: Authors (2016))

Table 24 COx emission results. NSGA-III – test system

CO _x emissions from each generating unit				
	Solution:			
	Classic	R. Cost	R. NO _x	R. CO _x
Emissions of CO _x :				
	(kg/h)	(kg/h)	(kg/h)	(kg/h)
PG1	2824.84	4883.65	3470.36	6165.76
PG2	2968.80	4056.88	3566.50	0.00
PG3	9496.17	0.00	17,019.61	22,755.42
PG4	3827.07	5367.70	4905.56	5826.98
PG5	10,770.72	20,450.29	16,285.27	22,433.13
PG6	6430.82	14,829.08	0.00	0.00
Total	36,318.43	49,587.60	45,247.31	57,181.28

Source: Authors (2016)

Table 24 presented the results of total CO_x emissions for each generating unit, comparing the classic solution with the new solution that turns off generators with higher fuel consumption (R. Cost), with a higher NO_x emission rate (R. NO_x), or with a higher rate of CO_x emissions (R. CO_x), after the execution of the NSGA-III for the test system.

The minimum number of generators with the lowest CO_x emission rates is selected to meet the total demand for active power P^D . Generators with the highest CO_x emission rates (PG3 and PG6) are turned off at the time of optimization.

The solution that turns off generators with the highest CO_x emission rates did not show reductions in emission rates, compared with the classic solution that uses all generators to meet the need for active power demand P^D . This phenomenon occurs because of the characteristics of the plant’s generators, making the classic solution

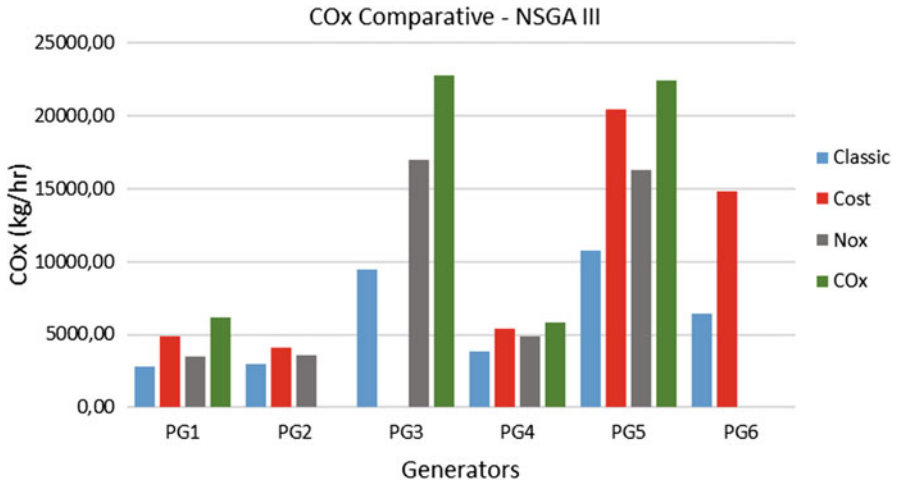


Fig. 36 Comparative chart of COx emissions, NSGA-III – test system. (Source: Authors (2016))

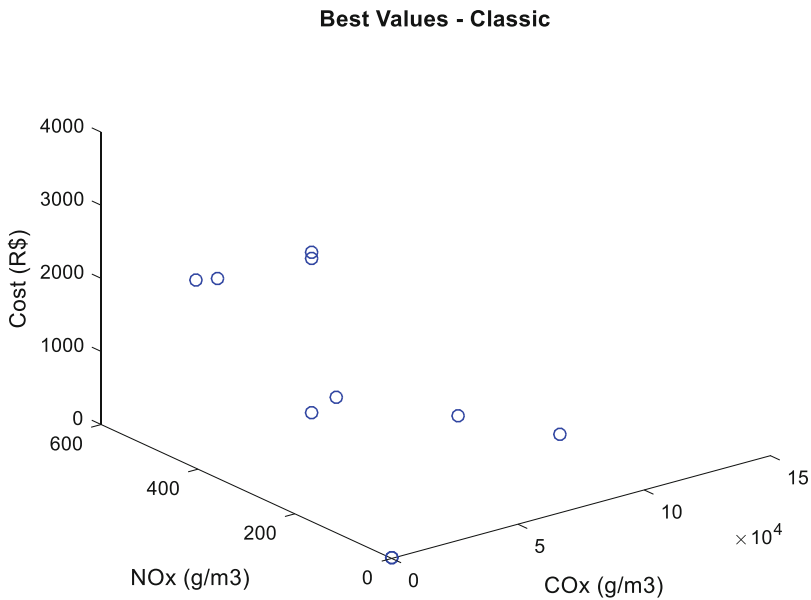


Fig. 37 Best individuals for classic solution, NSGA-III – test system. (Source: Authors (2016))

the one with the lowest total index of COx emissions. In Fig. 36, the comparative graph of COx emissions for each generator is displayed, between the classic solution and the new proposed solution implemented with NSGA-III for the test system.

In Fig. 37, the graph of the best individuals for the classic solution, implemented with NSGA-III for the test system is visualized.

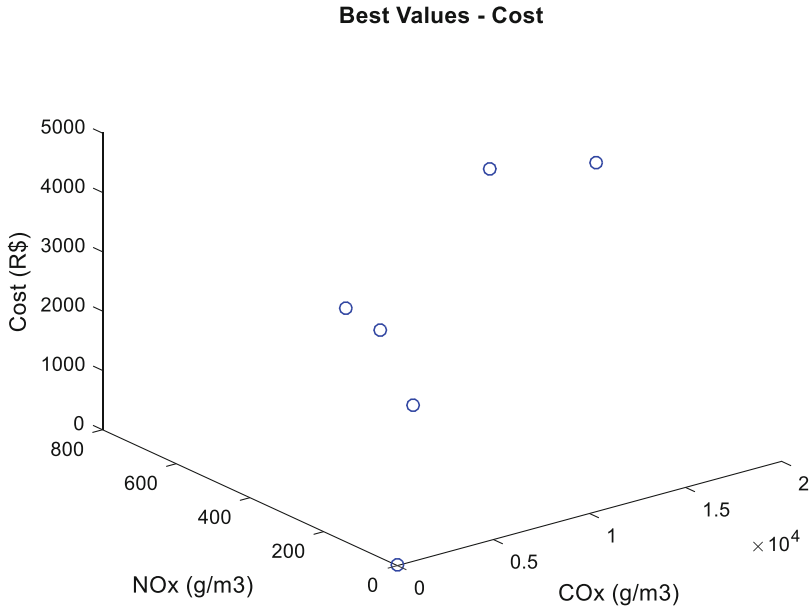


Fig. 38 Best individuals for cost reduction, NSGA-III – test system. (Source: Authors (2016))

In Fig. 38, the graph of the best individuals for the solution that turns off the generators with the highest fuel cost is visualized, implemented with NSGA-III for the test system.

In Fig. 39, the graph of the best individuals for the solution that turns off the generators with the highest COx emission rate is visualized, implemented with NSGA-III for the test system.

In Fig. 40, the graph of the best individuals for the solution that turns off the generators with the highest NOx emission rate is visualized, implemented with NSGA-III for the test system.

In this chapter, it can be seen that the new solution proposed for the EED optimization problem, which includes the shutdown of generators with higher fuel costs at the time of optimization to meet a certain power demand, proved to be efficient, with a reduction in the total cost of fuel in power generation in TPPs compared with other conventional methods that distribute power generation among all generators, including those with higher generation costs.

5.12 Conclusions

This chapter proposes to present a new solution for optimizing EED problems, based on bio-inspired metaheuristics. In this context, issues related to multi-objective

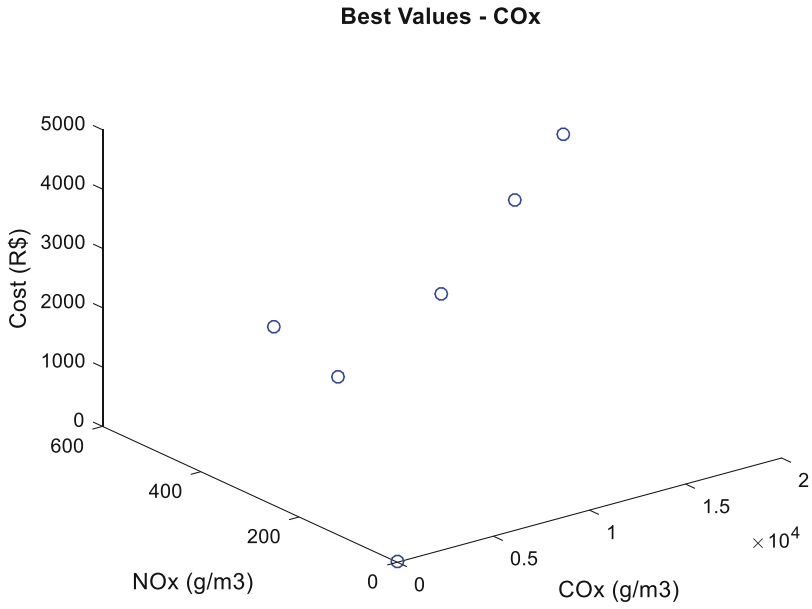


Fig. 39 Best individuals for COx reduction, NSGA-III – test system. (Source: Authors (2016))

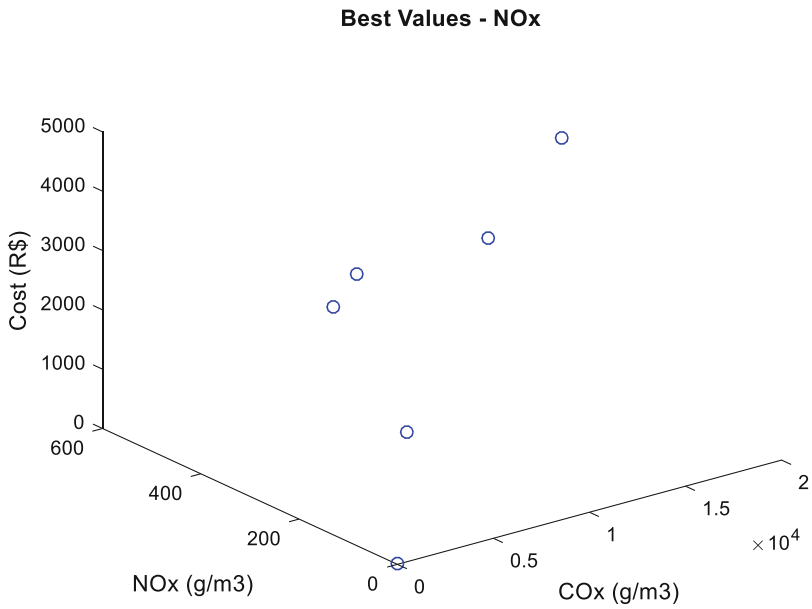


Fig. 40 Best individuals for NOx reduction, NSGA-III – test system. (Source: Authors (2016))

optimization and the conflicts that may exist within it were defined, in addition to the presentation of several methods based on conventional and unconventional analysis to solve the proposed problem.

One of the initial aspects that can be highlighted is the fact that the formulation of the EED problem, tested by heuristic methods, proved to be feasible and easy to implement, with low computational costs given the complexity of the problems.

Another important issue was the ease and feasibility of the computational implementation of the EED optimization problem modeling, through the use of the NSGA-II and NSGA-III. These algorithms showed that the EED multi-objective problem can be solved with a reasonable computational cost for the proposed problem.

To solve the EED MOOP, better results were also found, considering the shutdown of generators with the highest fuel costs and that are not necessary to meet the demand for active power P^D at the time of optimization. The proposal in this case proved to be efficient both for the application of the NSGA-II heuristic method, contemplating two objective functions (fuel cost and total emissions), and for the NSGA-III heuristic method, contemplating three objective functions (fuel cost, NOx emissions, and CO₂ emissions). In both cases there was a significant reduction of more than 30% in fuel and emission costs.

The new modified EED solution for shutting down generators with higher fuel costs at the time of optimization enables TPP specialists to carry out predictive maintenance on these machines that are not being used at the time of optimization, in order to improve efficiency not only in the generators, but in TPP generation planning.

Bio-inspired computing methods based on optimization techniques do not guarantee to find an optimal global solution, but produce feasible solutions at an acceptable computational cost (time), which is the reason why such techniques have been widely applied to solve the EED problem.

The positive results of this chapter, from the analysis of the application of several methods in several simulations, demonstrate the benefits of the proposed new method.

References

1. Abedin MJN et al (2013) Energy balance of internal combustion engines using alternative fuels. Centre for Energy Sciences, Faculty of Engineering, University of Malaya, 50603 Kuala Lumpur, Malaysia
2. Abou El Ela AA, Abido MA, Spea SR (2010) Differential evolution algorithm for emission constrained economic power dispatch problem. *Electr Power Syst Res* 80(10):1286–1292. 2010/10/01/. ISSN 0378-7796. Available from: <https://www.sciencedirect.com/science/article/pii/S0378779610001021>
3. Abusoglu A, Kanoglu M (2009) Exergetic and thermoeconomic analyses of diesel engine powered cogeneration: part 1 – formulations. *Appl Therm Eng* 29(2–3):234–241. ISSN 1359-4311. Available from: <http://www.sciencedirect.com/science/article/pii/S1359431108001038>

4. Ajayi O, Heymann R (2021) Day-ahead combined economic and emission dispatch with spinning reserve consideration using moth swarm algorithm for a data centre load. *Heliyon* 7(9):e08054. ISSN 2405-8440. Available from: < <https://www.sciencedirect.com/science/article/pii/S2405844021021575>
5. Alberto I, Coello CAC, Mateo PM (2014) A comparative study of variation operators used for evolutionary multi-objective optimization. *Inf Sci* 273:33–48
6. Antczak T (2011) A new characterization of (weak) Pareto optimality for differentiable vector optimization problems with *G*-invex functions. *Math Comput Model* 54(1–2):59–68. ISSN 0895-7177. Available from: <http://www.sciencedirect.com/science/article/pii/S0895717711000525>
7. Aragón VS, Esquivel SC, Coello Coello CA (2015) An immune algorithm with power redistribution for solving economic dispatch problems. *Inf Sci* 295(0):609–632. ISSN 0020-0255. Available from: <http://www.sciencedirect.com/science/article/pii/S0020025514010081>
8. Arul R, Velusami S, Ravi G (2015) A new algorithm for combined dynamic economic emission dispatch with security constraints. *Energy* 79(0):496–511. ISSN 0360-5442. Available from: <http://www.sciencedirect.com/science/article/pii/S0360544214012924>
9. Atashkari K et al (2007) Modelling and multi-objective optimization of a variable valve-timing spark-ignition engine using polynomial neural networks and evolutionary algorithms. *Energy Convers Manag* 48:1029–1041. Elsevier, 2007
10. Augusto OB, Bennis F, Caro S (2012) A new method for decision making in multi-objective optimization problems. *Pesquisa Operacional [Online]* 32. ISSN 1678-5142
11. Aydin D et al (2014) Artificial bee colony algorithm with dynamic population size to combined economic and emission dispatch problem. *Int J Electr Power Energy Syst* 54(0):144–153. ISSN 0142-0615. Available from: <http://www.sciencedirect.com/science/article/pii/S0142061513002809>
12. Barisal AK, Prusty RC (2015) Large scale economic dispatch of power systems using oppositional invasive weed optimization. *Appl Soft Comput* 29(0):122–137. ISSN 1568-4946. Available from: <http://www.sciencedirect.com/science/article/pii/S1568494614006462>
13. Basu M (2008) Dynamic economic emission dispatch using nondominated sorting genetic algorithm-II. *Int J Electr Power Energy Syst* 30(2):140–149
14. Basu M (2014a) Fuel constrained economic emission dispatch using nondominated sorting genetic algorithm-II. *Energy* 78(0):649–664. ISSN 0360-5442. Available from: <http://www.sciencedirect.com/science/article/pii/S036054421401202X>
15. Basu M (2014b) Improved differential evolution for economic dispatch. *Int J Electr Power Energy Syst* 63:855–861. ISSN 0142-0615. Available from: <http://www.sciencedirect.com/science/article/pii/S0142061514004359>
16. Bazgan C, Gourvès L, Monnot J (2013) Approximation with a fixed number of solutions of some multiobjective maximization problems. *J Discrete Algorithms* 22(0):19–29. ISSN 1570-8667. Available from: <http://www.sciencedirect.com/science/article/pii/S1570866713000439>
17. Behera S, Sahoo S, Pati BB (2015) A review on optimization algorithms and application to wind energy integration to grid. *Renew Sust Energ Rev* 48(0):214–227. ISSN 1364–0321. Available from: <http://www.sciencedirect.com/science/article/pii/S1364032115002191>
18. Caramia M, Dell’olmo P (2008) Multi-objective management in freight logistics. Springer, London., ISBN 978-1-84800-382-8
19. Carrano EG et al (2014) A multiobjective hybrid evolutionary algorithm for robust design of distribution networks. *Int J Electr Power Energy Syst* 63(0):645–656. ISSN 0142-0615. Available from: <http://www.sciencedirect.com/science/article/pii/S0142061514003810>
20. Castro ADO (2015) Otimização do Processo de Montagem de Componentes Eletrônicos de Superfície Utilizando Ferramenta Multicritério. Universidade Federal do Pará – Instituto de Tecnologia – Programa de Pós-Graduação em Engenharia Elétrica
21. Coello Coello CA (1999) An updated survey of evolutionary multiobjective optimization techniques: state of the art and future trends. In: *Proceedings of the 1999 Congress on Evolutionary Computation, CEC 99, Washington, DC, USA, 1999, Vol. 1.* p 13

22. CONAMA (2006) Resolução Conama no. 382. Publicada no DOU n° 1, de 2 de janeiro de 2007, Seção 1, p. 131–137
23. Deb K, Jain H (2014) An evolutionary many-objective optimization algorithm using reference-point-based nondominated sorting approach, part I: solving problems with box constraints. *IEEE Trans Evol Comput* 18(4):577–601. ISSN 1089-778X
24. Deb K et al (2002) A fast and elitist multiobjective genetic algorithm: NSGA-II. *IEEE Trans Evol Comput* 6(2):182–197. ISSN 1089-778X
25. Deligiannis VF, Manesis SA (2006) Modeling internal combustion engines using a hyper-class of hybrid automata: a case study. In: *Proceedings of the 2006 IEEE. Conference on Computer Aided Control Systems Design*. Munich, Germany, 4–6 October 2006
26. Destek MA (2016) Renewable energy consumption and economic growth in newly industrialized countries: evidence from asymmetric causality test. *Renew Energy* 95:478–484. ISSN 0960-1481. Available from: <http://www.sciencedirect.com/science/article/pii/S0960148116303512>
27. Dhamanda A et al (2013) A traditional approach to solve economic load dispatch problem of thermal generating unit using MATLAB programming. *Int J Eng Res Technol (IJERT)* 2(9)
28. Dhillon J, Jain SK (2011) Multi-objective generation and emission dispatch using NSGA-II. *Int J Eng Technol* 3(5):460–466
29. Dike DO, Adinfo MI, Ogu G (2013) Economic dispatch of generated power using modified lambda iteration method. *IOSR J Electr Electron Eng (IOSR-JEEE)* 7(1):49–54
30. Dincer I, Cengel Y (2001) Energy, entropy and exergy concepts and their roles in thermal engineering. *Entropy* 3(3):116. ISSN 1099-4300. Available from: <http://www.mdpi.com/1099-4300/3/3/116>
31. Du Q et al (2015) Effect of cooling design on the characteristics and performance of thermoelectric generator used for internal combustion engine. *Energy Convers Manag* 101(0):9–18. ISSN 0196-8904. Available from: <http://www.sciencedirect.com/science/article/pii/S0196890415004835>
32. Elattar EE (2015) A hybrid genetic algorithm and bacterial foraging approach for dynamic economic dispatch problem. *Int J Electr Power Energy Syst* 69(0):18–26. ISSN 0142-0615. Available from: <http://www.sciencedirect.com/science/article/pii/S0142061515000162>
33. Farhan Tabassum M et al (2021) Evolutionary simplex adaptive Hooke-Jeeves algorithm for economic load dispatch problem considering valve point loading effects. *Ain Shams Eng J* 12(1):1001–1015. ISSN 2090-4479. Available from: <https://www.sciencedirect.com/science/article/pii/S2090447920300903>
34. Fonseca C, Fleming P (1995) An overview of evolutionary algorithms in multiobjective optimization. *Evol Comput* 3(1):1–16. ISSN 1063-6560
35. Ghane-Kanafi A, Khorram E (2015) A new scalarization method for finding the efficient frontier in non-convex multi-objective problems. *Appl Math Model* (0). ISSN 0307-904X. Available from: <http://www.sciencedirect.com/science/article/pii/S0307904X15001742>
36. Ghasemi M et al (2015) Multi-objective optimal electric power planning in the power system using Gaussian bare-bones imperialist competitive algorithm. *Inf Sci* 294:286–304. ISSN 0020-0255. Available from: <http://www.sciencedirect.com/science/article/pii/S0020025514009633>
37. Gitizadeh M, Aghaei J (2014) Dynamic security consideration in multiobjective electricity markets. *Appl Soft Comput* 16:1–9, Elsevier B.V., 2013
38. Golchha A, Qureshi SG (2015) Non-dominated sorting genetic algorithm-II – a succinct survey. *Int J Comput Sci Inform Technol* 6(1):252–255
39. Gopalakrishnan R, Krishnan A (2012) An advanced genetic optimization algorithm to solve combined economic and emission dispatch problem. *Bonfring Int J Man Mach Interface* 2(1):11–19
40. He L et al (2020) Environmental economic dispatch of integrated regional energy system considering integrated demand response. *Int J Electr Power Energy Syst* 116:105525. ISSN 0142-0615. Available from: <https://www.sciencedirect.com/science/article/pii/S0142061519315352>

41. Hota PK, Barisal AK, Chakrabarti R (2010) Economic emission load dispatch through fuzzy based bacterial foraging algorithm. *Int J Electr Power Energy Syst* 32(7):794–803. ISSN 0142-0615. Available from: <https://www.sciencedirect.com/science/article/pii/S0142061510000256>
42. Hountalas DT et al (2014) Avaliação comparativa de várias metodologias para contabilizar o efeito da variação de carga durante a medição da pressão do cilindro de motores a diesel de grande porte de dois tempos. *Appl Energy* 113:1027–1042
43. http://ac.els-cdn.com/S0378779606002859/1-s2.0-S0378779606002859-main.pdf?_tid=9dea0210-cce4-11e4-aa87-00000aacb35d&acdnat=1426624480_378a4297c0fd67420a157aa134874b02
44. Idoumghar L et al (2013) Hybrid ICA–PSO algorithm for continuous optimization. *Appl Math Comput* 219(24):11149–11170. ISSN 0096-3003. Available from: <http://www.sciencedirect.com/science/article/pii/S009630031300547X>
45. Kalaivani L, Subburaj P, Willjuice Iruthayarajan M (2013) Speed control of switched reluctance motor with torque ripple reduction using non-dominated sorting genetic algorithm (NSGA-II). *Int J Electr Power Energy Syst* 53:69–77. ISSN 0142-0615. Available from: <http://www.sciencedirect.com/science/article/pii/S0142061513001646>
46. Li C (2021) Multi-objective optimization of space adaptive division for environmental economic dispatch. *Sustain Comput: Inform Syst* 30:100500. ISSN 2210-5379. Available from: <https://www.sciencedirect.com/science/article/pii/S2210537920302225>
47. Li L-L et al (2021) Improved tunicate swarm algorithm: solving the dynamic economic emission dispatch problems. *Appl Soft Comput* 108:107504. ISSN 1568-4946. Available from: <https://www.sciencedirect.com/science/article/pii/S1568494621004270>
48. Liu T, Gao X, Wang L (2015) Multi-objective optimization method using an improved NSGA-II algorithm for oil–gas production process. *J Taiwan Inst Chem Eng* (0). ISSN 1876-1070. Available from: <http://www.sciencedirect.com/science/article/pii/S1876107015002333>
49. Liu Z-F et al (2021) Dynamic economic emission dispatch considering renewable energy generation: a novel multi-objective optimization approach. *Energy* 235:121407. ISSN 0360-5442. Available from: <https://www.sciencedirect.com/science/article/pii/S0360544221016558>
50. Lora EES, Nascimento MAR (2004) Geração Termelétrica – Planejamento, Projeto e Operação. Editora Interciência, Rio de Janeiro, v. Volumes I and II, 1st edn
51. Meybodi MA, Behnia M (2011) Impact of carbon tax on internal combustion engine size selection in a medium scale CHP system. *Appl Energy* 88(12):5153–5163. ISSN 0306-2619. Available from: <http://www.sciencedirect.com/science/article/pii/S0306261911004703>
52. Mirjalili S, Lewis A (2015) Novel frameworks for creating robust multi-objective benchmark problems. *Inf Sci* 300(0):158–192. ISSN 0020-0255. Available from: <http://www.sciencedirect.com/science/article/pii/S0020025514011876>
53. Muccillo M, Gimelli A (2014) Experimental development, 1D CFD simulation and energetic analysis of a 15 kw micro-CHP unit based on reciprocating internal combustion engine. *Appl Therm Eng* 71(2):760–770. ISSN 1359-4311. Available from: <http://www.sciencedirect.com/science/article/pii/S1359431113008144>
54. Nascimento MHR et al (2016) A new solution to the economical load dispatch of power plants and optimization using differential evolution. *Electr Eng*:1–11. ISSN 1432-0487. Available from: <https://doi.org/10.1007/s00202-016-0385-2>
55. Nikhil R et al (2010) Model-based control of HCCI engines using exhaust recompression. SAE Technical Paper 2014-32-0079, 2014
56. Nwulu NI, Xia X (2015) Multi-objective dynamic economic emission dispatch of electric power generation integrated with game theory based demand response programs. *Energy Convers Manag* 89(0):963–974. ISSN 0196-8904. Available from: <http://www.sciencedirect.com/science/article/pii/S0196890414009510>
57. Palanichamy C, Babu NS (2002) Day-night weather-based economic power dispatch. *IEEE Trans Power Syst* 17(2):469–475
58. Palanichamy C., Srikrishna K. (1991) Economic thermal power dispatch with emission constraint. *J Indian Institute of Eng (India)* 72:11

59. Panigrahi BK et al (2010) Multiobjective fuzzy dominance based bacterial foraging algorithm to solve economic emission dispatch problem. *Energy* 34(12):4761–4770
60. Paul C, Roy PK, Mukherjee V (2020) Chaotic whale optimization algorithm for optimal solution of combined heat and power economic dispatch problem incorporating wind. *Renew Energy Focus* 35:56–71. ISSN 1755-0084. Available from: <https://www.sciencedirect.com/science/article/pii/S1755008420300351>
61. Postolov B, Iliev A (2022) New metaheuristic methodology for solving security constrained hydrothermal unit commitment based on adaptive genetic algorithm. *Int J Electr Power Energy Syst* 134:107163. ISSN 0142-0615. Available from: <https://www.sciencedirect.com/science/article/pii/S0142061521004026>
62. Rezaei H et al (2019) Solution of combined economic and emission dispatch problem using a novel chaotic improved harmony search algorithm. *J. Comput. Des. Eng.* 6(3):447–467. ISSN 2288-4300. Available from: <https://www.sciencedirect.com/science/article/pii/S2288430018301258>
63. Ruiz AB et al (2015) Multicriteria optimization of the investment in the auxiliary services of thermal power plants: a case study. *Energy Convers Manag* 93(0):339–348. ISSN 0196-8904. Available from: <http://www.sciencedirect.com/science/article/pii/S0196890415000345>
64. Sakthivel VP, Suman M, Sathya PD (2021) Combined economic and emission power dispatch problems through multi-objective squirrel search algorithm. *Appl Soft Comput* 100:106950. ISSN 1568-4946. Available from: <https://www.sciencedirect.com/science/article/pii/S1568494620308887>
65. Sánchez AS, Torres EA, Kalid RA (2015) Renewable energy generation for the rural electrification of isolated communities in the Amazon region. *Renew Sust Energy Rev* 49:278–290. ISSN 1364-0321. Available from: <http://www.sciencedirect.com/science/article/pii/S1364032115003457>
66. Shindell D, Smith CJ (2019) Climate and air-quality benefits of a realistic phase-out of fossil fuels. *Nature* 573(7774):408–411. ISSN 1476-4687. Available from: <https://doi.org/10.1038/s41586-019-1554-z>
67. Silva LRBD, Silva RPD (2014) Uma estratégia de implementação paralela eficiente de uma heurística de particionamento de grafos aplicados à simulação de escoamento multifásico. *Latin Am J Energy Res (Lajer)* 1:91–100
68. Srinivas N, Deb K (1993) Multiobjective optimization using nondominated sorting in genetic algorithms. *J Evol Comput* 2(3):221–248
69. Suksonghong K, Boonlong K, Goh K-L (2014) Multi-objective genetic algorithms for solving portfolio optimization problems in the electricity market. *Int J Electr Power Energy Syst* 58:150–159
70. Taghdisian H, Pishvaie MR, Farhadi F (2015) Multi-objective optimization approach for green design of methanol plant based on CO₂-efficiency indicator. *J Clean Prod* 103(0):640–650. ISSN 0959-6526. Available from: <http://www.sciencedirect.com/science/article/pii/S0959652614005009>
71. Talbi EH et al (2020) Solution of economic and environmental power dispatch problem of an electrical power system using BFGS-AL algorithm. *Procedia Comput Sci* 170:857–862. ISSN 1877-0509. Available from: <https://www.sciencedirect.com/science/article/pii/S1877050920306001>
72. Vahidinasab V, Jadid S (2008) Multiobjective environmental/techno-economic approach for strategic bidding in energy markets. *Appl Energy* 86:96–104
73. Wall G, Gong M (2001) On exergy and sustainable development, part I: conditions and concepts. *Exergy* 1(3)
74. Wang L, Singh C (2007) Environmental/economic power dispatch using a fuzzified multi-objective particle swarm optimization algorithm. *Electr Power Syst Res* 77:1654–1664. ISSN 0378-7796. Available from: <http://www.sciencedirect.com/science/article/pii/S0378779606002859>

75. Xin-Gang Z et al (2020) An improved quantum particle swarm optimization algorithm for environmental economic dispatch. *Expert Syst Appl.* 152:113370. ISSN 0957-4174. Available from: <https://www.sciencedirect.com/science/article/pii/S0957417420301950>
76. Yalcinoz, T., Altun, H. Environmentally constrained economic dispatch via a genetic algorithm with arithmetic crossover. In: *Africon Conference in Africa, 2002*. IEEE AFRICON. 6th, 2–4 October 2002. p. 923–928, vol. 2
77. Ying-Tung H et al (1994) A computer package for optimal multi-objective VAR planning in large scale power systems. *IEEE Trans Power Syst* 9(2):668–676. ISSN 0885-8950
78. Yokoyama R et al (1988) Multiobjective optimal generation dispatch based on probability security criteria. *IEEE Trans Power Syst* 3(1):317–324. ISSN 0885-8950
79. Zhoua A et al (2011) Multiobjective evolutionary algorithms: a survey of the state of the art. *Swarm Evol Comput* 1(1):32–49

A Stochastic Multi-period Transmission Expansion Planning Using Whale Optimization Algorithm



Mohamed M. Refaat, Muhyaddin Rawa, Yousry Atia, Ziad M. Ali, Shady H. E. Abdel Aleem , and Mahmoud M. Sayed

1 Introduction

1.1 Literature Review

Transmission network expansion planning (TEP) is a strategy to decide where, when, and how many transmission facilities are needed to extend the current power system transmission network [1]. TEP strategy always comprises economic and technical plans. The objective of the economic plan is to transport energy to distribution networks and load sites with low investment costs, whereas the technical

M. M. Refaat (✉) · Y. Atia
Photovoltaic Cells Department, Electronics Research Institute, Cairo, Egypt
e-mail: mrefaat@eri.sci.com

M. Rawa
Center of Research Excellence in Renewable Energy and Power Systems, King Abdulaziz University, Jeddah, Saudi Arabia

Department of Electrical and Computer Engineering, Faculty of Engineering, King Abdulaziz University, Jeddah, Saudi Arabia
e-mail: mrawa@kau.edu.sa

Z. M. Ali
Electrical Energy Department, College of Engineering, Prince Sattam Bin Abdulaziz University, Wadi Addawaser, Saudi Arabia
e-mail: dr.ziad.elhalwany@aswu.edu.eg

S. H. E. Abdel Aleem
Electrical Engineering Department, Valley High Institute of Engineering and Technology, Science Valley Academy, Qalubia, Egypt
e-mail: engyshady@ieec.org

M. M. Sayed
Electrical Power Department, Faculty of Engineering, Cairo University, Giza, Egypt

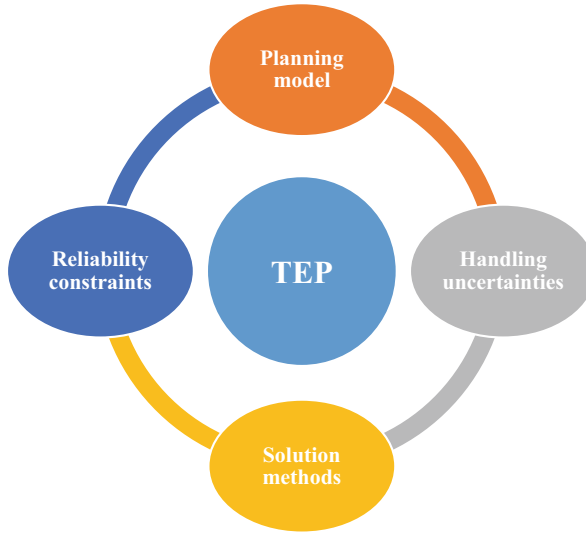


Fig. 1 Main factors impacting TEP

plan strives to keep power systems reliable at a reasonable level. Regarding the risks that threaten the transmission network, investors will be more interested in a strategy that has a lower investment risk and a better rate of return [1, 2].

TEP has been widely studied in the literature from different aspects such as the planning model, handling uncertainties, system reliability, and solution methods as shown in Fig. 1. Static or dynamic TEP-based AC or DC power flow models are commonly used to formulate TEP problems [1, 2]. In the static TEP (STEP) approach, the location and number of new lines are determined based on the demand for electrical power at the end of the planning horizon [1]. However, the planning horizon is divided into several time intervals in the dynamic TEP (DTEP) to take into account features such as annual load growth, inflation rate, market behavior, and environmental change, which lead to a more accurate and realistic assessment of the network. The implementation of DTEP increases the complexity and need for high computational effort

The ACTEP is a comprehensive and realistic model; however, it translates into a non-linear large-scale optimization problem [3]. DCTEP, in contrast to ACTEP, omits reactive power and transmission losses and assumes the buses' voltage is at its nominal value (1 pu) [4, 5]. As a result, the DCTEP model is linear and simple, but it has low accuracy compared to the AC model [3, 6].

The electric power system is not deterministic. Hence, the power system's uncertainties are yet another feature that must be considered in the TEP model [7]. Uncertain events, such as stochastic behavior of electrical loads and contingencies related to transmission lines and generation units, always occur randomly in an unexpected way [8, 9]. Furthermore, the output energy of renewable generation

sources (RGSs) like wind and PV units is highly unpredictable. RGSs, if widely used, might have a significant impact on power system operations and erode grid resilience. It is commonly treated loads and generation units as deterministic parameters in the traditional TEP models. Although the deterministic approach simplifies the problem, it fails to represent the random nature of the real power system and may produce unrealistic plans. In this regard, current research has focused on tackling this issue [7–9].

Stochastic and robust optimization approaches are commonly applied to deal with the system's uncertainties. The stochastic optimization approach specifically relies on an accurate probability distribution function (PDF) of the uncertain element. This approach has some limitations concerning large-scale power systems. For example, a precise PDF of the uncertainty element may be difficult to determine. A large number of scenario samples are also required to obtain reasonable accuracy, leading to an intense computational problem [9]. The robust programming methodology, on the other hand, does not require the precise PDF of uncertain variables, but rather merely the bound of uncertainty. As a result, this strategy will be extremely useful when the whole PDF of uncertain parameters is not provided [8, 9]. In other words, stochastic parameters take values inside an uncertainty set, and the solution to an optimization issue must be feasible in the worst case. As a result, the goal of this approach is to optimize the objective function under the worst-case realization of uncertainty [89].

Organizations, like the North American Electrical Reliability Corporation, have issued a set of guidelines to be adhered to by all to ensure the power network's reliability [10]. TEP models frequently have N-1 security, stability, and short circuit limiting constraints to maintain reliability [3, 4, 11, 12]. Energy storage systems and demand response programs are the most widely used sources of flexibility and reliability to achieve this objective [6, 13]. Both have demonstrated their capabilities in energy management roles, stabilizing the system and enhancing the reliability of the system as a whole, especially in the presence of RGSs. High voltage DC systems, thyristor-controlled compensators (TCCs), and phase-shifting transformers have been also used as power flow control technologies [3, 14]. Using these devices has allowed the system planner to achieve reliability at the lowest possible cost. On the other hand, the allocation of fault current limiters (FCLs) has recently been incorporated into the planning model to limit the short-circuit current to a pre-set value so that current protection devices are not replaced [3].

Because of the non-linearity of TEP's mathematical model, it poses various problems for system planners. The feasible search space for this decision-making problem is typically large, non-convex, and challenging to explore since it is characterized as a mixed-integer nonlinear programming (MINLP) optimization problem [1, 2]. Therefore, selecting a suitable solution method is a challenge facing the system planner to deal with the model's non-linearity and obtain the optimal configuration of the system. Several models and tools are used in the literature and can be organized into three classes: (1) mathematical, (2) heuristic, and (3) meta-heuristic methods.

Mathematical optimization methods are especially useful in solving simple and linear optimization problems with a relatively small search area. However, in combination with explosion problems with large search space, these methods require a high computational burden [3, 6, 12]. Furthermore, mathematical techniques could not guarantee the global optimum of a problem if non-convexities are contained within the search space. The implementation of a branch and bound (B&B) algorithm has been expressed by Lee et al. [15] to solve the MILP model. The B&B succeeds to solve the problem, but it slowly converges to the optimal solution and needs high computational efforts. Granville et al. [16] have introduced the bender decomposition technique (BD) to solve a STEP problem. This method is criticized because it does not guarantee convergence to optimal solutions. Romero et al. [17] have presented a hierarchical decomposition-based method to tackle this problem. In Alizadeh et al. [18], the BD method has been applied to solve a MILP model, taking into account generation reliability. The application of a branch-and-cut BD technique has been also introduced in Huang et al. [19] to solve the TEP problem. In addition, a modified scheme-based BD has been applied in Esmaili et al. [3] to solve a MILP model including FCLs and TCCS allocation. The adopted scheme has succeeded in reaching the best solution with low linearization errors as little time as possible compared to the other methods. A mixed-binary linear programming model has been introduced by Vinasco et al. [20] to solve the expansion problem. It is formulated as STEP in the first step, and then the results of STEP are applied to the DTEP problem in another step. As a result, the search space and the computing time of the solution algorithm are minimized. Özdemir et al. [21] have developed a hybrid approach that combines linear programming with the Gauss-Seidel method to solve a large-scale STEP problem.

In heuristic methods, streamlined procedures are employed to identify the best solutions. They have the advantage of being much computationally simpler, but they cannot guarantee either high quality or optimum solutions. Sensitivity analysis has been introduced by Pereira et al. [22] to solve the STEP problem. This approach saves time in contrast to mathematical methods, but its implementation on large-scale networks is difficult. A DTEP-based constructive heuristic algorithm has been presented by Romero et al. [23]. Moreover, Sousa et al. [24] have developed an algorithm that combines a fuzzy system with a B&B algorithm to solve a STEP problem. This approach has succeeded in obtaining high-quality solutions. A candidate line selection technique for TEP has been addressed by Zhang et al. [25]. This method has proved to be highly effective and accurate in finding optimal planning for large networks.

Meta-heuristic methods involve implementing heuristic techniques iteratively to find the optimal solution, using smart criteria. They need a higher computational effort, but they can lead to better solutions compared to heuristic algorithms [1, 26]. In contrast to mathematical approaches, meta-heuristic algorithms aim to get high-quality solutions with less computational burden, but they cannot ensure the global optimum [1]. Moreover, if they are unable to discover a solution, it is unclear if this is due to no possible solutions or to the algorithm's inability to locate one. Recently, several meta-heuristic approaches have been applied in the area

of TEP and can be categorized into four main groups. The first group comprises evolutionary algorithms such as genetic algorithms (GA) [26–28] and differential evolution [4, 26]. The second group includes swarm-based algorithms such as particle swarm optimization (PSO) [5, 29–32]. Human-based methods like a tabu search algorithm (TS) form the third group [33]. Whilst the fourth group involves physics-based techniques [34], Da Silva et al. [27] have introduced an improved GA to solve TEP problems. The extended GA (EGA) has been also employed by Escobar et al. [28] to determine the DTEP's projects. This sophisticated type of GA can find high-quality topologies for large-scale and high-complexity systems. A TEP-based discrete particle swarm optimization (DPSO) approach has been presented by Shayeghi et al. [29]. DPSO utilizes swarm intelligence and is regarded as a useful tool for solving many engineering problems. Nevertheless, it may fall into local optimums. An improved DPSO with mutation based on the similarity method has been presented by Shayeghi et al. [30] to resolve this shortcoming. In Torres et al. [31] and Huang et al. [32] the improved local PSO and the multi-group PSO algorithms have been implemented to solve the STEP problem, respectively. In addition, Da Silva et al. [33] have presented a TS-based method to reduce the investment cost in TEP. TS approach is feasible and powerful to solve the STEP problem. In Refaat et al. [4], DTEP and STEP using the success-history-based differential evolution with semi-parameter adaptation hybrid-covariance matrix adaptation evolution strategy algorithm (LSHADE-SPACMA) have been presented. The results have showed that LSHADE-SPACMA achieves superiority over the integer-based particle swarm optimization (IBPSO) technique [5], and the multiverse optimization (MVO) technique [34]. Shaheen et al. [35] have proposed the binary and integer coded backtracking search algorithm (CBSA) for solving the STEP. The results have demonstrated that the BSA outperforms IBPSO, and MVO in the area of TEP, while LSHADE-SPACMA still gives better performance compared to integer and binary CBSA.

In this chapter, a stochastic multi-period TEP model (SMTEP) for power systems planning is adopted. The whale optimization algorithm (WOA) is applied to solve the proposed problem. The WOA has been developed by Mirjalili et al. [36], and it has proven to be efficient in solving many complex problems. A reduction technique and an acceleration scheme are incorporated with the WOA to enhance its performance and to reduce the computational time. The WOA's efficacy is first validated to solve TEP and compared to LSHADE-SPACMA, IBPSO, MVO, and the binary and integer CBSA. Then, the impact of considering the system's uncertainties and N-1 reliability constraints in the planning model is introduced. All case studies are carried out on the Garver system and an equivalent system to the transmission network of West Delta (WDN) in Egypt.

The rest of this chapter is organized as follows: the problem formulation is presented in Sect. 12.2. The solution approach and the application of WOA for solving SMTEP are introduced in Sects. 12.3 and 12.4, respectively. Section 12.5 represents the numerical results, and the chapter is concluded in Sect. 12.6.

2 Problem Formulation

The SMTEP problem aims to minimize the total investment and operating costs and load shedding (LS), and to satisfy all the system's constraints. Due to the problem's complexity, the DC model is applied in this chapter [4].

The SMTEP problem is typically formulated as an optimization problem with an objective function and a set of constraints. The SMTEP model considering N-1 reliability and the LS is given as follows:

$$\text{Min. } F_1 + F_2 + F_3 \quad (1)$$

$$F_1 = \sum_{S=1}^{N_y} \sum_{i=1, j=1, i \neq j}^{i=n, j=n, i \neq j} \frac{C_{ij} (N_{ij}^s - N_{ij}^{s-1})}{(1 + \lambda)^{S-1}} \quad (2)$$

$$F_2 = \sum_{S=1}^{N_y} \sum_{i=1}^{i=n_D} \frac{C_r r_i}{(1 + \lambda)^{S-1}} \quad (3)$$

$$F_3 = \sum_{S=1}^{N_y} \sum_{i=1}^{i=n_G} \frac{C_{op,i} (P_{g,i}^s + P_{R,i}^s)}{(1 + \lambda)^{S-1}} \quad (4)$$

$$N_{G,i}^s (P_{g,i}^s + P_{R,i}^s) - P_{d,i}^s = \sum_{\substack{i, j \in N \\ i \neq j}} P_{ij}^s, \quad (5)$$

$$- P_{ij}^{\max} \leq \beta_{ij} N_{ij}^s (\theta_i^s - \theta_j^s) \leq P_{ij}^{\max}, \quad (6)$$

$$\theta_i^{\min} \leq \theta_i^s \leq \theta_i^{\max}, \quad (7)$$

$$P_{R,i}^{\min} \leq P_{R,i}^s \leq P_{R,i}^{\max}, \quad (8)$$

$$P_{g,i}^{\min} \leq P_{g,i}^s \leq P_{g,i}^{\max}, \text{ and} \quad (9)$$

$$N_{ij}^{s-1} \leq (N_{ij}^{\text{new},s}) \leq N_{ij}^{\max} \quad (10)$$

$$N_{G,i}^s \left(P_{g,i}^s + P_{R,i}^s \right) - P_{d,i}^s + r_i^s = \sum_{\substack{i, j \in N \\ i \neq j}} P_{ij}^s, \quad (11)$$

$$- P_{ij}^{\max} \leq \beta_{ij} \left(N_{ij}^s - 1 \right) \left(\theta_i^s - \theta_j^s \right) \leq P_{ij}^{\max}, \text{ and} \quad (12)$$

$$0 \leq r_i^s \leq P_{d,i}^s. \quad (13)$$

Where N_{ij}^s and N_{ij}^{s-1} are the total number of circuits between nodes i and j in scenarios S and $S - 1$, respectively. C_{ij} is the investment cost of installing a circuit between nodes i and j , while C_r is the penalty cost due to load shedding (\$/MW). $C_{op, i}$ is the operating cost of generation units (\$/MWh). $P_{g,i}^s$ and $P_{R,i}^s$ are the generated active power of thermal units and RGS, respectively (MW). $P_{d,i}^s$ and r_i^s are the load demand (MW) and the amount of load shedding (MW) at node i . θ_i^s and θ_j^s are the bus voltage angle for nodes i and j , respectively. P_{ij}^s is the power pass through-line between nodes i and j (MW). β_{ij} is the susceptance of the line between nodes i and j . The subscript max and min, respectively, represent the maximum and the minimum values for a variable.

The objective function (1) covers the cost due to the investment in new transmission lines as well as the operating cost and the cost of LS required to achieve the N-1 security. The planning horizon is split into many time intervals, and the planning cost in each interval is reasonably transferred to the base period using an interest rate λ .

Equations (5–10) represent the investment and operating constraints. Equations (5) and (6), respectively, limit the active power balance at bus i and power flows through transmission lines. While the voltage angles at bus i , the capacity of clean and thermal stations, number of circuits in each corridor are restricted by (7–10). The reliability constraints are represented in (11) to (13). Equations (11–12) show the nodal and power flow constraints to satisfy N-1 reliability, whilst (13) limits the LS at each bus.

3 Solution Approach

3.1 Proposed Model

The SMTEP problem in (1–13) is reformulated to a bi-level problem. The master problem determines TEP projects and calculates the LS to satisfy the N-1 reliability constraint as shown in (14–15). Whilst (16–17) represents the sub-problem that concerns the generation operating cost. The WOA is applied to solve the master problem, and the operating cost is obtained from DC optimal flow using MAT-

POWER toolbox [37].

$$\text{Min. } F_1 + F_2 \quad (14)$$

$$\text{s.t. (10), and (13)} \quad (15)$$

$$\text{Min. } F_3 \quad (16)$$

$$\text{s.t. (5)–(9), and (11)–(12)} \quad (17)$$

The proposed approach to solve the SMTEP problem is depicted in Fig. 2. It begins with selecting scenarios that represent the power system's uncertainties and defining the number of planning stages (*max_stage*). After that, branches, generation, and load data are prepared for the selected system. For each scenario, the WOA optimizes the number and the location of new circuits, and the generators dispatching are controlled using the MATPOWER toolbox [37]. The cost function is then calculated using (14). If the candidate solution does not fulfill the model constraints, it will be assigned at a higher cost. The preceding steps are repeated until the stopping criterion is achieved. This process is conducted for each stage.

3.2 Stochastic Model

The uncertainties in power systems relate to the daily variation of electrical demand and output power at each node. They are represented by scenarios that depict the hourly operating condition at each stage. Taking into account the 8760 hours of each stage in the proposed model increases the problem's complexity. As a result, using a clustering technique, the fuzzy C- means (FCM) algorithm [38, 39], the 8760 hours of the year are reduced to a smaller number of representative hours (e.g., 24). The number of representative hours should be chosen in such a way that it does not affect the accuracy of the planning [40].

The selected scenarios are represented by a matrix (S). Each row in S states the wind speed, solar radiation, temperature, and the percentage of the load for each scenario. Using the data given in S , the output power of wind turbines (WT) and PV units are given by (18) and (19) [41].

$$P_w^s(v_w^s) = \begin{cases} 0, & \text{for } v_w^s < v_w^{\text{in}} \text{ and } v_w^s > v_w^{\text{out}} \\ P_w^r \left(\frac{v_w^s - v_w^{\text{in}}}{v_w^r - v_w^{\text{in}}} \right), & \text{for } v_w^{\text{in}} \leq v_w^s \leq v_w^r \\ P_w^r, & \text{for } v_w^r \leq v_w^s \leq v_w^{\text{out}} \end{cases} \quad (18)$$

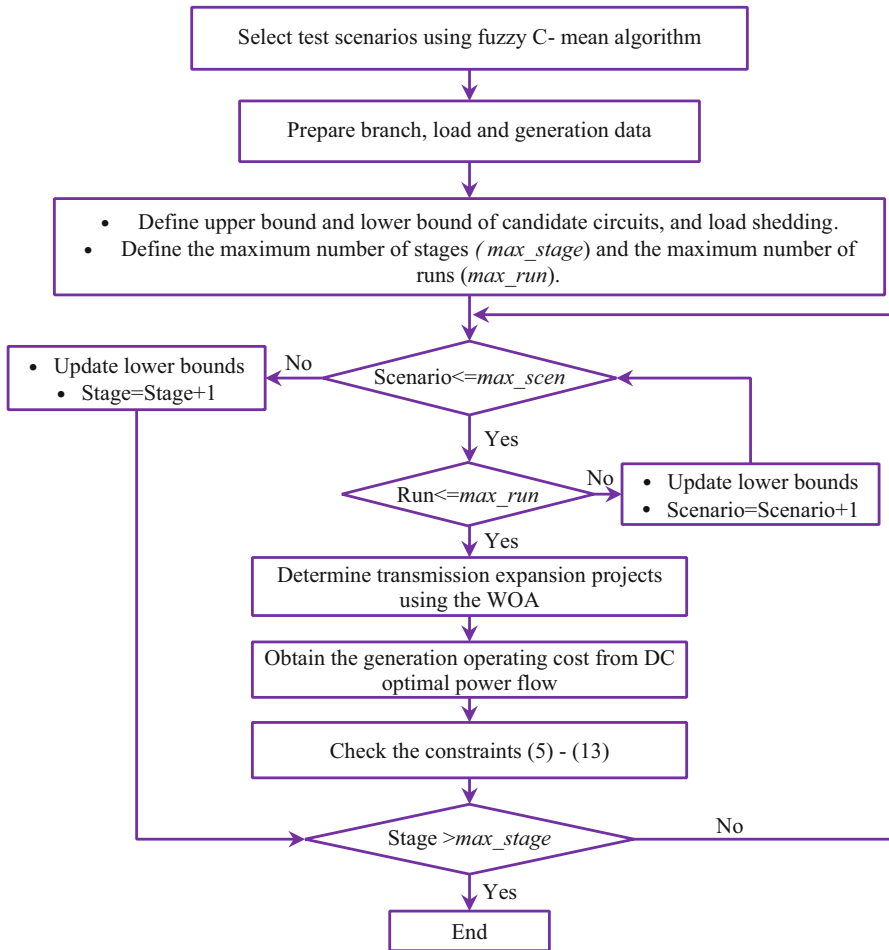


Fig. 2 The proposed approach to solve SMTEP

$$P_{PV}^s(G_s) = \begin{cases} P_{PV}^r \left(\frac{G_{PV}^s}{G_{std} R_c} \right)^2, & \text{for } 0 < G_s < R_c \\ P_{sr} \left(\frac{G_{PV}^s}{G_{std}} \right), & \text{for } G_s \geq R_c \end{cases} \quad (19)$$

where P_w^r and P_{PV}^r are the WT and PV units' rated powers. v_w^s , v_w^r , v_w^{in} , and v_w^{out} are the speed of WT at scenario s , rated speed, and cut-in and cut-out speeds of the WT, respectively. While G_{PV}^s is the solar irradiance, and G_{std} and R_c are set as 1000 and 120 W/m² [41].

• **Fuzzy C- Mean Algorithm**

In this study, a clustering technique known as the FCM method is applied to compile scenarios that represent the hourly variation of load and generation (Y) in a number of (y) groups. This method has been first developed by Dunn [38] and improved by Bezdek [39]. The data to be clustered is collected in a matrix M that has a set of column vectors m_j where $j \in \{1, 2, \dots, Y\}$. Two parameters are required by FCM clusters to group M : y and the component of fuzziness (d), where $d \in k$, and $d > 1$. The process is terminated if a pre-defined tolerance (eps) is reached. The adopted clustering technique undergoes the following steps [40]:

Step 1: A membership matrix ($k = [k_{ij}]_{y \times Y}$) is initialized randomly where the sum of each column j in k must equal to 1. y random centroids are chosen from the data. These centroids are gathered in a vector= $[y_i]_{1 \times y}$

Step 2: the new centroids are given by (20):

$$y_i = \frac{\sum_{j=1}^Y k_{ij}^d \times m_j}{\sum_{j=1}^Y k_{ij}^d} \tag{20}$$

Step 3: the membership matrix is calculated ($k = [k_{ij}]_{y \times Y}$) for each element in M , where:

$$k_{ij} = \frac{1}{\sum_{p=1}^y \left(\frac{\|m_j - y_i\|}{\|m_j - y_p\|} \right)^{\frac{2}{d-1}}} \tag{21}$$

Step 4: Determine $f_{\text{FCM}}^{(n)} = \sum_{j=1}^Y \sum_{i=1}^y k_{ij}^d \|m_j - y_i\|$, where $f_{\text{FCM}}^{(n)}$ shows the objective function value at the n th iteration.

Step 5: If $\|f_{\text{FCM}}^{(n)} - f_{\text{FCM}}^{(n-1)}\| < \text{eps}, \forall n$, terminate the optimization procedure, otherwise, the procedure is repeated starting from Step 2.

4 Application of WOA for Solving SMTEP

The inspiration and the mathematical model of WOA have been introduced in [36]. It is based on the idea of the hunting behavior of humpback whales to chase their prey using a unique bubble net attacking mechanism. The foraging is sought by creating distinct bubbles along a circle or path in the form of a “9.” It’s a unique behavior that can only be observed in humpback whales. WOA, similar to any meta-heuristic algorithm, begins with the process of initialization, followed by updates of decision variables and checking constraints, and then ends with the evaluation process. A reduction technique and an acceleration scheme are adopted in this

work to accelerate the convergence to the optimal solution and to decrease the computation time. SMTEP based WOA algorithm can be applied as follows:

Step 1: The whales' population vector x^t is randomly generated considering the lower and upper bounds of decision variables. Afterward, the fitness of each search agent $f_{i,j}^t$ is calculated. The search agent gives the minimum value is considered the best search agent and assigned with x_j^{t*} .

Step 2: Each search agent (x_j^t) in the population (x^t) is updated using (22). The former updating process is called the shrinking encircling mechanism and the spiral model.

$$x_j^{t+1} = \begin{cases} x_j^{t*} - A \cdot D_1, & \text{if } |A| < 1 \text{ and } p < 0.5 \\ x_{j,\text{rand}}^t - A \cdot D_2, & \text{if } |A| \geq 1 \text{ and } p < 0.5 \\ D \cdot e^{bl} \cdot \cos(2\pi l) + x_j^{t*}, & \text{if } p \geq 0.5 \end{cases} \quad (22)$$

p is a random number in $[0,1]$. D_1 and D_2 indicate the distance of i th whale to the prey (best solution obtained so far) and are calculated as follows:

$$D_1 = \left| C \cdot x_j^{t*} - x_j^t \right| \quad (23)$$

$$D_2 = \left| C \cdot x_{j,\text{rand}}^t - x_j^t \right| \quad (24)$$

D equals $\left| x_j^{t*} - x_j^t \right|$ and b is a constant for defining the shape of the logarithmic spiral, l is a random number in $[-1,1]$, and \cdot is an element-by-element multiplication.

Where A and C are coefficient vectors, x_j^{t*} is the position vector of the best solution obtained so far, and x_j^t is the position vector. The vectors A and C are calculated as follows:

$$A = 2a \cdot r - a \quad (25)$$

$$C = 2 \cdot r \quad (26)$$

where a is linearly decreased from 2 to 0 over the course of iterations (in both exploration and exploitation phases), and r is a random vector in $[0,1]$.

Step 3: Regarding generation units' output obtained by DC-optimal power flow, the DC power flow ($PF_i^{j,t+1}$) is calculated for each individual in the population using the MATPOWER toolbox [37], considering the system configuration under the updated variables.

Step 4: Reduce the number of circuits of each population using the following reduction formula applied in Fathy et al. [5]:

$$x_i^{j,t+1} = \frac{|\text{PF}_i^{j,t+1}|}{\text{PF}_i^{j,\text{MAX}}} \quad (27)$$

Where, $\text{PF}_i^{j,\text{MAX}}$ is maximum power can flow in the circuit i .

Step 5: Repeat Step 3 to check the constraints (5–7).

Step 6: To check the reliability constraints, an acceleration scheme is applied to speed up the convergence to the final solution. It can be summarized as follows. A binary index, indicating whether the line will participate in the N-1 contingency or not, is defined for each individual in the population. During the analysis, if the outage of a line (i) in the individual (j) does not meet power flow and generation constraints, the analysis is terminated. After that, a high penalty cost is assigned to this individual. A complete N-1 analysis was not performed for all individuals in the population by adding this function to the algorithm. Hence, the computational burden and the consumed time are reduced.

Step 7: For each individual in the population, the fitness value is calculated and compared with the best fitness. If the individual's fitness is better, it will be assigned with x_j^{t*} .

Step 8: Steps from 2 to 7 are repeated till the stop criterion is reached.

5 Results and Discussion

5.1 Validation of WOA in Solving TEP

To validate the WOA in solving TEP, it is implemented to identify the optimal configuration of the Garver system and the WDN, and the results are compared with the results introduced in the literature. The results are determined over 10 separate runs by MATLAB r2017a on a DELL PC, with a model name of OptiPlex7050, having an Intel® Core™ i7' CPU at 2.6 GHz and 16 GB RAM.

Garver system is a benchmark system and is composed of 3 generation units, 6 existing transmission lines, and 15 candidate lines, see Fig. 3 [5]. The dotted line in Fig. 3 represents candidate elements, and the solid line represents existing elements.

The initial configuration of WDN comprises 8 generating units, 52 loads, and 55 transmission lines as shown in Fig. 4 [5]. Regarding the prospective transmission projects, 31 candidates' lines are proposed to reinforce the network and incorporate additional links in the transmission system to supply the demand centres in the period 2016–2030. In terms of potential generation projects, it is planned for WDN to integrate a thermal unit at node 53.

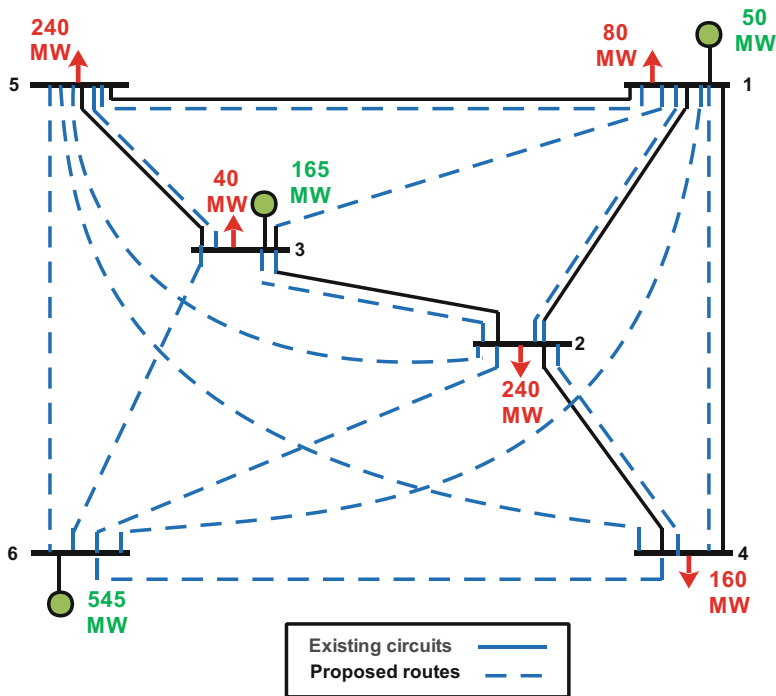


Fig. 3 Initial configuration of Garver system [5]

For both systems, the data are gathered from the databases provided in Fathy et al. [5]. Operating costs of power plants are reported in Saboori et al. [42].

• **TEP for Garver Network**

The STEP with and without including N-1 security is introduced in Table. 1. The WOA succeeds to get the same configuration proposed in Fathy et al. [5] and Silva et al. [43]. The convergence curves for WOA in both cases are depicted in Figs. 5 and 6, respectively. It may therefore be stated that the WOA is an effective algorithm for obtaining the optimal TEP of small-scale systems. Seven circuits are proposed for 200 million USD on the candidate paths 3-5, 2-6, and 4-6 if the N-1 security is ignored in the model. However, if reliability constraints are taken into account, ten circuits are proposed for 298 million USD on routes 3-5, 2-6, 3-6, and 4-6. This means that there is a 49% increase over the non-secure configuration. The secure plan requires three additional singular circuits on paths 3-6, 4-6, and 3-5 to satisfy the N-1 security. Neglecting this kind of constraints results in decreasing the economic cost, but the system becomes more susceptible to technical issues that may lead to rolling blackouts.

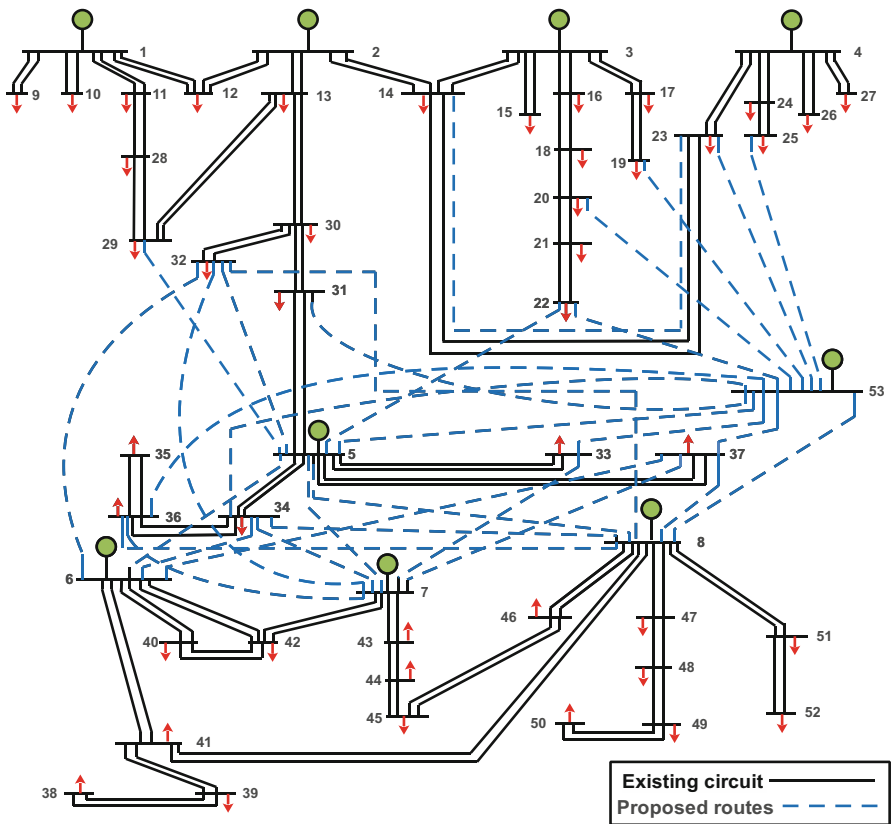


Fig. 4 Initial configuration of WDN [5]

• **TEP for WDN**

The STEP and DTEP for WDN are summarized in Tables 2 and 3, respectively. The WOA’s convergence curve to find the STEP’s optimal solution is illustrated in Fig. 7. The results of STEP are compared with results introduced in Refaat et al. [4], Fathy et al. [5], Shaheen et al. [34], and Shaheen et al. [35]. The configurations of WDN using WOA and LSHADE-SPACMA are identical and economically better than systems obtained by IBPSO, MVO, and integer and binary CBSA. Both WOA and LSHADE-SPACMA achieve investment costs of 17.28 million USD, whereas STEP projects using IBPSO, MVO, integer CBSA, and binary CBSA cost 22.19, 20.64, 18.605, and 18.455 million USD; respectively. WOA surpasses LSHADE-SPACMA in fast convergence to the optimal value. The WOA needs 115.1 s, while the LSHADE-SPACMA needs 164.78 s.

The DTEP for WDN listed in Table 3 is compared with the planning suggested in Refaat et al. [4]. The present study is concerned with in the results between 2016

Table 1 STEP for Garver system using WOA, IBPSO [5], and Ref. [43]

Candidate line	Without N-1 security		With N-1 security	
	WOA	IBPSO [5]	WOA	Ref. [43]
1-2	1	1	1	1
1-4	1	1	1	1
1-5	1	1	1	1
2-3	1	1	1	1
2-4	1	1	1	1
3-5	2	2	3	3
1-3	0	0	0	0
1-6	0	0	0	0
2-5	0	0	0	0
2-6	4	4	4	4
3-4	0	0	0	0
3-6	0	0	1	1
4-5	0	0	0	0
4-6	2	2	3	3
5-6	0	0	0	0
Added circuits	7	7	10	10
TEP cost (million USD)	200	200	298	298
Calculation time (sec)	4.2	NI*	9.3	NI

NI* not introduced

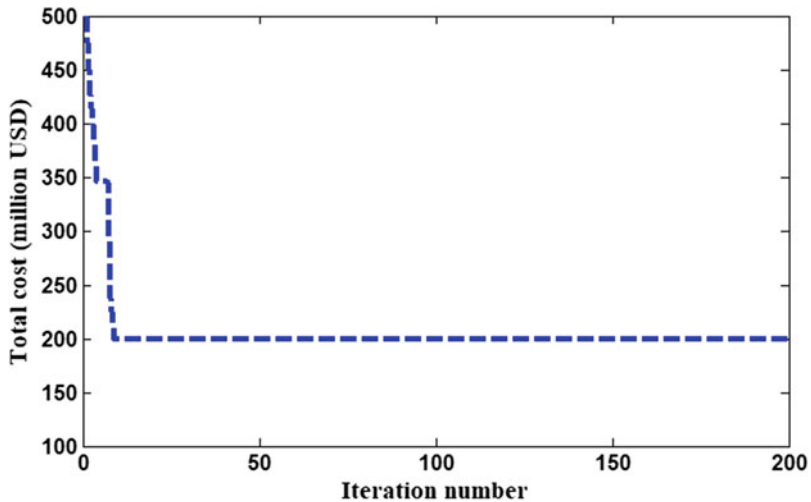


Fig. 5 Convergence curve of WOA during solving STEP for Garver system

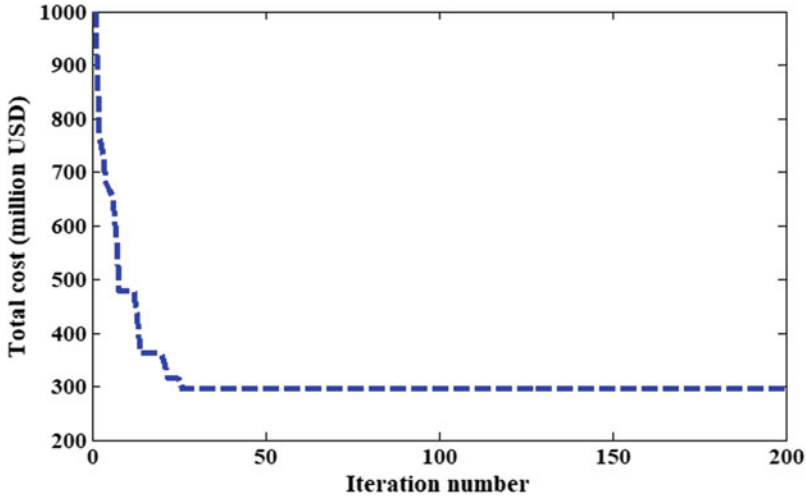


Fig. 6 Convergence curve of WOA during solving STEP for Garver system (N-1 security)

and 2030. The planning horizon is divided into three stages. Each stage consists of 5 years, and the interest rate is 0.2.

Regarding the WOA's results, two circuits, with investment costs of 2.45 million USD, are added at routes 6–34 and 5–53 to supply the predicted loads in the year 2020. While four circuits, with investment costs of 7.375 million USD on the routes 5–6, 33–53, and 5–53, are needed in the year 2025. At the end of the planning period, two circuits cost 4.305 million USD are suggested to be installed on routes 36–53. The WOA locates the optimal solution for a small number of runs. Figure 8 shows the WOA's convergence curves for the three stages.

The LSHADE-SPACMA, on the other hand, finds routes 6–34, 23–53, and 5–53 are the three vital options to add three circuits with investment costs of 4.71 million USD in the first stage. Moreover, three circuits with investment costs of 7.32 million USD, and two circuits with investment costs of 3.42 are established in the second and the third stages, respectively.

It is obvious that WOA, over the planning horizon, presents DTEP projects with a cost of 14.13 million USD which is lower than the DTEP's cost given by LSHADE-SPACMA. Based on the above stated, it can be concluded that WOA is an effective technique and outperform LSHADE-SPACMA in solving TEP problems.

Regarding the STEP and the DTEP for the WDN, the findings reveal that an additional circuit is required on routes 5–6, 6–34 for DTEP, whereas no circuits are needed on route 20–53. This difference is attributed to the fact that DTEP takes into account the time value of the money and the annual load growth, as illustrated in (1–4). In the first stage, the installation of circuits on routes 6–34 and 5–53 are essential to supply the loads in the best way that achieves the technical and economic requirements. Therefore, these circuits are a part of the system and are relied upon in the planning of the second stage. Similarly, the third stage depends on the data of

Table 2 STEP for WDN using WOA and some algorithms in the literature

Candidate lines	IBPSO [5]	MVO [34]	Integer CBSA [35]	Binary CBSA [35]	LSHADE-SPACMA [4]	WOA
5-6	0	0	0	0	1	1
5-7	0	0	0	1	0	0
5-8	0	0	0	0	0	0
5-22	1	0	0	0	0	0
5-29	0	0	0	0	0	0
5-32	0	0	0	0	0	0
6-32	0	0	0	0	0	0
6-34	2	1	1	1	0	0
6-37	0	0	0	0	0	0
7-32	0	0	1	0	0	0
7-33	0	0	0	0	0	0
7-34	0	0	0	0	0	0
7-36	0	1	0	0	0	0
7-37	0	0	0	0	0	0
8-38	0	0	0	0	0	0
8-33	0	0	0	0	0	0
8-34	0	0	0	0	0	0
8-36	0	0	0	0	0	0
8-37	0	0	0	0	0	0
25-53	0	0	0	0	0	0
23-53	0	0	0	0	0	0
22-53	0	1	1	0	0	0
19-53	0	0	0	0	0	0
37-53	0	1	0	0	0	0
33-53	2	1	1	1	1	1
5-53	0	0	2	2	2	2
31-53	0	0	0	0	0	0
34-53	2	1	0	0	0	0
36-53	2	2	2	2	2	2
20-53	0	0	0	2	1	1
8-53	0	0	0	0	0	0
TEP cost (million USD)	22.19	20.64	18.605	18.455	17.28	17.28
Calculation time (s)	NI	NI	NI	NI	164.78	115.1

the second stage to obtain the final configuration of the system. The DTEP is more realistic because it is not practical to install all TEP's projects in 1 year, and they also should be constructed at intervals to meet the annual load growth.

Table 3 DTEP for WDN using WOA and LSHADE-SPACMA

Candidate line	WOA			LSHADE-SPACMA [4]		
	Stage number			Stage number		
	1	2	3	1	2	3
5-6	0	2	2	0	1	0
5-7	0	0	0	0	0	0
5-8	0	0	0	0	0	0
5-22	0	0	0	0	0	0
5-29	0	0	0	0	0	0
5-32	0	0	0	0	0	0
6-32	0	0	0	0	0	0
6-34	1	1	1	1	1	1
6-37	0	0	0	0	0	0
7-32	0	0	0	0	0	0
7-33	0	0	0	0	0	0
7-34	0	0	0	0	0	0
7-36	0	0	0	0	0	0
7-37	0	0	0	0	0	0
8-38	0	0	0	0	0	0
8-33	0	0	0	0	0	0
8-34	0	0	0	0	0	0
8-36	0	0	0	0	0	0
8-37	0	0	0	0	0	0
25-53	0	0	0	0	0	0
23-53	0	0	0	1	1	1
22-53	0	0	0	0	0	0
19-53	0	0	0	0	0	0
37-53	0	0	0	0	0	0
33-53	0	1	1	0	1	1
5-53	1	2	2	1	1	2
31-53	0	0	0	0	0	0
34-53	0	0	0	0	0	0
36-53	0	0	2	0	1	2
20-53	0	0	0	0	0	0
8-53	0	0	0	0	0	0
Added circuits	2	4	2	3	3	2
Cost (million USD)	2.45	7.375	4.305	4.71	7.23	3.42
TEP cost (million USD)	14.13			15.36		

5.2 SMTEP for Garver System and WDN

Some assumptions are made in the Garver network and the WDN to increase the usage of clean electricity as shown in Figs. 9 and 10, respectively. For the Garver network, the thermal unit at node 3 is replaced with a 165 MW wind unit, and the

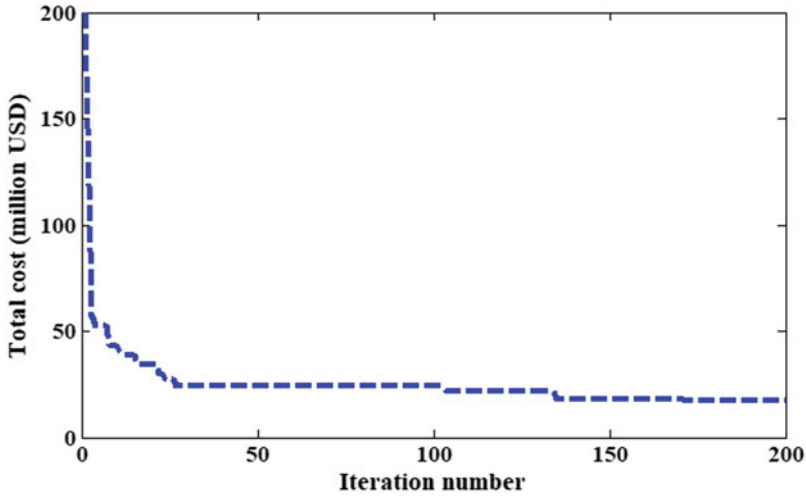


Fig. 7 Convergence curve for WOA during solving STEP for WDN

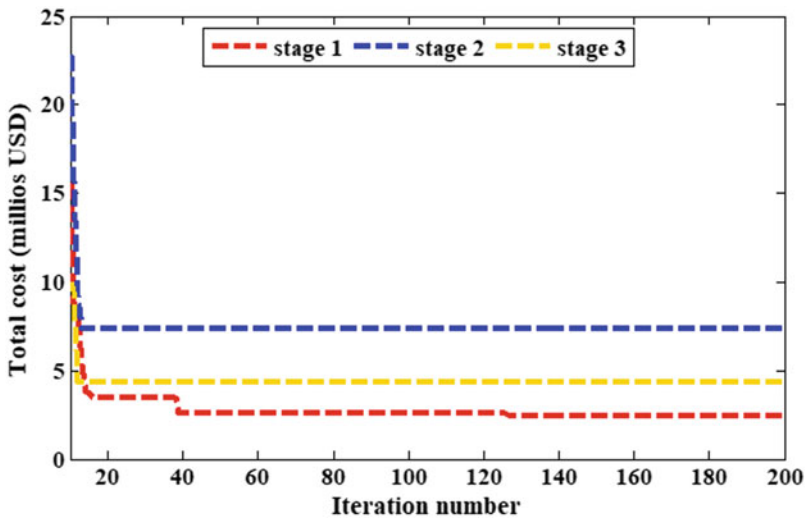


Fig. 8 Convergence curve for WOA during solving DTEP of WDN

capacity of the generation unit connected to node 1 is increased to 150 MW. The maximum capacity of the thermal unit at node 6 is also increased to 600 MW. The load and the generation data for each stage are given in Table 4.

For the WDN, two wind stations with a capacity of 200 MW are constructed at nodes 2 and 8, and two solar power stations are expected to be established at nodes 3 and 5. The capacity of each solar unit is 100 MW. Renewable and conventional energies are merged for buses where both types are available.

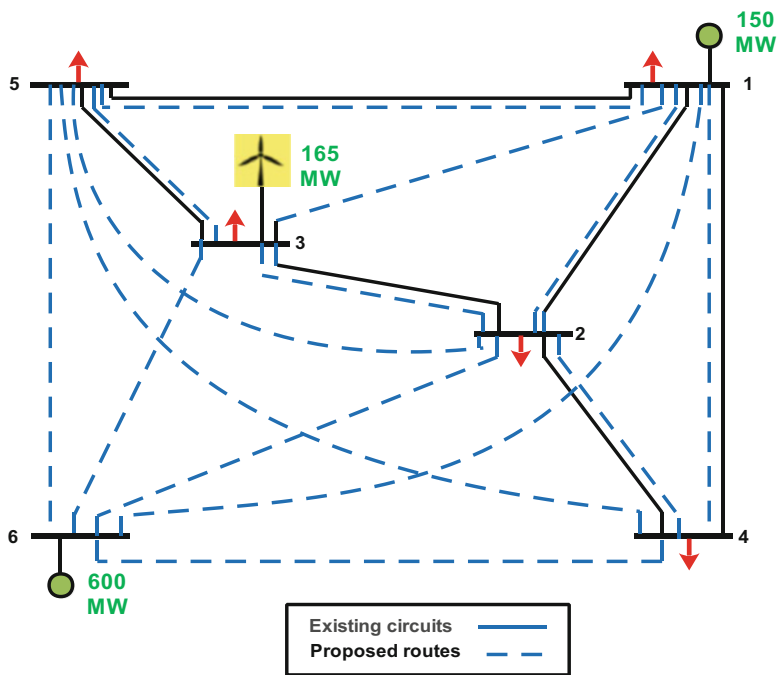


Fig. 9 The initial configuration of the Garver system in the presence of RGS

For the WDN, the wind speed, solar radiation, and temperature data are obtained from [44] to form 8760 scenarios representing operational conditions per hour at each stage. The 8760 scenarios are reduced to 24 scenarios using the FCM clustering technique. The selected scenarios are listed in Table 5. The Garver network is also planned using the wind and loads data provided in Table 5.

• **SMTEP for Garver Network**

The SMTEP for the Garver system is shown in Figs. 11 and 12. With regard to the N-1 security, it is planned, as depicted in Fig. 11, to have 4 circuits in the first stage and 3 circuits in the second and third phases. Table 6 indicates that one circuit is needed at routes 1-2, 1-5, 2-4, 3-5, and 1-6, whilst five circuits are needed between bus 2 and bus 6. TEP’s projects are expected to cost 283.889 million USD. Ignoring the reliability of the N-1 reveals that the total planning cost is down to 212.15 to million USD as 8 circuits at routes 2-5, 2-6, and 4-6 are needed during the planning horizon as described in Fig. 12. It is obvious that the reduction in the planning cost reaches 25.27% compared to the secure plan. The results found that no load shedding is applied for both strategies. This means that the candidate circuits and generation units are sufficient to meet the planning constraints. It can be concluded that omitting N-1 security in the model reduces the investment costs but makes it more prone to rolling electrical power outages.

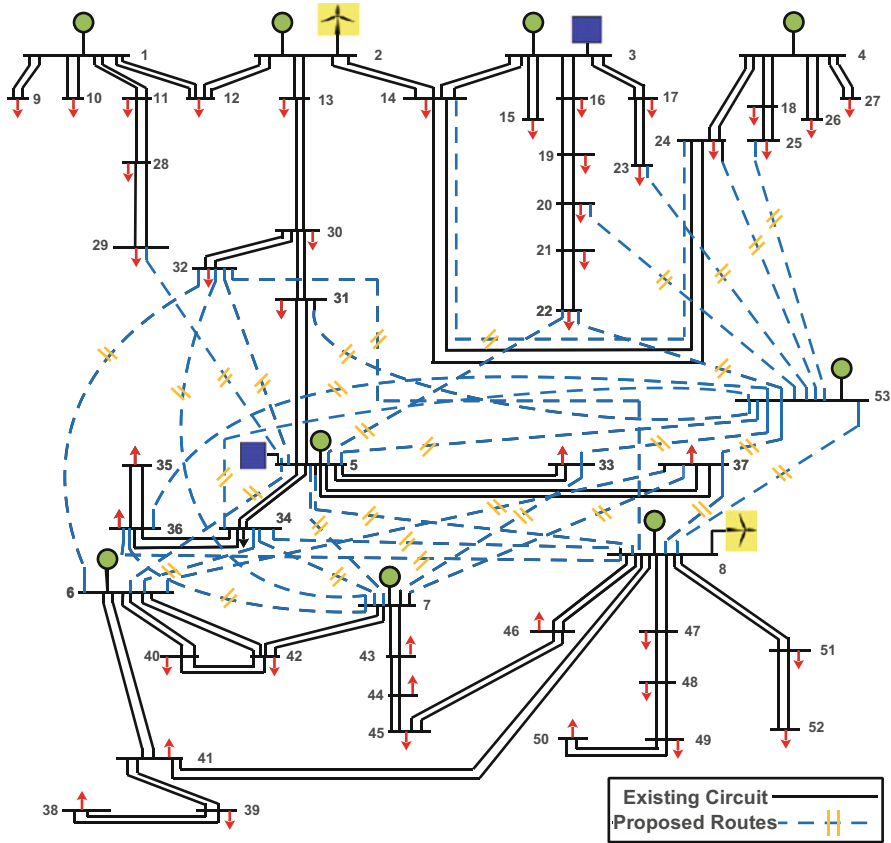


Fig. 10 The initial configuration of WDN in the presence of RGS

Table 4 Generation and load data for SMTEP

Bus no.	Stage 1		Stage 2		Stage 3	
	P_d (MW)	P_g^{\max} (MW)	P_d (MW)	P_g^{\max} (MW)	P_d (MW)	P_g^{\max} (MW)
1	64	150	72	150	80	150
2	192	0	216	0	240	0
3	32	165	36	165	40	165
4	128	0	144	0	160	0
5	192	0	216	0	240	0
6	0	600	0	600	0	600

Finally, the presence of RGSs considerably changes the final configuration of the Garver network. Regarding the non-secure configuration presented in Sect. 12.5.1, the added circuit in route 3–5 is omitted, while additional two single circuits are needed in routes 2–5 and 2–6. For the secure configuration, two single circuits

Table 5 Selected scenarios

Scenario no.	Wind speed	Solar irradiance	Temperature	Load/max. load
1	7.628	1.39e-09	19.243	1
2	7.009	0.194	16.796	0.891
3	6.60	9.170	16.675	0.923
4	7.167	4.440e-06	9.858	0.866
5	6.030	0.691	32.399	0.891
6	8.753	0.0187	25.012	0.953
7	6.190	0.029	17.4066	0.828
8	8.5734	2.460e-07	21.281	0.917
9	5.996	0.388	22.918	0.823
10	5.847	3.450e-06	21.238	0.866
11	5.400	0.224	26.177	0.824
12	5.717	0.629	32.023	0.863
13	7.523	1.460e-07	19.031	0.936
14	7.154	1.760e-05	10.022	0.888
15	6.758	0.129	12.409	0.824
16	7.637	0.615	30.138	0.949
17	6.948	0.530	18.072	0.863
18	6.056	1.350e-05	20.940	0.888
19	6.820	0.241	20.942	0.898
20	8.306	0.192	20.319	0.952
21	8.876	8.880e-07	22.781	0.939
22	7.242	1.620e-05	18.551	0.955
23	6.809	0.777	29.276	0.899
24	8.199	0.297	34.649	0.952

between nodes 3 and 5 and nodes 3 and 6 are not needed, whilst four circuits located in routes 1–2, 1–5, 2–4, and 2–6 are required.

Regarding the embedding of the acceleration scheme with the WOA, the results indicate that time spent solving the TEP problem is decreased by 22% compared to the full N-1 analysis for all individuals in the population. It has been found that the number of individuals meeting the security constraint increases as the algorithm moves towards the maximum iteration.

• SMTEP for WDN

The SMTEP's projects for the WDN are given in Table 7. The SMTEP with and without embedding the N-1 security are radically different from each other. Ignoring the N-1 condition, as shown in Fig. 13, results in installing one circuit in the first stage and two circuits in the subsequent stages, respectively. The TEP's cost is 13.78 million USD. It's worth mentioning that no-load shedding is required for this plan, but it, on the other hand, is essential for achieving the N-1 constraints as shown in Table 7. The secure configuration represented in Fig. 14 clarifies that there is an urgent need for 14 circuits during the planning period with load shedding estimated

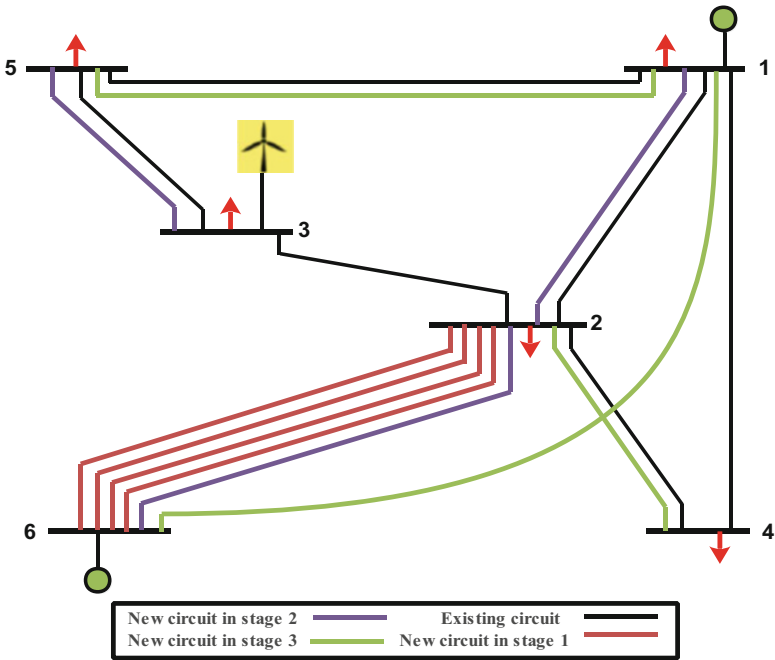


Fig. 11 Final configuration of Garver network using SMTEP model with considering N-1 security

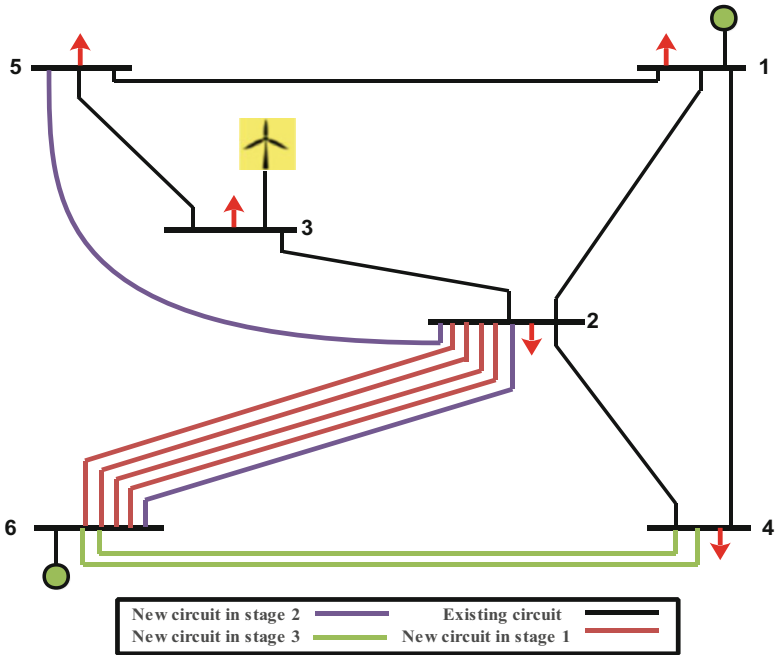


Fig. 12 Final configuration of Garver network using SMTEP model without considering N-1 security

Table 6 SMTEP for Garver system

Candidate line	Without N-1 reliability			With N-1 reliability		
	Stage number			Stage number		
	1	2	3	1	2	3
1-2	1	1	1	1	2	2
1-4	1	1	1	1	1	1
1-5	1	1	1	1	1	2
2-3	1	1	1	1	1	1
2-4	1	1	1	1	1	2
3-5	1	1	1	1	2	2
1-3	0	0	0	0	0	0
1-6	0	0	0	0	0	1
2-5	0	1	1	0	0	0
2-6	4	5	5	4	5	5
3-4	0	0	0	0	0	0
3-6	0	0	0	0	0	0
4-5	0	0	0	0	0	0
4-6	0	0	2	0	0	0
5-6	0	0	0	0	0	0
Added circuits	4	2	2	4	3	3
LS(MW)	0	0	0	0	0	0
Cost (million USD)	120	50.833	41.667	120	75	88.889
TEP costs (million USD)	212.15			283.889		

at 116.53 MW. It has been found that eleven circuits are installed in the first stage, and three circuits are constructed in the third stage. The results clarify that no circuits are needed in the second stage. The results also show that LS of 0.1157 MW and 56.64 MW are required in the first and the second stages, respectively, while LS of 116.53 MW is needed in the third stage. This implies that the expected load not supplied, for a single line outage, may reach to 5.3% of the total load demand. It is worth mentioning that the cost of this plan is 95.208 million USD. It is clear that the planning cost is about 6.9 times the non-secure plan. As expected, the time required to implement one run, using the acceleration scheme, is decreased. It is less than the conventional methods by 37%. The results found that the closer the algorithm gets to the terminated criteria the more individuals that satisfy N-1 security increases.

Comparing the results obtained in this section and the results introduced in Sect. 12.5.1 reveals that the presence of REGs reduces the need for TEP’s projects. For a non-secure plan, two circuits are not required in presence of wind and PV units.

Finally, the system planner and operator should set their priorities, either preserve the system’s safety and reliability or pay attention to the overall planning cost and make the system vulnerable to complete or partial blackouts [45–47].

Table 7 SMTEP for WDN

Candidate line	Without N-1 reliability			With N-1 reliability		
	Stage number			Stage number		
	1	2	3	1	2	3
5-6	0	0	0	0	0	0
5-7	0	0	0	0	0	0
5-8	0	0	0	0	0	0
5-22	0	0	0	0	0	0
5-29	0	0	0	0	0	0
5-32	0	0	0	0	0	0
6-32	0	0	0	0	0	0
6-34	0	0	0	2	2	2
6-37	0	0	0	0	0	0
7-32	0	0	0	1	1	2
7-33	0	0	0	0	0	0
7-34	0	0	0	0	0	0
7-36	0	0	0	2	2	2
7-37	0	0	0	0	0	0
8-38	0	0	0	0	0	0
8-33	0	0	0	0	0	0
8-34	0	0	0	0	0	0
8-36	0	0	0	0	0	0
8-37	0	0	0	0	0	0
25-53	0	0	0	0	0	0
23-53	0	0	0	2	2	2
22-53	1	1	1	0	0	0
19-53	0	0	0	0	0	0
37-53	0	0	0	0	0	0
33-53	0	1	1	2	2	2
5-53	0	0	0	0	0	0
31-53	0	0	0	0	0	0
34-53	0	0	0	0	0	2
36-53	0	0	2	2	2	2
20-53	0	0	0	0	0	0
8-53	0	1	1	0	0	0
Added circuits	1	2	2	11	0	3
LS (MW)	0	0	0	0.1157	56.64	116.53
Cost (million USD)	1.5	7.975	4.305	25.248	23.60	46.36
TEP costs (million USD)	13.78			95.208		

6 Conclusions

This chapter presented a SMTEP model for power systems planning that takes into account the power system’s uncertainties and N-1 security. To solve the proposed

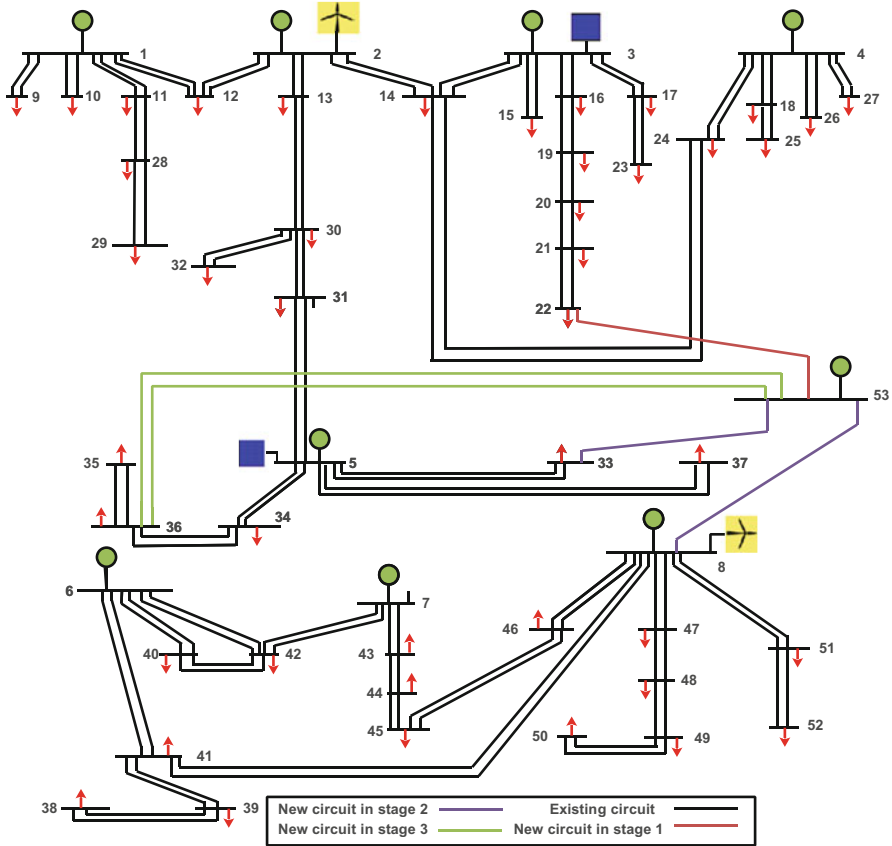


Fig. 13 Final configuration of WDN using SMTEP model without considering N-1 security

problem, reduction strategy and acceleration scheme were incorporated with the WOA to enhance the performance of the algorithm. Integrating uncertainties and reliability constraints into the planning model has become an urgent necessity that cannot be dispensed with to obtain a security system that is not exposed to rolling blackouts. Information, such as the date and number of installations of new transmission lines, and maintaining of the planned system security are among the most important features to the conducted strategy. In addition, the SMTEP model is economically welcome because investment costs are low, as the dynamic approach assumes the time value of money.

Two test systems, the Garver network and the WDN, were used to validate the proposed strategy. The application of the WOA algorithm was first investigated to solve the STEP and DTEP problems. Promising results were obtained and ensured the potential of this technique. The STEP results for the WDN demonstrated that the WOA algorithm gives a better (low-cost) solution than IBPSO, MVO, and integer and binary CBSA for the WDN. Both WOA and LSHADE-SPACMA achieved

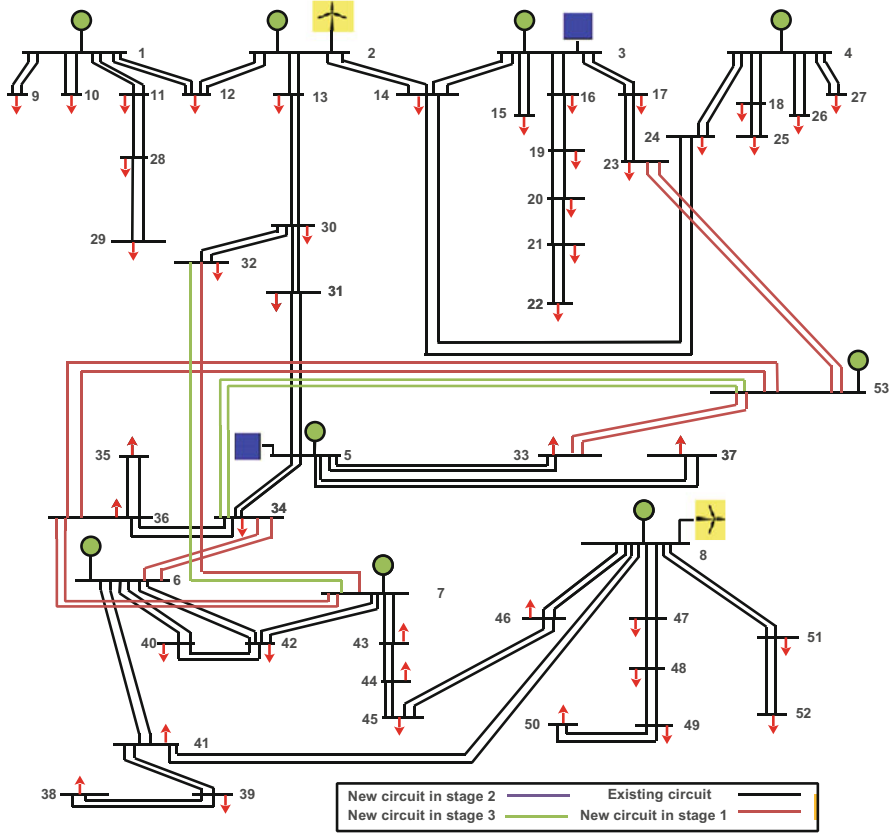


Fig. 14 Final configuration of WDN using SMTEP model with considering N-1 security

investment costs of 17.28 million USD, whereas the cost of STEP projects using IBPSO, MVO, integer CBSA, and binary CBSA was 22.19, 20.64, 18.605, and 18.455 million USD, respectively. However, the WOA reached optimum solution faster than the LSHADE-SPACMA. Regarding the DTEP, the WOA obtained a configuration for the WDN with a cost less than the LSHADE-SPACMA by 1.23 million USD. For the Garver system, the WOA succeeded to reach the optimal configuration presented in the literature.

The results showed that including the N-1 security with SMTEP model highly impacts the final configuration of power networks. The results also indicated that taking into account the system’s uncertainties increases the robustness of the system and reduces the probability of power outage. The SMTEP for the WDN revealed that incorporating the N-1 security into the planning model increased the cost by 81.48 million USD. Moreover, the presence of RGSs reduced the load shedding to 5.3%. For the Garver network, the SMTEP with the N-1 security increased the planning cost by 71.74 million USD compared to the non-secure configuration. Hence, the

system planner and operator have to set their priorities, either maintaining the integrity and reliability of the system or paying attention to the overall planning cost and making the system vulnerable to total or partial blackouts.

The results demonstrated that the reduction and the acceleration schemes contributed to speeding up the convergence to the optimal solution. The calculation time was reduced by 37% for the WDN and by 22% for the Garver network.

References

1. Mahdavi M, Sabillon Antunez C, Ajalli M, Romero R (2019) Transmission expansion planning: literature review and classification. *IEEE Syst J* 13(3):3129–3140
2. Gomes PV, Saraiva JT (2019) State-of-the-art of transmission expansion planning: a survey from restructuring to renewable and distributed electricity markets. *Int J Electr Power Energy Syst* 111:411–424
3. Esmaili M, Ghamsari-Yazdel M, Amjady N, Chung CY, Conejo AJ (2020) Transmission expansion planning including TCSCs and SFCLs: a MINLP approach. *IEEE Trans Power Syst* 35(6):4396–4407
4. Refaat MM, Aleem SHEA, Atia Y, Ali ZM, Sayed MM (2021) Multi-stage dynamic transmission network expansion planning using lshade-spacma. *Appl Sci* 11(5):1–22
5. Fathy AA, Elbages MS, El-Sehiemy RA, Bendary FM (2017) Static transmission expansion planning for realistic networks in Egypt. *Electr Power Syst Res* 151:404–418
6. Hamidpour H, Aghaei J, Pirouzi S, Dehghan S, Niknam T (2019) Flexible, reliable, and renewable power system resource expansion planning considering energy storage systems and demand response programs. *IET Renew Power Gener* 13(11):1862–1872
7. Wang Y, Zhou X, Shi Y, Zheng Z, Zeng Q, Chen L, Xiang B, Huang R (2021) Transmission network expansion planning considering wind power and load uncertainties based on multi-agent DDQN. *Energies* 14(19):6073
8. Ramirez JM, Hernandez-Tolentino A, Marmolejo-Saucedo JA (2021) A stochastic robust approach to deal with the generation and transmission expansion planning problem embedding renewable sources. In: *Uncertainties in modern power systems*. Elsevier, San Diego, pp 57–91
9. Mazaheri H, Ranjbar H, Saber H, Moeini-Aghaie M (2021) Expansion planning of transmission networks. In: *Uncertainties in modern power systems*. Elsevier, San Diego, pp 35–56
10. Zhu Y, Brown D (2013) Expanding transmission planning capabilities for NERC standard TPL-001-2 compliance. In: *IEEE power & energy society general meeting*, pp 1–5
11. Esmaili M, Ghamsari-Yazdel M, Amjady N, Chung CY (2021) Convex model for controlled islanding in transmission expansion planning to improve frequency stability. *IEEE Trans Power Syst* 36(1):58–67
12. Lee S, Kim H, Kim TH, Shin H, Kim W (2019) Fault current constraint transmission expansion planning based on the inverse matrix modification lemma and a valid inequality. *Energies* 12(24):4769
13. Nemat H, Latify MA, Yousefi GR (2021) Tri-level coordinated transmission and electrical energy storage systems expansion planning under physical intentional attacks. *J Energy Storage* 42:103095
14. Franken M, Barrios H, Schrief AB, Moser A (2020) Transmission expansion planning via power flow controlling technologies. *IET Gener Transm Distrib* 14(17):3530–3538
15. Lee STY, Hicks KL, Hnyilicza E (1974) Transmission expansion by branch-and-bound integer programming with optimal cost — capacity curves. *IEEE Trans Power Appar Syst PAS-93(5):1390–1400*

16. Granville S et al (1988) Mathematical decomposition techniques for power system expansion planning: Volume 2, analysis of the linearized power flow model using the bender decomposition technique, Stanford Univ., CA (USA). Systems Optimization Lab
17. Romero R, Monticelli A (1994) A hierarchical decomposition approach for transmission network expansion planning. *IEEE Trans Power Syst* 9(1):373–380
18. Alizadeh B, Jadid S (2015) A dynamic model for coordination of generation and transmission expansion planning in power systems. *Int J Electr Power Energy Syst* 65:408–418
19. Huang S, Dinavahi V (2017) A branch-and-cut benders decomposition algorithm for transmission expansion planning. *IEEE Syst J* 13(1):659–669
20. Vinasco G, Rider MJ, Romero R (2011) A strategy to solve the multistage transmission expansion planning problem. *IEEE Trans Power Syst* 26(4):2574–2576
21. Özdemir Ö, Munoz FD, Ho JL, Hobbs BF (2015) Economic analysis of transmission expansion planning with price-responsive demand and quadratic losses by successive LP. *IEEE Trans Power Syst* 31(2):1096–1107
22. Pereira MVF, Pinto LMVG (1985) Application of sensitivity analysis of load supplying capability to interactive transmission expansion planning. *IEEE Trans Power Appar Syst PAS-104(2):381–389*
23. Romero R, Rocha C, Mantovani M, Mantovani JRS (2003) Analysis of heuristic algorithms for the transportation model in static and multistage planning in network expansion systems. *IEE Proc-Gener Transm Distrib* 150(5):521–526
24. Sousa AS, Asada EN (2011) Combined heuristic with fuzzy system to transmission system expansion planning. *Electr Power Syst Res* 81(1):123–128
25. Zhang X, Conejo AJ (2018) Candidate line selection for transmission expansion planning considering long- and short-term uncertainty. *Int J Electr Power Energy Syst* 100:320–330
26. Abdi H, Moradi M, Lumbreras S (2021) Metaheuristics and transmission expansion planning: a comparative case study. *Energies* 14(12):3618
27. Da Silva EL, Gil HA, Areiza JM (2000) Transmission network expansion planning under an improved genetic algorithm. *IEEE Trans Power Syst* 15(3):1168–1174
28. Escobar AH, Gallego RA, Romero R (2004) Multistage and coordinated planning of the expansion of transmission systems. *IEEE Trans Power Syst* 19(2):735–744
29. Shayeghi H, Mahdavi M, Bagheri A (2010) Discrete PSO algorithm based optimization of transmission lines loading in TNEP problem. *Energy Convers Manag* 51(1):112–121
30. Shayeghi H, Mahdavi M, Bagheri A (2010) An improved DPSSO with mutation based on similarity algorithm for optimization of transmission lines loading. *Energy Convers Manag* 51(12):2715–2723
31. Torres SP, Castro CA (2014) Expansion planning for smart transmission grids using AC model and shunt compensation. *IET Gener Transm Distrib* 8(5):966–975
32. Huang S, Dinavahi V (2017) Multi-group particle swarm optimisation for transmission expansion planning solution based on LU decomposition. *IET Gener Transm Distrib* 11(6):1434–1442
33. Da Silva EL, Areiza Ortiz JM, De Oliveira GC, Binato S (2001) Transmission network expansion planning under a Tabu search approach. *IEEE Trans Power Syst* 16(1):62–68
34. Shaheen AM (2019) Application of multi-verse optimizer for transmission network expansion planning in power systems. In: 2019 International conference on innovative trends in computer engineering, pp 371–376
35. Shaheen AM, El-Sehiemy RA (2019) Binary and integer coded backtracking search optimization algorithm for transmission network expansion planning. *WSEAS Trans Power Syst* 14:47–54
36. Mirjalili S, Lewis A (2016) The whale optimization algorithm. *Adv Eng Softw* 95:51–67
37. Zimmerman RD, Murillo-Sánchez CE (2020) MATPOWER user's manual version 7.1. [Online]. Available: <https://matpower.org/doc/>
38. Dunn JC (1973) A fuzzy relative of the ISODATA process and its use in detecting compact well-separated clusters

39. Bezdek JC (2013) Pattern recognition with fuzzy objective function algorithms. Springer, United States
40. Mostafa MH, Ali SG, Calasan M, Abdelaziz AY, Aleem SHEA (2021) Scenario-based approach for efficient energy management in microgrids considering parameters uncertainty. In: 2021 25th international conference on information technology (IT), pp 1–7
41. Biswas PP, Sugathan PN, Mallipeddi R, Amaratunga GAJ (2019) Optimal reactive power dispatch with uncertainties in load demand and renewable energy sources adopting scenario-based approach. *Appl Soft Comput J* 75:616–632
42. Saboori H, Hemmati R (2016) Considering carbon capture and storage in electricity generation expansion planning. *IEEE Trans Sustain Energy* 7(4):1371–1378
43. Silva IDJ, Rider MJ, Romero R, Garcia AV, Murari CA (2005) Transmission network expansion planning with security constraints. *IEE Proc-Gener Transm Distrib* 152(6):828–836
44. <https://www.renewables.ninja/>
45. Zobaa AF, Aleem SA, Abdelaziz AY (eds) (2018) Classical and recent aspects of power system optimization. Elsevier, United Kingdom
46. Rizk-Allah RM et al (2017) A new sine cosine optimization algorithm for solving combined non-convex economic and emission power dispatch problems. *Int J Energy Convers* 5(6):180–192
47. Gandoman FH, Abdel Aleem SHE, Omar N, Ahmadi A, Alenezi FQ (2018) Short-term solar power forecasting considering cloud coverage and ambient temperature variation effects. *Renew Energy* 123:793–805

Energy Storage Devices



Samuel Raafat Fahim and Hany M. Hasanien

Abbreviations

ac	Alternating current
A-CAES	Adiabatic compressed air energy storage
AFC	Alkaline fuel cell
BMS	Battery management system
CAES	Compressed air energy storage
CHP	Combined heat and power
CO	Carbon mono-oxide
dc	Direct current
D-CAES	Diabatic compressed air energy storage
DLC	Double layered capacitor
DMFC	Direct methanol fuel cell
DMS	Device management system
DoD	Depth of discharge
EcSS	Electro-chemical energy storage
EES	Electrical energy storage
EMS	Energy management system
ESD	Energy storage devices
FES	Flywheel energy storage
GBES	Gravity battery energy storage
H ₂ S	Hydrogen sulfide
HFB	Hybrid flow battery
KOH	Potassium hydroxide

S. R. Fahim (✉) · H. M. Hasanien
Electrical Power and Machines Department, Faculty of Engineering, Ain Shams University,
Cairo, Egypt
e-mail: discoures@yahoo.com; hanyhasanien@ieee.org

LAES	Liquid air energy storage
LHES	Latent heat energy storage
Li-ion	Lithium ion battery
MCFC	Molten carbonate fuel cell
MSS	Mechanical Energy Storage System
NaS	Sodium sulfur battery
NASA	National aeronautics and space agency
PAFC	Phosphoric acid fuel cell
Pb-acid	Lead acid battery
PCS	Power conversion system
PEMFC	Proton exchange membrane fuel cell
PHES	Pumped hydro energy storage
PV	Photovoltaic
RFB	Redox flow battery
SHES	Sensible heat energy storage
SMES	Superconducting magnetic energy storage
SoC	State of charge
SOFC	Solid oxide fuel cell
SoH	Sate of health
STES	Sorption thermal energy storage
TCP	Transmission control protocol
TES	Thermal storage devices
TSS	Thermal storage system
VRFB	Vanadium redox flow battery
YSZ	Yttria stabilized zirconia

1 Introduction

In electrical grids, there is always a mismatch between generation and electrical load demand. It is a big challenge to mitigate this mismatch. There are many efforts that try to suppress the mismatch, among which supply/demand sides scheduling. In addition, this is done by using deterministic and probabilistic techniques and methodologies to decrease the estimation error in both sides. However, every electrical grid suffers from some sort of mismatch. The supply/demand mismatch can be positive type: supply exceeds the demand; or negative type: supply is deficit to cover the demand [1].

Here comes one of the promising solutions to the aforementioned problem, which is energy storage. The energy storage can offer a prominent tool to overcome the mismatch problem. The basic concept of energy storage is storing the energy when it is surplus to use when energy is deficit. Therefore, the storage converts the electrical energy to another energy form. Then, when needed, the storage technique shall restore it to electrical energy. The storage of electrical energy has a variety of forms that transfer the electrical energy either into another energy type or store

it as electrical energy. Storage devices range from: (a) chemical (ex: fuel cell); (b) electrostatic (ex: super capacitors); (c) electromagnetic (ex: superconducting magnetic energy storage “SMES”); (d) electrochemical (ex: various types of batteries); (e) thermal (ex: molten salt); and (f) electromechanical (ex: flywheel). This is just a brief on techniques; the chapter discusses many more techniques. Moreover, this chapter tries to cover them in the following aspects: theory of operation, modeling, and integration with electrical generation [2].

Regardless of the simplicity of the concept, it comes with concerns. Those concerns shall be handled and studied carefully. As there are a variety in storage techniques, there will be a need to develop selection criteria. Among the selection criteria are the upcoming aspects. First is the storing capacity of each methodology. As an example, the chemical storage has limited capacity in comparison with mechanical storage. Second is the time needed to discharge the stored energy, as electrical storage discharges much faster than other forms of storage. Third is the storage density per square meter. In the published literature, the fuel cell is the best in this issue. Fourth is the optimum type of energy storage to certain energy generation technology. Pumped storage is more suitable for hydro substation. Fifth is the cost of installing the energy storage. The electrochemical storage (Sodium Sulfur “NaS”) has a high installation cost. Sixth is the lifetime of the energy storage. The mechanical storage lasts longer than other forms. Seventh is whether storage is needed for utility scale or not. Mainly mechanical and electromechanical are widely used. Finally, special requirements are needed to install each storage type. Some mechanical techniques (ex: compressed air) are site specific [3, 4].

This chapter will cover the various categories of energy storage devices with the consideration of all the above aspects in a comprehensive way. That gives an overview to the reader, both experts and beginners.

2 Energy Storage Devices Technology

The electric grid aims to balance between energy demand (load) and energy generation. The energy demand is highly stochastic, and its prediction always has a marginal error. On the other side, energy generation is subject to two governing factors: the unit response time and unit intermittence. This means that there are times when energy demand is high and there is no supply, and vice versa.

To stabilize the electrical grid operation and balance generation/demand process, energy storage plays an important role. Energy storage aims to “store” the excess of energy generation to be used at a later time when there is a deficiency in generation. Therefore, this helps in increasing the overall system reliability and security.

The electrical energy can be stored either in its original form or in an alternative form. In this section, the devices used to store the electrical energy will be demonstrated. For every energy storage device, the following will be discussed:

- Theory of operation
- Advantages of the technology
- Disadvantages of the technology
- The field of application
- The mathematical model for each system will be presented whenever possible

2.1 Mechanical Energy Storage Devices

In this section, the mechanical energy storage system (MSS) is presented. This type of storage is one of the indirect ways of storing electrical energy. This is because the electrical energy is stored in another energy (mechanical) form either directly or through a thermodynamic process. The mechanical energy storage uses either kinetic energy, potential energy, or a mixture of the two.

Each system can store electrical energy in a certain manner and release it based on its own structure. For every mechanical storage device, there is a renewable storage that can use the potential of mechanical storage effectively.

2.1.1 Pumped Hydro Energy Storage

The pumped hydro energy (PHES) depends on potential energy. Two connected water reservoirs are used. One is located in elevated location with respect to the other. In case of low energy demand, the excess electrical generation is used to power water pumps. Those pumps transfer water from the lower reservoir to the upper one. This is called “charging mode” and typically happens at nighttime “off-peak hours” [5].

In cases of high energy demand and low electrical generation, the water gates at the higher reservoir are opened. The flow of water downwards operates turbines that help in generation of more electrical energy. This is called “discharging mode,” and typically happens at daytime “peak hours” [5].

This technology’s main advantages are as follows:

- It can discharge in several hours and up to several days.
- The system efficiency ranges from 70 to 85%.
- This technology has a very long lifetime and theoretically unlimited charge/discharge cycles [6].

While the disadvantages are as follows:

- The system response is relatively slow, due to the amount of water transferred and the startup of pumps/turbines.
- The amount of water needed to generate shall be calculated, including the evaporation rates and amount of energy needed.

- This technology is site-specific, which means if the location of the two reservoirs is not found naturally, the cost of constructing them can make the PHES cost unfeasible considering the benefits [6].

The main application is grid storage to achieve peak shaving.
The mathematical formula of this storage type is as follows:

$$P_{\text{PHES}} = QH\rho g\eta \quad (1)$$

Where,

P_{PHES} = generated output power (W)

Q = fluid flow (m^3/s)

H = hydraulic head height (m)

ρ = fluid density (Kg/m^3) (=1000 for water)

g = acceleration due to gravity (m/s^2) (=9.81)

η = efficiency

2.1.2 Compressed Air Energy Storage

The compressed air energy storage (CAES) analogies the PHES. The concept of operation is simple and has two stages: (1) the compression stage (charging/storage) – when power generation exceeds demand, the surplus power is used to compress the air using multistage compressors, thus reducing its volume and temperature and (2) the expansion stage (discharge/generation) – when the demand exceeds the generation, the compressed air is pumped into gas turbines, thus leading to the rotation of the generator that is coupled on the same shaft with the gas turbine.

This technology depends on the static energy that is stored by gas compression. The energy is stored by compressing air in large underground caverns or above-ground vessels [7].

The CAES analogies the PHES, as the elevated reservoir (storage reservoir) resembles the compression phase of the CAES, while the lower reservoir (discharge reservoir) is similar to the expansion phase [7].

The underground caverns can be either salt caves, hard rock, or porous rocks [8, 9].

During the compression of air, the excess heat shall be removed in order to reach the storage temperature of compressed air. The removal of heat can be either of the following:

- *Adiabatic (A-CAES)*: it is a thermodynamic process in which generated heat due to air compression is not transferred to any other system, thus fulfilling the first law of thermodynamics. In this process, the air is compressed in caverns hundreds of meters below the earth's surface to a pressure value of 100 bars. The produced heat is stored by transferring it into thermal storage devices (TES) to be used later

to reheat the compressed air during the expansion process. Thus, there is no need to burn any kind of fuel. This technique has the highest efficiency up to 70% [7].

- *Diabatic (D-CAES)*: in this method, the generated heat is permitted to be dissipated to the surrounding by means of intercoolers. The compressed air is stored in cavern in the same conditions as A-CAES. The only difference is that in the expansion phase, the compressed air might reach the gas turbine cooler than required, which can damage the turbine fins. Therefore, natural gas can be burnt with the compressed air to generate electricity from the turbine/generator set. This way, the efficiency is around 55% [7].

The advantages of CAES are [10] as follows:

- Fast response time; therefore, the power generation fluctuation is minimal.
- Large capacity, which can backup large wind farms, thus mitigating its intermittency.
- It can store hundreds of MWhr at a very low cost.
- The technology has the ability to black start.
- Can produce three times the power generated compared to burning natural gas in gas turbines for the same volume.
- The environmental impact is at its lower limit.

The disadvantages of CAES are [10] as follows:

- Geographical limitations to find a location with suitable cavern that can store the compressed air.
- Low round-trip efficiency.
- There are inevitable losses in the process of compression.
- An additional heating facility might be needed in order to operate the turbines in the expansion process, especially, the need for natural gas which is a fossil fuel with fluctuating market price.

It is mainly used for storing energy of utility scale wind farms [10].

For A-CAES, the mathematical modeling includes the compression mode, heat and air storage, and finally the expansion mode. To be brief, the compression and expansion models will only be listed hereunder. For compression mode [11]:

$$P_{CAES}^{Comp} = \frac{1}{\eta_c} \dot{m}_{c,a} c_{p,a} T_{ct,a}^{in} \left(\beta_c^{n_{ct}-1/n_{ct}} - 1 \right) \quad (2)$$

Where,

P_{CAES}^{Comp} = consumed power by compressor (W)

η_c = compressor efficiency

$\dot{m}_{c,a}$ = air mass flow (kg/s)

$c_{p,a}$ = specific heat capacity (J/kg.K)

$T_{ct,a}^{in}$ = input temperature of air (K)

β_c = compression ratio for each compressor

While for expansion mode [11]:

$$P_{CAES}^{Expa} = \eta_t \dot{m}_{t,a} c_{p,a} T_{t,a}^{in} \left(1 - \beta_c^{n_t-1/n_t} \right) \quad (3)$$

Where,

P_{CAES}^{Expa} = electrical power obtained from during expansion (W)

η_t = compression efficiency

$\dot{m}_{t,a}$ = air mass flow through turbines (kg/s)

$T_{t,a}^{in}$ = air temperature that enters the turbine (K)

2.1.3 Flywheel Energy Storage

Flywheel energy storage (FES) depends on kinetic energy stored in rotating mass. With the same concept of the pumped hydro storage, but the only difference is that the energy stored in rotating mass (a rim attached to shaft). The storage system is composed of a rotor connected to a huge mass via a transmission system. The mass is rotating at a constant speed; to store more energy, the rotation speed increases, and vice versa. The transmission system is responsible to charge/discharge, i.e., increase/decrease the mass speed [12].

The rotating mass speed reaches 20,000–50,000 rpm. Therefore, the rotating mass is kept in vacuum [13].

The advantages of FES energy storage are [14] as follows:

- The system has high reliability, as it can operate for charge/discharge cycles of the order of hundreds of thousands without degrading.
- FES has a lifespan that lasts for decades with minimal maintenance.
- Also, FES's response time is very fast.
- In addition, FES has high energy efficiency when considering charging/discharging phases.
- State of charge could be determined easily by measuring the rotation speed of the mass. The storage energy is neither affected by the device life time or ambient temperature.
- The stored energy could be drained completely, disregarding the depth of discharge concept.
- The materials used in manufacturing this type of energy storage devices are environmentally friendly.

While the disadvantages of FES's energy storage are [14] as follows:

- The energy losses in bearings could be countered by using superconducting magnetic bearings, which use the magnetic levitation concept to avoid touching between the rotating mass and conventional bearings. But this also puts the burden of using cryogenic cooling to support the operation of the superconducting magnets.

- The system shall be concealed in sealed tanks to enable the system operation in a vacuum, thus reducing the friction.
- They are limited to short duration (order of few seconds/several minutes) support of the system.
- They are more feasible to be used in utility scale levels.

They can be used as an alternative to UPS for data centers and hospitals, as well as for launching fighter jets from the deck of military aircraft carriers.

The mathematical formula of this storage type is as follows [12]:

$$E_{\text{FES}|_{\text{max}}} = \frac{1}{2} m r^2 \omega^2 \quad (4)$$

The useful stored energy in the system is as per the following equation [12]:

$$E = \eta_{\text{st}} E_{\text{FES}|_{\text{max}}} (1 - s^2) \quad (5)$$

$$s = \frac{\omega_{\text{min}}}{\omega_{\text{max}}} \quad (6)$$

Where,

$E_{\text{FES}|_{\text{max}}}$ = maximum energy the FES can store (Wh)

E = maximum useful stored energy (Wh)

m = mass of the rotating FES (kg)

r = radius of the rotating cylinder (m)

ω = angular velocity (rad/s)

ω_{min} = minimum angular velocity (rad/s)

ω_{max} = maximum angular velocity (rad/s)

η_{st} = efficiency of the system

s = limit of rotational torque

2.1.4 Gravity Battery Energy Storage

The gravity battery energy storage (GBES) depends on both potential and kinetic energies. The electrical energy is converted to gravitational potential energy in elevated mass. In the storing mode, the surplus energy is used to elevate certain mass to certain a height and keep it still, via pulleys. Thus the kinetic energy (due to surplus electrical power) is stored in the form of potential energy.

In the discharge mode, the mass is left to fall free, thus converting the potential energy into kinetic energy. The free-falling mass is connected to a generator shaft, thus generating electrical energy when there is a generation deficiency [15].

The large scale system contains:

- A large electrical generator that acts as winch in case of charge/discharge.
- Cables and pulleys.
- A large mass that can be concrete blocks, or any other heavy weight materials.
- A shaft that extends to several hundreds of meters. It can be a vertical shaft elevator of an old mine. That extends beneath the earth level.
- Or the location can be an inclined mountain, not a shaft. And the mass is moving on the inclined surface of the mountain.

The system can store several MWhr and release it within minutes for short support for the system.

Another variation of the system can be a water-filled cylinder equipped with weights, pulleys, and a generator [16].

For the system that uses vertical shafts, the mathematical model for stored energy is as follows:

$$E_{GBES|_{ver}} = mg (h_2 - h_1) \quad (7)$$

Where,

$E_{GBES|_{ver}}$ = maximum energy stored energy in vertical GBES (Wh)

m = mass of the object (kg)

g = acceleration of object to earth surface at sea level due to gravity (m/s²)

h_2 = final height (elevated) of the mass (m)

h_1 = initial height (lowest) of the mass (m)

For the system that uses the inclined mountains, the mathematical model for this storage energy type is as follows, in the case of charging [15]:

$$P_{GBES(mtr)|_{UP}} = mg (\sin \theta + \mu \cos \theta) v_{UP} \quad (8)$$

While in the case of discharging, the following equation can be used [15]:

$$P_{GBES(gen)|_{DOWN}} = mg (\sin \theta - \mu \cos \theta) v_{DOWN} \quad (9)$$

Where,

$P_{GBES(mtr)|_{UP}}$ = maximum motor power when the system is charging (W)

$P_{GBES(gen)|_{DOWN}}$ = maximum generator power the system is discharging (W)

θ = angle of inclination of the surface to the earth surface (degrees)

v_{UP} = rising speed (m/s)

v_{DOWN} = sliding speed (m/s)

μ = surface friction coefficient

This technology has the following advantages [17]:

- High efficiency (75–80%).
- Costs of production and maintenance are low per MWhr.
- Environmentally friendly as there is no emissions.

- No need for any fuel from any kind.
- Fast response.

While on the other hand, this technology suffers from the following disadvantages [17]:

- Site specific.
- They are not spread in various locations as the technology is still emerging.
- Hard and costly maintenance is required in the case of water version of this technology.

2.2 *Electro-Chemical Storage Devices*

In EcSS technology, the electrical energy is converted into chemical energy. In each battery, the state of charge determination is complex and extremely important. It determines if the battery either needs to be charged or the maximum permissible level of discharging. If care is not given to the state of charge issue, the battery performance and service life could be affected severely.

The battery is always defined by the amount of current that could be delivered within voltage and time limitation.

The battery mathematical formula could be defined as a set of voltage and current equations, or by power equation. The battery power equation is as follows [18]:

$$P_{\text{BAT}}(t) = P_{\text{BAT}}(t-1) \times (1 - \sigma) + \frac{D_s}{\text{DoD}_{\text{max}} \times \eta_T} \times \Delta t \eta_c \times \left(N_{R_1} P_{R_1}(t) \eta_{\text{acdc}} + N_{R_2} P_{R_2}(t) \eta_{\text{dcdc}} - \frac{P_L(t)}{\eta_{\text{wr}} \eta_{\text{inv}}} \right) \quad (10)$$

Where,

$P_{\text{BAT}}(t)$ = energy stored in battery stack (W)

N_{R_1} = number units of renewable technology with ac electrical output (ex: wind turbine)

N_{R_2} = number units of renewable technology with dc electrical output (ex: PV panel)

$P_{R_1}(t)$ = electrical power output from ac renewable unit (W)

$P_{\text{pv}}(t)$ = electrical power output from dc renewable unit (W)

$P_L(t)$ = AC load (W)

η_{acdc} = AC/DC converter efficiency

η_{dcdc} = DC/DC converter efficiency

η_{inv} = DC/AC inverter efficiency

η_c = charging efficiency

η_{wr} = wire loss (wire efficiency) = 0.98

D_s = days of autonomy (2 days)

DoD_{\max} = maximum depth of discharge (= 80%)

η_T = temperature correction factor (= 90%)

Δt = time interval of the study (= 1 hour)

The above mathematical model is suitable to estimate the stored energy in any chemical battery stack. It combines the previous state of charge plus the charging/discharging current from the generation units.

This type of energy storage contains three major categories; the first is the secondary batteries and has the following subcategories:

2.2.1 Lead Acid

This battery (Pb-acid) type has a positive electrode made of lead dioxide (PbO_2) and a negative electrode of metallic lead (Pb). The electrolytic medium is sulfuric acid (H_2SO_4), which comprises 37% of the total battery weight. This type of batteries is in standby emergency power systems, telecommunications, renewable applications (either PV or wind), and widely as a starter for vehicles. These batteries can achieve cycle efficiency levels of 80–90%. The battery has two common types: vented and sealed (valve regulated lead acid batteries – VRLA) [19].

The Pb-acid can have sizes that range from several hundreds of kWhr to several tens of MWhr [20].

The advantages of the Pb-acid batteries are as follows [21]:

- Low production cost.
- Available in many modular sizes.
- High performance thus used in starting internal combustion engines.
- High efficiency.
- High open circuit voltage >2.0 V.
- Some versions are maintenance free.
- Can be easily recycled.

While the disadvantages of the Pb-acid batteries are as follows [21]:

- Low life cycle (50–500) cycle compared to other battery designs. Some designs can reach 2000 cycle.
- Has energy density of 30–40 Wh/kg which is relatively low.
- Self-discharge when stored for elongated times.
- Can't be manufactured in tiny sizes like other batteries.
- Open types are hazardous due to hydrogen evolution.

2.2.2 Lithium – Ion

The invention of lithium-ion (Li-ion) battery revolutionizes the applications that need a secondary power source. The revolution lies in its numerous advantages in weight, capacity, and power compared to other competitors. The main usage is in

electronic-based customer appliances. Currently there is a global trend to be used in electric vehicles. The battery consists of a metallic cylinder casing that houses three sheets that are tightly spiraled together and immersed in liquid electrolyte. The positive electrode is made of lithium cobalt oxide (LiCoO_2), and the negative electrode is from graphite (C_6). Due to the high voltage of operation (3.7 V), the number of series cells can be reduced. On the other hand, there is a need to have a complex circuitry to avoid overcharging. The larger batteries suffer from heat issues due to requirements of cooling, which affect the performance of the battery [19].

The advantages of the Li-ion batteries are as follows [22]:

- As sealed batteries, it is maintenance free.
- Relatively long life cycle in order to tens of hundreds.
- Can operate at different temperatures.
- Low self-discharge, i.e., long shelf life.
- Capable of rapid charge.
- Large depth of discharge.
- High in efficiency, specific energy, and energy density.
- Can be housed in tiny aluminum casing.

While the disadvantage of the Li-ion batteries are as follows [22]:

- The initial cost is moderate.
- High temperatures cause the battery to degrade.
- Charging device must be equipped with charge controller to keep the battery safe.
- Has bad performance when overcharged.
- Crushing the cell can leak the material outside the casing, which may cause a fire hazard.
- Many become unstable in the case of rapid charged at sub-zero temperatures.

2.2.3 Sodium Sulfur

The Sodium Sulfur (NaS) battery technology has molten Sulfur as the positive electrode and molten sodium as the negative electrode. Both materials are separated by beta-alumina ceramic electrolyte. The battery has an operating temperature of 300–350 °C to keep both materials in molten state. The cells are arranged in blocks to have a commercial efficient size and use. The main use is in large scale utility-based generation. The main drawback is the high temperature required to maintain the cell in its molten state. The battery commercial size is in order to megawatts [19].

The advantages of the NaS batteries are as follows [17, 19]:

- Low cost compared to other batteries technologies.
- High number of charge/discharge cycle.
- High energy and power density.
- High energy efficiency.
- Relatively high resistivity to ambient conditions.

The disadvantages of the NaS batteries are as follows [17, 19]:

- Difficult thermal management due to high operating temperature.
- Large safety precautions shall be carried to ensure stable operation.
- The sulfur is corrosive; therefore, the battery shall be treated with strong corrosion resistance compounds.

While the second category has the following two subcategories:

2.2.4 Redox Flow

In redox flow battery (RFB), the electrical energy is stored in different molten electrolytes kept in separate tanks. These different electrolytes act as electrodes. The charging/discharging process is done by flowing of the electrolytes from the tanks to the electrochemical cell body. These batteries are rechargeable type as secondary batteries, but differ in operation concept. The number and size of the used tanks determine the size of the cell.

The most famous variation is the vanadium redox flow batteries (VRFB), which is most suitable for wind farms and solar park's application as the amount of power generated/time needed is highly stochastic. It is suitable for achieving both peak load shaving, load leveling to compensate for generation fluctuations due to meteorological variations daily and seasonally [19].

The advantages of redox flow batteries are as follows [17]:

- The battery has a modular design, as the power stored depends on the size of the battery, while the energy depends on electrolyte concentration.
- The battery is capable of very large depth of discharge (theoretically 100%) as the reactions occur in the liquid phase.
- Large number of charge/discharge cycles.
- Low operating cost.

Meanwhile, the redox flow batteries have the following disadvantages [17]:

- The battery needs a circulating pump to permit the electrolyte to continuously flow.
- The operating temperature shall be kept between 5 and 45 °C, in order to enable the electrolyte to work properly. Any change in this range affects the lifetime of the battery.
- The initial cost of the battery is relatively high.

2.2.5 Hybrid Flow

The hybrid flow battery (HFB) contains two parts, one is the electrochemical cell and the other is the liquid electrolyte. Therefore, this technology combines the secondary batteries and RFB. In the case of charging, the liquid electrolyte deposits

on the electrode, and vice versa in the case of discharging. The size of the battery is determined by the size of the electrochemical cell [23].

Finally, the third category, which is the electrochemical capacitor/ultracapacitor:

2.2.6 Ultracapacitor

Another electrochemical device is the ultracapacitor. This design closes the gap between ordinary electrical capacitors and general batteries. Electrochemical capacitors are different from the ordinary electrical capacitor. The first point of difference is the electrode; the electrode is covered with porous material that allows larger surface areas for the same volume, allowing a larger power density. Second point of difference is the supercapacitor contains a liquid electrolyte that is rich in positive and negative ions. The two electrodes, with separator, are immersed in the electrolyte [24].

The charge/discharge mechanism has three variations as follows:

Double Layered Capacitor

The double layered capacitor (DLC) is the first variation. In case of charging, the ions are polarized, forming separation of charges that acts as two additional “plates.” Thus the supercapacitor behaves as two ordinary capacitors connected in series. Therefore, a larger power density in smaller size. The energy is stored in electrostatic charges without any chemical reactions [24].

DLC can charge/discharge large amount of energy in order of milliseconds. This superior electrical performance aims to the low resistance in the insulating material, something that cannot be achieved in batteries [24].

They have the advantage of reliability, durability, absolute zero maintenance, and long life. Weather conditions do not affect their electrical performance. They have large specific power density that can reach ten times similar battery size [24].

One disadvantage is that the electrolyte needs to be replaced after 5 years regardless of the number of charge/discharge cycles. Also, they have high self-discharge rate that permits using them in long term storage [24].

With efficiency reaches to 90%, they are used in both electronics and power electronics customer-based device. In addition, they could be used in UPS to bridge the short circuit failures [24].

The mathematical model of ultracapacitors is as follows:

$$E_{SC} = \frac{1}{2} \times \epsilon A \frac{V^2}{d} = \frac{1}{2} C V^2 \quad (11)$$

Where,

E_{SC} = energy stored in supercapacitor

ε = permittivity

A = area of plate (m^2)

V = voltage across the plates (Volts (V))

d = spacing between plates (m)

C = capacitance of the capacitor (Farad (F))

Pseudo Capacitor

Another form of the ultracapacitors is the pseudo capacitor. It has a similar construction to DLC, but the energy is stored by means of faradaic mechanisms. Which means that the energy is stored by means of reversible chemical reactions between the electrode and the electrolyte. The chemical reactions have three types: surface adsorption, redox reactions, and doping/undoping in case using conductive polymers as electrodes. The first two processes happen near the electrode surface, while the third one happens in the bulk of the electrolyte [24].

It was named “pseudo” as the used materials are not entirely capacitive as in DLC or dependent on faradic reactions as in batteries [25].

Hybrid Capacitor

Final variation of electrochemical capacitors is the hybrid capacitor. It consists of two electrodes; one of them depends on the double layered capacitor concept, while the other depends on the pseudo capacitor concept [24].

2.3 Chemical Energy Storage

This energy technology is mainly concerned with fuel cells. The fuel cell is a chemical device that stores electrical energy in the form of chemical reactions. However, there are different types of fuel cells but the major difference lies in the type of fuel used. In principal, the fuel cell uses certain type of elements as fuel, while the other element is the oxidant. The main structures of a fuel cell are two electrodes and membrane that form the reaction chamber between the externally stored in tanks [26].

A single fuel cell can generate power at a very low voltage (≤ 1 V). Therefore, to generate required power and voltage, a stack of fuel cells is needed. This stack has fuel cells connected in series and parallel to obtain the desired power. The major difference between fuel cells and batteries is that the battery is a closed system, while the fuel cell needs replenishing its elements to continue operating [26].

The fuel cells can be classified referring to the type of fuel, oxidant, operating temperature, and the field of application. All the fuel cells types can be categorized into six types, as follows [27, 28]:

2.3.1 Proton Exchange Membrane Fuel Cell

PEMFC derived its name from the proton (positive ion) that is generated by using a catalyst with hydrogen gas. The positive ion travels to the anode through the electrolyte membrane that filters the protons from electrons. The remaining electron flow in the external circuit, thus generating electricity. Also, besides the generated electricity, the protons and electrons interact to create water molecules.

The PEMFC operates at a temperature range of 50–100 °C, which is relatively low.

The PEMFC has low electrical efficiency in the range of 40–45%. By applying CHP concept, the efficiency can increase to reach 70–90%.

The sizes of PEMFC vary based on the application. It has the range less than 10 kW for residential usage. For large buildings, the size can reach 50 kW, and for distributed generation application, the PEMFC reaches 250 kW.

The major advantages for PEMFC are light weight, high power density, and start-up rapidly, with solid low corrosion electrodes.

However, the major disadvantages are: low operating efficiency (40–45%), expensive platinum catalyst, and high sensitivity to fuel impurities (CO, H₂S).

The detailed mathematical modeling for this type of fuel cell can be found in reference [29].

2.3.2 Alkaline Fuel Cell

The AFC is considered as the one of the earlier models of fuel cells that was invented in the 1950s. The electrolyte in this fuel cell is the aqueous alkaline solution of potassium hydroxide (KOH). The operation follows the same principle of fuel cells. It was named the “Bacon Cell” after its British inventor Thomas Bacon.

AFC can operate in a temperature range of 50–200 °C. However, the new designs can operate at 70 °C.

It is characterized by high efficiency of 60–70%. And can reach 80% if combined heat and power (CHP) concept is applied.

It was used by NASA in its shuttles in Apollo mission in the 1960s. The uses are not only limited to electricity generation but also for producing potable water. It has limited commercial usage in transportation. The AFC sizes ranges from 10 to 100 kW.

AFC’s major advantages are high power density and quick startup.

Meanwhile, the major disadvantages are a short life span due to the use of corrosive electrolyte and the cell becoming easily poisonous to CO₂ and needing an external device to eliminate CO₂.

2.3.3 Phosphoric Acid Fuel Cell

The PAFC uses phosphoric acid (H_3PO_4) in liquid form and carbon paper as electrodes. The acid is a clear, colorless liquid with versatile applications of fertilizers to pharmaceuticals. The hydrogen is the input fuel and charge carrier as in PEMFC with the same operation concept. One of the reasons behind high operating temperature is to avoid the poisoning of the fuel with CO. On the contrary of other fuel cells, PAFC can use normal air as fuel rather than oxygen.

PAFC has an operating temperature range of 175–200 °C. However, the system start-up required a temperature of 40 °C.

Concerning the operational efficiency of PAFC, it ranges from 40% to 50%. Furthermore, by utilizing the CHP concept, efficiency can reach 85%.

The PAFC is used in commercial applications in ranges that reach 500 kW. Also, in some countries, the PAFC size reached 1.3 MW.

The main advantages of PAFC are used in heating water and as a CHP.

On the other hand, PAFC has the following disadvantages: all the points listed for PEMFC. Also, the initial cost is tripled as the input fuel is air rather than pure oxygen. Also, the cost increases due to the use of coating made from platinum catalyst.

2.3.4 Molten Carbonate Fuel Cell

The electrolyte in MCFC is molten carbonate salt, in which two porous ceramic electrodes are immersed.

MCFC operates at high temperatures that range from 600 to 700 °C.

This fuel cell has an efficiency greater than 50%. By applying the CHP concept, the efficiency can exceed 80%.

The MCFC mainly used for medium and large power applications ranges from hundreds of kilowatts to 1 MW. And in some sites, a system of size 2 MW is installed.

Among the advantages of MCFC are: high efficiency, and for electrochemical oxidation the MCFC doesn't need metal catalyst.

However, the disadvantages of MCFC are: slow start up and inability to handle fuel impurities.

2.3.5 Solid Oxide Fuel Cell

The SOFC uses a dense and solid ceramic material called yttria stabilized Zirconia (YSZ), as electrolyte. The YSZ is used due to the two main characteristics: the first is high chemical and thermal stability, while the second is its pure ionic conductivity.

SOFC operates at a very high temperature that ranges from 800 to 1000 °C.

The SOFC has an operating efficiency of 50–60%. In case of using CHP concept, the efficiency can reach 90%.

SOFC is mainly in wide range from small residential loads (1–5 kW) and medium range applications as micro-grids (100–250 kW). And finally, large utility sizes that reaches 1.7 MW.

The main advantage of SOFC is high efficiency and can be used in the generation of electricity using excess heat.

Meanwhile, the SOFC has the following disadvantages: slow start up, high cost, and intolerance of sulfur composed in the chemical reaction.

2.3.6 Direct Methanol Fuel Cell

The DMFC is a new technology compared to the aforementioned fuel cell technologies. It is an enhanced type of PEMFC, it can be considered as a clean renewable energy source. It uses liquid alcohol or methanol as fuel.

DMFC operates a low temperature that ranges from 60 to 200 °C.

The DMFC has a low operating efficiency of 40%. In case applying CHP concept the efficiency reaches 80%.

DMFC is mainly used to replace batteries in portable devices like cameras, laptops, and other electronic devices. As this type has a power range capacity ranges from 1 W to 1 kW.

The main advantages of SOFC are: low operating temperature, and the absence of the need of a catalyst (fuel reformer).

While the main disadvantages of SOFC are: low efficiency and low power density.

2.4 Thermal Energy Storage Devices

The thermal energy storage system (TSS) is another indirect way to store electrical energy. In this form, the energy is stored in form of heat that can be re-used to generate electrical energy.

2.4.1 Sensible Heat (Molten Salt)

The SHES (sensible heat energy storage) technology uses a mixture of salts (sodium nitrate, potassium nitrate, and calcium nitrate) as a latent heat storage and heat transfer fluid. The salt mixture is pumped from the *cold tank* (where molten salt temperature >220 °C) to solar troughs to absorb heat. The molten salt (after heating to 566 °C) is pumped to the *hot tank*. If there a need to retrieve the stored energy, the molten salt from the hot tank is pumped to steam turbine to create superheated steam which generates electrical power [30].

The system advantage is storing large amount of energy in small volumes. Also, the temperature difference is minimal, thus ensuring high heat transfer efficiency [30].

The system main disadvantage is that the molten salt could freeze in the pipes at low temperature (<200 °C). Also, the mixture might decompose at extremely high temperature [30].

As described, the system is used economically with concentrated solar power (CSP) plants [30].

2.4.2 Latent Heat (Cryogenic Energy Storage)

One of the applications of LHES (latent heat energy storage) is liquid air energy storage. LAES could be obtained by applying the same concept illustrated in the CAES. The LAES avoids many defects, such as the need of caverns, needed by CAES, and large reservoirs needed by PHES. This eliminated the geographical limitations imposed by both CAES and PHES. It is still a hot area of academic research with no practical implementations, only prototypes for academic research [31].

The ambient air is liquefied by removing the heat from it in a process called cryogen. In case more power is needed, a specific cryogenic pump is used to expand the air. Sometimes a fuel can be used (ex: natural gas) to heat-up the liquid air before entering the turbine/generator set [31].

The LAES possess a theoretical round trip efficiency of 70%. Also, it can be used for grid scale storage in ranges of several hundreds of MW [31].

The LAES have the following advantages [31]:

- In case of discharge, the technology can be beneficial in both generating electricity (using turbine/generator set) and use the low temperature in cooling purposes (using evaporator).
- The technology has high power and energy density in a smaller volume of storage (compared with CAES).
- Low initial cost.

On the other hand, LAES have the following disadvantages [31]:

- The system has limited applications (mainly in academic range). The challenge is to produce a competitive (technical and financial) alternative to the CAES.
- The technology has low efficiency in small size applications.
- The final challenge is to find the optimal liquefaction and thermodynamic process in the way to commercialize LAES.

2.4.3 Sorption Thermal Energy Storage

STES is considered as an emerging thermal technology besides SHES and LHES. It can play an important role with renewable energies to offer a more stable supply and mitigate intermittency. The technology depends on a reversible reaction between sorbent/sorbate materials. Among the used materials are: silica gel (SiO_2), zeolite (crystalline aluminosilicates), natural rocks, and activated carbon; these are considered as solid absorption materials. While the liquid absorption materials come in pairs, such as: $\text{CaCl}_2/\text{H}_2\text{O}$ or $\text{NaOH}/\text{H}_2\text{O}$, and many others. The technology is still under the academic research via prototypes with promising performance [32, 33].

The technology has two variations, closed STES and open STES:

- Closed system sorption energy storage [32, 33]:
 - It consists of the sorption reactor, evaporator, and condenser.
 - In case of charging (desorption), the heat energy is supplied to the system from an external source (ex: concentrated solar power). Then the energy is stored by breaking the chemical bond between sorbent/sorbate, which forms chemical potential. The breaking of the bond releases water vapor that flows from reactor to condensate in the condenser. The evaporation valve between the reactor and condenser is opened. The condenser stores the water and releases heat to the surrounding. Then both the sorbent and sorbate are isolated in separate tanks, and the evaporation valve is closed. This is used mainly in the summer season or hot days.
 - When heat is needed, the system is put into discharge mode (sorption). The tanks of sorbents and sorbates are put together and the evaporation valve is open the reaction between the materials release heat. This is mainly done in the winter season or night.
 - This technology has some advantages as follows: it has the ability to store heat for cold weathers or provide cooling via evaporation. Tanks containing the stored heat can be transferred over long distances.
 - While, there are disadvantages as follows: the system is complicated as it has many components. It occupies a large volume that adds to the manufacturing complexity.
- While the system is called open system sorption energy storage:
 - The system is much simpler than closed STES, in which both the condenser and evaporator are eliminated.
 - In charging mode, the hot ambient air is directly supplied to the sorbent reactor, thus releasing the water vapor to the ambient directly. This makes the ambient air warm. This makes the sorbent unsaturated.
 - In discharging mode, a fan is used to blow cold wet ambient air (may need a humidifier) to the unsaturated sorbent reactor, thus releasing the sorption heat into the surrounding. Therefore, heating is produced.

- The major advantages are: simple structure than closed STES. Easy to fabricate and maintain.
- On the other hand, the system disadvantages are: the manipulation of moisture of the ambient air (supplying can affect the thermal comfort of individuals).

Both systems can be used in deferring the need of electric energy for heating/-cooling.

2.5 Electrical Energy Storage Devices

EES is a direct form of electrical energy storage, as the stored energy is preserved in its original form (i.e., electrical charges/field).

2.5.1 Capacitor

Electrical capacitors store electrical energy in the form of static charges. They consist of two plates isolated with isolating material (mainly air). By applying electrical current, the magnetic field associated rearranges the positive and negative ions thus the energy is stored directly [34].

The mathematical formula for stored energy in capacitors is as follows [34]:

$$E_{\text{cap}} = \frac{1}{2} \varepsilon A \frac{V^2}{d} \quad (12)$$

Where,

E_{cap} = energy stored in capacitor

ε = permittivity

A = area of plate (m^2)

V = voltage across the plates (Volts (V))

d = spacing between plates (m)

And the capacitance can be expressed by the following equation [34]:

$$C = \varepsilon \frac{A}{d} \quad (13)$$

Therefore, the energy stored in terms of capacitance and voltage is as follows [34]:

$$E_{\text{cap}} = \frac{1}{2} C V^2 \quad (14)$$

2.5.2 Super Magnetic Energy Storage

As electrical current passes in any conductor, the electrons forming the current collides with the molecules of the conductor. Because of the electrical resistance of the material, some of them pass through and others do not. Electron passing thus creates collisions that heat the conductor up. The heat stresses the material up and could eventually cause failure in the material. This heating limits the amount of electrical current that can pass through the conductor [23, 35].

It was found that the materials if cooled, the harmful effect of the heat stress could be avoided. Moreover, the same material can bare more electrical current than in the absence of cooling. In other words, the electrical performance could be enhanced by cooling. Therefore, if we cooled the material well enough (reaching *superconducting critical temperature*), we can have zero resistance conductor. This conductor is called *superconductor* [23, 35].

The SMES is based on the previous idea. A coil enclosed in special container, in which the coil is operating at superconducting state by means of cryogenic fluid. The cryogenic fluid can be Helium/Nitrogen gas; that is cooled to reach 4 K. This process liquefies the gas. Then it is pumped to the *cryostat* “container containing the coil.” Now, there are materials that can be superconducting at 100°K [23, 35].

The coil is charged using direct current (dc) injected to the coil that generates a magnetic field.

The advantage of SMES is their very quick response. The stored power is instantaneously ready whenever discharge is requested. The system achieves 85–90% efficiency. As the overall system is stationary (i.e., no moving parts), but reliability is affected by the effectiveness of the cryogenic system [23, 35].

The disadvantage of the SMES is the energy demand to keep the cryogenic system operating [23, 35].

The SMES used for load frequency control, grid voltage stability, and as spinning reserve. The mathematical model for the SMES is as follows [35, 36]:

$$E_{SMES} = \frac{1}{2} \iiint L B dx dy dz = \frac{1}{2} L I^2 \quad (15)$$

Where,

E_{SMES} = energy stored

L = intensity of magnetic field (Henry (H)) (A/m)

B = induced magnetic field (Tesla (T)) (Wb/m²)

I = current (Ampere)

3 Classification of Energy Storage Devices

3.1 Classification Based on the Type of ESD Technology

In Fig. 1, the classification is done considering two parameters; the first one is the type of technology used to store the electrical energy. This led to five different categories: mechanical, electro-chemical, chemical, thermal, and electrical.

The aforementioned categories can be further classified into the state of the electrical energy. Those categories are indirect and direct storage. In *indirect storage*, the electrical energy is converted into another energy form and stored. This applies to mechanical, electro-chemical, chemical, and thermal. While in *direct storage*, the electrical energy is stored in its original form, and the electrical storage devices are the only ones that can achieve that [37].

3.2 Classification Based on ESD Role

The power grid is divided into three main parts: generation, transmission, and distribution. In this classification, the energy storage plays different roles based on their location in the power grid. This means that the energy storage (regardless of its type) can add benefits to whatever section it is in or will be added to.

The role/benefits of using energy storage are both technical and financial. It can help in facing both the planned/expected events and the sudden fluctuations. Thus enable the operators to have a flexible grid with resilient behavior.

The benefits can be extended to off grid networks which are far from municipal power grids. Also, the households that depend on electrical power generation from renewable resources [38, 39].

In Fig. 2, a demonstration of the different roles that the energy storage can play in various locations of the power grid.

While in Fig. 3, a depiction of the different energy storage devices that are assigned to each of the power grid functions and locations [40–42].

3.3 Classification Based on ESD Service Time

In Table 1, the energy storage devices are classified as per the discharge duration time. Also, for each time duration, there are certain applications that fit the mentioned time window. Finally, the table shows that some energy storage technologies can be used in any task regardless the duration time, ex: Pb-acid batteries. While SMES is only suitable for medium duration tasks only [42, 43].

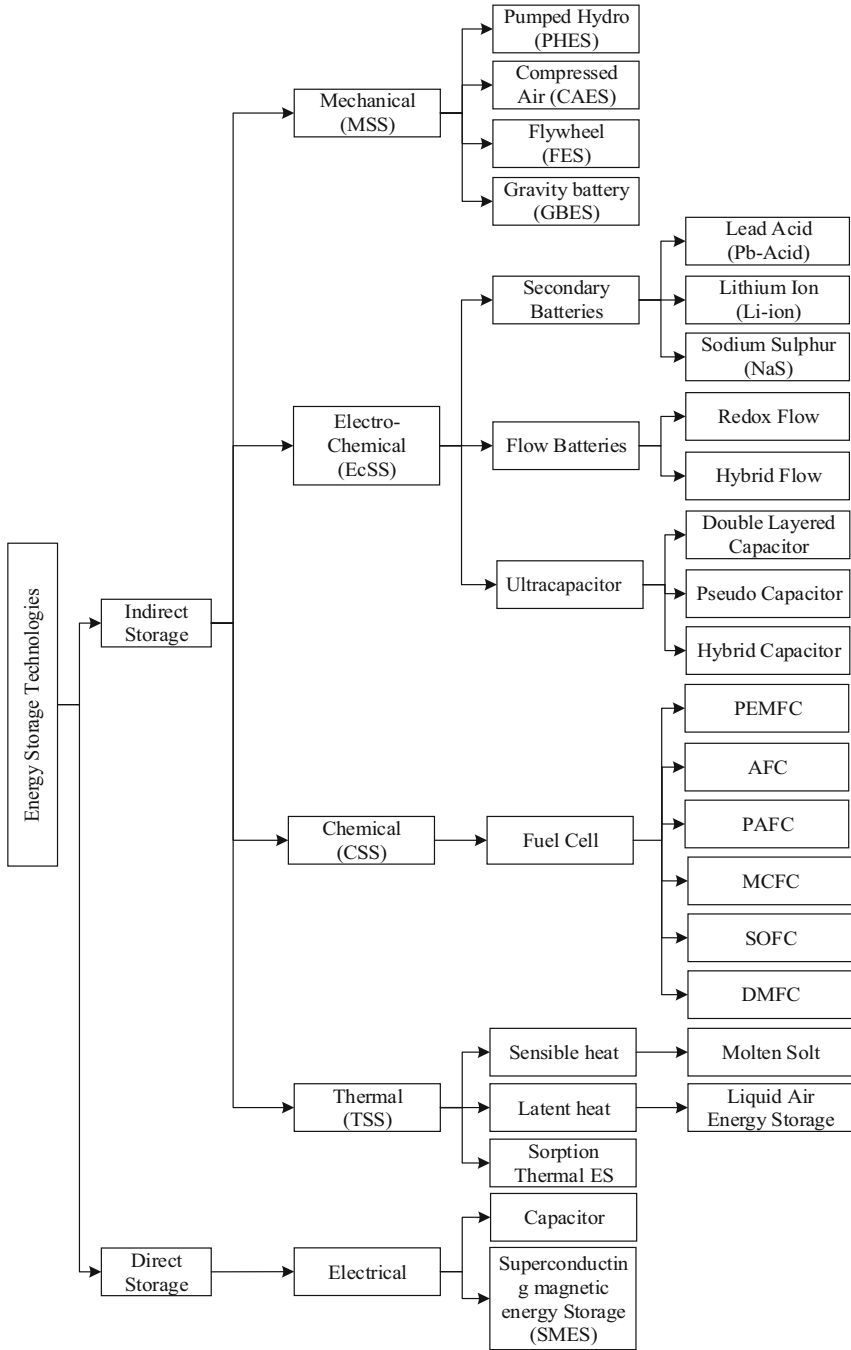


Fig. 1 Classification of ESD technologies

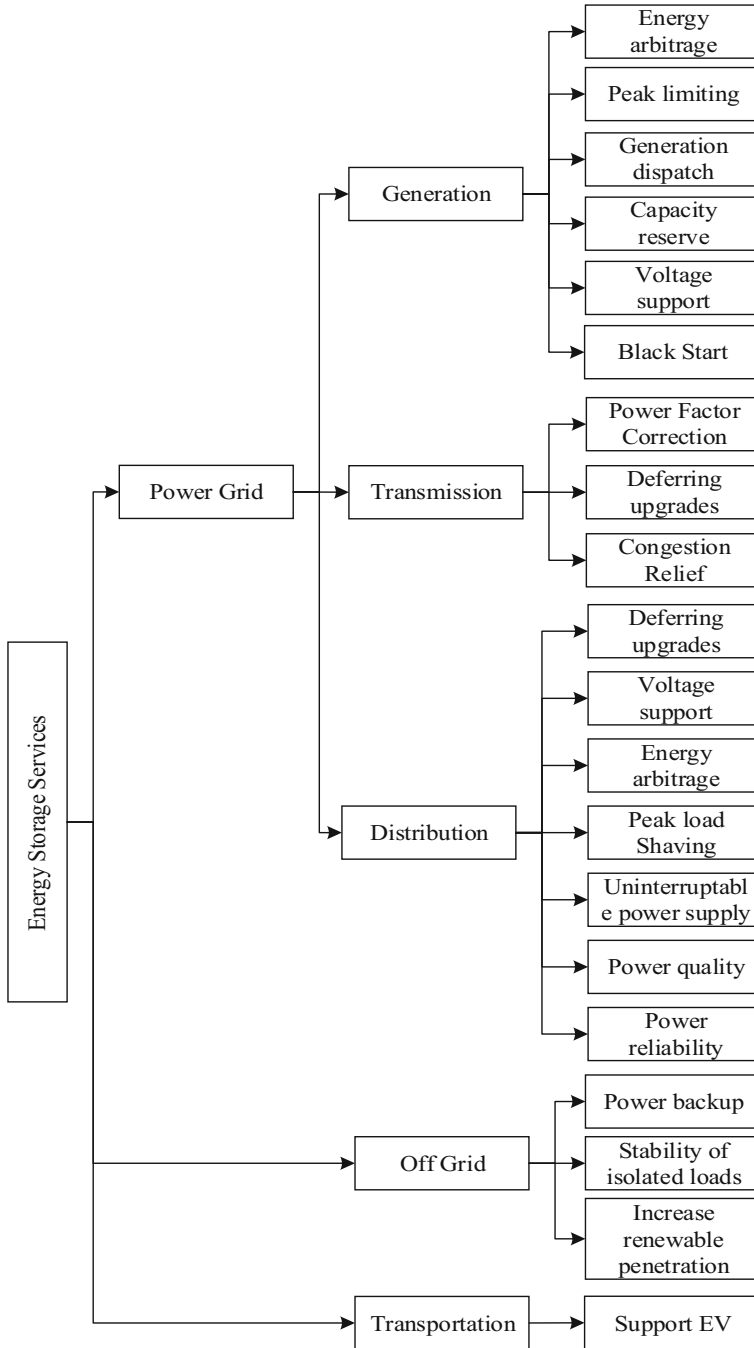


Fig. 2 Classification of ESD as per location in power grid

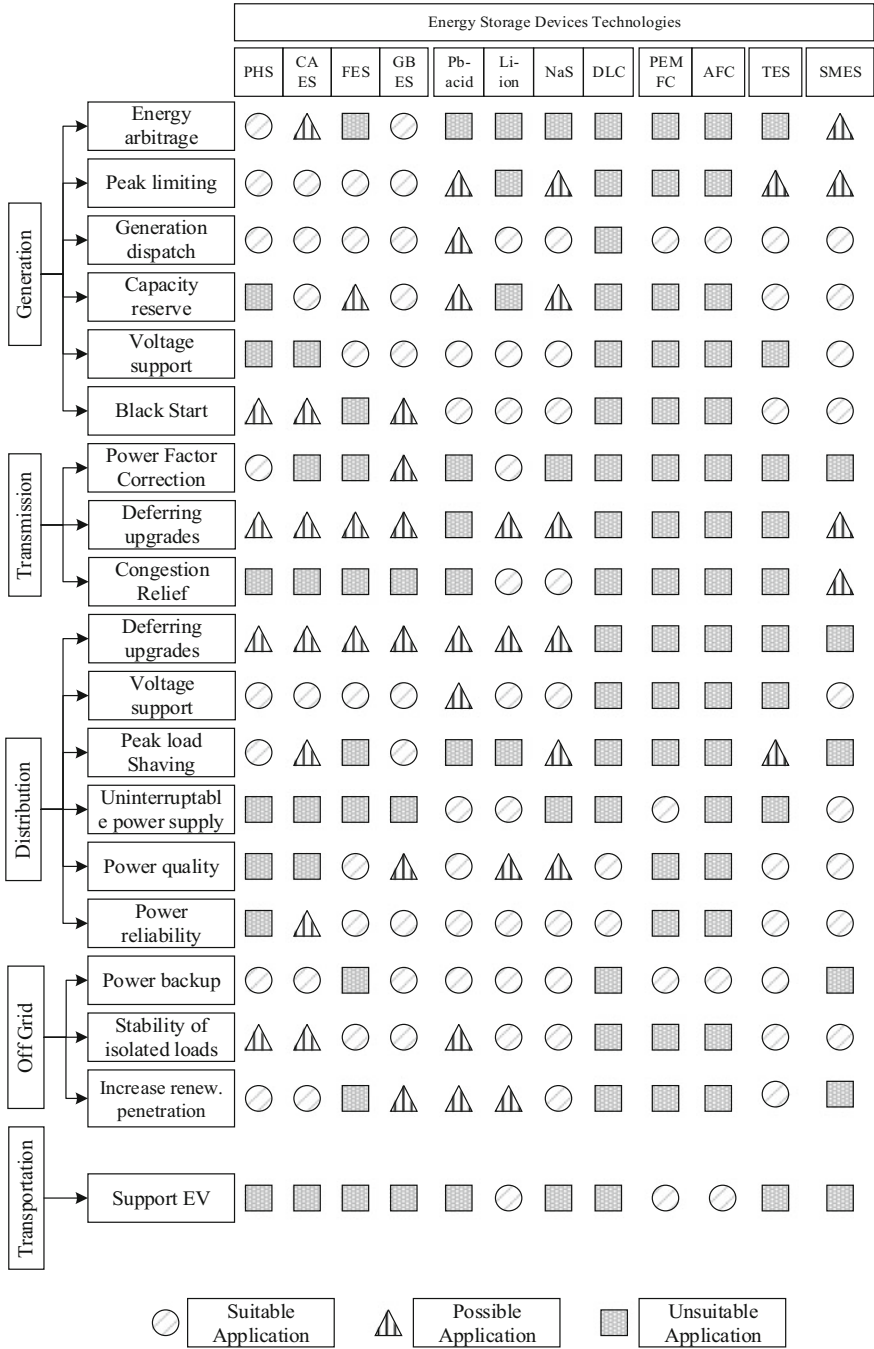


Fig. 3 ESD Technologies vs. power grid applications

Table 1 Classification of ESD based on service time

#	Service time	Application	Type of ESD
1.	Long duration	Load leveling Online reserve Energy arbitrage Peak shaving Frequency regulation Seasonal balancing Renewable penetration	PHS CAES RFB FCs Pb-acid NaS
2.	Medium duration	Black start Demand side management Distributed storage Investment deferral Contingency relief Spinning reserve Transmission support	Pb-acid Li-ion RFB FCs Thermal energy storage FES SMES
3.	Short duration	Power quality Intermittency mitigation Transient stability Frequency regulation Renewable penetration Smoothing fluctuation	FES Ultracapacitor Pb-acid Li-ion SMES

4 Evaluation and Selection Criteria for Energy Storage Devices

In selecting an energy storage device to certain application, some optimization models rely only on economic modeling. Despite the importance of this approach, the result may be biased. The following aspects shall be considered [43]:

- Modularity to enable future expansion.
- High energy capacity to allow long period energy storage.
- The ratio of power storage to energy storage to be high.
- High efficiency.
- Large number of charging/discharging cycles.
- High value of depth of discharge (DoD).
- Low rate of self-discharge.
- Environmentally friendly.
- Tolerance to (ambient temperature, humidity, etc. . . .).
- Simple in design and usage.
- Cost effective in initial, operation, and maintenance costs.

After selecting the proper energy storage, the selection is ready to undergo an evaluation (Fig. 4). In return, the evaluation has the following criteria's listed hereunder and depicted in Fig. 3 [3, 44, 45]:

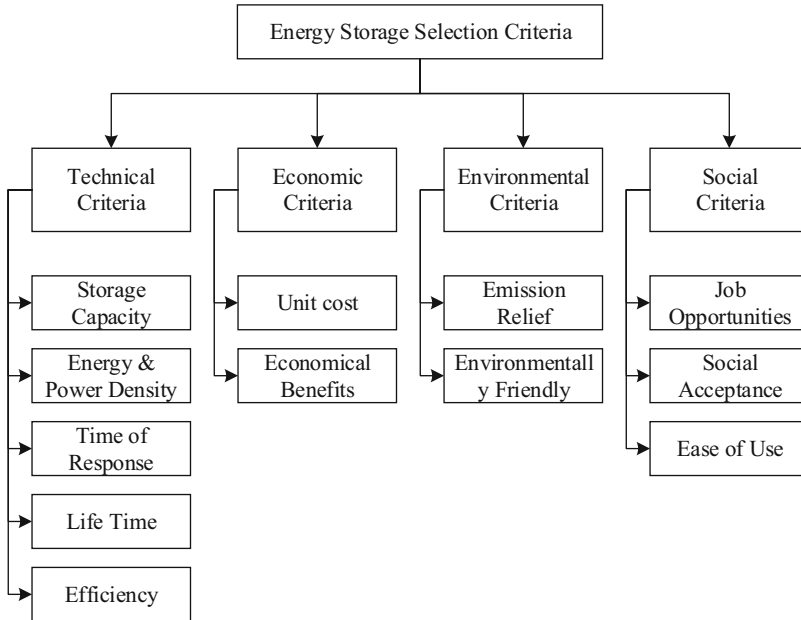


Fig. 4 Selection criteria for ESD

4.1 Technical Criteria

- Storage capacity: it indicates how much energy the device can store after finishing the charging phase.
- Energy and power density: both are the ratios of the storage to mass and weight respectively. Some energy storage devices have significant difference between the energy and power storage. This is referenced to either the technology used or the type of material.
- Time of response: it is the amount of time needed by the storage device to be operational when needed. As long as this value is low, the reliability of the used storage device increases.
- Lifetime: it is the operational period of time before the energy storage device is aged and need to be replaced.

4.2 Economic Criteria

- Unit cost: this feature represents all the costs needed by the energy storage device. From initial, to operation and maintenance costs. By varying the energy storage technology and size, this feature is affected considerably.

- Economic benefit: it can be the time needed to return the initial investment, the impact on energy market, price lowering as a result of supply stability and many more.

4.3 Environmental Criteria

- Emission relief: amount of solid, water, and gas wastes due to usage of energy storage. The lower the values of three waste types, the more convenient the storage device is. Also, the amount of pollution the energy storage produces as a result of its wastes.
- Environmentally friendly: it is the impact of installation, operation, vegetation, and land use on the ecosystem. All these impacts indicate how much the energy storage is friendly to the surrounding ecosystem.

4.4 Social Criteria

- Job opportunities: some energy storage projects are labor intensive in both nation-wide and to urban communities. These created opportunities may be of direct type, indirect type, short term, and long term.
- Social acceptance: it is important to investigate the acceptance of the surrounding communities to the installed energy storage projects. Some energy storage technologies are not accepted for their large land occupation, noisy operation, or any other environmental/health issues. Public acceptance shall contribute in the construction decision.

5 Energy Management of Energy Storage Devices

The energy management is concerned by some of the following aspects [46, 47]:

- Operation scheduling, as it should be optimized to ensure maximizing the benefits of the energy storage device.
- Operation coordination of multiple energy storage devices considering their various sizes, technologies, technical aspects, etc.
- Maximizing the energy efficiency of each energy storage device.
- Managing charging/discharging cycles to increase the lifetime of the energy storage device(s).
- Considering various operation constraints of each energy storage device. The constraints are dictated by the technology of the energy storage device.

A typical energy management architecture comprises many stages and component, which are: EMS, PCS, and DMS. Each with a specific function. The different control components are interconnected with Modbus/TCP. In the following section each component function and location in the control structure will be discussed [46].

5.1 Energy Management System

The energy management system (EMS) is the component responsible for the overall management of all the energy storage devices connected to a certain system. It is the supervisory controller that masters all the following components.

For each energy storage device or system, it has its own EMS controller. It is called the slave EMS. In this case, the slave EMS is supervised by the master EMS.

The master EMS takes the inputs from the customer/owner, market prices, and utility conditions. Among the outputs are the operating conditions for each energy storage device. These outputs are passed to the slave EMS of connected energy storage systems.

If the system has master/slave, EMS it is called centralized control structure. If the system has slave EMS only, it is called a decentralized structure.

The major role of master EMS is to coordinate the data flow of from/to each of the subsystem components. The data flow is (and not limited to) devices status, measurements, etc.

5.2 Power Conversion System

The power conversion system (PCS) is responsible for the interface between the energy storage device and the electrical grid, thus managing the power flow from the device to the grid. It has an intermediate location in any control structure. As most of the energy conversion systems produce DC current, the PCS has to integrate these devices to the AC grid. The mechanical energy storage can be excluded from DC/AC integration.

PCS receives the inputs from the EMS (real and reactive power status) and then delivers the output to the device management system (DMS). The PCS is responsible for the primary and secondary control functions; they are as follows:

- *Charging mode*, it is one of the secondary control functions. It happens when the master EMS give the charging command to the device PCS. The charging has three variants. The first is the bulk charge/current control, this happens in case of fast charging with the device has low state of charge. The second is the absorb charge/voltage control. This in case the state of charge is higher than a certain threshold. Finally, the floating charge/voltage control. In this case, the state of charge is close to maximum. In FES system, the terminology is slightly

different; the bulk charge is named torque control. While the absorb charge is called speed control. Finally, the floating charge is called power control.

- *Discharge mode*, it is another secondary control mode. The discharge shall consider the following aspects: the first one is the minimum allowable depth of discharge DOD. The second one, the available energy stored in the device.
- *Standby mode*, it is also one of the secondary control modes. In this mode the energy storage device is connected to the grid but it is not charging or discharging. This mode occurs when the SoC is at maximum.

After the PCS determines the above mentioned states, the primary control is performed. The primary control is performed either using transformer-based controllers or transformerless controllers. The transformerless controllers depend on power electronic devices. Primary control has the following functions:

- Charge control
- Voltage control
- Current control
- Combined voltage/control

The final task for PCS is the communication interface.

5.3 *Device Management System*

This component might be referred to as a BMS (battery management system) in the case of battery-based systems. The DMS is connected directly to the energy storage device. This is the final device in any control structure, before the device itself. The DMS is responsible for the following tasks:

- *Active safety protection*, thus to ensure the safe operation of the energy storage device. The active safety protects the device from overcharge, deep discharge, and over temperature. All these can reduce significantly the lifetime of energy storage device. If any of the above conditions are detected, DMS can disconnect the device from the grid as a protection measure.
- *Passive safety protection*, this stage occurs to prevent worst case scenario events. Examples on these events are short circuits, leakage of chemical materials, thermal runaway (batteries), over speed rotation (FES), etc. All energy storage systems are equipped with circuit breakers/fuses to protect against short circuits. Thermal insulation as a counter measure for thermal runaway. Speed sensors to avoid over rotation and reinforced casing to contain the system in case of damage of FES.
- *State of charge*, the SoC is the indication of how much energy is still within the device. SoC can be measured directly in mechanical systems such as PHES, by measuring the water level in reservoir. While in batteries (e.g., Li-ion), it cannot be measured, it can only be estimated using the measured battery

Table 2 Economic analysis of energy storage devices

#	Energy storage		Capital cost		O&M	Service years
	Category	Technology	Power (\$/kW)	Energy (\$/kWh)	(\$/kWh.yr)	
1.	MSS	PHS	403–4644	5–136	2–10	≤70
2.		CAES	432–1674	2–130	2–5	≤40
3.		FES	32–756	216–162,000	5–6	≤20
4.	EcSS	Pb-acid	211–648	132–915	3–26	≤20
5.		Li-ion	161–4320	282–4104	2–123	≤15
6.		NaS	221–3240	194–1080	2–54	≤15
7.		VRFB	351–1620	142–1080	4–51	≤10
8.		DLC	108–864	108–101	1–6	≤40
9.	CSS	PEMFC	<1500	–	1400–4200	≤15
10.	TES	Molten salt	3400–4500	–	120	≤30
11.		LAES	6000–15,000	–	250	≤30
12.		STES	1000–3000	–	20–60	≤30
13.	EES	SMES	120–150	–	14.5–22.2	≤40

parameters. This estimation depends on mathematical modeling. The precision of SoC estimation depends on the model accuracy.

- *State of health*, the SoH is the comparison between the current conditions of the energy storage device with reference to its ideal condition.
- *Specific applications*, as the energy storage technology operating concept and conditions varies, the DMS has to consider these variations.

6 Economic Analysis of Energy Storage Devices

This section will present the main contributing values of the economic analysis of energy storage device [2, 27, 40, 41, 48–53]. The parameters are depicted in Table 2.

7 Conclusions

From the aforementioned presentation, it is clear that energy storage is useful by all its forms and means. Energy storage is versatile in sizes and applications, which enables adding it to either generation, transmission, or distribution. Regardless of its location, the added energy storage device will be useful.

However, it is important to take care in selecting the energy technology. The selection shall consider all the mentioned aspects thus to harness benefits and avoid drawbacks. It is worth mentioning that the emerging technologies can contribute strongly in the field supply stabilization and mitigating fluctuations.

It is notably to consider the different economic parameters for each energy storage device. Starting from capital cost; through the operation and maintenance costs; finally, the salvage value costs. All these costs should be included in the decision maker consideration in order to select the proper energy storage device that suites well the required application.

Finally, the energy storage devices shall be selected via multi-criteria decision-making techniques. Those techniques incorporate the economic model, along with geographical location limitations, technical aspects of the energy storage, and finally, the decision maker preferences. Those aspects affect the selection considerably and make it more adequate from an economical point of view.

References

1. Kiptoo MK, Lotfy MS, Adewuyi OB, Conteh A, Howlader AM, Senjyu T (2020) Integrated approach for optimal techno-economic planning for high renewable energy-based isolated microgrid considering cost of energy storage and demand response strategies. *Energ Convers Manage* 215(1):16. <https://doi.org/10.1016/j.enconman.2020.112917>
2. Rahman MM, Oni AO, Gemechu E, Kumar A (2020) Assessment of energy storage technologies: a review. *Energ Convers Manage* 223(1):28. <https://doi.org/10.1016/j.enconman.2020.113295>
3. Liu Y, Du JL (2020) A multi criteria decision support framework for renewable energy storage technology selection. *J Clean Prod* 227(1):17. <https://doi.org/10.1016/j.jclepro.2020.122183>
4. Zhang C, Chen C, Streimikiene D, Bzlezentis T (2019) Intuitionistic fuzzy MULTIMOORA approach for multi-criteria assessment of the energy storage technologies. *Appl Soft Comput* 79:410–423. <https://doi.org/10.1016/j.asoc.2019.04.008>
5. Levine JG (2011) Pumped hydroelectric energy storage. In: Barnes FS, Levine JG (eds) *Large energy storage systems handbook*. CRC Press, Boca Raton, pp 51–76
6. Rehman S, Al-Hadhrami LM, Alam MM (2015) Pumped hydro energy storage system: a technological review. *Renew Sust Energ Rev* 44:586–598. <https://doi.org/10.1016/j.rser.2014.12.040>
7. Succar S (2011) Compressed air energy storage. In: Barnes FS, Levine JG (eds) *Large energy storage systems handbook*. CRC Press, Boca Raton, pp 111–152
8. Allen K (1985) CAES: the underground portion. *IEEE Trans Power Appar Syst* 104:809–812. <https://doi.org/10.1109/TPAS.1985.319078>
9. Mehta B (1992) CAES geology. *EPRI J* 17:38–41
10. Knoke S, Schänker R, van der Linden S (2003) Compressed air energy storage. In: Gotschall H, Mears D (eds) *EPRI-DOE handbook of energy storage for transmission & distribution applications*. EPRI, Palo Alto, pp 15.1–15.42
11. Arsie I, Marano V, Nappi G, Rizzo G (2005) A model of a hybrid power plant with wind turbines and compressed air energy storage. In: *The American Society of Mechanical Engineers, New York, PWR2005–50187*, pp 987–1000
12. Komarnicki P, Lombardi P, Styczynski Z (2017) *Electric energy storage systems: flexible options for smart grids*. Springer, Berlin, pp 136–140
13. Miyagawa Y, Kamenno K, Takahata R, Ueyama H (1999) A 0.5 kWh flywheel energy storage system using a high-T/sub c/superconducting magnetic bearing. *IEEE Trans Appl Supercond* 9:996–999
14. Kamath H, Key T, Bakis C, Richey S, Plater B, Townley D (2003) Flywheel energy storage. In: Gotschall H, Mears D (eds) *EPRI-DOE handbook of energy storage for transmission & distribution applications*. EPRI, Palo Alto, pp 13.1–13.42

15. Hou H, Xu T, Wu X, Wang H, Tang A, Chen Y (2020) Optimal capacity configuration of the wind-photovoltaic-storage hybrid power system based on gravity energy storage system. *Appl Energy* 271:1–9. <https://doi.org/10.1016/j.apenergy.2020.115052>
16. Berrada A, Loudiyi K, Zorkani I (2017) System design and economic performance of gravity energy storage. *J Clean Prod* 156:317–326. <https://doi.org/10.1016/j.jclepro.2017.04.043>
17. Wu F, Yang B, Ye J (2020) *Grid-scale energy storage systems and applications*, 1st edn. Academic, London, pp 17–56
18. Fahim SR, Hamid NM, Hegazy YG (2019) Statistical sizing of a 100% renewable energy system with battery energy storage system. In: *IEEE 7th international conference on smart energy grid engineering (SEGE)*, pp 309–314. <https://doi.org/10.1109/SEGE.2019.8859775>
19. Scott I, Lee S (2011) Battery energy storage. In: Barnes FS, Levine JG (eds) *Large energy storage systems handbook*. CRC Press, Boca Raton, pp 153–179
20. Enos DG (2015) Lead-acid batteries for medium and large-scale energy storage. In: Menictas C, Kazacos MS, Lim TM (eds) *Advances in batteries for medium and large scale energy storage*. Elsevier/Woodhead Publishing, Cambridge, pp 57–71
21. Salkind A, Zguris G (2011) Lead-acid batteries. In: Reddy TB, Linden D (eds) *Linden's handbook of batteries*, 4th edn. McGraw Hill, New York, pp 16.1–16.87
22. Dahn J, Ehrlich GMG (2011) Lithium-ion batteries. In: Reddy TB, Linden D (eds) *Linden's handbook of batteries*, 4th edn. McGraw Hill, New York, pp 26.1–26.79
23. The International Electrotechnical Commission (IEC) (2011) *Electrical energy storage*. White paper, Geneva
24. Burke AF (2011) Electrochemical capacitors. In: Reddy TB, Linden D (eds) *Linden's handbook of batteries*, 4th edn. McGraw Hill, New York, pp 39.1–39.44
25. Jiang Y, Liu J (2019) Definitions of pseudocapacitive materials: a brief review. *Energy Environ Mater* 2(1):30–37, Wiley Online Library. <https://doi.org/10.1002/eeem2.12028>
26. Petricca L, Ohlckers P, Chen X (2013) The future of energy storage systems. In: Zobia AF (ed) *Energy storage technologies and applications*. In Tech, Rijeka, pp 113–130
27. Kirubakaran A, Jain S, Nema RK (2009) A review on fuel cell technologies and power electronic interface. *Renew Sust Energ Rev* 13:2430–2440. <https://doi.org/10.1016/j.rser.2009.04.004>
28. Mekhilef S, Saidur R, Safari A (2012) Comparative study of different fuel cell technologies. *Renew Sust Energ Rev* 16:981–989. <https://doi.org/10.1016/j.rser.2011.09.020>
29. Fahim SR, Hasanien HM, Turky RA, Alkuhayli A, Al-Shamma'a AA, Noman AM, Tostado-Veliz M, Jurado F (2021) Parameter identification of proton exchange membrane fuel cell based on hunger games search algorithm. *Energies* 14(16):1–21. <https://doi.org/10.3390/en14165022>
30. Begeal C, Decker T (2011) Solar thermal energy storage. In: Barnes FS, Levine JG (eds) *Large energy storage systems handbook*. CRC Press, Boca Raton, pp 181–212
31. Callaghan OO, Donellan P (2021) Liquid air energy storage systems. *Renew Sust Energ Rev* 146:1–12. <https://doi.org/10.1016/j.rser.2021.111113>
32. Zhang Y, Wang R (2020) Sorption thermal energy storage: concept, process, applications and perspective. *Energy Storage Mater* 27:352–369. <https://doi.org/10.1016/j.ensm.2020.02.024>
33. Yu PN, Wang RZ, Wang LW (2013) Sorption thermal storage for solar energy. *Prog Energy Combust Sci* 39:489–514. <https://doi.org/10.1016/j.pecs.2013.05.004>
34. Huggins RA (2010) *Energy storage*. Springer, Germany, pp 69–93
35. Hassenzahl W, Schoenung S, Abel T (2003) Superconducting magnetic energy storage. In: Gotschall H, Mears D (eds) *EPRI-DOE handbook of energy storage for transmission & distribution applications*. EPRI, Palo Alto, pp 12.1–12.31
36. Hasanien HM, Muyeem SM (2015) Particle swarm optimization-based superconducting magnetic energy storage for low-voltage ride-through capability enhancement in wind energy conversion system. *Electr Power Compon Syst* 43(11):1278–1288. <https://doi.org/10.1080/15325008.2015.1027017>
37. Hannan MA, Hoque MM, Mohamed A, Ayoub A (2017) Review of energy storage for electric vehicle applications: issues and challenges. *Renew Sust Energ Rev* 69:771–789. <https://doi.org/10.1016/j.rser.2016.11.171>

38. International Renewable Energy Agency (IRENA) (2017) Electricity storage and renewables: costs and markets to 2030. IRENA, Abu Dhabi
39. Pearre NS, Swan LG (2015) Technoeconomic feasibility of grid storage: mapping electrical services and energy storage technologies. *Appl Energy* 137:501–510. <https://doi.org/10.1016/j.apenergy.2014.04.050>
40. Palizban O, Kauhaniemi K (2016) Energy storage systems in modern grids – matrix of technologies and applications. *J Energy Storage Rev* 6:248–259. <https://doi.org/10.1016/j.est.2016.02.001>
41. Mostafa MH, Abdel Aleem SHE, Ali SG, Ali ZM, Abdelaziz AY (2020) Techno-economic assessment of energy storage systems using annualized life cycle cost of storage (LCCOS) and levelized cost of energy (LCOE) metrics. *J Energy Storage Rev* 29:101345. <https://doi.org/10.1016/j.est.2020.101345>
42. Rezaei N, Ahmadi A, Afifi SN, Zobaa AF, Abdel Aleem SHE (2018) Overview of energy storage technologies. In: Zobaa AF, Ribeiro PF, Abdel Aleem SHE, Afifi SN (eds) *Energy storage at different voltage levels. Technology, integration, and market aspects*, 1st edn. The Institute of Engineering and Technology (IET), Stevenage Herts, pp 1–30
43. Jarnut M, Werminski S, Waskowicz B (2017) Comparative analysis of selected energy storage technologies for prosumer-owned microgrids. *Renew Sust Energ Rev* 74:925–937. <https://doi.org/10.1016/j.rser.2017.02.084>
44. Baumann M, Weil M, Peters JF, Chibeles-Martins N, Moniz AB (2019) A review of multi-criteria decision making approaches for evaluating energy storage systems for grid applications. *Renew Sust Energ Rev* 107:516–534. <https://doi.org/10.1016/j.rser.2019.02.016>
45. Acar C, Beskese A, Temur GT (2019) A novel multicriteria sustainability investigation of energy storage systems. *Int J Energy Res. Wiley Online Library* 43:6419
46. Tran D, Khmbadkone AM (2013) Management of lifetime extension of energy storage system in micro-grid applications. *IEEE Trans Smart Grid* 4(3):1289–1296
47. Bryne RH, Ngugen TA, Copp D, Chalamala BR, Gyuk I (2017) Energy management and optimization methods for grid energy storage systems. *IEEE Access* 6:13231–13260
48. Mostafa MH, Abdel Aleem SHE, Ali SG, Ali ZM, Abdelaziz AY (2019) Energy-management solutions for microgrids. In: *Distributed energy resources in microgrids*. Elsevier, pp 483–515. <https://doi.org/10.1016/B978-0-12-817774-7.00020-X>
49. Mostafa MH, Aleem SHEA, Ali SG, Abdelaziz AY, Ribeiro PF, Ali ZM (2020) Robust energy management and economic analysis of microgrids considering different battery characteristics. *IEEE Access* 8:54751–54775. <https://doi.org/10.1109/ACCESS.2020.2981697>
50. Schoenung SM, Hassenzahl WV (2003) Long-vs. short-term energy storage technologies analysis a life-cycle cost study a study for the DOE energy storage systems program. Sandia National Laboratories (SNL), Albuquerque/Livermore. <https://doi.org/10.2172/918358>
51. Ramsden T (2013) An evaluation of the total cost of ownership of fuel cell powered material handling equipment. National Renewable Energy Laboratory (NREL), Oak Ridge
52. Nomura S, Shintomi T, Akita S, Nitta T, Shimada R, Meguro S (2010) Technical and cost evaluation on SMES for electric power compensation. *IEEE Trans Appl Supercond* 20:1373–1378. <https://doi.org/10.1109/TASC.2009.2039745>
53. Carnegie R, Gotham D, Nderitu D, Preckel P (2013) Utility scale energy storage – benefits, applications, and technologies. State Utility Forecasting Group. West Lafayette, IN, USA.

Stochastic Approach for Economic-Technical-Environmental Operation of Microgrids with Battery Storage Considering Parameters Uncertainty



Mostafa H. Mostafa, Muhyaddin Rawa, Ahmed I. Omar, Shady H. E. Abdel Aleem , Almoataz Y. Abdelaziz, Ziad M. Ali, and Ahmed F. Zobaa 

Nomenclature

Abbreviations

BSS	Battery storage system
CO ₂	Carbon dioxide
DG	Distributed generators
EM	Energy management
ESS	Energy storage system
FC	Fuel cell
FCM	Fuzzy cognitive map
MG	Microgrid

M. H. Mostafa

Department of Electrical Power and Machines, International Academy for Engineering and media science, Cairo, Egypt

M. Rawa

Department of Electrical and Computer Engineering, Engineering College, King Abdulaziz University, Jeddah, Saudi Arabia
e-mail: mrawa@kau.edu.sa

A. I. Omar

Electrical Power and Machines Engineering, The Higher Institute of Engineering at El-Shorouk City, El-Shorouk Academy, Cairo, Egypt

S. H. E. Abdel Aleem (✉)

Electrical Engineering Department, Valley Higher Institute of Engineering and Technology, Science Valley Academy, Qalyubia, Egypt
e-mail: engyshady@ieee.org

A. Y. Abdelaziz

Faculty of Engineering and Technology, Future University in Egypt, Cairo, Egypt

MGCC	Microgrid central controller
MT	Micro-turbine
NO _x	Nitrogen dioxide
OF	Objective function
PV	Photovoltaic
RES	Renewable energy resource
SO ₂	Sulfur dioxide
SoC	State of charge
WT	Wind turbine

Symbols

b_{batt}	Bidding cost at period h of the battery
b_{FC}	Bidding cost at period h of the fuel cell
$b_{\text{grid}, s, h}$	Bidding cost at period h of the grid
b_{MT}	Bidding cost at period h of the micro-turbine
b_{PV}	Bidding cost at period h of the photovoltaic
b_{WT}	Bidding cost at period h of the wind turbine
Batt_p^t	Output power of the battery storage system
b_{BSS}^t	Bidding cost of the battery storage system
b_{grid}	Energy market price
$\text{Cost}_{\text{BSS}}^t$	Operation cost of battery storage system
$\text{Cost}_{\text{grid}}$	Operation cost of the grid
d	Component of fuzziness
DG_C	Costs of fuel cell and micro-turbine
DG_η	Efficiency of the distributed generation
$\text{DG}_{\text{invest}}$	Investment cost of micro-turbine or fuel cell
DG_p	Output power of the distributed generation
E_{batt}^h	Energy stored in the battery storage system at period h
$E_{\text{batt-max}}^h$	Maximum capacity of the battery storage system
$E_{\text{batt-min}}^h$	Minimum capacity of the battery storage system
$E_{\text{batt}}^{\text{in}}$	Initial stored energy
e_{batt}^f	Efficiency of the battery
η^{in}	Efficiency of the inverter

Z. M. Ali

Electrical Engineering Department, College of Engineering at Wadi Addawaser, Prince Sattam bin Abdulaziz University, Al-Kharj, Saudi Arabia

Electrical Engineering Department, Aswan faculty of Engineering, Aswan University, Qism Aswan, Egypt

A. F. Zobaa

College of Engineering, Design & Physical Sciences, Brunel University London, Uxbridge, UK

FC_{CSD}	Shut-down cost coefficient of fuel cost
FC_{CSU}	Start-up cost coefficient of fuel cell
FC_P^h	Power generated at period h by fuel cell
FC_{SD}^h	Shut-down cost of fuel cell
FC_{SU}^h	Start-up cost of fuel cell
fuel^{DG}	Cost of fuel to supply the micro-turbine or fuel cell
grid_P	Output power of the main grid
I	Global insolation
I_0	Standard solar irradiance under standard test conditions
s, h	Probabilities of wind turbine scenarios
$k_{batt}^{CO_2}$	CO_2 injected from the battery storage system
$k_{FC}^{CO_2}$	CO_2 injected from the fuel cell
$k_{grid, s, h}^{CO_2}$	CO_2 injected from the main grid
$k_{MT}^{CO_2}$	CO_2 injected from the micro-turbine
$k_{PV}^{CO_2}$	CO_2 injected from the photovoltaic
$k_{WT}^{CO_2}$	CO_2 injected from the wind turbine
$k_{batt}^{SO_2}$	SO_2 injected from the battery storage system
$k_{FC}^{SO_2}$	SO_2 injected from the fuel cell
$k_{grid, s, h}^{SO_2}$	SO_2 injected from the main grid
$k_{MT}^{SO_2}$	SO_2 injected from the micro-turbine
$k_{PV}^{SO_2}$	SO_2 injected from the photovoltaic
$k_{WT}^{SO_2}$	SO_2 injected from the wind turbine
$k_{batt}^{NO_x}$	NO_x injected from the battery storage system
$k_{FC}^{NO_x}$	NO_x injected from the fuel cell
$k_{grid, s, h}^{NO_x}$	NO_x injected from the main grid
$k_{MT}^{NO_x}$	NO_x injected from the micro-turbine
$k_{PV}^{NO_x}$	NO_x injected from the photovoltaic
$k_{WT}^{NO_x}$	NO_x injected from the wind turbine
m_{FC}^h	State of fuel cell
m_{MT}^h	State of micro-turbine
MS	Photovoltaic output power scenarios
MT_{CSD}	Shut-down cost coefficient of micro-turbine
MT_{CSU}	Start-up cost coefficient of micro-turbine
MT_P^h	Power generated at period h by micro-turbine
NS	Market price scenarios
O	Number of clusters
P_{batt}^h	Power generated at period h by the battery storage system
P_{batt}^{h-ch}	Power charged at h
P_{batt}^{h-dis}	Power discharged at h
$P_{batt-max}^{h-ch}$	Maximum power charging

$P_{\text{batt-max}}^{h-\text{dis}}$	Maximum power discharging
$P_{\text{grid}, h}$	Power generated at period h by the main grid
$P_{\text{load}, s, h}$	Total load scenarios
PV_{η}^{RPV}	Relative efficiency of the PV
PV^N	Number of the PV elements
PV_{Pr}	Rated PV power
$PV_{\text{P}, s}^h$	Power generated at period h by photovoltaic
PV_{P}^t	Photovoltaic output power
T_{am}	Ambient temperature of photovoltaic
T_{Co}	Temperature constant of the maximum photovoltaic power
$v_{\text{WT}}^{\text{in}}$	Cut-in speed of the wind turbine
$v_{\text{WT}}^{\text{out}}$	Cut-out speed of the wind turbine
v_{WT}^r	Rated speed of the wind turbine
v_{WT}^t	Speed of the wind turbine at time t
w_1	Weight factor of the total operation cost of the microgrid
w_2	Weight factor of pollution emission of the microgrid
$\omega^{s, h}$	Probabilities of photovoltaic scenarios
WS	Wind turbine output power scenarios
$WT_{\text{P}, s}^h$	Power generated at period h by wind turbine
WT_{SD}^h	Shut-down cost of wind turbine
WT_{SU}^h	Start-up cost of wind turbine
WT_{P}^t	Wind turbine output power
WT_{Pr}	Wind turbine rated power
$\chi^{s, h}$	Probabilities of market price scenarios

1 Introduction

One of the world's most pressing issues is climate change resulting from the emissions of fossil fuel power plants. Thus, converting conventional grids to smart grids has gotten a lot of interest [1, 2]. Since the smart grid brings excessive environmental profits: decreased greenhouse gases, decreased burning of fossil fuels, increased interaction between customers and intelligent grid operators, and enhanced integration of the different types of renewable energy resources (RESs) [3, 4]. Microgrid (MG) has a significant role in this conversion. A microgrid is a localized grid with various types of distributed generators (DG), the energy storage systems (ESS), and electrical loads [5–7].

Nowadays, the MG's energy management (EM) with minimizing the operating cost of the MG and best employment of the RES to reduce environmental pollution has become the center of the microgrid operating system [8]. MG operators can no longer manage the power of the MG with minimum cost as the only objective. The increasing environmental concern pressures the MG operator towards multi-objective energy management to achieve minimum cost and minimum emissions

[9]. Whereas power generation from fossil fuel releases numerous pollutants, like sulfur dioxide (SO₂), carbon dioxide (CO₂), and nitrogen dioxide (NO_x), into the atmosphere [10]. Thus, MGs’-EM is employed for getting an optimal generating schedule of the different DGs and ESS to achieve the objective function (OF) while fulfilling the operating restrictions. However, random demand, the nature of RES intermittency, and the volatile market price have an essential influence on the EM of MGs [11]. Thus, MG operators’ most crucial challenge is considering the uncertainty of future variables, like RESs, market pricing, and electrical loads. In the literature, some researchers [12–16] treated the management of MGs as an optimization issue with the goal of attaining the single lowest overall operating cost by assuming one uncertain parameter only. And others researchers [17–21] considered multi-OF for minimizing total operating cost and pollutant emission of the MG while ignoring the uncertain parameter.

To redress this gap, this chapter suggested a stochastic optimization model for scheduling the energy of MG considering random demand, the intermittent nature of RES, and the volatile market price. Also, this chapter aims to schedule the energy of the MG with only OF such as lessening the overall operating cost of the MG over a 24-h horizon or minimizing the pollutant emissions over a 24-h horizon and with multi-OFs minimizing the overall operating cost and the pollutant emission MG over a 24-h horizon at the same time with fulfilling the operating restrictions.

2 Microgrid Description

The typical MG considered includes MG central controller (MGCC) and different DGs like a photovoltaics (PV), wind turbines (WT), micro-turbines (MT), fuel cells (FC), and battery storage systems (BSSs), as illustrated in Fig. 1 [13].

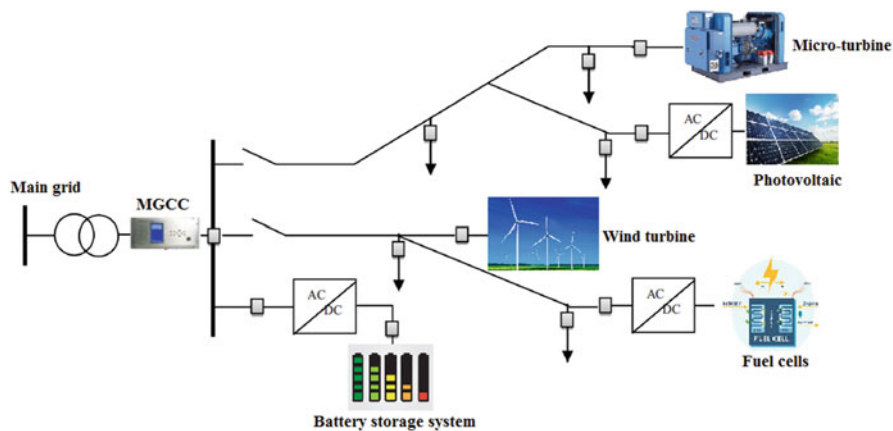


Fig. 1 Distribution network model

2.1 Wind Turbine

The WT's output power (WT_p^t) at period t depends on the period step wind velocity in a definite position is exemplified by (1) [13].

$$WT_p^t = \begin{cases} 0 & v_{WT}^t < v_{WT}^{in} \\ WT_{Pr} \left(\frac{(v_{WT}^t)^2 - (v_{WT}^{in})^2}{(v_{WT}^r)^2 - (v_{WT}^{in})^2} \right) & v_{WT}^{in} \leq v_{WT}^t < v_{WT}^r \\ WT_{Pr} & v_{WT}^r \leq v_{WT}^t < v_{WT}^{out} \\ 0 & v_{WT}^t > v_{WT}^{out} \end{cases} \quad (1)$$

where WT_{Pr} , v_{WT}^{out} , v_{WT}^{in} , v_{WT}^r , and v_{WT}^t are the WT rated power, cut-out speed, cut-in speed, rated speed of the WT, and the speed of WT at time t , respectively [12].

2.2 Photovoltaic

The temperature of the atmosphere and solar irradiance affects the output power of PV (PV_p^t) as shown in (2) [13].

$$PV_p^t = PV^N PV_{Pr} \left(\frac{I}{I_0} \right) (1 + T_{Co} (T_{am} - 25)) \eta^{in} PV_{\eta}^{RPV} \quad (2)$$

where T_{Co} and T_{am} symbolize the temperature constant of the PV's maximum power and the ambient temperature, respectively. PV^N and PV_{Pr} denote the number of the PV elements and the rated PV power, respectively. PV_{η}^{RPV} is the relative efficiency of the PV. η^{in} denotes the efficiency's inverter. I and I_0 represent the global irradiance and standard solar irradiance during standard test condition, respectively.

2.3 Fuel Cell and Micro-turbine

The costs of FC and MT (DG_C) are depending on the efficiency (DG_{η}) and output power (DG_P) of DG as exemplified in (3) [13].

$$DG_C = fuel^{DG} \times \frac{DG_P}{DG_{\eta}} + DG_{invest} \quad (3)$$

where $fuel^{DG}$ and DG_{invest} represent the cost of fuel (\$/kWh) to feed the FC or MT and their investing costs, respectively.

2.4 The Main Grid Operating Cost

The grid operating cost ($\text{Cost}_{\text{grid}}$) can be exemplified by the energy market pricing (b_{grid}) and the main grid output power (grid_p) as represented in (4).

$$\text{Cost}_{\text{grid}} = b_{\text{grid}} \times \text{grid}_p \quad (4)$$

2.5 Battery Storage System

The operation cost of BSS ($\text{Cost}_{\text{BSS}}^t$) is represented by the BSS output power (Batt_p^t) and its bidding cost (b_{BSS}^t) as represented in (5) [6].

$$\text{Cost}_{\text{Batt}} = b_{\text{Batt}} \times \text{Batt}_p \quad (5)$$

3 Uncertainty Modeling

Designing appropriate scenarios is critical in stochastic optimization to enable decisions based on real-world uncertainty measures [13]. Consequently, uncertainty estimations must imitate the measurement rule in a realistic approach. Each approach of uncertainty modeling would lead to a different system design. As a result, the appropriate choice of how to model uncertainty is critical. Rather than believing explicit knowledge of identified parameters as in the deterministic approach, uncertainty modeling uses random distributions as input to a random optimization issue to simulate the probability features of parameters [22].

In this chapter, a collection of situations is created to represent the many alternatives of system parameter uncertainties, and each one has a definite probability. A fuzzy cognitive map (FCM) is used to generate unpredictable situations of electricity demand, RESs production power, and market pricing, as well as to combine them into a smaller variety of situations [24].

As clarified in [22, 23], FCM a technique for organizing a large amount of data (M) into a small number of clusters (O) where $O = 5$. The task becomes increasingly complex and sophisticated as the possibilities grow, necessitating a larger computing package.

The information in a matrix Z required to be clustered that containing a group of column vectors z_j , where $j \in \{1, 2, \dots, M\}$. FCM needs two variables to group Z : O and the component of fuzziness (d), where $d \in k$ and $d > 1$. The operation is expected to conclude at a predetermined tolerance (eps). Five phases are included in the FCM clustering algorithm:

Stage 1: A membership matrix ($k = [k_{ij}]_{O \times M}$) is adjusted arbitrarily where the sum of each column j in k must equal 1. O random centroids can be selected from the data. These centroids are collected in a vector $= [O_i]_{1 \times O}$.

Stage 2: Compute the new centroids utilizing (6):

$$O_i = \frac{\sum_{j=1}^M k_{ij}^d \times z_j}{\sum_{j=1}^M k_{ij}^d} \quad (6)$$

Stage 3: Compute the elements of the membership matrix ($k = [k_{ij}]_{O \times M}$) for each element in Z , where:

$$k_{ij} = \frac{1}{\sum_{p=1}^O \left(\frac{\|z_j - O_i\|}{\|z_j - O_p\|} \right)^{\frac{2}{d-1}}} \quad (7)$$

Stage 4: Compute $f_{\text{FCM}}^{(n)} = \sum_{j=1}^M \sum_{i=1}^O k_{ij}^d \|z_j - O_i\|$, where $f_{\text{FCM}}^{(n)}$ at the n th iteration denotes the OF value.

Stage 5: If $\left\| f_{\text{FCM}}^{(n)} - f_{\text{FCM}}^{(n-1)} \right\| < \text{eps}$, $\forall n$, stop the optimization technique, otherwise repeat the procedure starting from stage 2.

4 Problem Formulation

In this section, the problem's single OF, multi-OF, and constraints are explained.

4.1 Cost Formulation

The main OF ($f(x)_1$) is minimizing the total expected cost of the MG during the day whereas taking into account RESs, market price, and electrical load uncertainties. The total operating cost of MG ($f(x)_1$) at period h taking into account numerous WT output power scenarios (WS) and their statistics ($^s, h$), multiple PV output power scenarios (MS) and their statistics ($^s, h$), and numerous market pricing scenarios (NS) and their statistics ($\chi^{s, h}$) is stated in (8–12).

$$\begin{aligned} \min f(x)_1 = & \sum_{h=1}^H \left[\sum_{s=1}^{\text{NS}} \left(\chi^{s, h} \times k_{\text{grid}, s, h} \times P_{\text{grid}, h} \right) + \sum_{s=1}^{\text{MS}} \left(b_{\text{PV}} \times \omega^{s, h} \times \text{PV}_{\text{P}, s}^h \right) \right. \\ & + \sum_{s=1}^{\text{WS}} \left(b_{\text{WT}} \times \Pi^{s, h} \times \text{WT}_{\text{P}, s}^h \right) + \left(m_{\text{FC}}^h \times b_{\text{FC}} \times \text{FC}_{\text{P}}^h + \text{FC}_{\text{SU}}^h + \text{FC}_{\text{SD}}^h \right) \\ & \left. + \left(m_{\text{MT}}^h \times b_{\text{MT}} \times \text{MT}_{\text{P}}^h + \text{WT}_{\text{SU}}^h + \text{WT}_{\text{SD}}^h \right) + \left(b_{\text{batt}} \times P_{\text{batt}}^h \right) \right] \quad (8) \end{aligned}$$

$$FC_{SU}^h = FC_{CSU} \times \max \left(0, \left(m_{FC}^h - m_{FC}^{h-1} \right) \right), \forall h \quad (9)$$

$$FC_{SD}^h = FC_{CSD} \times \max \left(0, \left(m_{FC}^{h-1} - m_{FC}^h \right) \right), \forall h \quad (10)$$

$$MT_{SU}^h = MT_{CSU} \times \max \left(0, \left(m_{MT}^h - m_{MT}^{h-1} \right) \right), \forall h \quad (11)$$

$$MT_{SD}^h = MT_{CSD} \times \max \left(0, \left(m_{MT}^{h-1} - m_{MT}^h \right) \right), \forall h \quad (12)$$

where $b_{WT}, b_{PV}, b_{MT}, b_{FC}, b_{grid, s, h}$, and b_{batt} are the cost's bidding at period h of the WT, PV, MT, FC, the main grid, and BSS (€ct /kWh), respectively. $WT_{P,s}^h, PV_{P,s}^h, MT_P^h, FC_P^h, P_{grid, h}$, and P_{batt}^h represent the power produced at period h by WT, PV, MT, FC, the main grid, and BSS. m_{MT}^h and m_{FC}^h are the state of MT and FC, in which m_{MT}^h or m_{FC}^h equals 1 when MT or FC is on; otherwise, m_{MT}^h or m_{FC}^h equals 0 when MT or FC is off. WT_{SD}^h and FC_{SD}^h are the cost's shut-down of WT and FC, respectively. WT_{SU}^h and FC_{SU}^h are the cost's start-up of WT and FC, respectively. $FC_{CSU}, FC_{CSD}, MT_{CSU}$, and MT_{CSD} denote cost's start-up and cost's shut-down factor of FC and MT, respectively.

4.2 Emission Formulation

The main OF ($f(x)_2$) is minimizing the overall MG emissions while also considering RESs, market price, and electrical load uncertainties. The pollutant emission exited from grid-connected MG is produced due to the generating sources. It is assumed that the emission comprises sulfur dioxide (SO₂), carbon dioxide (CO₂), and nitrogen dioxide (NO_x), the mathematical formula of the total emissions of grid-connected MG ($f(x)_2$) at period h can be expressed in (13).

$$\begin{aligned} \min f(x)_2 = & \sum_{h=1}^H \left[\sum_{s=1}^{NS} \left(\chi^{s,h} \times k_{grid,s,h}^{CO_2} \times k_{grid,s,h}^{SO_2} \times k_{grid,s,h}^{NO_x} \times P_{grid,h} \right) \right. \\ & + \sum_{s=1}^{MS} \left(\omega^{s,h} \times k_{PV}^{CO_2} \times k_{PV}^{SO_2} \times k_{PV}^{NO_x} \times PV_{P,s}^h \right) + \sum_{s=1}^{WS} \left(\Pi^{s,h} \times k_{WT}^{CO_2} \times k_{WT}^{SO_2} \times k_{WT}^{NO_x} \times WT_{P,s}^h \right) \\ & + \left(m_{FC}^h \times k_{FC}^{CO_2} \times k_{FC}^{SO_2} \times k_{FC}^{NO_x} \times FC_P^h \right) + \left(m_{MT}^h \times k_{MT}^{CO_2} \times k_{MT}^{SO_2} \times k_{MT}^{NO_x} \times MT_P^h \right) \\ & \left. + \left(k_{batt}^{CO_2} \times k_{batt}^{SO_2} \times k_{batt}^{NO_x} \times P_{batt}^h \right) \right] \quad (13) \end{aligned}$$

where, $k_{WT}^{CO_2}, k_{PV}^{CO_2}, k_{MT}^{CO_2}, k_{FC}^{CO_2}, k_{grid,s,h}^{CO_2}$, and $k_{batt}^{CO_2}$ are the CO₂ injected from the WT, PV, MT, FC, main grid, and BSS, respectively. $k_{WT}^{SO_2}, k_{PV}^{SO_2}, k_{MT}^{SO_2}, k_{FC}^{SO_2}, k_{grid,s,h}^{SO_2}$,

and $k_{\text{batt}}^{\text{SO}_2}$ are the SO_2 injected from WT, PV, MT, FC, the main grid, and BSS, respectively. $k_{\text{WT}}^{\text{NO}_X}$, $k_{\text{PV}}^{\text{NO}_X}$, $k_{\text{MT}}^{\text{NO}_X}$, $k_{\text{FC}}^{\text{NO}_X}$, $k_{\text{grid,s,h}}^{\text{NO}_X}$, and $k_{\text{batt}}^{\text{NO}_X}$ are the NO_X injected from the WT, PV, MT, FC, main grid, and BSS, respectively.

4.3 Multi-objective Function Formulation

This section introduces multi-OF for minimizing the overall operating cost and the pollutant emission grid-connected MG during the day at the same time. The multi-OF can be given as follows:

$$\min f(x)_3 = w_1 \times f(x)_1 + w_2 \times f(x)_2 \quad (14)$$

where w_1 and w_2 denote the weight factor of the overall operating cost of the MG and pollution emission of the MG during the day.

4.4 Constraints

The OF is constrained to the following restrictions:

4.4.1 Generation and Demand Balance

At period h , the total load scenarios ($P_{\text{load, s, h}}$) and their statistics (LS with statistics $\psi^{s, h}$) should be equal to the sum of the power produced from WT, PV, MT, FC, the grid, and power discharged from the battery as expressed in (15).

$$MT_{\text{P}}^h m_{\text{MT}}^h + FC_{\text{P}}^h m_{\text{FC}}^h + WT_{\text{P,s}}^h + PV_{\text{P,s}}^h + P_{\text{grid,h}} + P_{\text{batt}}^{h-\text{dis}} = \sum_{s=1}^{\text{LS}} \psi^{s, h} \times P_{\text{load,s,h}} + P_{\text{batt}}^{h-\text{ch}} \quad (15)$$

4.4.2 Generating Units Limit

The power produced by the WT, PV, MT, FC, and the main grid have to be within their bounds as expressed in (16–20).

$$P_{\text{grid,h}}^{\min} \leq P_{\text{grid,h}} \leq P_{\text{grid,h}}^{\max}, \quad \forall h \quad (16)$$

$$PV_{P,s}^{h-\min} \leq PV_{P,s}^h \leq PV_{P,s}^{h-\max}, \quad \forall h \quad (17)$$

$$WT_{P,s}^{h-\min} \leq WT_{P,s}^h \leq WT_{P,s}^{h-\max}, \quad \forall h \quad (18)$$

$$FC_p^{h-\min} \leq FC_p^h \leq FC_p^{h-\max}, \quad \forall h \quad (19)$$

$$MT_p^{h-\min} \leq MT_p^h \leq MT_p^{h-\max}, \quad \forall h \quad (20)$$

4.4.3 Storage Constraints

The discharged and charged power limits and the BSS's energy stored is formulated as follows:

$$P_{\text{batt}}^{h-\text{ch}} \leq P_{\text{batt-max}}^{h-\text{ch}}, \quad \forall h \leq H \quad (21)$$

$$P_{\text{batt}}^{h-\text{dis}} \leq P_{\text{batt-max}}^{h-\text{dis}}, \quad \forall h \leq H \quad (22)$$

$$E_{\text{batt-min}}^h \leq E_{\text{batt}}^h \leq E_{\text{batt-max}}^h, \quad \forall h \leq H \quad (23)$$

where $E_{\text{batt-max}}^h$, $E_{\text{batt-min}}^h$, and E_{batt}^h are the highest and lowest capacity of the BSS and the BSS's energy stored i at period h , respectively. $P_{\text{batt-max}}^{h-\text{ch}}$, $P_{\text{batt-max}}^{h-\text{dis}}$, $P_{\text{batt}}^{h-\text{ch}}$, and $P_{\text{batt}}^{h-\text{dis}}$ are highest power charging (kW), highest power discharging (kW), the charged power (kW) at h , and power discharged (kW) at h , respectively. Through the day, the sum of the charged power while considering the BSS efficiency (ef_{batt}) should equal the sum of discharged power, as expressed in (24).

$$\sum_{h=1}^H P_{\text{batt}}^{h-\text{ch}} \times \text{ef}_{\text{batt}} = \sum_{h=1}^H P_{\text{batt}}^{h-\text{dis}} \quad (24)$$

The initial stored energy ($E_{\text{batt}}^{\text{in}}$) is judged at ($h = 1$) as expressed in (25). The initial stored energy is obtained at the last hour ($h = 24$) as described in (26).

$$E_{\text{batt}}^h = E_{\text{batt}}^{\text{in}} + \text{ef}_{\text{batt}} P_{\text{batt}}^{h-\text{ch}} \Delta h - P_{\text{batt}}^{h-\text{dis}} \Delta h, \quad h = 1 \quad (25)$$

$$E_{\text{batt}}^h = E_{\text{batt}}^{\text{in}}, \quad h = 24 \quad (26)$$

The BSS stored energy (E_{batt}^h) depends on the previously stored energy (E_{batt}^{h-1}) and the quantities of charged and discharged powers at h , considering $e_{\text{f}_{\text{batt}}}$, expressed in (27).

$$E_{\text{batt}}^h = E_{\text{batt}}^{h-1} + e_{\text{f}_{\text{batt}}} P_{\text{batt}}^{h-\text{ch}} \Delta h - P_{\text{batt}}^{h-\text{dis}} \Delta h, 2 \leq h \leq H \quad (27)$$

5 Simulation Results and Discussion

According to the grid-connected MG shown in Fig. 1, Table 1 shows the highest and lowest power limits, the bids, emission data, and coefficients used WT, PV, MT, FC, main grid, and the BSS [14].

The stochastic method utilizes several scenarios with corresponding probabilities to get a purer picture of the influence of variations of parameters on the alternative. Depending on chronological information, 1000 situations are produced to imitate the intermittency of load demand, PV and WT, and market pricing. Next, a situation reduction dependent on the FCM clustering technique can be carried out to decrease the generated scenarios of market price, demand, PV, and WT to the most critical five scenarios.

The clustered scenarios of PV power and WT power at each time (1 hour) are shown in Fig. 2. The clustered scenarios of the market price and electrical loads at each time (1 hour) are shown in Fig. 3. The probability of the happening scenarios of market price, demand, PV, and WT is shown in Figs. 4, 5, 6, and 7, respectively.

Before applying the multi-OF, single-objective optimizations are executed to explain how each objective impacts the microgrid's daily energy scheduling. In the first single objective (Case 1), the optimal intermittent model for schedule the MG energy is executed for minimizing the overall MG operating cost, and in the second single objective (Case 2), the optimal intermittent model for schedule the MG energy is executed for minimizing the overall MG emissions. Then, the multi-

Table 1 Cost, emissions technical data of the grid and DGs

Units	WT	PV	MT	FC	BSS	Grid
Min. power (kW)	0	0	6	3	-30	-30
Max. power (kW)	15	25	30	30	30	30
Bid (€/kWh)	1.073	2.584	0.457	0.294	0.38	Figure 3
Cost's start-up/Cost's shut-down (€ct)	0	0	0.96	1.65	NA	NA
CO ₂ (Kg/MWh)	0	0	720	460	10	0
SO ₂ (Kg/MWh)	0	0	0.0036	0.003	0.0002	0
NO _x (Kg/MWh)	0	0	0.0075	0.0075	0.001	0

NA not applicable

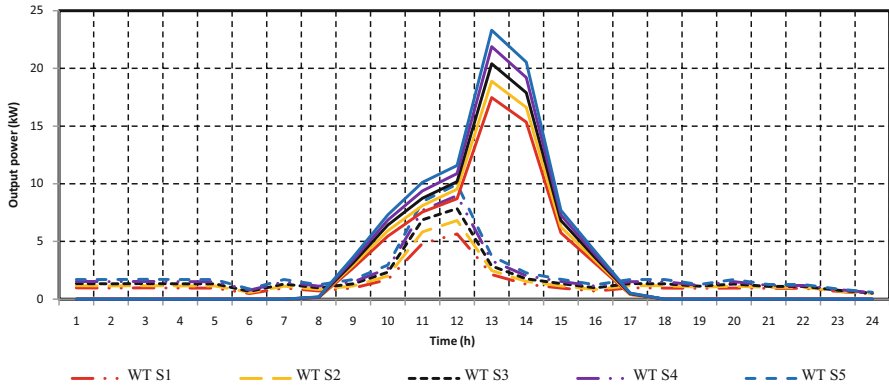


Fig. 2 Output power situations of PV and WT

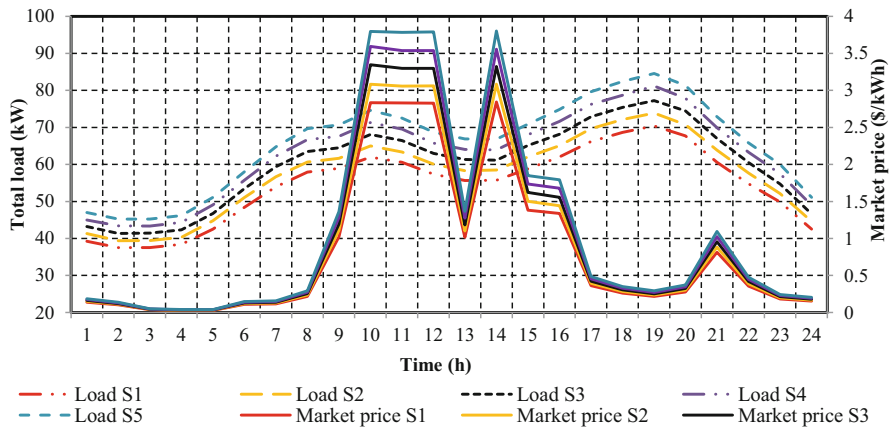


Fig. 3 Market pricing and electrical demand situations

objective optimization problem (Case 3) can be directed to integrate the two OFs, namely, minimizing total operation cost and emissions.

We can realize from Table 2 that the MG overall operating cost in Case 1 has offered the best effects in comparison with the outcomes attained utilizing the other cases, but the total emission of the MG, in this case, is very high. And vice versa in Case 2, the total emission of the MG is lower than in other cases, but the MG overall operating cost is very high. Therefore, Table 2 shows that the multi-objective optimization approach gives the best result from the overall operating cost and emissions viewpoints.

Figures 8, 9, and 10 show the optimum hourly powers output of the main grid, WT, PV, FC, and MT during parameters uncertainty in the three cases. The optimal hourly energy scheduling must be calculated to attain the minimal operating cost of the grid-connected MG through the day. Consequently, Fig. 8 depicts the

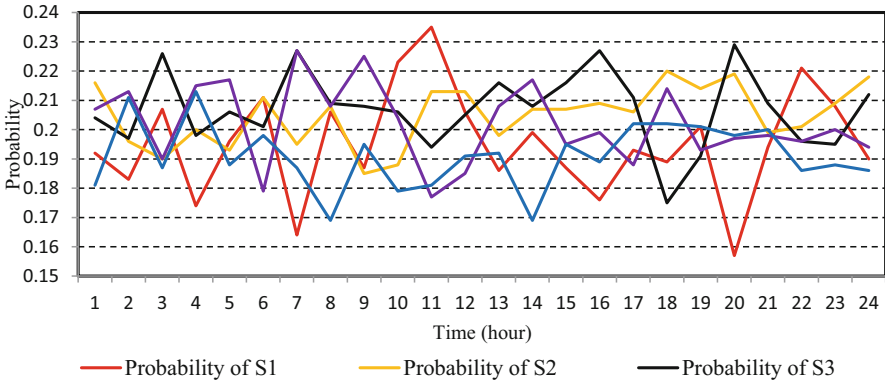


Fig. 4. Probability of market pricing situations.

Fig. 4 Probability of market pricing situations

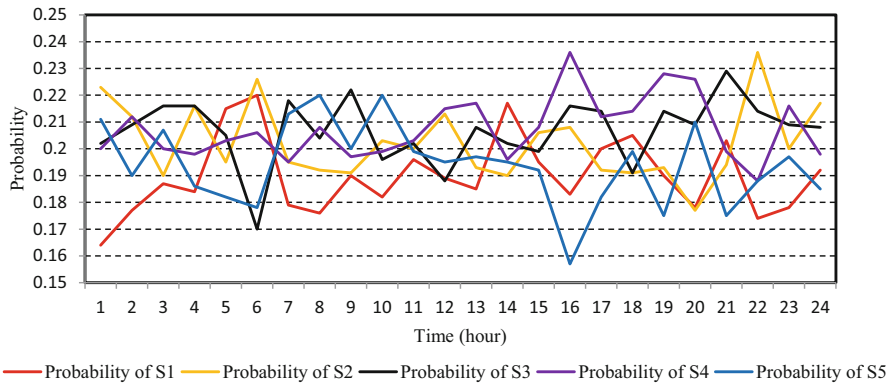


Fig. 5 Probability of electrical demand scenarios

power imported/exported from/to the main grid, the power output of each DG, and charging/discharging power of BSS relates to the bids of each DG and BSS and market pricing of the main grid in addition to the MG constraints. Figure 3 depicts the power imported/exported from/to the main grid based on the energy market pricing.

Figure 9 shows the optimal hourly output powers of the WT, PV, FC, MT, main grid, and BSS for lessening overall emissions of the grid-connected MG under considering the uncertainty parameters. Figure 9 displays the power imported/exported from/to the main grid, the power output of each DG, and the charging/discharging power of BSS depend on the number of emissions emitted from each source in addition to the MG constraints.

It is evident from Table 1 that the renewable sources (PV and WT) are zero-emissions sources. Thus, the power available from WT and PV is fully consumed

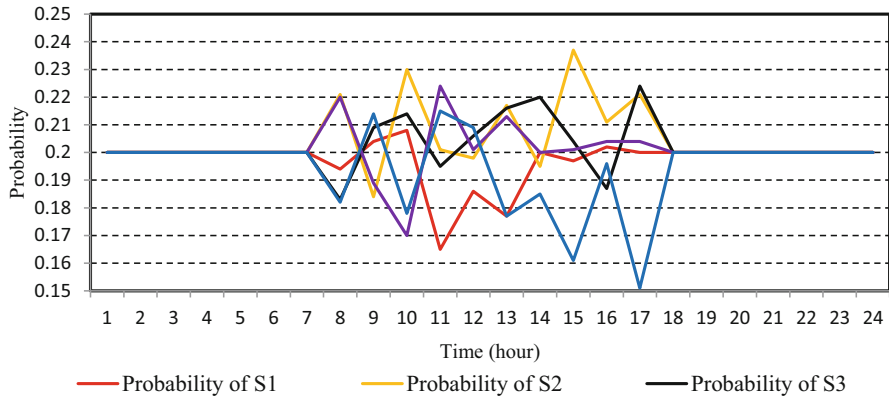


Fig. 6 Probability of PV situations

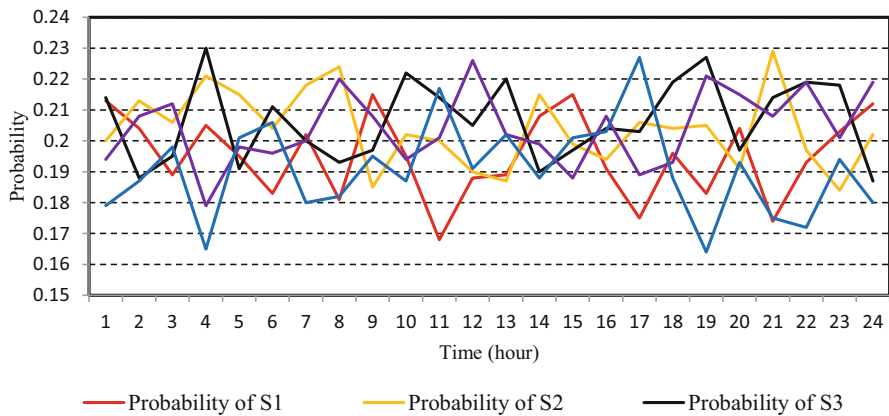


Fig. 7 Probability of WT situations

Table 2 The overall operating cost of the MG grid-connected in various cases

	Case 1	Case 2	Case 3
Overall operating cost (€ct/day)	148.26	1132.901	178.939
Overall emission (kg/day)	603.433	314.439	558.232

over a 24-h horizon, as shown in Fig. 9. It can be noted from Table 1 that the MT emission is high. Hence, the power consumed from the MT is low to create pollution-free environments. In the intervals with high load and low power output of renewable energy, it needs to consume power from the MT, although it pollutes the environment to satisfy the MG constraint. Also, Fig. 9 shows the BSS that did not affect the operating of the MG to achieve the minimization of the MG emission because the sum of available energy from renewable energy sources at each hour is less than the total electrical load, so it is fully used to supply the load electricity

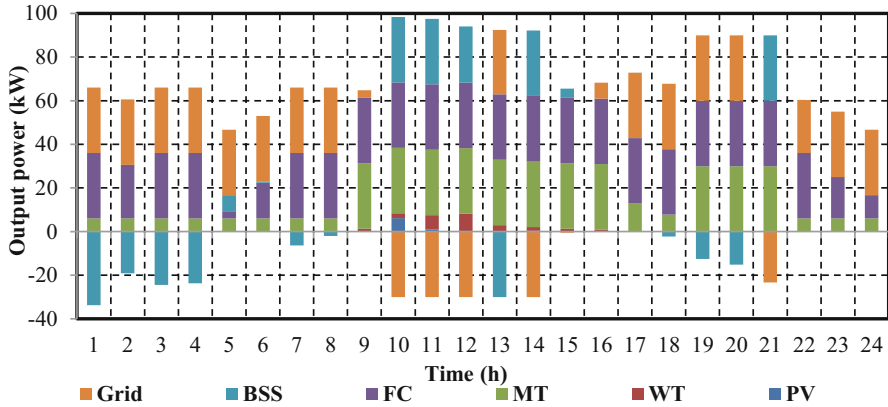


Fig. 8 Optimum hourly output powers of the WT, PV, FC, MT, main grid, and BSS for minimizing MG operating cost

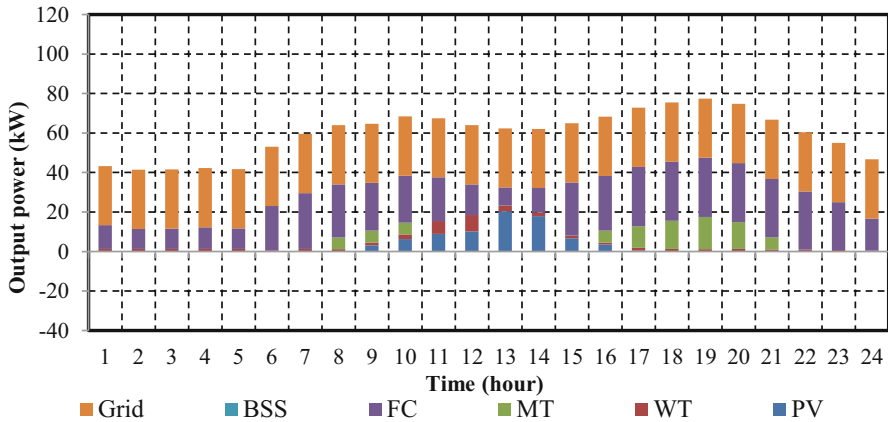


Fig. 9 Optimum hourly output powers of the WT, PV, FC, MT, main grid, and BSS for minimizing emissions

and also the use of MT and FC in cases of achieving electrical balance only because they are polluting sources of the environment.

Figure 10 shows the optimal hourly output powers of WT, PV, FC, MT, main grid, and BSS for lessening MG operating cost and emissions under uncertainty parameters. Therefore, Fig. 10 shows the power imported/exported from/to the main grid, the output power of each distributed generator, and BSS charging/discharging power based on the market pricing of the main grid, bids of each source, and emissions of each source, in addition to the MG constraints.

Figures 11 and 12 show the charging/discharging power of BSS at each hour and the state of charge (SoC) during the day in cases 1 and 3, respectively. It is notable from Figs. 11 and 12 that BSS is discharged from hour 10 to hour 12 and at hour

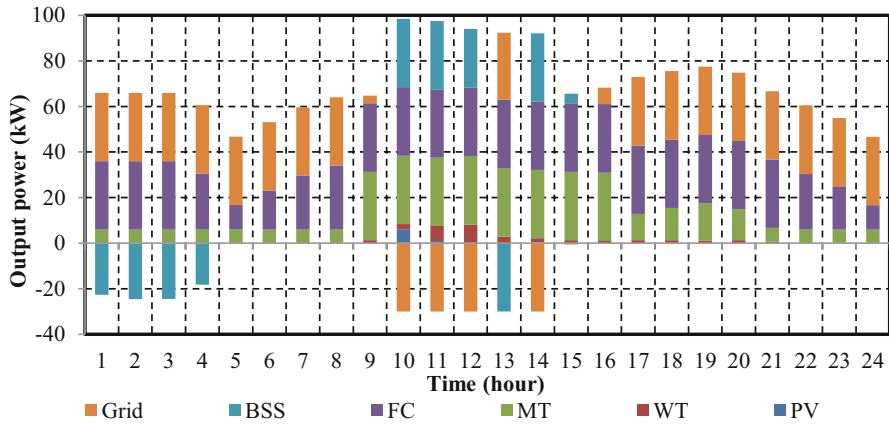


Fig. 10 Optimal hourly output powers of the WT, PV, FC, MT, main grid, and BSS for minimizing MG operating cost and emissions

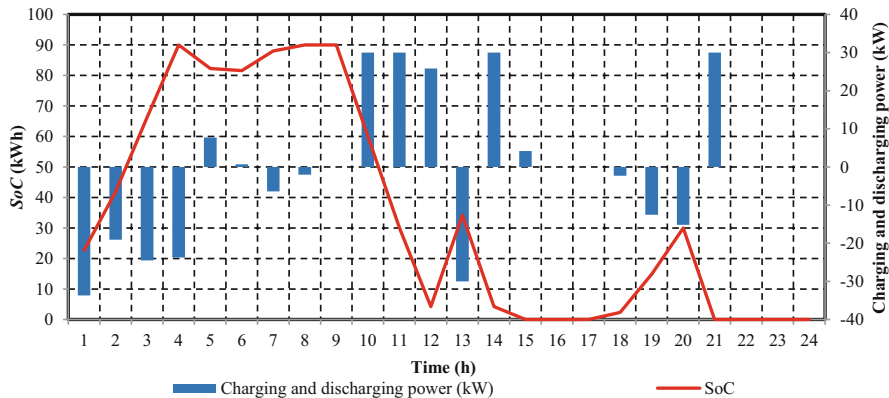


Fig. 11 Charging and discharging power and SoC of BSS in Case 1

14 since the market pricing is very high. Also, BSS is charging for the first moment since the energy market pricing is low and the overall MG demand is not great in these times.

6 Conclusions

A stochastic optimization model has been offered for schedule the grid-connected MG energy, considering the variation of market pricing, RESs, and load demand. The stochastic presentation is a scenario-based technique that GAMS solve. The FCM has been utilized to gather the produced scenarios of the load alteration, RESs

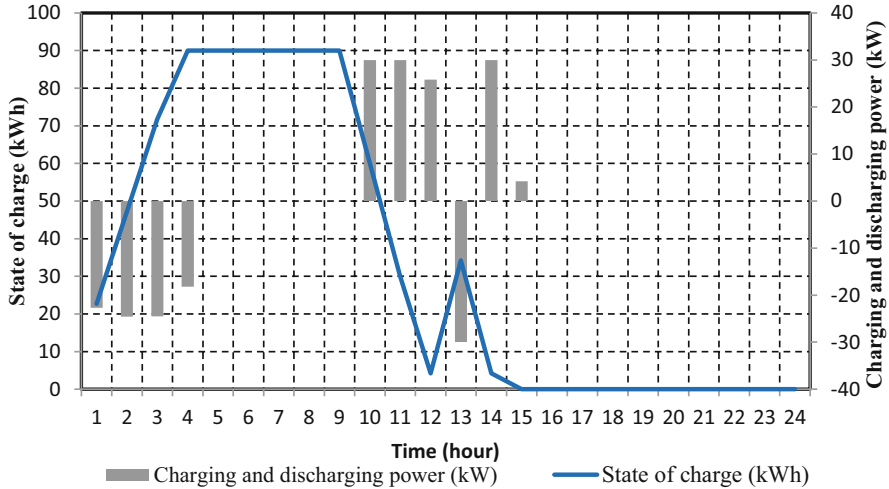


Fig. 12 Charging and discharging power and SoC of BSS in Case 3

output power, and market pricing variant during the day. This chapter introduces a schedule for the energy of the MG with only OFs such as lessening the overall MG operating cost over a 24-h horizon or minimizing the pollutant emissions over a 24-h horizon and with multi-OF minimize the MG overall operating cost and the pollutant emission over a 24-h horizon at the same time with tacking into account numerous constraints linked to the system operation and the uncertainty of parameters. The formula developed in this paper revealed that the variables OF and uncertainty degree have a substantial impact on the optimal hourly generation schedule of MG. This chapter demonstrates that a multi-OF is a suitable approach to the energy management of the MG.

References

1. Chen T, Cao Y, Qing X, Zhang J, Sun Y, Amaratunga GAJ (2022) Multi-energy microgrid robust energy management with a novel decision-making strategy. *Energy* 239:121840. <https://doi.org/10.1016/j.energy.2021.121840>
2. Mostafa MH, Abdel Aleem SHE, Ali SG, Abdelaziz AY (2019) Energy-management solutions for microgrids. In: *Distributed energy resources in microgrids*. Elsevier, London, pp 483–515. <https://doi.org/10.1016/B978-0-12-817774-7.00020-X>
3. Sharma DK, Rapaka GK, Pasupulla AP, Jaiswal S, Abadar K, Kaur H (2021) A review on smart grid telecommunication system. *Mater Today Proc*. <https://doi.org/10.1016/j.matpr.2021.05.581>
4. Silva JAA, López JC, Arias NB, Rider MJ, da Silva LCP (2021) An optimal stochastic energy management system for resilient microgrids. *Appl Energy*. <https://doi.org/10.1016/j.apenergy.2021.117435>

5. Ouammi A (2021) Model predictive control for optimal energy management of connected cluster of microgrids with net zero energy multi-greenhouses. *Energy* 234:121274. <https://doi.org/10.1016/j.energy.2021.121274>
6. Mostafa MH, Ali SG, Aleem SHEA, Abdelaziz AY (2018) Optimal allocation of energy storage system for improving performance of microgrid using symbiotic organisms search. In: 2018 twentieth international middle east power systems conference. IEEE, pp 474–479. <https://doi.org/10.1109/MEPCON.2018.8635265>
7. Mostafa MH, Abdel Aleem SHE, Ali SG, Ali ZM, Abdelaziz AY (2020) Techno-economic assessment of energy storage systems using annualized life cycle cost of storage (LCCOS) and levelized cost of energy (LCOE) metrics. *J Energy Storage* 29:101345. <https://doi.org/10.1016/j.est.2020.101345>
8. Rawa M, Abusorrah A, Al-Turki Y, Mekhilef S, Mostafa MH, Ali ZM, Aleem SHEA (2020) Optimal Allocation and economic analysis of battery energy storage systems: self-consumption rate and hosting capacity enhancement for microgrids with high renewable penetration. *Sustainability* 12:10144. <https://doi.org/10.3390/su122310144>
9. Li N, Hou W, Ghoreyshipour SE (2021) A secured transactive energy management framework for home AC/DC microgrids. *Sustain Cities Soc* 74:103165. <https://doi.org/10.1016/j.scs.2021.103165>
10. Polimeni S, Meraldi L, Moretti L, Leva S, Manzolini G (2021) Development and experimental validation of hierarchical energy management system based on stochastic model predictive control for off-grid microgrids. *Adv Appl Energy*. <https://doi.org/10.1016/j.adapen.2021.100028>
11. Kumar K, Alam M, Dutta V (2021) Energy management strategy for integration of fuel cell-electrolyzer technologies in microgrid. *Int J Hydrog Energy*. <https://doi.org/10.1016/j.ijhydene.2021.07.203>
12. Farzin H, Fotuhi-Firuzabad M, Moeini-Aghaie M (2017) Stochastic energy management of microgrids during unscheduled islanding period. *IEEE Trans Ind Inf* 13:1079–1087. <https://doi.org/10.1109/TII.2016.2646721>
13. Mostafa MH, Aleem SHEA, Ali SG, Abdelaziz AY, Ribeiro PF, Ali ZM (2020) Robust energy management and economic analysis of microgrids considering different battery characteristics. *IEEE Access* 8:54751–54775. <https://doi.org/10.1109/ACCESS.2020.2981697>
14. Mostafa MH, Abdel Aleem SHE, Ali SG, Abdelaziz AY (2019) Day-ahead optimal scheduling for grid-connected microgrid with energy storage systems. In: 2019 21st international middle east power systems conference. IEEE, pp 828–833. <https://doi.org/10.1109/MEPCON47431.2019.9007987>
15. de Bosio F, Luna AC, de Ribeiro LAS, Graells M, Saavedra OR, Guerrero JM (2016) Analysis and improvement of the energy management of an isolated microgrid in Lencois island based on a linear optimization approach. In: 2016 IEEE energy conversion congress and exposition. IEEE, pp 1–7. <https://doi.org/10.1109/ECCE.2016.7854871>
16. Narayan A, Ponnambalam K (2017) Risk-averse stochastic programming approach for microgrid planning under uncertainty. *Renew Energy* 101:399–408. <https://doi.org/10.1016/j.renene.2016.08.064>
17. Sedighzadeh M, Esmaili M, Jamshidi A, Ghaderi M-H (2019) Stochastic multi-objective economic-environmental energy and reserve scheduling of microgrids considering battery energy storage system. *Int J Electr Power Energy Syst* 106:1–16. <https://doi.org/10.1016/j.ijepes.2018.09.037>
18. Rabiee A, Sadeghi M, Aghaei J (2018) Modified imperialist competitive algorithm for environmental constrained energy management of microgrids. *J Clean Prod* 202:273–292. <https://doi.org/10.1016/j.jclepro.2018.08.129>
19. Zhou S, Zou F, Wu Z, Gu W, Hong Q, Booth C (2020) A smart community energy management scheme considering user dominated demand side response and P2P trading. *Int J Electr Power Energy Syst* 114:105378. <https://doi.org/10.1016/j.ijepes.2019.105378>
20. Chen C, Sun H, Shen X, Guo Y, Guo Q, Xia T (2019) Two-stage robust planning-operation co-optimization of energy hub considering precise energy storage economic model. *Appl Energy* 252:113372. <https://doi.org/10.1016/j.apenergy.2019.113372>

21. Rezvani A, Gandomkar M, Izadbakhsh M, Ahmadi A (2015) Environmental/economic scheduling of a micro-grid with renewable energy resources. *J Clean Prod* 87:216–226. <https://doi.org/10.1016/j.jclepro.2014.09.088>
22. Hazır Ö, Ulusoy G (2020) A classification and review of approaches and methods for modeling uncertainty in projects. *Int J Prod Econ* 223:107522. <https://doi.org/10.1016/j.ijpe.2019.107522>
23. Zhao Z, Zhao J, Song K, Hussain A, Du Q, Dong Y, Liu J, Yang X (2020) Joint DBN and fuzzy C-means unsupervised deep clustering for lung cancer patient stratification. *Eng Appl Artif Intell* 91:103571. <https://doi.org/10.1016/j.engappai.2020.103571>
24. Kim E-H, Oh S-K, Pedrycz W (2018) Design of reinforced interval type-2 fuzzy C-means-based fuzzy classifier. *IEEE Trans Fuzzy Syst* 26:3054–3068. <https://doi.org/10.1109/TFUZZ.2017.2785244>

A Resilient Hybrid Renewable Energy System for DC Microgrid with Inclusion of the Energy Storage



Siddharth Joshi, Praghnes Bhatt, Bhinal Mehta, and Amit Sant

1 Introductory Remarks

Recently, the energy demand has increased in a significant way so the renewable energy sources have been boosted by the increase of the price of conventional fuels and limited reserve capacity available for the foreseeable future. The energy crisis on the present day and inadequate nature of fossil fuel & sources led to an increased interest in power generation through renewable/non-conventional sources of energy. Renewable energy sources (RES) are the fastest-growing sources of energy which is used to supply the demand of electrical energy, with the increment rate of 2.9% per annum from 2012 to 2040 [1]. Nowadays, these renewable resources have become key players to electrify the loads, and some of the primary renewable sources are wind, solar, tidal, and biomass. The solar energy, or the energy from the sun, is one of the promising resources. The solar energy is available in the two forms; the first is in the thermal form which is used for water heating application and thermal to electrical energy conversion, and the second is solar photovoltaic, which converts light energy available in the photon to electrical energy.

The Indian government sets a target of 175 GW projection of RES by the year end of 2022 in installed capacity. The current status of the various renewable energy sources is shown in Fig. 1. To achieve the set target, 100 GW comprises of 60 GW roof top and 40 GW large scale power plant of solar PVES will be installed. The sector-wise Renewable Energy Cumulative Achievements for grid-interactive power is shown in Fig. 2 [2]. Among these RES, the contribution of renewable energy sources in the Indian grid is in shown in Fig. 3 [2].

S. Joshi (✉) · P. Bhatt · B. Mehta · A. Sant
School of Technology, Pandit Deendayal Energy University, Gandhinagar, Gujarat, India

Fig. 1 Indian renewable energy target for 2022

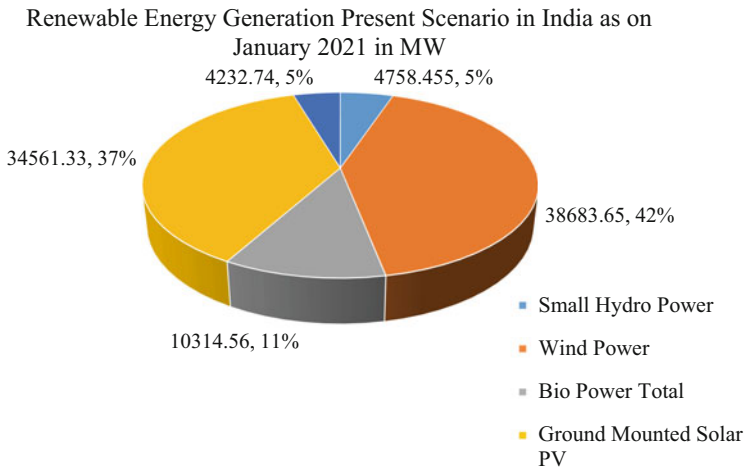
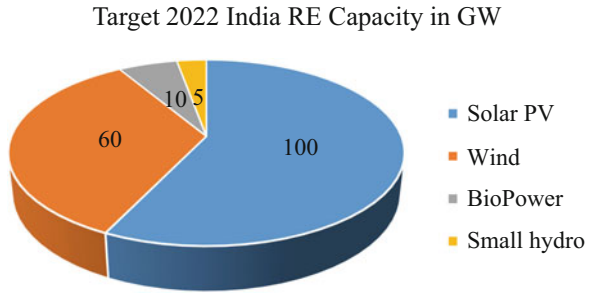


Fig. 2 Power sector scenario of India as of January 2021

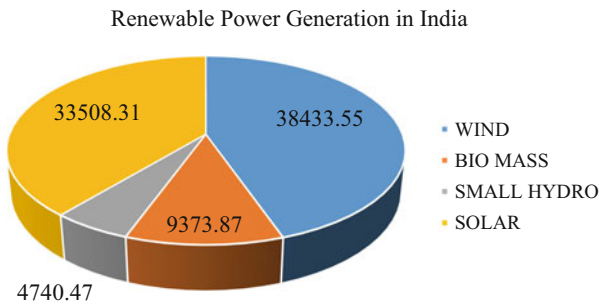


Fig. 3 Contribution of the renewable power sector in the Indian power sector as of January 2021

2 Review of Literature

The applications of RES in microgrids are many. The inclusion of RES plays significant role in the formation of microgrid. A DC microgrid comprises of a

DC bus, which feeds DC load. Normally, low-power devices like Internet routers, laptops, mobile phones, charging of small electrical vehicles, energy storage charging, and electronic gadgets are classified as DC loads.

This work contributes to the resilient hybrid RE system, which consists of photovoltaic energy system (PVES) and its converter assembly with the incorporation of battery energy storage system (BESS), which feeds the DC load to the DC load. The hybrid energy system (HES) may be defined as the system comprises of more than one power generating sources. The combined PVES and BESS form the DC microgrid [3]. These kinds of DC grids are useful for the isolated location where the grid power is not available and for those locations where frequent power outages are happening. Based on the concept of the PVES and BESS, the HES is formed and it is used to feed the DC load. To enhance the effectiveness and efficacy the MPPT algorithm is accommodated with PVES. From the above concept of the DC microgrid with PVES and BESS, the following literature are presented. The literature review covers the literature which comprises HRES, the application of MPPT algorithms in PVES, ES, and the analysis of HRES.

The adaptive MPPT algorithm for Solar Photovoltaics is proposed in [4] for fast varying climatic conditions using current perturbation method with estimation of short-circuit current of PV system. The proposed MPPT algorithm consists of two segments. The initial one is used to increase the tracking speed considering voltage as a perturbing variable to reach at MPP during steady climatic condition. The later segment focuses on the estimation of the short circuit current of solar PV under sudden changes in temperature and irradiance. The improvement in tracking speed towards maximum power point is considered as a variable. The modeling equations of a photovoltaic module have been solved using the NR method. The authors have checked the output of PV array with MPPT at standard test conditions (STC), i.e., 1000 W/m^2 and 25°C .

The author proposed a MPPT method with the incorporation of two MPPT algorithms in [5]. The calculation of the short circuit current is incorporated with a sudden change in insolation to establish the concept. The authors proposed the equation of current delivered by PV within upper and lower bounds/limits for current perturbation algorithm. They also derived the equation for PV within set limits for adaptive control algorithm. The comparison is done for conventional MPPT algorithm and proposed algorithm. They proposed ACA and VPA algorithms in the context of conventional algorithms like P & O (Perturb & Observed) and Fractional Short Circuit Current (FSCC) method. The activation signal is received by the ACA during sudden change in insolation. The controllers have fine-tuned with derivation of small signal modeling of the boost converter.

Authors have proposed the simulation and analysis for parallel connected PV system with MPPT in [6]. They established their proposed system with hardware demonstration. They claim the reduction in power loss using this topology. They employed a bidirectional converter for MPPT implementation, which has two main functions: charging the battery and acting as a step-up converter. For parallel-connected PV modules with MPPT algorithm, they proposed a dual way DC to DC converter for charging and discharging of the battery. They compared MPPT series

connections to parallel connections first, and afterwards, the author's simulated series connected multiple parallel MPPT. They first compared MPPT parallel connections, and then authors simulated series connections between multiple parallel MPPT. The proposed controller is tested for buck and boost converter. They have proposed and tested the bidirectional converter with five modes of operation. Various protection schemes to avoid charge and discharge of storage is discussed.

The operating principles of various MPPT techniques have proposed in [7] for solar photovoltaic applications. The MPPT methods are classified for uniform and non-uniform insolation levels. The comparative analysis among MPPT techniques has been done for their sampling rate, robustness, complexity, efficiency, their sampled parameters, requirement of a system or expert knowledge, and constant power operation for uniform and non-uniform solar insolation.

Comprehensive overview of MPPT approaches is reported in [8]. With the various control systems utilized for AC to DC and DC to AC conversion, the authors compared Tech-A to Tech-Z. The criteria of controlling variable, mode of conversation, form of the signal (analog or digital), cost, and level of complexity is taken into the consideration while comparing the MPPT methods.

Due to wide acceptance of the AC supply for AC loads, the hybrid energy systems were proposed and analyzed for supplying AC power. The PVES and BESS provide DC supply, whereas WES or diesel engine systems required AC-DC and then DC-AC conversion. The hybrid system with DC bus could be a substitute solution where the reduction in the power stage is considered. The remote and isolated locations, where the DC supply is used to feed the LED loads for lighting and DC fan. The merits of DC system are proposed in [9]. The low-voltage bipolar-type DC microgrid with PV, supercapacitor, gas engine, battery, fuel cell, etc. is proposed in [9] for high-quality power distribution.

The review of hybrid wind PV system is discussed in [10]; the authors have described various software/simulation tools used for hybridization methods with case studies. They considered the concept of the unit sizing of PVES, HRES, including aspects like meteorological data, load profile, modeling of PVES, modeling of WES, modeling of BESS, constraints of optimization, reliability analysis, economic analysis, converter design, controller design, performance assessment, and software tools. They have listed a summary of optimization studies, software tools for HRES.

The authors discussed the comparative investigation of stand-alone hybrid systems in [11]. The applications for off-grid and rural electrification using such renewable hybrid solar energy-based sources are discussed. The hybrid solar energy combined with conventional and non-conventional sources is discussed. Standalone PV-based system in the context of location of the project, load type, design capacity with their outcome from 2001 to 2013 has been discussed. The location for hybrid solar-PV/wind throughout the world has been discussed with its design capacity and outcome.

Regulation of DC link voltage across DC bus is important especially for significant in weak grids and isolated systems. An algorithm for the regulation of the DC link voltage irrespective of change in load or atmospheric conditions is discussed. The wind energy conversion system is hybridized with the battery bank,

fuel cell and electrolyser has been proposed in [12]. The effective control technique with unbalance loading conditions is used. The energy management system ensures the state of charge (SoC) of the battery.

The authors have analyzed the operation of the standalone PV/Wind/Battery system the weather data for 2 days by taking sample of wind speed, insolation, and temperature of solar PV at Calicut, India [13]. The DC link voltage is maintained with the help of proposed control algorithm. The study has been done for deferrable loads for primary, secondary, and tertiary control.

A micro rating DC power distribution system applicable for residential load is proposed in [13]. The major impact has focused on the DC power distribution system using RES such as PV, Wind, and Fuel cell for residential applications. The DC electrical system for clean energy house is located in the area of the industrial city Denizil, Turkey. The proposed DC system comprises of 400 W of a wind turbine, 5 kW of PV panels, and 2.4 kW of fuel cell used to run DC electric system for various electrical loads for which system is designed. The system also comprises of various sources with DC to DC converter, DC surge protector, monitoring devices, DC distribution power block, protective system, and data acquisition system.

The voltage control scheme for stand-alone HRES is proposed in [14] for the isolated area power system applications. The authors proposed novel algorithm for maintaining DC link voltage and the regulation of voltage at DC link voltage for hybrid RES. The standalone system with the BESS and the fuel cell is used by considering the meteorological changes such as PV insolation and temperature of PV, variation in wind speed, and impact of change in load.

Authors in [15] have presented a complete review on AC and DC microgrid. They have mentioned every aspect of building and configuring AC and DC microgrid. The various components for AC/DC microgrid and its general schemes are explained and compared. The various technologies with renewable and non-renewable energy sources, renewable DGs with primary energy, type of output, power from a module, efficiency (electrical), overall efficiency with its advantages, and disadvantages are discussed. They have also described the technology used in storage systems in context of its efficiency, capacity, energy density, capital, lifetime, environmental impact, and maturity with examples.

Microgrid architectures with the low voltage distribution generation are proposed in [16]. Authors have described the typical elements of a micro-grid, and its architectures with their topologies. The DC microgrid with various zones with incorporation of solar state transformer is discussed. A performance comparison of the microgrid architectures for various topologies like microgrid has been discussed.

Substantial issues of the HRES for the isolated load have discussed in [17]. Authors have mentioned various drivers for hybrid system development which comprises of economic factors, scarcity of electrical energy, policies, etc. They have also mentioned the benefits of hybrid systems and their viability as an option for rural electrification, the boosting of integration methods, power electronics interfacing methods, etc., with renewable sources like biomass, solar energy, wind

energy, and hydropower. The design related issues are also described. The key aspect for this article is to empower the homes for the population whom are living in the isolated areas.

The regulation in the DC link voltage in case of Photovoltaic system, fuel-cell, and supercapacitor-based hybrid system is proposed in [18]. They proposed the maintenance of DC link voltage with its regulation using the fuzzy logic controller.

The authors provide the solution to integrate the various renewable energy sources by formation of the micro-grids. The proposed micro-grid integration is done beyond the penetration depth limitations [19]. The energy management in hybrid system is proposed for islanding and grid connected modes are demonstrated in the work.

A novel active and reactive power control system for single-phase residential/commercial applications is proposed in [20] for HRES. The real time grid integration with the parameters like the voltage regulation, active & reactive power control, and its fault ride-through (FRT) with hybrid estimator is proposed.

PV, energy storage, and supercapacitor-based hybrid energy system for microgrid applications are proposed in [21]. The author proposed control strategies for fast regulation of DC link voltage for permutations and combinations of unpredictable changes in power from renewable and source as well, the reduction in current stress for battery management system, power management at PCC, current limit in battery and supercapacitors in case of hybrid energy system. They demonstrated the same with the hardware model of hybrid system.

The PVES with storage incorporated with novel decentralized control for power management is proposed in [22]. The droop control units are proposed in this work by authors to coordinate the hybrid system units for micro-grids. The multi-segment P-f characteristics are proposed in the article with frequency band. The overall coordinated control is proposed with simulation analysis for hybrid renewable power generation system.

PV Battery hybrid system-based reactive power scheduling using model predictive control is proposed in [23]. The main outcome of this paper comprises of the consideration of real time electricity pricing and its variation with real-time load and its demand with real time data for solar insolation. The MPC with function of the profit-cost is considered. Energy storage system is extended for peer-to-peer transmission like grid, vehicle or EVs, house, or any other application is proposed with MPC.

The hybrid PV and ESS is proposed with control and power management system in [24]. The proposed system ensures about succeeds in the regulation of the voltage on the DC & the AC Bus. The power management algorithm ensures the power flow for grid-connected and isolated mode.

A hybrid storage system combining battery and supercapacitor interfaced with DC bus for enabling the power flow is proposed in [25]. The primary source is the solar PV connected with high gain converter. The parallel operation of grid-side converters with PV source, battery energy storage, and supercapacitors are contributed in this work.

The authors proposed new energy management system implemented in hybrid system which comprises of solar PV, battery energy storage, and supercapacitor in [26]. The feature enhanced for novel energy management system are the restoration of DC link voltage in faster way, State of charge (SoC) limit for energy storage battery and super capacitors, BESS charging and discharging, and smooth transitions in the mode of operations for the sources.

The certain limitations of the fuzzy logic controller are the rules of scheduling are made without any standard approach with only human expert knowledge. The difficulty in the correct weight of the rules is also a challenge. For the complex system, the weight adjustment rules are quite complex [27].

The hybrid system usually employed with closed loop system to maintain the voltage and frequency. The fixed gain and adaptive gain techniques are used to fine tune the parameters of the controller. The gains are varying based on the error input in case of Gain scheduling to ensure that the degradation in the effectiveness which is minimized where disturbances are created by system or climatic conditions in present case as compared to fixed PI gain method [28]. While implementing this method, it is necessary to recognize the range over which the K_p and K_i would vary when the operating conditions change.

The basic idea of choosing a gain depends upon the error signal; it indicates that when the error signal is large, a value of the proportional gain is selected as high to increase the control effort; hence, there is an acceleration or deceleration in the parameter to be controlled. Similarly, vice-versa, for integral gain, the large value of the integral gain is chosen when the error is small. The gains are selected to tame the steady-state error.

The proposed work describes the Resilient Hybrid Renewable Energy for DC Microgrid fed to the DC load using PVES and BESS. The following objectives are taken into the consideration in the proposed work:

- To obtain an effective DC link voltage profile at DC bus for Photovoltaic Energy System and Battery Energy Storage-based hybrid DC Microgrid System.
- Incorporation of the quasi-double boost DC to DC converter interfaced between the PVES and the DC load with MPPT algorithm incorporated with fixed gain controller.
- To address the limitation of fixed gain controller through simulation with incorporation of adaptive Gain Scheduling PI controller technique.
- Application of Gain Scheduled Proportional Integral Controller-based PI controller is proposed for PVES and BESS system.
- Comparative analysis for fixed gain PI and GSPI controller under various climatic conditions, considering permutations and combinations of the solar insolation and temperature of the PV module.

3 Modeling of PV Cell/Module and Battery Energy Storage System

This segment covers the mathematical modeling of photovoltaic energy conversion system and energy storage. This portion is divided in to two parts. The first part covers the essentiality of energy storage system and its importance with energy storage system with PV. The second part covers the modeling equation of PVES, BESS, and power converter used in the system.

3.1 Need of ESS

At present, battery is used as an energy storage element in the PV power plant that has a small capacity. The commonly available rechargeable batteries are lead acid, nickel cadmium, nickel metal hydride, lithium ion, lithium-ion polymer, etc. Usually, for the PV systems incorporated with the Li-ion and the lithium-ion batteries. Among the available battery options, the Li-ion batteries are preferably used because of high energy storage capacity.

There are several aspects of energy storage integration in PV power plants. The first one is the incorporation of ES system connected with the grid and the second one is the importance of energy storage for off grid system and roof top power plants. In the case of grid connected solar PV power plants, the installation of energy storage battery bank results in to the quick release of the energy into the grid as and when needed. The incorporation of energy storage with grid-integrated power plants is used to make the power supply smoother, and energy stored in the battery banks can be used during the timing of the peak demands.

3.2 Modeling Equation of PV & BESS

3.2.1 Modeling of PV

The simple circuit of the PV cell is as shown in Fig. 4. The simplest equivalent circuit for a PV cell or module comprises of a current source drives through the Sun light. The important parameters for PV cell/module are open-circuit voltage (V_{OC}), short-circuit current (I_{SC}), rated or maximum-power point voltage (V_{MPP}), rated or maximum-power point current (I_{MPP}), and peak power capacity in watt (W_p). When the output terminals of the PV cell or module are shorted, the I_{SC} is measured for particular climatic conditions. Likewise, connecting terminals of voltmeters across the PV cell or module the V_{OC} will be computed. The IV and PV characteristics of Photovoltaic cell or module demonstrate the performance of PV module at various climatic conditions. The mathematical equations are obtained as

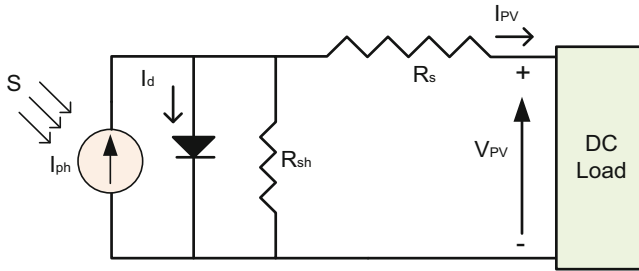


Fig. 4 Equivalent circuit diagram of PV cell/module [4]

under the simplified model of PV module. Similarly, to accommodate the effect of temperature and insolation, one has to model real PV cell or module. This requires the accommodation of the series resistance R_s is the series resistance of PV cell/module in ohm, the shunt resistance R_{sh} is the shunt resistance of PV cell in ohms. The series resistance causes adds the contact resistance and rear & top metal contacts and that too on shunt resistance results power losses. The relationship between V_{OC} , I_{SC} , and current delivered to the load is mentioned in Eqs. (1) and (2).

$$V_{OC} = 0.0257 \ln \left(\frac{I_{SC}}{I_0} + 1 \right) \tag{1}$$

$$I_{PV} = I_{ph} - I_{rs} \left(e^{\frac{q(V_{pv} + I_{pv} R_s)}{AKT}} - 1 \right) - \frac{V_{pv} + I_{pv} R_s}{R_{sh}} \tag{2}$$

3.2.2 Modeling of BESS

The ES is a key element for hybrid renewable energy system operating at standalone mode. The variable nature of insolation and temperature for PV system results variability in voltage level with change in climatic conditions. However, the battery banks encounter certain disadvantages like life cycle of battery, charging & discharging pattern, cost of large-scale development, lack of maintenance, etc. The BESS integrated with variable renewable sources like PVES in the present case ensures buffer when the sun is not shining and provides the voltage support at DC link /DC bus. Taking into consideration the modeling aspect, the battery storage can be modeled as controlled voltage source with series resistance [29]. The open circuit voltage equation is calculated by non-linear Eq. (3);

$$E = E_0 - K \frac{Q}{Q - it} + A \exp(-B*it) \tag{3}$$

Equation (3) represents various quantities like E is the no-load or open circuit voltage in Volt, $E_0 =$ constant voltage of battery in Volt, K is the polarization voltage in Volt, Q is storage capacity in Ah, $\int idt$ is the actual battery charge in Ah, A is the exponential zone amplitude in Volt, B is the exponential zone time constant inverse in $(\text{Ah})^{-1}$, V_{batt} is the battery voltage in Volt, R is the internal resistance of battery storage in ohm (Ω), i is the battery current in Ampere.

4 Description of Hybrid System

The hybrid PV & BESS-based energy system comprises of Photovoltaic array which comprises of 3 kW PV array and 72 V, 25 Ah BESS. The PVES consists of PV array connected with the quasi-double boost DC to DC converter, which is connected with DC bus which is then connected with the DC load. The purpose of incorporating the quasi-double boost converter is to acquire the high voltage ratio so that the range of output voltage will increase [30] and the reduction in the voltage stress on the power electronic switches of the converters and the pairs of inductor and capacitors. The BESS is interfaced with bidirectional DC to DC converter which is an interfacing medium between BESS and DC bus.

The PVES system comprises of 3 kW of peak power PV array. The PV array will generate 3 kW power at the standard test conditions which is 1000 W/m² insolation and 25 °C temperature. The quasi-double boost converter of 3.3 kW considering 90% efficiency of static quasi-double boost converter. The DC to DC converter operate with a gate pules. To drive the DC to DC boost converter, the voltage and current samples are taken from PV array output. These samples are fed to the MPPT algorithm. The MPPT proposed in [4] is used in this work. The MPPT algorithm is coded in simplified C block in PSIM[®] 11.1.3 software. The reference current is generated through MPPT algorithm and it is compared with actual PV current, the error signal is fed to controller which then compared with saw tooth waveform for the generation of gate pulse.

The BESS system comprises rating of 72 V, 25 Ah and is interfaced with the bidirectional DC to DC converter, which is interfaced with DC bus. The PVES and BESS are interfaced with common DC bus. The diagram of the HES is shown in Fig. 5. To maintain constant voltage across DC bus the reference voltage of 200 V is selected.

5 PI Tuning by Gain Scheduling, Mathematical Model

The proportional integral gain is usually incorporated in closed loop to regulate the DC link voltage and generation of duty cycle. The fixed or conventional gain controller has disadvantages of the high probability of failure with change in

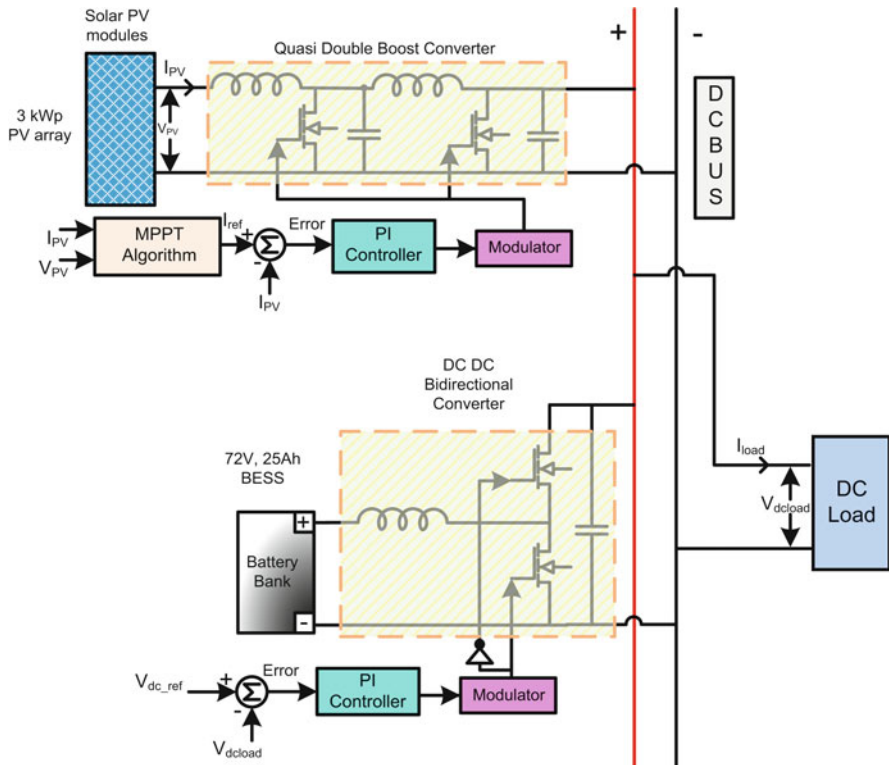


Fig. 5 PVES and BESS hybrid system fed to DC load with PI controller

climatic conditions. If the climatic conditions change, the controller may saturate which results undesired output. This problem can be addressed using various PI controller tuning methods. This analysis focuses on the integration of the GSPI controller applied in hybrid PV and BESS standalone system and its comparison with incorporation of fixed gain controller. The incorporation of fixed gain controlled with PVES and BESS is shown in Fig. 7. The value of load resistance is taken as 20Ω . The 50 kHz switching frequency is selected. The State of Charge (SoC) of the energy storage is considered as 0.8. The modulator signal is generated from the controller output.

The operation with the GSPI controller is divided into two stages. The first stage determines the gains of the controller with the error input and the second one decides the controller output.

The controller is modeled mathematically with respect to change in controller gain based upon error input is mentioned in Eq. (4).

$$u_{dc}(t) = k_p(t) * e(t) + k_i(t) \int e(t)dt \tag{4}$$

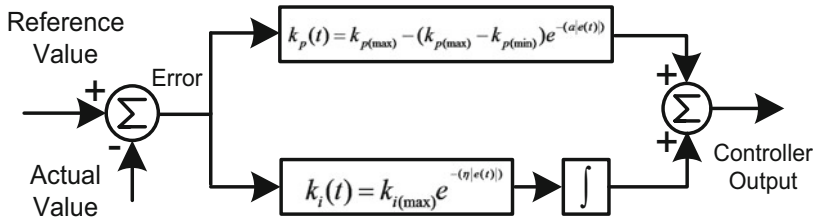


Fig. 6 Implementing GSPI

The Eq. (4) represents various parameters like $u_{dc}(t)$ denotes the output of the controller, $e(t)$ is error signal, $k_p(t)$ and $k_i(t)$ are the instantaneous values for PI, and t is time. $k_p(t)$ can be represented as a function of the input error signal $e(t)$ as in Eq. (5), where, ‘a’ is a constant, k_{pmax} and k_{pmin} are the maximum and the minimum values of k_p . Similarly, Integral gain, $k_i(t)$, in Eq. (6) as a function of error signal $e(t)$ can be expressed. The structure of GSPI controller is shown in Fig. 6.

$$k_p(t) = k_{p(max)} - (k_{p(max)} - k_{p(min)}) e^{-a|e(t)|} \tag{5}$$

$$k_i(t) = k_{i(max)} e^{-(\eta|e(t)|)} \tag{6}$$

The graphical and logical response for GSPI controller with change in error is as shown in Fig. 7a, b for k_p & k_i based upon error signal. The GSPI offers the benefits of variation of k_p & k_i with change in error input with variations in the climatic conditions. The performance of GSPI controller rejects the degradation in output under disturbance. The only disadvantage is that the GSPI needs an extra calculation for the identification of k_p and k_i at every iteration.

6 Simulation Results and Discussions

The model for simulation is developed in PSIM[®] 11.1.3 environment. The PVES is interfaced with quasi-double boost DC to DC converter with DC load. The incorporation of MPPT algorithm ensures MPPT operation of PVES. To maintain the constant voltage at the DC link, the incorporation of the BESS with bidirectional DC to DC converter is simulation. The system is tested for fixed gain controller and with incorporation of GSPI controller under sudden change in load variations and climatic conditions. The quantities which are measured for the simulation and its analysis purpose are PV module voltage, voltage level after first stage of quasi-double boost, voltage after second stage of quasi-double boost, load voltage (load voltage and output of DC to DC converter is same.), load current, power shared by

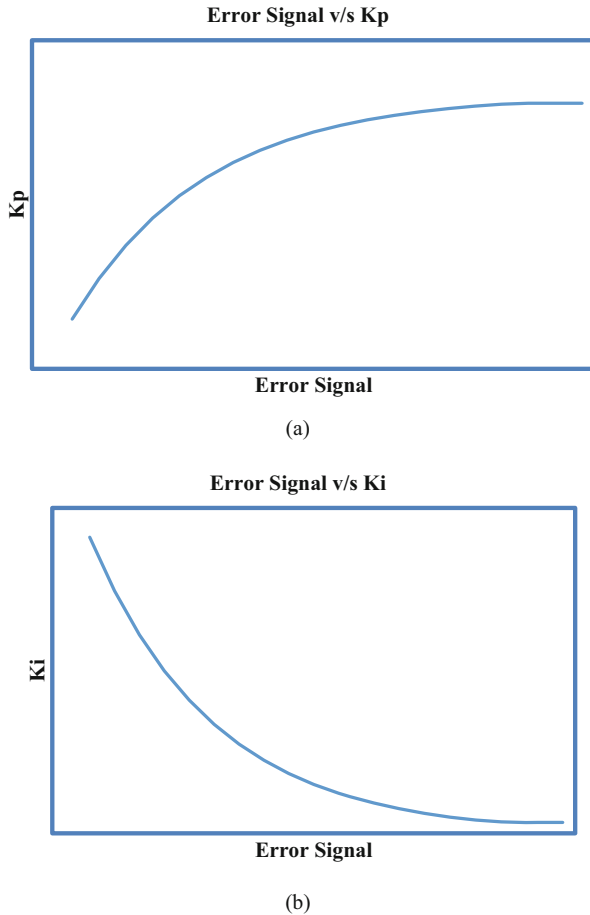


Fig. 7 Response of GSPI controller for (a) K_p with error signal $e(t)$ and (b) K_i with error signal $e(t)$

PVES, BESS voltage, power shared by BESS, etc. The DC bus along with PV and energy storage forms a DC microgrid with incorporations of balance of systems for PVES and BESS.

The system is first tested with fixed gain PI controller for variations in climatic conditions and change in load. The schematic diagram of the HRES is shown in Fig. 5. The system is then tested through the incorporation of GSPI controller instead of fixed gain PI method. The schematic diagram is shown in Fig. 8. The simulation analysis of PVES and BESS is done by considering three cases. The first case incorporates comparative analysis of the fixed gain PI controller and GSPI controller in case of the hybrid PVES and BESS system at 1000 W/m^2 insolation and $25 \text{ }^\circ\text{C}$ temperature for PVES and SoC for BESS is taken as 0.8. The second case deals with the comparative analysis for change in insolation, temperature, and change in load

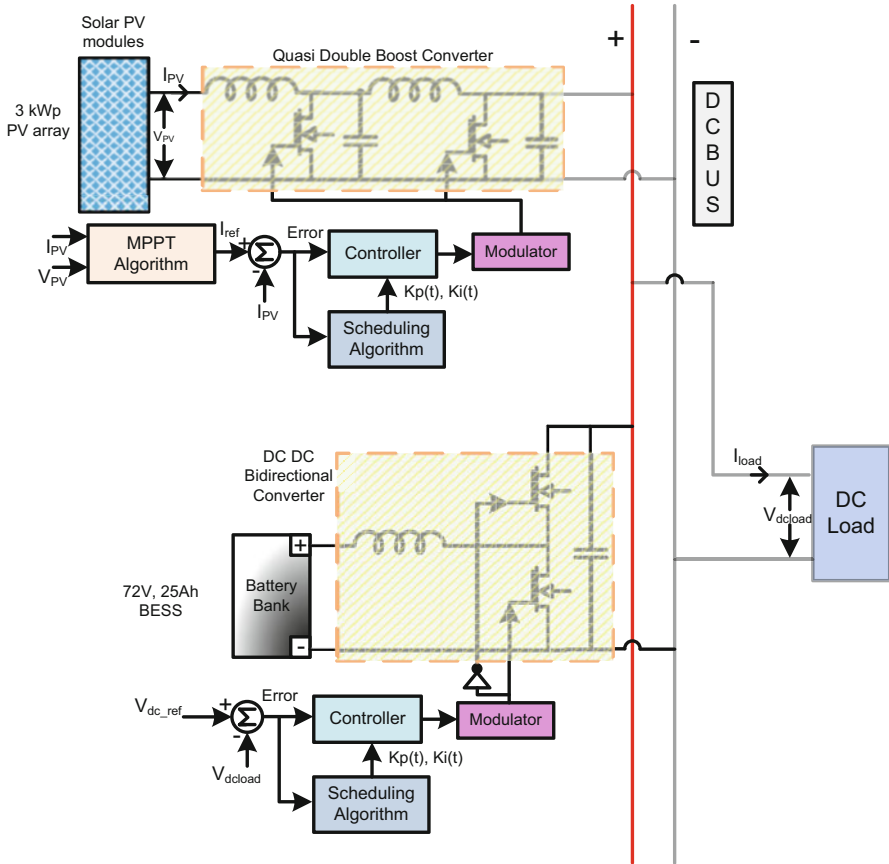
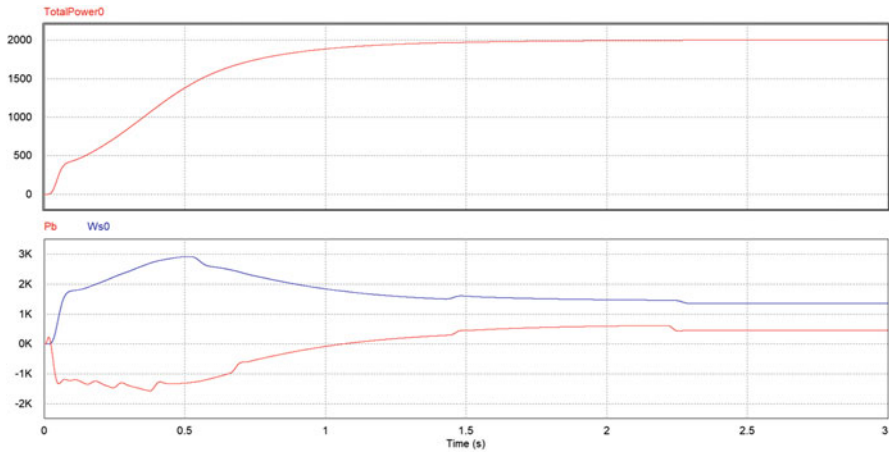


Fig. 8 PVES and BESS hybrid system fed to DC load with GSPI controller for DC microgrid

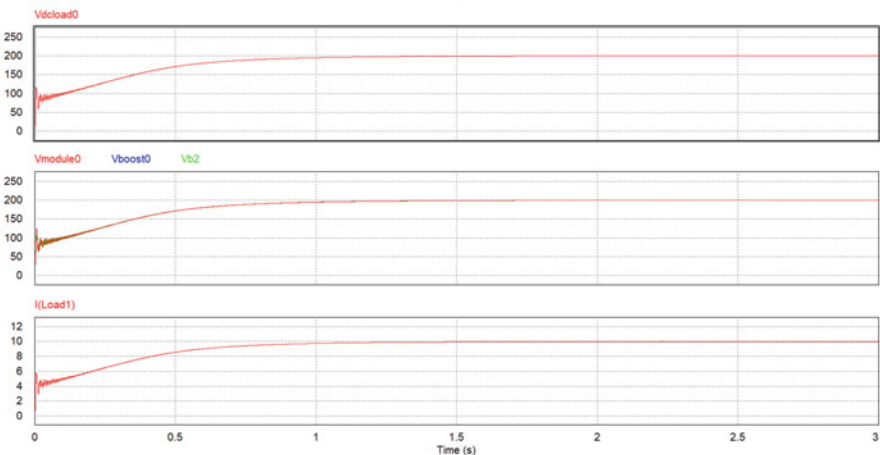
for the fixed gain controller and GSPI controller. The third case comprises a GSPI controller for change in insolation, change in temperature, and change in load.

Case 1: Performance of PVES and BESS for constant insolation, temperature, and constant load for fixed gain controller and GSPI controller.

This case represents the performance of hybrid system which is tested for constant insolation of 1000 W/m^2 and temperature $25 \text{ }^\circ\text{C}$ for PVES. The connected load at DC bus is $2 \text{ kW}/20 \text{ } \Omega$. Figure 9a shows the power sharing by the PVES and BESS with the incorporation of the fixed gain PI controller. The power shared by PVES (P_{s0}) and BESS (P_b) are Fig. 9b shows the voltage profile at DC bus (V_{dload0}), the voltage after first stage of the boost converter (V_{boost0}) and second stage of the boost converter (V_{b2}) connected with PVES and total current drawn by the system (I_{load1}).



(a)

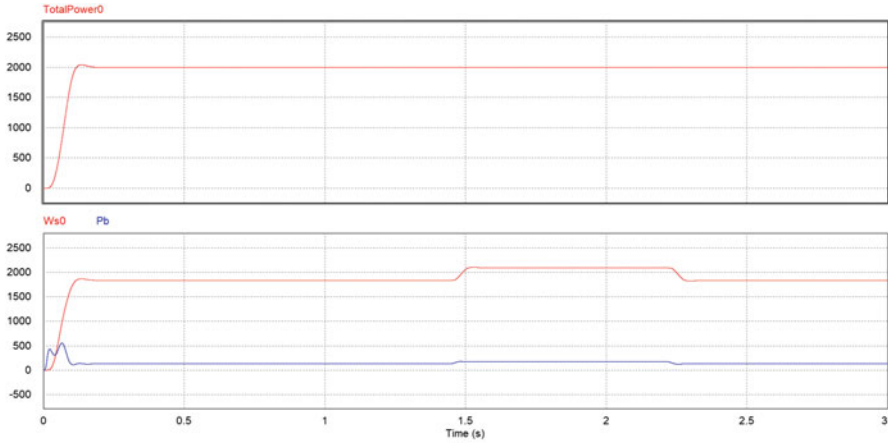


(b)

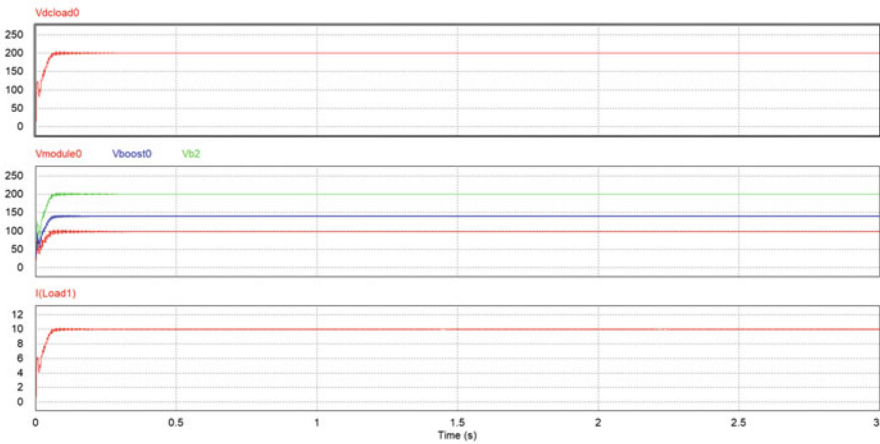
Fig. 9 Results for hybrid system with fixed gain controller: (a) Power shared by the PVES and BESS (in Watt) and (b) voltage profile at DC bus, voltage levels in quasi double boost converters (in V), total current drawn by load (in A)

Similarly, the hybrid system is tested for similar climatic conditions and load conditions for GSPI controller. Figure 10a, b demonstrate the results for the GSPI controller which is used in place of fixed gain controller.

Figure 9a shows the power sharing between PVES and BESS for 2 kW load. The DC resistance has modeled and taken as a load for DC microgrid. The power sharing between PVES and BESS is 74.93% and 25.06%, respectively, to cater the load demand of 2 kW. The load voltage has maintained at 200 V. The incorporation of PI controller regulates the voltage around 200 V DC. The limitation of the fixed gain controllers in the context of steady-state behavior of the quantities is observed



(a)



(b)

Fig. 10 Results for hybrid system with GSPI controller: (a) Power shared by the PVES and BESS (in Watt) and (b) voltage profile at DC bus, voltage levels in quasi double boost converters (in V), total current drawn by load (in Amp.)

in Fig. 9a, b. The system takes much longer time to gain its steady value of respective electrical quantities. Figure 9a, b demonstrate the same for voltage, power drawn by the load, contribution of the power by the PVES and BESS, and load current. This increases the voltage stress across switching MOSFET.

To address this issue, the incorporation of adaptive proportional integral controller is adapted. The hybrid DC microgrid system is now incorporated with the GSPI controller. Section V depicts the mathematical model of GSPI controller. This effect of GSPI controller is demonstrated in Fig. 10a, b. The time required to reach at steady state mode by the system is less with less transients for incorporation of

GSPI as compared to fixed gain controller. The output of GSPI controller drives the gate pulse of the quasi-double boost converter for PVES and the gate pulse of the bidirectional converter in case of the BESS.

The effect of the quasi-double boost converter is observed in Fig. 10b which results in reduction in the voltage stress across the quasi-double boost converter. The other advantage is the reduction in the DC ripple in case of DC voltage profile which demonstrates the effectiveness of the controller. The constant DC link voltage profile in DC microgrid application is essential to strive a goal for further connection with other power electronic components and the grid.

Case 2: Performance of PVES and BESS for change in insolation, temperature, and change in load for fixed gain controller and GSPI controller.

This case represents the performance of the PVES and the BESS-based hybrid DC system under dynamic conditions. The system is tested for change in insolation, change in temperature, and change in load as well. Initially, the system is tested for fixed gain PI controller and then it is compared with GSPI controller for similar variations climatic and load conditions. Figure 11 shows simulation analysis for the PVES and the BESS-based DC microgrid with fixed gain controller and Fig. 12 shows simulation analysis with GSPI controller.

The simulation analysis is done using change in insolation and temperature for fixed gain controller. The input applied to the PVES is shown in Fig. 11a. The insolation changes from 1000 to 900 W/m² to 800 W/m² within 3 seconds. Similarly, the increment in temperature is shown in Fig. 11a which varies between 25 °C and 30 °C within 3 seconds. The power sharing between PVES and BESS is shown in Fig. 11b and similarly, like case 1, the voltage at different nodes are observed in Fig. 11b.

The simulation analysis is done for GSPI controller by considering the above mentioned climatic conditions. The responses shown in Fig. 12b, c typify the effectiveness of the GSPI controller incorporated with the MPPT algorithm. The effectiveness of the algorithm and response of controller can be seen with the help of the results shown in Fig. 12. The variations in the climatic conditions can be observed in the results. The responses are as shown in Fig. 12c the change in climatic conditions (insolation and temperature) there is little deviation in voltage profile across DC load or at the DC bus; again the value of the voltage is regained to the reference value which is set as 200 V DC. Similar observations can be done in current profile when the load changes and in voltage profile for quasi double boost converter.

Case 3: Performance of PVES and BESS for change in insolation and constant temperature for GSPI controller and change in temperature and constant insolation with change in load.

This case describes the analysis for PVES and BESS-based DC microgrid for change in insolation & constant temperature and change in temperature and constant insolation with change in load.

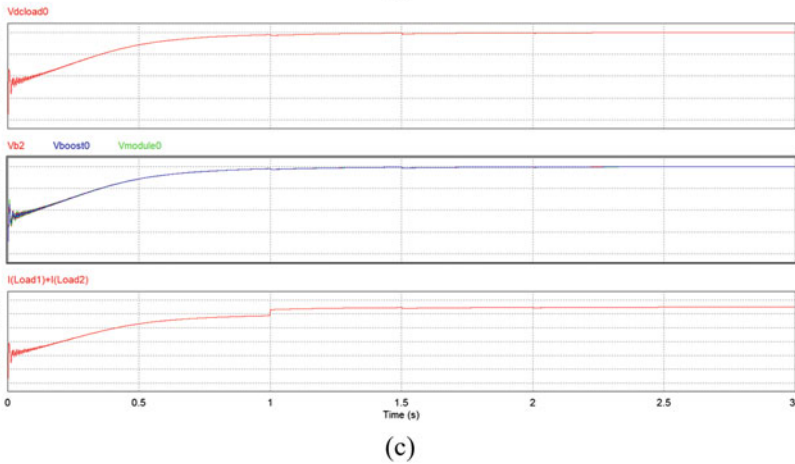
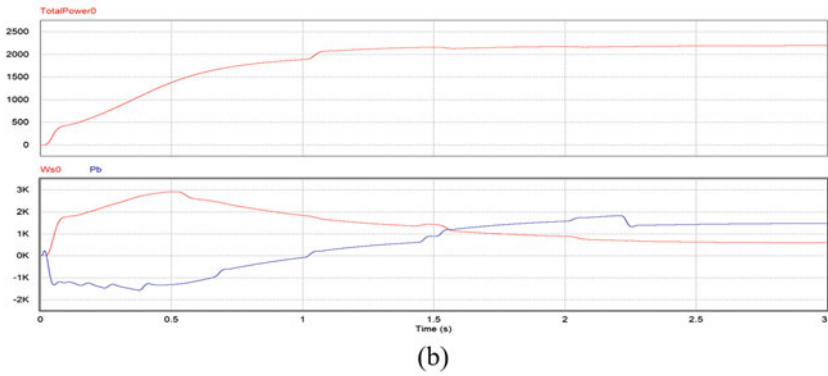
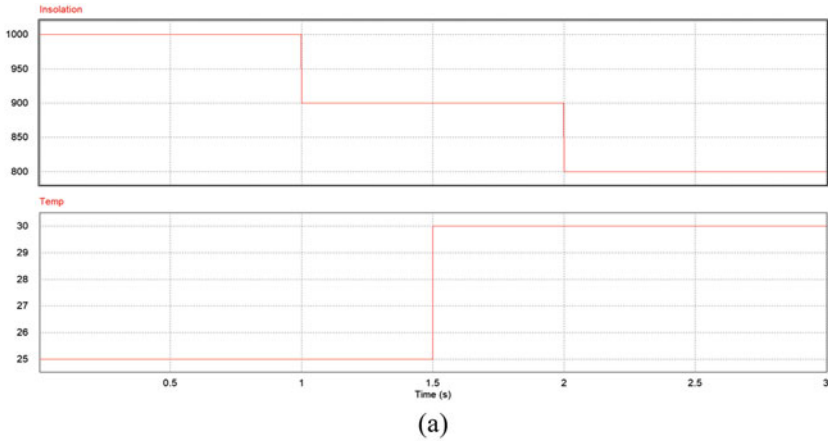


Fig. 11 Results for hybrid system with fixed gain controller: **(a)** Input solar insolation (in Watt/m^2) and temperature (in $^{\circ}\text{C}$), **(b)** power shared by the PVES and BESS (in Watt), and **(c)** voltage profile at DC bus, voltage levels in quasi double boost converters (in V), total current drawn by load (in Amp)

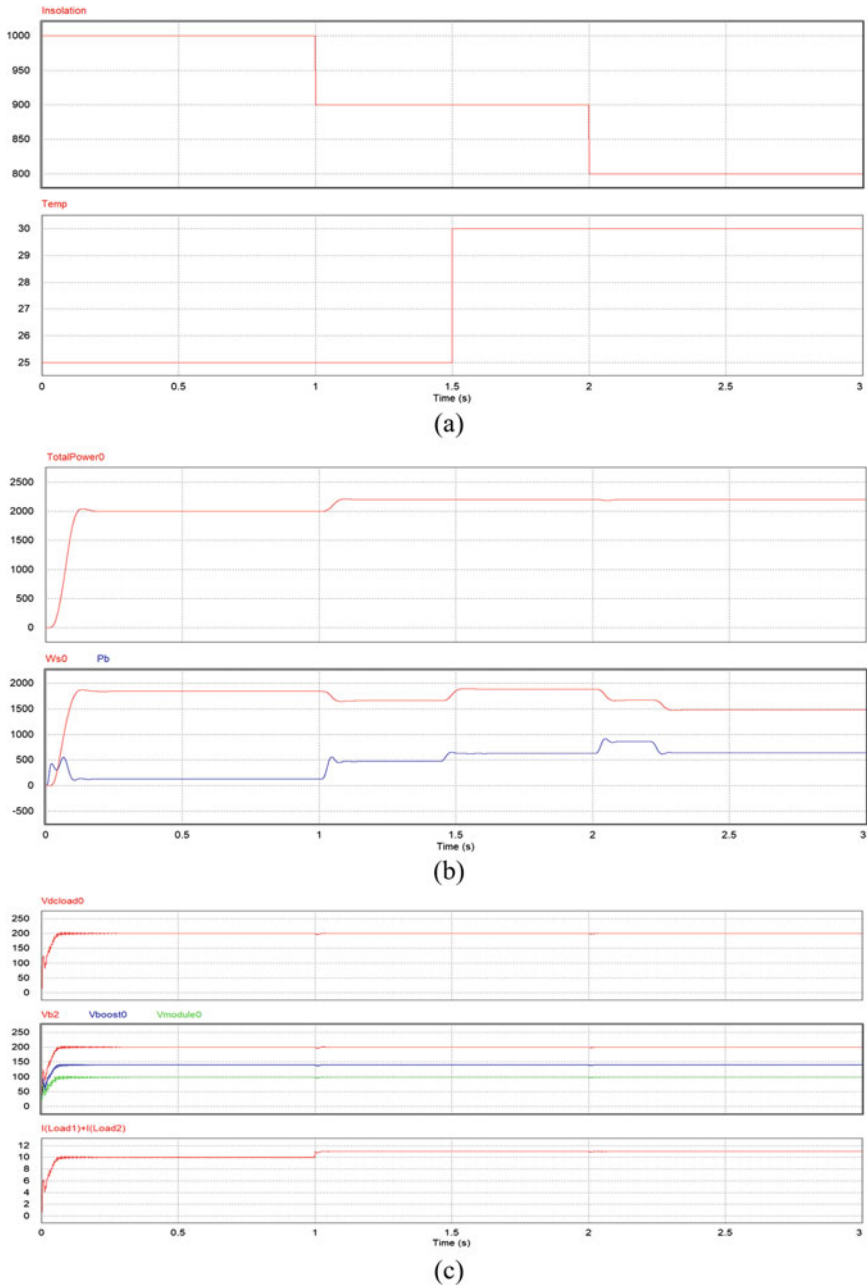
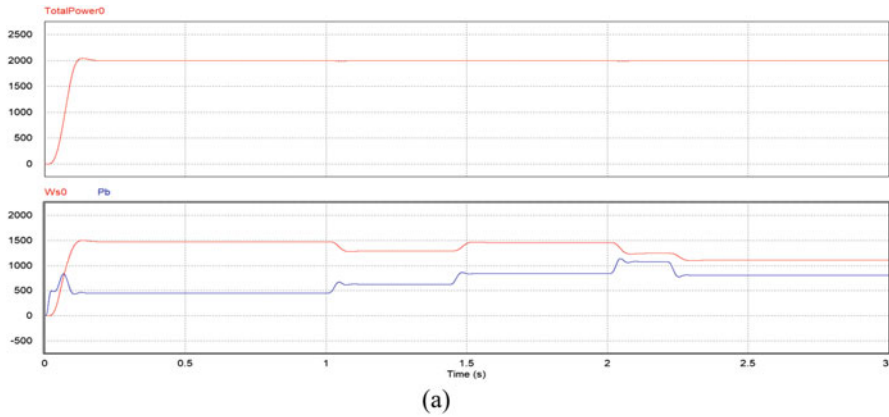
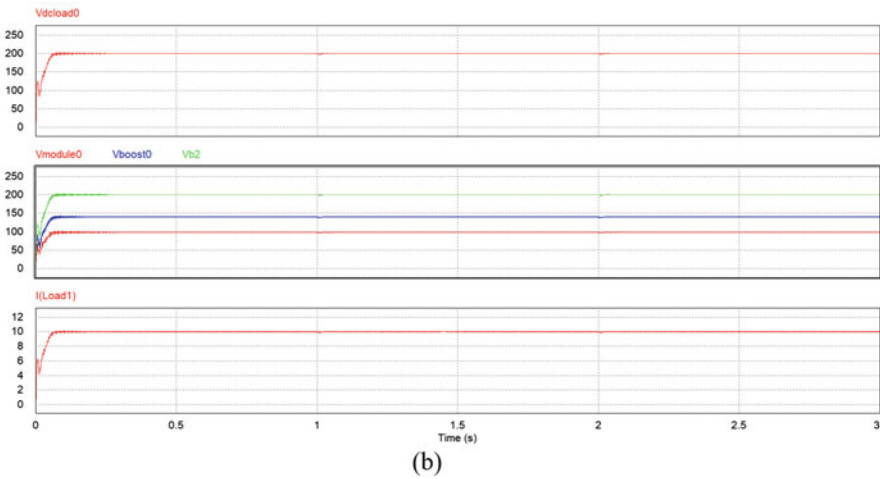


Fig. 12 Results for hybrid system with GSPI controller: (a) input solar insolation (in Watt/m^2) and temperature (in $^{\circ}\text{C}$), (b) power shared by the PVES and BESS (in Watt), and (c) voltage profile at DC bus, voltage levels in quasi double boost converters (in V), total current drawn by load (in Amp)



(a)

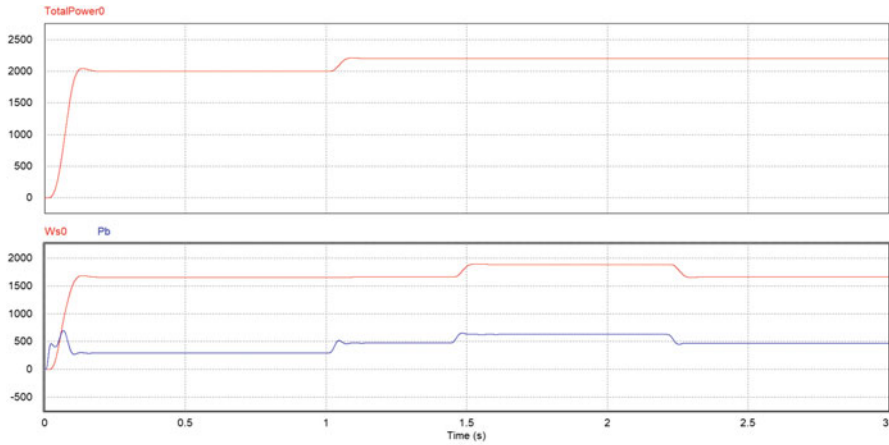


(b)

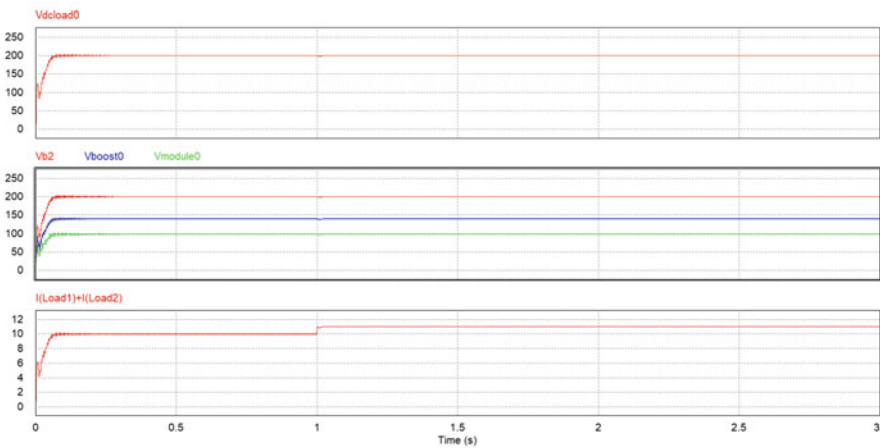
Fig. 13 Results for hybrid system with GSPI controller: (a) power shared by the PVES and BESS (in Watt) and (b) voltage at DC bus, response of the quasi double boost converters (in V), total current drawn by load (in Amp)

3.1 Performance of PVES and BESS for change in insolation and constant temperature.

This case describes the testing of system for change in insolation from 1000 to 900 W/m² to 800 W/m², constant temperature of 30 °C and constant loading condition. The responses are shown in Fig. 13a, b. The effect of the quasi double boost converter is observed in Fig. 13b which regulates the DC link voltage around 200 V.



(a)



(b)

Fig. 14 Results for hybrid system with GSPI controller: (a) power shared by the PVES and BESS (in Watt) and (b) voltage profile at DC bus, voltage levels in quasi double boost converters (in V), total current drawn by load (in Amp)

3.2 Performance of PVES and BESS for change in temperature and constant insolation with change in load.

The case 3.2 describes the testing of system for constant insolation and the variation in temperature from 25 to 30 °C with combination of change in load. The equivalent load resistance of 18 Ω is considered as a DC load. The increment in total power is observed in Fig. 14a after 1 second. After 1 second the additional load of 250 W is connected at DC bus. The responses are shown in Fig. 14a, b. The effect of the quasi-double boost converter is observed with change in temperature and loading conditions in Fig. 14b which regulates the DC link voltage around 200 V. The

GSPI controller ensures the voltage regulation and the BESS maintains the DC link voltage profile at reference value of 200 V.

7 Concluding Remarks

This effort reports the PVES and the BESS-based HRE system for DC microgrid application. The PVES and the BESS incorporates the closed loop control with the accommodation of fixed gain controller. To address the limitations of fixed gain controller, the GSPI control is proposed for the PVES and BESS-based hybrid renewable power system fed to DC load. Like fixed gain controller the GSPI controller is incorporated for PVES and BESS to control the quasi-double boost converter and the bidirectional DC to DC converter respectively to ensure the voltage regulation at the DC bus. The gains of GSPI vary during transient conditions like change in insolation and temperature for PVES and change in load at DC bus in order to keep the voltage regulation within the limit at DC bus and MPPT operation of PVES. This addresses the limitations of fixed gain PI controller. The performance of HES is checked under the change in climatic conditions and change in load to check the effect on of the change in DC bus voltage profile and operation of MPPT. The PVES and BESS-based DC bus is designed to feed the rural communities which are away from the national grid and forms its own DC microgrid. Hence, the PVES and BESS-based hybrid renewable energy system is suitable for DC microgrid application is resilient and sustainable for local DC load.

References

1. IEA, I (2019) World energy outlook 2019–analysis-IEA. International Energy Agency, France.
2. <https://powermin.gov.in/en/content/power-sector-glance-all-india>
3. Sechilariu M, Locment F (2016) Urban DC microgrid: intelligent control and power flow optimization. Butterworth-Heinemann, Oxford. isbn: 978-0-12-803736-2
4. Kollimalla SK, Mishra MK (2014) Variable perturbation size adaptive P&O MPPT algorithm for sudden changes in irradiance. *IEEE Trans Sustainable Energy* 5(3):718–728. <https://doi.org/10.1109/TSTE.2014.2300162>
5. Kollimalla SK, Mishra MK (2014) A novel adaptive P&O MPPT algorithm considering sudden changes in the irradiance. *IEEE Trans Energy Convers* 29(3):602–610. <https://doi.org/10.1109/TEC.2014.2320930>
6. Gules R, Pacheco JDP, Hey HL, Imhoff J (2008) A maximum power point tracking system with parallel connection for PV stand-alone applications. *IEEE Trans Ind Electron* 55(7):2674–2683. <https://doi.org/10.1109/TIE.2008.924033>
7. Koutroulis E, Blaabjerg F (2015) Overview of maximum power point tracking techniques for photovoltaic energy production systems. *Electr Power Compon Syst* 43(12):1329–1351. <https://doi.org/10.1080/15325008.2015.1030517>
8. Subudhi B, Pradhan R (2012) A comparative study on maximum power point tracking techniques for photovoltaic power systems. *IEEE Trans Sustainable Energy* 4(1):89–98. <https://doi.org/10.1109/TSTE.2012.2202294>

9. Kakigano H, Miura Y, Ise T (2010) Low-voltage bipolar-type DC microgrid for super high quality distribution. *IEEE Trans Power Electron* 25(12):3066–3075. <https://doi.org/10.1109/TPEL.2010.2077682>
10. Mahesh A, Sandhu KS (2015) Hybrid wind/photovoltaic energy system developments: critical review and findings. *Renew Sust Energ Rev* 52:1135–1147. <https://doi.org/10.1016/j.rser.2015.08.008>
11. Akikur RK, Saidur R, Ping HW, Ullah KR (2013) Comparative study of stand-alone and hybrid solar energy systems suitable for off-grid rural electrification: a review. *Renew Sust Energ Rev* 27:738–752. <https://doi.org/10.1016/j.rser.2013.06.043>
12. Kumaravel S, Ashok S (2015) Optimal power management controller for a stand-alone solar PV/wind/battery hybrid energy system. *Energy Sources Part A* 37(4):407–415. <https://doi.org/10.1080/15567036.2011.576414>
13. Cetin E, Yilanci A, Ozturk HK, Colak M, Kasikci I, Iplikci S (2010) A micro-DC power distribution system for a residential application energized by photovoltaic–wind/fuel cell hybrid energy systems. *Energy Buildings* 42(8):1344–1352. <https://doi.org/10.1016/j.enbuild.2010.03.003>
14. Malla SG, Bhende CN (2014) Voltage control of stand-alone wind and solar energy system. *Int J Electr Power Energy Syst* 56:361–373. <https://doi.org/10.1016/j.ijepes.2013.11.030>
15. Planas E, Andreu J, Gárate JI, De Alegría IM, Ibarra E (2015) AC and DC technology in microgrids: a review. *Renew Sust Energ Rev* 43:726–749. <https://doi.org/10.1016/j.ijepes.2013.11.030>
16. Patrao I, Figueres E, Garcerá G, González-Medina R (2015) Microgrid architectures for low voltage distributed generation. *Renew Sust Energ Rev* 43:415–424. <https://doi.org/10.1016/j.rser.2014.11.054>
17. Mohammed YS, Mustafa MW, Bashir N (2014) Hybrid renewable energy systems for off-grid electric power: review of substantial issues. *Renew Sust Energ Rev* 35:527–539. <https://doi.org/10.1016/j.rser.2014.04.022>
18. Thounthong P, Luksanasakul A, Koseyaporn P, Davat B (2012) Intelligent model-based control of a standalone photovoltaic/fuel cell power plant with supercapacitor energy storage. *IEEE Trans Sustainable Energy* 4(1):240–249. <https://doi.org/10.1109/TSTE.2012.2214794>
19. Liu B, Zhuo F, Zhu Y, Yi H (2014) System operation and energy management of a renewable energy-based DC micro-grid for high penetration depth application. *IEEE Trans Smart Grid* 6(3):1147–1155. <https://doi.org/10.1109/TSG.2014.2374163>
20. Pahlevani M, Eren S, Guerrero JM, Jain P (2015) A hybrid estimator for active/reactive power control of single-phase distributed generation systems with energy storage. *IEEE Trans Power Electron* 31(4):2919–2936. <https://doi.org/10.1109/TPEL.2015.2453350>
21. Tummuru NR, Mishra MK, Srinivas S (2015) Dynamic energy management of renewable grid integrated hybrid energy storage system. *IEEE Trans Ind Electron* 62(12):7728–7737. <https://doi.org/10.1109/TIE.2015.2455063>
22. Mahmood H, Jiang J (2017) Autonomous coordination of multiple PV/battery hybrid units in islanded microgrids. *IEEE Trans Smart Grid* 9(6):6359–6368. <https://doi.org/10.1109/TIE.2015.2455063>
23. Lupangu C, Justo JJ, Bansal RC (2020) Model predictive for reactive power scheduling control strategy for PV–battery hybrid system in competitive energy market. *IEEE Syst J* 14(3):4071–4078. <https://doi.org/10.1109/JSYST.2020.2968926>
24. Yi Z, Dong W, Etemadi AH (2017) A unified control and power management scheme for PV–battery-based hybrid microgrids for both grid-connected and islanded modes. *IEEE Trans Smart Grid* 9(6):5975–5985. <https://doi.org/10.1109/TSG.2017.2700332>
25. Yallamilli RS, Mishra MK (2018) Instantaneous symmetrical component theory based parallel grid side converter control strategy for microgrid power management. *IEEE Trans Sustainable Energy* 10(2):682–692. <https://doi.org/10.1109/TSTE.2018.2845469>
26. Manandhar U, Ukil A, Gooi HB, Tummuru NR, Kollimalla SK, Wang B, Chaudhari K (2017) Energy management and control for grid connected hybrid energy storage system under different operating modes. *IEEE Trans Smart Grid* 10(2):1626–1636. <https://doi.org/10.1109/TSG.2017.2773643>

27. Bisht DC, Srivastava PK, Ram M (2018) Role of fuzzy logic in flexible manufacturing system. In: Diagnostic techniques in industrial engineering. Springer, Cham, pp 233–243. https://doi.org/10.1007/978-3-319-65497-3_9
28. Panda SK, Lim JMS, Dash PK, Lock KS (1997) Gain-scheduled PI speed controller for PMSM drive. In: IEEE proceedings of the IECON'97 23rd international conference on industrial electronics, control, and instrumentation, vol 2, pp 925–930. <https://doi.org/10.1109/IECON.1997.672113>
29. Tremblay O, Dessaint LA, Dekkiche AI (2007) A generic battery model for the dynamic simulation of hybrid electric vehicles. In: IEEE vehicle power and propulsion conference, pp 284–289. <https://doi.org/10.1109/VPPC.2007.4544139>
30. Lohmeier C, Zeng J, Qiao W, Qu L, Hudgins J (2011) A current-sensorless MPPT quasi-double-boost converter for PV systems. In: IEEE energy conversion congress and exposition, pp 1069–1075. <https://doi.org/10.1109/ECCE.2011.6063892>

High Impedance Fault Detection and Classification Based on Pattern Recognition



Zahra Moravej and Mehrdad Ghahremani

1 Introduction

The high-impedance fault (HIF) in electrical energy distribution networks is caused by the connection of an electrified conductor to the ground via an object with relatively high impedance and is usually associated with an electric arc [1]. This type of fault can also occur when an electrified conductor in overhead power lines comes into contact with an object such as a tree or when it is cut and falls to the ground. Due to the low voltage in the grid and the high impedance between the ground and the electrified conductor, the current flowing at the fault location is small and on the order of the load currents in the lines. HIF can be defined as a fault that does not draw sufficient current to activate common protective devices (such as fuses and relays).

Various sources have reported the HIF current to be from 0.5 to 75 A and sometimes up to 100 A [2]. Accordingly, current-based protection schemes cannot detect this fault. Upon the occurrence of this fault, an electric arc forms at the location of contact between the conductor and the object. The HIF can be distinguished from normal loads in the distribution grid via the features of the arc current. However, detecting all HIFs in a distribution grid is a formidable task and requires careful preparations and accurate measurements. Examples of HIF current are shown in Figs. 1 and 2.

Some features of the HIF are as follows:

- The current at the fault location is low due to the high impedance between the ground and the conductor and can vary according to the conditions of the contact

Z. Moravej (✉) · M. Ghahremani
Faculty of Electrical and Computer Engineering, Semnan University, Semnan, Iran
e-mail: zmoravej@semnan.ac.ir; mehrdad_ghahremani@semnan.ac.ir

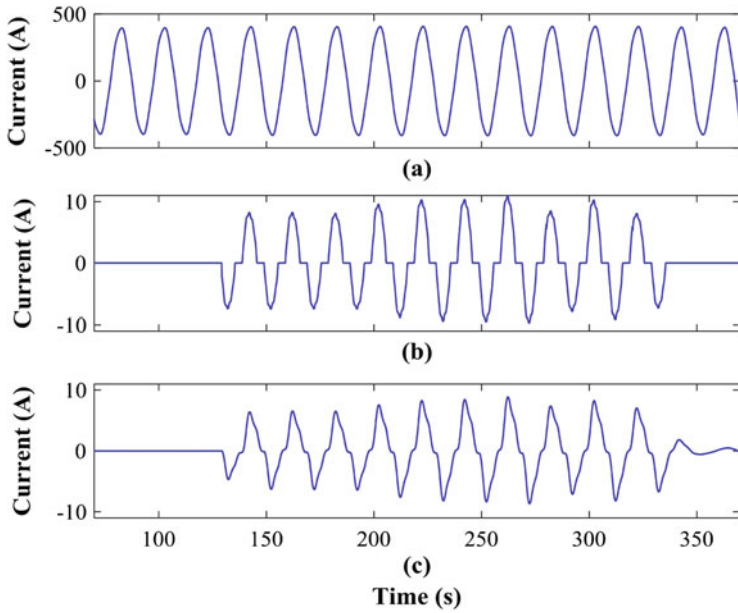


Fig. 1 Simulated HIF current waveforms: (a) faulty phase current in substation (measuring point), (b) the HIF current at the fault location, (c) superimposed component of the measured phase current at substation due to the HIF (obtained by subtracting the faulty phase current and the phase current without HIF) [3]

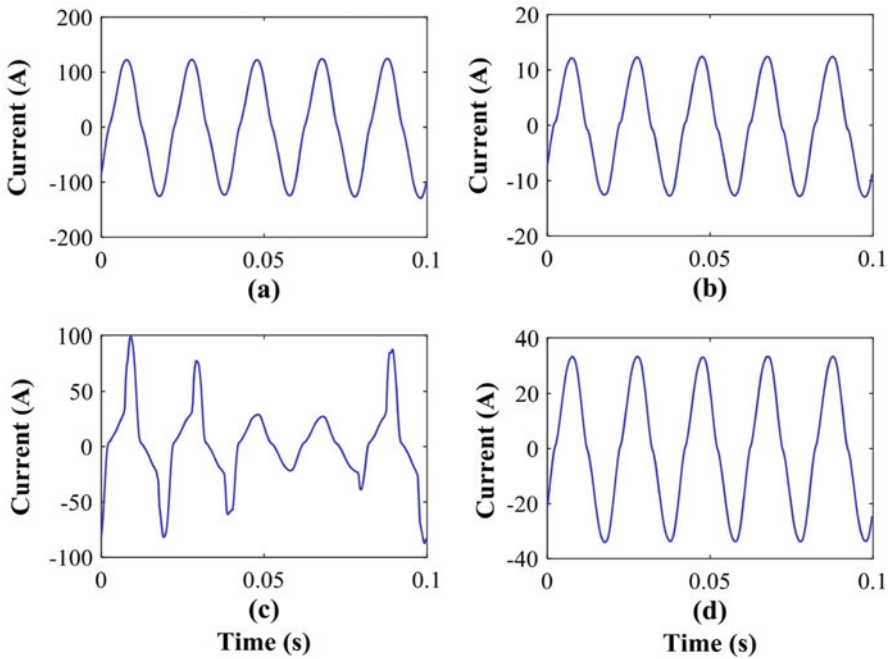


Fig. 2 HIF current waveforms with 20 kV conductor connection on several different surfaces: (a) dry asphalt with 2 cm thickness, (b) plain (non-reinforced) concrete with 10 cm thickness, and (c) reinforced concrete with 10 cm thickness [3]

Table 1 Different HIF currents [2]

Contact surface	Fault current (A)
Dry asphalt	0
Plain (non-reinforced) concrete	0
Dry sand	0
Wet sand	15
Dry grassland	20
Dry grass	25
Wet grassland	40
Wet grass	50
Reinforced concrete	75

location and the grid. Table 1 displays HIF currents over various surfaces reported by the Power System Relaying Committee (PSRC) of IEEE [2].

- HIFs are usually accompanied by electric arcs.
- HIF currents are not sinusoidal. Therefore, their harmonic and inter-harmonic components are more than those of load currents. Although the fault current waveform is different for different contact surfaces, there are similarities between the features of HIFs for different surfaces due to the manner of arc formation.
- The fault current differs in positive and negative half-cycles: the current amplitude is usually smaller in negative cycles.
- The HIF has a dynamic nature, i.e., the fault current amplitude varies in different cycles and behaves randomly.
- Moreover, the HIF is single-phase, and the fault current normally increases when more than one phase is involved in the fault.
- Also, this fault has a resistive characteristic.

1.1 History of HIF Protection

Research on detecting HIFs began in about the mid-1970s. The advent of numerical relays in the early 1990s began with the fabrication of an HIF relay by University of Texas and General Electric researchers [4]. Later, other protective relay manufacturers, such as ABB and Schweitzer, offered relays capable of detecting HIFs.

The initially used methods were mostly based on energy and the statistical specifications of current frequency components. However, the developments in discrete signal processing and digital signal processors (DSPs) in later years led to the use of various signal processing, artificial intelligence, and pattern recognition algorithms in detecting HIFs.

In recent decades, numerous academics have researched this topic and have reported various techniques to detect HIFs. A review of papers indexed throughout the years in authoritative journals indicates the significance of HIF detection as a challenge faced by distribution networks companies [5]. Fault detection methods

can perform differently under different conditions and in different grids. This performance refers to the reliability indexes of protective systems, the two aspects of which are dependability and security. Dependability represents the adequate performance of the system when it is needed. Security refers to the inaction of the system when it is not needed. Another commonly used index is sensitivity, which denotes the ability to detect faults defined for the relay under various abnormal conditions.

2 Goals in HIF Protection

Similar to other faults, the HIF must be detected in a grid. In distribution networks, protective devices are generally used to protect grid equipment, such as transformers or overhead and underground power lines, against fault currents, which exceed the allowable current limits of this equipment. However, the HIF is within these limits and, thus, does not damage grid equipment. The primary goal in detecting this fault in traditional distribution networks is to prevent injury caused by electrocution. Nevertheless, other motivations come into play with the privatization of electricity companies and the creation of a competitive market. In general, the goals in detecting HIFs are the following:

- *Prevention of injury*: As mentioned in older references, the most important reason for detecting HIFs is to prevent injury due to electrocution from contact with a broken conductor.
- *Prevention of fire*: An electric arc caused by the fault, especially when the conductor breaks and falls onto a tree, can result in fire.
- *Prevention of potential outages*: Timely detection of HIFs can prevent damage to equipment due to electric arcs caused by fault currents and potential outages and decrease outage penalties and losses from reduced electricity sales.
- *Reduction of outage duration*: A common method of detecting conductor breakage in distribution networks is through telephone calls from customers. This method suffers from delays, especially in areas with a smaller customer presence. Faster detection of conductor breakage decreases losses due to reduced electricity sales and potential outage penalties.

However, protection against HIFs is not carried out merely by detecting the fault since a short-lived occurrence of this fault does not damage grid equipment considering the small current that passes through this equipment as a result of an HIF. On the other hand, HIF detection algorithms are less error-prone than protection methods such as overcurrent protection and distance protection. Hence, issuing a trip command via the HIF protection immediately after fault detection is not recommended. As a result, when an HIF is detected in the distribution grid, appropriate measures must be taken automatically or by the operator. Usually, the protection system transmits an alarm signal after detecting a fault and issues a trip command if it detects a repeated fault and conductor breakage. Factors such as

hazard probability and the quantity and importance of the loads connected to the feeder in which the fault has been detected must be considered before issuing a trip command. For example, the possibility of electrocution due to conductor breakage is significantly higher in a residential area than a non-residential one, or additional considerations must be made for disconnecting a feeder that supplies the load of a hospital. The location of the fault must be specified to perform these actions. In addition, the approximate location of the fault must be known for the rapid resolution of the factors causing the fault and the dispatching of repair teams.

Moreover, given the privatization of the electricity industry, electricity companies must pay fines to their customers in cases of outage. Also, they are held responsible for accidents, such as electrocution or fire, caused by their distribution networks equipment. Therefore, the rapid detection and resolution of faults are important aspects for reaching the reliability indexes required to become a smart grid.

3 Methods of HIF Detection in Distribution Networks

Various algorithms have been proposed for detecting HIFs. These algorithms consist of three main steps, as shown in Fig. 3. They can be classified and analyzed in different ways. To avoid repetition, not all of these algorithms have been introduced in this section. Only those proposed for HIF detection in distribution networks have been reviewed in Fig. 3 according to the method used in each of the three steps.

3.1 Input Data Preparation

The three-phase voltages and currents in a distribution grid are measured using instrument transformers. The current in the neutral wire is also measured if it is present in four-wire distribution networks. Other parameters, such as active power, reactive power, and currents of positive, negative, and zero sequence voltages may be computed via the measured values. Different signals can be used for fault detection given that any event in the grid affects all signals to different degrees. Since an HIF directly impacts the phase and earth currents, most references, such as [4, 6–15], have used only the three-phase current or residual current signal to detect the fault.

On the other hand, some references have utilized (three-phase or residual) voltage signal features in addition to current signals for fault detection [16–18]. Voltage signals have rarely been used on their own [19, 20].

An arc forms as a result of electric discharge in the gap between two surfaces with a potential difference (such as an electrified conductor and tree branches) due to an HIF. Electromagnetic waves are radiated as the electric charges pass through space. These waves can be received via special antennae and sensors, and faults in the power system can be detected based on their amplitude and features. Electric-

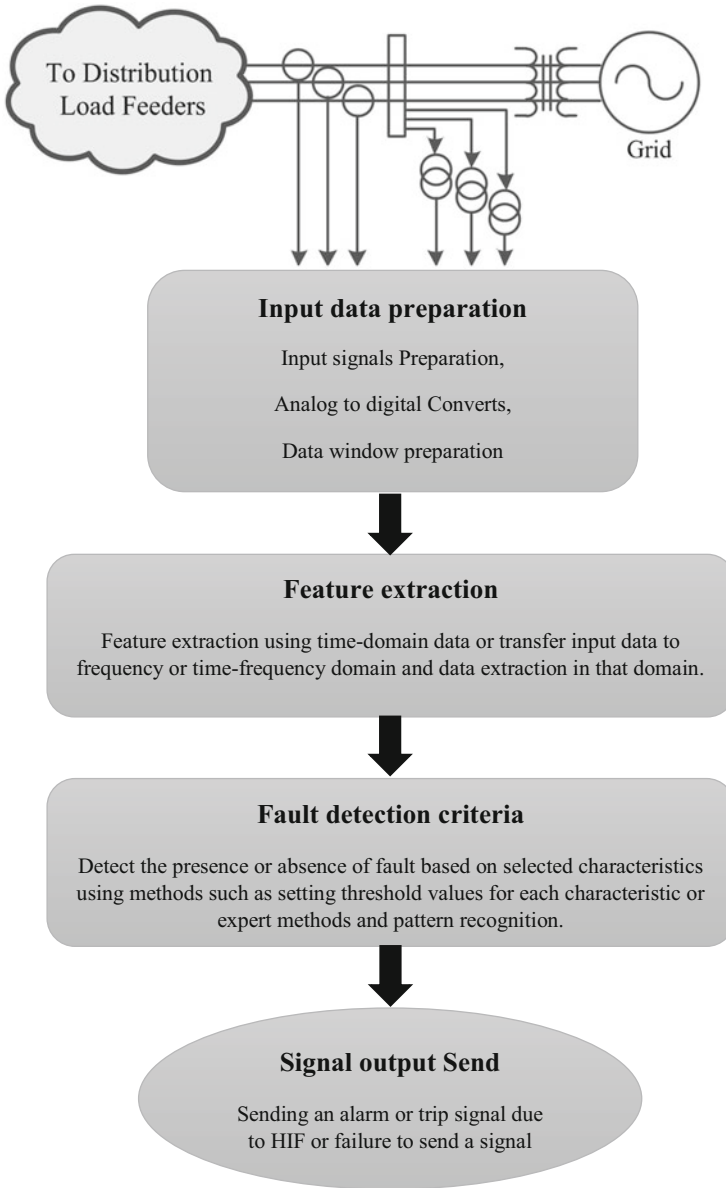


Fig. 3 Schematic of HIF detection in distribution networks

arc-induced electromagnetic waves received by various antennae in a laboratory have been analyzed in [21].

3.1.1 Determining the HIF-Induced Signal

It is very difficult to measure HIFs in an operational distribution grid since there might be several month intervals between their occurrences. Therefore, it is common practice to create artificial fault conditions in real feeders in order to be able to measure and store signals caused by HIFs. For this purpose, the feeder is connected to various surfaces, and the resulting signals are measured. Such tests are usually conducted on insignificant or non-operational feeders since obtaining a permit for causing an error in operational feeders due to the possibility of an outage in the feeder and damage to the equipment.

Another technique for measuring the arc current due to contact between a medium-voltage conductor and various surfaces is laboratory simulation. In this technique, a conductor is electrified with the desired voltage in a laboratory and brought into contact with different surfaces.

However, the arc fault due to this contact can be obtained only at one point in the distribution grid and only under no-load or low-load conditions in this method. Fault measurement at different points in a distribution grid and under different operating conditions is a formidable task that requires considerable time and money. In addition, it is very hard to simulate other events possible in distribution networks.

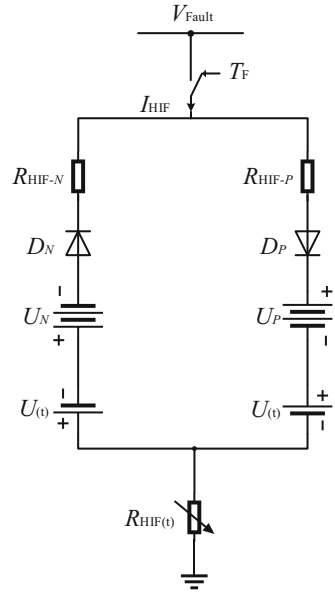
To design an HIF-detection scheme, one must first examine the features of the errors, events, and disruptions occurring in the distribution grid so that suitable features can be selected and an appropriate decision-making criterion can be designed. In addition, large numbers of input and output data are required to train the decision-maker and the classifier in expert methods. For this reason, most references have considered software simulation. Many references, such as [6, 14, 17, 22–26], have used simulation results to analyze faults and design fault detection algorithms. Some other references have first measured HIF values in real feeders or in the laboratory and, then, used simulation data along with measured data to design and test their proposed algorithm [9, 27–29]. Most of these references have employed measured HIF signals for comparison with simulated error models and have trained their algorithms using simulation data. For this purpose, the tested part of the distribution system is simulated in software such as EMTP, PSCAD, or MATLAB.

3.1.2 HIF Model

Numerous researchers have used the double-diode model to model HIF due to its simplicity and ability to provide the main features of the HIF, presented in Sect. 1 [3, 10, 29–31]. The circuit model of the simulated HIF is displayed in Fig. 4.

$R_{\text{HIF-P}}$ and $R_{\text{HIF-N}}$ represent the arc resistance, and U_P and U_N denote the fault threshold values during positive and negative half-cycles $U_P < U_N$. When the fault voltage is larger than the fault threshold voltage during the positive half-cycle $V_{\text{Fault}} > U_P$ and smaller than the fault threshold voltage during the negative half-cycle $V_{\text{Fault}} < U_N$, the fault current will flow in the circuit. However, if

Fig. 4 Circuit model of the simulated HIF



$U_N < V_{Fault} < U_P$, the HIF current will be zero, and no current will flow in the circuit. $R_{HIF}(t)$ represents the time-varying resistance, the value of which varies randomly in each cycle, and $U(t)$ expresses the dynamic and time-varying nature of the HIF.

3.1.3 Distribution Grid Modeling

Software simulation is used because it is impossible to simulate and measure various HIF cases and other events in an actual distribution grid. To this end, first, a distribution grid, including the loads and the accessories, must be modeled. References that have measured HIFs in actual feeders have mostly first modeled the feeder in a software environment and then carried out the simulations on the feeder. As an example, Fig. 5 displays a distribution grid in which HIF tests were performed, after which these tests were modeled in software for further simulations.

Many papers that have utilized only software simulation have modeled part of an actual distribution system in software or used sample distribution networks introduced in authoritative references, such as the IEEE 34-bus distribution grid, for simulation and measurement. Figure 6 displays one sample distribution network used for simulating and measuring an HIF in software.

The larger and more complex a distribution grid is, the more diverse the feeders and loads will be, and the better the fault detection algorithm can be evaluated. Moreover, the presence of various linear and nonlinear single-phase and three-phase loads with different harmonic properties helps better evaluate the reliability of the proposed method. In some references, the proposed method has been studied only

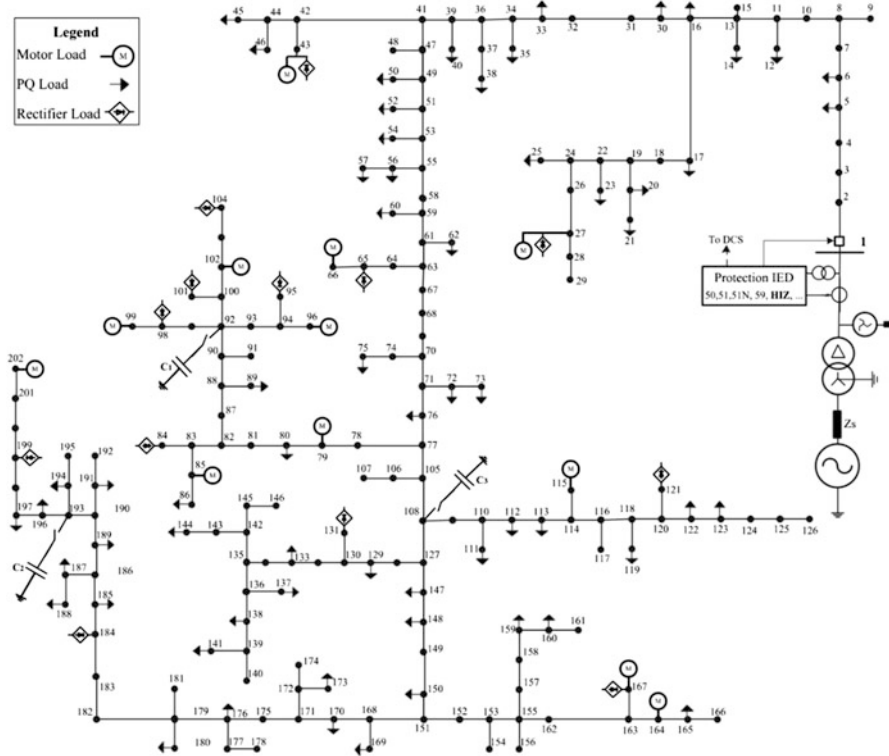


Fig. 5 A sample distribution grid for software simulation of HIFs [3]

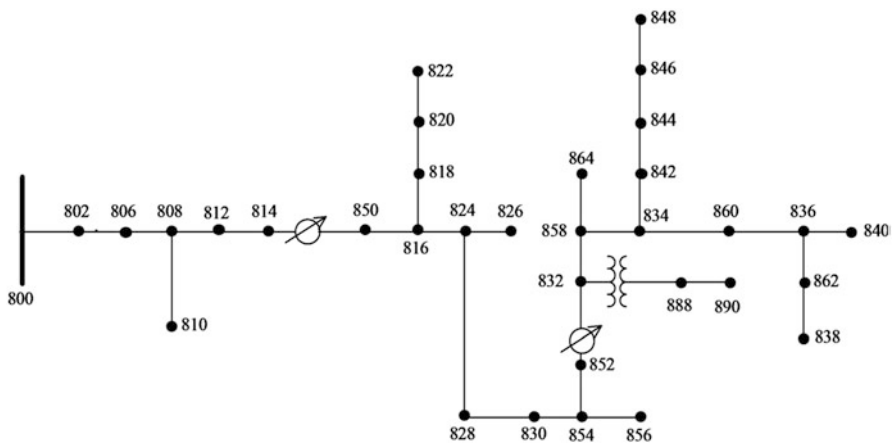


Fig. 6 A sample IEEE 34-bus distribution grid for software simulation of HIFs [30]

for one or two events, such as the disconnection and reconnection of a linear load and a capacitor bank, or the system loads have been considered fixed and a fixed amount of harmonic load has been modeled in the system. Hence, the efficiency of the methods proposed in these references cannot be judged without further examination.

3.1.4 Modeling of Distribution Grid Loads

Distribution grid feeders feed various types of domestic and industrial loads. The distribution grid loads play a key role in the performance of the fault detection algorithm. More specifically, some of the algorithms designed and evaluated for HIF detection in grids with linear loads may not perform well in those with nonlinear loads. The more power electronic instruments, rectifiers, and converters are used in industrial workshops and household loads, the more the harmonics will be in the grid. Since a major feature for HIF detection are the harmonic components of the current, nonlinear loads significantly affect the performance indexes of these algorithms. Furthermore, the presence of dynamic loads influences the data utilized by fault detection algorithms due to the variation in the currents associated with these loads after an event in the grid. Numerous references have evaluated their proposed techniques only in grids with linear loads, and some references have considered a number of rectifiers for generating load harmonics in the distribution grid.

Consider Possible Events in a Distribution Network

The following events are considered in the simulations:

- Disconnection and reconnection of linear loads.
- Disconnection and reconnection of a capacitor bank.
- Low-impedance faults.
- Consideration of nonlinear loads.
- Line electrification.
- Transformer electrification.

Some references have simulated only one or two events, while some others, such as [3, 9, 11, 26, 27, 30] etc. have considered more events. The more diverse the events are, the more complicated training will become, and the higher the error probability of the algorithm will be. On the other hand, the performance of the proposed method will be better evaluated.

3.2 Feature Extraction

Feature extraction refers to the selection and calculation of numerical quantities from measured or simulated data for the purpose of fault detection. Given that the HIF current amplitude is on the order of the distribution line load current amplitude, one cannot use the current amplitude to detect faults and must extract certain features from HIFs to be able to distinguish them from other events, such as disconnection and reconnection of the capacitor bank and nonlinear loads. These features constitute data that are input to the fault detection algorithm.

Appropriate feature selection plays a significant role in correctly distinguishing faults from non-fault events. Those features must be selected the fault-state characteristics of which are different from those of other power grid events, such as capacitor bank switching, disconnection and reconnection of various linear and nonlinear loads, and disconnection and reconnection of transformers. Since one cannot utilize only one feature for a distribution grid consisting of various loads, previous works have chosen more than one feature or even many features (e.g., 24 features in [15]). This section examines the features selected for HIF detection according to the domains from which they have been selected.

Selecting unique features for fault detection is extremely difficult. This is because it is virtually impossible to select quantities produced only due to HIFs at locations where measurement instruments are installed.

Hence, one can improve the chances of correct detection via the selection of a number of features that might be affected also by other events, the relationship between sets of these features, or even their statistical characteristics, such as standard deviation and randomness. For example, [4, 15] have employed the energy and the statistical characteristics of the odd and even low-order harmonics and inter-harmonics of the current and the high-frequency current components to ensure the presence of an HIF.

In the employed algorithm, one can directly use input signal data in the time domain for fault detection, a method called the time-domain method. Alternatively, the time-domain data may be taken via a transform to the frequency or time-frequency domain where the features may be calculated.

3.2.1 Time-Domain Methods

Time-domain methods here refer to those algorithms that employ time-domain signal features to detect faults. Some of the time domain HIF detection techniques are introduced in this section:

- Using circuit models and differential equations in this method, the lines and the HIF are modeled based on the electrical characteristics of the system, and the electrical relationships between the measured voltage and current values and the modeled system are obtained as differential equations. These equations can

then be solved using numerical methods and recursive algorithms to estimate the resistance and location of an existing arc fault along the lines [22].

- Using a correlation function a technique for HIF detection using the correlation function of measured voltage and current signals in the time domain has been presented in [6]. In the proposed method, the auto-correlation and the partial auto-correlation functions of the voltage and current signals and the first and second derivatives of the voltage and current are calculated first. Then, the sets of each of these correlation functions are computed for a given number of samples (10 or 20 samples), and the calculation indexes are utilized for HIF detection.

Using mathematical morphology algorithms Mathematical morphology (MM) was introduced in the mid-1970s as an image processing tool. Morphology is based on extracting the spatial structures of images and signals. It affects the signal itself and does not make use of a transform to transfer the signal from the time domain to another domain, such as the frequency domain, for feature extraction. For this reason and for the use of simple mathematical operators to extract the signal features, it is fast to implement. Morphology-based filters have been employed in power engineering for eliminating the DC component for phasor estimation, detecting instrument transformer saturation, distinguishing between an inrush current and a fault to protect power transformers, locating faults in transmission lines, and denoising power signals. Moreover, mathematical morphology has been utilized in [19, 31] to detect HIFs.

3.2.2 Frequency Domain Methods

Frequency domain methods are the most common HIF detection techniques found in authoritative sources [5]. As mentioned in Sect. 1, an HIF is usually associated with an electric arc. The energy of the harmonic components of an arc current can be used as a criterion for distinguishing faults from load currents. These methods commonly utilize Fourier-based transforms to compute the frequency spectrum of the measured signals or the amplitudes of the harmonics included therein. Subsequently, the fault conditions are discerned from non-fault ones using the components extracted according to the relationship between the amplitudes (energy) of the frequency components and that of the main signal frequency and by defining the appropriate threshold or via other decision-making techniques.

Several references have considered the energies of the second and third harmonics as major HIF indicators. Furthermore, the energies of even- and odd-order harmonics and inter-harmonic components have also been used as indicators that can distinguish fault and non-fault conditions. Given the random characteristics of HIF currents and the differences in the amplitude and form of the current in different cycles, one can also use the statistical characteristics, such as standard deviation, of the harmonics as fault indicators.

The HIF is resistive in nature; hence, the phase difference between some of the harmonics can be utilized as a feature that detects HIF. The Fourier transform has been used in the majority of frequency-domain methods to extract the harmonics.

Some HIF indicators based on harmonic components are as follows:

- The ratio of the second and third harmonics of the three-phase current to the fundamental component [7].
- The ratio of the second harmonic of the three-phase current to the fundamental component.
- The change in the variance of the low-order even harmonics of Current $3I_0$ during 600 consecutive cycles.
- The energy of the mean variance of Harmonics 2, 3, 4, 4, 7, and 9 of Current $3I_0$ [2].
- The energies of the 180 Hz component and the 210 Hz inter-harmonic component (in the 60 Hz system).
- The magnitude and angle of the third harmonic of the voltage and current [32].
- The energy and statistical characteristics of the low-order odd and even harmonics and inter-harmonics of the current and the high-frequency components of the current [4, 15].
- The sum of the energies of even harmonics of order 6–32, the ratio of these energies to those of odd harmonics of order 7–33, and the increase in the variances of even harmonics of order 6–32 [14].
- Magnitudes of zero sequence and negative sequence harmonics of order 2, 3, and 5 and the ratio of zero sequence harmonics to negative sequence harmonics for current and voltage signals [22].
- The energy and statistical characteristics of the low-order odd and even harmonics and inter-harmonics of the current [8].
- The energy of the third harmonic of three-phase currents, the phase difference of the third harmonic of the current and voltage, and the ratio of the energy of the third harmonic to that of the fifth harmonic of the current.
- The magnitude of the first and third current harmonics, the magnitude of the first voltage harmonic, and the phase difference between the magnitudes of the first and third current harmonics and the first and third voltage harmonics.
- The increase in the sum of the energies of harmonic and inter-harmonic components of up to the 15th order (the frequency range of 25–375 Hz in the 50 Hz system) and the durability and randomness of the harmonic energies [9].
- The magnitude of the third and fifth harmonics of the current [33].

Given the variation in the harmonic current components in distribution networks, some references have suggested using the Kalman filter to estimate the frequency components. The application of the Kalman filter to extracting the harmonics of the HIF current signal has been investigated in [10]. The proposed method has used two of these filters, one to estimate the fundamental component and the other to estimate the current signal harmonics under steady-state working conditions. Also, a Kalman filter has been used to estimate the fundamental and the harmonics under disturbance

conditions and changes in the current signals. Subsequently, the amplitudes of the low-order harmonics corresponding to the HIFs have been studied.

3.2.3 Time-Frequency Domain Methods

Time-frequency domain methods refer to those that process signals and extract features using transforms that transfer signal data from the time domain to the time-frequency domain. One of the first time-frequency transforms was the short-time Fourier transform (STFT). STFT or the windowed Fourier transform provides information regarding the frequency components of the considered signal in limited ranges in the time and frequency domains. The wavelet transform was introduced in 1980 as a time-frequency transform and gained popularity in engineering with the introduction of the discrete wavelet transform and its implementation using filter banks. This transform was first used in power engineering in the mid-1990s. It started to be increasingly used in denoising, fault detection, fault location, etc., as its features, such as fast implementation, provision of signals with various time and frequency accuracies, excellent detection of the disturbance and edges in a signal, provision of a compressed and signal with minimum data loss. Using the wavelet transform has been reported in most areas of signal processing and signal feature extraction in various sources. Also, numerous sources have reported using the wavelet transform to detect HIFs. Most of these references have utilized this transform to decompose electric signals at various levels, after which they have used features such as the energy or variance of various decomposition levels to distinguish faults from other conditions in distribution networks [34].

The following are some instances of the features extracted via the wavelet transform for HIF detection, as reported in the literature:

- Using the number and jump intervals of the exact coefficients of the current signal discrete wavelet transform at the first and second decomposition levels during two cycles.
- Using the amplitude and phase difference between the continuous wavelet transforms of the I_0 and V_0 signals at the jump points of the continuous wavelet transform of the I_0 signal for the detection of an HIF and its direction [16, 25].
- Using three consecutive continuous wavelet transforms of I_0 and V_0 signals [17].
- Decomposing four current signal cycles up to two levels using the discrete wavelet transform and using the average of the exact coefficients of the first-level decomposition of each cycle and the RMS of the exact coefficients of the second-level decomposition of each cycle to discern between HIFs and other events.
- Decomposing the current signal up to three levels using the discrete wavelet transform, dividing the exact coefficients into four parts at each level, and using the RMS of the first two parts at decomposition level [27].
- Using the sum of the third-level exact coefficients obtained from decomposing the residual current using the discrete wavelet transform during two cycles and

the sum of the absolute values of the third-level exact coefficients obtained from decomposing the residual voltage during one cycle [18].

- Using the absolute values of the exact coefficients from third- and fifth-level decomposition of the residual current via the discrete wavelet transform during one cycle [35].
- Using the standard deviation of the first to seventh-level exact coefficients and seventh-level approximate coefficients resulting from decomposing three-phase currents [28].
- Using the sum of the absolute values of the exact coefficients of third-level decomposition of the three-phase current and voltage during one cycle [36].
- Using the standard deviation of the fourth- to seventh-level exact coefficients and the approximate coefficients of the last decomposition level of current, voltage, and power signals [37].

Some works have selected a combination of frequency and time-frequency domain features. For instance, the method presented in [11] makes use of the discrete wavelet transform and the Fourier transform for current signal decomposition. In this method, first, the current signals are decomposed down Level 2 via the discrete wavelet transform. Then, the exact coefficients of each level are grouped into 5 parts, after which the ratio of the energy of the third part to that of the second part and the ratio of the energy of the third part to that of the fourth part for each level are selected for distinguishing HIFs from other events. In addition, the ratio of the amplitude of the third current harmonic to that of the fundamental and the DC component of the current signal (sum of all signals) during one cycle have been applied to HIF detection.

3.3 Decision-Making Techniques for HIF Detection

The features used in various references to distinguish between the HIF and non-fault conditions in distribution networks were discussed in Sect. 3.2. A fault detection criterion must be specified after feature selection. Selecting a feature capable of setting a clear boundary for fault detection using signals measured at the location of the protective equipment in the distribution grid is a daunting task. For this purpose, several features are usually selected and analyzed or compared to the set values to detect the fault. Establishing boundaries for decision-making requires thorough investigations given that HIF features, such as the second, third, or fifth harmonics, are present in the grid load at different levels of energy. This section introduces some of the decision-making techniques used for HIF detection in distribution networks.

3.3.1 Threshold-Based Decision-Making

This type of decision-making refers to specifying a clear boundary between the values of the selected features under fault and non-fault conditions. Examples include conventional protection in power systems, such as overcurrent and distance protections. As mentioned previously, the frequency spectrum of the HIF is different from those of the load signal, capacitor bank switching, etc. Accordingly, boundary values can be selected by analyzing and comparing the frequency components of these events.

For instance, [1] has used the relative energies of the frequency components from 2 to 10 kHz as a decision-making criterion for fault detection although not all HIFs could be detected using this method. Specifying thresholds for the chosen features was the decision-making criterion for fault detection in [3, 9, 10, 38–40]. The simplest solution for cases with more than one feature is using the AND gate. Specifically, a fault is detected when all the values have exceeded their thresholds. However, in most papers, in case the threshold conditions are not met, the HIF counter is activated, and the fault detection signal is activated if fault detection is repeated within a specified time (e.g., 3 consecutive cycles or after a specific delay). This is for improving the safety of the algorithm and to prevent performance errors in case of transient faults and computational errors.

To be able to specify a threshold, one must first select features for HIFs and other events and, then, select parameters providing the highest sensitivity and safety as the final configuration. The thresholds can also be determined using smart methods and optimization algorithms, such as the genetic algorithm.

In this case, different features can be assigned different weights, and a fault can be recorded if the sum of the products of the weights and the features exceeding their thresholds violates a specified threshold.

The criterion for relay performance and issuing HIF signals in references that have fabricated relays and tested them on actual feeders is complicated and based on several algorithms and other criteria. For example, the relay fabricated by General Electric and the University of Texas [4, 15] employs decision-making and expert systems along with a large number of different features and algorithms.

3.3.2 Decision-Making Using Smart Pattern Recognition Techniques

The use of pattern recognition for HIF detection involves employing artificial intelligence techniques to analyze the features extracted from the measured signals and to distinguish between the fault-related features from those associated with normal operational events in power systems. In pattern recognition methods, a dataset consisting of the patterns and the classifiers corresponding to each pattern must be prepared after the technique is selected. A pattern refers to the features selected from a process. In this case, they include features associated with various events in a distribution grid, such as HIF, disconnection and reconnection of a capacitor bank, and disconnection and reconnection of various linear and nonlinear

loads. In its simplest form, the class of each pattern consists of the presence and absence of an HIF. Accordingly, a set of different data from various events must be prepared so that pattern recognition methods can be used. A part of this data is used for training and another part for testing the selected pattern recognition technique. The larger the range of the provided data and the more the event conditions it includes, the better the pattern recognition performance.

An advantage of pattern recognition methods over threshold-based ones is their lack of need for an expert to configure the thresholds. In such methods, the pattern recognition parameters are determined automatically, and during training, after technique selection and data preparation, such that the false detection error is limited to a range.

One of the most rudimentary classifiers is the Bayes classifier, which classifies the input patterns based on the Bayes conditional probability, and is sometimes used to measure the performance of other classifiers. Some pattern recognition methods used for HIF detection in distribution networks are those based on support vector machine (SVM), artificial neural networks (ANNs), fuzzy logic, decision tree, and hybrid methods, such as neural-fuzzy networks.

Methods Based on Neural Networks

ANNs are one of the oldest and most popular smart classifiers and have been used in a large number of fields owing to their numerous advantages, such as adaptive learning, self-organization, fault tolerance, generalizability, and stability. These networks include different types, such as multi-layer perceptron (MLP), probabilistic neural networks (PNNs), and radial basis function (RBF) networks, each of which has specific capabilities. In addition to pattern recognition, they have found application in various areas, such as modeling. ANNs have also been used to detect HIFs, as discussed in the following.

A feed forward network with 18 inputs from Fourier transform components, a hidden layer consisting of 15 neurons, and one output for HIF detection has been used in [22]. The network was trained using the back propagation algorithm.

Three MLP networks consisting of four inputs, two middle layers made of ten neurons in the first layer and five neurons in the second, and two output neurons (presence and absence of fault) have been used in [31] for fault detection. The linear sigmoid function was selected as the activation function, and the numbers of layers and neurons were determined by trial and error. The input of each network was obtained from the multi-resolution morphology gradient of three current half-cycles (each for one network), and the networks were trained through the Levenberg-Marquardt algorithm. The final decision on the presence of an HIF in the network was made using the combined output of the three networks. After various methods were used to combine the classification networks, the best result was obtained via the mean output.

A neural network (NN) composed of 24 inputs obtained from 8 features resulting from the discrete wavelet transform of three-phase current signals, 2 middle layers

consisting of 14 neurons in the first layer and 6 neurons in the second, and 3 output neurons (related to the presence and absence of a fault) has been employed in [28]. The selected outputs corresponded to HIF, low-impedance fault (LIF), and normal operation, and the Levenberg-Marquardt algorithm was used for training. Moreover, [12, 17, 22, 25, 30, 31, 35–37, 41–44] have also used NNs for HIF detection.

Support Vector Machine

SVM is a pattern recognition technique that is more recent than NNs and fuzzy logic. It is based on a linear classification of data and attempts to select pattern boundary lines that provide a larger safety margin.

For complex nonlinear patterns, one can first transfer the nonlinear input vector to a high-dimensional space via a kernel function and then calculate the inner product such that the patterns can be separated by lines in the new space. This considerably reduces the computational burden. For instance, MLP or RBF can act as the kernel function. Simpler training is an advantage of SVM compared to NNs. Moreover, it does not become trapped in local extremum, unlike NNs.

SVM has been used as the main classifier for HIF detection in [29]. The performance of the SVM classifier has been compared to those of Bayesian and MLP classifiers in terms of safety and dependability. The results indicated the significant advantage of the SVM. Moreover, [3, 45–47] have also used SVM for HIF detection.

Fuzzy Logic

Since it is difficult to specify a deterministic threshold for each feature as the boundary between faulty and non-faulty conditions, fuzzy variables can be used instead of deterministic ones.

A method for HIF detection based on the fuzzy inference system (FIS) has been proposed in [27]. In this method, 4 features are selected using the discrete wavelet transform; then, a set of input data, consisting of the features extracted in every simulation and output, is prepared for various events. Based on the 4 selected features, 4 membership functions are selected for each class, making up a total of 12 Gaussian membership functions for the fuzzy system inputs. Moreover, [33, 48, 49] have also used fuzzy logic for HIF detection.

Hybrid Fuzzy-Neural Method

Given that each NN technique has unique advantages, one can combine different techniques to benefit from all these advantages.

ANFIS systems have been utilized in [11] to classify nonlinear disturbances in a distribution grid, including HIF, current transformer (CT) saturation, nonlinear

loads, and inrush current caused by transformer electrification. Four features obtained using the discrete wavelet transform and two obtained from the Fourier transforms of current signals have been selected as the inputs of the proposed system. In addition, [22, 41] have also used Hybrid fuzzy-neural for HIF detection.

Decision Tree

The decision tree is an expert system for pattern recognition or decision-making based on several different features. To use this method, one must select features and specify thresholds for each feature. Then, a feature at the root of the tree is selected, and the threshold condition is examined for that feature to guide the input toward various branches. Subsequently, a feature in each branch is inspected to determine the branch (leaf) the input belongs to. There is software for training a decision tree. This software determines the thresholds for the conditions of each branch based on the input data, which consist of the selected features and the class of each data group. The decision tree has been employed in [26, 50] to detect HIFs in distribution networks.

4 Summary of HIF Detection Methods

This section introduced the HIF detection techniques presented in authoritative references and categorized them in different respects. The methods proposed in the literature performed well within the limits of the corresponding experiment. However, given the lack of comprehensiveness of these methods, they might perform differently in most cases when exposed to various linear and nonlinear single-phase and three-phase loads in the grid.

A wide range of features, including features in the time, frequency, and time-frequency domains, have been utilized for HIF detection in different sources. An advantage of time-domain methods is that they can directly use the signals in the domain they were measured. Hence, they are less likely to lose data in addition to executing the algorithm faster. However, extracting HIF-related features in the time domain without the use of intermediate transforms is a formidable task due to the small amplitude of the fault current relative to that of the normal load current. In addition, it is difficult to separate noise and disturbance from the signal.

The Fourier transform and fault feature extraction in the frequency domain are techniques also used in HIF detection relays. A property of Fourier-transform-based methods is the accurate estimation of the frequency components, especially when the nominal frequency of the system varies. This is especially effective in estimating the amplitudes of higher frequency components. Moreover, the data window significantly affects the phase magnitude estimation in methods that use the phases of the harmonics. A property of frequency domain features is their independence from time. In other words, the Fourier transform results provide only

the magnitude and phase of the frequency components along the data window and no information on the time and quality of these components with time.

The special waveform of the arc fault current signal Fig. 1 is that the arc fault current stops flowing around the point passing through zero voltage at specific periods. This produces frequency components, such as the third and fifth components, and can be used to detect faults in frequency domain methods. The lack of current flow in the region passing through zero voltage can be exploited as a feature of the arc current. This is impossible in the Fourier transform.

Time-frequency transforms can provide time-frequency data in different intervals. This feature and the localization property of time-frequency transforms can be used to detect HIFs, the features and quality of which differ in different intervals (during one cycle). The relative energies of various frequency ranges, obtained from decomposing the measured signals using the wavelet transform. In addition to energy, other features, such as the statistical characteristics of the decomposition coefficients, can be employed to distinguish between faults and other events.

An important point about many of the proposed methods is that the amplitude of the HIF current is significant compared to that of the load current at the measurement location. Hence, the features of HIF are prominent in the phase current signal. On the other hand, the principal difficulty in detecting this fault is its small amplitude. Specifically, the fault features are covered by the load currents in high-load distribution networks, and various features must be used to distinguish them. This is especially true in the case of feature extraction in the time domain. These features will be ineffective in reliable HIF detection if the fault current amplitude is smaller than that the load current amplitude. Another important point about feature extraction for HIF detection is that the values computed for the parameters selected as features by the measured signals in the main feeder of the distribution grid are considerably affected by the operational conditions of the distribution grid. For instance, the energies of the harmonics, which have been utilized as main fault detection features, are dependent on nonlinear loads in the grid. In addition, the connection or disconnection of the capacitor bank in the grid strongly affects the values of the features.

After feature extraction, decisions must be made on the existence of an HIF based on the calculated features. Selecting a criterion for decision-making about the presence of an HIF based on the chosen features is very important. The sensitivity and safety of fault detection algorithms depend on the selected decision-making criterion. Configuring various thresholds for different features is a common technique in protective systems. The decision-making criterion is linear in these techniques; thus, their performance in features meeting the threshold conditions is reliable. Selecting the threshold criterion and configuring different thresholds for different features cannot single-handedly constitute a sufficient decision-making criterion since some of the selected features may not satisfy the threshold condition depending on the fault and grid conditions. Accordingly, despite the fact that selecting more features may increase the certainty about the fault, some faults may still go unnoticed. Therefore, one must use decision-making techniques, such as those in [4, 15], in order to be able to apply the threshold criterion.

The main issue related to methods that use thresholds for fault detection is specifying these thresholds in the first place. This task requires an extensive study on the distribution grid and the features of the connected load and the HIFs in the feeders. This study must be conducted over a long interval since the loads in a system might differ throughout the year. Finally, an increase in the security of threshold-based methods, aimed at preventing false detection, reduces the sensitivity and dependability of these methods, especially for low-amplitude faults.

Smart classifiers may constitute a suitable solution to address the complexity and nonlinearity of the feature space. If appropriate features are extracted and the classifiers are properly trained, one can expect the good performance of these methods in different faults based on their generalizability. However, more complicated cases may require yet more complex decision-making algorithms that use various classifiers.

Table 2 lists some of the major techniques used for HIF detection in distribution networks. These methods have been selected based on highly cited papers published in authoritative journals and those accepted by these journals. Appropriate indexes have been included in this table for results analysis and comparison. One of the most important indexes for classifier evaluation is accuracy, which is calculated by dividing the correctly classified cases by the total number of test cases. Nevertheless, it is not sufficient for evaluating and comparing classifiers, and other criteria must be taken into account. Two important indexes for evaluating protection schemes are dependability and security. The dependability of a protection scheme in HIF detection is obtained by dividing the number of detected HIFs by the total number of HIFs in the utilized datasets. The security index is determined by dividing the non-fault events not identified as faults by the total number of non-fault events in the used datasets. Given that a considerable number of journal and conference papers have been published on HIF protection, conference papers and journal papers without the parameters necessary to determine the above criteria were excluded to avoid excessively enlarging Table 2.

5 Conclusions

This chapter book presented a comprehensive study of HIF detection schemes. Rapid and highly reliable HIF detection in distribution networks can prevent human disasters and fire in addition to increasing the reliability indexes of the grid and customer satisfaction and entailing technical and economic benefits. The most important problem in HIF protection in distribution networks is the grid loads and their impact on parameters measured against HIFs. Therefore, the following is suggested as extensions of the present study on HIF protection in distribution networks:

Investigating the degree of certainty of HIFs and other grid events will improve the security of the proposed protection scheme and reduce incorrect detections:

Table 2 Compare the results of some published methods

References.	Analysis domain	Measurement	Classifier	A (%)	D (%)	S (%)	Data
[7]	Time	Current and voltage	Threshold				Simulation
[13]			Current	Threshold and counter			
[31]		Neural network	97.3	98.3	96.3	Experimental	
[49]		Fuzzy classifier	99.4	99.78	99.07	Simulation	
[50]		Decision tree	99.34	98.77	100	Simulation	
[19]		Voltage	Threshold and counter		100	100	Simulation
[1]		Frequency	Current	Threshold			
[10]							Experimental
[14]	Threshold and counter						Experimental
[12]	Neural network		99.8	99	100	Simulation	
[26]	Decision tree					Simulation	
[48]	Fuzzy classifier			81.0		Experimental	
[22]	Current and voltage		Neural network				Simulation
[41]							Simulation
[33]			Fuzzy classifier	98.8			Simulation
[3]			Time-frequency	Current	SVM	97.2	98.8
[45]		93.6			100	81.5	Experimental
[36]	Neural network				93.8	81.5	Simulation
[40]	Current and voltage	Threshold					Simulation
[44]		Neural network		100	100	100	Simulation
[47]		SVM		100	100	–	Simulation
[4]		Hybrid		Current and voltage	Threshold		
[11]	Current		Fuzzy classifier	99.5	99	99.8	Simulation

(continued)

Table 2 (continued)

References.	Analysis domain	Measurement	Classifier	A (%)	D (%)	S (%)	Data
[28]	Wavelet	Current	Neural network	99.7	99.5		Simulation
[30]				96.1	98.5	93.5	Simulation
[35]				98.0			Simulation
[42]				98.27	97.14	100	Simulation
[43]				97.14			Simulation
[29]				SVM		99.6	99.8
[46]			94.86			Simulation	
[17]		Current and voltage	Neural network				Simulation
[25]							Simulation
[18]		Multiple measurement	Threshold				Experimental
[20]	Voltage	Threshold and counter				Simulation	

- Using statistical and state estimation methods for uncertainty in the grid loads.
- Studying HIFs in the presence of distributed generation (DG).
- Introducing a technique for HIF location.
- More accurate and realistic models of the grid elements are recommended due to the significance of modeling in the tested grid.

References

1. Aucoin B, Russell B (1982) Distribution high impedance fault detection utilizing high frequency current components. *IEEE Trans Power Appar Syst* 6:1596–1606
2. Tengdin J, Westfall R (1994) High impedance fault detection technology report of PSRC working group D15
3. Mortazavi S, Moravej Z, Shahrtash S (2018) A hybrid method for arcing faults detection in large distribution networks. *Int J Electr Power Energy Syst* 94:141–150
4. Kim CJ, Russell BD, Watson K (1990) A parameter-based process for selecting high impedance fault detection techniques using decision making under incomplete knowledge. *IEEE Trans Power Delivery* 5(3):1314–1320
5. Ghaderi A, Ginn III, Mohammadpour H (2017) A high impedance fault detection: a review. *Electr Power Syst Res* 143:376–388
6. Patterson R, Tyska W, Russell B (1994) A microprocessor-based digital feeder monitor with high-impedance fault detection. No. CONF-941089-Vol. 1. USDOE, Washington, DC (United States); Korea Electric Power Corp. (KEPCO), Seoul (Korea, Republic of)
7. Faridnia N, Samet H, Doostani Dezfuli B (2012) A new approach to high impedance fault detection based on correlation functions. In: *IFIP international conference on artificial intelligence applications and innovations*. Springer, Berlin, pp 453–462

8. Russell B, Mehta K, Chinchali R (1988) Fault detection technique using low frequency current components-performance evaluation using recorded field data. *IEEE Trans Power Delivery* 3(4):1493–1500
9. Kim C, Russell B (1993) High-impedance fault detection system using an adaptive element model. *IEE Proceedings C-Generation, Transmission and Distribution* 140(2):153–159
10. Sarlak M, Shahrtash S, Khaburi D (2010) Design and implementation of a systematically tunable high impedance fault relay. *ISA Trans* 49(3):358–368
11. Yang M, Gu J, Guan J (2005) Detection of downed conductor in distribution system. In: *IEEE power engineering society general meeting*
12. Etemadi A, Sanaye-Pasand M (2008) High-impedance fault detection using multi-resolution signal decomposition and adaptive neural fuzzy inference system. *IET Gener Transm Distrib* 2(1):110–118
13. Keyhani R, Deriche M, Palmer E (2001) A high impedance fault detector using a neural network and subband decomposition. In: *Proceedings of the sixth international symposium on signal processing and its applications (Cat. No. 01EX467)*, vol 2
14. Sultan A, Swift G, Fedirchuk D (1992) Detection of high impedance arcing faults using a multi-layer perceptron. *IEEE Trans Power Delivery* 7(4):1871–1877
15. Lee R, Osborn R (1985) A microcomputer based data acquisition system for high impedance fault analysis. *IEEE Trans Power Appar Syst* 10:2748–2753
16. Michalik M, Rebizant W, Lukowicz M, Lee S, Kang S (2005) Wavelet transform approach to high impedance fault detection in MV networks. In: *IEEE Russia Power Tech*
17. Michalik M, Rebizant W, Lukowicz M, Lee S, Kang S (2006) High-impedance fault detection in distribution networks with use of wavelet-based algorithm. *IEEE Trans Power Delivery* 21(4):1793–1802
18. Elkalashy N, Lehtonen M, Darwish H, Taalab A, Izzularab M (2007) DWT-based detection and transient power direction-based location of high-impedance faults due to leaning trees in unearthened MV networks. *IEEE Trans Power Delivery* 23(1):94–101
19. Gautam S, Brahma S (2012) Detection of high impedance fault in power distribution systems using mathematical morphology. *IEEE Trans Power Syst* 28(2):1226–1234
20. Bakar A, Ali M, Tan C, Mokhlis H, Arof H, Illias H (2014) High impedance fault location in 11 kV underground distribution systems using wavelet transforms. *Int J Electr Power Energy Syst* 23:723–730
21. Kim C (2008) Electromagnetic radiation behavior of low-voltage arcing fault. *IEEE Trans Power Delivery* 24(1):416–423
22. Sharaf A, Snider L, Debnath, K (1993) A neural network based relaying scheme for distribution system high impedance fault detection. In: *Proceedings 1993 the first New Zealand international two-stream conference on artificial neural networks and expert systems*, pp 1226–1234
23. Sharaf A, Wang G (2003) High impedance fault detection using feature-pattern based relaying. In: *2003 IEEE PES transmission and distribution conference and exposition (IEEE Cat. No. 03CH37495)*, vol 1, pp 222–226
24. Radojevic Z, Terzija V, Djuric N (2000) Numerical algorithm for overhead lines arcing faults detection and distance and directional protection. *IEEE Trans Power Delivery* 15(1):31–37
25. Michalik M, Lukowicz M, Rebizant W, Lee S, Kang S (2007) Verification of the wavelet-based HIF detecting algorithm performance in solidly grounded MV networks. *IEEE Trans Power Delivery* 22(4):2057–2064
26. Shahrtash S, Sarlak M (2006) High impedance fault detection using harmonics energy decision tree algorithm. In: *International conference on power system technology, IEEE*, pp 1–5
27. Haghifam M, Sedighi A, Malik O (2006) Development of a fuzzy inference system based on genetic algorithm for high-impedance fault detection. *IEE Proc-Gener Transm Distrib* 153(3):359–367
28. Baqui I, Zamora I, Mazón J, Buigues G (2011) High impedance fault detection methodology using wavelet transform and artificial neural networks. *Electr Power Syst Res* 81(7):1325–1333

29. Sarlak M, Shahrtash S (2011) SVM-based method for high-impedance faults detection in distribution networks. In: *COMPTEL-The international journal for computation and mathematics in electrical and electronic engineering*
30. Moravej Z, Mortazavi S, Shahrtash S (2015) DT-CWT based event feature extraction for high impedance faults detection in distribution system. *Int Trans Electr Energy Syst* 25(12):3288–3303
31. Sarlak M, Shahrtash S (2011) High impedance fault detection using combination of multi-layer perceptron neural networks based on multi-resolution morphological gradient features of current waveform. *IET Gener Transm Distrib* 5(5):588–595
32. Bretas A, Moreto M, Salim R, Pires L (2006) A novel high impedance fault location for distribution systems considering distributed generation. In: *IEEE/PES transmission and distribution conference and exposition: Latin America*, pp 1–6
33. Sulaiman M, Tawfan A, Ibrahim Z (2013) Detecting high impedance fault in power distribution feeder with fuzzy subtractive clustering model. *Aust J Basic Appl Sci* 7(8):81–91
34. Torres-Garcia V, Guillen D, Olveres J, Escalante-Ramirez B, Rodriguez-Rodriguez J (2020) Modelling of high impedance faults in distribution systems and validation based on multiresolution techniques. *Comput Electr Eng* 83:106576
35. Vijayachandran G, Mthew B (2013) Arcing fault detection in feeder networks using discrete wavelet transform and artificial neural network. *Int J Emerg Sci Eng* 1(10):93–102
36. Samantaray S, Panigrahi B, Dash P (2008) High impedance fault detection in power distribution networks using time–frequency transform and probabilistic neural network. *IET Gener Transm Distrib* 2(2):261–270
37. Kar S, Samantaray S (2014) Time-frequency transform-based differential scheme for microgrid protection. *IET Gener Transm Distrib* 8(2):310–320
38. Silva S, Costa P, Gouvea M, Lacerda A, Alves F, Leite D (2018) High impedance fault detection in power distribution systems using wavelet transform and evolving neural network. *Electr Power Syst Res* 154:474–483
39. Ramos M, Bretas A, Bernardon D, Pfitscher L (2017) Distribution networks HIF location: a frequency domain system model and WLS parameter estimation approach. *Electric power systems research, distribution networks HIF location: a frequency domain system model and WLS parameter estimation approach*. *Electr Power Syst Res* 146:170–176
40. Zhang S, Xiao X, He Z (2020) Detection of high-impedance fault in distribution network based on time–frequency entropy of wavelet transform. *IEEJ Trans Electr Electron Eng* 15(6):844–853
41. Snider L, Yuen Y (1998) The artificial neural-networks-based relay algorithm for the detection of stochastic high impedance faults. *Neurocomputing* 23(1–3):243–254
42. Mohammadnian Y, Amraee T, Soroudi (2019) A fault detection in distribution networks in presence of distributed generations using a data mining–driven wavelet transform. *IET Smart Grid* 2(2):163–171
43. Silva S, Costa P, Santana M, Leite D (2020) Evolving neuro-fuzzy network for real-time high impedance fault detection and classification. *Neural Comput & Applic* 32(12):7597–7610
44. Gadanayak D, Mallick R (2019) Interharmonics based high impedance fault detection in distribution systems using maximum overlap wavelet packet transform and a modified empirical mode decomposition. *Int J Electr Power Energy Syst* 112:282–293
45. Ghaderi A, Mohammadpour H, Ginn H, Shin Y (2014) High-impedance fault detection in the distribution network using the time-frequency-based algorithm. *IEEE Trans Power Delivery* 30(3):1206–1268
46. Sahoo S, Baran M (2014) A method to detect high impedance faults in distribution feeders. In: *2014 IEEE PES T&D conference and exposition*, pp 1–6
47. Sarwar M, Mehmood F, Abid M, Khan A, Gul S, Khan AS (2019) A High impedance fault detection and isolation in power distribution networks using support vector machines *J King Saud University-Engineering Sci* 32(2020): 524–535
48. Jota F, Jota P (1998) High-impedance fault identification using a fuzzy reasoning system. *IEE Proc-Gener Transm Distrib* 145(6):656–661

49. Sekar K, Mohanty N (2020) A fuzzy rule base approach for high impedance fault detection in distribution system using morphology gradient filter. *J King Saud University-Engineering Sci* 32(3):177–185
50. Sekar K, Mohanty N (2018) Data mining-based high impedance fault detection using mathematical morphology. *Comput Electr Eng* 69:129–141

Designing of Efficient Lighting System for Smart Homes



Suprava Chakraborty and Abhishek Nemani

1 Background

In the future, everything in the built environment may be “linked” and “smart.” Smart lighting has become popular in commercial and industrial settings during the last decade, with a focus on energy conservation. Smart lighting in the house, in a larger sense, is part of the “smart home” concept, which attempts to meet and encourage user comfort, convenience, and security while also satisfying the requests of residents [1]. Smart lighting systems (SLS) are defined by Rossi [2] as “lighting systems with the capacity to govern, communicate, and interconnect data, capable of providing new methods of interacting with the luminous performances in new luminaires, equipped to give extra service.” “Solid-state sources – in particular, LED-based sources – offer what was previously inconceivable with conventional sources: controllability of their spectral, spatial, temporal, and polarization properties, as well as their color temperature” [3]. When compared to other protocols like Wi-Fi, the ZigBee protocol, which is currently extensively used, utilizes less power [4, 5]. As a result, it is observed that a Wi-Fi communication-based network consumes more energy compared to one based on the ZigBee protocol [6–8]. According to research investigations on smart lighting and controls, smart lighting systems are mostly employed in non-residential settings, with a focus on energy savings. Based on the behavior of the user, activity patterns, and different types of control systems, such as daylight harvesting and occupancy management systems, studies in office settings indicated potential energy savings ranging from 17% to 94% compared to conventional (manual) control systems [9–15]. Manoj Mohan et al. [16] show that a less difficult variant of lighting control can be utilized in homes.

S. Chakraborty (✉) · A. Nemani
TIFAC-CORE, Vellore Institute of Technology Vellore, Katpadi, Tamil Nadu, India
e-mail: suprava.chakraborty@vit.ac.in

An innovatively progressed studio can be made utilizing a comparable arrangement for controlling the foundation and side lighting of an expert studio and furthermore physical encompassing can be done by utilizing a NFC empowered cell phone. Mario Collotta et al. [17] have proposed that energy executives approach for smart homes that joins a Bluetooth-based Low Energy WSHAN, for the correspondence among home machines, with a HEM conspire. Indeed, private energy the board, savvy machines, WSHANs, and their reconciliation to keen framework applications are turning out to be mainstream subjects in light of the fact that in recent years a movement to keen matrices is occurring. Whereby, a HEM execution can prompt socially and financially valuable climate by tending to shoppers' and utilities concerns. Enrique Rodriguez-Diaz et al. [18] and her team have conceivable outcomes that can be acquired from the reconciliation of the high level metering framework with the idea of Smart Home. An entire genuine AMI framework has been depicted, showing the data stream, the correspondence structure, and the various factors that can be observed in the framework. Karam M.Al-Obaidi et al. [19] have approached to a progression of area concentrates in a standard sized room. Three distinctive material frameworks are researched to recognize the IRS execution in both dull and sunshine conditions to decide the impact of normal light on the indoor climate. The results of the investigation indicate that the IRS had the option to less than the indoor air temperature contrasted and customary material framework by around 2.1 °C under sunlight condition. The distinction in the IRS (light dim) condition was 0.31 °C contrasted with that in the customary material framework at 0.8 °C. Besides, the degree of mean brilliant temperature analyzed with indoor temperature under sunlight condition was 2.61 °C for the IRS, though 4.05 °C for ordinary rooftop. A case study in Nanchang, China, is used to calculate the energy-saving potential and identify efficiency improvement options for metro lighting applications [20]. Arun et al. [21] installed a sophisticated LED lighting system that used several energy-saving approaches without compromising occupants' visual comfort. Gerhardsson et al. [22] looked into the various reasons for lighting consumption in Swedish homes and came to the conclusion that leaving lights on, in unoccupied rooms serves a variety of purposes, such as prevention of visual and aesthetic discomfort, provides safety, and makes the home more inviting. Smart lighting-based homes are projected to increase from little over 2.0% in 2020 to almost 8.0% in 2025 [23]. Market study indicates a rise in smart home appliances, but not user uptake or long-term usage. To take use of lighting devices smart capabilities and potential, houses must embrace, appreciate, and utilize them. Consumer health concerns, performance expectations, and compatibility, according to Juric and Lindenmeier [24], are the key factors driving customer acceptance or opposition to smart lighting systems.

1.1 Motivation

The inspiration for creating savvy home frameworks comes from numerous reasons, yet, most noticeable are accommodation, security, energy the executives, network

furthermore, extravagance. Shrewd Home frameworks are one of the more recent areas of investigation that have not yet been fully integrated into our general public. This is due to the fact that the examination necessitates a number of distinct tiers of examination and design in order to offer a functionally sound dwelling. The cost of constructing a brilliant house is also a significant impediment to the introduction of brilliant home frameworks into the market. The additional expense of the introduction stems from the fact that, despite the fact that the majority of homes were built recently, innovation has accelerated considerably. This suggests that most homes were built before this innovation was available, posing a barrier to the development and sale of smart home frameworks. In any case, technology is improving and becoming less expensive, which will help to make smart house frameworks a worthwhile investment when new homes are built. Comfort is the finest source of inspiration for amazing house structures. Wastage of power at home is high wattage tube lights and bulbs. When we use lower wattage light, its power and intensity are reduced. What's more, another issue is with less daylight we feel the necessity of light, wattage can't be changed so we need to utilize the same high wattage bulb or tube light. So we need a light whose power can be changed by the power of daylight. The power of the light can without much of a stretch be changed by controlling the voltage to the light.

2 Material and Methods

In this work, an alternate sort of light utilizing drove strips are assemble. As indicated by each drove is of 0.08 watt. This segment of drove can be utilized to construct the light. Thirty LEDs can be utilized to shape a solitary square of drove, each drove of 12 V. Such three squares can be utilized for various degrees of power.

2.1 Technical Specifications

2.1.1 Software

The Arduino Integrated Development Environment (IDE)

The Arduino Integrated Development Environment (IDE) is a cross-platform application created in the C and C++ programming languages. It's utilized to execute and convert projects to Arduino feasible sheets, as well as other seller improvement sheets with the support of outsider centres. The source code of IDE is released under the GNU General Public License, version 2. The Arduino IDE is executable through the C and C++ programming languages and employs unique code organisation techniques. The Arduino IDE includes a product library from the wiring project that includes a variety of standard data and yield systems. Client-written code requires

just two essential capabilities: the start of the sketch and the primary programme circle, which are built and integrated with a programme stub idea into an executable cyclic leader programme using the GNU toolchain, which is inbuilt with the IDE version. The Arduino IDE utilises the avrdude software to transform executable code into a hexadecimal book document, which is subsequently stacked into the firmware of the Arduino board by a loader application. Naturally, avrdude is used as the transferring tool for moving client code to official Arduino sheets. Arduino IDE is a subsidiary of the Processing IDE, anyway as of rendition 2.0, the Processing IDE will be supplanted with the Visual Studio Code-based Eclipse Theia IDE system.

Blynk

Blynk is an internet service. It indicates that the chosen device should be able to connect to the internet. Some of the sheets, such as the Arduino Uno, will require an Ethernet or Wi-Fi Shield to communicate, while others, such as the ESP32, Raspberri Pi with WiFi dongle, Particle Photon, or SparkFun Blynk Board, are already Internet-capable. However, even if it doesn't have a safeguard, users can connect it to a PC or work area by USB (comparatively more complicated for beginners, but it can be covered). The amazing benefit is that the list of Blynk-compatible equipment is extensive and will continue to grow.

Blynk App

Blynk App – permits to connect astounding interfaces for it's activities using various gadgets.

Blynk Server

Blynk Server is in charge of all communications between the phone and the equipment. It can use our Blynk Cloud or operate locally using a private Blynk worker. It's open-source, can manage a large number of devices without difficulty, and can even run on a Raspberry Pi.

Blynk Libraries

It is used for all the famous equipment categories, empower correspondence with the worker and interacts with all the approaching and outcoming orders.

Whenever a Button is pushed on the Blynk app, the message is sent to the Blynk Cloud, where it is miraculously delivered to the hardware. In the other direction, it works similarly and everything executed in the blink of an eye.

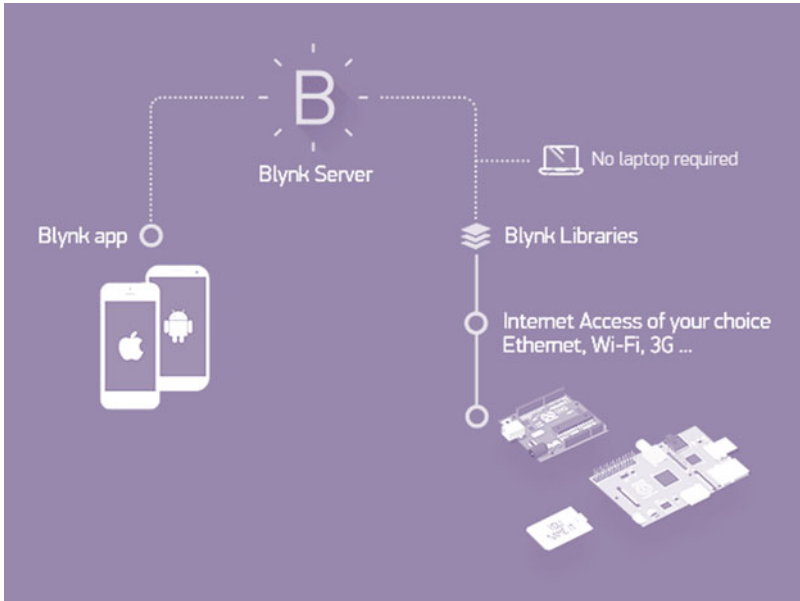


Fig. 1 About Blynk application

According to the Fig. 1, whenever a Button in the Blynk program is pressed, the message is sent to the Blynk Cloud, where it immediately finds its way to the equipment and same executed in the other direction in the blink of an eye.

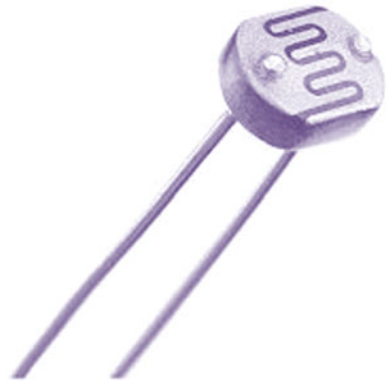
2.1.2 Hardware

PIR Sensor

The PIR sensor has inbuilt two holes, each one of them is composed of an unusual IR-sensitive substance. The PIR sensor gets triggered, when a warm body, such as a human or animal, passes by one section which causes a positive differential change between the two portions (Fig. 2).

LDR

A photograph resistor or LDR is a Light Controlled variable resistor. The obstruction of a photograph resistor Decreases With Increasing light power (Fig. 3).

Fig. 2 PIR sensor [25]**Fig. 3** LDR sensor [26]

AdaFruit 12 NEOPiXEL RING

The driver of the LED string is included in the strip itself. Each LED has an 18 mA constant current drive, thus the shade will be exceptionally dependable independent of voltage variations, and no exterior gag resistors are necessary, resulting in a very small footprint. Each LED drives at a constant current of 18 mA, ensuring that the colour remains steady even if the voltage fluctuates. We can run the entire system on 5 V_{DC} (4–7 V) (Fig. 4).

2.2 Design Approach and Codes

2.2.1 Light Detecting Using LDR

The light sensor, which is used as a lighting detector in this circuit, is a hypothetical concept. The LDR is a resistor, and the amount of light falling on its surface varies

Fig. 4 Neo ring [27]

its blockage. When the LDR detects light, its opposition decreases; on the other hand, if it detects dimness, its obstruction increases.

2.2.2 Ada Fruit Light Ring

Its eight ultra-bright smart LED NeoPixels are grouped in a circle with an outside circumference of 1.75" (44.5 mm). The rings can be chained together to connect one ring's output pin to another ring's input pin. Only one pin can be connected to the microcontroller in order to control as many as possible. Each LED may be addressed since the driver-chip is built in the LED. Each one uses an 18 mA continuous current to drive the color, which is extremely consistent even when the voltage varies, and there is no need for an external choke, resulting in a tiny design. The complete system can run on 5VDC (4 V–7 V).

2.2.3 PIR Sensor

The PIR sensor is made up of two holes, each of which is made up of an IR-sensitive material. We can see that the two regions can "look" out past a certain amount since the focal point chosen here isn't doing anything (essentially the affectability of the sensor). At switch off condition, the two regions of the sensor detect the same amount of IR from inside of the room, dividers, or the outside. When a warm body, such as a human or an animal, passes by, one area of the PIR sensor is obstructed, causing a positive differential change between the two sections. When the heated body departs the detecting zone, the sensor produces a negative differential change, and when the heated body returns, the sensor produces a positive differential change.

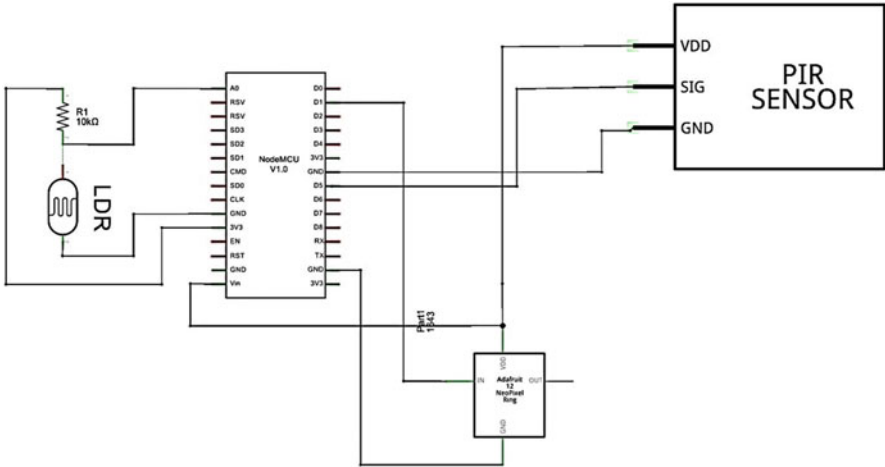


Fig. 5 Light control schematic diagram

2.2.4 Blynk App

It's the mobile in built app which can control our hardware and we can see what amount of light falling on the LDR (Fig. 5).

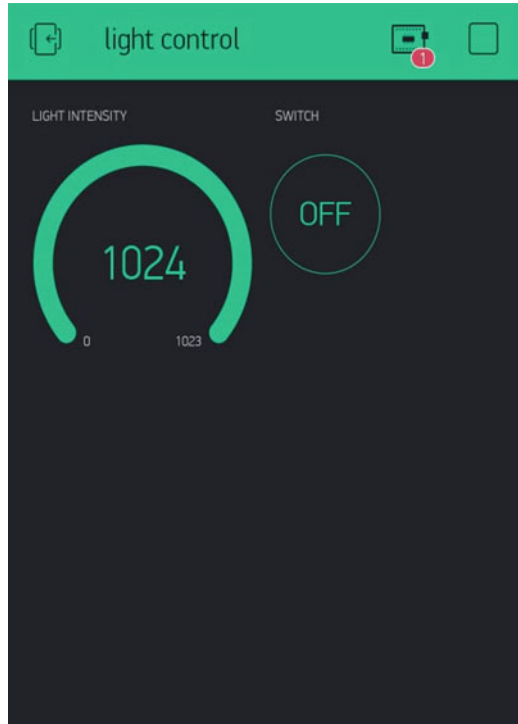
As there are two modules in this maintaining the room light using sunlight with object detection and smart plug.

2.3 Maintaining the Room Light

This project contain of an adfruit neo ring to that have been fabricated to nodemcu and LDR, and it is connected with PIR motion sensor. Then code has been written in Aurdino IDE to control light intensity of neo ring. As it is a smart lighting control, an online app has been created which is very user-friendly on the BLYNK platform in that only two keys have been assigned – one where the light intensity can be displayed (i.e., how much light falls on LDR) accordingly and the other one ON/OFF switch: when the switch is off PIR, i.e., motion sensor gets activated when any object like human or animal (heat emitting) moves, then light glows automatically and when the switch is on, the light falls on LDR and the brightness increases or decreases accordingly (Fig. 6).

Initially, we have declared the required pixels, the particular address through which it can connect to the mobile application, the code, and network details that our device needs to be connected with both our mobile and the hardware in one single network.

Fig. 6 BLYNK app



3 Result and Discussion

When a PIR sensor recognizes some heat-emitting objects, then the light glows. When there is no obstacle to PIR sensor, it will emit no heat. So LED will not glow (Figs. 7 and 8).

3.1 Light Intensity at Different Level of Light Range

The luminaire tested at different intensity of light to get different output intensity (Fig. 9) (Table 1).

4 Conclusions

Energy utilized for lighting is one of the significant segments of absolute energy utilization in structures. These days, structures have an extraordinary potential to lessen their energy utilization, yet to accomplish this reason extra endeavors are

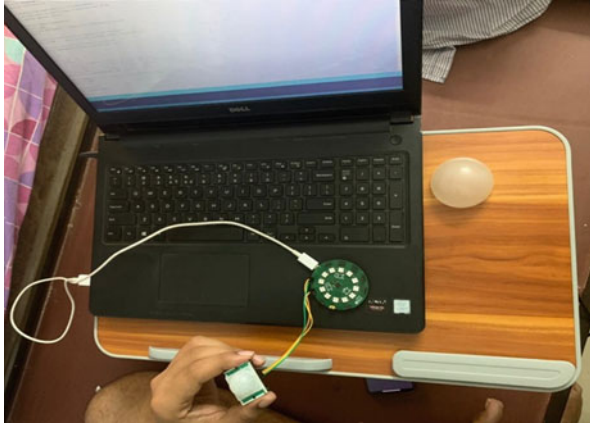


Fig. 7 With obstacle

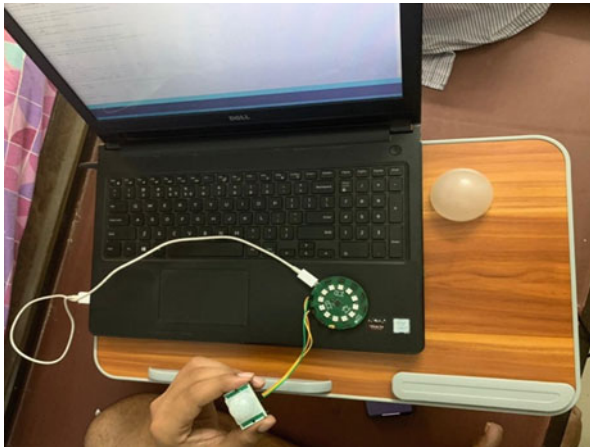


Fig. 8 Without obstacle

crucial. The requirement for energy reserve funds assessment before the execution of lighting control calculations for a predefined constructing is featured. To make the application all the more straightforward, the web and android-based progressions have gained their importance in this bleeding edge development.

This study is aimed to reduce the power consumption of lighting loads. A novel solution is proposed which assembles an alternate sort of light utilizing drove strip. As indicated, each drove is of 0.08 W. This segment of drove can be utilized to construct the light. Thirty LEDs can be utilized to shape a solitary square of drove, each drove of 12 V. Such three squares can be utilized for various degrees of power.

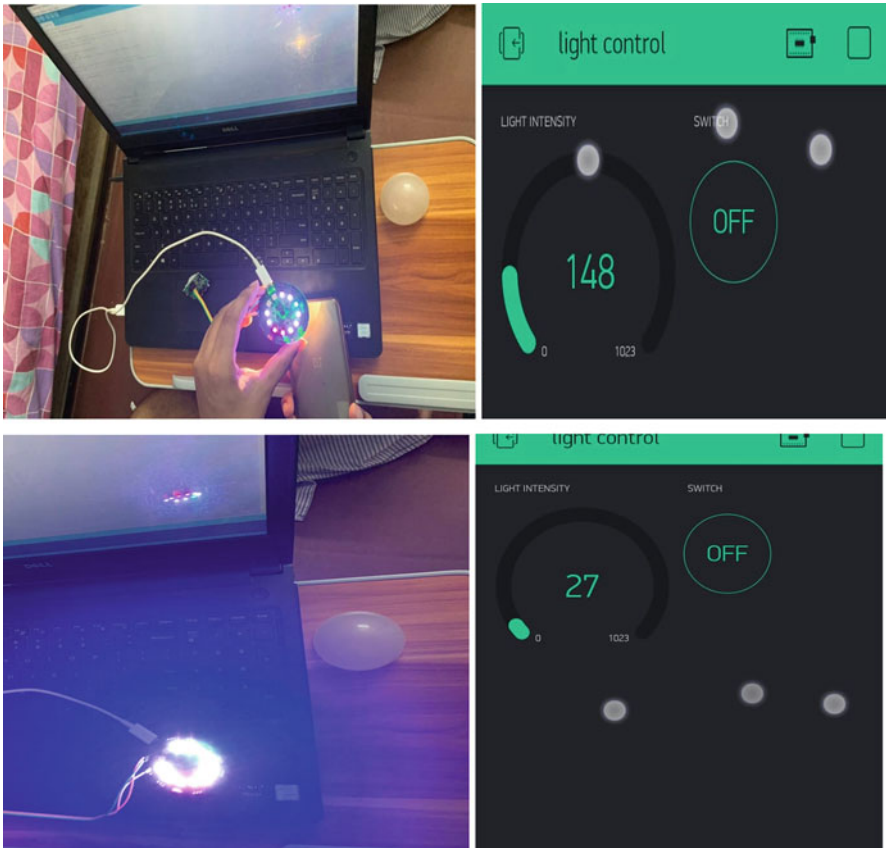


Fig. 9 Testing at different light intensity

Table 1 Output of light intensity

Light intensity	Light calculated in pixel
1024	255
855	200
635	150
754	170
520	120
450	90
950	235

References

1. Solaimani S, Keijzer-Broers W, Bouwman H (2015) What we do – and don’t – know about the smart home: an analysis of the smart home literature. *Indoor Built Environ* 24(3):370–383
2. Rossi M (2019) LEDs and new technologies for circadian lighting. In: *Research for development*. Springer, Cham, pp 157–207

3. Schubert EF, Kim JK (2005) Solid-state light sources getting smart. *Science* 308(5726):1274–1278
4. Alobaidy HAH, Malaysia JSM, Nordin R, Abdullah NF (2020) A review on ZigBee based WSNs: concepts, infrastructure, applications, and challenges. *Int J Electr Electron Eng Telecommun* 9:189–198
5. Van Bommel WJM (2019) *Interior lighting: fundamentals, technology and application*. Springer, Berlin/Heidelberg
6. Chew I, Karunatilaka D, Tan CP, Kalavally V (2017) Smart lighting: the way forward? Reviewing the past to shape the future. *Energy Buildings* 149:180–191
7. ul Haq MA et al (2014) A review on lighting control technologies in commercial buildings, their performance and affecting factors. *Renew Sustain Energy Rev* 33:268–279
8. Pandharipande A, Caicedo D (2015) Smart indoor lighting systems with luminaire-based sensing: a review of lighting control approaches. *Energy Buildings* 104:369–377
9. de Bakker C, Aries M, Kort H, Rosemann A (2017) Occupancy-based lighting control in open-plan office spaces: a state-of-the-art review. *Build Environ* 112:308–321
10. Nagy Z, Yong FY, Frei M, Schlueter A (2015) Occupant centered lighting control for comfort and energy efficient building operation. *Energy Buildings* 94:100–108
11. Galasiu AD, Newsham GR, Suvagau C, Sander DM (2007) Energy saving lighting control systems for open-plan offices: a field study. *LEUKOS* 4(1):7–29
12. Higuera J, Hertog W, Peralvarez M, Polo J, Carreras J (2015) Smart lighting system ISO/IEC/IEEE 21451 compatible. *IEEE Sensors J* 15(5):2595–2602
13. Jennings J, Colak N, Rubinstein F (2002) Occupancy and time-based lighting controls in open offices. *J Illum Eng Soc* 31(2):86–100
14. Roisin B, Bodart M, Deneyer A, D’Herdt P (2008) Lighting energy savings in offices using different control systems and their real consumption. *Energy Buildings* 40(4):514–523
15. Zou H, Zhou Y, Jiang H, Chien S-C, Xie L, Spanos CJ (2018) WinLight: a WiFi-based occupancy-driven lighting control system for smart building. *Energy Buildings* 158:924–938
16. Chandrakar N, Kaul S, Mohan M, Sai Vamsi C, Prabhu KR (2015) NFC based profiling of smart home lighting system. In: 2015 international conference on industrial instrumentation and control (ICIC)
17. Collotta M, Pau G (2015) A novel energy management approach for smart homes using Bluetooth low energy. *IEEE J Sel Areas Commun* 33(12):2988–2996
18. Rodriguez-Diaz E, Palacios-Garcia EJ, Savaghebi M, Vasquez JC, Guerrero JM, Moreno-Munoz A (2015) Advanced smart metering infrastructure for future smart homes. In: 2015 IEEE 5th international conference on consumer electronics, Berlin (ICCE-Berlin)
19. Al-Obaidi KM, Ismail M, Abdul Rahman AM (2014) Design and performance of a novel innovative roofing system for tropical landed houses. *Energy Convers Manag* 85:488–504
20. Lai X, Dai M, Rameezdeen R (2020) Energy saving based lighting system optimization and smart control solutions for rail transportation: Evidence from China. *Res Eng* 5(100096):100096
21. Kumar A, Kar P, Warriar R, Kajale A, Panda SK (2017) Implementation of smart LED lighting and efficient data management system for buildings. *Energy Procedia* 143:173–178
22. Gerhardsson KM, Laike T, Johansson M (2021) Leaving lights on – a conscious choice or wasted light? Use of indoor lighting in Swedish homes. *Indoor Built Environ* 30(6):745–762
23. Statista comfort and lighting—worldwide|statista market forecast. Available online: <https://www.statista.com/outlook/392/100/comfort-and-lighting/worldwide>. Accessed on 18 Oct 2021
24. Juric J, Lindenmeier J (2019) An empirical analysis of consumer resistance to smart-lighting products. *Light Res Technol* 51(4):489–512
25. <https://www.Elektor.Com/Hc-Sr501-Pir-Motion-Sensor-Module>
26. <https://www.indiamart.com/proddetail/ldr-sensor-15345628591.html>
27. https://www.digikey.in/product-detail/en/adafruit-industries-llc/2852/1528-1604ND/5878294?cur=INR&lang=en&utm_adgroup=General&utm_source=google&utm_medium=cpc&utm_campaign=Smart%20Shopping_Product_Zombie%20SKUS&utm_term=&productid=5878294&gclid=Cj0KCQjwktKFBhChARIsAJeDT0iS4PvL_RRJTg2AEOfZlqhRkMeDHIBNVaQ8WhGt_pguVtoR70O9QsaAkpIEALw_wcB

Reliability Analysis of a Group of Internal Combustion Engines (ICM) in Thermoelectric Power Plants Using Optimization Methods for Artificial Neural Networks (ANN)



Ítalo Rodrigo Soares Silva, Ricardo Silva Parente, Paulo Oliveira Siqueira Junior, Manoel Henrique Reis Nascimento, Milton Fonseca Júnior, Jandecy Cabral Leite, and David Barbosa de Alencar

1 Introduction

One of the factors that contribute to the environmental, social, and economic impacts of the commercial and industrial sectors is the failure of machines and/or generators [1], which provide power generation for several consumers through load dispatch. As a result, machine downtime or failure in cases where there are no predictive maintenance tools can lead to irreversible losses or damage such as loss of life [2].

This sector becomes important due to the generation and dispatch of energy, since the stoppage of the machine causes irreversible losses or damage, and in the cases of hospitals and clinics, the scenario tends to be worse where the lack of energy supply can lead to the death of a patient. Consequently, the entrepreneur incurs even greater losses due to the high cost of the stopped machines, besides the penalties sanctioned and provided by law, which can even reach the loss of physical guarantee and imply the reduction of energy sold [3, 4].

Therefore, the research is justified by the opportunity to improve prediction methods in the maintenance of Internal Combustion Machines in Thermoelectric Power Plants. Maintenance programs are methodologies that make use of tools to maintain or increase the life expectancy of a given piece of equipment; therefore, they are useful in the equipment maintenance process [5].

Thus, when it comes to machines, some techniques are taken into consideration, such as vibration analysis, thermographic analysis, oil analysis, ultrasound, and others, are effective measures to identify failures; however, demand time, strict

Í. R. S. Silva (✉) · R. S. Parente · P. O. S. Junior · M. H. R. Nascimento · M. F. Júnior · J. C. Leite
D. B. de Alencar
Institute of Technology and Education Galileo of the Amazon (ITEGAM), Manaus, Amazonas,
Brazil
e-mail: italo.silva@itegam.org.br; ricardo.parente@itegam.org.br; paulo.siqueira@itegam.org.br;
hreys@itegam.org.br; jandecy.cabral@itegam.org.br; david.alencar@itegam.org.br

control of the measurement points, and personnel training to perform the evaluation procedures.

To obtain accurate control and management in the maintenance plan, the main performance indicators specified by the Brazilian Standard 5462 are used, among them is reliability, which refers to the probability of efficient work of an equipment through a certain period of time acceptable by the elements of the production chain [6]. Bringing to light the reality of this research, it is noteworthy for its innovation in implementing, testing, and analyzing Artificial Neural Networks (ANN) techniques using Training Algorithms.

Its contribution comes from the problem of failures and the investigation of the Reliability method, to evaluate the probability of equipment functioning over a period of time. In addition, it is worth mentioning the use of Machine Learning, Pattern Recognition, Pattern Classification, Deterministic Methods, Systematic Heuristics, and Optimization Algorithms [7–11].

This research presents a focus on the maintenance scenario of internal combustion machines in Thermoelectric Power Plants, where the Reliability rate of the group of 20 machines is analyzed by using optimization methods to find the best convergence state of the ANN and present results close to the real function.

2 Theoretical Reference

This section presents the main topics for scientific and theoretical background that are determinant in the processes and elements used in the research, among which are highlighted: the mathematical basis for the acquisition of the Reliability Indicator regulated by the Brazilian Standard 5462 and the optimization methods Levenberg-Marquardt and Bayesian Regularization used to train ANN models for the acquisition of the best configuration and performance when considering the number of neurons, iterations, hidden layers, activation functions, and training algorithms.

2.1 *Reliability as an Indicator in Predictive Maintenance*

According to [6], reliability is a quality metric that analyzes the performance of an item, equipment, machine, or system, provided that a period of time is specified. The method is used to assess the degree of reliability or useful life of the material; its analysis is based on mathematical calculations that indicate values relevant to their performance [12, 13].

The analysis method uses a database of values for material/equipment performance to find the estimated future performance. In this way, it is possible to increase the object's lifetime, reduce costs with corrective maintenance, improve the operational performance, and improve the quality of the maintenance programs

executed by a technical team [14, 15]. The definition of the reliability parameter relative to the observation data can be expressed by Eq. (1):

$$\lambda_i^x = \frac{N_{fi}}{t_i^x \cdot n} \tag{1}$$

Where N_{fi} is the number of failures before the i -th point of failure, t_i^x is the i th point of failure time for subsystem x , and n is the number of subsystem failures [16–18]. The failure rate for each failure point in subsystem x can be expressed by Eq. (2):

$$\lambda^x = [\lambda_1^x, \lambda_2^x, \lambda_3^x \dots \lambda_i^x, \dots \lambda_{n-1}^x, \lambda_n^x]^t \tag{2}$$

For [16], among the various techniques of failure analysis and investigation concerning a material/equipment, there is the bathtub curve. This technique uses mathematical models with combinatorial radial basis functions performed to approximate complex calculation functions in a continuous and multivariate way. This method is adjustable to a RBF Neural Network [17, 18], being expressed by Eq. (3).

$$\hat{y}(x) = \sum_{i=1}^n \beta_i f(\|x - x_i\|) = f(x)^T \beta \tag{3}$$

Where $\hat{y}(x)$ is the forecast response vector, x , β is the vector of radial basis coefficients β_i is the i th component β , $f(x)$ is the RBF vector $f(\|x - x_i\|)$ is the i th component of $f(x)$, $r = \|x - x_i\|$ is the Euclidean distance between two vectors [14, 16]. The Eq. (3) can be rewritten to find the failure rate, this application in a RBF must be defined as a custom activation function to approximate functions and calculate reliability, the Eq. (4) expresses the mathematical model:

$$\hat{\lambda}^x(t) = \sum_{i=1}^n \beta_i f(\|x - x_i\|) = f(x)^T \beta \tag{4}$$

Where $\hat{\lambda}^x(t)$ is the subsystem failure rate x at the time. The reliability of the unit is defined as its cumulative probability of success [16–18], The reliability represented in a quantitative way can be expressed by the probability of survival of the unit for a set time; the set term $R(t)$ must assume values between 0 and 1, the longer the set time the lower will be the $R(t)$. Analytically, this is defined by the integral of the probability density function $F(t)$, being expressed by Eq. (5):

$$R(t) = \frac{n_s(t)}{n_s(t) + n_f(t)} = \frac{n_s(t)}{n_0} \tag{5}$$

The defined term $F(t)$ is understood as the probability accumulation, this being the complement of $R(t)$; in this way, it can be defined that this term accumulates the failure rate probability of the unit in operation, starting from this principle the same mathematical logic of $R(t)$ is applied to $F(t)$, this model is expressed by Eq. (6):

$$R(t) = 1 - F(t) = 1 - \int_0^t f(u)du = \int_t^{+\infty} f(u)du \quad (6)$$

The distribution of terms that make up the reliability function or $R(t)$ obtained by Eq. (6) has as viés present values that relate measures of qualitative classification for a piece of equipment x in a period y , correlating the failure rate in this same period, this leads to state that the construction and application of this model becomes viable for simple and complex systems with units that present failure behavior aiming at the qualitative analysis of the system in question [14, 16].

The application of the reliability function as a method of systems analysis must consider the use of performance data, taking into account the parameters that make up the distribution of the mathematical function. In this way, the model must obtain results in series to analyze a temporal behavior [17–19].

2.2 Artificial Neural Networks (ANN)

The Artificial Neural Networks are computational techniques that aim to predict events, recognize or classify patterns. They have architectures and topologies, besides being inspired in the neural structure of intelligent organism,s and with the necessary adjustments in their weights, it is possible to acquire knowledge [20, 21].

Its operation is simple each unit is connected by communication channels, the unit is responsible for performing operations on data passed as input [22]. As a result, neural networks can improve decision processes in many areas [20, 23, 24]:

- Credit card and health care fraud detection
- Logistics optimization for transportation networks
- Voice and character pattern recognition
- Targeted marketing
- Financial predictions
- Data classification
- Computer vision for photo identification

The behavior of the results presented by an ANN is in accordance with the elements that execute its processes, often stochastic, heuristic, iterative, or optimization processes [23].

2.2.1 Learning an ANN

A very important factor to be pointed out for a neural network is the learning process that depends on how it relates to the environment [20, 23]. Thinking in this perspective, some learning paradigms are taken into consideration:

- *Supervised Learning*: With the help of an external agent, the network learns the desired pattern
- *Unsupervised Learning*: It is a form of self-organization, where there is no external agent to infer in the learning process
- *Reinforcement*: when an external evaluator analyzes or defines the response provided by the network

The learning of an ANN occurs when the error rate is constant or minimal according to the previously defined restriction criteria to converge to a state equivalent to the real function. Among these ways, a neural network can learn are error correction, competition, Hebbian models, and machine learning [23, 25].

Thus, in this research, two optimization approaches are presented to evaluate the best convergence state of the ANN and increase the approximation rate between simulated and real functions, achieving error rates close to 0 and correlation rates between output variables close to or equal to 100%.

2.2.2 Levenberg-Marquardt Method

Be $R : \mathbb{R}^n \rightarrow \mathbb{R}^m$, a residual function, Eq. (7) expresses a nonlinear least squares problem.

$$\min_{x \in \mathbb{R}^n} f(x) = \frac{1}{2} \|R(x)\|^2 \tag{7}$$

This optimization method aims at solving nonlinear least squares problems. *Levenberg* initially proposed to introduce a parameter $\lambda_k > 0$ on the diagonal of $J^T(x_k)J(x_k)$ to the Gauss-Newton system [26–28], expressed by Eq. (8).

$$\left(J^T(x_k) J(x_k) + \lambda_k I \right) d_k = -J^T(x_k) R(x_k) \tag{8}$$

One way to determine the position of a matrix is by applying the Decomposition of *Cholesky*, in which it is applied in cases of positive definite matrices [26, 29]. The *damping* introduced by Levenberg has a direct influence on the direction $d(\lambda)$, and as a consequence, allows a feasible performance as a function of the convergence of the algorithm [26, 30, 31].

As the parameter λ increases in the system represented by Eq. (8), the direction d_k tends to the direction of maximum descent, while λ approaches zero, the minimization direction tends to the Gauss-Newton direction [26, 27].

The determination of the parameter λ_k can be done as a function of Eq. (9), however, in the technical literature, other formulations of the *damping* parameter are found, which are contributions according to different problems and performance improvements [26, 30, 31].

$$\lambda_k = \frac{g_k^T v_k}{f'(x_k)} \quad (9)$$

Another way to interpret *Levenberg's* method is, consider $S(x) = \sum_{i=1}^m r_i(x) \nabla^2 r_i(x)$, consider also the quadratic model of the objective function $f(x)$, in a neighborhood of the point x_k such that it is possible to approximate the Hessian matrix [26, 30, 31], as expressed by Eq. (10).

$$\nabla^2 f(x) = \sum_{i=1}^m r_i(x) \nabla r_i(x)^T + \sum_{i=1}^m r_i(x) \nabla^2 r_i(x)^T = J(x)^T J(x) + S(x) \quad (10)$$

By Eq. (11),

$$\nabla^2 f(x_k) \approx J(x_k)^T J(x_k) + \lambda_k I \quad (11)$$

Thus, it is possible to obtain the model expressed by Eq. (12):

$$m_k(d) := \frac{1}{2} R(x_k)^T R(x_k) + J(x_k)^T R(x_k) d + \frac{1}{2} \left(J(x_k)^T J(x_k) + \lambda_k I \right) d^2 \quad (12)$$

The Eq. 12 evidence the acquired model in such a way that by minimizing it, it is possible to obtain the same direction $d(\lambda_k)$, when $\lambda_k = 0$, the direction d^{LM} obtained by the *Levenberg-Marquardt* method coincides with the *Gauss-Newton* direction d^{GN} [26, 32], the *Gauss-Newton* method can be defined and expressed by Eqs. (13), (14) and (15).

$$\frac{\partial}{\partial d} \left(\frac{1}{2} \left(R(x_k)^T R(x_k) + 2d^T J(x_k)^T R(x_k) + d^T J(x_k)^T J(x_k) d \right) \right) = 0, \quad (13)$$

$$J(x_k)^T R(x_k) + J(x_k)^T J(x_k) d = 0, \quad (14)$$

$$J(x_k)^T J(x_k) d = -J(x_k)^T R(x_k) \quad (15)$$

In such a way that the minimization direction expressed by Eq. (16), satisfies:

$$\frac{\partial}{\partial d} \left(\frac{1}{2} \|R(x_k) + J(x_k) d\|_2^2 \right) = 0 \quad (16)$$

If $J(x_k)^T J(x_k)$ has a satisfactory approximation rate in relation to the hessian matrix, it is understood that the convergence rate of the optimization will be quadratic, that is, it finds a model with the approximate value of the solution [26, 32].

However, if d^{LM} tends to infinity, it is understood that the optimization will tend to a maximum downward direction, in other words, $-\nabla f(x_k)$, which is denoted by $-g_k$. Therefore, an algorithm for the *Classical Levenberg-Marquardt Method* is presented [27, 30] for better understanding.

Algorithm 1: *Classic Levenberg-Marquardt*

```

Input:  $R(x), J(x)$ , when  $x_0 \in \mathbb{R}^n$ , with initial values  $\lambda_0 \in \mathbb{R}_+$ , update parameters  $k_1, k_2 > 1$  and tolerance  $\epsilon > 0$ 
Output:  $x_* \in \mathbb{R}^n$ , with stationary point of  $f(x) = \frac{1}{2} \|R(x)\|_2^2$ 
1 begin
2  $k \rightarrow 0$ ;
3 while  $J(x_k)^T R(x_k) > \epsilon$  do
4   Get  $d(\lambda_k)$  solution of:  $J(x_k)^T J(x_k) d = -J(x_k)^T R(x_k)$ ;
5   Do  $x_n = x_k + d(\lambda_k)$ ;
6   If  $R(x_n) < R(x_k)$  then
7      $x_{k+1} = x_n$ ;
8      $\lambda_{k+1} = \frac{\lambda_k}{k_1}$ 
9   else
10     $\lambda_{k+1} = \lambda_k k_2$ 
11  end
12 Do  $k \rightarrow k + 1$ 
13 end
14 end
15 return  $x_k$ 

```

Source: Refs. [27, 30]

The classical method spread by Levenberg and later improved by Marquardt gave rise to other contributions that are now used in various applications for function approximation and as a least squares solution.

2.2.3 Bayesian Regularization Method

The Regularization is a name for methods that involve modifying the performance function of neural networks and has emerged as a way to solve ill-conditioned problems [33], with the main objective of reducing the sum of the quadratic errors, such that it is possible to minimize a combination of the quadratic errors and the weights, and then produce a generalized network [34, 35].

Based on this principle, regularization involves two terms: standard error term and regularization term, the former measuring the standard error between the desired and the actual response obtained [8, 36], expressed by Eq. (17). The second depends on the geometric properties of the approximated function $F(x)$, as expressed in Eq. (18).

$$E_D(w) = \frac{1}{2} \sum_{i=1}^m [d_i - F(x_i)]^2 \quad (17)$$

$$E_s(w) = \frac{1}{2} \|DF\|^2 \quad (18)$$

Where:

$E_D(w)$ = standard error term

$E_s(w)$ = regularization term

d_i = desired response

$F(x_i)$ = approximate function

D = stabilizer.

The D parameter referred to as the regularization term stabilizer has the function of solving the regularization problem, in order to smooth the continuity property [8, 34, 36]. Therefore, the function to be minimized by the regularization theory is expressed by Eq. (19).

$$\xi(w) = E_D(w) + \lambda E_s(w) \quad (19)$$

Where:

λ = positive real number

$E_D(w)$ = standard error term

$E_s(w)$ = regularization term

The smoothing parameter λ assumes a value between the two extremes $(0, \infty)$ so that there is a balance between the data sample and the previous information. This method represents a form of complexity punishment [37, 38], whose influence on the final value is controlled and can be expressed by Eq. (20).

$$E_s(w, k) = \frac{1}{2} \int \left\| \frac{\partial^k}{\partial x^k} F(x, w) \right\|^2 \mu(x) dx \quad (20)$$

Where:

$F(x, w)$ = input-output mapping

$\mu(x)$ = weighting function

The objective of the formulated problem is to estimate the optimal value for the smoothing parameter in such a way that it is possible to find the balance between variance and bias [34, 37]. In the technical literature, there are reformulated regularization models, known as: *Tikhonov and Maximum Entropy Principle* [34, 37, 39].

The process of learning a neural network by means of Bayesian Regularization is given by methods such as the worst-case density $p(w)$. This information is expressed

in the form of a function [40, 41]. Other distributions are found in the literature such as Gaussian, likelihood, and parameter optimization [11, 42].

The Gaussian distribution generates a wide class of a priori information due to its ease of formulation, analytical treatment and versatility of use [34, 37, 41]. Since minimizing a functional $J(x)$ is the same as maximizing $J'(x) = \exp\left(-\frac{1}{2}J(x)\right)$, the function to be minimized relative to the regularized solution is expressed by Eq. (21).

$$x_\alpha = \arg \min_x \left\{ \left\| Ax - y \right\|_2^2 + \alpha^2 \left\| L_r (x - x^*) \right\|_2^2 \right\} \tag{21}$$

Where:

α = when greater than 0, smoothing parameter

$\left\| Ax - y \right\|$ = minimization residue

A point to note about the minimization function is that Eq. (21) will only be unique or stable, if $\ker(A) \cap \ker(L_r) = \{0\}$. Thus, using the a priori information as a solution to Eq. (21), it can be expressed by Eq. (22).

$$J'(x) = \exp\left(-\frac{1}{2}(Ax - y)^T (Ax - y) - \frac{\alpha^2}{2}(x - x^*)^T L_r^T L_r (x - x^*)\right) \tag{22}$$

Therefore, the regularization can be interpreted statically as a Gaussian density [11, 34, 37, 42], in such a way as to obtain the formulation expressed by Eq. (23).

$$f_x^{\text{priori}} \propto \exp\left(\frac{\alpha^2}{2} \left\| L_r (X - x^*) \right\|_2^2\right) = N(x^*, \Gamma^{xx}) \tag{23}$$

Where Γ^{xx} is the covariance matrix and expressed by Eq. (24),

$$\Gamma^{xx} = \frac{1}{\alpha^2} \left(L_r^T L_r \right)^{-1} \tag{24}$$

Thus, if $\ker(A) \cap \ker(L_r) \neq \{0\}$, the classical regularization would not reach the optimal solution to the problem; however, other methods can be used that over the years have been introduced in Bayesian methods [11, 34, 37, 42], in such a way as to acquire information a priori as distribution conditioned to the realization of fixed components.

In cases where the a priori information holds over time, as in the case of spatial information, it is necessary to modify the iteration step to introduce $f_{x_{k+1}}^{\text{priori}}$ in the propagation stage [41, 43].

The main objective of the Bayesian Optimization Algorithm (BOA) s to learn a network that conforms to the dependencies and independence that make up a

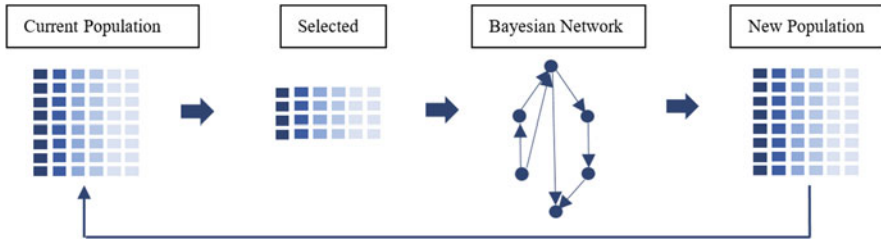


Fig. 1 BOA summary. (Source: Adapted from Refs. [10, 44])

given problem as shown in Fig. 1 [10, 44], so the optimization performs two tasks: Learning to structure and learning conditional probabilities.

In short, the BOA has no prior knowledge of the structure of the parameters; therefore, the feasible solution is given by the candidate element, that is, a candidate solution is proposed, it uses a complex model that can identify relationships of order n among the genes of the population, the main challenge of the algorithm, is the computational cost, which meets the estimated time to find the candidate solution [10, 44].

In order to model promising solutions and consequently guide the exploration of the search space, the Algorithm 2 demonstrates the pseudocode of the BOA.

Algorithm 2: BOA pseudocode

```

1   $g=1$ ;
2  InitializePopulation ( $Pg$ );
3  while Stop criterion not met do
4  EvaluatePopulation ( $Pg$ );
5   $g=g+1$ ;
6   $S = Selection(Pg-1)$ ;
7   $BN = BayesianNetwork(S)$ ;
8   $Pg = NewPopulation(BN)$ ;
9  end

```

Source: Ref. [44]

3 Materials and Methods

This section presents the materials acquired and used to carry out the research, covering the main methods used to achieve the specific objectives, in such a way that the general objective was reached. It is worth mentioning that this section covers the optimization methods used to select the best ANN model.

3.1 Machine Group Characteristics

The characteristics of the set of machines were acquired through reports from the Thermoelectric Power Plants; this information was necessary to support the research and facilitate the acquisition process of specific indicators for each engine. Each engine is from the manufacturer Wartsila NSD Corporation 4-stroke Diesel model. The average efficiency is approximately 42.3%, each unit has approximately 237 tons.

The maintenance indicators meet the availability and the frequency of failures that each unit can obtain, so the other characteristics of each unit are presented in Table 1.

3.2 Maintenance Management Indicators

The Key Performance Indicators (KPI) are acquired through an analysis in relation to the failure history and that meet the UTE’s maintenance procedures. The Table 2 presents the list of acquired indicators.

These indicators are requirements for acquiring the Reliability Rate calculation, and Table X categorizes the indicators as Input and Output so that it is possible to map a data structure to the Neural Network training model.

The mapped indicators are regulated by the Brazilian Standard 5462 of 1994, which provides the necessary information about the Reliability and Maintainability of equipment. That said, each indicator has a mathematical formulation that determines its value.

Total Stop Time This indicator aims to measure the time spent for each machine stopped in decimal hours. It is expressed by Eq. (25).

Table 1 Group of 20 machine features

Manufacturer	<i>Wartsila NSD Corporation</i>
Model	18 V46
Engine type	4-stroke diesel cycle
Nominal power	15,75 MW
Efficiency	42,3%;
Cylinder configuration	V;
Number of cylinders	18
Cylinder bore	460 mm
Velocity	514 rpm
Length	13,58 m
Width	5347 m
Height	5488 m
Weight	237 Tons

Source: Authors (2021)

Table 2 Input and output variables for the ANN

Variable	Indicator
Input	Total Occurrences – TO
Input	Total Downtime – TP
Input	Total Machine Operation Time – TTOM
Input	Mean Time Between Failures – MTBF
Input	Average Repair Time – MTTR
Input	Availability – D
Input	Failure Rate – TF
Input	Total Days Analyzed – TD
Input	Forecast Days – DA
Output	Reliability – CO

Source: Authors (2021)

$$TTP = \sum_{i=1}^n tpf - tpi \tag{25}$$

Where:

- TTP = total stop time in hours
- tpf = final stop time in hours
- tpi = initial stop time in hours
- n = number of stops

Total Attendance Time This indicator aims to measure in units the number of times that the machine stoppage occurred according to the analyzed time, in this case in days. It is expressed by Eq. (26).

$$TF = \sum_{i=1}^n f_i \tag{26}$$

Where:

- TF = Total Attendance Time in units (quantity)
- f_i = failure unit
- n = number of failures

Days Analyzed This indicator aims to measure the number of days evaluated as a function of the start date and the end date. It is expressed by Eq. (27).

$$DA = DF - DI \tag{27}$$

Where:

- DA = Days analyzed

DF = end date

DI = start date

Operating Hours This indicator aims to measure the total number of hours that the machine was stopped. The values are acquired according to the analyzed days. It is expressed by Eq. (28).

$$HO = DA * 24 \quad (28)$$

Where:

HO = Operating hours

DA = days analyzed

24 = daylight hours

MTBF This indicator aims to measure the average time between failures as a function of the Total Downtime and Total Frequency. It is expressed by Eq. (29).

$$MTBF = \frac{TTP - TF}{HO} \quad (29)$$

Where:

MTBF = Mean Time Between Failures

TTP = Total Stop Time

TF = Total Attendance Time

HO = Operation hours

MTTR This indicator aims to measure the average time to repair. The values are acquired as the function of total downtime and total frequency time. It is expressed by Eq. (30).

$$MTTR = \frac{TTP}{TTF} \quad (30)$$

Where:

MTTR = Average Time to Repair

TTP = Total Stop Time

TTF = Total Attendance Time

Failure Rate This indicator aims to measure the failure rate as a function of the mean time between failures and projection time. It is expressed by Eq. (31).

$$\lambda(t) = \frac{1}{MTBF} \quad (31)$$

Table 3 Computer/
Simulator settings

Resource	Value
RAM memory	6 GB
Processor	I5 third generation
Processing clock	2.90 GHz
L3 cache memory	6 MB
Storage technology	HD
Secondary memory	500 GB

Source: Authors (2021)

Where:

$\lambda(t)$ = Failure Rate

MTBF = Mean Time Between Failures

T = projection time

Reliability This indicator is acquired by applying it together with the other equations using a sample performance base of equipment that evidences faulty behaviors. This model is expressed by Eq. (32).

$$R(t) = e^{-\lambda * t} \tag{32}$$

Where:

$R(t)$ = Reliability

e = Nepierian logarithm

λ = failure rate

t = projection time

3.3 Test Machine Features

The configurations of the machines used for the simulations were important, mainly in relation to the use of computational resources such as: Parallelism and Data processing with memory allocation in graphics processing units (GPU). Table 3 shows the settings of the machine used.

3.4 Training Algorithms

The ANN training algorithms were extremely important to find the best convergence state based on the number of neurons, layers, activation functions and errors such

Table 4 Training algorithms

Algorithm	Method
<i>Levenberg-Marquardt</i>	Optimization
<i>Bayesian Regularization</i>	Optimization

Source: Authors (2021)

as MSE and RMSE. Table 4 presents the algorithms used characterizing their convergence methods.

3.5 Activation Functions

The transfer functions are extremely important to evaluate and reduce the gradient explosion in the transfer layers between neurons, in which iteration control, less error and better model are stopping criteria of the used algorithm. The functions used are presented below:

- Linear
- Sigmoid
- Hyperbolic tangent

3.6 Error Analysis by Statistical Models

The factor for choosing the best algorithm is based on the smallest mean square error (MSE) and the mean square error (RMSE) [45], where each neural network model is trained, a filtering is performed to identify the one with the lower.

For each iteration performed, a validation of the network performance is performed, where a function responsible for simulating the output result of the network with the output vector is called, according to Eqs. (33) and (34):

$$MSE = \frac{\sum_{i=1}^n (ra_i - rs_i)^2}{n} \tag{33}$$

$$RMSE = \sqrt{\frac{\sum_{i=1}^n (ra_i - rs_i)^2}{n}} \tag{34}$$

Where:

- MSE = Mean Squared Error
- RMSE = Root Mean Square Error
- n = number of elements of the output vector
- ra = target result
- rs = simulated result

The purpose of the implemented computational model is:

- Read the fault data set.
- Perform the processing of this data, to find and calculate the Maintenance Management indicators.
- Separate the processed dataset based on the number of engines, i.e., each engine will have an observed input and output set for ANN training.
- The computational model determines which ANN is best based on the MSE and RMSE to then run simulations over periods of days and months.

For the execution of the tests, the two ANN learning algorithms were evaluated. Each one was submitted to a series of three training sessions to evaluate the best network topology conditions considering the number of neurons and the transfer function in the input and intermediate layers.

4 Results and Discussions

This section presents the main results of the application of the Levenberg-Marquardt and Bayesian Regularization algorithms for prediction in days and months, analyzing the performance of the ANN as a function of the MSE and RMSE to arrive at the best model considering the values (data) of the relative failures for the 20 engine group.

4.1 Application of the Algorithms for Forecasting in Days

This section presents the results of the application of the learning algorithms for the best ANN model, applied to the forecast of 1, 5, 10, 15, and 20 days, where the data set for training the neural network includes: 66,000 fault records considering the years 2018 and 2019.

The ANN input set has 11 variables, described as follows: Total Frequency; Downtime; Opening hours; MTBF; MTTR; Availability; Failure rate; Days analyzed; Current month; Current year; Forecast time, both validated by mathematical models, which are dynamically calculated during the algorithm execution process, which is done in the data processing step.

The ANN output set has a variable, described as: Reliability, which is the result of Eq. (8), and is dynamically calculated in the data processing step.

The Table 5 presents a summary of the training results for each engine, where the columns represent: *Engine* is the engine identifier number; *FT1* is the activation function used in hidden layer 1; *FT2* is the activation function used in hidden layer 2; *NC1* is the number of neurons used in hidden layer 1; *NC2* is the number of neurons used in hidden layer 2; *MSE* is the Root Mean Square Error; *RMSE* is the Root Mean Square Error; *trainLM* is the Levenberg-Marquardt method; *trainBR* is the Bayesian

Table 5 Error indicators for the group of 20 machines

Engine	Algorithm	Epochs	FT1	FT2	NC1	NC2	MSE	RMSE
1	trainBR	871	tansig	tansig	9	9	9,57e-14	3,09e-07
2	trainBR	366	logsig	tansig	9	9	8,78e-13	9,37e-07
3	trainBR	690	tansig	tansig	10	10	7,89e-14	2,80e-07
4	trainBR	631	tansig	tansig	10	10	9,86e-14	3,14e-07
5	trainBR	669	tansig	tansig	10	10	5,54e-14	2,36e-07
6	trainLM	64	tansig	tansig	10	10	2,63e-13	5,13e-07
7	trainBR	1000	tansig	logsig	5	5	6,53e-13	8,08e-07
8	trainLM	73	logsig	logsig	8	8	7,77e-12	2,79e-06
9	trainBR	708	tansig	tansig	6	6	4,82e-14	2,20e-07
10	trainBR	307	tansig	tansig	10	10	1,55e-13	3,93e-07
11	trainBR	239	logsig	logsig	8	8	8,01e-13	8,95e-07
12	trainBR	845	tansig	logsig	5	5	1,64e-13	4,05e-07
13	trainBR	361	logsig	logsig	10	10	4,48e-13	6,70e-07
14	trainBR	675	tansig	tansig	10	10	4,86e-14	2,21e-07
15	trainLM	86	logsig	logsig	10	10	1,60e-14	1,27e-07
16	trainBR	343	tansig	tansig	8	8	4,01e-13	6,33e-07
17	trainBR	458	tansig	tansig	7	7	3,69e-13	6,07e-07
18	trainBR	1000	tansig	tansig	10	10	1,19e-13	3,45e-07
19	trainBR	802	tansig	tansig	10	10	4,38e-13	6,62e-07
20	trainBR	402	logsig	logsig	8	8	4,64e-13	6,81e-07

Source: Authors (2021)

Regularization method; *logsig* is the Sigmoid transfer function; *purelin* is the Linear transfer function; and *tansig* is the hyperbolic Tangent transfer function.

As Table 5 presents the results of the 20 best algorithms classified according to the best training for each engine, it is possible to identify that engine 15 obtained 1.60e-14 of MSE, 1.27e-07 of RMSE, and 100% of correlation between the output and the observed variables, characterizing the total proximity to the real projected function.

From the results presented in Table 5, engine 9 obtained the second best performance rate, when using the Bayesian Regularization algorithm, with 4.82e-14 for the MSE and 2.20e-07 for the RMSE using the training functions hyperbolic tangent in the two hidden layers. In the first hidden layer, 6 neurons were used, and in the second layer, 6 neurons too; these results were acquired when reaching 708 training epochs.

The engine that obtained the third best error rate was 14, using the Bayesian Regularization algorithm, where it was possible to reach 4.86e-14 for the MSE and 2.21e-07 for the RMSE, training function used in the two hidden layers was the Hyperbolic Tangent, the first hidden layer used 10 neurons and the second hidden layer also used 10 neurons, the results were acquired when reaching 675 epochs of training.

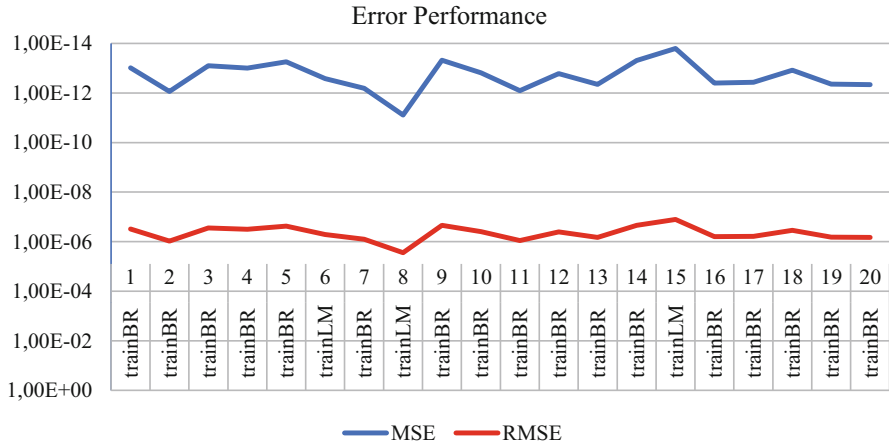


Fig. 2 Error rates for training the ANN for the group of engines. (Source: Authors (2021))

In view of the results presented in Table 5, Fig. 2 presents a relation of the MSE and RMSE indicators for the group of 20 machines, the blue curve indicates the first indicator and the red curve indicates the second indicator. Comparison between engines and error indicators allows an accurate view of the rates achieved by training the algorithms for each engine.

It is possible to identify a high error rate for engine 8, reaching 7.77e-12 for RSM and 2.79e-06 for RMSE, a fact that indicates a variation in the correlation between the variables observed and predicted by the winning algorithm, in this case the Levenberg-Marquardt, by the way, through the behavioral analysis of the graph, it is possible to state that engine 1 obtained lower error rates compared to engine 20 where the first obtained 9.57e-14 for the RSM and 3.09e-07 for the RMSE, while the latter reached 4.64e-13 for the RSM and 6.81e-07 for the RMSE.

The error rates of the training algorithms used in the ANN model, which are closer to the upper limit of 1.00e-14 in Fig. 2, are the ones with the lowest error rates for the MSE and RMSE indicators, that is, they are more accurate in the which concerns the values of the observed and predicted desired variable, characterized mainly by the engine 15.

The error rates of the motors that are closer to the lower limit of 1.00 and +00 in Fig. 2 are the ones with the highest error rates, that is, they are less accurate with respect to the desired observed and predicted values variable, characterized by a variation of values in which it influences the performance of the network and the approximation function.

4.1.1 Characteristics of the Winning ANN Model

Figure 3 illustrates the neural network architecture model evidenced by the winning ANN considering the engine 15 training data when using the previously mentioned configurations. In this figure, it is possible to identify 4 columns of neurons characterized respectively as: input layer, first hidden layer, second hidden layer, and output layer.

The network convergence process depends on the parameters used in modeling the neural network, the training algorithm and the application of activation functions in hidden or output layers, as shown in Fig. 3.

Considering that ANN’s best configuration is engine 15 where it was possible to obtain lower error rates, detailed results for this engine will be presented.

Figure 4 illustrates 4 graphs representing respectively the results of training, validation and testing, and the average between the two, where each one obtained 100% correlation between the observed and predicted output variables.

These values come from a linear regression analysis; the black markings around the trend line are very close, characterizing the correlation between them, where the points of each variable are equal.

The first graph represented by the motor training 15 achieves 100% correlation between the observed and predicted variable, that is, the values coordinated by the abscissa and ordered axes are equal as a function of the inputs inferred in the neural network.

The second, third, and fourth graphs also show 100% reliability in the correlation between the observed and predicted variables so that the division of data to carry out this step is performed in order to prove the efficiency of the model through

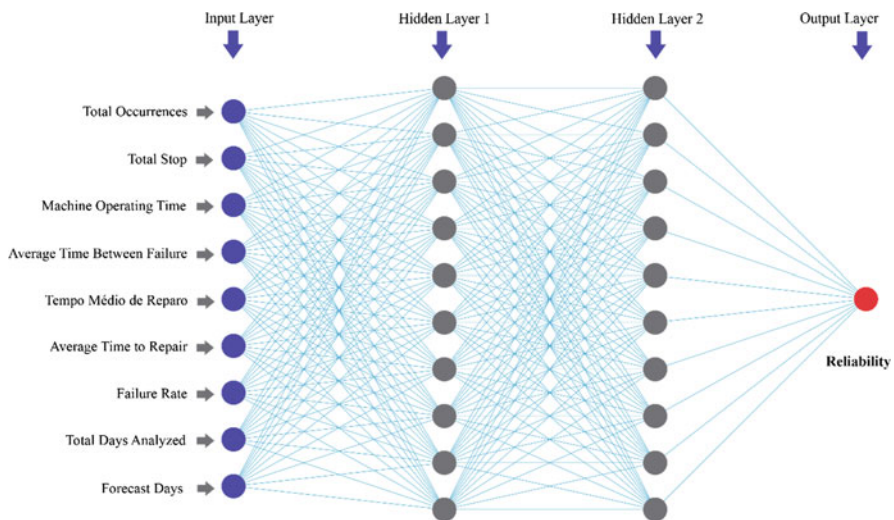


Fig. 3 Winning ANN architecture (Source: Authors (2021))

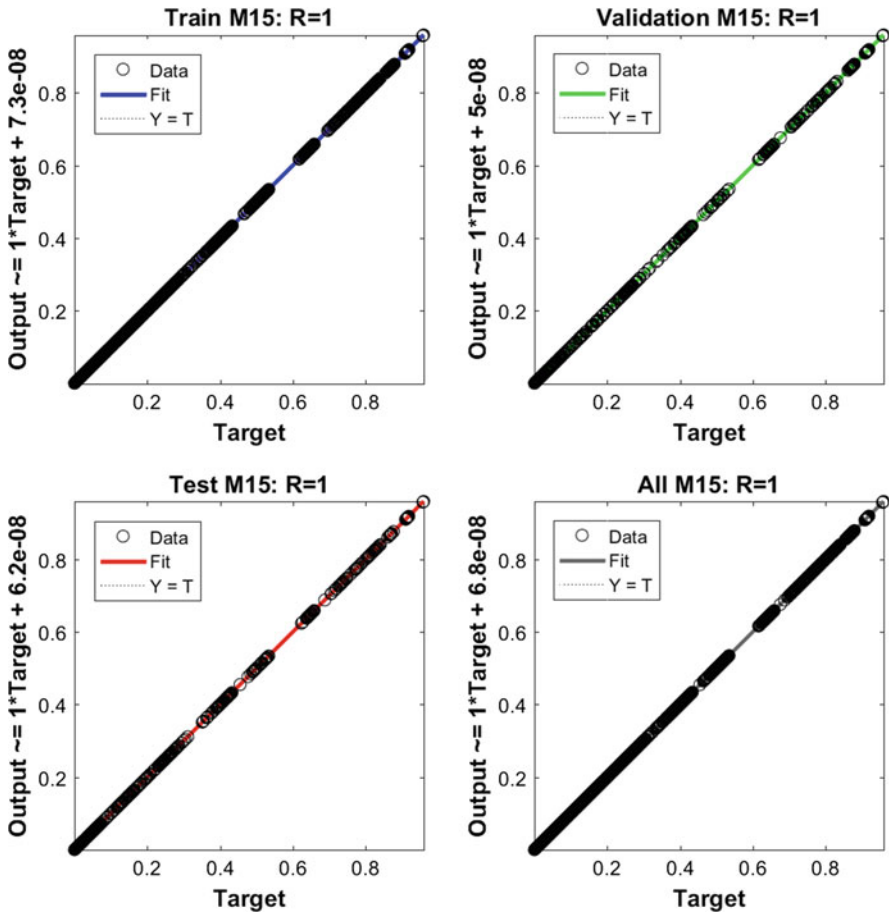


Fig. 4 Correlation model of the observed and simulated output variables (Source: Authors (2021))

its configurations and validate the prediction through a mathematical technique called Linear Regression. The last graph characterized as “All” aims to demonstrate an average between the previous steps, where 100% correlation or reliability is evidenced.

The main characteristic of the Levenberg-Marquardt algorithm is the minimization by minimum damping methods, which is fundamental for the solution of nonlinear problems, that is, it acts directly in the adjustment of the curve slip; however, this algorithm does not find a global minimum.

4.1.2 Simulation for 1 Day

Figure 5 presents a comparison of the Reliability of the group of 20 engines, where a sample of 16 failure units is listed to represent the percentage rate, in which a range of 69 to 96% of Reliability can be identified for the 1 day model of prediction.

Therefore, Table 6 presents the data related to Fig. 5 of the Reliability forecast for the group of 20 engines. Table 6 shows the samples of 16 failures for the years 2018 and 2019, on a scale from 0 to 100% according to the forecast proposal, in this case, 1 day.

In Table 6, it is possible to identify variations between 70.34 and 95.84% for the line representing the 2018 failure sample as a function of the probability of the machine operating in the 1 day forecast. For the line representing the 2018 failure sample 2019, it is possible to observe a variation between 69.56% and 95.83% of the machine operating in the 1 day forecast.

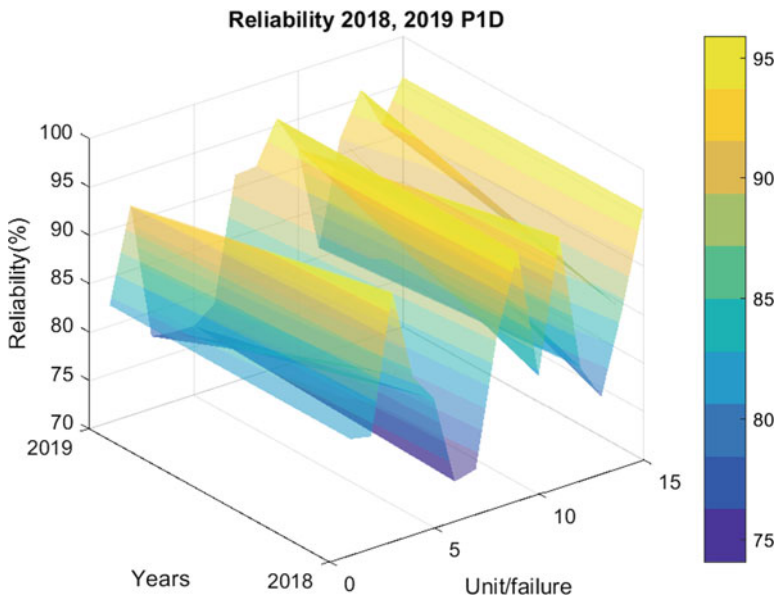


Fig. 5 1-day reliability forecast. (Source: Authors (2021))

Table 6 Simulated data for 1-day forecast

Failure	U1	U2	U3	U4	U5	U6	U7	U8
2018	95.77	70.34	77.44	75.35	71.70	95.84	91.39	91.17
2019	69.56	91.61	82.68	82.62	91.26	71.22	71.32	78.90
Failure	U9	U10	U11	U12	U13	U14	U15	U16
2018	87.14	91.60	87.57	71.70	81.99	83.10	82.71	78.67
2019	95.63	85.42	90.82	85.94	95.83	77.75	95.71	80.27

Source: Authors (2021)

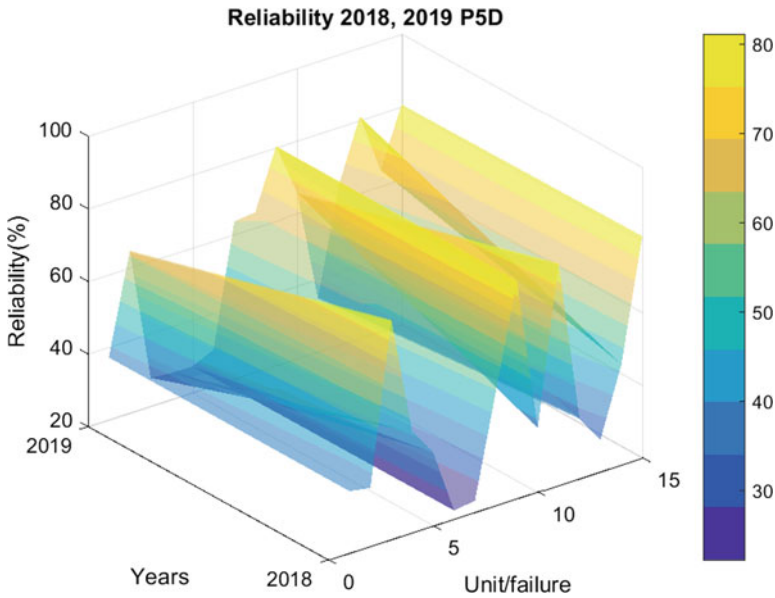


Fig. 6 5-day reliability forecast. (Source: Authors (2021))

Table 7 Simulated data for 5-day forecast

Failure	U1	U2	U3	U4	U5	U6	U7	U8
2018	80.56	17.22	27.85	24.29	18.95	80.86	63.76	62.98
2019	16.29	64.52	38.64	38.51	63.30	18.33	18.45	30.57
Failure	U9	U10	U11	U12	U13	U14	U15	U16
2018	50.25	64.50	51.49	18.95	37.05	39.63	38.72	30.12
2019	79.97	45.49	61.78	46.89	80.83	28.41	80.33	33.33

Source: Authors (2021)

4.1.3 Simulation for 5 Days

Figure 6 presents a comparison of the Reliability of the group of 20 engines, where a sample of 16 failure units is listed to represent the percentage rate, in which it is possible to identify a Reliability range from 16% to 81% for the 5 models of day forecast.

Therefore, Table 7 presents the data related to Fig. 6 of the Reliability Forecast for the group of 20 engines. The table shows the samples of 16 failures for the years 2018 and 2019, on a scale from 0% to 100% according to the forecast proposal, in this case, 5 days.

In Table 7, it is possible to identify variations between 17.22% and 80.86% for the line representing the 2018 failure sample due to the probability of the machine operating within a 5-day forecast. For the line representing the failure sample of

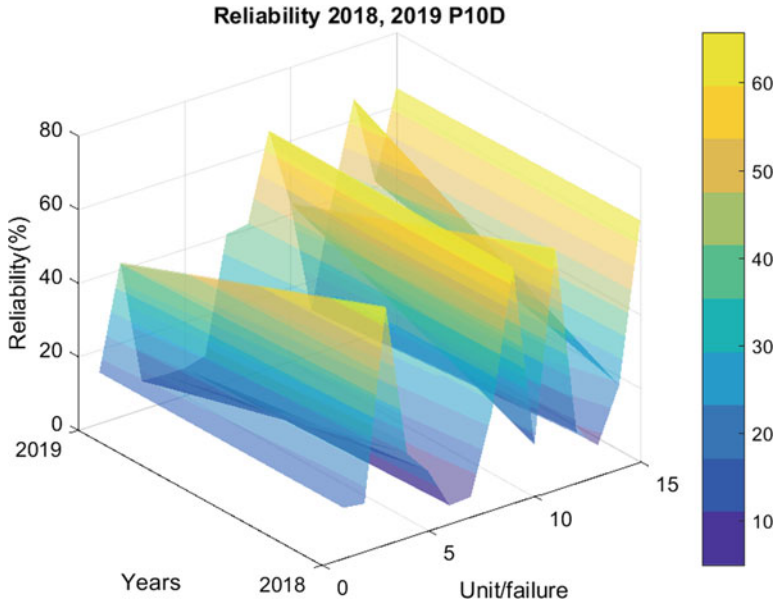


Fig. 7 10-day reliability forecast. (Source: Authors (2021))

Table 8 Simulated data for 10-day forecast

Failure	U1	U2	U3	U4	U5	U6	U7	U8
2018	64.89	2.97	7.76	5.90	3.59	65.38	40.66	39.66
2019	2.65	41.62	14.93	14.83	40.07	3.36	3.41	9.35
Failure	U9	U10	U11	U12	U13	U14	U15	U16
2018	25.25	41.60	26.51	3.59	13.73	15.71	14.99	9.08
2019	63.95	20.69	38.16	21.98	65.33	8.07	64.53	11.11

Source: Authors (2021)

2019, it is possible to observe a variation between 16.29% and 80.83% of the machine operating in a 5-day forecast.

4.1.4 Simulation for 10 Days

Figure 7 presents a comparison of the Reliability of the 20 engine group, where a sample of 16 failure units is listed to represent the percentage rate, in which a range of 2–66% of Reliability can be identified for the 10 model days of prediction.

Therefore, Table 8 presents the data related to Fig. 7 of the Reliability forecast for the group of 20 engines. The table shows the samples of 16 failures for the years 2018 and 2019, on a scale from 0% to 100% according to the forecast proposal, in this case, 10 days.

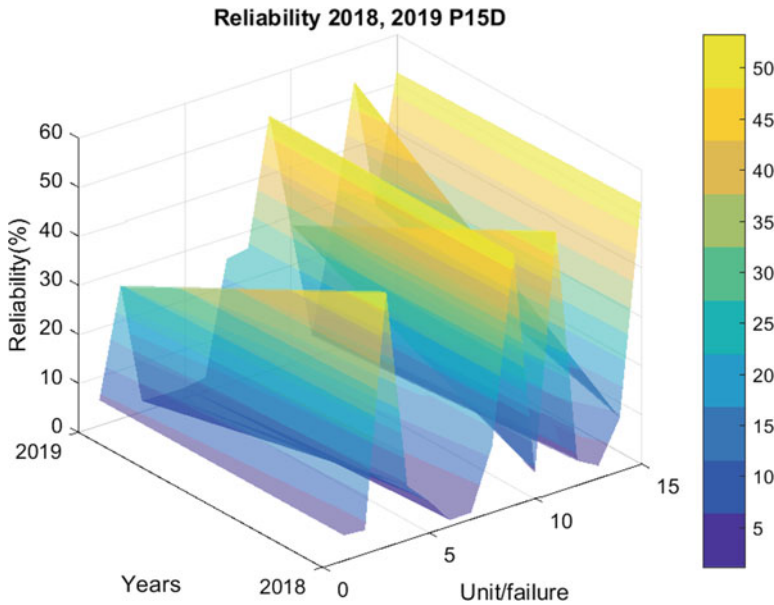


Fig. 8 15-day reliability forecast. (Source: Authors (2021))

In Table 8, it is possible to identify variations between 2.97% and 65.38% for the line representing the 2018 failure sample due to the probability of the machine operating within a 10-day forecast. For the line representing the failure sample of 2019, it is possible to observe a variation between 2.65% and 65.33% of the machine operating in a 10-day forecast.

4.1.5 Simulation for 15 Days

Figure 8 presents a comparison of the Reliability of the group of 20 motors, where a sample of 16 fault units is listed to represent the index in percentage, in which it is possible to identify a Reliability range from 0.40% to 53% for the 15 day forecast model.

Therefore, Table 9 presents the data related to Fig. 8 of the Reliability forecast for the group of 20 engines. The table shows the samples of 16 failures for the years 2018 and 2019, on a scale from 0% to 100% according to the forecast proposal, in this case, 15 days.

In Table 9, it is possible to identify variations between 0.51% and 52.86% for the line representing the 2018 failure sample due to the probability of the machine operating within a 15-day forecast. For the line representing the failure sample of 2019, it is possible to observe a variation between 0.43% and 52.81% of the machine operating in a 15-day forecast.

Table 9 Simulated data for 15-day forecast

Failure	U1	U2	U3	U4	U5	U6	U7	U8
2018	52.28	0.51	2.16	1.43	0.68	52.86	25.92	24.98
2019	0.43	26.86	5.77	5.71	25.37	0.62	0.63	2.86
Failure	U9	U10	U11	U12	U13	U14	U15	U16
2018	12.69	26.83	13.65	0.68	5.09	6.22	5.80	2.73
2019	51.15	9.41	23.58	10.31	52.81	2.29	51.84	3.70

Source: Authors (2021)

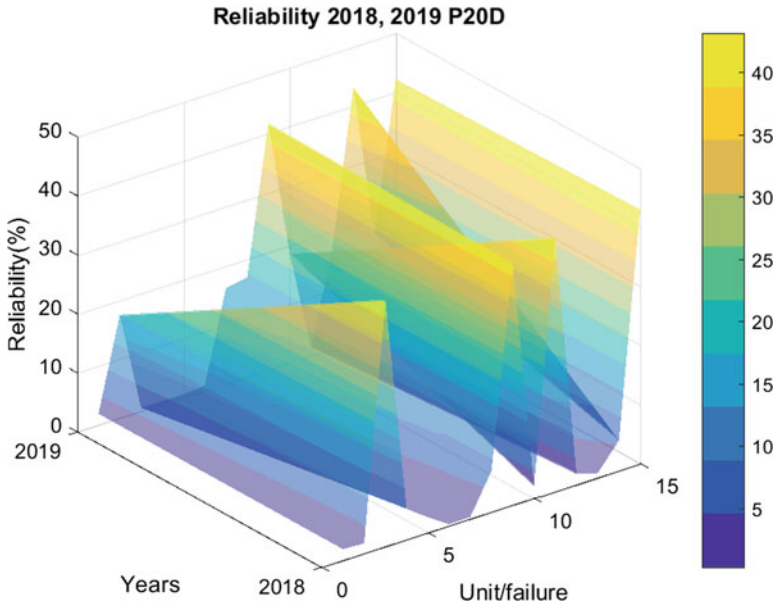


Fig. 9 20-day reliability forecast. (Source: Authors (2021))

4.1.6 Simulation for 20 Days

Figure 9 presents a comparison of the Reliability of the 20 motor group, where a sample of 16 failure units is listed to represent the percentage rate at which a range of 0.07–42.69% Reliability can be identified for the 20-day prediction model.

Therefore, Table 10 presents the data related to Fig. 9 of the Reliability projection for the group of 20 engines. The table shows the samples of 16 failures for the years 2018 and 2019, on a scale from 0% to 100% according to the proposed forecast, in this case, 20 days.

In Table 10, it is possible to identify variations between 0.09% and 42.74% for the line representing the 2018 failure sample, depending on the probability of the machine operating in a 20-day forecast. For the line representing the 2018 failure

Table 10 Simulated data for 20-day forecast

Failure	U1	U2	U3	U4	U5	U6	U7	U8
2018	42.11	0.09	0.60	0.35	0.13	42.74	16.53	15.73
2019	0.07	17.33	2.23	2.20	16.06	0.11	0.12	0.87
Failure	U9	U10	U11	U12	U13	U14	U15	U16
2018	6.38	17.31	7.03	0.13	1.89	2.47	2.25	0.82
2019	40.90	4.28	14.57	4.83	42.69	0.65	41.64	1.23

Source: Authors (2021)

sample 2019 failure, it is possible to observe a variation between 0.07% and 42.69% of the machine operating in a 20-day forecast.

4.2 Comparison of Simulations

As a result of the simulations carried out, according to the proposal of 1, 5, 10, 15, and 20 days of forecast, it was possible to analyze the behavior of engine 15 failures as a function of the years 2018 and 2019, in such a way that the that the forecasting step increases also increases the Reliability loss rate, a true and true fact, which occurs due to unmapped eventualities that can occur that are not mapped in the data collection step.

4.2.1 Depending on Engine 15 (2018 and 2019)

Due to these anomalies, the Exponential Reliability calculated as a function of the failure frequency of the motor group tends to lose its prediction step over time. However, this exponential distribution becomes effective when the frequency of failures is higher, that is, if the database is well formulated and the forecast stage is short (prediction in days) or average (normalized forecast in months).

Given these situations of loss of Reliability over the forecast time and the failure rate required in the forecast calculation, Fig. 10 presents two graphs referring to the 1, 5, 10, 15, and 20 day simulations, where the calculated model and the year 2018 forecast model are compared.

The graphs in Fig. 10 show the same Reliability values as a function of the prediction steps. The sample of 50 failure units allows a localized analysis of the Reliability dispersion as a function of the predictions, where PD20 is less than PD15 and the others.

The curves for the DP1, DP5, DP10, DP15, and DP 20 simulations are characterized by the colors: blue, red, green, yellow, and blue (dash), the loss of Reliability between DP1 and DP5 is noticeable in such a way that the lower limits are closer to other DP's.

Figure 11 shows a comparison with the proposed forecast of 1, 5, 10, 15, and 20 days as a function of 2019 and engine 15, where the similarity between the calculated and predicted models can be identified, confirming the 100% correlation between the output variables.

Compared with the year 2018, the year 2019 obtained reliability indices for nearby engines, this is confirmed by the previous tables regarding the simulations performed; however, this indicates that engine 15 has a frequent variation depending on the available machine time, as can be illustrated in Figs. 10 and 11, where the meeting points that characterize the Reliability rate as a function of Unit / failure tend to suffer disturbances that impact the behavior of the graph. In Fig. 11, a sample of 50 failure units is used to present the results achieved and efficiently compare the calculated model and the predicted model. In Fig. 11, it is also possible to identify the loss of reliability rate as a function of prediction time due to unmapped events in the dataset.

4.2.2 Depending on the Engine Group (2018 and 2019)

The comparative analyzes carried out in Figs. 10 and 11 prove the loss of the Reliability Index due to the prediction time. In addition, they express the availability characteristics that impact the frequency of failure, which is a determining factor for decision making regarding the engine, i.e., the engine efficiency may be compromised by the prediction step.

However, motor 15 data due to failures and the Levenberg-Marquardt algorithm determined the model with the lowest error rate when analyzing the MSE and RMSE indicators, which differs from the other motors because it uses other configurations (number of neurons, hidden layers, activation functions and training algorithm) that allowed higher error rates so that the model was unusable for the context of the best model.

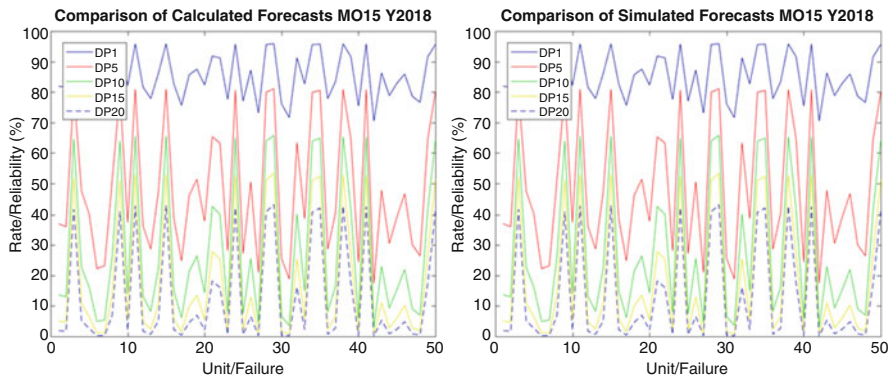


Fig. 10 Calculated model (2018) x forecasted model (2018) (Source: Authors (2021))

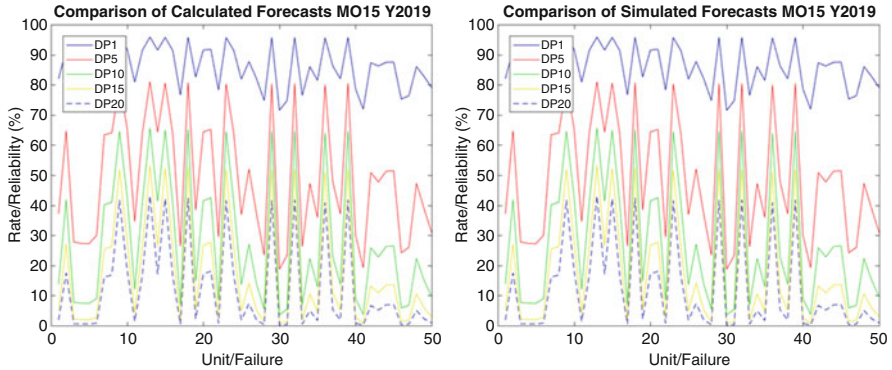


Fig. 11 Calculated model (2019) x forecasted model (2019) (Source: Authors (2021))

Although the optimization methods implemented in the training algorithms are taken into account to obtain satisfactory results, the simulations reached 100% reliability indices (correlation between the output variables), which allows analysis of the behavior of the frequency of failure due to motor group.

Figure 12 presents four graphs that characterize the behavior of a sample of 30 fault units as a function of 20 motors for the years 2018 and 2019. The mesh graph indicates the correlation of three variables, in the X, Y, and Z axes, respectively: Motors, Unit/Failure, and Reliability (%).

Graphs 1 and 2 in Fig. 12 (top left and top right) show the results of the 1-day simulations for the year 2018 (left) and 2019 (right), the first and second graphs achieve reliability variations between 70% and 96%, in the same way, however, different when relating values and behavior.

The year 2018 of graph 1 in Fig. 12 (top left) has higher rates compared to graph 2 in Fig. 12 (top right), the behavior of the graphs and the way they are arranged is distinctly different, the rates The lowest reliability indexes are characterized by Dark colors ranging between 70% and 80%, indicated by the depth of the graph format, the highest reliability indexes are characterized by the lighter colors ranging between 86 and 96%, indicated by the formed edges by the graph.

The distorted shapes of the curves as a function of variations are due to the availability of the engine, which influences Reliability. This indicates that each engine has a different working and stopping time, which can be perceived by the non-linear behavior of the graph formed.

Graphs 3 and 4 in Fig. 12 (bottom left and bottom right) show the results of the 20-day simulations for the year 2018 (left) and 2019 (right), the first and second graphs achieve reliability variations of approximately 0.07–42.69%, also in the same way, however, different when relating values and behaviors.

The year 2018 graph 3 in Fig. 12 (bottom left) has less variation compared to graph 4 in Fig. 12 (bottom right). The behavior of the graphs and the way they are arranged is distinctly different; the reliability rates of the lower ones are characterized by dark colors touching the X and Y axes, where the rate of change

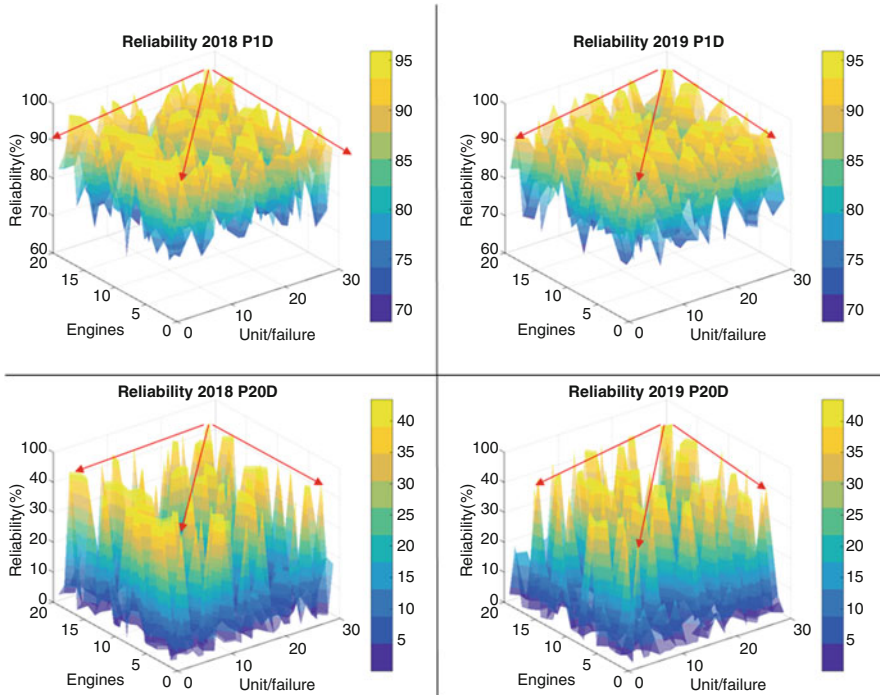


Fig. 12 Reliability behavior as a function of engine group. (Source: Authors (2021))

is approximately 0.07 and 20, indicated by the depth of the graph format, while the highest reliability rates are characterized by lighter colors that vary between 21% and 42.69%, indicated by the borders formed by the graph.

The arrows highlighted in red indicate the location of the peak values of the failure units with respect to Reliability, considering the largest and smallest peaks on the X, Y, and Z axes for each graph shown in Fig. 12.

5 Final Considerations

The objective of this research was to present an analysis of the Reliability of a Group of Internal Combustion Engines of Thermoelectric Power Plants due to the requirement of elements that enable new strategies for decision making regarding the predictive maintenance of machines.

The maturation of the forecast model was made possible by performing accurate analysis of machine failure records, in addition to tests carried out for the acquisition and calculation of Maintenance Management indicators such as: MTTR, MTBF, Availability, and Reliability.

The strategy of using optimization methods as research elements and as a tool to build the prediction model allowed satisfactory results, due to stochastic procedures and mathematical models to improve the ANN convergence state, other prediction horizons were determined, reaching results with 100% confidence in the model.

The development of the prediction model brought elements of innovation by using Artificial Intelligence and Machine Learning techniques and procedures. Furthermore, the use of optimization methods such as Levenberg-Marquardt and Bayesian Regularization are of worldwide relevance for using mathematical mechanisms to provide prediction results and approximation of a real function.

The application of these methods as an integrating element of customized algorithms that allow their use in Intelligent Systems is necessary and extremely important, since the improvement in the decision process in a maintenance program tends to reduce costs with machine stoppages in a Thermoelectric Plant.

Finally, the simulation of the data and the prediction of Reliability allowed the development of precise analyzes on the efficiency of the engine group. In addition, the Maintenance Management indicators were essential elements to support the justification of the results achieved with graphics and comparisons regarding the best model (lowest error rate achieved), considering the motor group.

In summary, the results presented here are satisfactory as they meet the established objectives and prove to be beneficial for application in predictive maintenance using Artificial Neural Network (ANN) techniques.

Acknowledgments We would like to thank the Postgraduate Program in Engineering, Processes, Systems and Environmental Management (PPG-EGPSA) and to Institute of Technology and Education Galileo of the Amazon for enabling the development of this research.

References

1. Elavarasan RM, Shafiullah G, Raju K, Mudgal V, Arif MT, Jamal T et al (2020) COVID-19: impact analysis and recommendations for power sector operation. *Appl Energy* 279:115739
2. Vereide K, Stevanovic U, Digerud E, Blancarte C (2020) Perez R Strategy and application of new technologies for condition monitoring and predictive maintenance of hydro units
3. Shah YT (2021) Hybrid power: generation, storage, and grids. CRC Press, Boca Raton
4. Yang Z, Li L, Yuan H, Dong Y, Liu K, Lan L et al (2020) Evaluation of smart energy management systems and novel UV-oriented solution for integration, resilience, inclusiveness and sustainability. In: 2020 5th international conference on universal village (UV), pp 1–49
5. Ochella S, Shafiee M, Sansom C (2021) Adopting machine learning and condition monitoring PF curves in determining and prioritizing high-value assets for life extension. *Expert Syst Appl* 176:114897
6. ABDNT (1994) (ABNT), NBR 5462: confiabilidade e manutenibilidade – terminologia, ed
7. Can A, Dagdelenler G, Ercanoglu M, Sonmez H (2019) Landslide susceptibility mapping at Ovacık-Karabük (Turkey) using different artificial neural network models: comparison of training algorithms. *Bull Eng Geol Environ* 78:89–102
8. Medeiros TD (2004) Treinamento de redes neurais artificiais com otimização multi-objetivo e regularização Baesiana: Um estudo comparativo. In: Universidade Federal de Minas Gerais- Pós Graduação em Engenharia Elétrica

9. Mehlig B (2019) Artificial neural networks. arXiv e-prints, p. arXiv: 1901.05639
10. Nascimento MBD 2013 Aplicação do algoritmo de otimização bayesiano ao problema de alocação de berços
11. Shin S, Lee Y, Kim M, Park J, Lee S, Min K (2020) Deep neural network model with Bayesian hyperparameter optimization for prediction of NOx at transient conditions in a diesel engine. *Eng Appl Artif Intell* 94:103761
12. Lu X-Q, Yan H-F, Su Z-L, Zhang M-X, Yang X-H, Ling H-F (2021) Metaheuristics for homogeneous and heterogeneous machine utilization planning under reliability-centered maintenance. *Comput Ind Eng* 151:106934
13. Shi Y, Zhu W, Xiang Y, Feng Q (2020) Condition-based maintenance optimization for multi-component systems subject to a system reliability requirement. *Reliab Eng Syst Saf* 202:107042
14. Lughofer E, Sayed-Mouchaweh M (2019) Predictive maintenance in dynamic systems: advanced methods, decision support tools and real-world applications. Springer, Cham
15. Zou G, Faber MH, González A, Banisoleiman K (2021) Fatigue inspection and maintenance optimization: a comparison of information value, life cycle cost and reliability based approaches. *Ocean Eng* 220:108286
16. Bai B, Li Z, Wu Q, Zhou C, Zhang J (2020) Fault data screening and failure rate prediction framework-based bathtub curve on industrial robots. *Industrial Robot: the International Journal of Robotics Research and Application* 47:867
17. Wang X, Zhao X, Wang S, Sun L (2020) Reliability and maintenance for performance-balanced systems operating in a shock environment. *Reliab Eng Syst Saf* 195:106705
18. Wang Y, Liu Y, Chen J, Li X (2020) Reliability and condition-based maintenance modeling for systems operating under performance-based contracting. *Comput Ind Eng* 142:106344
19. Soltanali H, Rohani A, Abbaspour-Fard MH, Farinha JT (2021) A comparative study of statistical and soft computing techniques for reliability prediction of automotive manufacturing. *Appl Soft Comput* 98:106738
20. Al-AbdulJabbar A, Elkatatny S, Abdulhamid Mahmoud A, Moussa T, Al-Shehri D, Abughaban M et al (2020) Prediction of the rate of penetration while drilling horizontal carbonate reservoirs using the self-adaptive artificial neural networks technique. *Sustainability* 12:1376
21. Zhang Y, Ma H, Xu J (2021) Neural network-based fuzzy vibration controller for offshore platform with random time delay. *Ocean Eng* 225:108733
22. Suganthan PN, Katwal R (2021) On the origins of randomization-based feedforward neural networks. *Appl Soft Comput* 105:107239
23. He W, Ruhani B, Toghraie D, Izadpanahi N, Esfahani NN, Karimipour A et al (2020) Using of artificial neural networks (ANNs) to predict the thermal conductivity of zinc oxide–silver (50%–50%)/water hybrid Newtonian nanofluid. *Int Commun Heat Mass Transfer* 116:104645
24. Parente RS, de Alencar DB, Junior POS, Silva ÍRS, Leite JC (2021) Application of the narx model for forecasting wind speed for wind energy generation. *Int J Dev Res* 11:46461–46466
25. Bulaghi ZA, Navin AH, Hosseinzadeh M, Rezaee A (2021) World competitive contest-based artificial neural network: a new class-specific method for classification of clinical and biological datasets. *Genomics* 113:541–552
26. Benatti KA (2017) O Método de Levenberg-Marquardt para o problema de Quadrados Mínimos não Linear. In: II Simpósio de Métodos Numéricos em Engenharia
27. Marquardt DW (1963) An algorithm for least-squares estimation of nonlinear parameters. *J Soc Ind Appl Math* 11:431–441
28. Junior POS, Nascimento MHR, Silva ÍRS, Parente RS, Júnior MF, Leite JC (2021) Computational meta-heuristics based on machine learning to optimize fuel consumption of vessels using diesel engines. *Int J Innov Educ Res* 9:587–606
29. Schwertner AE (2019) O método de Levenberg-Marquardt para problemas de otimização de menor valor ordenado
30. Calandra H, Gratton S, Riccietti E, Vasseur X (2020) On a multilevel Levenberg–Marquardt method for the training of artificial neural networks and its application to the solution of partial differential equations. *Optim Methods Softw* 37:1–26

31. Umar A, Sulaiman I, Mamat M, Waziri M, Zamri N (2021) On damping parameters of Levenberg-Marquardt algorithm for nonlinear least square problems. *J Phys Conf Ser* 1734:012018
32. Särkkä S, Svensson L (2020) Levenberg-Marquardt and line-search extended Kalman smoothers. In: ICASSP 2020–2020 IEEE international conference on acoustics, speech and signal processing (ICASSP), pp 5875–5879
33. Kalhori H, Tashakori S, Halkon B (2021) Experimental study on impact force identification on a multi-Storey tower structure using different transducers. *Vibration* 4:101–116
34. Boeira EC (2018) Sintonia de controladores multivariáveis pelo método da referência virtual com regularização Bayesiana
35. Silva ÍRS, Nascimento MHR, Júnior MF, Parente RS, Júnior POS, Leite JC (2021) Bayesian Regularizers of artificial neural networks applied to the reliability forecast of internal combustion machines in the short-term. *Int J Innov Educ Res* 9:460–477
36. Samadi F, Woodbury K, Kowsary F (2021) Optimal combinations of Tikhonov regularization orders for IHCPs. *Int J Therm Sci* 161:106697
37. Moura FSd (2013) Estimação não linear de estado através do unscented Kalman filter na tomografia por impedância elétrica. Universidade de São Paulo
38. Noshad M, Choi J, Sun Y, Hero A, Dinov ID (2021) A data value metric for quantifying information content and utility. *J Big Data* 8:1–23
39. Rioux G, Choksi R, Hoheisel T, Maréchal P, Scarvelis C (2020) The maximum entropy on the mean method for image deblurring. *Inverse Problems* 37:015011
40. Colón-Ruiz C, Segura-Bedmar I (2020) Comparing deep learning architectures for sentiment analysis on drug reviews. *J Biomed Inform* 110:103539
41. Ma X, Xie M, Suykens JA (2021) A novel neural grey system model with Bayesian regularization and its applications. *Neurocomputing* 456:61–75
42. Gai J, Shen J, Hu Y, Wang H (2020) An integrated method based on hybrid grey wolf optimizer improved variational mode decomposition and deep neural network for fault diagnosis of rolling bearing. *Measurement* 162:107901
43. Guhaniyogi R (2020) High dimensional Bayesian regularization in regressions involving symmetric tensors. In: International conference on information processing and management of uncertainty in knowledge-based systems, pp 347–357
44. Crocomo MK, Delbem ACB (2011) Otimização Bayesiana com detecção de comunidades
45. Chicco D, Warrens MJ, Jurman G (2021) The coefficient of determination R-squared is more informative than SMAPE, MAE, MAPE, MSE and RMSE in regression analysis evaluation. *PeerJ Comput Sci* 7:e623

Index

A

Analytic hierarchy process (AHP), 203, 209
Artificial Neural Network Techniques (ANN),
237, 503, 528–534, 554

B

Bald eagle search (BES), 238, 251
Battery Energy Storage System (BESS), 137,
236, 465, 470–472
Bio-inspired Computing, 371
Blynk, 516–518, 520

C

Chemical storage, 409
Classification, 4, 83, 100, 312, 314, 315, 331,
332, 429–433, 487–509, 528
Complex linearization, 162, 163, 169–170, 179
Computational intelligence, 270, 327
Controllers, 2, 3, 45, 437, 465, 477
Convex optimization, 171, 178, 179
Cost-benefit analysis, 105, 137

D

Data balancing, 270
Data mining, 270, 280, 283–285, 291
DC load, 465, 469, 472–474, 476, 479, 483,
484
Decision making, 317, 319, 551, 553
Decision tree, 270, 283–291, 294, 296, 505
Detection, 272, 487–509, 520, 528

Distributed generation (DG), 40, 87, 89, 90,
96, 99–105, 117, 124, 128, 131, 137,
142, 236, 246, 253, 255, 256, 260, 446,
447, 454, 467
Distribution networks, 79, 96, 141–159, 162,
179, 209, 243, 280, 487, 490–493, 499,
501, 503, 506
Distribution power flow, 146–149, 151, 237
Distribution systems, 207, 236–238, 243,
247–249, 253, 261–265
D-STATCOM, 141–159, 237

E

Economic and environmental dispatch (EED),
305–371
Economic dispatch, 306–308
Efficient lighting, 513–523
Electrical power networks, 136, 379, 403
Electrical storage, 409, 429
Electro-Chemical Storage (EcSS), 416–421
Energy management (EM), 379, 435–438, 446,
460, 467–469
Energy storage, 31, 137, 162, 184, 408–421,
429–433, 435–438
Energy storage economics, 438
Energy storage evaluation, 433–435
Energy storage management, 435–438
Energy storage role, 409, 429
Energy storage system (ESS), 31, 231, 379,
470
Energy storage technology selection, 429
EN 50160, 191, 197–201, 203

F

Fault current, 49–75, 137, 489, 493, 506
 Feature extraction, 497–501
 Finite element method, 57, 74
 Flexible Alternating Current Transmission System (FACTS), 1–45
 Flux density distribution, 66–68, 72–74
 Fuzzy logic, 86, 90, 237, 468, 469, 503, 504

G

Gain Scheduled Proportional Integral Controller, 469

H

Harmonic distortion, 103, 196, 207, 208, 235, 236, 238, 270, 273, 280
 Harmonics, 2, 142, 197, 235–238, 243–245, 248–251, 261–265, 274, 496–500, 506
 Heuristic methods, 162, 327, 371, 379, 380
 High impedance fault (HIF), 487–509
 Hosting capacity (HC), 101, 161, 163–168, 174–179, 215
 Hybrid fuzzy-neural, 504–505
 Hybrid Renewable energy system, 463–484

I

Integrated Development Environment (IDE), 515, 516
 Internal Combustion Engines (ICM), 306, 313, 314, 317, 525–554

K

Key Performance Indicators (KPI), 535
 Knowledge discovery in database (KDD), 269–302

L

LDR, 517–518, 520
 LED, 273, 466, 513–515, 518, 519, 521, 522
 Light ring, 519

M

Machine Learning, 270, 526, 529, 554
 Magnetic field, 52, 54, 55, 64, 65, 69, 74, 427, 428
 Magnetic separation, 57–61
 Mathematical models, 237, 527, 554

Maximum Power Point Tracking (MPPT), 186, 465, 470
 Mean Time Between Failures (MTBF), 537, 538
 Mean Time To Repair (MTTR), 537, 540, 553
 Measurements, 197, 198, 312, 336, 436, 487
 Mechanical storage, 409, 410
 Microgrid (MG), 87, 161, 162, 237, 446–460, 463–484
 Mitigation of emissions (CO₂), 207, 306–309, 344, 356–365, 371, 454
 Mixed-integer non-linear optimization problem, 83, 102, 379
 Modeling, 1–45, 51, 142, 143, 154, 162, 166, 237–240, 254, 371, 409, 422, 449, 465, 470, 471, 496
 Multi-Objective Optimization (MOO), 260–263

N

Naïve Bayes, 270, 283, 295–296, 300–301
 Neural networks, 237, 270, 503
 Nitrogen oxide (NO_x), 306, 310, 344–346
 N-1 security, 379, 383, 389, 392, 396, 398–403
 Nonlinear loads, 103, 142, 208, 236–238, 243–245, 248, 249, 253, 262, 496, 506
 NSGA-II and III, 328, 329, 331–340, 345–371

O

Optimal relay coordination, 87
 Optimization, 83, 102, 141, 162, 208, 237, 306, 378, 433, 447, 466, 502, 526
 Optimization methods, 103, 105, 208, 265, 307, 308, 380, 525–554

P

Parameters uncertainty, 446–460
 Pattern recognition, 270, 487–509, 526, 528
 Permeability, 53–55
 Perturb and Observe, 465
 Photovoltaic energy system, 469
 Photovoltaics (PV), 104, 161, 163–167, 173–177, 179, 182–189, 198, 200, 201, 236, 447, 448, 463, 465, 466, 468–470, 472
 PIR, 517–521
 Point of common coupling (PCC), 235, 270, 273, 276, 279, 281, 282, 284, 289, 299, 468
 Power flow solution, 1–45, 153, 159

Power loss, 2, 17, 52, 101–103, 105, 117, 127, 129, 131, 135–137, 141, 154, 158, 186, 207, 208, 214–216, 219, 226, 231, 237, 238, 248, 250, 254, 255, 257, 261–263, 265, 335, 347, 352, 357, 364, 465, 471

Power quality (PQ), 4, 6, 8, 21, 22, 100, 101, 142, 143, 148, 149, 152, 156, 161, 181–203, 208, 219, 222, 223, 226, 235–266, 269–272, 274, 275, 284, 431–423

Power system planning (PSP), 106

Power systems, 3, 19, 50, 52, 54, 57, 61, 74, 79–96, 106, 109, 117, 142, 161, 170, 181–203, 207, 209, 235–237, 269, 306, 307, 317, 377–379, 381, 384, 401, 417, 467, 484, 489, 491, 502

Power system's uncertainties, 384, 401

Predictive maintenance, 526–528, 553, 554

Problem formulations, 381–383, 450–454

R

Radial distribution networks (RDNs), 141, 142, 144–146, 149–159, 207–210, 212, 219–227, 229, 230

Reliability, 79, 101, 161, 208, 226, 269, 313, 378–383, 388, 389, 396, 400–402, 404, 409, 413, 420, 428, 431, 432, 434, 466, 490, 491, 494, 507, 525–554

Renewable energy, 99, 104, 162, 207, 238, 305, 307, 426, 457, 463–484

Renewable energy sources (RES), 141–159, 182, 238, 446, 447, 456, 463, 464, 467

Renewable generation sources (RGSS), 378–379, 383, 396, 397, 403

Renewables, 99–101, 104, 105, 136, 141–159, 161, 200, 207–209, 236, 238, 305, 307, 410, 416, 417, 429, 431, 433, 456, 457, 463–484

Resilient, 429, 463–484

S

Saturated Core Fault Current Limiter, 49–75

Security, 3, 99, 101, 188, 379, 383, 389, 391, 392, 396, 398–403, 490, 507, 513, 514

Sensor, 187, 190, 437, 491, 517–521

Short circuit currents, 49, 379, 465, 470

Shunt capacitor banks, 141

Shunt capacitors, 141, 205–231

Sine-cosine algorithm, 205–231

Single-objective optimization (SOO), 255–260, 311, 454

Smart home, 513–523

Smart lighting systems (SLS), 513, 514

Stochastic approach, 446–460

Stochastic multi-period transmission expansion planning, 377–404

Support Vector Machine (SVM), 503, 504, 508, 509

T

Techno-economic metrics, 103, 105, 137, 214, 226

THDv, 276, 280, 282, 286–289

Thermal storage, 411

Thermoelectric Power Plants (TPP), 306, 525–554

Threshold, 89, 436, 493, 498, 502–509

Total harmonic distortion (THD), 197, 235, 270, 276, 282

Transmission line, 1, 13, 15, 16, 22, 41, 51, 52, 55, 68, 99, 378, 383, 388, 402, 498

V

Voltage regulators, 99–137, 208

Voltage stability (VS), 4, 99, 101, 102, 106–109, 123, 208, 237, 428

Voltage stability index (VSI), 108, 143

W

Whale optimization algorithm (WOA), 105, 118–122, 223, 225, 381

Windings, 50, 51, 54, 55, 57, 58, 68–74

Wirtinger's calculus, 170